

Micro-Drops and Digital Microfluidics

Micro-Drops and Digital Microfluidics

Second Edition

Jean Berthier



ELSEVIER

AMSTERDAM • BOSTON • HEIDELBERG • LONDON
NEW YORK • OXFORD • PARIS • SAN DIEGO
SAN FRANCISCO • SINGAPORE • SYDNEY • TOKYO
William Andrew is an imprint of Elsevier



William Andrew is an imprint of Elsevier
The Boulevard, Langford Lane, Kidlington, Oxford OX5 1GB, UK
225 Wyman Street, Waltham, MA 02451, USA

First edition 2008
Second edition 2013

Copyright © 2013 Elsevier Inc. All rights reserved

No part of this publication may be reproduced, stored in a retrieval system or transmitted in any form or by any means electronic, mechanical, photocopying, recording or otherwise without the prior written permission of the publisher

Permissions may be sought directly from Elsevier's Science & Technology Rights Department in Oxford, UK: phone (+44) (0) 1865 843830; fax (+44) (0) 1865 853333; email: permissions@elsevier.com. Alternatively you can submit your request online by visiting the Elsevier web site at <http://elsevier.com/locate/permissions>, and selecting *Obtaining permission to use Elsevier material*.

Notice

No responsibility is assumed by the publisher for any injury and/or damage to persons or property as a matter of products liability, negligence or otherwise, or from any use or operation of any methods, products, instructions or ideas contained in the material herein. Because of rapid advances in the medical sciences, in particular, independent verification of diagnoses and drug dosages should be made

British Library Cataloguing-in-Publication Data

A catalogue record for this book is available from the British Library

Library of Congress Cataloging-in-Publication Data

A catalog record for this book is available from the Library of Congress

ISBN: 978-1-4557-2550-2

For information on all Elsevier publications
visit our web site at books.elsevier.com

Typeset by MPS Limited, Chennai, India

www.adi-mps.com

Printed and bound in United States of America

12 13 14 15 16 10 9 8 7 6 5 4 3 2 1

Working together to grow
libraries in developing countries

www.elsevier.com | www.bookaid.org | www.sabre.org

ELSEVIER

BOOKAID
International

Sabre Foundation

Preface

This book deals with the physics of microdrops and its application to micro-electro-mechanical systems (MEMS), especially digital microfluidics (DMF) systems, and to some extent to droplet microfluidics. Many of the physical principles on which this book is based have not been recently discovered; they were stated between the end of the eighteenth century and the beginning of the twentieth century. Interface and capillarity laws are based on the successive theories of Laplace, Young, Dupré, Wenzel, Cassie and Baxter, Jurin, Concus, and Finn between the years 1780 and 1940; the electrowetting effect was discovered by Lippmann at the end of the nineteenth century, and dielectrophoresis (DEP) by Pohl in the middle of the twentieth century.

However, all these theories have been recently subject to new attention and increasing interest with the development of microfluidics. This development has been first promoted by the generalization of ink-jet printing and, to some extent, by the space industry where droplets are used to feed micromotors; and more recently by the formidable expansion of biotechnology. This expansion follows the development of microfabrication techniques pioneered by the microelectronic industry. Microsystems like MEMS and labs-on-chips (LOC) have been built to address the many goals of biotechnology, from bioanalysis and recognition, to DNA, protein and cell handling, and to screening and drug discovery. All these systems make extensive use of microfluidic principles, like microflows, digital, or droplet microfluidics.

Hence, the early interface and capillarity laws have been revisited and further developed to conform to their new environment of microsystems. Israelachvili has worked on molecular interactions and improved the notion of interface, de Gennes has clarified the notion of surface tension and developed an understanding of the mechanical behavior of colloids; Lippmann's law has been revisited by Berge to give birth to DMF systems. Pohl's DEP and liquid dielectrophoresis (LDEP) has been reinterpreted by Jones. Coupling between hydrodynamic and electric forces has given birth to electro-osmotic actuation. Interactions between a force field (electric, acoustic) and a liquid–fluid interface have been investigated, and the modeling of the shape and deformation of interfaces has seen considerable progress with the energy minimization approach for static problems (EVOLVER) and the volume of fluid (VOF) and level set approaches for dynamic problems. A huge volume of new information has been produced covering all these domains.

Because they constitute historically the first microfluidic approach, microflows—continuous flows in microchannels—have been the subject of hundreds of publications. Many books have been published concerning the different applications of microflows for MEMS and LOC. The situation is very different for the techniques more recently developed using microdrops instead of continuous microflows. Although many publications and some reviews in journals are

addressing these techniques, a comprehensive book seemed necessary. After the first edition published in the year 2008, this new edition includes five new chapters linked to recent developments of DMF.

In the introductory chapter, the different types of microfluidics are presented and categorized, specifying the place of digital and droplet microfluidics in the global picture of today's microfluidics.

In the second chapter, the notions of interface and surface tension are exposed, and the theory of capillarity is presented. Laplace's, Young's, and Jurin's laws are derived, and it is shown how they are used for the determination of the shape of interfaces in complex geometries. It is shown how the principle of energy minimization governs the shape of a static interface.

These prerequisites constitute the basis of the third chapter, which deals with the physics of microdrops and their behavior in microsystems comporting either lyophilic, lyophobic—or both—surfaces, textured and patterned surfaces comporting micropillars, arêtes, and grooves. Especially, the importance of the pinning of droplets by sharp edges is pointed out.

The fourth chapter is devoted to the theory of electrowetting, with a focus on electrowetting on dielectric (EWOD). In spite of its apparent simplicity, it is shown that Lippmann's law hides complex physical phenomena, some being still debated. The most important constraints for the functioning of EWOD actuation are analyzed: first, the saturation limit of the electrowetting effect at large voltages; this phenomenon is still poorly understood and the different explanations that have been proposed are discussed. Second, it is shown how contact angle hysteresis hinders electrowetting at low voltages. Finally, the limitations brought by the breakdown limit of the dielectric are discussed.

Global applications of the electrowetting theory are presented in Chapter 5. The mechanisms enabling the basic operations on an EWOD-based chip are investigated: these operations consist in moving, merging, splitting, mixing, and diluting droplets on EWOD-based microsystems. Based on these results, fabrication and design constraints are discussed.

Chapter 6 has been introduced in this second edition with the aim of clarifying the role of AC actuation and the effect of the electric actuation frequency. Indeed, the frequency of the electric actuation has recently been found to produce either electrowetting effect or LDEP.

So far DMF systems have been using planar surfaces; hence, the name "planar microfluidics" for DMF. Recently, progress has been made in the adaptation of these systems to nonplanar surfaces. In this new edition, Chapter 7 presents the state of the art of the development of EWOD on curved substrates.

Applications of EWOD-based microchips to biotechnology and biology are the subject of Chapter 8. Some typical applications in the different domains of sample collection, DNA analysis, DNA repair, protein analysis, and cell handling have been chosen amongst all the possible applications. Because it is a good comparison test with other systems (conventional and continuous microfluidics), a special focus is made on DNA analysis using the polymerase chain reaction.

It is a general trend in biotechnology that microsystem developments evolve toward the manipulation of cells. DMF follows this trend, and an additional chapter (Chapter 9) on this topic has been introduced in this new edition.

Chapter 10 is devoted to the study of the behavior of chemical components on EWOD-based chips, especially of organic solvents and ionic liquids. The maneuverability of these different liquids on the substrate of a microsystem is analyzed, and it is shown how these carrier fluids can be used to realize controlled chemical reactions in microdrops.

Another extremely important field of application of DMF relates to optics: in this new edition, liquid lenses, screen display systems, and EWOD actuated micromirrors are the subject of a new chapter, Chapter 11.

The new, more fundamental Chapter 12 focuses on the interaction of a sessile droplet and a soft, deformable substrate. The duality between Young's law and Neumann's construction is investigated. Applications to elasto-capillarity with capillary origami, and electro-elasto-capillarity are presented.

Acoustic wave actuation of droplets constitutes another mode of actuation, and Chapter 13 presents its principle. It is shown how it can be used to design a digital droplet microsystem. Applications to biology, biotechnology, and electronics are discussed.

Chapter 14 is an introduction to another approach to the use of microdrops, based on the merging of microflows in T-junctions or flow focusing devices (FFD) to form controlled microdroplets transported by the continuous phase. First, the physical behavior of two-phase flow droplets and plugs is investigated, with a focus on plugs moving in capillary tubes, and on immiscible fluids flowing in parallel. Pressure loss is determined in both cases. Finally, we analyze how droplets are produced in T-junctions or FFD and what parameters control the size and reproducibility of these droplets.

The Epilog (Chapter 15) reflects on the potential of DMF, and future trends and perspectives are discussed.

This book has been conceived and written to enable the reader to acquire a solid understanding of the physical behavior of droplets in complex microsystems, and a profound knowledge of the functioning of digital and droplet microfluidic systems.

*Jean Berthier
July 3, 2012*

Acknowledgments

It is a very common statement to say that writing a scientific book is a long and difficult task. I would like to add my contribution to this statement. And this is no less the case for a second edition. However, I had the chance not to be alone in this enterprise and, first of all, I express here my gratitude to Ken Brakke, Hsueh-Chia Chang, Achim Wixforth, and to my colleagues Raphaël Renaudot and Vincent Agache.

In the first place, I would like to thank Ken Brakke. Chapters 2, 3, 9, and 11 would not have been the same without him. I have recently worked with him writing the book “The Physics of Microdroplets” and I admire his capacity to tackle difficult problems and solve them in a very short time. I thank him for his help in using Surface Evolver numerical software on tricky cases. I emphasize here the potentialities of this software for the analysis of droplet and interface behavior.

Many thanks also to Hsueh-Chia Chang. I had the chance to be welcomed by Chia at the University of Notre-Dame and to visit his laboratory. I was extremely impressed by the high standard of the research and developments going on there. So when I looked for someone to back me up in writing Chapters 4 and 5 dedicated to electrowetting theory and applications, I immediately thought of him. I express to him here all my gratitude for his help.

I am also very much indebted to Achim Wixforth and his colleagues Thomas Frommelt and Matthias Schneider from Augsburg University and Advalytix for writing the chapter dedicated to acoustic actuation of droplets. This chapter brings another view of digital microfluidics, and I was keen to have it in this book. Many thanks to all three.

I also thank my colleagues Raphaël Renaudot and Vincent Agache for helping me with the delicate chapter on liquid dielectrophoresis and on its links with electrowetting.

I am grateful to all the persons who have contributed photographs, David Hu, Thomas Frommelt, Anthony Mescher, Michael Bestehorn, Jenifer Elisseeff, Gady Fishel, and my colleagues Olivier Raccourt, Philippe Clementz, Yves Fouillet, Dorothée Jary, Roland Bavière, Nicolas Chiaruttini, Raphaël Renaudot, and Vincent Agache.

I express my gratitude to my management at the CEA-Leti for their support, especially Guillaume Delapierre, Christine Peponnet, and Laurent Malier.

Finally, and not least, I thank all the reviewers of the first edition who made useful suggestions for this new edition and all the prominent researchers in the field, C.-J. Kim, A. Wheeler, T.B. Jones, Ya-Pu Zhao, Hsueh-Chia Chang, J. Heikenfeld, Richard Fair, Robin Garrell, and others whose international publications I have repeatedly used in this book.

Introduction: Digital Microfluidics in Today's Microfluidics

1

CHAPTER OUTLINE

1.1 The development of microfluidics	1
1.2 The advantages of digital and droplet microfluidics compared to conventional microflows.....	2
1.2.1 From microflows to microdrops	2
1.2.2 Microdrops: comparison between digital and droplet microfluidics	3
1.3 The respective place of digital and droplet microfluidics in today's microfluidics	5
1.4 Summary	6
References	6

1.1 The development of microfluidics

The development of microfluidics has been remarkable since the 1980s. Historically, in the 1980s, the first applications of microfluidics were triggered by the generalization of ink-jet printing, and also to some extent by space applications, where droplets are used to feed micromotors. Today, the developments are boosted by biotechnology. Indeed, microfluidics is the basis of most biotechnological developments, simply because biological samples are in a liquid state and biological organisms live in an aqueous environment. Compared to conventional techniques, the use of microfluidic devices has many advantages [1]: the volumes of sample and reagents are significantly reduced—which is practical and diminishes the cost of the process; the results (diagnostic) or the products (biochemistry) are obtained in a much shorter time—which also contributes to reducing costs, or can be necessary for medical emergency reasons; the level of sensitivity is increased due to higher precision and selectivity of the process; the risks with the manipulation of toxic or dangerous products are decreased. Besides, miniaturization allows for an increase in automation and parallelization, which

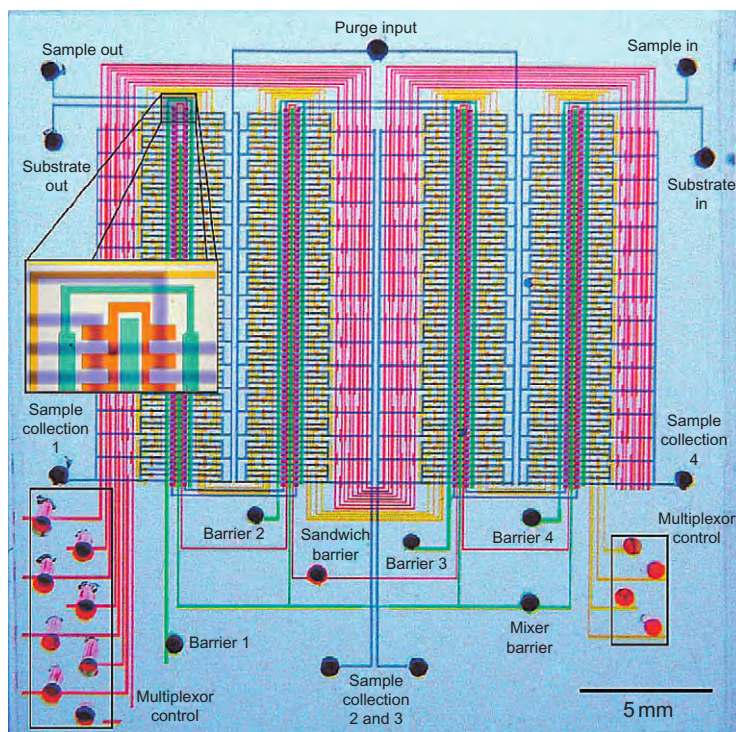
opens the way to screening and systematic testing in the domain of drug discovery. Finally, portability is a unique feature that will permit diagnostic and bioanalysis in the field.

However, the revolution that fluidic microsystems brings to biotechnology depends on the response to some challenges, the most important being the integration of all the components of the system on the same chip. Hence, pumps, valves, mixers, etc. must be miniaturized in order to obtain an integrated system, introducing a complicated choice between active methods—efficient, but difficult to miniaturize and requiring energy sources—and passive methods—easier to integrate, but less efficient. Another challenge is the growing complexity of the microfabrication required to support all the functions of the system: it is foreseen that composite materials will have to be assembled and connected. In biotechnology, the volume reduction from the macroscopic environment where the targets are located to the microscopic environment of the microsystem is also a huge challenge. Molecules and/or particles existing in macroscopic volumes have to be concentrated in microvolumes in order to be introduced in a biochip. Miniaturization of the whole chain of treatment is still to be done. Finally, the very large surface/volume ratio of miniaturized systems modifies the physical behavior of the system and some new problems arise, like, for instance, the adherence of target molecules to the solid walls, or the effect of capillary forces that may prevent the fluid from entering microchannels.

1.2 The advantages of digital and droplet microfluidics compared to conventional microflows

1.2.1 From microflows to microdrops

The most common—and historically first—microsystems, such as microelectrical-mechanical systems (MEMS) or lab-on-a-chip (LOC), are using microflows; conceptually, they are more or less derived from macroscopic devices, taking into account the particularities brought by the reduction of the dimensions and the physical modifications due to the influence of the solid walls. In such systems, microfluidics is often combined with electrics, magnetics, optics, acoustics, and chemistry in order to perform adequate functions. These systems have brought considerable progress to biotechnology. A striking example is that of screening that consists in searching for a specific component in a sample. Conventionally, screening is performed in microplates comprising tenth of 10 µL wells. With this format, when screening for 100,000 components, the process can last for about 4 months and require up to 10 L of reagent. Using microflow systems such as the one described in [Figure 1.1 \[2\]](#), the duration of the same screening is reduced to a week and the quantities of sample are reduced by 100 times. However, a week is still a long time; nowadays, the use of droplet or digital microfluidics reduces the time to about 20 min. This is the case for example of the digital microfluidic

**FIGURE 1.1**

Scheme of a complex microflow system governed by pressure actuated microvalves.

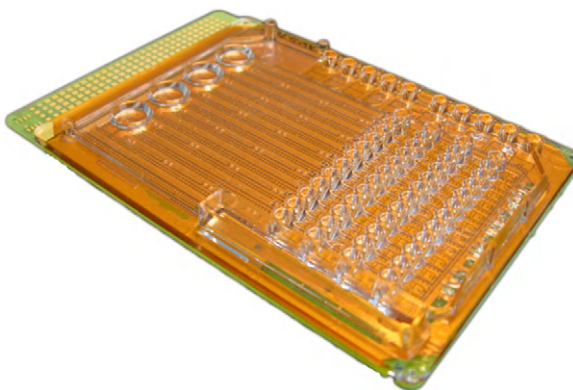
Source: From Ref. [2]. Reprinted with permission from AAAS (American Association for the Advancement of Science).

(DMF) device shown in Figure 1.2. We see here the considerable advantage brought by digital or droplet microfluidics that is closely linked to the dramatic reduction of volume. The working volumes can be reduced down to 50 nL and probably less than that in the near future.

An advantage brought by the use of microdroplets is the reduction of the contact with the solid walls: a large part of the contact surface of the liquid with the solid wall being replaced by a liquid–liquid or liquid–gas interface, the solid contact surface to liquid volume ratio is reduced compared to that of microflow systems; hence, adherence and adhesion problems are reduced (but not suppressed).

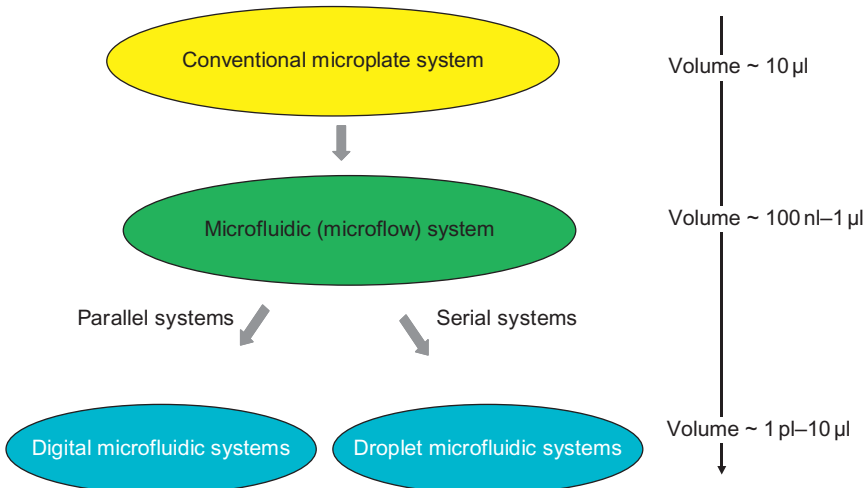
1.2.2 Microdrops: comparison between digital and droplet microfluidics

Digital and droplet microfluidics have in common the use of microdrops and the associated reduction of volume (Figure 1.3). However, they differ considerably. Droplet microfluidics is a particular example of two- or multiphase microflows,

**FIGURE 1.2**

DMF system from advance liquid logic, capable of rapidly and simultaneously performing 5 assays on 40 dried blood spot extracts along with 4 controls and 4 calibrators.

Source: From <http://www.liquid-logic.com>.

**FIGURE 1.3**

Scheme of the different scales of fluidic microsystems.

where droplets are transported by a carrier flow, whereas DMF is based on a totally different approach, inspired by microplate systems where the manipulation robot would be incorporated; in such systems, the microdrops are moved and treated individually as digital entities on a planar surface (hence the other name of DMF is planar microfluidics), allowing for a very reconfigurable system [3].

Contrary to microflow and droplet microfluidic systems, where pumps and valves are actuated by mechanical, electrical, magnetic, or acoustic forces, pumping and valving functions are inherent in the DMF construction. A unique actuation force (electric or acoustic) performs all the different tasks like pumping, valving, and motioning the liquid samples [4].

In the conclusions of Chapter 15, it is shown that digital and droplet microfluidic systems are in fact very complementary. DMF can handle extremely small volumes of liquids and realize operations and manipulation in parallel, and with great accuracy, whereas droplet microfluidics is well adapted to perform operations in series, like screening or encapsulation.

1.3 The respective place of digital and droplet microfluidics in today's microfluidics

It seems interesting to position the place of DMF in the global panel of state-of-the-art microfluidics. The different “toolboxes” proposed by today's microfluidics are shown in Figure 1.4. The first and most important toolbox is the “microflow”

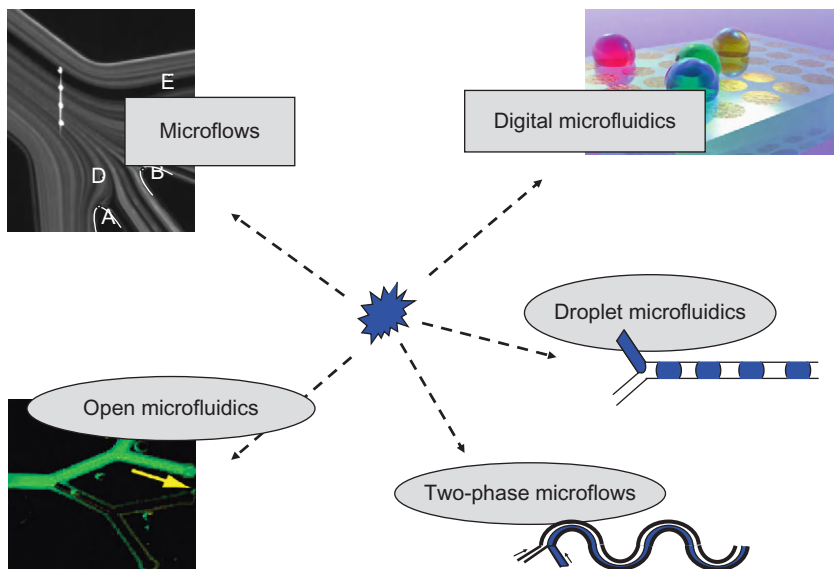


FIGURE 1.4

The different domains (toolbox) of microfluidics; the arrows between the different toolboxes symbolize the connections; continuous arrows correspond to established links; dotted arrows to not yet established links.

Source: Photo bottom left reprinted with permission from Ref. [5] © 2005, American Chemical Society.

Photo top right courtesy Advalytix.

toolbox (top left in [Figure 1.4](#)). It is now mature and has already been the object of a few books and numerous publications. DMF (top right) is a new toolbox that is the subject of this book. It is still at a developing stage, and its possibilities have not all been determined. More recently, new concepts have been developed to complement the possibilities offered by microfluidics: on the one hand, the two toolboxes, constituted by two-phase microflows and droplet microfluidics that will be the object of Chapter 14, are schematized on the bottom right of [Figure 1.4](#); on the other hand, “open” microfluidics [5], i.e., microflows in partially opened channels, where the flow is stabilized by capillarity forces in the absence of a solid boundary, is at the crossroads between single- and two-phase microflows (bottom left in [Figure 1.4](#)). Open microfluidics is probably the less advanced type of microfluidics today.

1.4 Summary

The aim of this book is to provide the reader with the background for the physical behavior of microdrops in general, with a focus on DMF. A profound understanding of the physics of microdrops—subjected only to surface tension and capillary forces, and to a lesser extent to gravity—is required to be able to tackle the study of DMF—in which electric or acoustic forces are involved. In Chapter 14, an introduction to droplet microfluidics has been inserted in order to give a more complete view of the use of droplets in microsystems.

References

- [1] P.S. Dittrich, A. Manz, Lab-on-a-chip: microfluidics in drug discovery, *Nat. Rev. Drug Discov.* 5 (2006) 210–218.
- [2] T. Thorsen, S.J. Maerkl, S.R. Quake, Microfluidic large-scale integration, *Science* 298 (2002) 580–584.
- [3] K. Chakrabarty, F. Su, *Digital Microfluidic Biochips: Synthesis, Testing, and Reconfiguration Techniques*, Taylor and Francis, Boca Raton, FL, 2007.
- [4] R.B. Fair, Digital microfluidics: Is a true lab-on-a-chip possible?, *Microfluid. Nanofluid.* 3 (2007) 245–281.
- [5] W. Satoh, H. Hosono, H. Suzuki, On-chip microfluidic transport and mixing using electrowetting and incorporation of sensing functions, *Anal. Chem.* 77 (2005) 6857–6863.

Theory of Wetting*

2

CHAPTER OUTLINE

2.1 Introduction	8
2.2 Interfaces and surface tension.....	11
2.2.1 The notion of interface.....	11
2.2.2 Surface tension	14
2.2.2.1 <i>The effect of temperature on surface tension</i>	15
2.2.2.2 <i>The effect of surfactants</i>	17
2.3 Laplace's law and applications	20
2.3.1 Laplace's law	20
2.3.1.1 <i>Radius of curvature and curvature</i>	20
2.3.1.2 <i>Derivation of Laplace's law</i>	22
2.3.2 Examples of application of Laplace's law	24
2.3.2.1 <i>Liquid transfer from a smaller drop to a bigger drop</i>	24
2.3.2.2 <i>Precursor film and coarsening</i>	24
2.3.2.3 <i>Pressure in droplets constrained between two parallel plates.....</i>	27
2.3.2.4 <i>Zero pressure surfaces: example of a meniscus on a wire</i>	28
2.3.2.5 <i>Self-motion of a liquid plug between two nonparallel wetting plates</i>	30
2.3.2.6 <i>Laplace's law in medicine: normal and shear stress in blood vessels.....</i>	32
2.3.2.7 <i>Laplace's law in medicine: the example of lung alveoli</i>	34
2.4 Wetting—partial or total wetting	36
2.5 Contact angle—Young's law	38
2.5.1 Young's law	38
2.5.2 Nanobubbles on hydrophobic walls, line tension, and the modified Young's law	39

*This chapter was written with the collaboration of Kenneth A. Brakke (Mathematics Department, Susquehanna University, Selinsgrove, PA).

2.6 Work of adhesion, work of cohesion, and the Young–Dupré's equation	41
2.6.1 Work of adhesion	41
2.6.2 Work of cohesion	42
2.6.3 Young–Dupré's equation	42
2.7 Capillary force, force on a triple line	43
2.7.1 Introduction	43
2.7.2 Capillary force between two parallel plates	43
2.7.3 Capillary rise in a tube	45
2.7.4 Capillary rise between two parallel vertical plates	48
2.7.5 Capillary rise in a pipette	50
2.7.6 Force on a triple line	52
2.7.7 Examples of capillary forces in microsystems	53
2.8 Measuring surface tension of liquids.....	53
2.8.1 Using pressure (bubble pressure method)	54
2.8.2 Using the capillary rise on a plate—Wilhelmy plate	55
2.8.3 Using gravity: the pendant drop method	57
2.8.3.1 Bond number.....	58
2.8.3.2 Method	59
2.8.4 Using shear stress in a microflow	60
2.9 Surface tension of solids	62
2.9.1 Introduction	62
2.9.2 Surface free energy	62
2.9.2.1 Method of Good–Girifalco	62
2.9.2.2 Fowkes method	63
2.9.3 CST and SFE	64
2.9.3.1 Zisman plot	64
2.9.3.2 Disjoining pressure	66
2.10 Minimization of the surface energy and minimal energy surface	68
2.10.1 Minimal surfaces	68
2.10.2 Minimization of the surface energy	69
2.11 Summary	70
References	71

2.1 Introduction

The understanding, development, and design of fluidic microsystems require dealing with forces that are usually overlooked and neglected at the macroscopic scale. In the case of DMF, interfaces are omnipresent and capillary and surface tension forces have a tremendous influence. These forces are of utmost importance at the microscopic level, whereas at a macroscopic scale, they are usually

neglected in front of forces like pressure or gravity. **** Stteger Typical ranges of pressure in macroscopic applications are 1–100 bars, i.e., 10^5 – 10^7 Pa, whereas pressure levels seldom reach 0.1 bar (10^4 Pa) above atmospheric pressure in microfluidic systems. Most of the time gravity has no or little consequence in the design of fluidic microdevices.

Numerous examples of the importance of capillarity can be found in existing microsystems for biotechnology, or microchemistry, and in space applications. In order to point out the importance of capillary forces, we give in [Figures 2.1–2.4](#) some examples illustrating the importance of capillary forces in microsystems.

A starting point for many analyses of biological substances is the deposition, i.e., dispensing or spotting, of liquids in microwells ([Figure 2.1A](#)). In each of

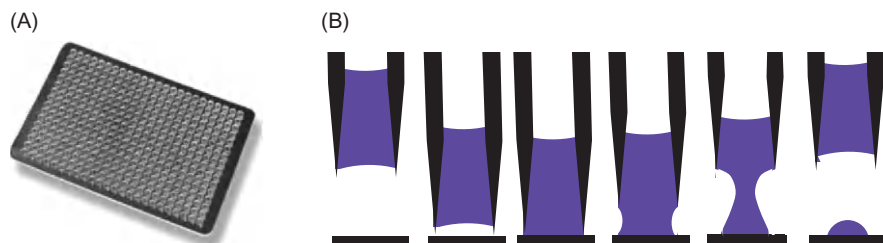


FIGURE 2.1

(A) View of a microplate for biotechnology applications. (B) Capillarity is a determining force when spotting a droplet on a microplate.

Sources: (A) From Ref. [1] © 2004, JALA. (B) From Ref. [2]. Reprinted with permission.

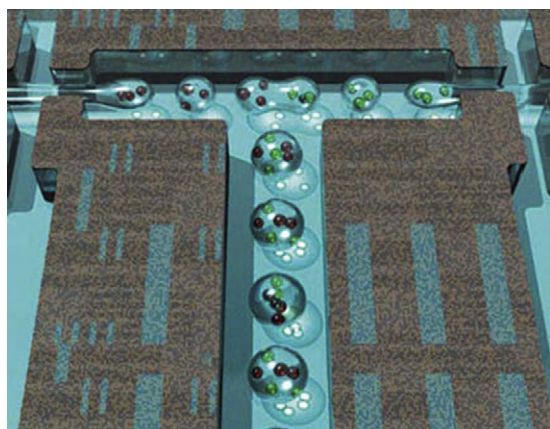
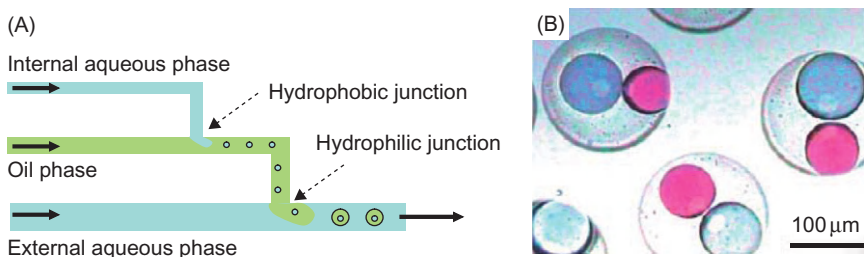


FIGURE 2.2

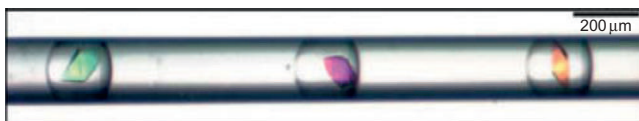
Schematic view of a DMF system based on electrowetting.

Source: Courtesy Rain Dance Technology Inc. [3].

**FIGURE 2.3**

(A) Successive use of T-junctions with wetting and nonwetting walls results in the encapsulation of two liquids in a droplet [4]; (B) clever use of T-junctions can be used to obtain simultaneous encapsulation.

Source: Reprinted with permission from Ref. [4] © 2004, American Chemical Society.

**FIGURE 2.4**

Droplets in a glass capillary: crystals of proteins were grown under microbatch condition in these droplets.

Source: From Ref. [5] © 2004, Wiley, reprinted with permission.

these microwells, biological reactions take place simultaneously, leading to a high-efficiency parallelization of the reactions. Spotting of liquids in microwells requires a careful control of the wettability of the surfaces as shown in Figure 2.1B. The amount of liquid deposited on the plate is both a function of the wettability of the pipette and the plate, and a function of the applied pressure in the pipette.

A second example is that of electrowetting-based microsystems. Electrowetting is a combination of capillary and electric forces, where electric forces modify the apparent capillarity; such a technique has been found to be a promising way to realize DMF devices. Such microsystems are being developed for biological applications and microchemistry. This technique will be detailed in Chapters 4 and 5. A schematic view of a DMF system is shown in Figure 2.2 [3]. Liquid droplets are displaced on a digital grid—or along a path—paved with electrodes and displaced by electric actuation of the electrodes.

Another illustration of the use of capillarity in microfluidic systems is the use of T-junctions to produce droplets immersed in a carrier fluid; such systems are principally devoted to performing chemical reactions or the encapsulation of biological objects. The principle is to use a contrast of wettability of the solid walls

at microfluidic T-junctions to create microdroplets (Figure 2.3). At each step, the wettability of the walls of the carrier liquid should be chosen so that the carrier liquid wets the walls, forcing the incoming immiscible liquid to form droplets (Figure 2.3A). By a clever combination of multiple junctions, encapsulation of two aqueous liquids in an oil droplet can be achieved [4–6].

Encapsulation of biomolecules in their liquid environment is now foreseen as a tool for targeted drug delivery [6]; it is also a tool for protein crystallization. Figure 2.4 shows how proteins can be continuously crystallized in microdroplets, using the preceding technique.

All these examples clearly show the essential role of surface tension and capillary forces in microsystems.

In this chapter, the fundamentals of capillarity are presented. Surface tension of an interface is the fundamental notion in capillarity theory; this notion leads naturally to that of wetting and to the introduction of capillarity and capillary forces. Next, different applications of capillary forces are shown, and the keystone problem of the measurement of surface tensions is presented. The consequences of surface tension and capillary forces for microdrop shape and behavior are presented in Chapter 3.

2.2 Interfaces and surface tension

2.2.1 The notion of interface

Mathematically speaking, an interface is the geometrical surface that delimits two fluid domains. This definition implies that an interface has no thickness and is smooth (i.e., has no roughness). As practical as it is, this definition is in reality a schematic concept. The reality is more complex and the separation of two immiscible fluids (water/air, water/oil, etc.) depends on molecular interactions between the molecules of each fluid [7] and on Brownian diffusion (thermal agitation).

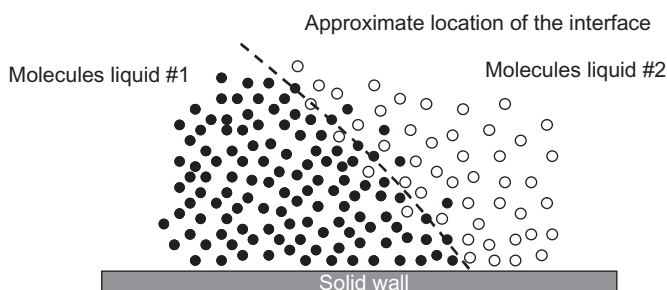
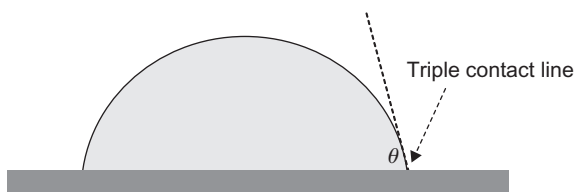
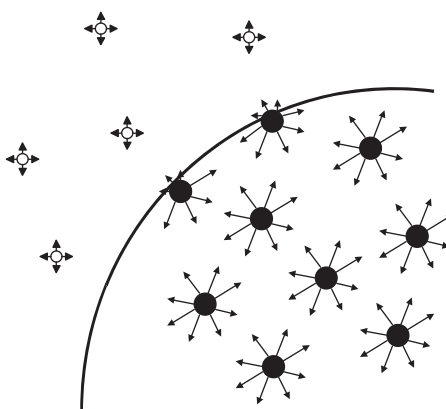


FIGURE 2.5

Schematic view of an interface at the molecular size.

**FIGURE 2.6**

Macroscopic view of the interface of a drop.

**FIGURE 2.7**

Simplified scheme of molecules near an air–water interface. In the bulk, molecules have interaction forces with all the neighboring molecules. At the interface, half of the interactions have disappeared.

A microscopic view of the interface between two fluids looks more like the scheme of [Figure 2.5](#).

However, in engineering applications, it is the macroscopic behavior of the interface that is the focus of attention, and the mathematical concept regains its utility. At a macroscopic size, [Figure 2.5](#) can be replaced by that of [Figure 2.6](#), where the interface is a mathematical surface without thickness and the contact angle θ is uniquely defined by the tangent to the surface at the contact line.

In a condensed state, molecules attract each other. Molecules located in the bulk of a liquid have interactions with all neighboring molecules; these interactions are mostly van der Waals attractive interactions for organic liquids and hydrogen bonds for polar liquids like water [7]. However, molecules at an interface have interactions in a half-space with molecules of the same liquid, and in the other half-space interactions with the molecules of the other fluid or gas ([Figure 2.7](#)).

Consider an interface between a liquid and a gas. In the bulk of the liquid, a molecule is in contact with 4–12 other molecules depending on the liquid (4 for water and 12 for simple molecules); at the interface, this number is divided by 2. Of course, a molecule is also in contact with gas molecules, but, due to the low densities of gases, there are less interactions and less interaction energy than in the liquid side. The result is that there is locally a dissymmetry in the interactions, which results in a defect of surface energy. At the macroscopic scale, a physical quantity called “surface tension” has been introduced in order to take into account this molecular effect. The surface tension has the dimension of energy per unit surface and in the International System it is expressed in J/m^2 or N/m (sometimes, it is more practical to use mN/m as a unit for surface tension). An estimate of the surface tension can be found by considering the molecules’ cohesive energy. If U is the total cohesive energy per molecule, a rough estimate of the energy loss of a molecule at the interface is $U/2$. Surface tension is a direct measure of this energy loss, and if δ is a characteristic molecular dimension and δ^2 the associated molecular surface, then the surface tension is approximately

$$\gamma \approx \frac{U}{2\delta^2}. \quad (2.1)$$

This relation shows that surface tension is important for liquids with large cohesive energy and small molecular dimension. This is why mercury has a large surface tension, whereas oil and organic liquids have small surface tensions.

Another consequence of this analysis is the fact that a fluid system will always act to minimize surface areas: the larger the surface area, the larger the number of molecules at the interface and the larger the cohesive energy imbalance. Molecules at the interface always look for other molecules to equilibrate their interactions. As a result, in the absence of other forces, interfaces tend to adopt a flat profile, and when it is not possible due to capillary constraints at the contact of solids, they take a convex rounded shape, as close as possible to that of a sphere. Another consequence is that it is energetically costly to expend or create an interface: we will come back on this problem in Chapter 5 when dividing a droplet into two “daughter” droplets by electrowetting actuation.

The same reasoning applies to the interface between two liquids, except that the interactions with the other liquid will usually be more energetic than a gas and the resulting dissymmetry will be less. For example, the contact energy (surface tension) between water and air is 72 mN/m, whereas it is only 50 mN/m between water and oil (Table 2.1). Interfacial tension between two liquids may be zero: fluids with zero interfacial tension are said to be miscible. For example, there is no surface tension between fresh and salt water. Salt molecules will diffuse freely across a boundary between fresh and salt water.

The principle applies for a liquid at the contact of a solid. The interface is just the solid surface at the contact of the liquid. Molecules in the liquid are attracted toward the interface by van der Waals forces. But usually these molecules do not “stick” to the wall because of Brownian motion. However, impurities contained

Table 2.1 Values of Surface Tension of Different Liquids on Contact with Air at a Temperature of 20°C and Thermal Coefficient α

Liquid	Temperature of 20°C (γ_0)	Thermal Coefficient (α)
Acetone	25.2	-0.112
Benzene	28.9	-0.129
Ethanol	22.1	-0.0832
Ethylene glycol	47.7	-0.089
Glycerol	64.0	-0.060
Methanol	22.7	-0.077
Mercury	425.4	-0.205
Perfluorooctane	14.0	-0.090
Polydimethylsiloxane	19.0	-0.036
Pyrrol	36.0	-0.110
Toluene	28.4	-0.119
Water	72.8	-0.1514

in the fluid, like particles of dust or biological polymers like proteins, may well adhere permanently to the solid surface because, at the contact with the solid interface, they experience more attractive interactions. The reason is that the size of polymers is much larger than water molecules and van der Waals forces are proportional to the number of contacts.

Usually surface tension is denoted by the Greek letter γ with subscripts referring to the two components on each side of the interface, e.g., γ_{LG} at a liquid–gas interface. Sometimes, if the contact is with air, or if no confusion can be made, the subscripts can be omitted. It is common to speak of “surface tension” for a liquid at the contact with a gas, and “interfacial tension” for a liquid at the contact with another liquid.

According to the definition of surface tension, for a homogeneous interface (same molecules at the interface all along the interface), the total energy of a surface is

$$E = \gamma S, \quad (2.2)$$

where S is the interfacial surface area.

2.2.2 Surface tension

In the literature or on the Internet, there exist tables for surface tension values [8,9]. Typical values of surface tensions are given in Table 2.1. Note that surface tension increases as the intermolecular attraction increases and the molecular size decreases. For most oils, the value of the surface tension is in the range

$\gamma \sim 20\text{--}30 \text{ mN/m}$, while for water, $\gamma \sim 70 \text{ mN/m}$. The highest surface tensions are for liquid metals; for example, liquid mercury has a surface tension $\gamma \sim 500 \text{ mN/m}$.

2.2.2.1 The effect of temperature on surface tension

The value of the surface tension depends on the temperature. The first empirical equation for the surface tension dependence on temperature was given by Eötvös in 1886 [10]. Observing that the surface tension goes to zero when the temperature tends to the critical temperature T_C , Eötvös proposed the semiempirical relation

$$\gamma = \left(\frac{1}{\nu_L} \right)^{2/3} (T - T_C),$$

where ν_L is the molar volume. Katayama (1915) and later Guggenheim (1945) [11] improved Eötvös's relation to obtain

$$\gamma = \gamma^* \left(1 - \frac{T}{T_C} \right)^n, \quad (2.3)$$

where γ^* is a constant for each liquid and n is an empirical factor, whose value is 11/9 for organic liquids. Equation (2.3) produces very good results for organic liquids. If temperature variation is not very important, and taking into account that the exponent n is close to 1, a good approximation of the Guggenheim–Katayama formula is the linear approximation

$$\gamma = \gamma^* (1 + \alpha T). \quad (2.4)$$

It is often easier and more practical to use a measured reference value (γ_0 , T_0) and consider a linear change of the surface tension with the temperature

$$\gamma = \gamma_0 (1 + \beta(T - T_0)). \quad (2.5)$$

Comparison between Eqs. (2.4) and (2.5) requires

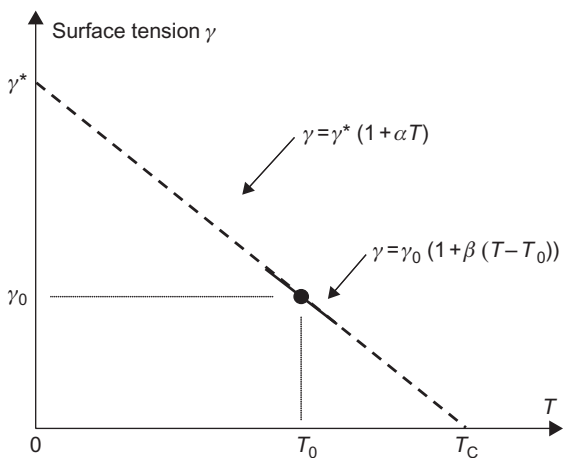
$$\beta = -\frac{1}{T_C - T_0}. \quad (2.6)$$

Relations (2.4) and (2.5) are shown in Figure 2.8. The value of the reference surface tension γ_0 is linked to γ^* by the relation

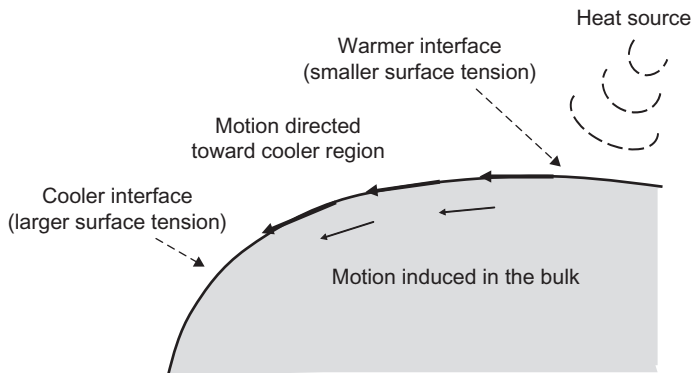
$$\gamma_0 = \gamma^* \frac{T_C - T_0}{T_C}.$$

Typical values of surface tensions and their temperature coefficients α are given in Table 2.1.

The coefficient α being always negative, the value of the surface tension decreases with temperature. This property is at the origin of a phenomenon that is called either Marangoni convection or thermocapillary instabilities (Figure 2.9). If an interface is locally heated by any heat source (like radiation, convection, or conduction), the surface tension is reduced on the heated area according to

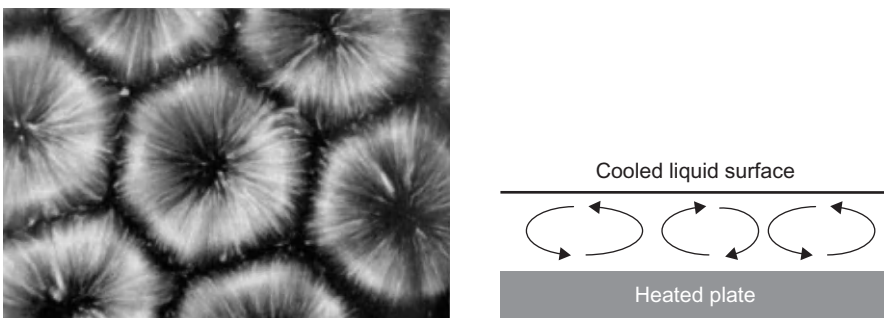
**FIGURE 2.8**

Representation of the relations (2.4) and (2.5).

**FIGURE 2.9**

Sketch of interface motion induced by a thermal gradient between two regions of the surface. The motion of the interface propagates into the bulk under the action of the viscous forces.

Eq. (2.4) or (2.5). A gradient of surface tension is then induced at the interface between the cooler and the warmer interface. We will show in [Section 2.7](#), surface tensions can be viewed as forces; as a consequence, there is an imbalance of tangential forces on the interface, creating a fluid motion starting from the warm region (smaller value of the surface tension) toward the cooler region (larger value of the surface tension). This surface motion propagates to the bulk under the influence of viscosity.

**FIGURE 2.10**

Marangoni flow (thermocapillary instabilities) patterns in a thin film of liquid.

Source: Reused with permission from Ref. [12] © 2005, American Institute of Physics.

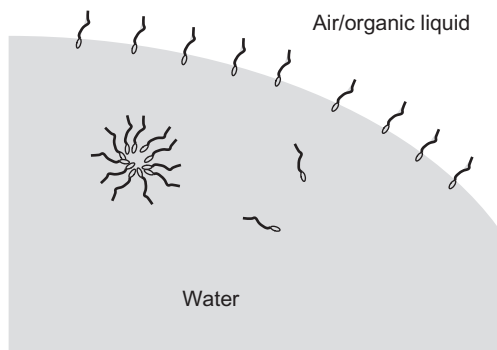
If the temperature source is temporary, the motion of the fluid tends to homogenize the temperature and the motion progressively stops. If a difference of temperature is maintained on the interface, the motion of the fluid is permanent; this is the case of a film of liquid spread on a warm solid. Depending on the contrast of temperature between the solid surface and the liquid surface, the motion of the liquid in the film has the morphology of convective rolls, hexagons, or squares. Figure 2.10 shows hexagonal patterns of Marangoni convection in a film of liquid heated from below [12]. The white segments show the trajectories of the liquid molecules. In Chapter 3, we will look in more details at Marangoni convection inside droplets.

2.2.2.2 The effect of surfactants

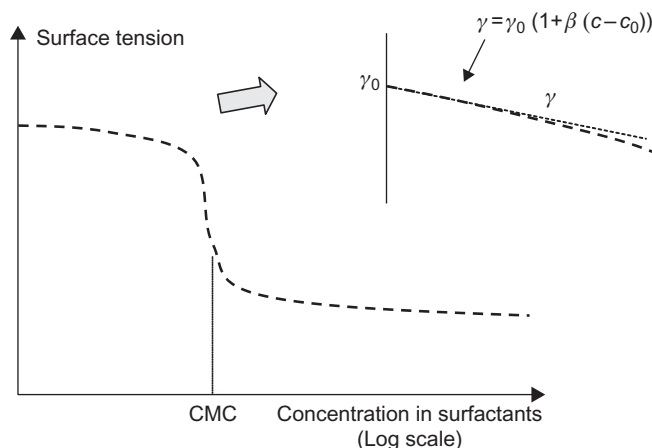
Surfactant is the short form for surface active agent. Surfactants are long molecules characterized by a hydrophilic head and a hydrophobic tail and are for this reason called amphiphilic molecules. Very often surfactants are added to biological samples in order to prevent the formation of aggregates and to prevent target molecules from adhering to the solid walls of the microsystem (remember that microsystems have extremely large ratios between the wall surfaces and the liquid volumes). Surfactants diffuse in the liquid and when reaching the interface they are captured because their amphiphilic nature prevents them from escaping easily from the interface. As a consequence, they gather on the interface as is shown in Figure 2.11, lowering the surface tension of the liquid.

As the concentration in surfactants increases, the surface concentration increases too. Above a critical value of the concentration, called critical micelle concentration (CMC), the interface is saturated with surfactants and surfactant molecules in the bulk of the fluid group together to form micelles.

The evolution of the value of the surface tension as a function of the concentration in surfactants is shown in Figure 2.12. At very low concentration, the slope is nearly linear. When concentration approaches the CMC, the value of the

**FIGURE 2.11**

Schematic view of surfactants in a liquid drop.

**FIGURE 2.12**

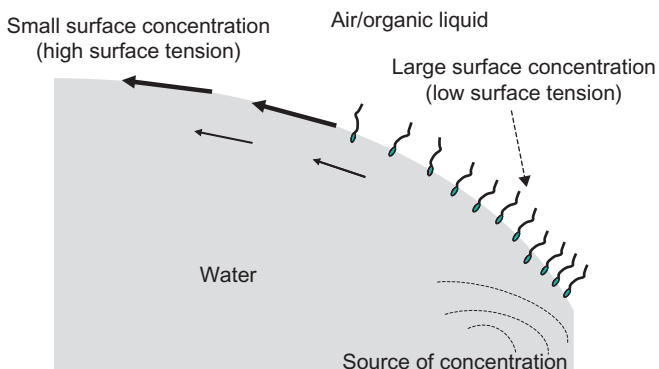
Evolution of the value of the surface tension as a function of the surfactant concentration.

surface tension drops sharply; above CMC, the value of the surface tension is nearly constant [13]. For example, pure water has a surface tension 72 mN/m and water with Tween 10 at a concentration above the CMC has a surface tension of only 30 mN/m.

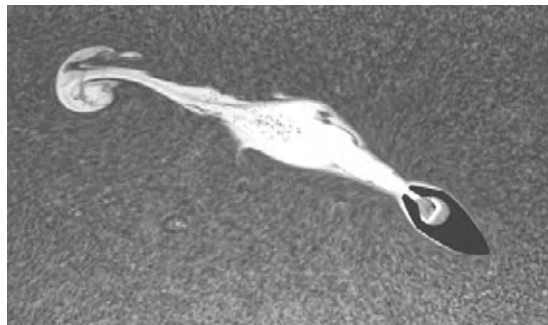
In the limit of small surfactant concentration ($c \ll \text{CMC}$), the surface tension can be expressed as a linear function of the concentration

$$\gamma = \gamma_0(1 + \beta(c - c_0)). \quad (2.7)$$

Equation (2.7) is similar to Eq. (2.5). We have seen how a temperature gradient results in a gradient of surface tension leading to Marangoni type of

**FIGURE 2.13**

Schematic of Marangoni convection induced by a gradient of concentration.

**FIGURE 2.14**

Soap boat: a floating body contains a small volume of soap. At first, the soap exits the rear of the boat under Marangoni stress. Hence, a low surface tension region is created behind the boat, whereas the unsoaped region in front of the boat has a larger surface tension. This difference of surface tension pulls the boat forward [14].

convection. Similarly, a concentration gradient results in a gradient of surface tension, and consequently to a Marangoni convection. Note that the direction of the motion is always toward the largest value of surface tension (Figure 2.13).

Spreading of surfactant molecules on an interface can be easily seen experimentally: an instructive example is that of a thin paper boat with a cavity at the rear (Figure 2.14). When the boat is placed gently on the surface of water, it rests on the surface of water suspended by surface tension forces. When a drop of soap solution/detergent is put on the notch, the boat accelerates rapidly. Soap molecules try to spread over the surface of water. Since they are confined in the cavity of the boat with only one way out, they jet from the rear end creating a reaction force that drives the boat forward.

2.3 Laplace's law and applications

2.3.1 Laplace's law

Laplace's law is fundamental when dealing with interfaces and microdrops. It relates the pressure inside a droplet to the curvature of the droplet. Let us first describe the notion of curvature.

2.3.1.1 Radius of curvature and curvature

For a planar curve, the radius of curvature is the radius of the osculating circle—the circle which is the closest to the curve at the contact point ([Figure 2.15](#)). The curvature of the curve is defined by:

$$\kappa = \frac{1}{R}. \quad (2.8)$$

Note that the curvatures as well as the curvature radii are signed quantities. Curvature radius can be positive or negative depending on the orientation (convex or concave) of the curve.

In the case of a parametric curve $c(t) = (x(t), y(t))$, the curvature is given by the relation [\[15\]](#):

$$\kappa = \frac{\dot{x}\ddot{y} - \dot{y}\ddot{x}}{(\dot{x}^2 + \dot{y}^2)^{3/2}}, \quad (2.9)$$

where the dot denotes a differentiation with respect to t . For a plane curve given implicitly as $f(x, y) = 0$, the curvature is

$$\kappa = \nabla \cdot \left(\frac{\nabla f}{\|\nabla f\|} \right) \quad (2.10)$$

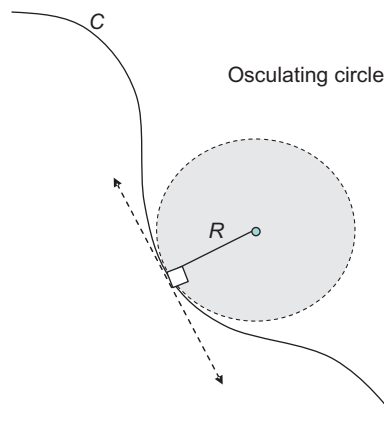


FIGURE 2.15

Radius of curvature and osculating circle.

that is, the divergence of the direction of the gradient of f . And for an explicit function $y = f(x)$, the curvature is defined by:

$$\kappa = \frac{(\mathrm{d}^2y/\mathrm{d}x^2)}{(1+(\mathrm{dy}/\mathrm{dx})^2)^{3/2}}. \quad (2.11)$$

The situation is more complex for a surface. Any plane containing the vector normal to the surface intersects the surface along a curve. Each of these curves has its own curvature. The mean curvature of the surface is defined using the principal (maximum and minimum) curvatures κ_1 and κ_2 (Figure 2.16) in the whole set of curvatures

$$H = \frac{1}{2}(\kappa_1 + \kappa_2). \quad (2.12)$$

It can be shown that the principal curvatures κ_1 and κ_2 are located in two perpendicular planes. Introducing the curvature radii in Eq. (2.12) leads to

$$H = \frac{1}{2}(\kappa_1 + \kappa_2) = \frac{1}{2}\left(\frac{1}{R_1} + \frac{1}{R_2}\right). \quad (2.13)$$

For a sphere of radius R , the two curvatures are equal to $1/R$ and the mean curvature is $H = 1/R$. For a cylinder of base radius R , the maximum curvature is R and the minimum curvature zero, hence $H = 1/2R$. For a plane, the two curvatures are zero and $H = 0$: a plane has no curvature.

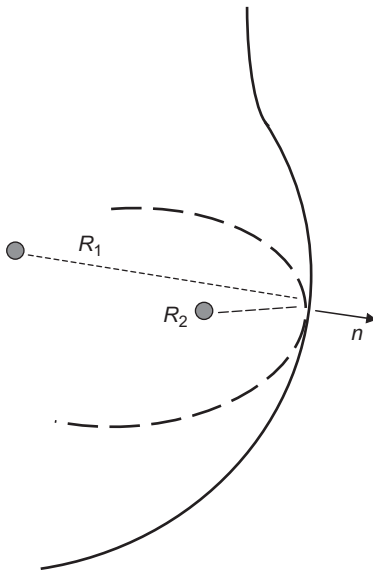
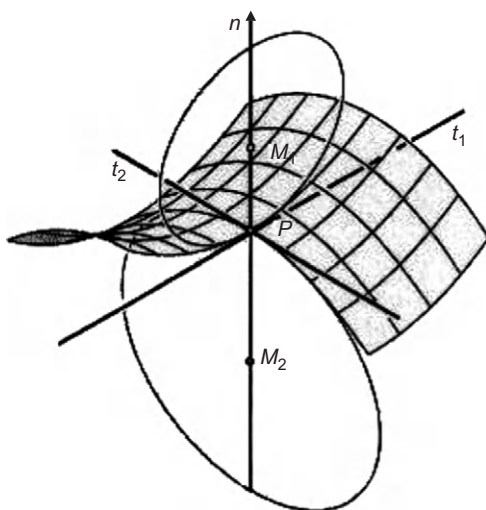


FIGURE 2.16

Schematic view of the radius of curvature of a surface.

**FIGURE 2.17**

Mean curvature at a saddle point is zero if $|R_1| = |R_2|$.

At a saddle point of a surface (Figure 2.17), one of the curvature radii is positive because it corresponds to a convex arc, whereas the other is negative, because it corresponds to a concave arc. If $|R_1| = |R_2|$, the mean curvature H is zero:

$$H = \frac{1}{2} \left(\frac{1}{R_1} + \frac{1}{R_2} \right) = \frac{1}{2} \left(\frac{1}{|R_1|} - \frac{1}{|R_2|} \right) = 0.$$

2.3.1.2 Derivation of Laplace's law

Suppose there is a spherical droplet of liquid surrounded by a fluid. Let us calculate the work necessary to increase its volume from the radius R to the radius $R + dR$ (Figure 2.18). The part of the work due to the internal volume increase is

$$\delta W_i = -P_0 dV_0,$$

where dV_0 is the increase of the volume of the droplet

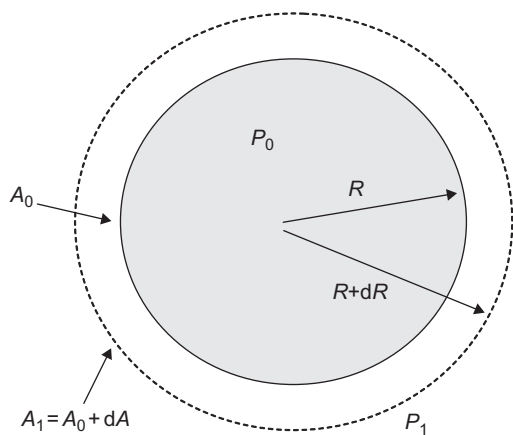
$$dV_0 = 4\pi R^2 dR.$$

The work to pull out the external fluid is

$$\delta W_e = -P_1 dV_1,$$

where dV_1 is the decrease of the external volume, equal to dV_0 . The work corresponding to the increase of interfacial area is

$$\delta W_s = \gamma dA,$$

**FIGURE 2.18**

Schematic of a liquid drop immersed in a fluid; initially, the droplet radius is R and its surface area A_0 . An increase of its radius by a quantity dR corresponds to the new surface area A_1 and the pressure P_1 .

where dA is the increase of the surface area $dA = 8\pi R dR$. The mechanical equilibrium condition is then,

$$\delta W = \delta W_i + \delta W_e + \delta W_s = 0. \quad (2.14)$$

Substituting the values of the work found previously, it follows that

$$\Delta P = P_0 - P_1 = \frac{2\gamma}{R}. \quad (2.15)$$

[Equation \(2.15\)](#) is the Laplace's equation for a sphere.

The reasoning we have used to obtain [Eq. \(2.15\)](#) can be generalized as

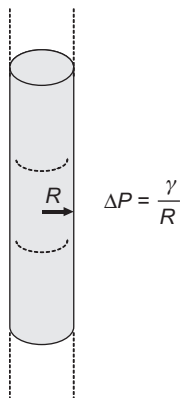
$$\Delta P = \gamma \frac{dA}{dV}. \quad (2.16)$$

For simplicity, we have derived Laplace's equation for the case of a sphere, but we can use [Eq. \(2.16\)](#) for an interface locally defined by two (principal) radii of curvature R_1 and R_2 ; the result would then be

$$\Delta P = \gamma \left(\frac{1}{R_1} + \frac{1}{R_2} \right). \quad (2.17)$$

For a cylindrical interface, as shown in [Figure 2.19](#), one of the two radii of curvature is infinite, and Laplace's law reduces to

$$\Delta P = \frac{\gamma}{R}. \quad (2.18)$$

**FIGURE 2.19**

Laplace's law for cylindrical interface.

Equation (2.17) is called Laplace's law. Keep in mind that it is closely linked to the minimization of the energy. Laplace's law is fundamental when dealing with interfaces, microdrops, and in DMF. In the following section, we give some examples of application of Laplace's law.

2.3.2 Examples of application of Laplace's law

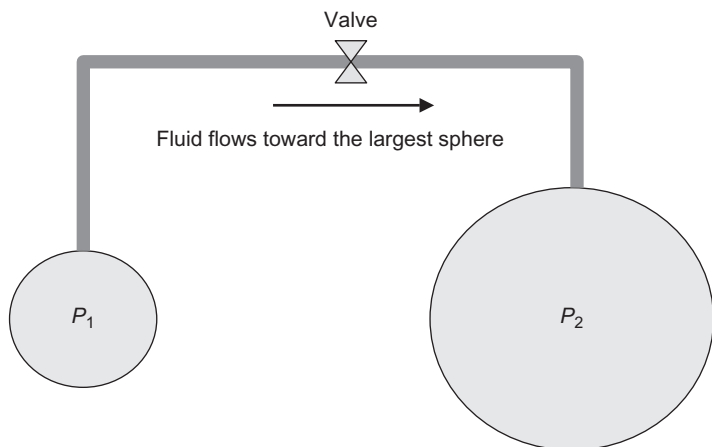
Amongst other things, Laplace's law explains many phenomena occurring during electrowetting actuation. The use of Laplace's law for electrowetting will be detailed in Chapter 5. In the following section, applications of Laplace's law outside the electrowetting domain are presented.

2.3.2.1 Liquid transfer from a smaller drop to a bigger drop

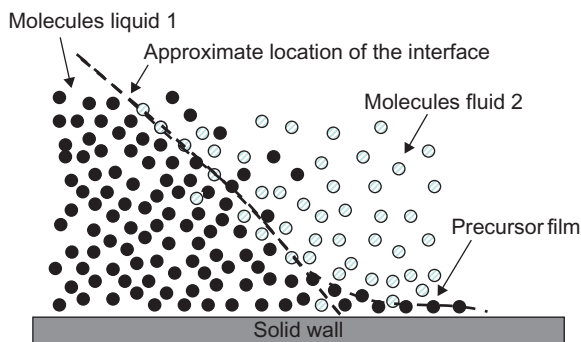
It has been observed that when two bubbles or droplets are connected together, there is a fluid flow from the small bubble/droplet to the larger one (Figure 2.20). This is a direct application of Laplace's law: the pressure inside the small bubble/droplet is larger than that of the larger bubble/droplet, inducing a flow from the former toward the latter. This flow continues until the smaller bubble/droplet disappears to the profit of the larger one.

2.3.2.2 Precursor film and coarsening

The concept of infinitely thin interface and unique contact angle presented at the beginning of this chapter is a mathematical simplification of the reality. When a partially wetting droplet is deposited on a flat solid surface, a very thin film of a few nanometers spreads before the contact line, and the contact between the liquid and the solid resembles the sketch of Figure 2.21. The precursor film can be explained by thermodynamic considerations, because a jump between the

**FIGURE 2.20**

Fluid flow from the smaller bubble/droplet to the larger is a direct application of Laplace's law.

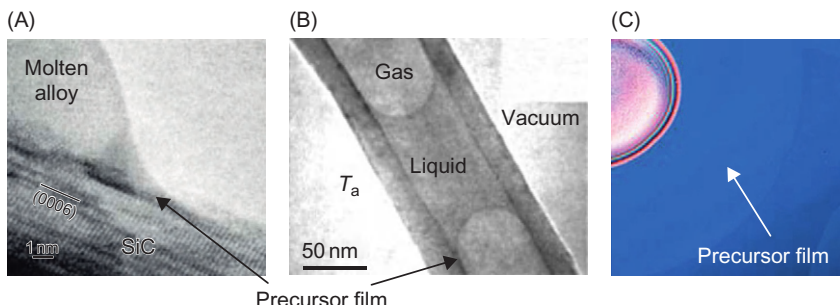
**FIGURE 2.21**

Interface with precursor film.

chemical potential of the gas and of the solid is not physical, liquid molecules intercalate between the gas and the solid [16]. Molecules of liquids progressively spread under the action of the “disjoining pressure” caused by the van der Waals interactions between the liquid and the solid molecules [17].

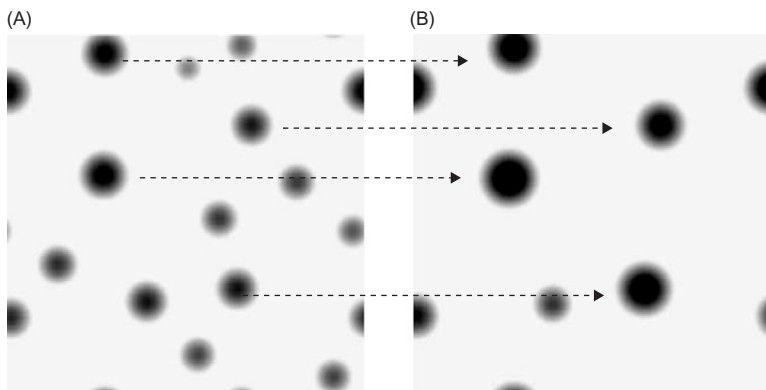
Such precursor films have been observed for different wetting situations, as shown in [Figure 2.22](#). Note the extreme thinness of the film in the photographs.

When droplets of different size are deposited on a flat solid surface, if the droplets are sufficiently close to one another, it is observed that the smaller droplets disappear to the benefit of the large droplets. This phenomenon is called “coarsening.” Experimental evidence of coarsening is shown in [Figure 2.23](#).

**FIGURE 2.22**

(A) Precursor film of spreading molten alloy; (B) precursor film of a liquid plug inside a carbon nanotube [18]; (C) scan of a liquid crystal precursor film; the precursor film spreads on a distance of 1 mm.

Sources: (A) From Ref. [19] © 2002, Elsevier, reprinted with permission. (B) Reused with permission from Ref. [18] © 2005, American Institute of Physics. (C) From Ref. [20], Sarfus Image: Courtesy Nanolane.

**FIGURE 2.23**

Experimental observation of coarsening: the number of droplets diminishes; only the largest droplets remain: (A) beginning of the observation, (B) increase in size of the large droplets and vanishing of the smaller droplets [21].

Source: Courtesy Michael Bestehorn.

The explanation of the phenomenon requires two steps: first, the existence of a precursor film (extremely thin film on the solid surface spreading around each droplet) that links the droplets together. The second step is identical to that of the previous section: the pressure is larger in a small droplet according to the Laplace's law, and there is a liquid flow toward the largest droplet (Figure 2.24). The precursor film is very thin, thus the flow rate between droplets is very small and mass transfer is extremely slow. Hence, experimental conditions require that the droplets do not evaporate.

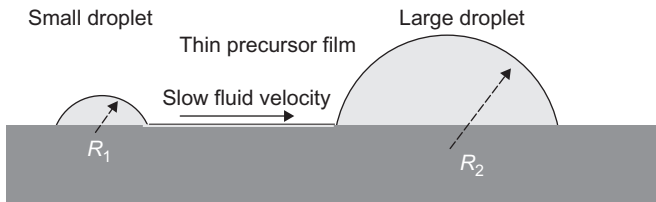


FIGURE 2.24

When two droplets are linked by a precursor film, a fluid flow is established from the smaller droplet to the larger droplet. The smaller droplet progressively disappears.

2.3.2.3 Pressure in droplets constrained between two parallel plates

When using Laplace's law, one should be careful of the orientation of the curvature. A convex surface has two positive radii of curvature. A “saddle” surface has one positive and one negative curvature radius. Take the example of a water droplet flattened between two horizontal plates (we will see in Chapter 4 that this situation is frequent in electrowetting on dielectrics (EWOD)-based microsystems [22]). Suppose that the droplet is placed at the intersection of a hydrophobic band and a hydrophilic band. As a result, the droplet is squashed by the hydrophobic band and elongated on the hydrophilic band (Figure 2.25). The pressure in the droplet is given by Laplace's law

$$P_{\text{droplet}} - P_0 = \gamma \left(\frac{1}{R_1} + \frac{1}{R_2} \right) = \gamma \left(\frac{1}{R_3} + \frac{1}{R_4} \right), \quad (2.19)$$

where R_1 , R_2 , R_3 , and R_4 are respectively the horizontal curvature radius in the hydrophilic region, the vertical curvature radius in the hydrophilic region, the horizontal curvature radius in the hydrophobic region, and the vertical curvature radius in the hydrophobic region. Taking into account the sign of the curvatures, we obtain

$$P_{\text{droplet}} - P_0 = \gamma \left(\frac{1}{|R_1|} - \frac{1}{|R_2|} \right) = \gamma \left(\frac{1}{|R_4|} - \frac{1}{|R_3|} \right). \quad (2.20)$$

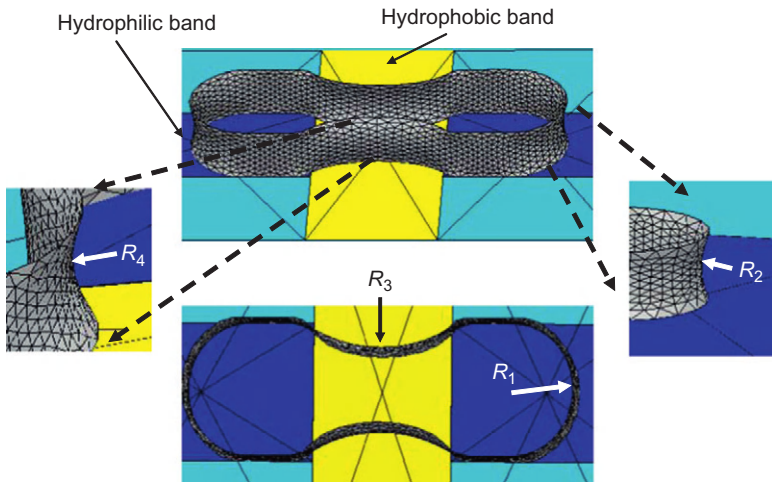
The pressure in the drop being larger than the exterior pressure, the following relations must be satisfied:

$$|R_4| < |R_3| \quad (2.21)$$

and

$$|R_2| > |R_1|. \quad (2.22)$$

The vertical curvature radius R_4 in the hydrophobic region is smaller than the concave horizontal radius R_3 and the vertical curvature radius in the hydrophilic region R_2 is larger than the convex horizontal radius R_1 . We shall see in Chapter 5 the use of a hydrophobic band to “cut” the droplet into two daughter

**FIGURE 2.25**

Sketch of a water droplet pinched by a hydrophobic surface. Case of a droplet constrained between two parallel planes (the upper plane has been dematerialized for visualization). Simulation performed with the Surface Evolver numerical software [23].

droplets. For that to happen, the curvature radius R_3 must be sufficiently small, so that the two concave contact lines contact each other. The inequality (2.21) then produces a condition on the level of hydrophobicity required to obtain droplet division.

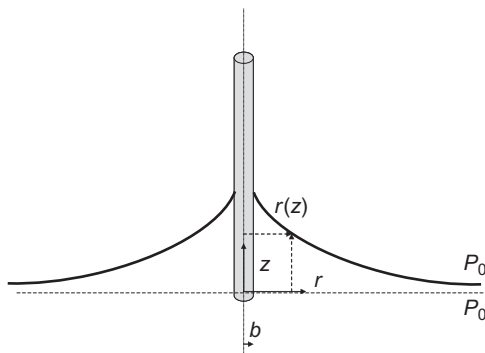
2.3.2.4 Zero pressure surfaces: example of a meniscus on a wire

Laplace's law is often seen as determining a pressure difference on the two sides of the interface from the observation of curvature. But it is interesting to look at it the other way: knowing the pressure difference, what conclusion may be reached on the curvature of the interface?

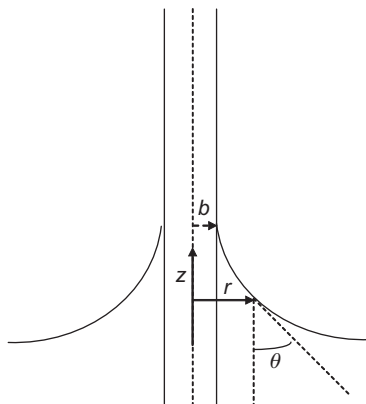
We consider an example in which the pressure difference is zero: this is the case of a cylindrical wire dipped in a wetting liquid. We suppose that the angle between the surface and the wire (contact angle) is $\theta = 0$. We shall develop the notion of contact angle in [Section 2.5](#). The liquid rises along the wire, deforming the free surface ([Figure 2.26](#)). What is the shape of the surface? Laplace's law combined with the hydrostatic pressure yields

$$P_0 + \gamma \left(\frac{1}{R_1} + \frac{1}{R_2} \right) = P_0 - \rho g z, \quad (2.23)$$

where R_1 and R_2 are the two (signed) principal curvature radii. $R_1(z)$ is the horizontal (positive) radius of the circle delimited by the intersection of a horizontal plane and the surface, while $R_2(z)$ is the (negative) curvature radius of the vertical

**FIGURE 2.26**

Sketch of wire dipped into a liquid (wetting case).

**FIGURE 2.27**

Vertical profile of liquid surface at the vicinity of a vertical rod.

profile at the elevation z . Assuming that the system is small enough that the gravity term can be neglected compared to the pressure P_0 , we are left with

$$\frac{1}{R_1} + \frac{1}{R_2} = 0. \quad (2.24)$$

This is the equation of a zero curvature surface, also called a minimal surface. The equation of the surface can be obtained by writing that the vertical projection of the surface tension force is constant [23]. Using the notations of Figure 2.27, we find

$$2\pi r\gamma \cos \theta = 2\pi b\gamma. \quad (2.25)$$

Substituting the relation $\tan \theta = dr/dz = \dot{r}$, we are left with

$$\frac{r}{\sqrt{1 + \dot{r}^2}} = b. \quad (2.26)$$

Integration of Eq. (2.26) yields the equation of the vertical profile

$$r = b^* \cosh \frac{z - h^*}{b^*}, \quad (2.27)$$

where b^* and h^* are constants depending on the contact angle with the vertical cylinder. In the case of a wetting contact ($\theta = 0$), the exact solution is

$$r = b \cosh \frac{z - h_0}{b}, \quad (2.28)$$

where b is the wire radius and h_0 is the height of the interface along the wire. We note that Eq. (2.28) is the equation of a catenoid [23]. However, this equation describes the surface close to the wire (for $r = b$, $z = h_0$) but not far from the wire. Far from the wire, the value of z increases again in Eq. (2.28). This is not physical, and we should take into account gravity that flattens the surface. We shall see in Chapter 3 that the expression

$$\kappa^{-1} = \sqrt{\frac{\gamma}{\rho g}} \quad (2.29)$$

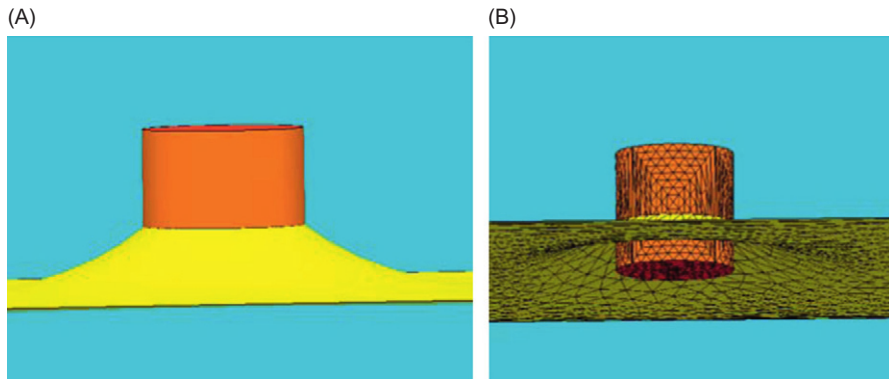
is a characteristic length of the capillarity, called the capillary length. Scaling the horizontal extent of the surface deformation with the capillary length $r_{\max} \approx \kappa^{-1}$, Eq. (2.28) yields $\kappa^{-1} = b \cosh(-h_0/b)$. Assuming that $b \ll h_0$, we obtain an approximate value for the maximum height h_0 [24]:

$$h_0 \approx b \ln \left(\frac{2\kappa^{-1}}{b} \right). \quad (2.30)$$

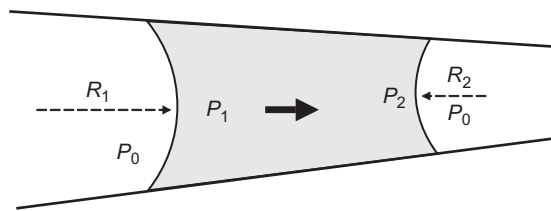
Figure 2.28 shows the deformed surface obtained by a numerical simulation. Relation (2.30) shows that the elevation h_0 along the wire increases with the surface tension γ . At first sight, this may seem a paradox because the surface is pulled tighter when the surface tension increases. However, we show later in this chapter that the capillary force exerted by the wire is proportional to the surface tension. The force pulling the surface is thus larger for high surface tension liquids.

2.3.2.5 Self-motion of a liquid plug between two nonparallel wetting plates

It was first observed by Hauksbee [25] that a liquid plug limited by two nonparallel wetting plates moves toward the narrow gap region. A sketch of the plug is shown in Figure 2.29. Laplace's law furnishes a very clear explanation of this

**FIGURE 2.28**

Vertical wire dipped into a fluid. The surface is deformed depending on the surface tension of the liquid and on the contact angle (Surface Evolver calculation). (A) View of the surface in the vicinity of the wire. (B) View from below showing the gain in elevation of the surface at the contact of the wire.

**FIGURE 2.29**

Sketch of a liquid plug moving under capillary forces between two plates. The contact angle is $\theta < 90^\circ$.

phenomenon. Supposing that Figure 2.29 is a wedge (2D situation), let us write Laplace's law for the left-side interface

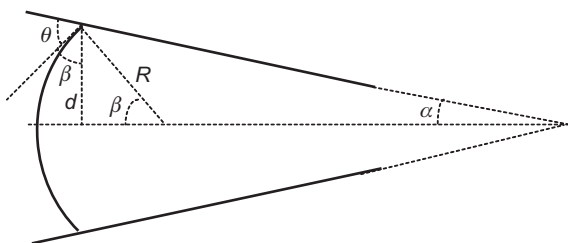
$$P_0 - P_1 = \frac{\gamma}{R_1} \quad (2.31)$$

and for the right-side interface

$$P_0 - P_2 = \frac{\gamma}{R_2}. \quad (2.32)$$

Subtraction of the two relations leads to

$$P_1 - P_2 = \gamma \left(\frac{1}{R_2} - \frac{1}{R_1} \right). \quad (2.33)$$

**FIGURE 2.30**

Curvature of the interface in a dihedral.

Next, we show that $R_2 < R_1$. Looking at Figure 2.30, we have

$$R_2 \sin \beta = d_2,$$

where d_2 is the half-distance between the plates.

The angle β is linked to θ and α by the relation

$$\beta = \frac{\pi}{2} + \alpha - \theta.$$

Finally, we obtain

$$R_2 = \frac{d_2}{\cos(\alpha - \theta)}. \quad (2.34)$$

Using the same reasoning with a meniscus oriented in the opposite direction, we obtain the expression of R_1 :

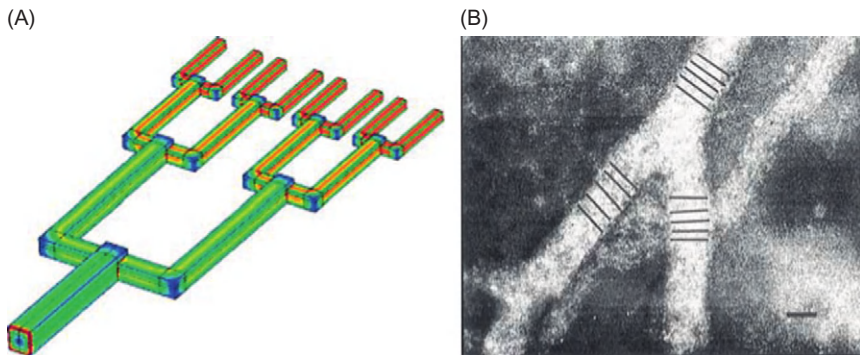
$$R_1 = \frac{d_1}{\cos(\alpha - \theta)}. \quad (2.35)$$

Comparing relations (2.34) and (2.35), remarking that $d_2 < d_1$ and $\cos(\alpha - \theta) > \cos(\alpha + \theta)$, we deduce that R_2 is then smaller than R_1 , and $P_1 > P_2$. The situation is not stable. Liquid moves from the high- to the low-pressure region, and the plug moves toward the narrow gap region. It has also been observed that the plug accelerates; it is due to the fact that the difference of the curvatures in Eq. (2.33) is increasing when the plug moves to a narrower region. Bouasse [25] has remarked that the same type of motion applies for a cone, where the plug moves toward the tip of the cone. In reality, Bouasse used a conical frustum (slice of cone) in order to let the gas escape during plug motion.

2.3.2.6 Laplace's law in medicine: normal and shear stress in blood vessels

2.3.2.6.1 Shear stress

A human body—or any mammalian organism—respects the rules of physics. Take the example of blood vessels. The arrangement of blood vessel networks

**FIGURE 2.31**

(A) Schematic of blood vessel system. (B) Photograph of blood vessel division in chickens.

Source: From Ref. [26] © 2001, Elsevier, reprinted with permission.

very often satisfies Murray's law (Figure 2.31). In 1926, Murray observed the morphology of the blood system and found a very general relation between the dimensions of a "parent" branch and of a "daughter" branch, and he found that the same relation applies at any level of bifurcation.

Soon after, he published this discovery [27]. Since that time, this relation has been known as Murray's law and can be written as

$$d_0^3 = d_1^3 + d_2^3, \quad (2.36)$$

where d_0 , d_1 , and d_2 are the "parent" and "daughter" channel diameters. Usually, daughter branches have the same dimension $d_1 = d_2$. A recurrence relation can be deduced from Eq. (2.36); it shows that the diameter, flow rates, and average velocities at the n th generation, i.e., at a bifurcation rank n (Figure 2.31), are related to the "origin" diameter, flow rate, and average velocity by the relations

$$\begin{aligned} d_n &= \frac{d_0}{2^{n/3}} \\ Q_n &= \frac{Q_0}{2^n} \\ V_n &= \frac{V_0}{2^{n/3}}. \end{aligned} \quad (2.37)$$

Relation (2.37) can be developed further to show that the wall friction is the same at each level [26,28]. This property simply stems from the expression of the shear stress of a cylindrical duct:

$$\tau_n = \frac{8\eta V_n}{d_n} = \frac{8\eta V_0}{d_0} = \tau_0. \quad (2.38)$$

The equality of the shear stress still stands if we take into account the non-Newtonian character of blood. Murray showed that, from a physiological point of view, such a relation minimizes the work of the blood circulation. The important thing here is that the shear stress is constant in most blood vessel networks. Now what about the normal stress?

2.3.2.6.2 Normal stress

In the particular case of human or mammalian blood systems, the normal stress is simply the internal pressure, because, in a first approximation, the flow is purely axial and there is no radial component of the velocity. It has been observed that the thickness of the walls of blood vessels satisfies Laplace's law (Figure 2.32). In this particular case, the surface tension is replaced by the wall tension T , and Laplace's law becomes

$$P = \frac{T}{R}. \quad (2.39)$$

At a given distance from the heart, the pressure is approximately the same and Laplace's equation (2.39) has the consequence that the wall tension increases together with the curvature radius. As a consequence, arteries have larger wall thickness than veins, and similarly veins compared to capillaries.

2.3.2.7 Laplace's law in medicine: the example of lung alveoli

It is very tempting to refer systematically to Laplace's law because of its simplicity. But one should refrain from doing that systematically. A striking example is that of lung ventilation.

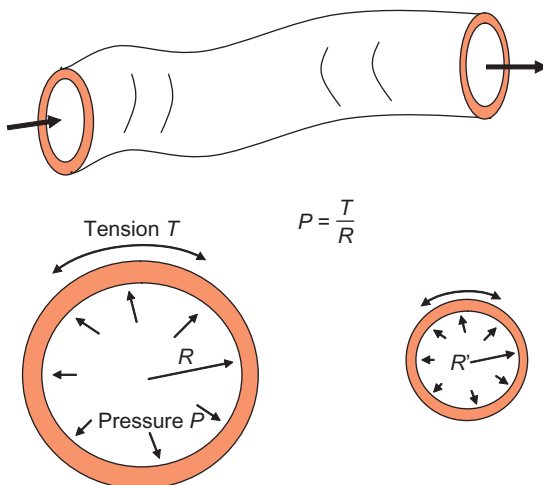


FIGURE 2.32

Schematic view of a blood vessel: if the internal pressure is P , the tension in the wall is $T = PR$. Small blood vessels have smaller walls than large blood vessels.

Ventilation of lungs has been widely studied for medical purposes. It was usual to consider the alveoli to be like spherical balloons inflated during lung ventilation (Figure 2.33). The problem is that the alveoli are connected, and when applying Laplace's law, the air in the smaller alveoli should be driven to the larger alveoli and a general collapse of the lungs would occur. Because the collapse of the alveoli does not—luckily—correspond to the reality, it has been suggested that the concentration of surfactant in the alveoli is not uniform and compensates for the different Laplace's pressures.

Recently, a different, more realistic analysis has been made [29]: the alveoli are not “free” spheres but are packed together (Figure 2.34), and there are pores

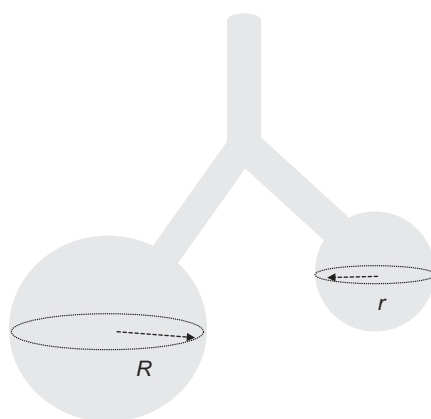


FIGURE 2.33

Wrong sketch for the alveoli leading to a biased Laplace's law application.

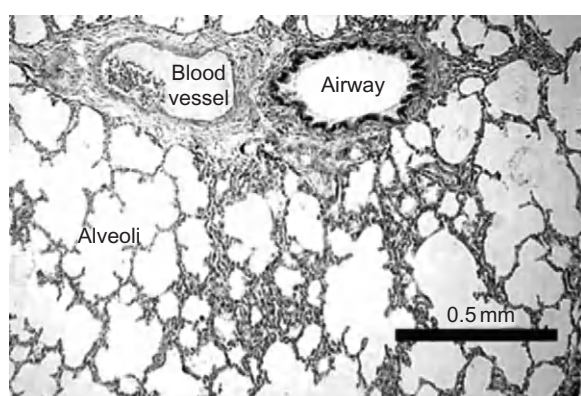


FIGURE 2.34

Image of lung alveoli.

Source: Detail from an original slide generously provided by A. Mescher.

in the alveoli walls. Alveoli cannot expand freely, and they are limited in their inflation. As a result, the smallest alveoli do not collapse during ventilation, because large alveoli cannot grow indefinitely and Laplace's law is not the answer in this kind of problem.

2.4 Wetting—partial or total wetting

So far, we have dealt with interfaces between two fluids. Triple contact lines are the intersections of three interfaces involving three different materials: for example, a droplet of water on a solid substrate has a triple contact line.

Liquids spread differently on a horizontal plate according to the nature of the solid surface and that of the liquid. In reality, it depends also on the third constituent, which is the gas or the fluid surrounding the drop. Two different situations are possible: either the liquid forms a droplet and the wetting is said to be partial, or the liquid forms a thin film wetting the solid surface, with the horizontal dimension of the film depending on the initial volume of liquid (Figure 2.35). For example, in the environment of a room, water spreads like a film on a very clean and smooth glass substrate, whereas it forms a droplet on a plastic substrate. In the case of partial wetting, there is a line where all three phases come together. This line is called the *contact line* or the *triple line*.

A liquid spreads on a substrate in a film if the energy of the system is lowered by the presence of the liquid film (Figure 2.36). The surface energy per unit surface of the dry solid surface is γ_{SG} ; the surface energy of the wetted solid is $\gamma_{SL} + \gamma_{LG}$. The spreading parameter S determines the type of spreading (total or partial):

$$S = \gamma_{SG} - (\gamma_{SL} + \gamma_{LG}). \quad (2.40)$$

If $S > 0$, the liquid spreads on the solid surface; if $S < 0$, the liquid forms a droplet.

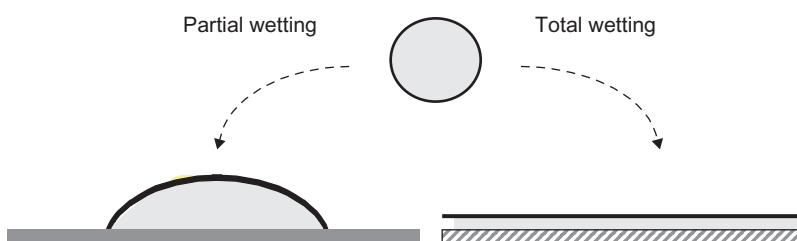


FIGURE 2.35

Wetting is said to be total when the liquid spreads like a film on the solid surface.

When a liquid does not totally wet the solid, it forms a droplet on the surface. Two situations can occur: if the contact angle with the solid is less than 90° , the contact is said to be “hydrophilic” if the liquid has a water base, or more generally “wetting” or “lyophilic.” In the opposite case of a contact angle larger than 90° , the contact is said to be “hydrophobic” with reference to water or more generally “not wetting” or “lyophobic” (Figures 2.37 and 2.38).

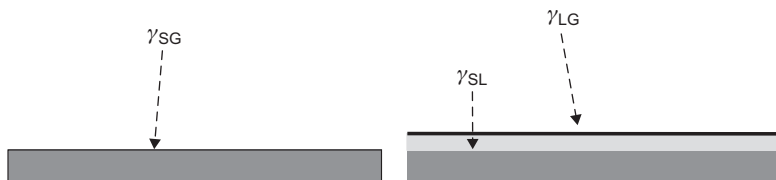


FIGURE 2.36

Comparison of the energies between the dry solid and the wetted solid.

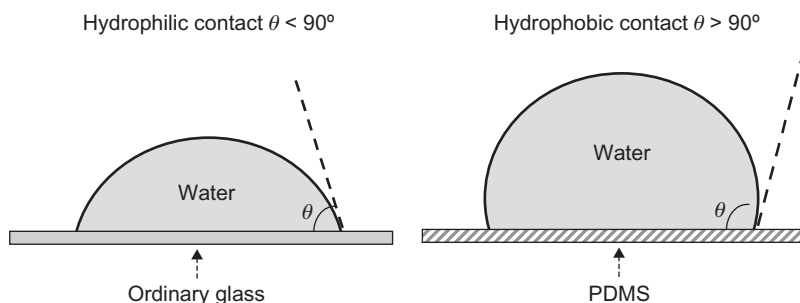


FIGURE 2.37

Water spreads differently on different substrates.

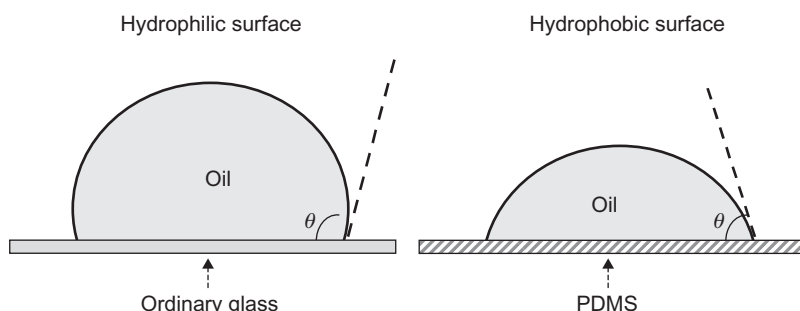


FIGURE 2.38

Silicone oil has an opposite wetting behavior than water.

2.5 Contact angle—Young's law

2.5.1 Young's law

Surface tension is not exactly a force; its unit is N/m. However, it represents a force that is exerted tangentially to the interface. Surface tension can be looked at as a force per unit length. This can be directly seen from its unit. But it may be interesting to give a more physical feeling by making a very simple experiment (Figure 2.39) [24]. Take a solid frame and a solid tube that can roll on this frame. If we form a liquid film of soap between the frame and the tube—by plunging one side of the structure in a water-soap solution—the tube starts to move toward the region where there is a liquid film. The surface tension of the liquid film exerts a force on its free boundary.

However, we can increase the film surface by exerting a force on the tube. The work of this force is given by the relation

$$\delta W = F dx = 2\gamma L dx. \quad (2.41)$$

The coefficient 2 stems from the fact that there are two interfaces between the liquid and the air. This relation shows that the surface tension γ is a force per unit length, perpendicular to the tube, in the plane of the liquid and directed toward the liquid.

We can then draw the different forces that are exerted by the presence of a fluid on the triple line (Figure 2.40).

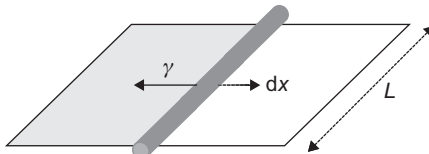


FIGURE 2.39

A tube placed on a rigid frame whose left part is occupied by a soap film requires a force to be displaced toward the right; this force opposed the surface tension that tends to bring the tube to the left.

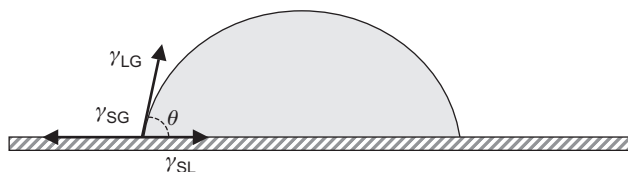


FIGURE 2.40

Schematic of the forces at the triple contact line.

At equilibrium, the resultant of the forces must be zero. We use a coordinate system where the x -axis is the tangent to the solid surface at the contact line (horizontal) and the y -axis is the perpendicular (vertical). At equilibrium, the projection of the resultant on the x -axis is zero and we obtain the relation

$$\gamma_{LG} \cos \theta = \gamma_{SG} - \gamma_{SL}. \quad (2.42)$$

This relation is called Young's law and is very useful for understanding the behavior of a drop. Especially, it shows that the contact angle is determined by the surface tensions of the three constituents. For a microdrop on a solid, the contact angle is given by the relation

$$\theta = \arccos \frac{\gamma_{SG} - \gamma_{SL}}{\gamma_{LG}}. \quad (2.43)$$

Note that sometimes it happens that, in real experimental situations when we deal with real biological liquids, one observes unexpected changes in the contact angle with time. This is just because biological liquids are inhomogeneous and can deposit a layer of chemical molecules on the solid wall, thus progressively changing the value of the tension γ_{SL} , and consequently the value of θ , as stated by Young's law.

Young's law can be more rigorously derived from free energy minimization. Consider a sessile droplet large enough for the effect of the triple line to be neglected. The change of free energy due to a change in droplet size can be written as [30]

$$\begin{aligned} dF &= \gamma_{SL} dA_{SL} + \gamma_{SG} dA_{SG} + \gamma_{LG} dA_{LG} \\ &= (\gamma_{SL} - \gamma_{SG} + \gamma_{LG} \cos \theta) dA_{SL}, \end{aligned} \quad (2.44)$$

where θ is the contact angle. At mechanical equilibrium, $dF = 0$ and

$$\gamma_{SL} - \gamma_{SG} + \gamma_{LG} \cos \theta = 0. \quad (2.45)$$

Equation (2.45) is the Young's law, identical to Eq. (2.42).

2.5.2 Nanobubbles on hydrophobic walls, line tension, and the modified Young's law

It has been observed that bubbles often form along hydrophobic walls, even when the surface is smooth. The size of these bubbles is in the mesoscopic range—between the microscopic and the nanoscopic scales: bubble dimension is usually less than 200 nm. A paradox arises when calculating the internal pressure. Using Laplace's law with a curvature radius of the order of the observed contact at the wall, one finds that the internal pressure should be of the order of

$$P \approx \frac{\gamma}{R} \approx \frac{70 \times 10^{-3}}{200 \times 10^{-9}} \approx 5 \times 10^5 \text{ Pa.}$$

At this level of pressure, the gas should dissolve, and the bubble would disappear rapidly in the liquid. So, why are these bubbles stable? From a Laplace's

law point of view, either their surface tension should be smaller than that of a “macroscopic” bubble, or their curvature radius should be larger. It is easy to see that a reduced surface tension is not sufficient to find a sustainable internal pressure. However, at this scale, contact angle measurements are very tricky. Recent measurements [31] have shown that nanobubbles have very flat profiles—the base radius is 5–20 times larger than the height—because the contact angle of the bubble is much smaller than the macroscopic contact angle of the bubble on the same substrate (Figure 2.41).

The problem has now shifted from Laplace’s law to Young’s law. What has changed in Young’s law for the contact angle between the nanometric scale and the microscopic/macrosopic scale? The answer to this question is not yet clear. A plausible answer is connected to the notion of “line tension” and to the so-called modified Young’s law. Young’s law has been derived for a triple line without consideration of the interactions near the triple contact line. A sketch of the interactions leading to surface tension and line tension is shown in Figure 2.42. The molecules close to the triple line experience a different set of interactions than at the interface. To take into account this effect, a line tension term has been introduced in Young’s law [32]:

$$\gamma_{SG} = \gamma_{SL} + \gamma_{LG} \cos \theta^* + \frac{\gamma_{SLG}}{r}, \quad (2.46)$$

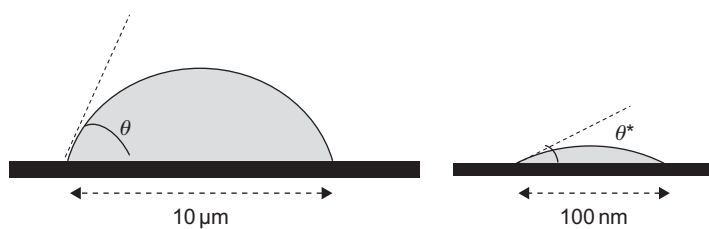


FIGURE 2.41

Comparative sketches of microbubble and nanobubble (not to scale).

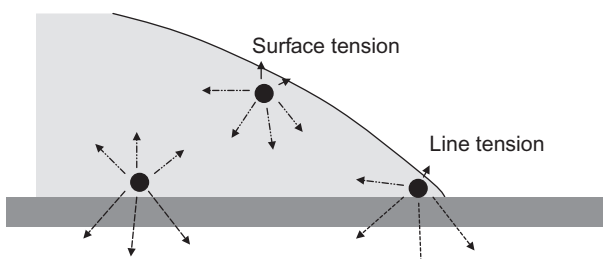


FIGURE 2.42

Sketch of interactions leading to surface tension and line tension.

where r is the contact radius, γ_{SLG} is the line tension (unit N), and θ^* is the real contact angle. The contact angle is then changed by the line tension according to

$$\cos \theta^* = \cos \theta - \frac{\gamma_{\text{SLG}}}{r \gamma_{\text{LG}}}. \quad (2.47)$$

For droplet contact radius larger than $10 \mu\text{m}$, the effect of the line tension is negligible; the value of the term $\tau/r = \gamma_{\text{SLG}}/r \gamma_{\text{LG}}$ is of the order of 10^{-4} [24]. But it is not the case for nanodrops and nanobubbles.

2.6 Work of adhesion, work of cohesion, and the Young–Dupré's equation

In this section, we introduce the notions of work of adhesion and work of cohesion. These notions are valid for solids or immiscible liquids. When applied to a solid and a liquid, the concept of work of adhesion combined with Young's law produces the Young–Dupré's equation. Work of adhesion and Young–Dupré's equation have been widely used to determine the surface tension of solids ([Section 2.9](#)).

2.6.1 Work of adhesion

Imagine a body contacting another body on a surface S ([Figure 2.43](#)). The surface energy of S when there is contact is

$$E_{12} = \gamma_{12} S.$$

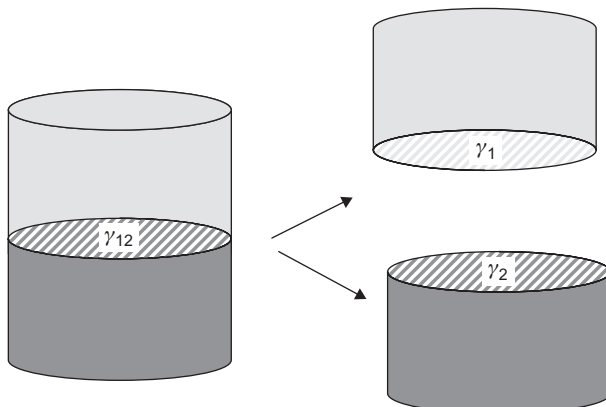


FIGURE 2.43

Work of adhesion is the work done to separate two surfaces of incompatible substances.

The work of adhesion is the work required to separate the two bodies. After separation, the surface energies are

$$E = E_1 + E_2 = (\gamma_1 + \gamma_2)S.$$

The work of adhesion is then

$$W_a = \gamma_1 + \gamma_2 - \gamma_{12}. \quad (2.48)$$

2.6.2 Work of cohesion

The work of cohesion is obtained similarly, but this time the body being split is homogeneous ([Figure 2.44](#)). The same reasoning yields

$$W_c = 2\gamma_1. \quad (2.49)$$

In other words, the surface energy is half the work of cohesion.

2.6.3 Young–Dupré's equation

Let us express the work of adhesion for a liquid and a solid ([Figure 2.45](#)). Using [Eq. \(2.48\)](#) with the surface tensions $\gamma_1 = \gamma_{LG} = \gamma$, $\gamma_2 = \gamma_{SG}$, and $\gamma_{12} = \gamma_{SL}$, we obtain

$$W_a = \gamma + \gamma_{SG} - \gamma_{SL}. \quad (2.50)$$

Upon substitution of Young's law, we derive the Young–Dupré's equation:

$$W_a = \gamma(1 + \cos \theta). \quad (2.51)$$

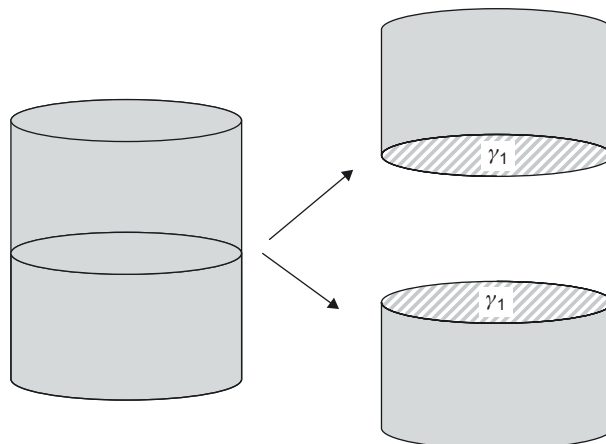
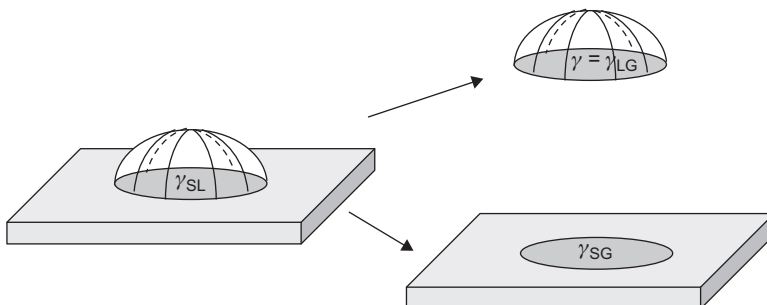


FIGURE 2.44

Work of cohesion is the work done to separate two surfaces of the same substance.

**FIGURE 2.45**

Sketch of the Young–Dupré's equation for the work of adhesion of a liquid and a solid:
 $W_a = \gamma (1 + \cos \theta)$.

For a superhydrophobic contact, $\theta = \pi$ and $\cos \theta = -1$; we deduce that $W_a = 0$: there is no work to separate a superhydrophobic liquid from a solid. Concretely, a droplet of water rolls freely over a superhydrophobic surface. The Young–Dupré's equation indicates that the more hydrophobic (nonwetting) is the contact between a liquid and a solid, the smaller is the work of adhesion.

2.7 Capillary force, force on a triple line

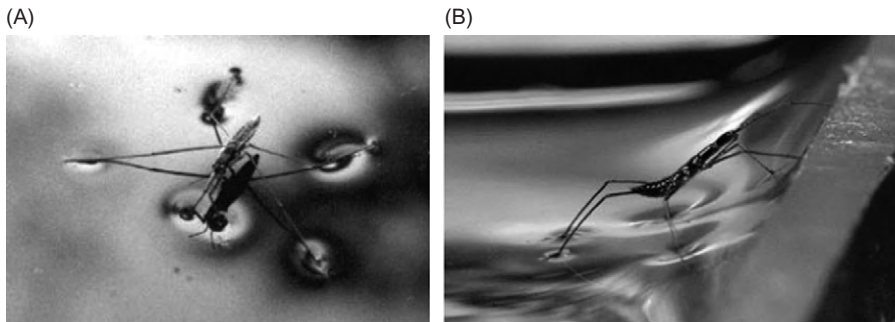
2.7.1 Introduction

We have seen in [Section 2.5](#) the correspondence between surface tension and capillary forces. Capillary forces are extremely important at a microscale. We have all seen insects “walking” on the surface of a water pond ([Figure 2.46](#)). Their hydrophobic legs do not penetrate the water surface and their weight is balanced by the surface tension force. More than that, it is observed that some insects can walk up meniscus, i.e., can walk inclined water surface. The explanation of this phenomenon was recently given by Hu and Bush [\[33\]](#) and refers to complex interface deformation under capillary forces.

In the domain of microfluidics, capillary forces are predominant; some examples of the action of capillary forces are given in the following sections.

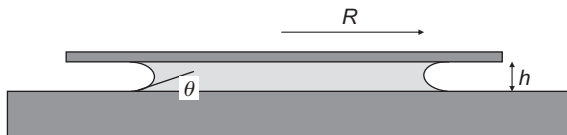
2.7.2 Capillary force between two parallel plates

A liquid film placed between two parallel plates makes the plates very adhesive. For instance, when using a microscope to observe objects in a small volume of liquid deposited on a plate and maintained by a secondary glass plate, it is very difficult to separate the plates. This situation is schematized in [Figure 2.47](#). In the first place, it is observed that the meniscus has a round shape (in order to minimize the free energy).

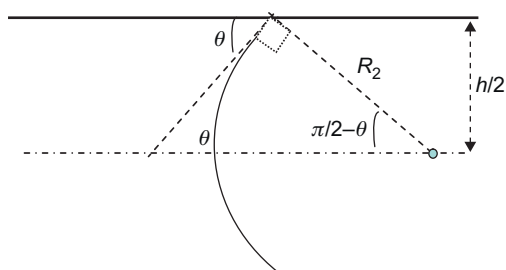
**FIGURE 2.46**

(A) Capillary forces make the water surface resist the weight of an insect. (B) An insect walking up a meniscus [33].

Source: Photo courtesy David Hu.

**FIGURE 2.47**

Film of water between two glass plates.

**FIGURE 2.48**

Calculation of the vertical curvature.

Let us write Laplace's law at the free interface. The first (horizontal) radius of curvature is approximately R . The second (vertical) radius of curvature, shown in Figure 2.48, is calculated by:

$$R_2 \sin\left(\frac{\pi}{2} - \theta\right) = \frac{h}{2}$$

or

$$R_2 = \frac{h}{2 \cos \theta}. \quad (2.52)$$

Laplace's law states that

$$\Delta P = \gamma \left(\frac{1}{R} - \frac{2 \cos \theta}{h} \right). \quad (2.53)$$

In Eq. (2.53), the minus sign is derived from the concavity of the interface. Because the vertical gap h is much less than the horizontal dimension R , we have the approximation

$$\Delta P \approx -\frac{2\gamma \cos \theta}{h}.$$

And the capillary force that links the plates together is

$$F \approx \frac{2\gamma \cos \theta}{h} \pi R^2. \quad (2.54)$$

This capillary force can be quite important; for $h = 10 \mu\text{m}$ and $R = 1 \text{ cm}$, the force F is of the order of 2.5 N.

2.7.3 Capillary rise in a tube

When a capillary tube is plunged into a volume of wetting liquid, the liquid rises inside the tube under the effect of capillary forces (Figures 2.49 and 2.50). It is observed that the height reached by the liquid is inversely proportional to the radius of the tube.

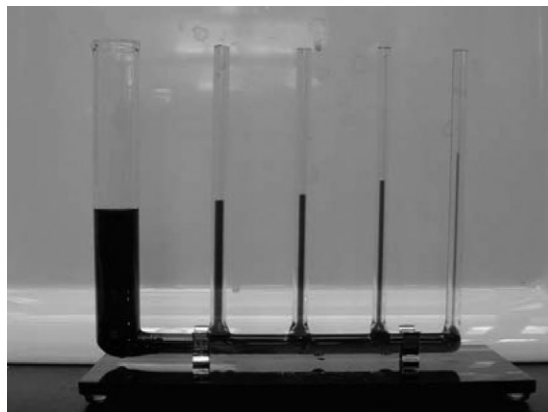
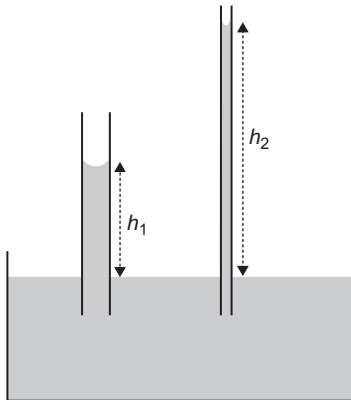


FIGURE 2.49

Capillary rise in tubes of different internal cross-section.

**FIGURE 2.50**

Capillary rise is inversely proportional to the capillary diameter.

Historically, many scientists have investigated this phenomenon, from Leonardo da Vinci to Hauksbee and Jurin. This property is now referred to as Jurin's law.

Using the principle of minimum energy, one can conclude that the liquid goes up in the tube if the surface energy of the dry wall is larger than that of the wetted wall. If we define the impregnation criterion I by:

$$I = \gamma_{SG} - \gamma_{SL}. \quad (2.55)$$

The liquid rises in the tube if $I > 0$, otherwise the liquid descends in the tube. Using Young's law, the impregnation criterion can be written under the form

$$I = \gamma \cos \theta. \quad (2.56)$$

When the liquid rises in the tube, the system gains potential energy—because of the elevation of a volume of liquid—and loses capillary energy—due to the reduction of the surface energy. The balance is [24]

$$\begin{aligned} E &= \frac{1}{2} \rho g h V_{\text{liquid}} - S_{\text{contact}} I = \frac{1}{2} \rho g h (\pi R^2 h) - 2\pi R h I \\ &= \frac{1}{2} \rho g \pi R^2 h^2 - 2\pi R h \gamma \cos \theta. \end{aligned} \quad (2.57)$$

Note that we have not taken into account in Eq. (2.57) the detailed shape of the meniscus for the height h . The equilibrium elevation of the liquid is given by:

$$\frac{\partial E}{\partial h} = 0,$$

which results in

$$h = \frac{2\gamma \cos \theta}{\rho g R}. \quad (2.58)$$

Equation (2.58) is called Jurin's law. The capillary rise is inversely proportional to the tube radius. It can be also applied to the case where the liquid level in the tube decreases below the outer liquid surface; this situation happens when $\theta = 90^\circ$.

The maximum possible height that a liquid can reach corresponds to $\theta = 0$ and is $h = 2\gamma/\rho g R$.

In microfluidics, capillary tubes of 100 μm diameter are currently used; if the liquid is water ($\gamma = 72 \text{ mN/m}$), and using the approximate value $\cos \theta \sim 1/2$, the capillary rise is of the order of 14 cm, which is quite important at the scale of a microcomponent.

Equation (2.58) characterizes the capillary rise; note that the capillary rise can be important. What is the corresponding capillary force? The capillary force balances the weight of the liquid in the tube. This weight is given by:

$$F = \rho g \pi R^2 h.$$

Replacing h by its value from Eq. (2.54), we find the capillary force

$$F = 2\pi R \gamma \cos \theta. \quad (2.59)$$

The capillary force is the product of the length of the contact line $2\pi R$ times the line force $f = \gamma \cos \theta$. This line force is sketched in Figure 2.51.

Note that the capillary force per unit length f is identical to the impregnation criterion

$$f = \gamma \cos \theta = I. \quad (2.60)$$

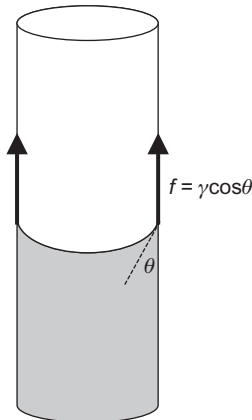
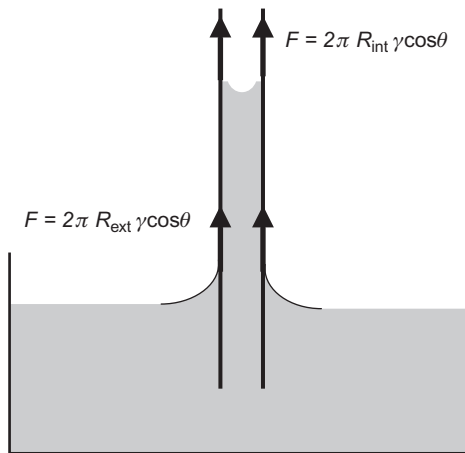


FIGURE 2.51

Sketch of the capillary force of a liquid inside a tube.

**FIGURE 2.52**

Capillary forces act also on the tube exterior, raising the level of the liquid around the tube (if the liquid wets the solid it would be the opposite if the liquid were not wetting).

For $f > 0$, the liquid goes up in the tube, and for $f < 0$, the liquid goes down. Note that Figure 2.50 is not quite exact. There are also capillary forces on the outside of the tube, as shown in Figure 2.52.

To derive the expression of the capillary rise inside the tube, a control volume corresponding to the liquid volume inside the tube was first considered. Let us consider now a control volume defined by the pipette (Figure 2.53). The force to maintain the pipette is

$$F = P - P_A + P_{c,e} + P_{c,i}, \quad (2.61)$$

where P is the weight of the tube, P_A the floatation force, and $P_{c,i}$ and $P_{c,e}$ are respectively the interior and exterior capillary forces *exerted on the solid*.

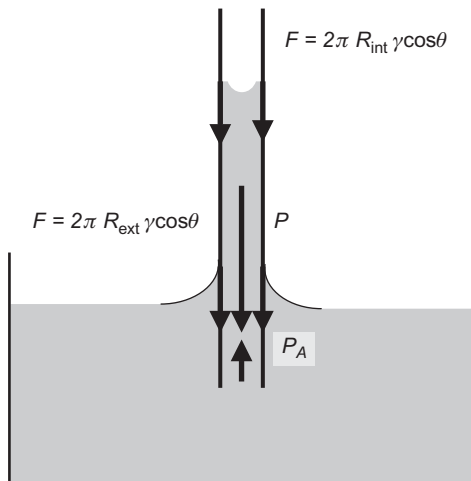
$$F = P - P_A + 2\pi R_i \gamma \cos \theta + 2\pi R_e \gamma \cos \theta. \quad (2.62)$$

This force is a function of the surface tension γ . In Section 2.8, we will see that the measure of such a force constitutes a way to determine the surface tension.

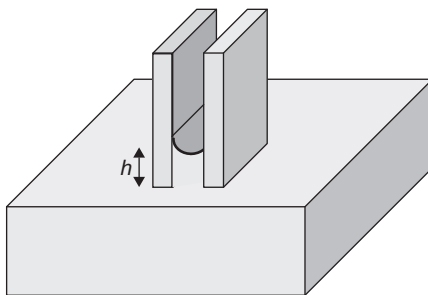
2.7.4 Capillary rise between two parallel vertical plates

The same reasoning can be made for a meniscus between two parallel plates (Figure 2.54) separated by a distance $d = 2R$. It is easy to show that in this case

$$h = \frac{\gamma \cos \theta}{\rho g R}. \quad (2.63)$$

**FIGURE 2.53**

Forces acting on the pipette.

**FIGURE 2.54**

Capillary rise between two parallel vertical plates.

If we introduce the capillary length defined by:

$$\kappa^{-1} = \sqrt{\frac{\gamma}{\rho g}} \quad (2.64)$$

we can rewrite Eq. (2.63) under the form

$$h = \kappa^{-2} \frac{\cos \theta}{R}. \quad (2.65)$$

Note: The expressions for the two geometries (cylinder and two parallel plates) are similar. If we use the coefficient c , with $c = 2$ for a cylinder and $c = 1$ for parallel plates [34], we have

$$h = c\kappa^{-2} \frac{\cos \theta}{R}, \quad (2.66)$$

where R is either the radius of the cylinder or the half-distance between the plates.

2.7.5 Capillary rise in a pipette

The analysis of the capillary rise—or descent—in cylindrical tubes or between two parallel plates has been recently extended by Tsori [34] to the case where the walls are not parallel, as, for instance, for a conical pipette (Figure 2.55).

The mechanic equilibrium states that the Laplace's pressure is balanced by the hydrostatic pressure

$$P_0 + \frac{c\gamma}{r} = p_0 - \rho gh, \quad (2.67)$$

where c is the index defined previously, $c = 2$ for cones and $c = 1$ for wedges, and r is the curvature radius of the meniscus. Note that the depth h is counted negatively from the surface. Using the same approach as that of Section 2.3.2.5, the curvature radius is expressed by:

$$r(h) = -\frac{R(h)}{\cos(\theta + \alpha)} \quad (2.68)$$

with

$$R(h) = R_0 + h \tan \alpha, \quad (2.69)$$

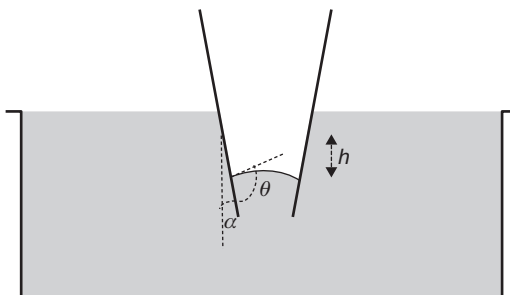


FIGURE 2.55

Capillary descent inside a hydrophobic pipette.

where R_0 is the internal radius of the pipette at $h = 0$. Substituting Eq. (2.69) in Eq. (2.68) and then in Eq. (2.67), we obtain

$$\cos(\theta + \alpha) = \frac{1}{c} h(R_0 + h \tan \alpha) \frac{\rho g}{\gamma}. \quad (2.70)$$

Using capillary length κ^{-1} to scale the variables, we obtain the dimensionless variables $\bar{R} = \kappa R$ and $\bar{h} = \kappa h$. Equation (2.70) then becomes

$$\tan \alpha \bar{h}^2 + \bar{R}_0 \bar{h} - c \cos(\theta + \alpha) = 0. \quad (2.71)$$

This is a quadratic equation in \bar{h} . The discussion of this equation is somewhat complex. Depending on the values of α and θ , the meniscus may be stable or not stable; in this latter case, the meniscus jumps to the top or the bottom of the pipette where it gets stabilized by pinning (anchoring to an angle). Figure 2.56 summarizes the meniscus behavior.

The important information here is that there are two domains where the meniscus “jumps” inside the pipette until it finds a pinning edge. The first case is that of a cone/wedge angle α larger than a critical value α^* (and contact angle θ sufficiently large); the meniscus stays pinned at the bottom of the pipette, and no

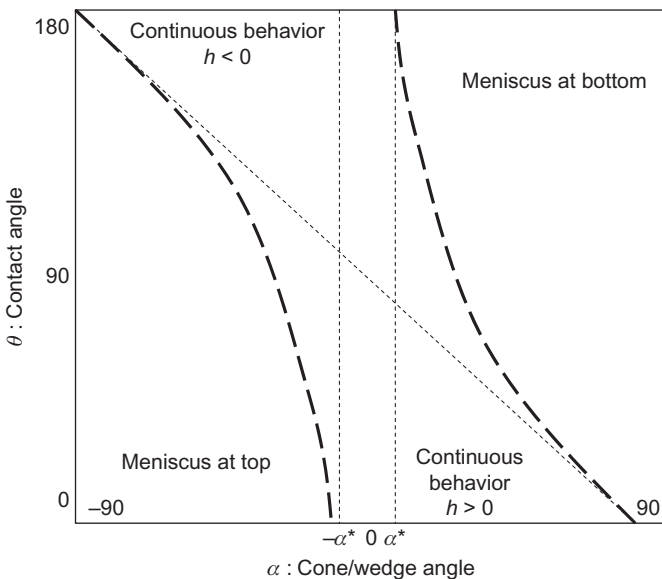


FIGURE 2.56

Diagram of meniscus behavior in the (θ, α) plane. The angle α^* is defined by $\sin \alpha^* = \bar{R}_0^2 / 4c$. Depending on the contact angle, if the angle of a pipette is sufficiently large, whether it is hydrophobic or hydrophilic, the meniscus will stay at the bottom. No liquid will penetrate the pipette unless a negative pressure is established in the pipette [34].

liquid penetrates the pipette, unless a negative pressure is established. On the other hand, when the angles α and θ are sufficiently small (α smaller than a negative critical value— α^*), the liquid jumps to the top of the cone/wedge. The critical values depend on the internal radius R_0 of the pipette at $h = 0$.

In conclusion, a cone-shaped micropipette dipped into a liquid does not always have the expected behavior, i.e., there might not be the expected capillary rise.

2.7.6 Force on a triple line

The analysis of the capillary rise in tubes has shown the expression of the capillary force on the triple contact line [35]. This expression can be generalized to any triple contact line [36]. For a triple contact line Ω —as shown in Figure 2.57—the capillary force is

$$\vec{F} = \int_{\Omega} \vec{f} \, dl = \int_{\Omega} \gamma \cos \theta \, \vec{n} \, dl. \quad (2.72)$$

Suppose that we want to find the value of the resultant of the capillary forces in a particular direction, say x -direction. Using the notations of Figure 2.58, the projection along the x -direction of Eq. (2.68) can be written as

$$F_x = \int_{\Omega} \vec{f} \cdot \vec{i} \, dl = \int_{\Omega} \gamma \cos \theta \, \vec{n} \cdot \vec{i} \, dl. \quad (2.73)$$

Equation (2.73) can be simplified and cast under the form

$$F_x = \int_{\Omega} \gamma \cos \theta \, \vec{n} \cdot \vec{i} \, dl = \gamma \cos \theta \int_{\Omega} \vec{n} \cdot \vec{i} \, dl = \gamma \cos \theta \int_{\Omega} \cos \alpha \, dl = \gamma \cos \theta \int_0^e dl'.$$

Finally, we obtain the expression

$$F_x = e \gamma \cos \theta. \quad (2.74)$$

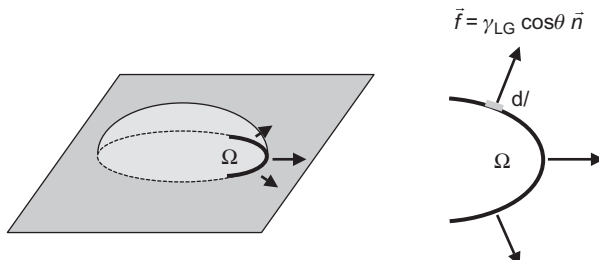
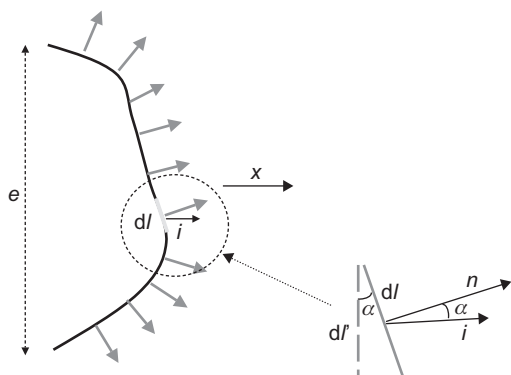


FIGURE 2.57

Schematic of the capillary force on a triple line.

**FIGURE 2.58**

Capillary force on a triple contact line in the x -direction.

Equation (2.74) shows that the resulting force on a triple contact line in any direction does not depend on the shape of the interface [36]; it depends only on the distance between the two ends of the triple line normal to the selected direction.

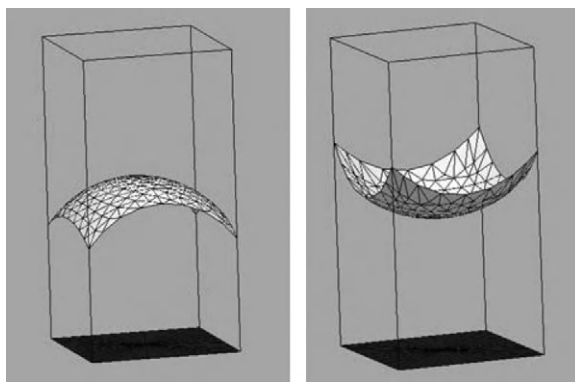
2.7.7 Examples of capillary forces in microsystems

It is very common in biotechnology to use plates comprising thousands of micro-holes or cusps. The position of the free surface of the liquid in the cusps is of utmost importance. In particular, the liquid must not exit the holes under the action of capillary forces.

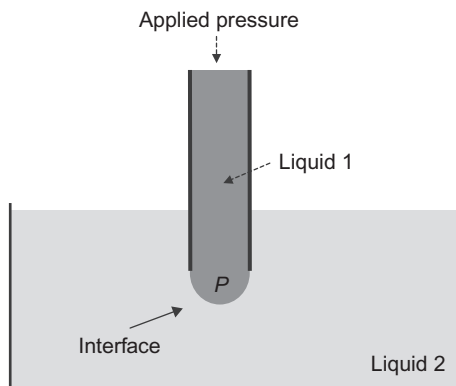
As an example, Figure 2.59 shows a free liquid interface in a square hole, calculated with the Surface Evolver numerical software [23]. In Chapter 3, we will study in more detail the position of an interface in a hole, as a function of the wetting characteristics of the solid surfaces and the shape of the hole.

2.8 Measuring surface tension of liquids

It has already been mentioned that surface tension can be seen as a force. Surface tension can then be measured by comparison with another known and calibrated force. This other force can be pressure as in the “bubble pressure method,” also known as the Schrödinger method, can be a capillary force as in the Wilhelmy plate method, or can be gravity as in the pendant drop method, and more recently it can be fluid stress as in the drop deformation method. In the following, we analyze these methods. Devices that are used to measure the surface tension are called tensiometers.

**FIGURE 2.59**

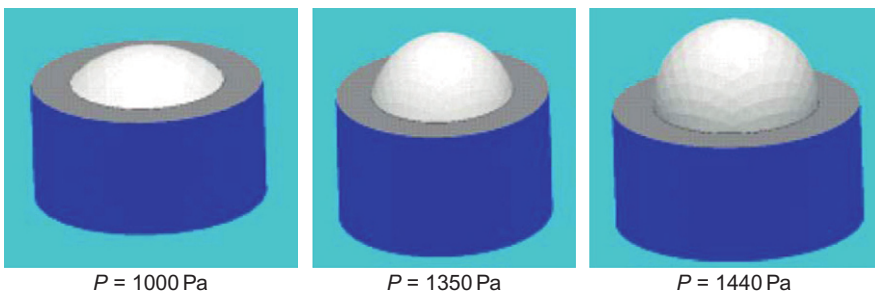
The surface of a liquid in a microwell is not flat due to capillary forces. The figure is a simulation with the Surface Evolver software. (A) Case of water in a hydrophilic well (contact angles of 140°) and (B) case of water in a hydrophilic well (contact angles 60°). The “free” surface is tilted downward or upward depending on the contact angle. The walls have been dematerialized for clarity.

**FIGURE 2.60**

Principle of surface tension measurement using pressure: the maximum pressure that a liquid interface can support is when the interface has the shape of a half-sphere. This pressure is related to the surface tension by Laplace’s law.

2.8.1 Using pressure (bubble pressure method)

The idea of using pressure to balance surface tension was first proposed by Erwin Schrödinger. The principle is based on the maximum pressure that an interface can support. A sketch of the experimental set up is shown in [Figure 2.60](#).

**FIGURE 2.61**

Result of a calculation with Surface Evolver: the surface deforms with increasing pressures, until it reaches a half-sphere.

A tube filled with liquid 1 is plunged into a beaker containing liquid 2. As pressure in liquid 1 is increased, the interface at the tube outlet deforms until it reaches the form of a half-sphere. Above this maximum pressure, the interface blows out and liquid 1 breaks down into droplets flowing through liquid 2. The maximum pressure is related to the surface tension between liquid 1 and liquid 2 by the Laplace's relation

$$P = 2 \frac{\gamma_{\text{L1L2}}}{R_{\text{tube}}} \quad (2.75)$$

This value can be found numerically by using the Surface Evolver software ([Figure 2.61](#)). We have used a capillary tube of 100 μm radius so that the gravity force does not introduce a bias in the result. Using a surface tension value of 72 mN/m (water in air), we find a maximum critical pressure of 1440 Pa, which is the value expected from [Eq. \(2.75\)](#).

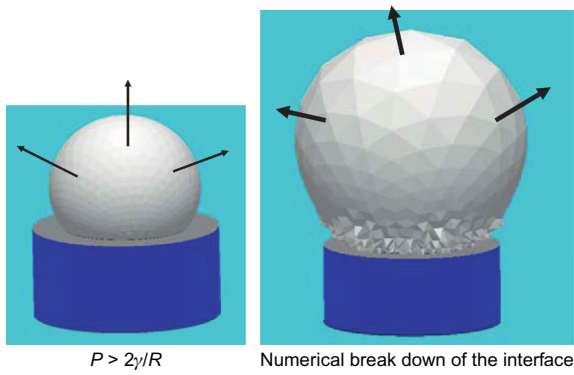
Remark: Theoretically, when the pressure is increased above the value defined by [Eq. \(2.71\)](#), the interface is no longer stable. It expands suddenly ([Figure 2.62](#)) and breaks down. Physically, it corresponds to the instability of the interface and the formation of droplets.

Experimentally, the maximum pressure before the interface breaks is difficult to determine very precisely. This is the reason why other methods of measuring surface tension have been developed.

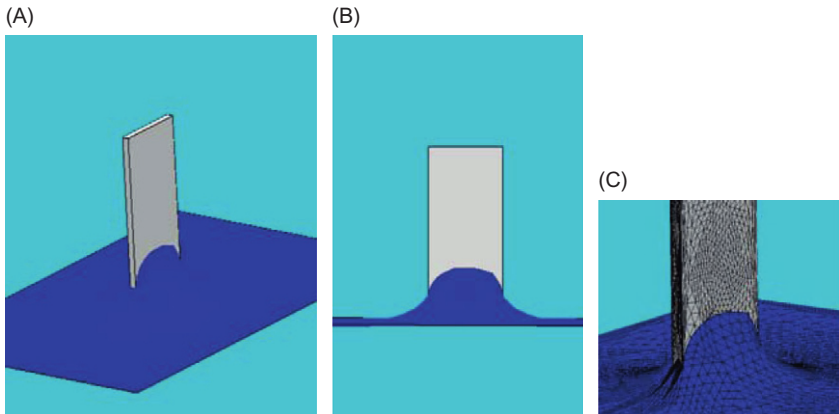
2.8.2 Using the capillary rise on a plate—Wilhelmy plate

Surface tension of a liquid can be determined by measuring the capillary force exerted by the liquid on a solid plate. The principle is that already described in [Section 2.7.3](#): the surface of the liquid rises along a vertical plate and the height reached by the liquid on the plate is proportional to the surface tension as shown in [Eq. \(2.58\)](#).

In the standard method, a thin plate (perimeter about 40 mm) is lowered to the surface of a liquid and the downward force directed to the plate is measured.

**FIGURE 2.62**

Above the threshold value $P = 2\gamma_{L1L2}/R_{\text{tube}}$ the interface is no longer stable; it starts expanding and breaks down.

**FIGURE 2.63**

Simulation of the capillary rise along a Wilhelmy plate using the Surface Evolver software: (A) perspective view, (B) front view, and (C) close up on the contact line in the angle.

Surface tension is directly the force divided by the perimeter of the plate. A couple of very important points with this method must be noted. First, the plate must be completely wetted before the measurement to ensure that the contact angle between the plate and the liquid is zero. If this is not true, the Wilhelmy method is not valid. Second, one must be sure that the position of the plate is correct, meaning that the lower end of the plate is exactly on the same level as the surface of the liquid. Otherwise, the buoyancy effect must be calculated separately. Figure 2.63 shows a numerical simulation of the Wilhelmy method.

2.8.3 Using gravity: the pendant drop method

By definition, a pendant drop is a drop suspended from a fixed solid, as shown in [Figure 2.64](#).

The two forces acting on the drop are gravitation and surface tension. The shape of such a drop is then a function of the surface tension ([Figure 2.65](#)). The pendant drop method consists of extracting the surface tension from an image of the drop shape.



FIGURE 2.64

Image of a pendant drop.

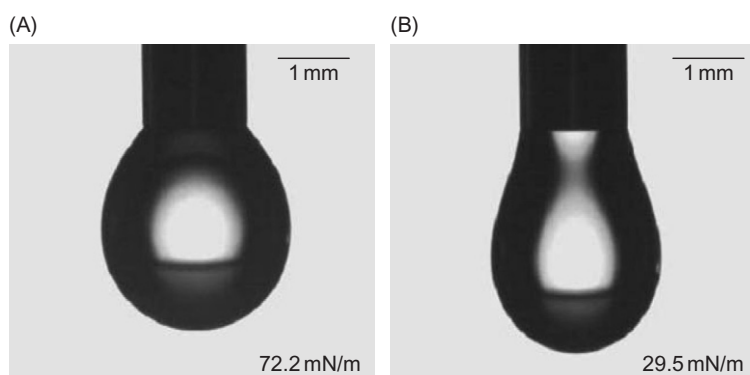


FIGURE 2.65

Experimental view of two drops: (A) water droplet in air and (B) oil droplet in air.

2.8.3.1 Bond number

For a pendant drop, the ratio of the gravitational and surface tension forces is scaled by a dimensionless number, the Bond number, defined by:

$$Bo = \frac{\Delta\rho g R^2}{\gamma}, \quad (2.76)$$

where $\Delta\rho$ is the difference of the density of the liquid and the surrounding fluid, g is the gravitational constant, γ is the surface tension, and R is a typical dimension of the droplet. Here, we choose R to be the maximum horizontal radius of the pendant drop. The shape of the pendant drop is shown in [Figure 2.66](#) for different Bond numbers.

[Figure 2.66](#) shows that, for a well-chosen Bond number, the competition between the gravitational force and the surface tension determines the shape of the droplet. On one hand, the gravitational force, i.e., the weight of the drop, tends to elongate the droplet vertically; on the other hand, the surface tension tends to minimize the interface by making it spherical. From an image analysis, the volume—and consequently the weight—of the drop can be determined, and also a vertical profile which is a function of the surface tension and the weight of the drop ([Figure 2.67](#)) can be found. In the following section, the numerical approach used to determine the surface tension is detailed.

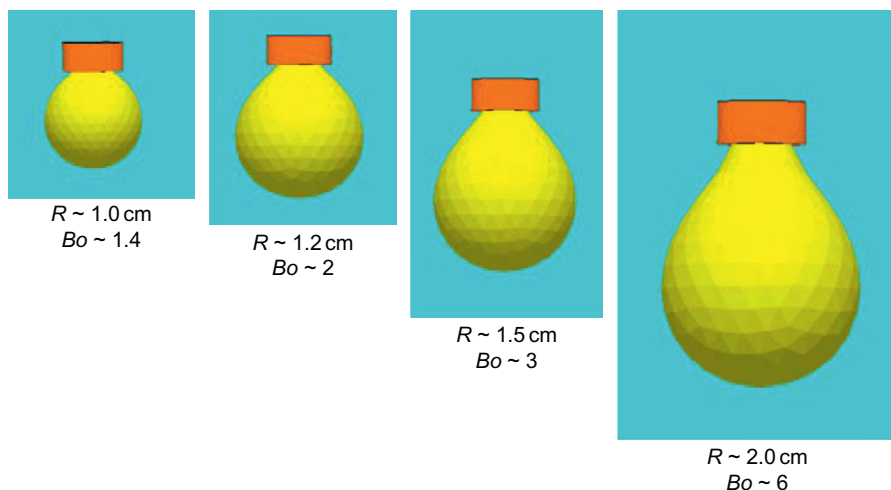
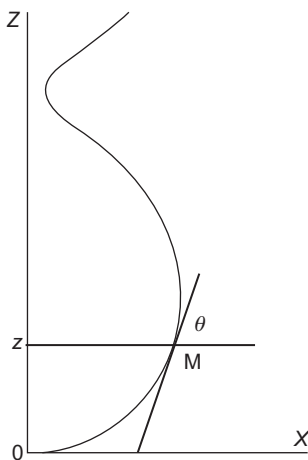


FIGURE 2.66

Shape of a pendant drop versus bond number: the drop shape departs from that of a sphere when its volume increases, until it detaches from the solid support. The liquid of the drop is water and is immersed in silicone oil; the surface tension is $\gamma = 33 \text{ mN/m}$. Calculation performed with Surface Evolver software.

**FIGURE 2.67**

Typical drop contour in the pending drop method.

2.8.3.2 Method

There exist different numerical schemes to extract the surface tension from the pendant drop shape. A well-known software is that pioneered by del Rio and Neumann [37] called ADSA (Axisymmetric Drop Shape Analysis). We do not give here the details of the method—which would be long—but just the main lines.

The drop pressure is determined by writing the Laplace's equation at the bottom of the droplet. Due to axisymmetry

$$\Delta P = \gamma \left(\frac{1}{R} + \frac{1}{R'} \right) = \frac{2\gamma}{R}. \quad (2.77)$$

The curvature radius being derived from an image analysis, Eq. (2.77) produces the internal pressure of the drop.

Second, we write the equilibrium equation of the drop in any horizontal section. Because of axisymmetry, this equilibrium imposes a zero vertical resultant

$$2\pi R\gamma \sin \theta = V(\rho_h - \rho_l)g + \pi R^2 P. \quad (2.78)$$

In Eq. (2.78), R is the horizontal radius in the considered section, θ is the angle of the tangent at M to the contour of the image of the drop, V is the volume of the fluid under the plane of altitude z , ρ_h and ρ_l are the densities of the two fluids, and g is the gravitational acceleration. The left-hand side term in Eq. (2.78) corresponds to the surface tension force; the first term to the right-hand side, to the weight of the liquid below the considered section; and the second term to the right-hand side to the pressure force. For each section, Eq. (2.78) produces a value for the surface tension γ . An averaging of all the values of γ determines precisely the real value of the surface tension.

Because the pendant drop method reacts very quickly, it is even possible to determine the surface tension as a function of the surface concentration in surfactants [38]. When CMC is reached, the shape of the drop does not evolve any more.

In conclusion, the advantages of the pendant drop method are the following:

- small volume of liquid,
- easy to spread a known amount of surfactant at the surface, and
- rapid rates of surface area change compared to Langmuir–Wilhelmy balance.

However, one must be very careful that the capillary is very smooth and cylindrical to preserve axisymmetry.

2.8.4 Using shear stress in a microflow

Hydrodynamic forces are usually difficult to control and to monitor accurately. However, the situation has changed drastically with the use of microflows. Such flows are completely laminar and their velocity is largely predictable [39]. With this in mind, and observing that a droplet/bubble changes its shape according to the change in the flow mean velocity, a method for measuring surface tensions between two immiscible liquids or between a liquid and a gas has been proposed [40,41]. The principle is sketched in Figure 2.68.

An experimental view of the phenomenon is shown in Figure 2.69. A droplet traveling in the middle of the tube exerts a very small shear stress. However, when it reaches a constricted section, the flow accelerates and the shear stress increases. As a result, the droplet takes an ellipsoidal shape oriented along the axis of the tube. At the entrance of the divergent section, the shear stress acts oppositely and the droplet takes an ellipsoidal shape oriented perpendicularly to the tube axis. After a while, the spherical shape is regained.

Let us define the drop deformation by:

$$D = \frac{a - b}{a + b}, \quad (2.79)$$

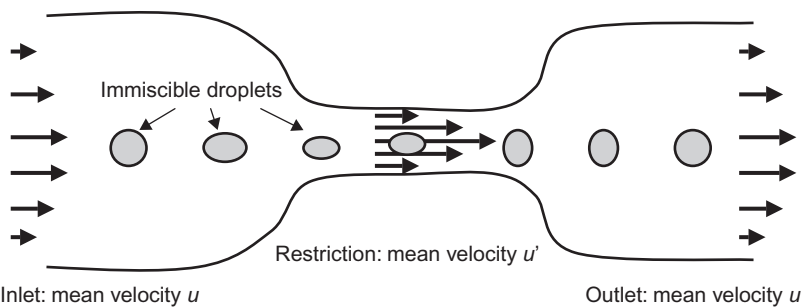
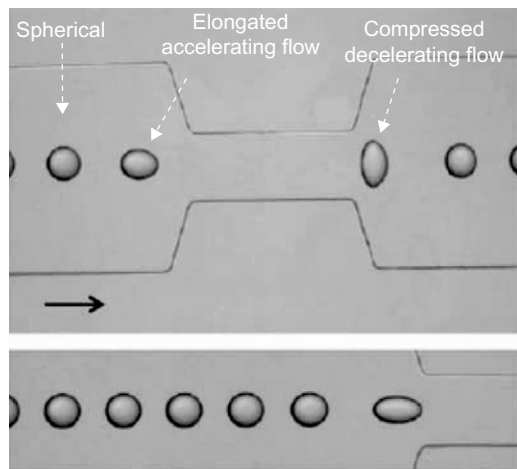


FIGURE 2.68

Schematic of droplet stretching in a contracted section for surface tension measurement.

**FIGURE 2.69**

Experimental image of droplets in accelerated and decelerated fluid flows.

Source: From Ref. [41], reproduced by permission of the Royal Society of Chemistry.

where a and b are the two vertical dimensions of the droplet. When the droplet is spherical $D = 0$. Let $\dot{\varepsilon}$ be the extension rate given by the change of axial velocity u

$$\dot{\varepsilon} = \frac{du}{dx}.$$

Then, it can be shown that D is given by the solution of the differential equation

$$\frac{dD}{dt^*} = \frac{5}{2\hat{\eta} + 3} \tau \dot{\varepsilon} - D, \quad (2.80)$$

where t^* is a nondimensional time defined by $t^* = t/\tau$, and $\hat{\eta} = \eta_{\text{drop}}/\eta_{\text{carrier}}$ and η denotes the dynamic viscosity. Finally, τ is defined by:

$$\tau = \frac{\alpha \eta_c a_0}{\gamma},$$

where a_0 is the undistorted radius and α is a rational function of $\hat{\eta}$. Instead of solving Eq. (2.80), it is convenient to rewrite it under the form

$$\alpha \eta_c \left[\frac{5}{2\hat{\eta} + 3} \dot{\varepsilon} - u \frac{\partial D}{\partial x} \right] = \gamma \frac{D}{a_0}. \quad (2.81)$$

D and its axial evolution $\partial D/\partial x$ are estimated by image analysis. Then, a plot of the quantity $\alpha \eta_c [5/2\hat{\eta} + 3\dot{\varepsilon} - u\partial D/\partial x]$ as a function of D/a_0 is a linear curve with slope γ . Figure 2.70 shows experimental results of the method.

This microfluidic tensiometer is particularly interesting, because it produces the instantaneous surface tension on line.

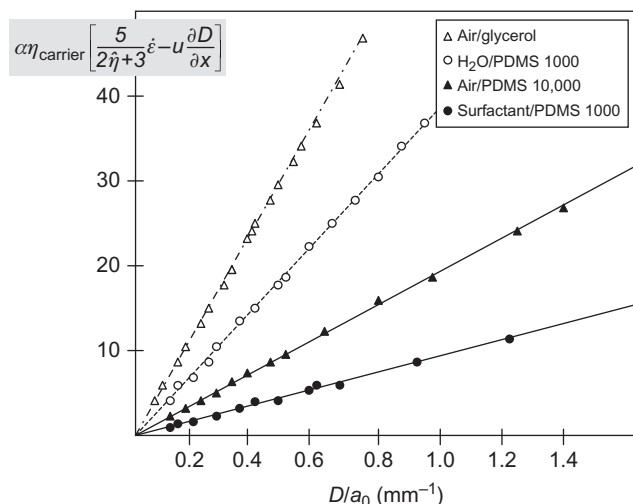


FIGURE 2.70

Plot of the flow extension rate versus the droplet deformation. The slope is the surface tension.

Source: From Ref. [41], reproduced by permission of the Royal Society of Chemistry.

2.9 Surface tension of solids

2.9.1 Introduction

In the preceding sections, the concept of surface tension of solids has been extensively used in Young's law. However, surface tension of solids is a complex notion; on one hand, it is very difficult to measure intrinsically, and on the other hand, different analytical relations have been proposed, but their results are still not completely satisfactory [42]. In our microfluidic approach, we will avoid as much as possible having to use surface tension of solids. We shall use Young's law as soon as it is possible to eliminate the solid surface tension, and make our approaches depend on only two values: γ_{LG} and θ . Still we present the notion of *surface free energy* (SFE) and in particular the notion of *critical surface tension* (CST) that is important for wetting analysis.

2.9.2 Surface free energy

2.9.2.1 Method of Good—Girifalco

The approach of Good and Girifalco [43] consists in expressing the work of adhesion in terms of γ_{LG} and γ_S

$$W_a = 2\Phi(\gamma_{LG}\gamma_S)^{1/2}, \quad (2.82)$$

where Φ is a function of the molar volumes of the liquid and the solid. Inserting Eq. (2.82) in the Young–Dupré's relation (2.51) yields

$$W_a = 2\Phi(\gamma_{LG}\gamma_S)^{1/2} = \gamma_{LG}(1 + \cos \theta) \quad (2.83)$$

leading to

$$\gamma_S = \gamma_{LG} \frac{(1 + \cos \theta)^2}{4\Phi^2}. \quad (2.84)$$

The remaining problem is to estimate Φ . Kwok and Neumann [44] made a systematic study of the contact between organic fluids and low energy surfaces. They based their approach on a dependency of the type

$$\Phi = e^{-\beta(\gamma_{LG} - \gamma_S)^2} \approx 1 - \beta(\gamma_{LG} - \gamma_S)^2, \quad (2.85)$$

where β is a constant slightly depending on the substrate. Substitution of Eq. (2.85) in Eq. (2.83) and using Young's law yields

$$\cos \theta = -1 + 2 \sqrt{\frac{\gamma_S}{\gamma_{LG}} e^{-\beta(\gamma_{LG} - \gamma_S)^2}}.$$

For any given substrate, γ_S is constant, and by using many different liquids and measuring γ_{LG} and θ , a least-squares analysis leads to the values of β and γ_S . The parameter β was found to be of the order of 0.000100 – 0.000130 (m^2/mJ)² for low energy substrate such as polystyrene and polymethacrylate.

2.9.2.2 Fowkes method

The preceding approach does not take into consideration the polar or apolar nature of the solid. The different components of the surface energy can be taken into account by writing [45]

$$\gamma_S = \gamma_S^D + \gamma_S^P, \quad (2.86)$$

where the superscripts D and P respectively stand for “diffusive” (nonpolar) and polar. Neumann's approach [46] consists in subdividing the polar component into a Lewis acid and a Lewis base, so that the work of adhesion can be cast under the form

$$W_a = \gamma_{LG}(1 + \cos \theta) = 2(\gamma_{LG}^D \gamma_S^D)^{1/2} + 2(\gamma_{LG}^- \gamma_S^-)^{1/2} + (\gamma_{LG}^+ \gamma_S^+)^{1/2}. \quad (2.87)$$

Equation (2.87) contains eight parameters. The contact angle θ can be measured, and the properties of the liquid are also known (they can be measured). Then, we are left with three unknowns describing the solid. If we first use a nonpolar liquid ($\gamma_{LG}^+ = \gamma_{LG}^- = \gamma_{LG}^P = 0$), then (2.87) simplifies to

$$\gamma_{LG}(1 + \cos \theta) = 2(\gamma_{LG}^D \gamma_S^D)^{1/2}$$

and we deduce γ_s^D . More generally, if we use three liquids—including a nonpolar one—we find a system of three equations with the three unknowns $(\gamma_s^D, \gamma_s^-, \gamma_s^+)$. The total solid surface tension is then given by the relation

$$\gamma_s = \gamma_s^D + \gamma_s^P = \gamma_s^D + 2(\gamma_s^+ \gamma_s^-)^{1/2}. \quad (2.88)$$

A very instructive example has been given by Combe et al. [47] for measuring the surface tension of the enamel of human teeth.

2.9.3 CST and SFE

A very general question in capillary studies is: would a given liquid completely wet a given solid or not? In other words, what is the condition for spreading? Zisman and coworkers [48] pioneered this problem in the 1950s, with the introduction of the notion of “critical surface tension,” denoted here CST for simplicity, and defined by the proposition: a solid surface cannot be completely wetted by a liquid if the value of the liquid surface tension is above the CST.

2.9.3.1 Zisman plot

Zisman [48] established an empirical connection between the cosine of the contact angle $\cos \theta$ and the liquid–air interfacial tension γ . For a given low energy solid surface, they measured the contact angle θ for many different liquids. The plot of $\cos \theta$ as a function of γ is approximately a straight line; it has the shape shown in Figure 2.71.

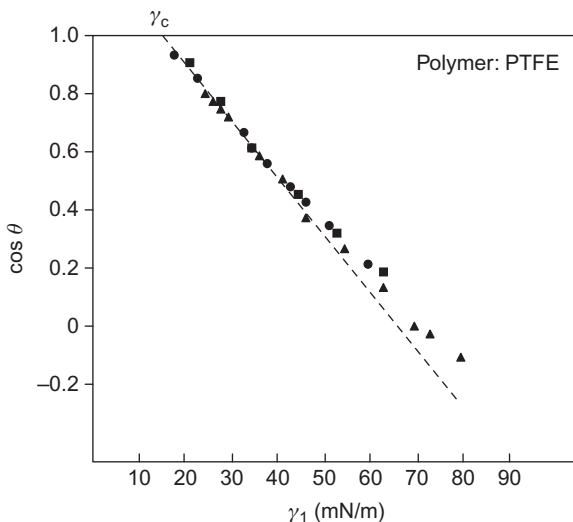


FIGURE 2.71

Zisman plot of the contact angle of different liquids on a polytetrafluoroethylene (PTFE) surface.

When the contact angle is such that $\cos \theta = 1$, i.e., $\theta = 0$, the liquid wets the solid surface. If we note γ_C the point where $\cos \theta = 1$, obtained by a linear extrapolation of Zisman's curves, then a liquid with a surface tension smaller than γ_C wets the surface. As a matter of fact, this nearly linear behavior is valid not only for pure liquids, but also for aqueous solutions.

Zisman's approach was later refined by Bargeman and van Voorst Vader [49]. Observing that the Zisman's curves were not exactly linear, especially for aqueous solutions, they have shown that linearity could be achieved by considering the relation between $\gamma \cos \theta$ and γ instead of the relation between $\cos \theta$ and γ (Figure 2.72).

In summary, there is a linear relation between adhesion tension and surface tension of aqueous solutions

$$\gamma_{LG} \cos \theta = a\gamma_{LG} + b, \quad (2.89)$$

where a and b are constants depending on the solid surface.

Zisman's approach is very practical; it easily produces the value of the CST. It has been observed that the value of the CST is often close to that of the surface tension of the solid, i.e., the SFE. For a liquid whose surface tension approaches the CST, Young's law can be written

$$\gamma_{LG} = \gamma_C = \gamma_{SG} - \gamma_{SL}. \quad (2.90)$$

In partial wetting conditions, there is a precursor film on the solid substrate; this is evidently the case at the onset of total wetting. This precursor film has a film pressure P_e^* (we discuss the film pressure in the next section) so that the surface tension γ_{SG} is given by:

$$\gamma_S - P_e^* = \gamma_{SG}. \quad (2.91)$$

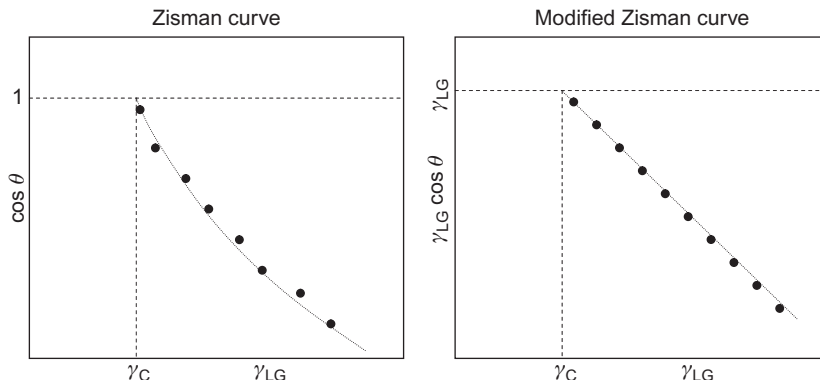


FIGURE 2.72

Modified Zisman's plot for polymethyl methacrylate (PMMA) and PTFE.

And Eq. (2.90) can be cast under the form

$$\gamma_s = \gamma_c + (\gamma_{SL} + P_e^*). \quad (2.92)$$

For a liquid having a surface tension γ_c , the term inside the parentheses on the right-hand side of Eq. (2.92) is often small [13]. This is, in particular, the case when the solid surface is apolar, i.e., the polar component of the SFE is negligible. For example, PMMA has a CST of 33.1 mN/m and an SFE of 39 mN/m; PTFE has a CST of 20 mN/m and an SFE of 23.4 mN/m. In such cases, the CST is a good approximation of the SFE. The advantage is that the CST can easily be obtained by Zisman plots.

2.9.3.2 Disjoining pressure

2.9.3.2.1 Definition

When a liquid film on a solid is very thin (like the precursor film), all the liquid molecules have an interaction with the solid wall, as sketched in Figure 2.73. We are then at a very small scale (less than 1 nm). The energy of the film takes a special form. For a thick film, the energy is $\gamma + \gamma_{SL}$. For a thin film of thickness e the film energy is [23]

$$E = \gamma + \gamma_{SL} + P_e(e), \quad (2.93)$$

where $P_e(e)$ is a function of e such that $P_e(\infty) = 0$ and $P_e(0) = \gamma_s - (\gamma + \gamma_{SL})$.

From a thermodynamic point of view, Derjaguin [50] has introduced the notion of “disjoining pressure” in the chemical potential

$$\mu = \mu_0 + \frac{dP_e}{de} v_0 = \mu_0 - \Pi_e v_0, \quad (2.94)$$

where v_0 is the molar volume in the liquid phase. The quantity Π_e in Eq. (2.94) defined by:

$$\Pi_e = -\frac{dP_e}{de} \quad (2.95)$$

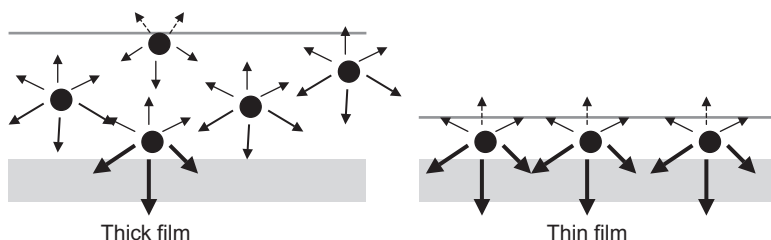


FIGURE 2.73

In a thin film, all the molecules in the liquid interact with molecules of the solid wall.

has the dimension of a pressure. Π_e is called the “disjoining pressure.” With this definition, and using Eq. (2.92), de Gennes [24] shows that the total surface tension of a thin film is given by:

$$\gamma_{\text{film}} = \gamma_{\text{LG}} + \gamma_{\text{SL}} + P_e + e\Pi_e. \quad (2.96)$$

2.9.3.2.2 Example

Bubbles and droplets at equilibrium tend to take a spherical shape. If this were not the case, the internal pressure would not be uniform, since Laplace’s law applied in regions of different curvatures would produce different internal pressures. In consequence, there is liquid motion inside the bubble/droplet in order to equilibrate the internal pressure (Figure 2.74).

But what about adjacent droplets or bubbles? The sketch of Figure 2.74 shows that a droplet is deformed by the presence of the neighboring droplet and its curvature is not constant. A first analysis using Laplace’s law would conclude that the internal pressure is not uniform. In reality, the pressure in the thin film between the droplets/bubbles is not the external pressure P_0 but a different pressure related to the “disjoining pressure.” According to the Laplace’s equation, the film pressure equilibrates the pressure jump across the interface, and we have the relations

$$\begin{aligned} \Delta P_1 &= \gamma \left(\frac{1}{R_1} + \frac{1}{R'_1} \right) = P - P_0 \\ \Delta P_2 &= \gamma \left(\frac{1}{R_2} + \frac{1}{R'_2} \right) = P - P_i, \end{aligned} \quad (2.97)$$

where indices 1 and 2 refer to two locations, a first one far from the deformed interface and the other close to the deformed interface. In Eq. (2.97), P_i is the film pressure.

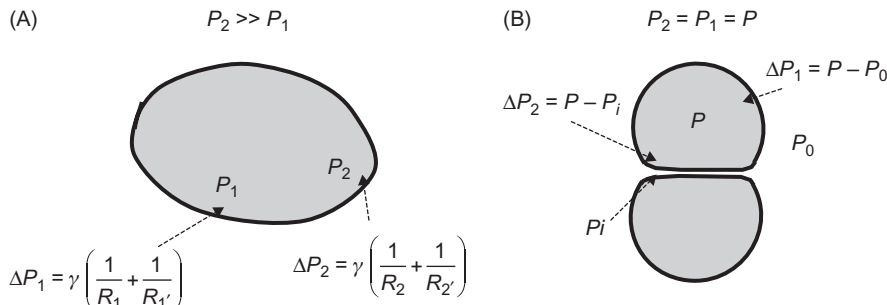


FIGURE 2.74

(A) Schematic of a droplet outside equilibrium and (B) an assembly of two droplets/bubbles at equilibrium.

2.10 Minimization of the surface energy and minimal energy surface

2.10.1 Minimal surfaces

Minimal surfaces are a particular type of surface. From a mathematical standpoint, a minimal surface is a surface with zero mean curvature. This definition is very restrictive: there are not many surfaces that are minimal surfaces. One can find a description of these surfaces in Ref. [51]. These surfaces locally minimize their area. In the domain of physics of liquid interfaces, we have already seen an example of a minimal surface in Section 2.3.2.4 with the surface of a liquid rising along a cylindrical vertical tube (Figure 2.75).

Another example of minimal surface is that of the catenoid (Figure 2.76). Physically, a catenoid is the surface formed by a liquid film maintained by two solid circles.

It is a general thermodynamic principle in physics that systems evolve to their minimal energy level. In particular, this is the case of interfaces. Surfaces of droplets in static equilibrium have a minimal free energy. Thus, in the domain of liquid interfaces, we are tempted to give a less restrictive definition for minimal surfaces. A minimal surface is a surface that minimizes its area under some constraints. The goal is to minimize the energy of the system (surface, gravitational, etc.) under some constraints imposed by external conditions, like walls, wires, fixed volume, or fixed pressure. With this definition, minimal surfaces comprise a much larger set of surfaces and describe liquid films and interfaces [36]; when gravity is negligible, these surfaces have a constant mean curvature [52].

Note that “minimal surfaces” present a general interest, not only in the domain of microfluidics. For example, they have a great appeal in architecture and arts. The “Cloud Gate” sculpture of Anish Kapoor in downtown Chicago is having a huge success and has been adopted by the public as the new symbol of Chicago

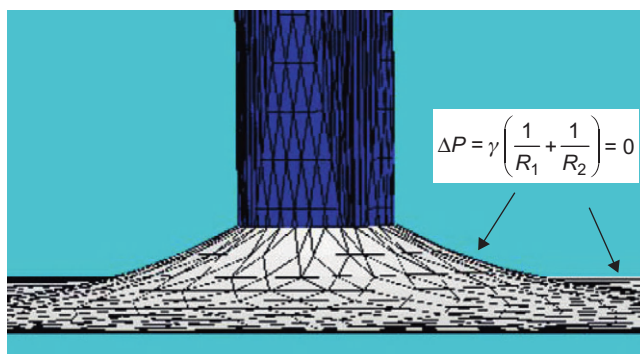
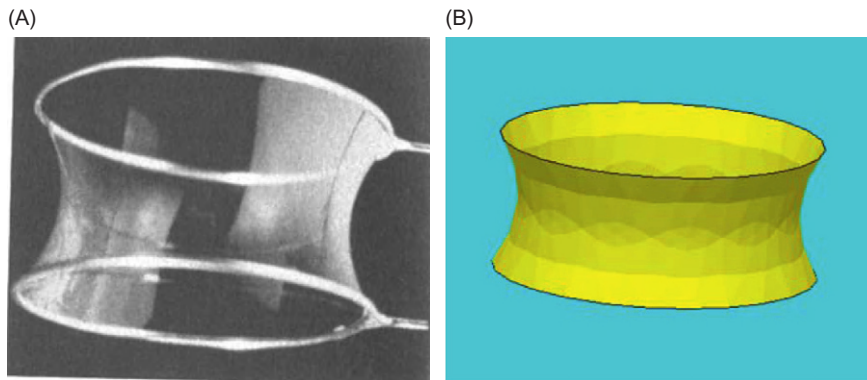
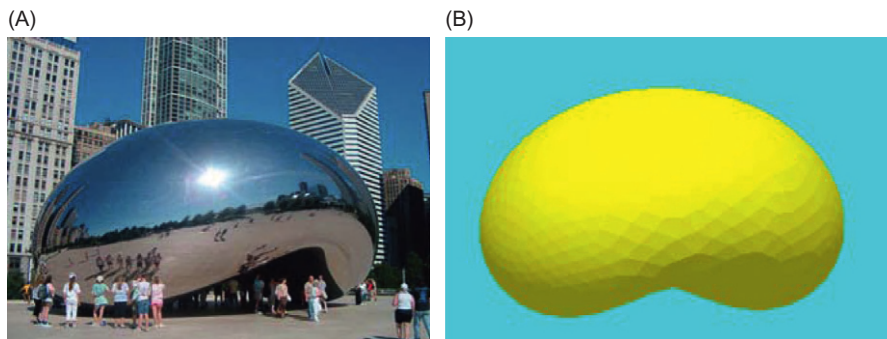


FIGURE 2.75

Minimal surface formed by the interface of a liquid with a vertical rod.

**FIGURE 2.76**

(A) Image of a soap film between two solid circles and (B) result of the calculation with the Surface Evolver software.

**FIGURE 2.77**

(A) Striking example of minimal surfaces in architecture: the “Cloud Gate” sculpture by Anish Kapoor in the Millennium Park of Chicago. (B) Calculation of a similar surface with the Surface Evolver numerical software.

(Figure 2.77). It can be shown that it is a minimal surface—in the extended sense—corresponding to the magnification of a droplet sitting on a solid cylinder.

2.10.2 Minimization of the surface energy

According to the extended definition of a minimal surface, the droplet interface can be calculated by minimization of its surface energy. In the absence of a droplet on the surface of the solid substrate, the surface energy is

$$E_{SG,0} = \gamma_{SG} S_{SG,0}. \quad (2.98)$$

After deposition of the droplet, the surface energy is the sum of the three surface energies

$$E = E_{LG} + E_{SL} + E_{SG,1}, \quad (2.99)$$

where $E_{SG,1}$ is the surface energy of the solid surface in contact with the gas. Then, we have

$$E = \gamma_{LG}S_{LG} + \int_S \int_{SL} (\gamma_{SL} - \gamma_{SG})dA + E_{SG,0}. \quad (2.100)$$

The last term to the right-hand side of Eq. (2.96) does not depend on the drop shape. Thus, we have to minimize

$$E = \gamma_{LG}S_{LG} + \int_S \int_{SL} (\gamma_{SL} - \gamma_{SG})dA. \quad (2.101)$$

Taking into account Young's law, the energy to be minimized is [22,53]

$$E = \gamma_{LG}S_{LG} - \gamma_{LG} \int_S \int_{SL} \cos \theta dA. \quad (2.102)$$

As mentioned earlier, the parameters intervening in Eq. (2.102) are θ and γ_{LG} . Thanks to Young's equation, we do not need the surface tension of the solid with the liquid or the gas. This is a real simplification, since we have shown that θ and γ_{LG} can be measured relatively easily.

Equation (2.102) constitutes the basis for the calculation of droplet shapes that we develop in Chapter 3.

2.11 Summary

This chapter was devoted to the study of surface tensions and capillary forces. The main notions presented in this chapter are the relation between curvature and pressure expressed by Laplace's law, and the relation between the different surface tensions and contact angle at the triple line expressed by Young's law. From these two relations, an expression for the capillary force on a triple line has been deduced. Such an expression has a key role in determining the behavior of droplets on different substrates and geometry in microsystems that we shall consider in Chapter 3.

This chapter has shown the essential role of surface tension and capillarity at the microscale. These forces often screen out forces like gravity or inertia that are predominant at the macroscopic scale. Although we have taken the stance of presenting capillarity and surface tension from an engineering point of view by considering global effects, one has to keep in mind that interactions at the nanoscopic scale are the real underlying causes of these global effects.

References

- [1] R. Steger, B. Bohl, R. Zengerle, P. Koltay, The dispensing well plate: a novel device for nanoliter liquid handling in ultra high-throughput screening, *J. Assoc. Lab. Autom.* 9 (2004) 291–299.
- [2] J. Zeng, M. Deshpande, H.-C. Kan, J.R. Gilbert, A dynamic spotting method for SPLIT-PIN based microarrays. *Micro Total Analysis (MicroTas) Conference*, Monterey, Ca, USA, 2001.
- [3] Rain Dance Technology. <<http://www.raindancetechnologies.com/tech.html>>.
- [4] S. Okushima, T. Nisisako, T. Torii, T. Higuchi, Controlled production of monodisperse double emulsions by two-step droplet breakup in microfluidic devices, *Langmuir* 20 (2004) 9905–9908.
- [5] B. Zheng, J.D. Tice, L.S. Roach, R.F. Ismagilov, A droplet-based, composite PDMS/glass capillary microfluidic system for evaluating protein crystallization conditions by micro-batch and vapor-diffusion methods with on-chip X-ray diffraction, *Angew. Chem. Int. Ed. Engl.* 43 (2004) 2508–2511.
- [6] J. Atencia, D.J. Beebe, Controlled microfluidic interfaces, *Nature* 437 (2005) 648–654.
- [7] J.N. Israelachvili, *Intermolecular and Surface Forces*, Academic Press, London, 1992.
- [8] Table of surface tension for chemical fluids, 2006. <<http://www.surface-tension.de/>>.
- [9] G. Navascués, Liquid surfaces: Theory of surface tension, *Rep. Prog. Phys.* 42 (1979) 1133–1183.
- [10] R. Eötvös, *Wied. Ann. Phys.* 27 (1886) 445–459.
- [11] E.A. Guggenheim, The principle of corresponding states, *J. Chem. Phys.* 13 (1945) 253–261.
- [12] A. Alexeev, T. Gambaryan-Roisman, P. Stephan, Marangoni convection and heat transfer in thin liquid films on heated walls with topography: Experiments and numerical study, *Phys. Fluids* 17 (2005) 062106.
- [13] K. Szymczyk, A. Zdiennicka, B. Janczuk, W. Wocik, The wettability of polytetrafluoroethylene and polymethyl methacrylate by aqueous solution of two cationic surfactants mixture, *J. Colloid Interface Sci.* 293 (2006) 172–180.
- [14] MIT, Lecture 4, Marangoni flows, 2008. <<http://web.mit.edu/1.63/www/Lec-notes/Surfacetension/Lecture4.pdf>>.
- [15] E. Weisstein, 2012. <<http://mathworld.wolfram.com/Curvature.html>>.
- [16] L.M. Pismen, B.Y. Rubinstein, I. Bazhlekov, Spreading of a wetting film under the action of van der Waals forces, *Phys. Fluids* 12 (3) (2000) 480–483.
- [17] P.G. de Gennes, Wetting: statistics and dynamics, *Rev. Mod. Phys.* 57 (1985) 827.
- [18] A.L. Yarin, A.G. Yazicioglu, C.M. Megaridis, Thermal stimulation of aqueous volumes contained in carbon nanotubes: experiment and modelling, *Appl. Phys. Lett.* 86 (2005) 013109.
- [19] C. Iwamoto, S. Tanaka, Atomic morphology and chemical reactions of the reactive wetting front, *Acta Mater.* 50 (2002) 749.
- [20] Nanolane, 2012. <<http://www.nano-lane.com/wetting-afm.php>>.
- [21] L. Pismen, Dewetting patterns, moving contact lines, and dynamic diffuse interfaces, *CISM lecture notes*, 16–20 October 2006, Udine, Italy.
- [22] J. Berthier, Ph. Clementz, O. Racourt, P. Claustre, C. Peponnet, Y. Fouillet, Computer aided design of an EWOD microdevice, *Sens. Actuators A* 127 (2006) 283–294.

- [23] K. Brakke, The surface evolver, *Exp. Math.* 1 (1992) 141.
- [24] P.G. de Gennes, F. Brochart-Wyart, D. Quéré, *Drops, Bubbles, Pearls and Waves*, Springer, New York, 2005.
- [25] A.A. Darhuber, S.M. Troian, Principles of microfluidic actuation by modulation of surface stresses, *Annu. Rev. Fluid Mech.* 37 (2005) 425–455.
- [26] L.A. Taber, S. Ng, A.M. Quesnel, J. Whatman, C.J. Carmen, Investigating Murray’s law in the chick embryo, *J. Biomech.* 34 (1) (2001) 121–124.
- [27] C.D. Murray, The physiological principle of minimum work. 1. The vascular system and the cost of blood volume, *Proc. Natl. Acad. Sci. U.S.A.* 12 (1926) 207–214.
- [28] K.A. Mc Culloh, J.S. Sperry, F.R. Adler, Water transport in plants obeys Murray’s law, *Nature* 421 (2003) 939–942.
- [29] H.D. Prange, Laplace’s law and the alveolus: a misconception of anatomy and a misapplication of physics, *Adv. Physiol. Educ.* 27 (2003) 34–40.
- [30] J.Y. Wang, S. Betelu, B.M. Law, Line tension approaching a first-order wetting transition: experimental results from contact angle measurements, *Phys. Rev. E* 63 (2001) 031601-1–031601-10.
- [31] X.H. Zhang, X.D. Zhang, S.T. Lou, Z.X. Zhang, J.L. Sun, J. Hu, Degassing and temperature effects on the formation of nanobubbles at the mica/water interface, *Langmuir* 20 (9) (2004) 3813–3815.
- [32] J. Drehlich, The significance and magnitude of the line tension in three-phase (solid–liquid–fluid) systems, *Colloids Surf. A Physicochem. Eng. Asp.* 116 (1996) 43–54.
- [33] D.L. Hu, J.W.M. Bush, Meniscus-climbing insects, *Nature* 437 (2005) 733–736.
- [34] Y. Tsori, Discontinuous liquid rise in capillaries with varying cross-sections, *Langmuir* 22 (2006) 8860–8863.
- [35] Jun Zeng, T. Korsmeyer, Principles of droplet electrohydrodynamics for lab-on-a-chip, *Lab Chip* 4 (2004) 265–277.
- [36] J. Berthier, Ph. Dubois, Ph. Clementz, P. Claustre, C. Peponnet, Y. Fouillet, Actuation potentials and capillary forces in electrowetting based microsystems, *Sens. Actuators A Phys.* 134 (2) (2007) 471–479.
- [37] O.I. del Rio, A.W. Neumann, Axisymmetric drop shape analysis: Computational methods for the measurement of interfacial properties from the shape and dimensions of pendant and sessile drops, *J. Colloid Interface Sci.* 196 (1997) 134–147.
- [38] H.A. Wege, J.A. Holgado-Terriza, M.J. Galvez-Ruiz, M.A. Cabrerizo-Vilchez, Development of a new Langmuir-type pendant drop film balance, *Colloids Surf. B Biointerfaces* 12 (1999) 339–349.
- [39] J. Berthier, P. Silberzan, *Microfluidics for Biotechnology*, Artech House, Norwood, MA, 2005.
- [40] S.D. Hudson, J.T. Cabral, W.J. Goodrum Jr., K.L. Beers, E.J. Amis, Microfluidic interfacial tensiometry, *Appl. Phys. Lett.* 87 (2005) 081905.
- [41] J.T. Cabral, S.D. Hudson, Microfluidic approach for rapid multicomponent interfacial tensiometry, *Lab Chip* 6 (2006) 427–436.
- [42] L. Makkonen, On the methods to determine surface energies, *Langmuir* 16 (2000) 7669–7672.
- [43] R.J. Good, L.A. Girifalco, A theory for estimation of surface and interfacial energies. 3. Estimation of surface energies of solids from contact angle data, *J. Phys. Chem.* 64 (1960) 561–565.
- [44] D.Y. Kwok, A.W. Neumann, Contact angle interpretation in terms of solid surface tension, *Colloids Surf. A Physicochem. Eng. Asp.* 161 (1) (2000) 31–48.

- [45] F.M. Fowkes, Additivity of intermolecular forces at interfaces.1. Determination of contribution to surface and interfacial tensions of dispersion forces in various liquids, *J. Phys. Chem.* 67 (12) (1963) 2538.
- [46] A.W. Neumann, R.J. Good, C.J. Hope, M. Seipal, Equation of state to determine surface tensions of low energy solids from contact angles, *J. Colloid Interface Sci.* 49 (1974) 291–304.
- [47] E.C. Combe, B.A. Owen, J.S. Hodges, A protocol for determining the surface energy of dental materials, *Dent. Mater.* 20 (2004) 262–268.
- [48] W.A. Zisman, Contact angle, wettability and adhesion, *Advances in Chemistry Series*, vol. 43, American Chemical Society, Washington, DC, 1964. p. 1
- [49] D. Bargeman, F. van Voorst Vader, Tensile strength of water, *J. Coll. Sci.* 42 (1973) 467–472.
- [50] A. Adamson, A. Gast, “Physical Chemistry of Surfaces”, 6th edition, John Wiley and Sons Inc., p. 247, 1997.
- [51] Brandeis University, 2010. <http://rsp.math.brandeis.edu/3D-XplorMath/Surface/gallery_m.html>.
- [52] D.E. Hewgill, Computing surfaces of constant mean curvature with singularities, *Computing* 32 (1984) 81–92.
- [53] N.A. Patankar, Y. Chen, Numerical simulation of droplets shapes on rough surfaces, Nanotech 2002. Technical Proceedings of the 5th International Conference on Modeling and Simulation of Microsystems, San Juan, Puerto Rico, USA, 2002, pp. 116–119.

The Physics of Droplets^{*}

3

CHAPTER OUTLINE

3.1 Introduction	77
3.2 The shape of microdrops	77
3.2.1 Sessile droplets	77
3.2.1.1 Height of a “large droplet”: $Bo \gg 1$	79
3.2.1.2 Microscopic drops: $Bo \ll 1$	80
3.2.2 Droplets constrained between two plates	85
3.2.2.1 Shape of a droplet constrained between two horizontal planes	85
3.2.2.2 Curvature radius of the free interface	85
3.2.2.3 Volume of a droplet constrained between two parallel planes and having the same contact angle with both planes	87
3.2.2.4 Free surface of a droplet constrained by two horizontal planes with different contact angles with the two planes	89
3.2.2.5 Droplet constrained by two planes and bounded by a hydrophilic/hydrophobic boundary	90
3.2.3 Droplet at a liquid interface—Neumann’s construction	90
3.2.4 Droplet in a corner	92
3.2.4.1 Concus–Finn relation	94
3.2.4.2 Extended Concus–Finn relation	96
3.2.4.3 Droplet in a wetting/nonwetting corner	97
3.2.5 Droplet in a groove	98
3.2.6 Droplet in a microwell	100
3.2.7 Droplet on striped surface domains	102
3.2.8 Droplet pierced by a microwire (catena)	107
3.3 Drops on inhomogeneous surfaces	108
3.3.1 Wenzel’s law	109
3.3.2 Cassie–Baxter’s law	110
3.3.3 Contact on fabricated surfaces: the transition between the Wenzel and Cassie laws	113

*This chapter was written with the collaboration of Kenneth A. Brakke (Mathematics Department, Susquehanna University, Selinsgrove, PA).

3.3.3.1 <i>Introduction</i>	113
3.3.3.2 <i>Contact angle on a microfabricated substrate: case of hydrophobic contact</i>	115
3.3.3.3 <i>Example of a square lattice</i>	117
3.3.3.4 <i>Superhydrophobicity</i>	119
3.3.3.5 <i>Irregularly patterned and fractal surfaces</i>	120
3.3.3.6 <i>Contact angle on a microfabricated substrate: case of hydrophilic contact</i>	122
3.3.3.7 <i>Conclusion/discussion</i>	123
3.4 Drops moving by capillarity	124
3.4.1 Drop moving over a transition of wettability.....	125
3.4.2 Drop moving uphill	127
3.4.3 Drop moving up a step	128
3.4.4 Drop moving over a gradient of surface concentration of surfactant	129
3.4.5 Conclusion.....	129
3.5 Contact angle hysteresis	130
3.6 Droplet pinning	134
3.6.1 Droplet pinning on a surface defect.....	134
3.6.2 Droplet pinning at a wettability separation line.....	135
3.6.3 Droplet pinning on an edge.....	136
3.7 The effect of surfactants.....	137
3.7.1 Introduction	137
3.7.2 From partial wetting to total wetting	138
3.8 Marangoni convection	138
3.8.1 Marangoni convection due to thermal nonuniformity	139
3.8.2 Marangoni convection due to concentration gradient.....	142
3.8.3 Marangoni convection due to an electric field	143
3.9 Evaporation	144
3.9.1 Evaporation of sessile droplets.....	144
3.9.1.1 <i>Experimental observations</i>	144
3.9.1.2 <i>Theoretical model</i>	146
3.9.1.3 <i>Discussion</i>	150
3.9.2 Evaporation rings.....	151
3.9.3 Evaporation stains	152
3.9.4 Marangoni convection during evaporation	152
3.9.5 The use of droplet evaporation in biotechnology, biology, and nanoassembly	153
3.9.5.1 <i>Drop evaporation as a tool for DNA stretching</i>	154
3.9.5.2 <i>Drop evaporation as a tool for nanoassembly</i>	154
3.9.5.3 <i>Conclusion</i>	156
3.10 Summary	157
References	157

3.1 Introduction

The importance of droplets in microfluidics has been pointed out in the introduction of the preceding chapter, where we presented the principles of capillarity and surface tension effects. This chapter is particularly devoted to the behavior of droplets and microdrops.

In this chapter, the shape of microdrops in different situations typical of microsystems is investigated, assuming that these microdrops are in an equilibrium state, i.e., at rest, or moving at a sufficiently low velocity that the inertial forces can be neglected. Different situations will be examined: sessile droplets deposited on a plate, droplets constrained between two horizontal planes, pendant droplets, droplets on lyophilic strips, in corners and dihedrals, in wells and cusps, etc.

Because microfabricated substrates are not ideally smooth, the microscopic state of the solid substrate that the droplets contact has to be taken into account. Its effect is described by the Wenzel and Cassie laws, and we describe the applications to the case of micropatterned substrates.

In the next section, the effect of capillarity forces on microdrops is investigated, and it is shown how such forces can displace microdrops on smooth surfaces. However, it is shown that such capillarity induced motions can be hindered by hysteresis of contact angle (difference between the advancing and the receding contact angles) and by pinning on the solid surface.

Finally, a focus is made on two very common phenomena occurring when working with microdrops: the Marangoni convection induced by a gradient of surface tension and the evaporation process which applies to volatile liquids such as water in air or organic solvent—octane, benzene—in air.

3.2 The shape of microdrops

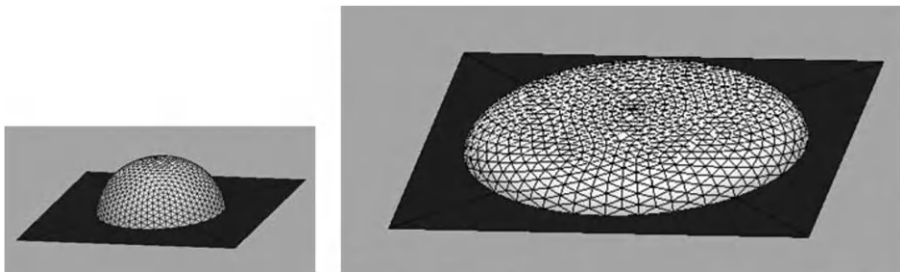
3.2.1 Sessile droplets

It is easily observed that large droplets on horizontal surfaces have a flattened shape, whereas small droplets have a spherical shape (Figure 3.1). This observation is linked to the balance between gravity and surface tension. A microscopic drop is governed solely by surface tension, whereas the shape of a larger droplet results from a balance between the two forces. The scale length of this transition l is the “capillary length”. This length is defined by the ratio of the Laplace pressure—characterizing the size of a microscopic drop—to the hydrostatic pressure [1]. If we compare the two pressures for a drop, we obtain

$$\frac{\Delta P_{\text{Laplace}}}{\Delta P_{\text{hydrostatic}}} \approx \frac{(\gamma/\ell)}{\rho g \ell}, \quad (3.1)$$

**FIGURE 3.1**

Comparison of the shape between microdrops and macrodrops (not to scale): microdrops have the shape of spherical caps, whereas larger drops are flattened by the action of gravity and their height is related to the capillary length.

**FIGURE 3.2**

Numerical simulations of a microdrop ($Bo \ll 1$) and a larger drop ($Bo \gg 1$) obtained with Surface Evolver software (not to scale).

where γ is the surface tension, ρ is the density, and g is the gravitational constant. The two pressures are of the same order when

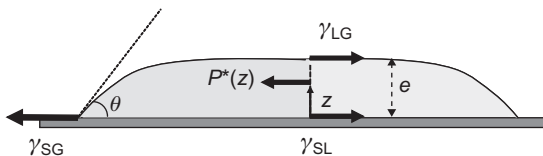
$$\ell \approx \sqrt{\frac{\gamma}{\rho g}} \quad (3.2)$$

ℓ is the capillary length. A drop of dimension smaller than the capillary length has a shape resembling that of a spherical cap. A drop larger than the capillary length is flattened by gravity. A dimensionless number—the Bond number—can be derived from Eq. (3.2) yielding a similar meaning. The Bond number is expressed by:

$$Bo = \frac{\rho g R^2}{\gamma}, \quad (3.3)$$

where R is of the order of the drop radius. If $Bo < 1$, the drop is spherical, or else the gravitational force flattens the drop on the solid surface. A numerical simulation of the two shapes of droplets obtained with the numerical software Surface Evolver [2] is shown in Figure 3.2.

The capillary length is of the order of 2 mm for most liquids, even for mercury. In the following sections, we analyze successively the characteristics of drops having respectively large and small Bond number.

**FIGURE 3.3**

Equilibrium of the forces (per unit length) on a control volume of the drop.

3.2.1.1 Height of a “large droplet”: $Bo \gg 1$

According to the observation of the preceding section, a “large” droplet has a flat upper surface and its shape is shown in Figure 3.3.

Let us calculate the height of such a droplet as a function of contact angle and surface tension. Take the control volume shown in Figure 3.3 and write the balance of the forces that act on this volume [1]. The surface tension contribution is

$$S = \gamma_{SG} - (\gamma_{SL} + \gamma_{LG}). \quad (3.4)$$

And the hydrostatic pressure contribution is

$$P^* = \int_0^e \rho g(e-z)dz = \frac{1}{2}\rho ge^2. \quad (3.5)$$

The equilibrium condition yields $P^* + S = 0$ which results in the relation

$$\frac{1}{2}\rho ge^2 + \gamma_{SG} - (\gamma_{SL} + \gamma_{LG}) = 0. \quad (3.6)$$

Recall that Young’s law imposes a relation between the surface tensions

$$\gamma_{SG} - \gamma_{SL} = \gamma_{LG} \cos \theta. \quad (3.7)$$

Upon substitution of Eq. (3.7) into Eq. (3.6), we obtain

$$\gamma_{LG}(1 - \cos \theta) = \frac{1}{2}\rho ge^2.$$

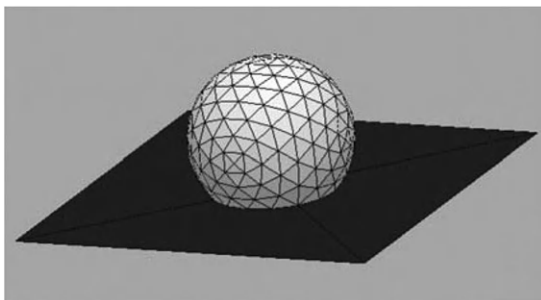
Using the trigonometric expression

$$1 - \cos \theta = 2 \sin^2 \frac{\theta}{2},$$

we finally find

$$e = 2 \sqrt{\frac{\gamma_{LG}}{\rho g}} \sin \frac{\theta}{2} = 2\ell \sin \frac{\theta}{2}. \quad (3.8)$$

Relation (3.8) shows that the height of a “large” droplet is proportional to the capillary length. The capillary length is of the order of 2 mm, and the height of large droplets is less than 4 mm.

**FIGURE 3.4**

Shape of a microdrop calculated with the software Surface Evolver.

3.2.1.2 Microscopic drops: $\text{Bo} \ll 1$

3.2.1.2.1 Shape of the droplet

As was mentioned earlier, a microdrop has the form of a spherical cap. A spherical cap is a surface of minimum energy if only surface tension is taken into account. This can be checked by using the Surface Evolver software. The result is shown in [Figure 3.4](#) for a contact angle of 110° .

3.2.1.2.2 Volume of a sessile droplet

[Figure 3.5](#) shows a cross-section of the droplet, on nonwetting and wetting surfaces. The volume V of such a droplet is a function of two parameters in the set of the four parameters $\{\theta, a, R, h\}$, where θ is the contact angle, a is the contact radius (i.e., the radius of the circular base), R is the curvature radius (i.e., the sphere radius), and h is the height of the droplet. First, we observe that the height of the droplet is expressed by the same relation in the wetting and nonwetting case:

$$\begin{aligned} h &= R + R \cos(\pi - \theta) = R(1 - \cos \theta) \\ h &= R - R \cos \theta = R(1 - \cos \theta). \end{aligned} \quad (3.9)$$

The contact radius a —radius of the circular base—is in both cases

$$a = R \sin(\pi - \theta) = R \sin \theta. \quad (3.10)$$

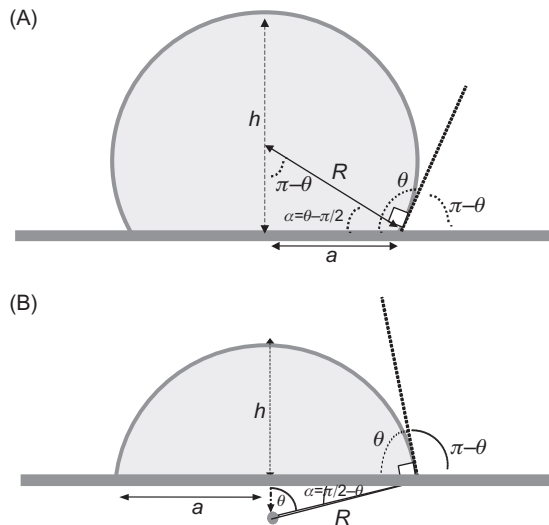
Thus, in the set $\{\theta, a, R, h\}$, h and a are functions of R and θ .

Using the Pythagorean theorem,

$$|h - R| = \sqrt{R^2 - a^2}. \quad (3.11)$$

Another useful relation can be obtained by combining [Eqs. \(3.9\)](#) and [\(3.10\)](#):

$$h = a \frac{1 - \cos \theta}{\sin \theta} = a \tan\left(\frac{\theta}{2}\right). \quad (3.12)$$

**FIGURE 3.5**

Cross-section of a microdrop sufficiently small to be a spherical cap: (A) nonwetting droplet; (B) wetting droplet. Notice that $\alpha = \theta - \pi/2$ in the first (nonwetting) case and $\alpha = \pi/2 - \theta$ in the second (wetting) case.

The volume of the spherical cap is calculated by the formula applied to the sketch of Figure 3.6 [3,4]

$$V = \int_{R-h}^R \pi r^2 dz. \quad (3.13)$$

Integration of Eq. (3.13) leads to

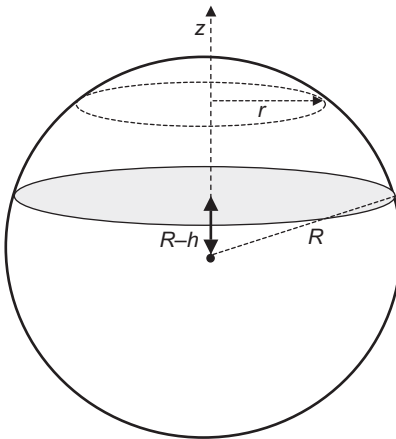
$$V = \int_{R-h}^R \pi r^2 dz = \int_{R-h}^R \pi(R^2 - z^2) dz = \frac{\pi h^2}{3} (3R - h). \quad (3.14)$$

Using relation (3.9), one finds an expression for the volume as a function of R and θ :

$$V(R, \theta) = \frac{\pi}{3} R^3 (2 - 3 \cos \theta + \cos^3 \theta). \quad (3.15)$$

Besides expressions (3.14) and (3.15), other expressions for the volume of the spherical cap are

$$V(a, h) = \frac{\pi}{6} h(3a^2 + h^2) \quad (3.16)$$

**FIGURE 3.6**

Schematic of the volume for the integration of relation (3.14).

and

$$V(a, R) = \frac{\pi}{6} \left(R \pm \sqrt{R^2 - a^2} \right) \left(3a^2 + \left(R \pm \sqrt{R^2 - a^2} \right)^2 \right). \quad (3.17)$$

Note that in Eq. (3.17) the + sign corresponds to a nonwetting case (lyophobic) and the - sign corresponds to the wetting case (lyophilic). For $\theta = 90^\circ$, $a = R$ and Eq. (3.17) reduces to the half sphere volume $V = (2\pi/3)R^3$. Other expressions of the volume are [4]

$$V(a, \theta) = \frac{\pi}{3} a^3 \frac{(2 - 3 \cos \theta + \cos^3 \theta)}{\sin^3 \theta} \quad (3.18)$$

and

$$V(h, \theta) = \frac{\pi}{3} h^3 \frac{(2 - 3 \cos \theta + \cos^3 \theta)}{(1 - \cos \theta)^3}. \quad (3.19)$$

3.2.1.2.3 Surface area of the spherical cap

The spherical cap is a surface of revolution obtained by rotating a segment of a circle. More generally, any surface obtained by rotating the curve $y = f(x)$ about the x -axis has the following expression for area [4]

$$S = 2\pi \int f(x) \sqrt{1 + [f'(x)]^2} dx. \quad (3.20)$$

In our case, with the same notations as in [Figure 3.6](#), the curve is defined by $r = f(z)$ and is rotated about the z -axis, so that the preceding formula becomes

$$S = 2\pi \int r\sqrt{1+r^2} dz.$$

Upon integration between the two limits $R-h$ and R —one obtains

$$S(R, h) = 2\pi Rh. \quad (3.21)$$

Other forms of the expression of the surface of the spherical cap are useful. Using [Eq. \(3.9\)](#), we find

$$S(\theta, h) = \frac{2\pi h^2}{1 - \cos \theta}. \quad (3.22)$$

Then, using [Eq. \(3.11\)](#), we obtain

$$S(a, h) = \pi(a^2 + h^2). \quad (3.23)$$

After eliminating h in the preceding relation:

$$S(a, \theta) = \frac{2\pi a^2}{1 + \cos \theta}. \quad (3.24)$$

The surface energy of the spherical cap with surface tension γ is

$$E_{\text{surf}} = \gamma S, \quad (3.25)$$

where S is given by any of the preceding relations.

3.2.1.2.4 Measurement of the volume of a droplet from a single image (hydrophobic case)

When observing a nonwetting droplet vertically downward with a microscope, two circles appear ([Figure 3.7](#)).

A simulation with Evolver leads us to think that the large circle corresponds to the horizontal cross-section of the droplet at its equator, and the smaller circle to the contact circle ([Figure 3.8](#)).

The radius of the spherical cap is

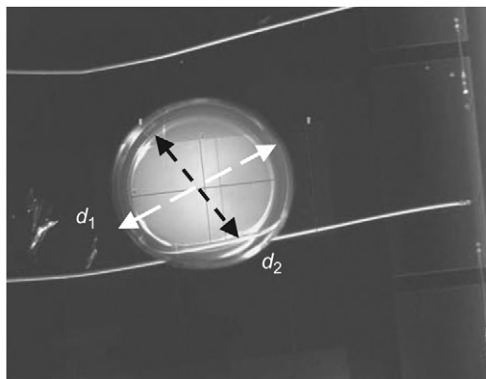
$$R = \frac{d_1}{2}$$

and the contact radius

$$a = \frac{d_2}{2}.$$

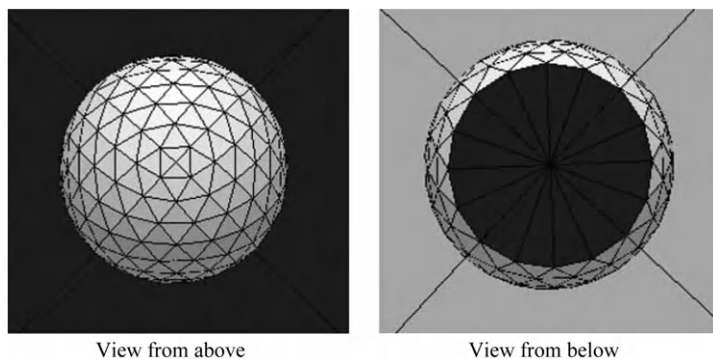
The information contained in these two relations is enough to determine completely the characteristics of the drop. Using the relation,

$$h = R + \sqrt{R^2 - a^2}$$

**FIGURE 3.7**

Microscope image of a sessile droplet on a hydrophobic surface: the larger diameter d_1 is the diameter of the sphere and d_2 is the diameter of the contact circle of the drop with the substrate.

Source: Photo Ph. Clementz, CEA/LETI.

**FIGURE 3.8**

Surface Evolver numerical simulation of a sessile droplet: the two diameters are clearly seen on an image taken from below (right).

we find the height of the drop and consequently the drop volume is given by:

$$V = \frac{\pi}{48} \left(d_1 + \sqrt{d_1^2 - d_2^2} \right) \left[3d_2^2 + \left(d_1 + \sqrt{d_1^2 - d_2^2} \right)^2 \right]. \quad (3.26)$$

Thus, the contact angle is

$$\theta = \arcsin\left(\frac{a}{R}\right) = \arcsin\left(\frac{d_2}{d_1}\right). \quad (3.27)$$

In conclusion, a single image (from above) of the drop produces all the characteristics of the droplet. The method can be quite accurate depending on the quality of the image. For example, an estimate of the diameters in the image of Figure 3.7 is $d_1 = 1332 \mu\text{m}$, and $d_2 = 1146 \mu\text{m}$, leading to a drop volume of $V = 1.05 \mu\text{L}$ and a contact angle $\theta = 120.6^\circ$. The expected values were $V = 1.0 \mu\text{L}$ and $\theta = 120^\circ$.

3.2.2 Droplets constrained between two plates

It happens very often in biotechnology that DMF devices have a planar cover, and the droplets are constrained between two horizontal solid surfaces. Such droplets have a relatively SFE than sessile droplets and are easier to handle. This is particularly the case for electrowetting. We consider here only the case of microsystems where the vertical gap δ is small (usually 50–500 μm); their Bond number, given by:

$$Bo = \frac{\rho g \delta^2}{\gamma}$$

is less than 0.1, and the free interfaces have circular cross-sections.

3.2.2.1 Shape of a droplet constrained between two horizontal planes

A droplet squashed between two parallel plates has two types of contact, one with the bottom plate and another with the top plate; these contacts can independently be either wetting or nonwetting depending on the material of the substrates. Figure 3.9 shows different possibilities and the corresponding shapes calculated using the Surface Evolver numerical software.

In all cases—due to a small Bond number and the flat upper and lower surfaces—the profile of the droplet in a vertical cross-section is nearly a circular arc. Taking advantage of this observation, we can derive a formulation for the calculation of the volume of the droplet.

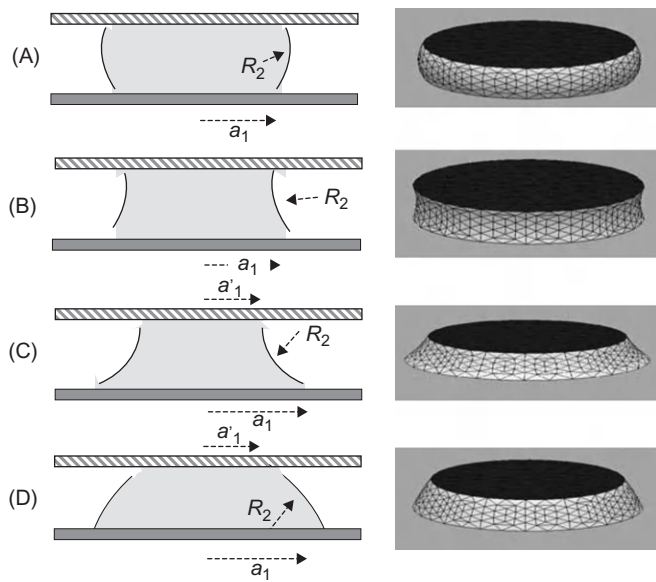
3.2.2.2 Curvature radius of the free interface

Here, “free interface” denotes the liquid–gas interface as opposed to the liquid–solid interfaces. Referring to Laplace’s law, the pressure in a constrained droplet is deduced from the two curvature radii. The expression of the curvature radius in the vertical plane is derived in this section. This curvature radius is shown in Figure 3.10. Remarking that angles with perpendicular sides are equal, we can write as follows:

$$R \cos \theta_1 = H - \delta,$$

where H is the distance between the curvature center and the upper plate and δ the gap between the plates; similarly,

$$R \cos(\pi - \theta_2) = -R \cos \theta_2 = H.$$

**FIGURE 3.9**

Sketch of the shape of a drop between two horizontal plates. (A) Nonwetting droplet—hydrophobic wetting for a water drop; (B) partial wetting—hydrophilic wetting for a water drop; (C) drop not wetting the top plate and wetting the bottom plate showing a concave interface (negative curvature radius), corresponding to the relation $\theta_1 < \pi/2$, $\theta_2 > \pi/2$, and $\theta_1 + \theta_2 < \pi$; and (D) same situation as (C), but the interface is convex because $\theta_1 < \pi/2$, $\theta_2 > \pi/2$, and $\theta_1 + \theta_2 > \pi$.

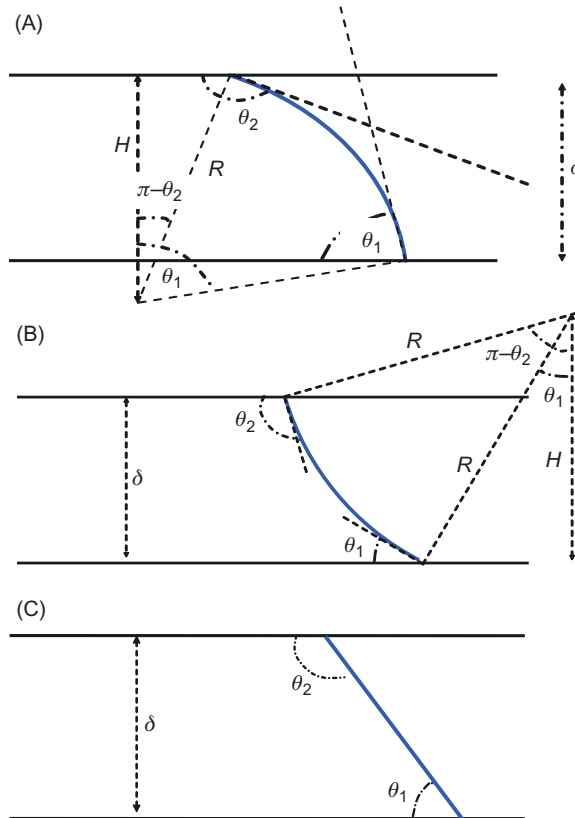
We deduce the value of the curvature radius R

$$R = -\frac{\delta}{\cos \theta_1 + \cos \theta_2}. \quad (3.28)$$

In the case of a concave interface corresponding to $\theta_1 < \pi/2$, $\theta_2 > \pi/2$, and $\theta_1 + \theta_2 < \pi$ (Figure 3.10B), similar reasoning leads to the negative curvature radius:

$$R = \frac{\delta}{\cos \theta_1 + \cos \theta_2}.$$

In the particular case where $\theta_1 + \theta_2 = \pi$ (Figure 3.10C), the vertical profile of the interface is flat (the interface has a conical shape) and the curvature radius is infinite.

**FIGURE 3.10**

Schematic of the geometry of a droplet constrained between two parallel planes: (A) case of a convex interface $\theta_1 < \pi/2$, $\theta_2 > \pi/2$, and $\theta_1 + \theta_2 > \pi$; (B) case of a concave interface $\theta_1 < \pi/2$, $\theta_2 > \pi/2$, and $\theta_1 + \theta_2 < \pi$; and (C) case of a flat interface $\theta_1 + \theta_2 = \pi$.

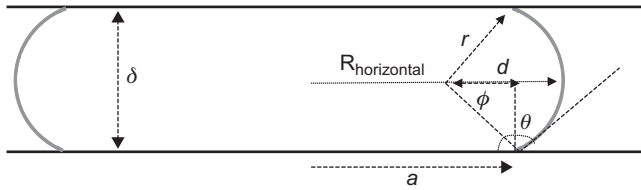
3.2.2.3 Volume of a droplet constrained between two parallel planes and having the same contact angle with both planes

In this section, we calculate the volume of the droplet sketched in [Figure 3.11](#). We will see that we obtain a relation of the type:

$$V = f(a, \theta, \delta) = g(R, \theta, \delta), \quad (3.29)$$

where a is the contact radius, θ is the contact angle, R is the maximum horizontal radius, i.e., the horizontal curvature radius, and δ is the vertical gap between the plates. Knowing the volume V , the horizontal curvature radius R can be deduced from [Eq. \(3.29\)](#). Using [Eq. \(3.28\)](#), we deduce the internal pressure:

$$\Delta P = \gamma \left(\frac{1}{R_{\text{vertical}}} + \frac{1}{R_{\text{horizontal}}} \right). \quad (3.30)$$

**FIGURE 3.11**

Cross-section of a droplet constrained by two parallel plates and having the same contact angle with both planes.

First, let us introduce the angle ϕ defined by:

$$\phi = \theta - \frac{\pi}{2}.$$

The curvature radius r of the interface is given by:

$$\cos \theta = -\sin \phi = -\frac{\delta/2}{r}. \quad (3.31)$$

On the other hand, we have

$$\sin \theta = \cos \phi = \frac{d}{r}$$

and we obtain a relation between d and δ :

$$d = -\frac{\delta}{2} \tan \theta.$$

The contact radius a is then,

$$a = R - r + d = R + \frac{\delta(1 - \sin \theta)}{2 \cos \theta}. \quad (3.32)$$

It can be verified that if $\theta = 90^\circ$, then the radius r is infinite and $a = R$. At first glance, the relation (3.32) is indeterminate but using a Taylor development, we find the limit:

$$\lim_{\theta \rightarrow \pi/2} \frac{(1 - \sin \theta)}{\cos \theta} \approx \frac{-((\pi/2) - \theta)^2}{(2!)((\pi/2) - \theta)} = 0.$$

The droplet volume is obtained through the following integral:

$$V = 2 \int_0^{\delta/2} \pi \tilde{R}^2(y) dy, \quad (3.33)$$

where $\tilde{R}(y)$ is the horizontal droplet radius at the vertical coordinate y . Using the equation for a circular segment, one finds that $\tilde{R}(y)$ is given by:

$$\tilde{R}(y) = (R - r) + \sqrt{r^2 - y^2}$$

and the volume is then,

$$V = 2 \int_0^{\delta/2} \pi \left[(R - r) + \sqrt{r^2 - y^2} \right]^2 dy. \quad (3.34)$$

Integration of Eq. (3.34) is somewhat lengthy. We finally find

$$V = 2\pi \left\{ (R^2 - 2rR + 2r^2) \frac{\delta}{2} - \frac{1}{3} \left(\frac{\delta}{2} \right)^3 + (R - r)r^2 \left[\theta - \frac{\pi}{2} + \frac{\sin(2\theta - \pi)}{2} \right] \right\}. \quad (3.35)$$

We notice that, for a droplet constrained by two parallel planes, the droplet volume depends on three independent parameters R , δ , and θ .

A similar relation can be found by replacing the equatorial radius R by the contact radius a :

$$V = \pi a^2 \delta + 2\pi \left(\frac{\delta}{2 \cos \theta} \right)^2 \left\{ a f_1(\theta) + \frac{\delta}{2} f_2(\theta) \right\}, \quad (3.36)$$

where:

$$f_1(\theta) = \theta - \frac{\pi}{2} + \frac{\sin(2\theta - \pi)}{2} + 2 \sin \theta \cos \theta$$

and

$$f_2(\theta) = \tan \theta \left(\theta - \frac{\pi}{2} + \frac{\sin(2\theta - \pi)}{2} + 2 \cos \theta \right) - \frac{1}{3} \cos^2 \theta + (1 - \sin \theta)^2.$$

3.2.2.4 Free surface of a droplet constrained by two horizontal planes with different contact angles with the two planes

This case is schematized in Figure 3.12. The volume V of the droplet now depends on four parameters: a , δ , θ_1 , and θ_2 .

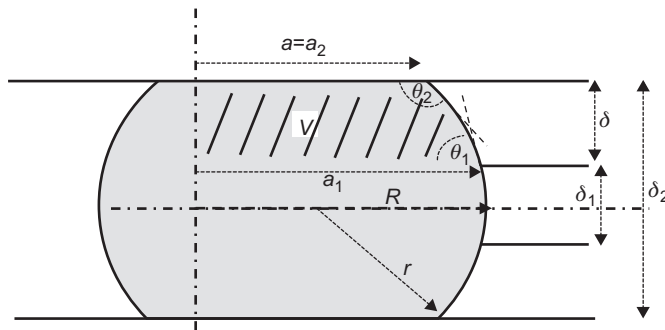
$$V = V(a, \delta, \theta_1, \theta_2).$$

Completing the figure to obtain a symmetrical droplet, the droplet volume is given by:

$$V(a, \delta, \theta_1, \theta_2) = \frac{V_{\text{sym}}(R, \delta_2, \theta_2) - V_{\text{sym}}(R, \delta_1, \pi - \theta_1)}{2}, \quad (3.37)$$

where V_{sym} is the volume of a symmetrical droplet, relation (3.36). We now have to express the parameters R , δ_1 , δ_2 as functions of a , θ_1 , θ_2 , and δ . Using Eq. (3.28), we can write

$$\begin{aligned} \delta_1 &= -\frac{\delta \cos \theta_1}{\cos \theta_1 + \cos \theta_2} \\ \delta_2 &= \frac{\delta \cos \theta_2}{\cos \theta_1 + \cos \theta_2}. \end{aligned} \quad (3.38)$$

**FIGURE 3.12**

Sketch of the droplet (hatched area). The volume V of the droplet is obtained by considering the volume of symmetrical droplet.

Using Eq. (3.32) and substituting Eq. (3.38), we find

$$R = a - \frac{\delta_2(1 - \sin \theta_2)}{2 \cos \theta_2} = a - \frac{\delta}{2(\cos \theta_1 + \cos \theta_2)}. \quad (3.39)$$

So, starting from the knowledge of the vector $\{a, \delta, \theta_1, \theta_2\}$, the volume of the droplet is obtained by solving Eqs. (3.38) and (3.39) to obtain $\{R, \delta_1, \delta_2\}$, and substituting these values in Eq. (3.37).

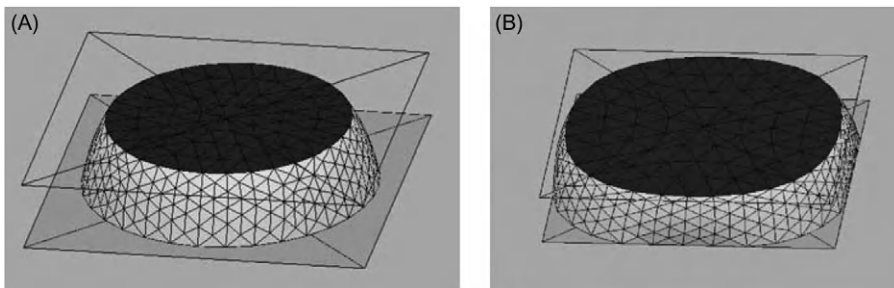
3.2.2.5 Droplet constrained by two planes and bounded by a hydrophilic/hydrophobic boundary

As will be seen in the next chapters, in DMF applications, droplets are often placed on a hydrophilic surface bounded by hydrophobic regions. In such a case, depending on its volume, either the droplet is small enough and stays far from the hydrophilic/hydrophobic boundary or it mimics the shape of the hydrophilic substrate (Figure 3.13). If the volume of liquid increases, the droplet will finally spread over onto the hydrophobic region.

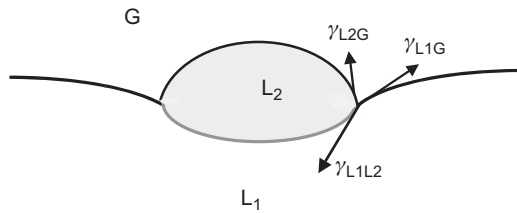
This phenomenon is related to contact line pinning and will be discussed in Section 3.6.

3.2.3 Droplet at a liquid interface—Neumann's construction

In Chapter 2, it was shown that Young's law is obtained by projection of the surface tension forces at the triple line on the plane defined by the solid surface. However, no mention is made for the projection on the normal to the solid surface. In reality, there is a normal constraint in the solid at its surface to balance the normal component of the surface tensions [1]. But, there is no visible effect if the substrate is a solid. This is not the case for a droplet at a liquid surface, and the resultant of the surface tensions should vanish.

**FIGURE 3.13**

Droplet on a bounded wetting region: (A) the droplet has a volume small enough not to touch the boundary and (B) the droplet is deformed by pinning on the boundary.

**FIGURE 3.14**

Droplet on a liquid surface.

Take two immiscible liquids, denoted 1 and 2, with the droplet of liquid 2 deposited on the interface between liquid 1 and a gas. Even if the density of liquid 2 is somewhat larger than that of liquid 1, the droplet may “float” on the surface, as shown in [Figure 3.14](#).

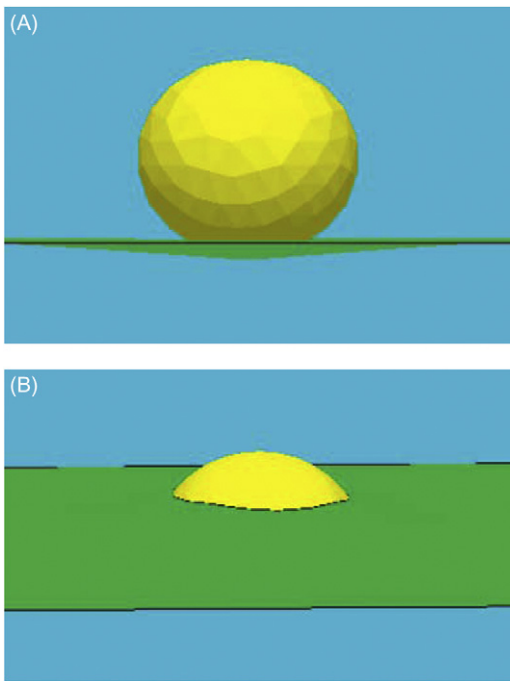
The situation is comparable to that of Young’s law with the difference that the situation is now two-dimensional. It is called Neumann’s construction, and the following equality holds

$$\vec{\gamma}_{L1L2} + \vec{\gamma}_{L1G} + \vec{\gamma}_{L2G} = 0. \quad (3.40)$$

The position of a floating droplet depends on the three interfacial tensions and on the density of each liquid.

In [Figure 3.15](#), we show some pictures of floating droplets obtained by numerical simulation (Surface Evolver software).

In microfluidic applications for biotechnology, two categories of liquids are used most of the time: the first category consists of aqueous liquids like deionized water (DIW), biological solutions (water with a few tenths of molar concentration of salt), and biological buffers with surfactants; the second category comprises

**FIGURE 3.15**

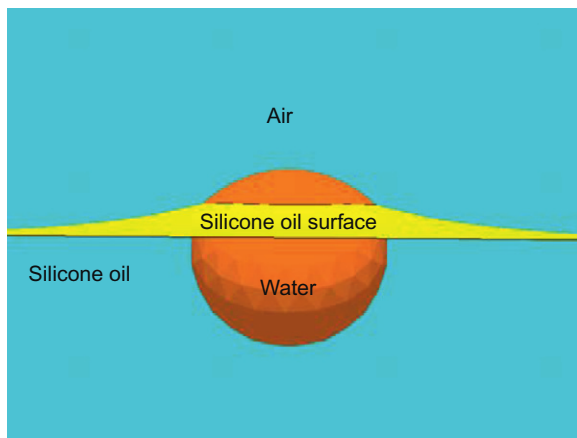
Numerical simulations of different positions of a droplet (1 mm) on a liquid surface depending on the three surface tensions: (A) the surface tension of the droplet is very large and (B) the surface tension of the droplet with the other liquid has been reduced; the drop is at equilibrium due to the balance of buoyancy and surface tensions.

organic liquids like silicone oil. It is interesting to know how a microscopic droplet of water behaves at an oil–air interface and a droplet of oil behaves at a water–air interface.

[Figure 3.16](#) shows the behavior of a droplet of water at an oil–air interface, and [Figure 3.17](#) shows that oil spreads at the surface of water.

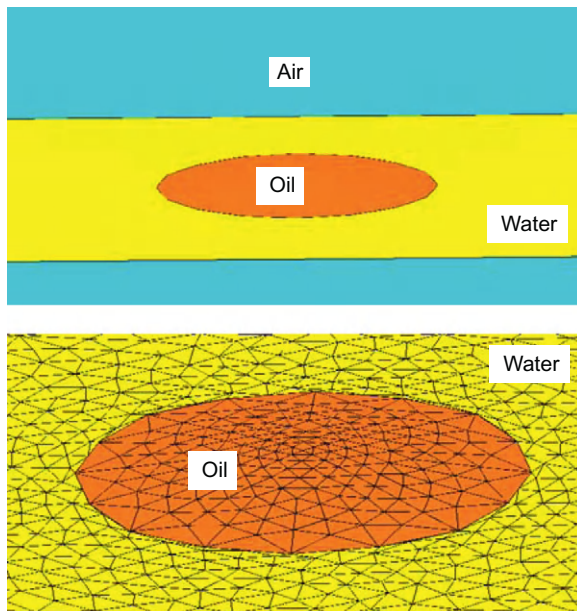
3.2.4 Droplet in a corner

Microfluidic channels and chambers are etched in silicon, glass, or plastic. Let us investigate first the effect of a corner—or a wedge—on the droplet interface. Take the case of a 90° wedge. The shape of the droplet is shown in [Figure 3.18](#) depending on the Bond number $Bo = \rho g R^2 / \gamma$, where R is a characteristic dimension of the droplet, which can be scaled as the 1/3 power of the value of the volume of liquid: $R^3 \approx 3\text{Vol}/\pi$.

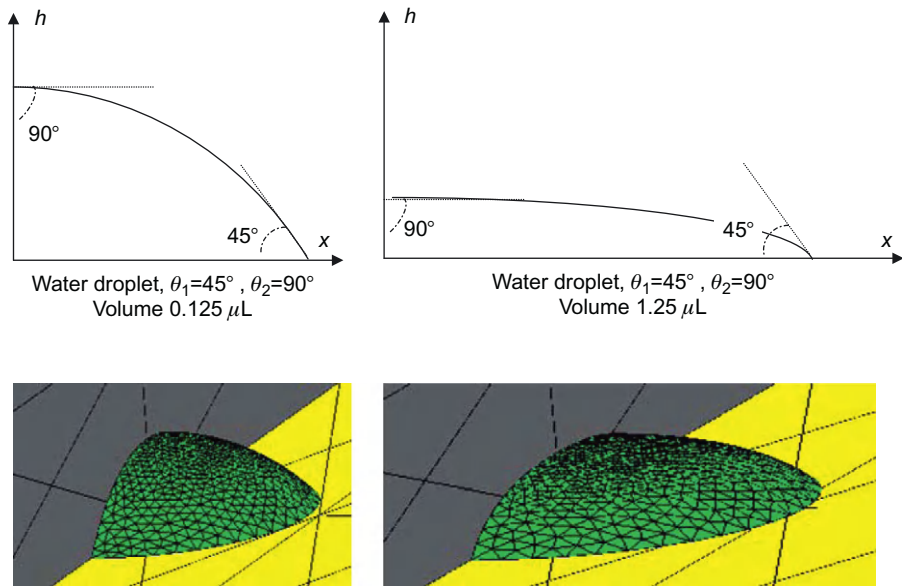
**FIGURE 3.16**

Droplet of water at the surface of silicone oil.

Source: *From Surface Evolver*.

**FIGURE 3.17**

A droplet of oil spreads out at a water interface.

**FIGURE 3.18**

Shape of a liquid drop in a 90° wedge. Left, a small droplet (volume $0.125 \mu\text{L}$) tends to take a spherical shape despite the different contact angles on the two planes; right, a larger droplet (volume $1.25 \mu\text{L}$) is flattened by gravity. In the first case, the Bond number is 0.04, and 4 in the second case.

3.2.4.1 Concus–Finn relation

It has been observed that liquid interfaces in contact with highly wetting solid walls forming a wedge tend to spread in the corner (Figure 3.19). This motion results from the fact that the interface curvature is strongly reduced in the corner (in the case of Figure 3.19, the vertical curvature radius is small): the Laplace's pressure is low in the corner and liquid tends to spread in the corner.

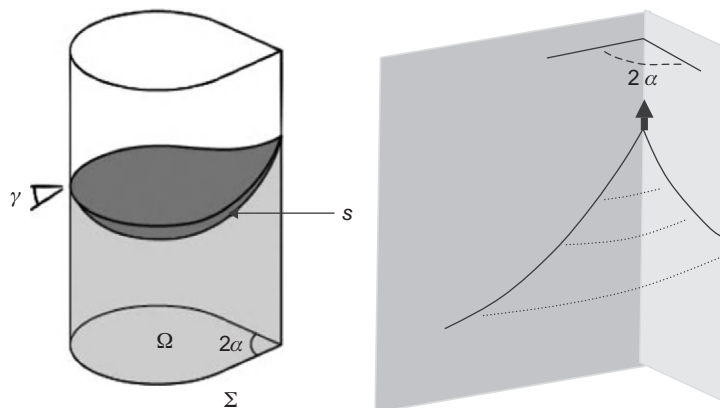
Concus and Finn [5] have investigated this phenomenon, and they have derived a criterion for capillary motion in the corner of the wedge. If θ is the Young's contact angle on both planes and α the wedge half-angle, the condition for capillary self-motion is

$$\theta < \frac{\pi}{2} - \alpha. \quad (3.41)$$

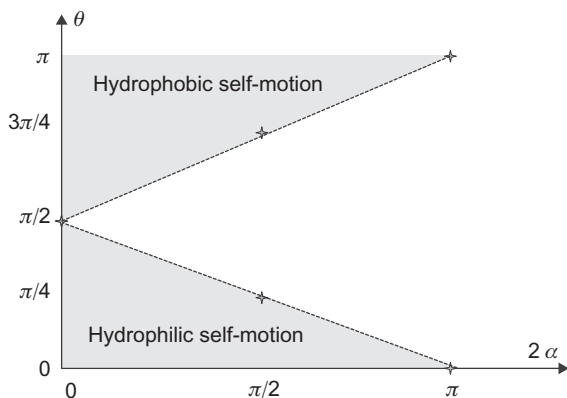
This case corresponds to wetting walls. Conversely, when the walls are non-wetting, the condition for dewetting of the corner is

$$\theta > \frac{\pi}{2} + \alpha. \quad (3.42)$$

In Figure 3.20, the Concus–Finn relations have been plotted in a (θ, α) coordinate system. One verifies that, for a flat angle, the Concus–Finn relations reduce to the usual capillary analysis.

**FIGURE 3.19**

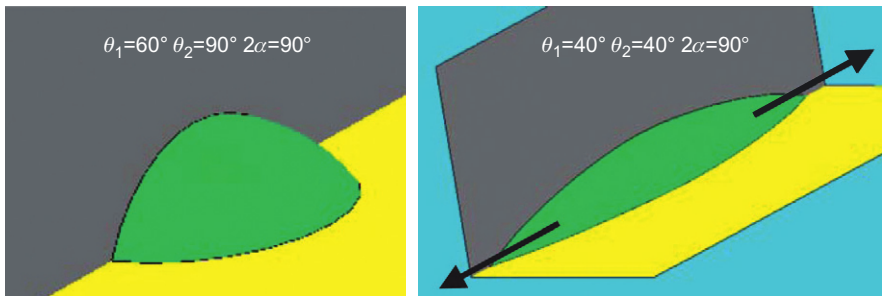
A liquid interface is deformed in the corner of a wedge made of two wetting plates. This phenomenon is due to a decrease of curvature at the edge.

**FIGURE 3.20**

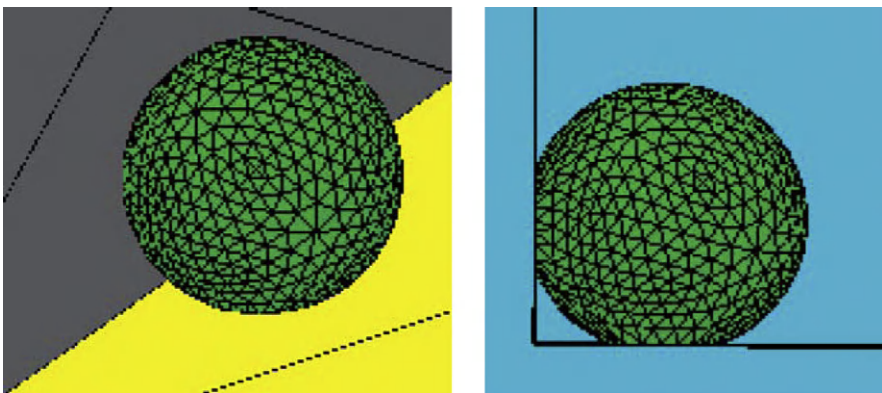
Plot of the domains of self-motion in a corner, according to the Concus–Finn relations.

The Concus–Finn relations can be numerically verified using the Surface Evolver software. Figure 3.21 shows the spreading of the liquid in the corner when condition (3.41) is met.

In microtechnology, wedges and corners most of the time form a 90° angle, so that a droplet disappears in the form of filaments if the wetting angle on both planes is smaller than 45° . One must be wary that, when coating the interior of microsystems with a strongly wetting layer, in order to have a very hydrophilic (wetting) surface, droplets may disappear; they are transformed into filaments in the corners.

**FIGURE 3.21**

A droplet spreads in a corner when the contact angles verify the Concus–Finn condition.

**FIGURE 3.22**

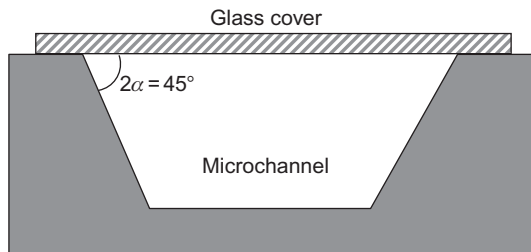
Droplet in a strongly hydrophobic corner: the droplet does not wet the tip of the corner, in accordance to the Concus–Finn relation.

The converse can also be verified: for a rectangular channel, if the coating is strongly hydrophobic, and the contact angles on both planes larger than 135° , the drop detaches from the corner, and does not wet the corner any more ([Figure 3.22](#)).

3.2.4.2 Extended Concus–Finn relation

A generalization of the Concus–Finn relation can be derived from the work of Brakke [\[6\]](#). When the two planes do not have the same wettability (contact angles θ_1 and θ_2), the relation [\(3.41\)](#) becomes

$$\frac{\theta_1 + \theta_2}{2} < \frac{\pi}{2} - \alpha. \quad (3.43)$$

**FIGURE 3.23**

Cross-section of a trapezoidal microchannel.

Remember that α is the wedge half-angle. An important consequence of relation (3.43) applies to trapezoidal microchannels, a form easily obtained by micro-fabrication (Figure 3.23).

When a glass cover is sealed on top, the upper corners form 45° angles and the extended Concus–Finn condition indicates the following limit:

$$\frac{\theta_1 + \theta_2}{2} < \frac{\pi}{2} - \alpha = 67.5^\circ.$$

The glass cover may be quite hydrophilic, say $\theta_1 \sim 60^\circ$, and if the channel is also hydrophilic, say $\theta_2 \sim 70^\circ$, then $(\theta_1 + \theta_2)/2 \sim 65^\circ$ and the liquid spreads in the upper corners, leading to unwanted leakage.

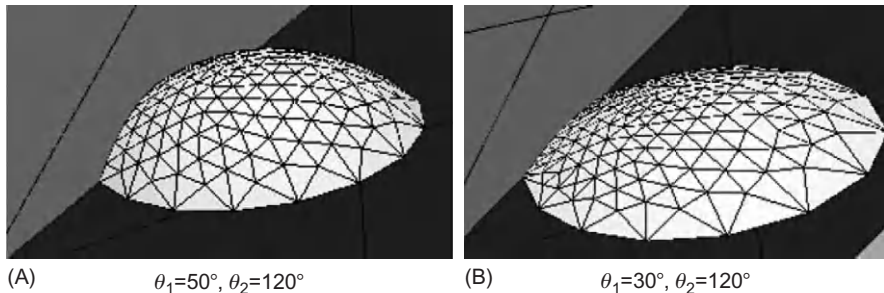
The same extension applies to the nonwetting case. The extended Brakke–Concus–Finn dewetting condition for a corner is

$$\frac{\theta_1 + \theta_2}{2} > \frac{\pi}{2} + \alpha. \quad (3.44)$$

In a general way, the surface tension does not appear in the Brakke–Concus–Finn relations. Thus, these relations also apply for two-phase liquids. If we consider water and oil, the contact angles with hydrophilic, respectively hydrophobic, surfaces are of the order of $\theta_1 \sim 60^\circ$, respectively $\theta_2 \sim 130^\circ$. Relation (3.41) shows that a droplet of oil surrounded by water is likely to form in hydrophilic channels, because the water spreads on the solid wall, and relation (3.42) shows the opposite for hydrophobic channels, i.e., oil spreads and a water droplet is formed. This point will be dealt with in more detail in Chapter 14, where solid walls of T-junctions should be hydrophilic or hydrophobic depending on the liquid that must be encapsulated in a droplet.

3.2.4.3 Droplet in a wetting/nonwetting corner

In this section, the behavior of a droplet in a wedge is investigated, in the case where one side of the wedge is wetting and the other nonwetting. It is expected that, if the contact angle on the wetting side is small and that on the nonwetting

**FIGURE 3.24**

Droplet in a corner with wetting and nonwetting sides: (A) the droplet stays attached to the corner and (B) the droplet is at equilibrium on the wetting side.

side is large, the drop will be positioned on the wetting side. It is intuitive to think that this will happen if the difference between the nonwetting contact angle and the wetting contact angle is large.

By referring to Ref. [6], a criterion for the drop to be positioned on the wetting side only is

$$\theta_2 - \theta_1 > \pi - 2\alpha \quad (3.45)$$

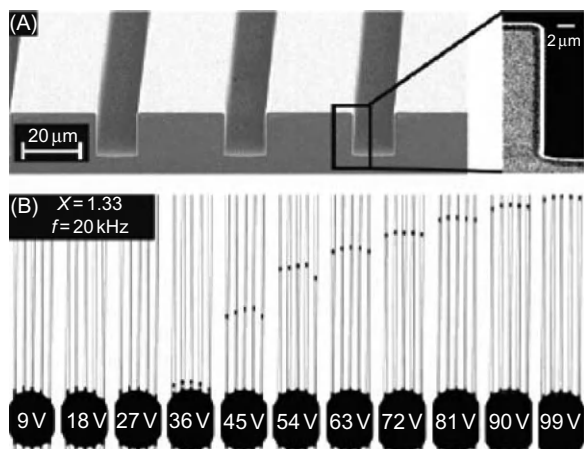
α being the wedge half-angle. Relation (3.45) can be verified by numerical simulation as shown in Figure 3.24.

The next logical step is to investigate the behavior of droplets in grooves.

3.2.5 Droplet in a groove

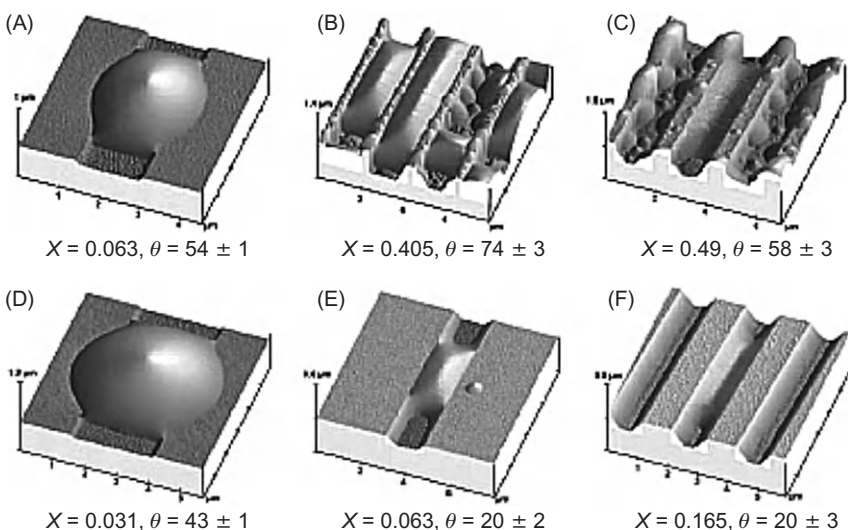
“Open” microfluidics is a relatively new concept which has gained momentum recently. The idea is to use either planar textured surfaces with different wettabilities or nonplanar substrates fabricated by available photolithography methods. In a general way, grooves and cusps present the advantages of being easily accessible and easily washable, and they confine the liquid in small volumes, due to pinning of the upper edges. An example is the electrocapillary grooves designed by Baret et al. [7], shown in Figure 3.25, where a liquid flows in microgrooves under the actuation of an electric field.

In this section, we investigate the shapes of droplets in microgrooves. Different types of morphology have been experimentally observed in rectangular grooves (Figure 3.26) [8,9]. Seemann et al. [8] and Lipowsky et al. [9] have observed that two parameters govern the morphology of the liquid in a groove: (i) the aspect ratio X of the groove geometry, i.e., the ratio of the groove depth to the groove width and (ii) the contact angle θ of the liquid with the solid substrate. Basically, the three morphologies are filaments, wedges, and droplets. Filaments correspond to the case where the liquid spreads in the groove, either in corners if the volume of liquid is small or in the whole groove if the volume of liquid is

**FIGURE 3.25**

Liquid flowing in microgrooves under the action of electrocapillary forces: (A) shape of the channels and (B) liquid filaments progress in the grooves depending on the applied voltage.

Source: Reprinted with permission from Ref. [7] © 2005, American Chemical Society.

**FIGURE 3.26**

AFM (atomic force microscopy) observation of a droplet in grooves [8,9]; X is the aspect ratio (depth divided by width) and theta the contact angle.

Source: © 2005, National Academy of Sciences, USA

sufficient (Figure 3.27); filaments are obtained for contact angles smaller than 45° , according to the Concus–Finn relation

$$\theta \leq \frac{\pi}{2} - \alpha,$$

where α is the corner half-angle. The liquid remains in the form of droplets or stretched droplets if the contact angle is larger than 45° . If the volume of liquid is small compared to the dimensions of the groove, the liquid goes to the corners of the groove, forming wedges. For more details on these morphologies, a complete diagram can be found in Seemann et al. [8].

3.2.6 Droplet in a microwell

In biotechnology, LOC and immunoassays are microdevices aimed at the recognition of DNA and proteins, and for the culture of cells (Figure 3.28). These devices are constituted of thousands of microwells or microcups. Biological liquids—called buffers—are deposited in microscopic wells and biological recognition

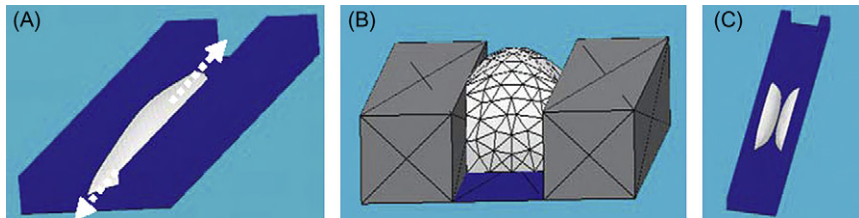


FIGURE 3.27

The different morphologies of liquid in grooves: filament (A), droplet (B), and wedges (C).

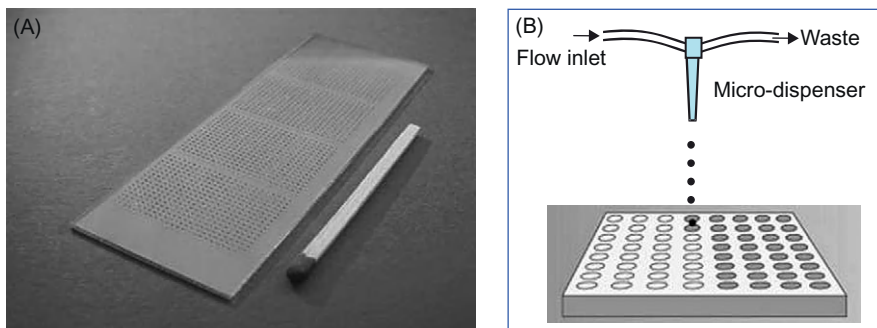
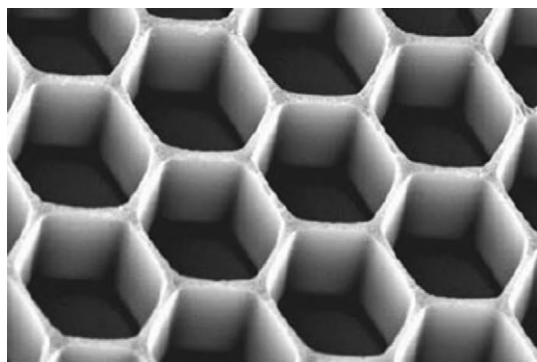


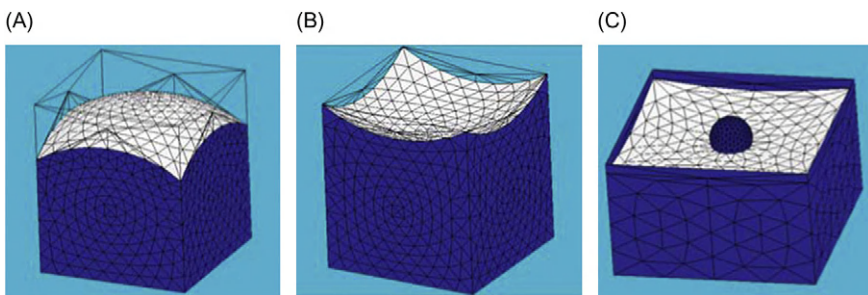
FIGURE 3.28

(A) DNA microarray made by SCIENION. (B) The wells are filled with biological buffers by droplet spotting.

**FIGURE 3.29**

Microwells for spatial confinement of avidin used to the immobilization and housing of single cells.

Source: From Ref. [10], reproduced by permission of the Royal Society of Chemistry.

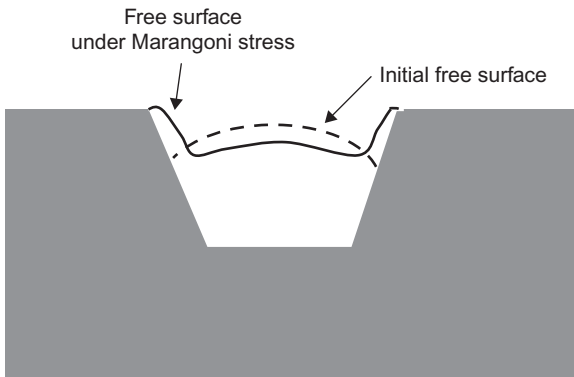
**FIGURE 3.30**

Numerical simulation of a droplet in a microwell: (A) case of water in a hydrophobic well; (B) case of water in a hydrophilic well; and (C) case of a water droplet at the surface of silicone oil in a hydrophobic well (Surface Evolver software).

reactions take place—or not—in each of these wells [10] (Figure 3.29). It is of importance to be sure that no liquid of a particular well leaks to a neighboring well. The shape of the droplet in a well is then of great importance.

Due to capillary forces at the walls of the well, the free surface of a droplet is never horizontal, but bent depending on the chemical nature of the walls. The convexity/concavity of the surface depends on the wetting/nonwetting nature of the walls (Figure 3.30). Nonwetting walls produce convex liquid surfaces; wetting walls produce concave liquid surfaces.

Attention should be given to the fact that the liquid should not overflow on the plate out of the cusp. This can happen when the contact angle in the corners is smaller than the Concus–Finn limit.

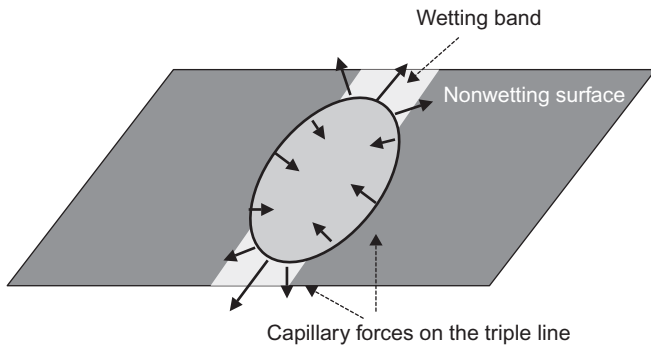
**FIGURE 3.31**

Marangoni effect in a microwell of a DNA array. Remark that in the case of a uniform temperature, the surface tension is constant and the interface is a spherical cap with contact angles defined by the Young's relation, whereas in the case where the drop is heated, the interface has a more complicated shape determined by the surface tension distribution.

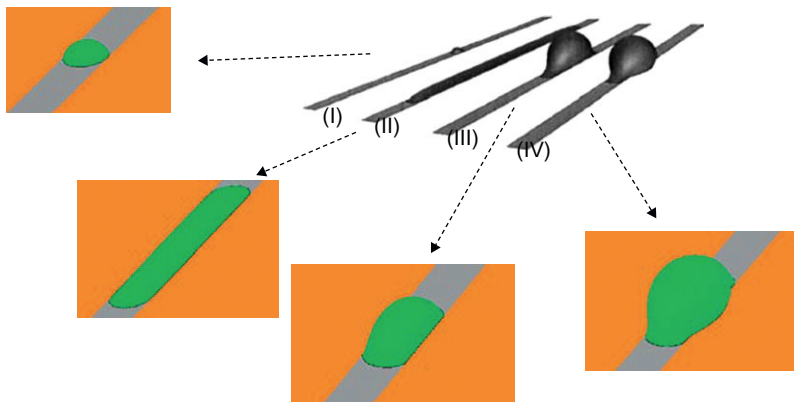
Another case for overspilling can occur when the liquid in the cusp is heated. This is particularly the case of DNA microsystems. DNA arrays are designed for the recognition of DNA segments. The principle is simple: it is based on the matching between a target DNA and its complementary sequence. When the target DNA finds its complementary sequence, there is a binding between the two DNA segments due to hydrogen bonds. Each well is grafted with a predetermined DNA sequence so that each well aims at a specific target. The target can be identified by fluorescence when it binds in a well. Grafting of complementary sequences in the bottom of a cusp requires successive operations of deposition of liquid drops and heating for evaporation. As the heating of the drop is not uniform, surface tension is lower at the walls and the liquid rises along the walls due to increased capillarity ([Figure 3.31](#)). Cusps should then be designed in a way that the liquid cannot exit by capillarity and overflow in the neighboring cusps [\[11\]](#).

3.2.7 Droplet on striped surface domains

In this section, the behavior of a droplet located on a wetting (lyophilic) band on the surface of an otherwise nonwetting (lyophobic) horizontal plate is investigated. In [Figure 3.32](#), we have schematized the forces on the contact line and we observe that the contribution of the wetting region (band) tends to elongate the droplet; this effect is reinforced by the forces exerted by the nonwetting region that want to pinch the droplet. However, there is a resisting force to this phenomenon: it is the droplet/air surface tension, whose contribution is to bring back the surface toward that of a sphere.

**FIGURE 3.32**

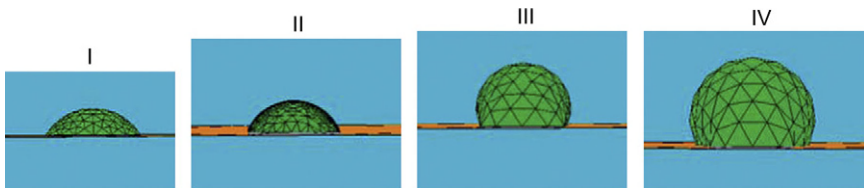
Sketch of the capillary forces on the triple contact line.

**FIGURE 3.33**

Different shapes of a droplet on a lyophilic band: results of a numerical simulation [14].

In Chapter 5, we will see that stretching droplets on lyophilic bands is a very important issue. In particular, it will be shown that this is one way to cut a droplet into two “daughter” droplets.

Then, the question is: can a droplet be stretched by capillary forces to a point where it is completely resting on the wetting band? This question has been answered in a series of articles by Gau et al., Lenz et al., Brinkman et al., and Klingner et al. [12–16]. They have shown that four morphologies are possible depending mostly on the lyophilic contact angle and the volume of the drop. These four morphologies are shown in Figure 3.33: (I) when the liquid volume is small, the droplet has a spherical shape and is totally located on the lyophilic band; for larger volumes, the morphology depends on the lyophilic contact angle: if

**FIGURE 3.34**

Transverse shape of the droplet in the different morphologies: (I) the drop is a spherical cap with Young's contact angle; (II) the drop has a circular transverse shape with $h \sim L/2$; (III) the droplet bulge over the hydrophobic band, but its contact surface lies within the hydrophilic band; (IV) curvature is reduced by liquid overflowing onto the lyophobic surfaces.

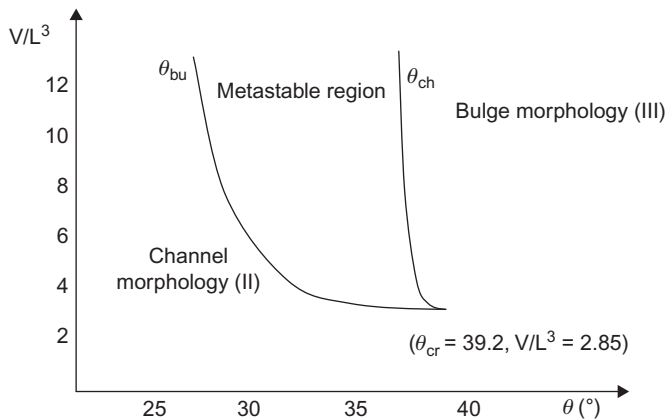
the contact angle is smaller than a threshold value $\theta_{lyo} < \theta_{lim}$ (V) the droplet spreads like a *channel* on the hydrophilic surface without overflowing on the hydrophobic surface (case II). If $\theta_{lyo} > \theta_{lim}$ (V) the droplet stays localized in a *bulge* state, i.e., does not spread, and two morphologies are possible depending on the volume of the droplet: (III) the volume is sufficiently small and the droplet is constrained by the hydrophilic surface limits; (IV) the volume is sufficiently large and the droplet spreads over the transition line onto the hydrophobic surface.

The cross-sectional profiles of the droplet in the different types of morphologies are shown in Figure 3.34. These profiles are circle arcs in all cases, with different curvatures. The curvature (and the internal pressure according to Laplace's law) is maximal in the bulge morphology III, where the ratio of the height of the drop to the base width is maximal.

In microfluidic systems, it is interesting to know if a volume of liquid deposited on a striped surface will spread on the hydrophilic stripe or will remain in a bulge form. An investigation of the bifurcation between morphologies II and III has been done by Brinkmann and Lipowsky [14] and the result is shown in Figure 3.35. The two main parameters are the hydrophilic contact angle θ_{lyo} and the dimensionless volume V/L^3 , where L is the width of the band. It is easy to show that when $V/L^3 < \pi/6$, the morphology of the droplet is a spherical cap (number I in Figure 3.33). For volumes in the range

$$\frac{\pi}{6} \leq \frac{V}{L^3} \leq 2.85$$

there is a continuous smooth change from “channel” droplet to “bulge” droplet. Above the critical volume $V/L^3 = 3.85$, the transition between morphologies II and III is abrupt. It appears that there is a metastable region where the droplet can be in either one of the two morphologies II and III; this metastable region is comprised between the two curves denoted θ_{bu} and θ_{ch} in Figure 3.35. What is particularly interesting is that the curve θ_{ch} (V) is nearly vertical, meaning a large

**FIGURE 3.35**

Bifurcation diagram for morphologies II and III.

volume droplet deposited on the stripe totally spreads on the stripe (channel morphology), if the contact angle is smaller than the approximate value of 38° .

Note that the value of 38° has a physical meaning: if we assume that the liquid in morphology II is a long cylinder of length L' , and if we neglect the two ends, the interfacial free energy is approximately

$$E = \gamma S_{LG} - \gamma_{SG} S_{base} + \gamma_{SL} S_{base} \quad (3.46)$$

corresponding to the energy of the liquid–gas surface plus the energy of the base (where solid–gas contact has been replaced by solid–liquid contact). Using Young's law, we find

$$E = \gamma(S_{LG} - \cos \theta_{lyo} S_{base}). \quad (3.47)$$

Using the relations

$$\begin{aligned} S_{base} &= LL' \\ S_{LG} &= LL' \frac{\theta}{\sin \theta} \\ S_{cross-section} &= \frac{L^2(\theta - \sin \theta \cos \theta)}{4 \sin^2 \theta}, \end{aligned} \quad (3.48)$$

where θ is the contact angle on the side of the cylindrical droplet. After substitution in Eq. (3.47), and introduction of the volume V , we deduce the expression of the surface energy as a function of the side contact angle θ :

$$E = \gamma \left[\frac{4V}{L} \sin \theta \frac{\theta - \sin \theta \cos \theta}{\theta - \sin \theta \cos \theta} \right]. \quad (3.49)$$

Stability of the interface is obtained by minimizing the surface energy relative to the angle θ , i.e., writing $\partial E/\partial\theta = 0$, and we find the implicit relation

$$\theta_{lyo} = \arccos\left(\frac{\theta}{2 \sin \theta} + \frac{\cos \theta}{2}\right). \quad (3.50)$$

Laplace's law indicates that the energy is always smaller than that obtained for the value of $\theta = \pi/2$, corresponding to a minimum curvature radius; and the maximum value of θ_{lyo} for having channel-type morphology is

$$\theta_{lyo} = \arccos\left(\frac{\pi}{4}\right) \approx 38^\circ$$

which is the value found by the numerical simulations. Note that 38° is quite a small value for a contact angle, and channel-type morphology requires very hydrophilic surfaces for water droplets.

The case of two parallel stripes has also been investigated [14], showing four different possible morphologies (Figure 3.36). These morphologies are in direct similarity with the preceding morphologies for the case of a single stripe. Morphology (a) corresponds to a small volume of liquid for which the drop is nearly spherical with the exception of the trace of the middle lyophobic line. If this lyophobic band is very thin, the drop is unstable and moves toward one of the two lyophilic bands. In morphology (b), the stripes are close and the contact angle is small so that the liquid spreads, almost like the channel case (II). When the volume of liquid is increased and the contact angle is larger, the drop bulges and can either be pinned on the two outer limits of the lyophilic bands (c) or spread over onto the lyophobic surfaces.

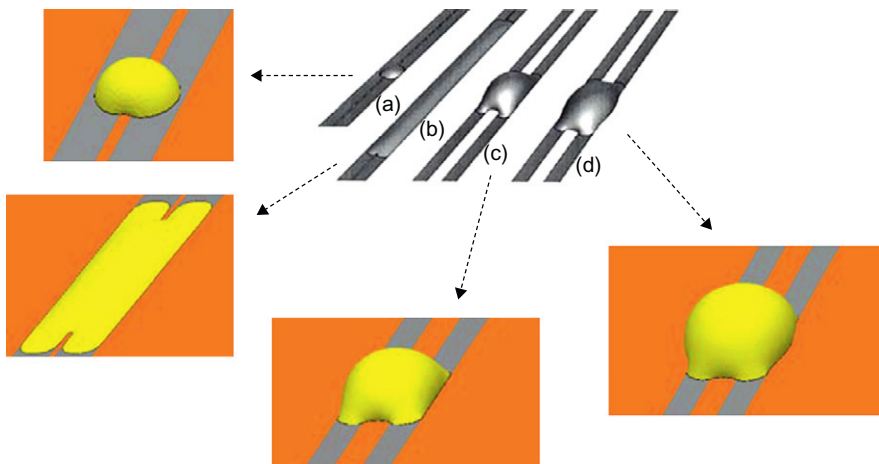


FIGURE 3.36

Different morphologies of a droplet on two lyophilic bands: results of a numerical simulation [14].

3.2.8 Droplet pierced by a microwire (catena)

A catena is sometimes used as a zero-potential contact for open EWOD systems (Figure 3.37) [17]. The catena should be electrically conducting and is usually made of gold. The presence of a catena should not modify too much the functioning of the microsystem by its action on the droplets. In this section, we investigate the effect of the catena on the droplet.

It has been observed that the catena modifies the behavior of the drop. In the case of a hydrophobic contact, a water drop adopts a position tangential to the catena. After adding surfactants, the contact becomes hydrophilic and the drop moves to a position centered on the wire (Figure 3.38).

Why does the presence of a catena modify the position and shape of drops? A very simple approach is to consider the capillary forces on the contact lines between the catena and the drop.

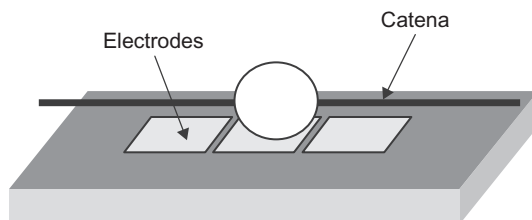


FIGURE 3.37

Schematic view of an open EWOD microsystem with catena.

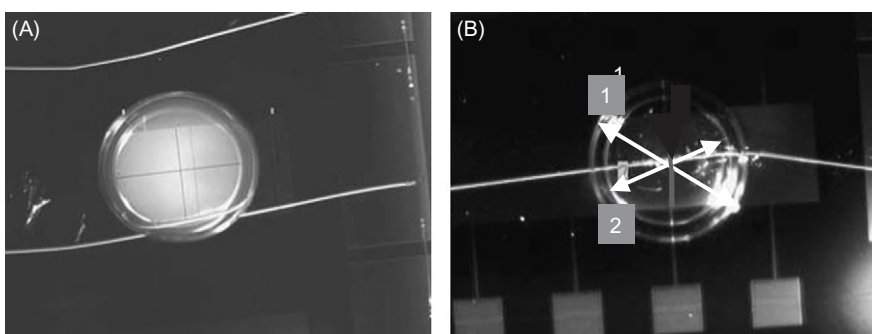
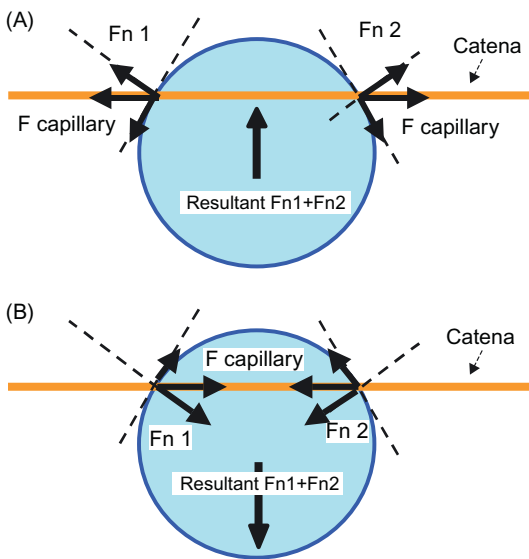


FIGURE 3.38

(A) The microdrop is tangent to the catena due to a hydrophobic contact and (B) the catena intersects the drop in its middle when the contact is hydrophilic due to the addition of surfactants: (1) diameter of the droplet; (2) diameter of contact circle.

Source: Photo Ph. Clementz.

**FIGURE 3.39**

In the case of a hydrophilic contact (A), the resultant of the normal forces moves the drop until it becomes symmetrical for the catena. In the hydrophobic case (B), the droplet moves till it is tangent to the catena.

In the case of a hydrophilic catena, these forces can be schematically represented as shown in Figure 3.39; their resultant is a force that pushes the drop into a symmetry position on the catena. The same reasoning may be done for a hydrophobic contact and the resultant of the forces is directed in the opposite direction and the drop moves aside to stop at an equilibrium position when the catena is tangent to the drop surface.

As a conclusion, the position of the catena above the electrodes has to be carefully chosen depending on its wettability. A hydrophilic catena should be located above the median of the electrode row, whereas a hydrophobic catena is best located above the edge of the electrode row. A catena at a nonoptimized position can block the drop motion.

This approach is confirmed by the results of the Evolver numerical simulation (Figure 3.40).

3.3 Drops on inhomogeneous surfaces

The reasoning used to establish Young's law supposed a perfectly flat homogeneous surface. This is somewhat an abstraction, and surfaces—even when carefully microfabricated—have some roughness and may not be chemically

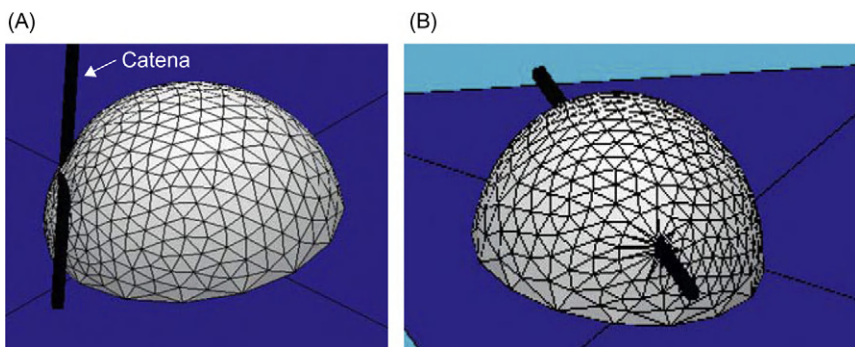


FIGURE 3.40

Numerical simulation of a droplet pierced by a catena using the Surface Evolver software: (A) the contact of the liquid and the catena is hydrophobic and the catena tangents the drop and (B) the contact is hydrophilic and the catena intersects the droplet symmetrically.

homogeneous. The following sections deal with rough and chemically inhomogeneous surfaces. It will be shown that Young's law should be corrected to take into account the imperfections of the surface.

3.3.1 Wenzel's law

It has been observed that roughness of the solid wall modifies the contact between the liquid and the solid. But the effect of roughness on the contact angle is not intuitive. It is surprising—and also a very useful observation as we will see later on—that roughness amplifies the hydrophilic or hydrophobic character of the contact.

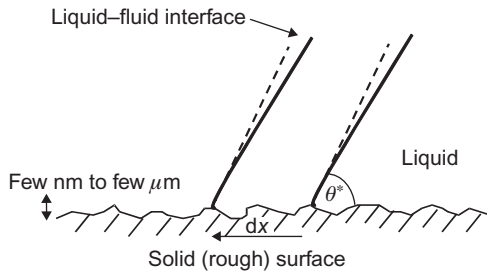
Suppose that θ^* is the angle with the surface with roughness and θ the angle with the smooth surface (in both cases, the solid, liquid, and gas are the same). One very important point here is that we have made the implicit assumption that the size of the roughness is very small, so that the molecules of the liquid are macroscopically interacting with a plane surface but microscopically with a rough surface. This explains why we can use the unique angle of contact θ^* .

Suppose a very small displacement of the contact line (Figure 3.41). Then, the work of the different forces acting on the contact line is given by:

$$dW = \sum \vec{F} \cdot d\vec{l} = \sum F_x dx = (\gamma_{SL} - \gamma_{SG})r dx + \gamma_{LG} \cos \theta^* dx, \quad (3.51)$$

where r is the roughness ($r dx$ is the real distance on the solid surface when the contact line is displaced by dx). Note that by definition, $r > 1$. Thus, the change in energy is

$$dE = dW = (\gamma_{SL} - \gamma_{SG})r dx + \gamma_{LG} \cos \theta^* dx. \quad (3.52)$$

**FIGURE 3.41**

Contact on a rough surface.

In fact, if we imagine that the drop finds its equilibrium state after the small perturbation dx , it finally stops at a position where its energy is minimum, so that

$$\frac{dE}{dx} = 0$$

and we obtain the relation

$$\gamma_{LG} \cos \theta^* = (\gamma_{SG} - \gamma_{SL})r. \quad (3.53)$$

If we recall that Young's law for a smooth surface,

$$\gamma_{LG} \cos \theta = \gamma_{SG} - \gamma_{SL}$$

then we obtain Wenzel's law

$$\cos \theta^* = r \cos \theta. \quad (3.54)$$

Taking into account that $r > 1$, this relation implies that

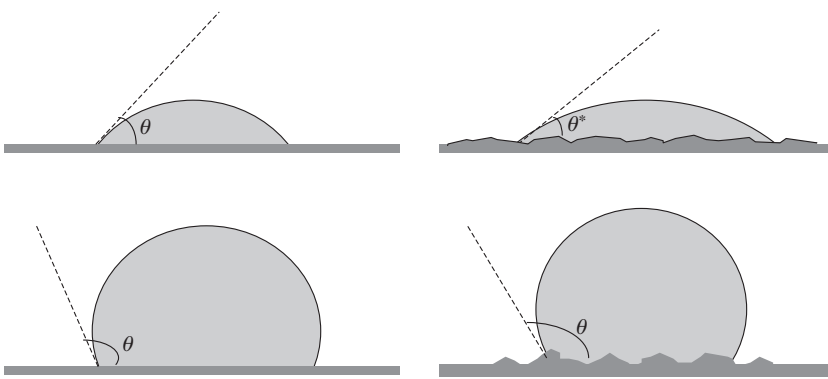
$$|\cos \theta^*| > |\cos \theta|. \quad (3.55)$$

We can deduce that if θ is larger than 90° (hydrophobic contact), then $\theta^* > \theta$ and the contact is still more hydrophobic due to the roughness. If θ is smaller than 90° (hydrophilic contact), then $\theta^* < \theta$ and the contact is still more hydrophilic ([Figure 3.42](#)). In conclusion, surface roughness increases the wetting character.

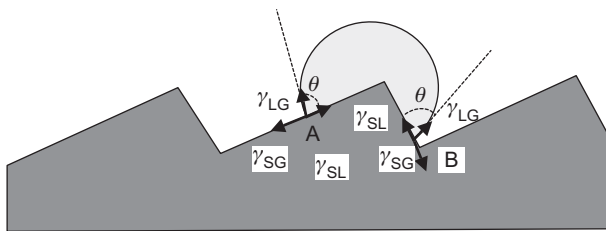
An important observation at this stage is that the scale of the roughness on the solid surface is very small compared to that of the drop [11]. Indeed, if not, it would not be possible to define a unique contact angle; the drop would no longer be axisymmetrical, and the contact could be sketched as in [Figure 3.43](#) (the position of the drop might not be stable).

3.3.2 Cassie–Baxter's law

The same analysis of Wenzel was done by Cassie for chemically inhomogeneous solid surfaces. As for Wenzel's law, the same requirement of small size

**FIGURE 3.42**

Contact of a liquid drop on a rough surface.

**FIGURE 3.43**

Large scale roughness: schematic view of a drop located on an angle of the solid surface. The position of the drop might not be stable.

heterogeneities compared to interaction size between liquid and solid wall applies. For simplicity, we analyze the case of a solid wall constituted by microscopic inclusions of two different materials. If θ_1 and θ_2 are the contact angles for each material at a macroscopic size, and f_1 and f_2 are the surface fractions of the two materials (Figure 3.44), then the energy to move the interface by dx is

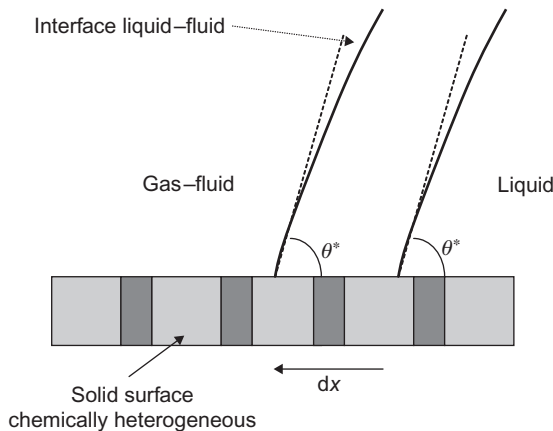
$$dE = dW = (\gamma_{SL} - \gamma_{SG})_1 f_1 dx + (\gamma_{SL} - \gamma_{SG})_2 f_2 dx + \gamma_{LG} \cos \theta^* dx. \quad (3.56)$$

The equilibrium is obtained by taking the minimum of E

$$\gamma_{LG} \cos \theta^* = (\gamma_{SG} - \gamma_{SL})_1 f_1 + (\gamma_{SG} - \gamma_{SL})_2 f_2$$

and by comparison with Young's law, we obtain the Cassie–Baxter's relation

$$\cos \theta^* = f_1 \cos \theta_1 + f_2 \cos \theta_2. \quad (3.57)$$

**FIGURE 3.44**

Displacement of the contact line of a drop on an inhomogeneous solid surface.

This relation may be generalized to a more inhomogeneous material

$$\cos \theta^* = \sum_i f_i \cos \theta_i. \quad (3.58)$$

Note that

$$f_1 + f_2 = 1 \quad \text{or} \quad \sum_i f_i = 1.$$

The Cassie–Baxter's relation shows that the cosine of the contact angle on a microscopically inhomogeneous solid surface is the barycenter of the cosine of the contact angles on the different chemical components of the surface.

The Cassie–Baxter's law explains some unexpected experimental results. Sometimes—if not enough care was taken during microfabrication—a microfabricated surface may present chemical inhomogeneity and the wetting properties are not those that were intended. For example, if a uniform layer of Teflon is deposited on a rough substrate, the surface should become hydrophobic. However, if the layer is too thin, the Teflon layer may be porous and the coating inhomogeneous; the wetting properties are then modified according to the Cassie–Baxter's law and the gain in hydrophobicity may not be as large as expected.

As for Wenzel's law, an important remark at this stage is that the scale of change of the different chemical materials of the solid surface is very small compared to that of the drop [11]. Indeed, if not, it would not be possible to define a unique contact angle any more. This latter type of inhomogeneity is related to drop pinning or to drop motion depending on the morphology of the inhomogeneity.

3.3.3 Contact on fabricated surfaces: the transition between the Wenzel and Cassie laws

3.3.3.1 Introduction

We have seen in the preceding sections that the contact angle of a liquid on a solid surface depends on the roughness and the chemical homogeneity of the surface; this contact angle is given by the Wenzel and Cassie laws. These laws have been established at a mesoscopic scale. For example, Wenzel's law shows that rugosities of the surface increase the hydrophobic/hydrophilic characteristics of a surface. In biotechnology, the materials used are limited—polydimethyl-siloxane (PDMS), Teflon, SU8, glass, silicon, gold. Plastics (Teflon, SU8, PDMS) are generally hydrophobic, whereas glass and metals are hydrophilic and silicon neutral. A way to force the surface to be hydrophobic/hydrophilic is to chemically deposit a hydrophobic/hydrophilic coating on top of the substrate. For example, Uelzen and Müller [18] have developed a technique that consists of growing microscopic tin crystals on a silicon substrate—in order to increase the roughness (Figure 3.45)—and then a hydrophobic coating of TFE (tetrafluoroethylene) or a hydrophilic coating of gold is deposited by chemical vapor deposition (CVD). The result is an enhanced hydrophobic or hydrophilic contact.

Another example of obtaining a superhydrophobic substrate is to deposit a coating of $\text{CF}_4\text{--H}_2\text{--He}$ (Figure 3.46) by plasma discharge [19]. The hydrophobic character increases with the numbers of discharges. Note that in this case, the increase in roughness of the surface is moderate. The rugosities created by the plasma coating are only 10 nm (Figure 3.47). This method can be applied to very different substrates, like silicon, gold, or even cotton.

Another way to increase the hydrophilic/hydrophobic character of a surface is to artificially create patterned microstructures in order to increase the roughness

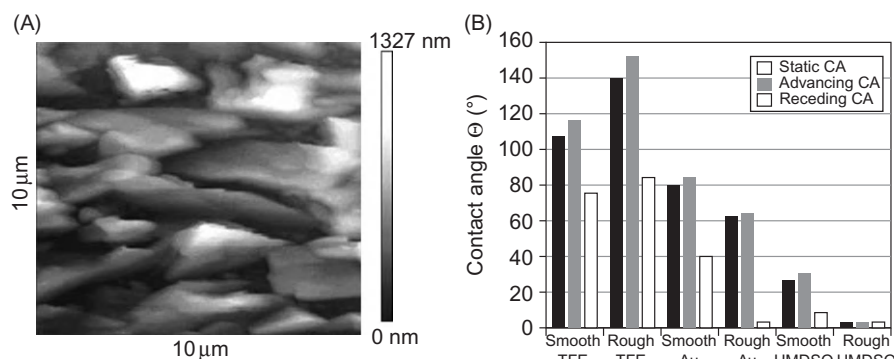
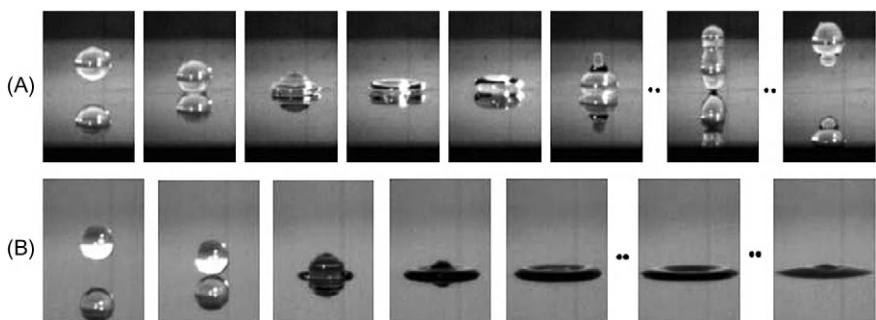


FIGURE 3.45

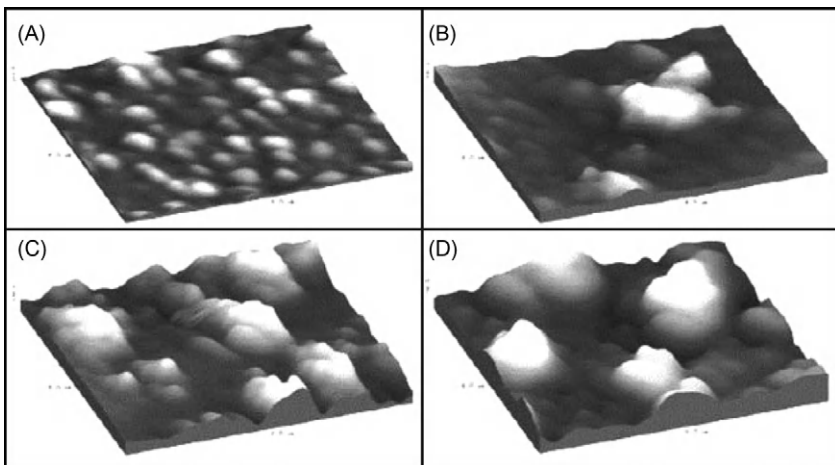
(A) Tin crystals on top of a silicon substrate [18] and (B) CVD deposition of TFE or gold renders the surface hydrophobic or hydrophilic. In the figure, CA stands for contact angle.

Source: From Ref. [18] © 2003, Elsevier, reprinted with permission.

**FIGURE 3.46**

A flat gold plate treated with $\text{CF}_4\text{--H}_2\text{--He}$ plasma deposition becomes very hydrophobic: (A) a water droplet bounces back from the surface treated with $\text{CF}_4\text{--H}_2\text{--He}$ plasma deposition, (B) whereas it spreads on the original gold surface.

Source: Reprinted with permission from Ref. [19] © 2005, American Chemical Society.

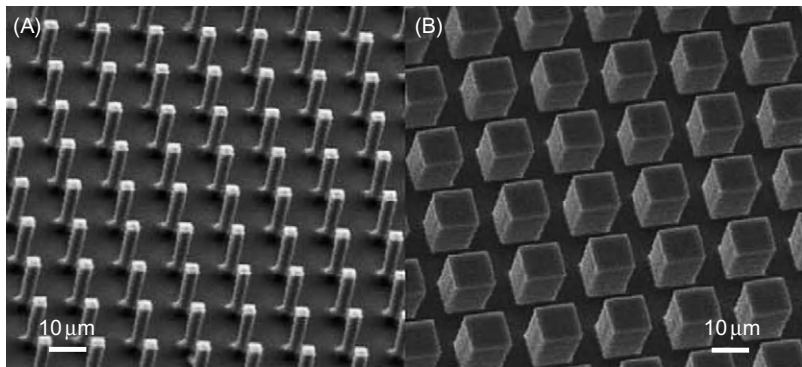
**FIGURE 3.47**

AFM image of a gold surface treated with $\text{CF}_4\text{--H}_2\text{--He}$ plasma discharges. The number of discharges is (A) 0, (B) 3, (C) 7, and (D) 11. After 10 discharges, the surface is superhydrophobic and the rugosities are still very small, of the order of 10 nm.

Source: Reprinted with permission from Ref. [19] © 2005, American Chemical Society.

of the surface—by creating micropillars or grooves. Figure 3.48 shows an example of patterning a silicon surface with micropillars [20].

If Wenzel's law is applicable at such a roughness scale, it is expected that the hydrophilic/hydrophobic character will be increased. So the question is: can Wenzel's formula, taking into account a roughness based on the shape of the microstructures, be used to derive the contact angle? The answer is not that

**FIGURE 3.48**

View of two microfabricated pillared surfaces. Left: small aspect ratio micropillars; right, large aspect ratio micropillars

Source: From Ref. [20] © 2006, Elsevier, reprinted with permission.

**FIGURE 3.49**

(A) Droplet penetrating between the pillars, and (B) droplet sitting on top of the pillars (fakir effect). θ_W is the Wenzel's contact angle and θ_C is the Cassie's contact angle.

straightforward. It has been observed that the droplet does not always contact the bottom plate and sometimes stays on top of the pillars—which is called the “fakir effect” (Figure 3.49). In such a case, should not Cassie’s law, based on a juxtaposition of solid surface and air, have been used? And what is the limit between a Wenzel’s droplet and a Cassie’s droplet? All these questions are discussed next.

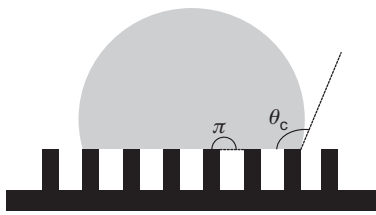
3.3.3.2 Contact angle on a microfabricated substrate: case of hydrophobic contact

Recently, the contact angle of a sessile drop sitting on microfabricated pillars has been the subject of many investigations. As we have seen previously, Young’s law defines the contact angle on the substrate material

$$\cos \theta = \frac{\gamma_{SG} - \gamma_{SL}}{\gamma_{LG}}. \quad (3.59)$$

If the drop penetrates between the pillars, one can write the Wenzel’s angle as

$$\cos \theta_W = r \cos \theta, \quad (3.60)$$

**FIGURE 3.50**

Sketch of a Cassie's drop (fakir effect). The interface between the pillars is roughly horizontal.

where θ_W is the “Wenzel’s” contact angle and r is the roughness of the surface. If the drop stays on top of the pillars, one can write Cassie’s law under the form

$$\cos \theta_C = f \cos \theta + (1 - f)\cos \theta_0, \quad (3.61)$$

where θ_C is the “Cassie’s” contact angle, θ_0 is the contact angle with the layer of air, and f is the ratio of the contact surface (top of the pillars) to the total horizontal surface. If the pillars are not too far from each other, the value of θ_0 is roughly $\theta_0 = \pi$ (Figure 3.50).

Equation (3.61) then simplifies to

$$\cos \theta_C = -1 + f(1 + \cos \theta). \quad (3.62)$$

It is usual to plot the two relations (3.60) and (3.62) in Figure 3.50 [21–26]. In such a representation, the two equations correspond to two straight lines, the first one with a slope r , and the second one with a slope f . The two lines intersect, because

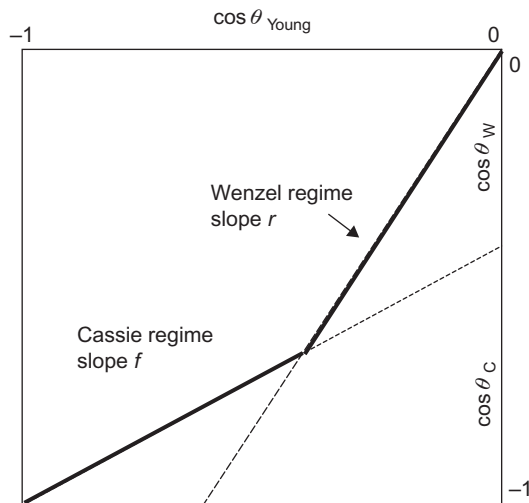
$$r = \frac{S_{\text{total}}}{S_{\text{horizontal}}} > f = \frac{S_{\text{top}}}{S_{\text{horizontal}}}.$$

The two lines intersect at a Young’s contact angle θ_i defined by $\theta_C = \theta_W$, so that

$$\cos \theta_i = \frac{f - 1}{r - f}. \quad (3.63)$$

In Figure 3.51, for a given Young’s angle, there are two contact angles. The question is now: which one is the real one? From energy considerations—e.g., by using Laplace’s law—it can be deduced that the real contact angle is the smaller one, so when the Young’s contact angle is not very hydrophobic ($\theta < \theta_i$), the contact corresponds to a Wenzel’s regime and the drop wets the whole surface. When the Young’s contact angle is more hydrophobic ($\theta > \theta_i$), the drop is in a Cassie’s regime and sits on top of the pillars.

Note that the situation we have just described does not always correspond to reality. It happens that a droplet is not always in its lowest energy level and that

**FIGURE 3.51**

Plot of the Wenzel and Cassie laws for a sessile droplet sitting on a surface textured with micropillars. Using Laplace's law, it can be seen that the energy of the drop is lower when the contact angle is the smallest. The physical situation then corresponds to the continuous lines, with a Wenzel's drop at small Young's contact angle and a Cassie's drop for large Young's contact angle.

droplets are sometimes in metastable regimes. One example was given by Bico et al. [21–23]. It is that of a drop deposited by a pipette on a pillared surface. Even if it should be in a Wenzel's regime and the droplet should penetrate between the pillars, it stays on top of the pillars. It needs an impulse, mechanic, electric, or acoustic to join the expected Wenzel's regime.

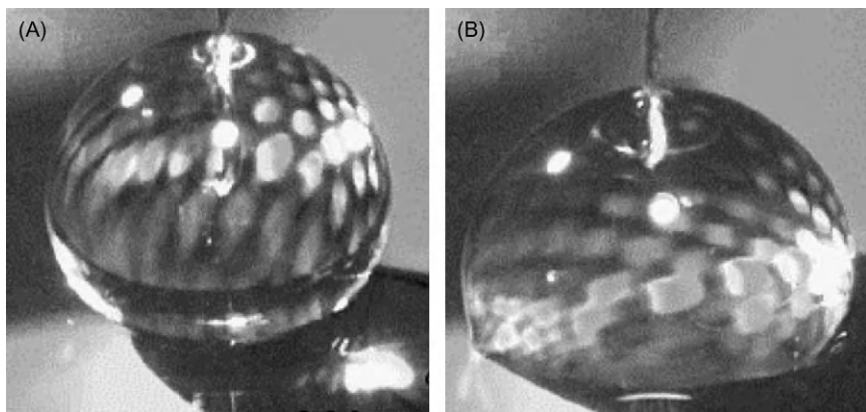
Transition from a Cassie's droplet to a Wenzel's droplet can be obtained by electrowetting actuation. Krupenkin et al. [27] have shown that a droplet sitting on pillars in a Cassie's regime, i.e., sitting only on the top of the pillars, sinks down as soon as electrowetting actuation is turned on ([Figure 3.52](#)).

3.3.3.3 Example of a square lattice

Take the case of a lattice of square pillars disposed along a square grid; this case has been studied by Patankar et al. [25,26] and Zhu et al. [28]. Suppose the rugosities are constituted of square pillars of size $a \times a$, height H , and spacing b similar to that of [Figure 3.48](#) and symbolized in [Figure 3.53](#).

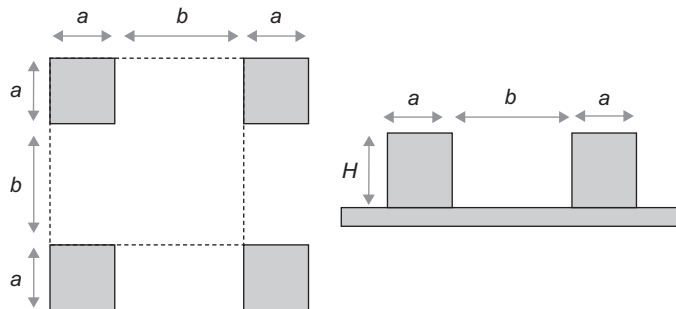
By considering one “motif” in [Figure 3.53](#), the roughness r is determined by:

$$r = \frac{S_{\text{total}}}{S_{\text{horizontal}}} = \frac{(a+b)^2 + 4aH}{(a+b)^2} = 1 + \frac{4A}{(a/H)}, \quad (3.64)$$

**FIGURE 3.52**

Sessile droplet sitting on micropillars: (A) when no electric actuation, the drop sits on top of the pillars and (B) electrode actuated with 22 V electric potential: the droplet wets the flat part of the substrate. The wire at the top is the zero-potential electrode.

Source: Reprinted with permission from Ref. [27] © 2005, American Chemical Society.

**FIGURE 3.53**

Top and cross-sectional schematic sketches of a square pillars patterning.

where

$$A = \left(\frac{a}{a+b} \right)^2.$$

On the other hand, the Cassie's coefficient f is given by:

$$f = \frac{S_{\text{top}}}{S_{\text{horizontal}}} = \frac{a^2}{(a+b)^2} = A. \quad (3.65)$$

Substitution of Eq. (3.64) in Eq. (3.60) and Eq. (3.65) in Eq. (3.62) leads to the Wenzel and Cassie formulas for square pillars in a square “motif”

$$\cos \theta_W = \left[1 + \frac{4A}{(a/H)} \right] \cos \theta \quad (3.66)$$

and

$$\cos \theta_C = -1 + A(1 + \cos \theta). \quad (3.67)$$

Using Eqs. (3.66), (3.67), and (3.63), one finds that the shift from Wenzel to Cassie droplet occurs when

$$\cos \theta_i = \frac{-1}{1 + 4(aH/b^2)}. \quad (3.68)$$

Let us estimate the influence of the parameters a , H , and b in Eq. (3.68).

If the height of the pillars is decreased, $H \rightarrow 0$, and we find $r \rightarrow 1$ using Eq. (3.64), meaning that the roughness induced by the pillars has disappeared and, using Eq. (3.68), $\theta_i \rightarrow \pi$. Reducing the height of the pillars increases the transition angle between Cassie and Wenzel’s regimes and favors the Wenzel’s regime.

When the pillars are thin, $a \rightarrow 0$, and we find $A \rightarrow 0$ and, using Eq. (3.65), $f \rightarrow 0$. Then, using Eq. (3.63), we have the relation $\cos \theta_i \approx (-1/r)$. Because $r \rightarrow 1$ from Eq. (3.64), we conclude that the Wenzel’s regime is predominant.

Finally, when the pillars are very close to one another, $b \rightarrow 0$, using Eq. (3.68), we find that $\theta_i \rightarrow 0$ and we observe a Cassie’s regime. A droplet on a hydrophobic surface does not penetrate small holes in the wall. A membrane pierced with very small holes has to be hydrophilic for water to penetrate the holes.

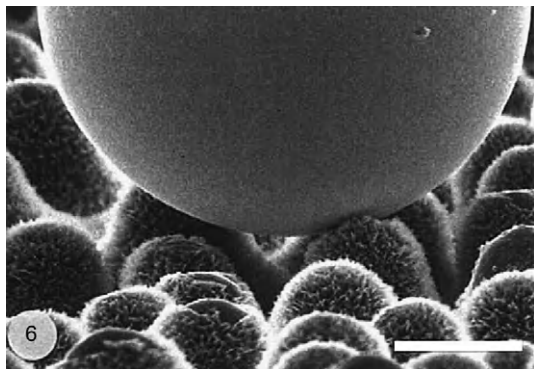
3.3.3.4 Superhydrophobicity

A surface is said to be superhydrophobic when the contact angle of aqueous liquid is close to 180° . In nature, some tree leaves in wet regions of the globe have superhydrophobic surfaces in order to force water droplets to roll off the leaves, preventing rotting of the leaves, as shown in Figure 3.54 taken from Barthlott and Neinhuis [29].

Superhydrophobicity requires either a superhydrophobic Young’s contact angle or a Cassie’s regime. Superhydrophobicity corresponds to $\theta_{\text{real}} = \pi$ and $\cos \theta_{\text{real}} = -1$. It cannot be obtained in the Wenzel’s regime except if $r = 1$ and $\theta_{\text{Young}} = \pi$. Otherwise, it can only be approached in a Cassie’s regime when the value of f is very small (Figure 3.54). Using Eq. (3.65), f can be cast in the form

$$f = \frac{a^2}{(a+b)^2} = \frac{1}{(1+(b/a))^2}. \quad (3.69)$$

From Eq. (3.69), f is small when $b/a \gg 1$. In such a case, the pillars are very thin, and the contact area of the droplet with the solid substrate is very small. The

**FIGURE 3.54**

Mercury droplet on the papillose adaxial epidermal surface of *Colocasia esculenta* demonstrating the effect of roughness on wettability. Due to the decreased contact area between liquid and surface, air is enclosed between the droplet and the leaf, resulting in a particularly strong water-repellent surface. The bar is $20\text{ }\mu\text{m}$.

Source: From Ref. [29] © 1997, Springer, reprinted with permission.

best situation for superhydrophobicity for a geometrically textured surface is f as small as possible and r as large as possible (Figure 3.55). We have already seen the condition for f . Using the approximation $b/a \gg 1$ in the expression of the roughness r , we find $r \approx 1 + 4(aH/b^2)$. This latter relation shows that if H is sufficiently high, r will be large.

3.3.3.5 Irregularly patterned and fractal surfaces

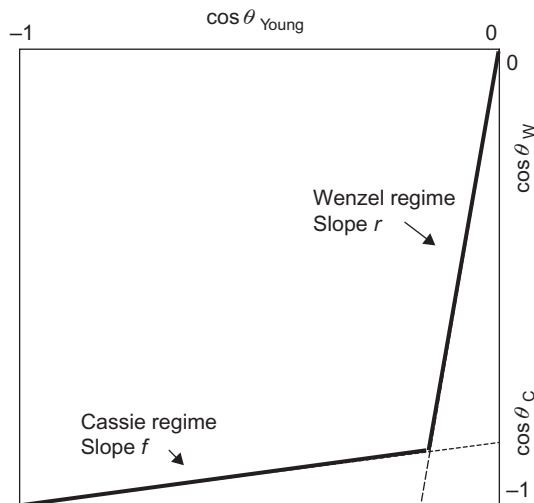
In Section 3.3.3.1, we have seen that an irregular coating was obtained by growing crystals on a surface. In this case, the rugosities were not important and the Wenzel's regime was the regime for any water droplet on this surface. In this section, we analyze the situation when the rugosities are irregular and sufficient to obtain the Cassie's regime.

The first example is that of Fan et al. [30] who made pillars grow from a surface (Figure 3.56) using a glancing angle deposition (GLAD) technique. GLAD is a physical vapor deposition technique along an angle.

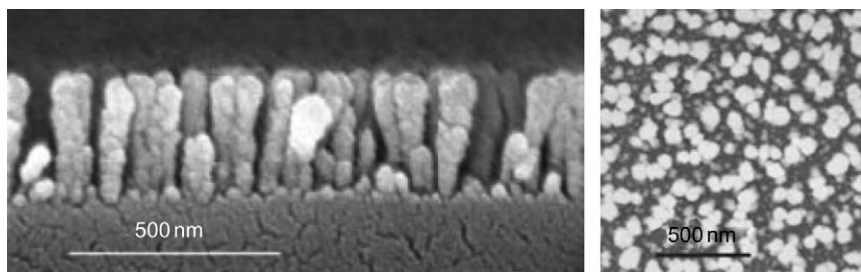
The contact of the water with the pillars has roughly the shape described in Figure 3.57.

Typically, this is a Cassie's droplet. However, due to the roughness of the tops of the pillars, the Cassie's contact angle can then be defined by an improvement of relation (3.61), taking into account the local roughness r^* in the area of contact.

$$\cos \theta_C = r^* f \cos \theta + (f - 1). \quad (3.70)$$

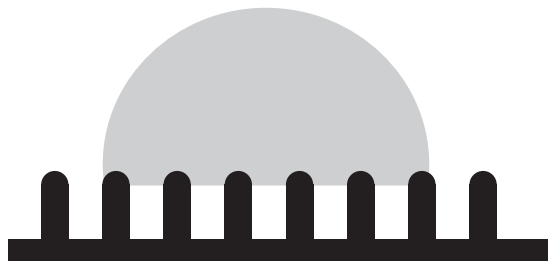
**FIGURE 3.55**

Superhydrophobicity requires a Cassie's/Wenzel's diagram with a very small coefficient f and a large coefficient r .

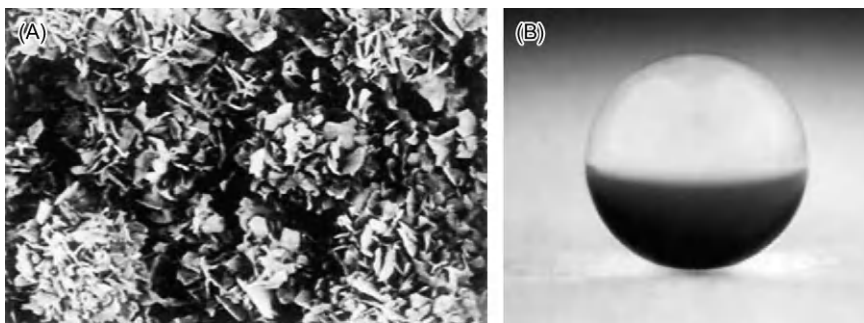
**FIGURE 3.56**

Irregular pillars obtained by Fan et al. [30].

Source: From Ref. [30] © 2004, IOP, reprinted with permission.

**FIGURE 3.57**

Sketch of droplet sitting on pillars similar to those of Figure 3.55.

**FIGURE 3.58**

(A) AFM image of a highly fractal surface made of AKD; (B) the contact angle is larger than 174° .

Source: Reprinted with permission from Refs. [31,32] © 1996, American Chemical Society.

In the case where the tops of the pillars are spherical, Bico et al. [22] have shown that Eq. (3.70) becomes

$$\cos \theta_C = -1 + f(1 + \cos \theta)^2. \quad (3.71)$$

This situation combines the effects of Cassie and Wenzel regimes. Note that Eq. (3.72) shows that the Cassie's regime is not linear in $\cos \theta$ but quadratic.

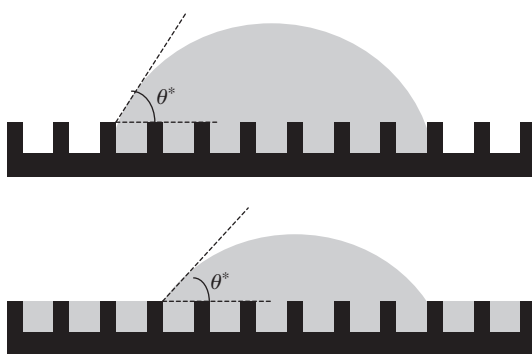
Similarly, Onda et al. and Shibuichi et al. [31,32] have fabricated fractal surfaces (Figure 3.58) using alkylketene dimer (AKD). These surfaces may be called biomimetic, because they resemble the structure of hydrophobic leaf surfaces which are also fractal. Using fractal dimensions, they have deduced a relation similar to Wenzel's law

$$\cos \theta_W = \left(\frac{L}{l}\right)^{D-2} \cos \theta, \quad (3.72)$$

where L and l are the largest and smallest fractal size limits of surface, respectively and D is the fractal dimension ($D = 2.3$ in their case). It is typically a case of superhydrophobicity, since the coefficient $r = (L/l)^{D-2}$ is large and the value of f is very small.

3.3.3.6 Contact angle on a microfabricated substrate: case of hydrophilic contact

In the preceding sections, we have dealt with nonwetting textured surfaces. Here, we examine the case of a hydrophilic (wetting) textured surface. This case refers to the theory of impregnation [23]: a droplet on a rough wetting surface has a smaller contact angle than the Young's contact angle, according to Wenzel's law. However, it has been observed that in some cases, spreading occurs, i.e., a part of the liquid forms a film on the substrate.

**FIGURE 3.59**

The two possible morphologies of a droplet on a wetting textured surface.

If we keep the same notations, r the roughness of the surface defined by Eq. (3.64) and f the Cassie's ratio defined by Eq. (3.65), one can define a critical contact angle by:

$$\cos \theta_{\text{crit}} = \frac{1-f}{r-f}. \quad (3.73)$$

If the Young's contact angle θ is such that $\theta < \theta_{\text{crit}}$, then the liquid wets the surface, i.e., a liquid film spreads on the surface. The two possible morphologies are shown in Figure 3.59.

Relation (3.73) is very similar to the case of the hydrophobic critical angle defined by Eq. (3.63). Then, for a flat surface $r \rightarrow 1$ and the surface is wetted only if the Young's contact angle is $\theta = 0$. For a porous medium (r infinite), Eq. (3.73) indicates that wetting occurs when $\theta < \pi/2$. More generally, Eq. (3.73) defines a critical angle comprised between 0 and $\pi/2$.

In the Wenzel's regime ($\theta > \theta_{\text{crit}}$), the contact angle is

$$\cos \theta^* = r \cos \theta \quad (3.74)$$

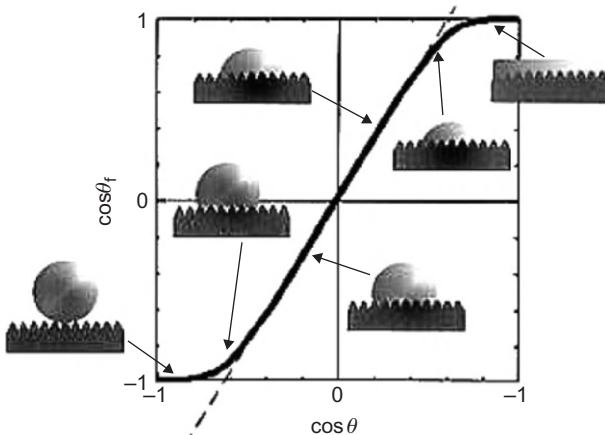
and, above the critical value θ_{crit} , a film forms, but the remaining droplet has a contact angle defined by:

$$\cos \theta^* = 1 - f(1 - \cos \theta). \quad (3.75)$$

This expression shows that the presence of a film improves the wetting ($\theta^* < \theta$), but it is not possible to induce a wetting transition (total wetting) by texturing a solid: Eq. (3.75) shows that complete wetting $\theta^* = 0$ requires $\theta = 0$.

3.3.3.7 Conclusion/discussion

A complete diagram of wetting transitions is shown in Figure 3.60 [31,32]. On the hydrophobic side, if the Young's angle θ is such that $\theta > \theta_i$, where θ_i

**FIGURE 3.60**

Plot of the relation between $\cos(\theta_{\text{real}})$ and $\cos(\theta_{\text{Young}})$ for patterned surfaces.

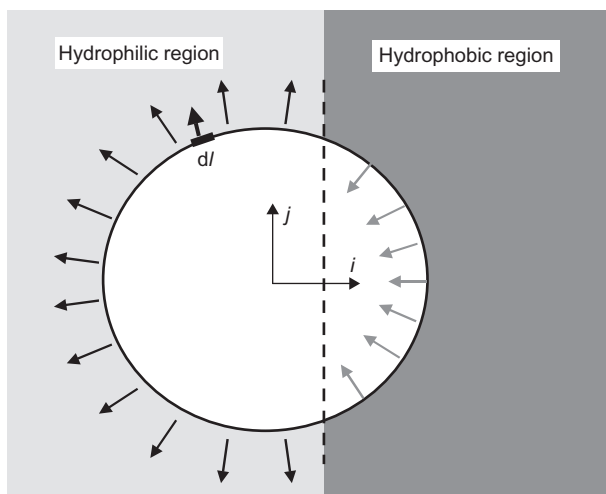
Source: Reprinted with permission from Ref. [32] © 1996, American Chemical Society.

is defined by $\cos \theta_i = (f - 1/r - f)$ (Eq. (3.63)), the droplet stays on the pillar tops (fakir effect) producing a superhydrophobic situation. If $\pi/2 < \theta < \theta_i$, the droplet is in the Wenzel's regime, completely in contact with the surface of the pillars, with a contact angle larger than the Young's contact angle. On the hydrophilic side, if the Young's contact angle θ is such that $\pi/2 > \theta > \theta_{\text{crit}}$ the droplet is in the Wenzel's regime, with a real contact angle θ^* smaller than θ . For $\theta < \theta_{\text{crit}}$, where θ_{crit} is defined by Eq. (3.73), the liquid spreads between the pillars and leaves a droplet above the pillars with a very small contact angle.

3.4 Drops moving by capillarity

Macroscopic flows are usually moved by hydrodynamic forces like pressure or mechanical forces like pistons or moving parts. The same types of forces can also be employed to actuate microfluidic flows. Peristaltic micropumps and syringe pumps are the microscopic versions of pumps and pistons. However, at the microscopic scale there are other forces to move fluids that are not efficient at the macroscopic scale. These forces are electro-osmosis and capillarity. In particular, capillarity is widely used for actuating droplets.

In the following, we deal with capillarity as a force to displace droplets. This problem is extremely difficult. In order to simplify the approach, we do not focus on the dynamics of the droplets but on the equilibrium state. In doing so, we assume slow motion and confine the study to quasi-static displacements.

**FIGURE 3.61**

Schematic view of a water droplet standing above a hydrophilic/hydrophobic contact. There is a resulting force directed toward the hydrophilic region.

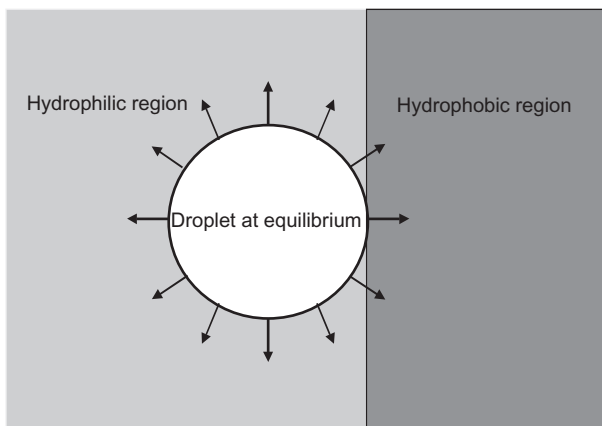
3.4.1 Drop moving over a transition of wettability

It is a well-established fact that microdrops can be put into motion by hydrophilic and hydrophobic forces. Let us suppose for instance that a water droplet is placed on a perfectly smooth horizontal plane (Figure 3.61) at the boundary between two different chemical coatings: hydrophilic on one side and hydrophobic on the other. In such a case, we have the following scheme for the contact forces (as we do not know exactly what is the shape of the drop at the very instant it is placed on the surface, we have drawn an approximate shape, close to—but not exactly—a circle; however, the reasoning will stand, whatever the shape).

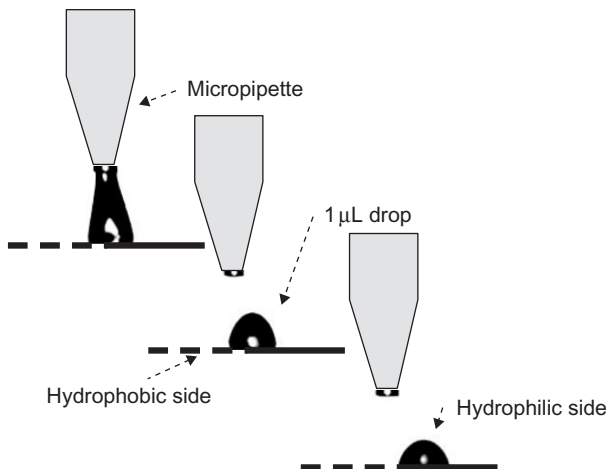
From this scheme, it results that the droplet moves toward the hydrophilic surface. If L_1 and L_2 are the contact lines, respectively in the hydrophilic and hydrophobic planes, and θ_1 and θ_2 the contact angles, the force acting on the drop is

$$\begin{aligned} F_x &= \int_{L_1} (\gamma_{SG} - \gamma_{SL})_1 (\vec{i} \cdot d\vec{l}) - \int_{L_1} (\gamma_{SG} - \gamma_{SL})_2 (\vec{i} \cdot d\vec{l}) \\ &= \int_{L_1} \gamma_{LG} \cos \theta_1 (\vec{i} \cdot d\vec{l}) - \int_{L_2} \gamma_{LG} \cos \theta_2 (\vec{i} \cdot d\vec{l}) < 0. \end{aligned} \quad (3.76)$$

So, the resulting force is directed toward the left in the scheme of Figure 3.26, and the drop moves to the left. The motion stops when the resultant of the contact forces is zero, i.e., when the drop is entirely on the hydrophilic region, as shown in Figure 3.62.

**FIGURE 3.62**

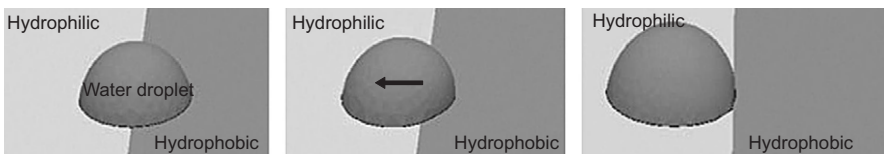
The water droplet is at equilibrium when it is entirely located on the hydrophilic region.

**FIGURE 3.63**

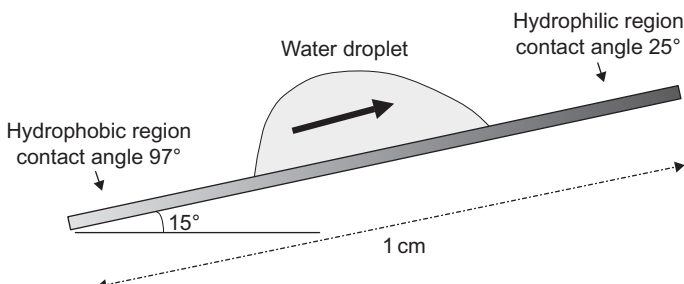
Experimental view of the relocation of a microdrop ($1 \mu\text{L}$) deposited on a hydrophilic/hydrophobic boundary.

Experimental evidence confirms the preceding analysis. In [Figure 3.63](#), a drop is deposited with a micropipette on a flat horizontal surface, at the boundary of two regions with different contact angles.

The preceding analysis is numerically confirmed by a calculation with the Evolver code ([Figure 3.64](#)). We can start with any volume of water spread over a hydrophilic/hydrophobic boundary. After a few iterations, the drop is formed, but

**FIGURE 3.64**

Motion of a drop toward the hydrophilic plane (simulation with Surface Evolver). The microdrop is initially deposited over the hydrophilic/hydrophobic transition line and it is not an equilibrium state. Drop moves to find an equilibrium state on the hydrophilic plate, just at the boundary between the two regions.

**FIGURE 3.65**

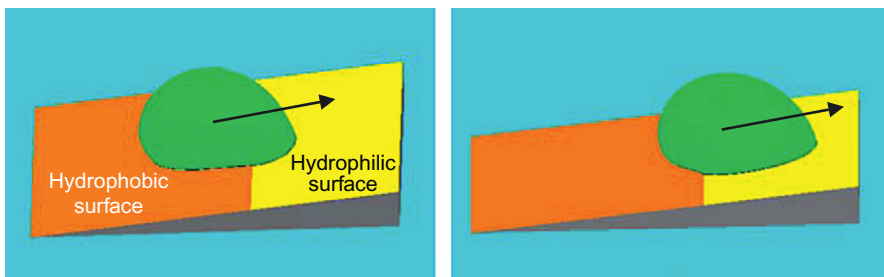
An oil drop may run uphill toward the more hydrophobic region.

it is not at equilibrium because of the global force directed toward the hydrophilic region. The drop evolves to find its equilibrium location which is located just at the boundary of the transition line, on the hydrophilic side.

Note that the direction of the motion of a water drop is toward the hydrophilic region, whereas the motion of an oil droplet would be toward the hydrophobic region in the same geometrical conditions. Note also that the drop behavior would be similar if the transition between the two regions were not abrupt, but smooth, and if there were a wettability gradient between the two regions [33]. In the next section, we investigate the effect of a gradient of wettability.

3.4.2 Drop moving uphill

Capillary forces may be sufficient to make microdrops move upward on an inclined plane. Chaudhury and Whitesides [34] have shown that a droplet can go up a slightly inclined plate presenting a wettability gradient (Figure 3.65). They have shown that a surface having a spatial gradient in its SFE was capable of causing drops of water placed on it to move uphill. This motion was the result of an imbalance in the forces due to surface tension acting on the liquid–solid

**FIGURE 3.66**

Droplet moving up a plane at a wettability transition (simulation made with Surface Evolver).

contact line on the two opposite sides (“uphill” or “downhill”) of the drop. The required gradient in SFE was generated on the surface of a polished silicon wafer by exposing it to the diffusing front of a vapor of decyltrichlorosilane, $\text{Cl}_3\text{Si}(\text{CH}_2)_9\text{CH}_3$. The resulting surface displayed a gradient of hydrophobicity (with the contact angle of water changing from 97° to 25°) over a distance of 1 cm. When the wafer was tilted from the horizontal plane by 15° , with the hydrophobic end lower than the hydrophilic, and a drop of water ($1\text{--}2\mu\text{L}$) was placed at the hydrophobic end, the drop moved toward the hydrophilic end with an average velocity of approximately $1\text{--}2\text{ mL/s}$.

A similar motion can be obtained at a wettability transition on a tilted plane. If a droplet is initially deposited over a wettability transition, it moves uphill from the lyophobic region (hydrophobic for a water droplet) toward the lyophilic region (hydrophilic for a water droplet). [Figure 3.66](#) shows that the droplet is not stable when located on the transition line and moves uphill. The slope angle a microdrop can move uphill depends on the size of the droplet (in case gravity intervenes) and the contact angles on both sides of the transition line.

3.4.3 Drop moving up a step

Another interesting demonstration of the power of capillary forces may be seen by making a drop move up a step. In such a case, a microdrop of water is initially located on a step at the boundary of a hydrophilic region (on top of the step) and a hydrophobic region (at the base of the step). The calculation with the Evolver code shows that the drop progressively moves toward the hydrophilic region, even if this region is located at a higher level ([Figure 3.67](#)). Capillary forces dominate gravity in this example.

In biotechnology, wells, cusps, and grooves are used to confine microdrops. This confinement must be efficient. The preceding analysis has shown that attention should be given to the wettability of surfaces and that the combination of a

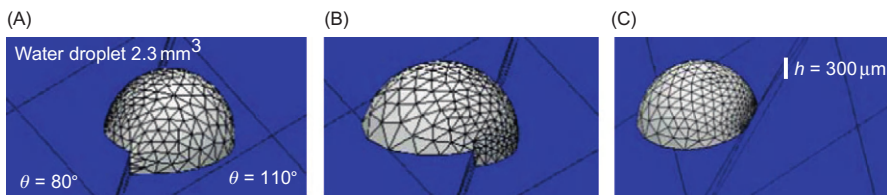


FIGURE 3.67

Motion of a drop up a step toward the hydrophilic plane (simulation made with Surface Evolver): (A) the droplet is located on the lower surface, with a part of it overlapping on the upper plane; (B) the droplet is not in an equilibrium state, and moves up the step pulled by hydrophobic forces of the upper plate; and (C) motion continues until an equilibrium state is reached when the drop is entirely on the upper plate.

nonwetting bottom of the well/groove and a wetting upper surface can result in poor confinement.

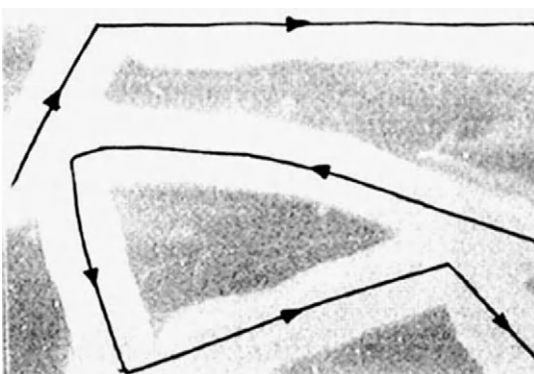
3.4.4 Drop moving over a gradient of surface concentration of surfactant

In the preceding sections, the capillary forces inducing droplet motion were linked to a local change of contact angle of the substrate. In this section, we show how chemical reactions between the liquid of the droplet and the substrate can create droplet motion. To this extent, the experiment of Dos Santos and Ondarçuhu [35] is characteristic. Suppose that a droplet of *n*-alkanes containing silane molecules is placed on a hydrophilic surface. It is well known that silane molecules form dense grafted monolayers on silicon or glass, rendering the surface hydrophobic. If we deposit such a droplet on a glass surface and initiate a motion by pushing it with a pipette, then the droplet continues to move on the substrate. It moves in nearly linear segments and changes its direction each time it encounters a hydrophobic barrier (Figure 3.68). The droplet cannot cross its own tracks.

The motion is governed by an imbalance of capillarity: the advancing contact line has a hydrophilic Young's contact angle. On the other end, molecules of silane concentrate at the vicinity of the receding contact line and form a hydrophobic layer. The Young's angle at the receding line is then a hydrophobic contact angle (Figure 3.69). As a result, the droplet moves in a straight line, except if it encounters surface defects or an existing hydrophobic trail.

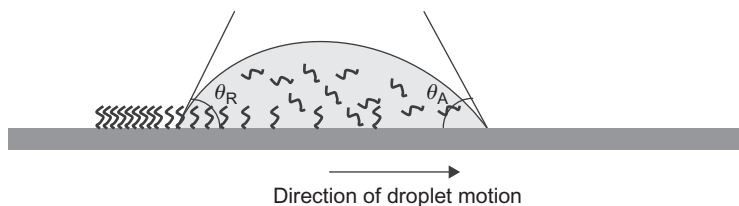
3.4.5 Conclusion

We have seen that capillary forces are often powerful enough to induce motion of microdrops. However, we have considered perfect, smooth surfaces and have

**FIGURE 3.68**

Free running *n*-alkane droplet on a horizontal hydrophilic substrate.

Source: From Ref. [35] © 1995, APS, reprinted with permission.

**FIGURE 3.69**

Advancing and receding Young's contact angles are not identical. The hydrophobic monolayer changes the receding Young's contact angle.

neglected the effect of hysteresis—local change of contact angle—and its extreme form which is droplet pinning—blockage of a droplet due to defects of the surface. In reality, a drop does not move as soon as there is a gradient of wettability. It moves as soon as the gradient of wettability is sufficient for the capillary forces to dominate opposite reaction forces like gravity, hysteresis, and pinning. In the following section, we concentrate on the forces preventing droplet motion linked to the state of the surface.

3.5 Contact angle hysteresis

The concept of hysteresis for triple contact lines is difficult to define with accuracy. Indeed, it is not clear how to set the boundaries for such a concept. Let us start with a droplet sitting on a perfectly horizontal, clean, smooth plane. In such a case, as we have seen in Chapter 2, the contact angle of the liquid is defined by Young's law

$$\cos \theta = \frac{\gamma_{SG} - \gamma_{SL}}{\gamma}$$

However, no surface is ideally perfect; microscopic defects—morphological as well as chemical—are usually present. We have also seen in the preceding section that the Young's contact angle is modified if the surface is rough (Wenzel's law) or chemically heterogeneous (Cassie's law). Some authors have associated the change of contact angle according to Wenzel's or Cassie's law to hysteresis [36]; however, the concept of hysteresis is preferentially associated to *local* defects [1]. These *local* defects can be isolated point defects, surface defects, or line defects. A point defect can be an isolated roughness due to adherence of a microparticle; a surface defect can be a stain of a chemical product; a line defect can be a long chain of polymer adhering to the surface.

Suppose we have a plane surface with dispersed local point defects. Let us deposit a droplet of water on the surface with a pipette in a first phase, and in a second phase, remove the water with the pipette ([Figure 3.70](#)).

We observe that the contact angle is not the same during the two phases. If θ_A denotes the contact angle during the first—advancing—phase and θ_R the contact angle during the second—receding—phase, we have

$$\theta_A \geq \theta_{Young} \geq \theta_R. \quad (3.77)$$

[Figure 3.71](#) shows typical evolution of the advancing and receding contact angles corresponding to the experiment of [Figure 3.70](#).

Intuitively, the advancing front has a larger contact angle because it is locally “slowed down” by inhomogeneities on the surface, whereas the receding front has a smaller contact angle because it is locally “pulled back” by these same inhomogeneities. Note that the same type of behavior is observed during the electrowetting process, with a similar method. More details will be given in Chapter 4.

Values of the change of contact angle are very difficult to predict, because they depend on many parameters. This situation is very different from the case of a plug flow where the Hoffmann–Tanner law links the advancing and receding contact angles to the plug velocity.

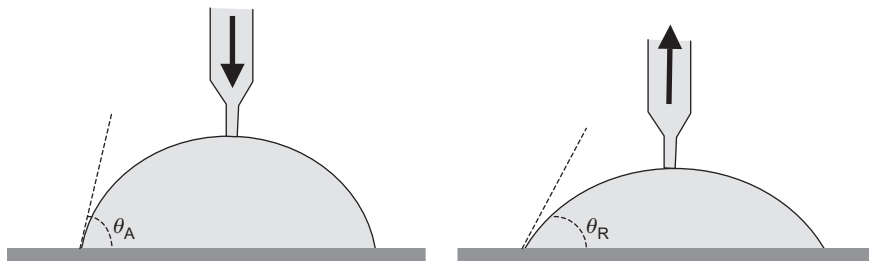
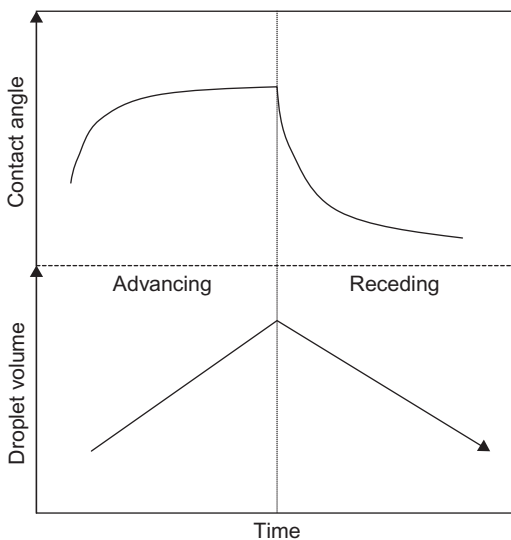


FIGURE 3.70

Contact angle is not the same when the droplet grows or recedes due to hysteresis of the triple line.

**FIGURE 3.71**

Typical time evolution of the contact angle during the growing and shrinking phase of a droplet on a flat substrate according to Wege et al. [37], Lam et al. [38] and Tavana and Neumann [39].

Cubaud and Fermigier [40] proposed a very instructive approach by showing that, in the presence of surface defects, the contact line can be separated between a three-phase—far from the defect or heterogeneity—and a four-phase contact line at the contact of the defect. An image of local hysteresis at extremely low speed of motion is shown in [Figure 3.72](#).

The contact line Λ is the union of the set of the triple contact lines Λ_3 and of the set of four-phase lines Λ_4 . This can be analytically described by:

$$\Lambda = g(t)\Lambda_3 + (1 - g(t))\Lambda_4, \quad (3.78)$$

where $g(t)$ is a function of time and surface geometry. For a quasi-static motion, with a small capillary number $Ca = (\mu U / \gamma) \ll 1$, the contact angle varies between the Young's contact angle θ_3 of the triple line and the contact angle θ_4 corresponding to the defect. [Figure 3.72](#) shows an enlarged view of the interface when it advances past defects. The deformation of the interface and the modified contact angle can be seen in black in the figure.

This situation can be simulated by the Surface Evolver numerical software. These defects can be geometrical as well as chemical. In the model, the defect is a local change of value of the wettability. As in the approach of Cubaud et al. [40], the contact angle is locally modified by the defect ([Figure 3.73](#)), resulting in a loss of capillary force.

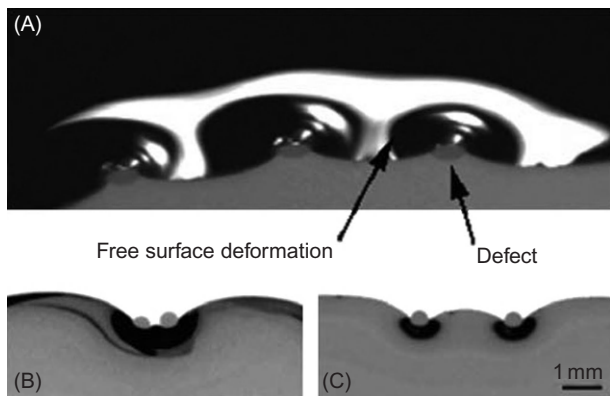
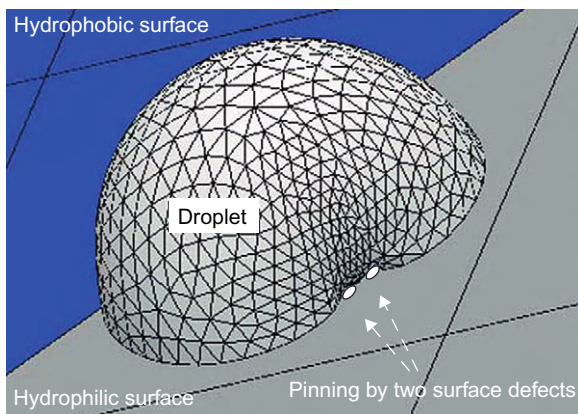
**FIGURE 3.72**

Image of an interface slowly moving over defects. Far from the defect, the contact angle is equal to the Young's contact angle θ_3 , close to the defect the interface is twisted, and the contact angle varies between θ_3 and that of the defect θ_4 . (A) interface moving towards the bottom of the figure, the three defects modify the shape of liquid surface (white region); (B) and (C) a liquid moving towards the top of the figures is blocked by the presence of the defects

Source: From Ref. [40] © 2004, Elsevier, reprinted with permission.

**FIGURE 3.73**

Evolver simulation of a water droplet encountering defects during its motion from a hydrophobic surface toward a hydrophilic surface. This case is similar to that of [Figure 3.72](#).

If we imagine now that there are many defects, we can easily understand that the global contact angle is an average between θ_3 and θ_4 , resulting in a larger advancing contact angle because θ_4 is larger than θ_3 .

In the next section, we investigate droplet pinning, which is the extreme form of hysteresis where the droplet is totally blocked in its motion by defects on the solid surface.

3.6 Droplet pinning

Young's law determines the contact angle at a triple line between a liquid, a fluid, and a solid. It is important to keep in mind that Young's law is valid only if there are no other forces applied on the triple line. In DMF, there are cases where Young's law is violated: this is the case in hysteresis, as we have seen in the previous section, and this is also the case in droplet "pinning". In the following we show that droplets can be pinned by "point-like" defects or by wettability boundary lines.

3.6.1 Droplet pinning on a surface defect

Local chemical and/or geometrical defects locally modify the contact angle. If the defect is sufficiently important, or if there are sufficient numbers of defects, the droplet cannot move even if capillary—or electrocapillary—forces are applied on it. This phenomenon is called pinning. We show in [Figure 3.74](#) a numerical simulation of pinning of a droplet during its motion from a hydrophobic to a hydrophilic substrate.

Note that an important defect does not always pin the droplet. Depending on the relative location of the defect, the droplet may be pinned or just deviated in its motion, as is shown in [Figure 3.75](#).

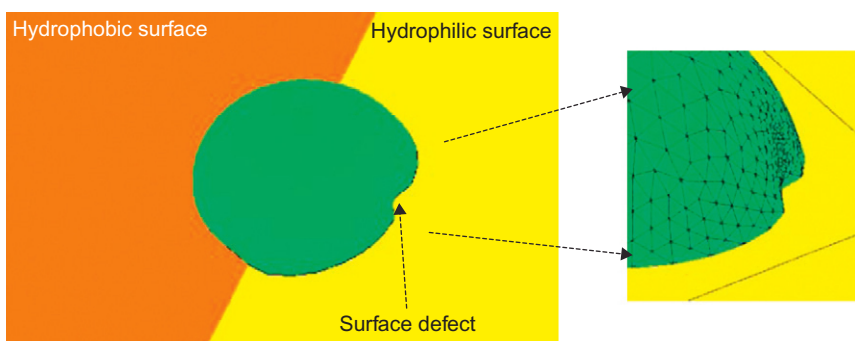
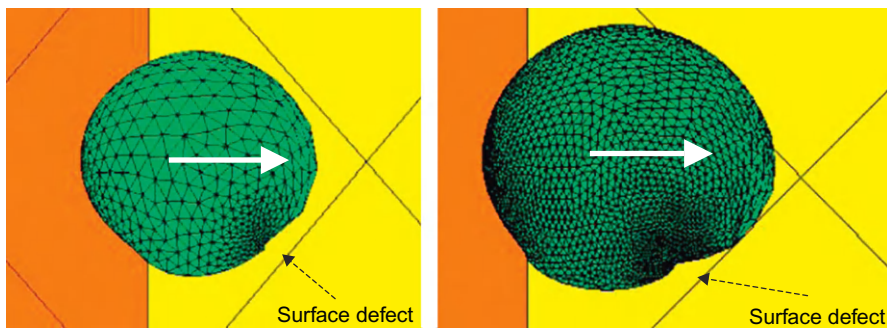
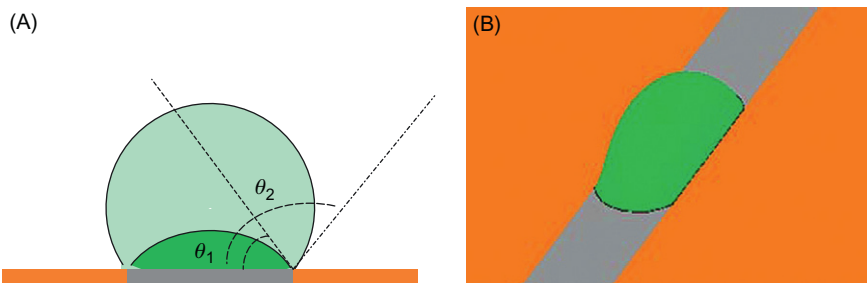


FIGURE 3.74

Pinning of a drop moving from a hydrophobic area toward a hydrophilic surface due to a defect of the surface.

**FIGURE 3.75**

Depending on its location, a surface defect does not always prevent the water droplet from moving to the hydrophilic surface.

**FIGURE 3.76**

Quadruple contact line pinning on a wettability boundary: (A) vertical cross-section of the droplet with the limiting contact angles θ_1 and θ_2 and (B) an Evolver simulation of the droplet.

3.6.2 Droplet pinning at a wettability separation line

Pinning may also occur at a transition line between two surfaces with different chemical coatings, inducing a sharp transition of wettability [41]. We have already seen this phenomenon in Section 3.2.7. This effect is also known as “canthotaxis”, and is due to the fact that, when the contact line reaches the separation line, we have a four-phase contact line. An analysis of the boundary conditions shows that there is equilibrium as long as the contact angle is comprised between the Young’s angles on both sides θ_1 and θ_2 as shown in Figure 3.76 [13,41]

$$\theta_1 \leq \theta \leq \theta_2. \quad (3.79)$$

Equation (3.79) can be written in terms of surface energy

$$\arccos\left(\frac{\gamma_{S1G} - \gamma_{S1L}}{\gamma}\right) \leq \theta \leq \arccos\left(\frac{\gamma_{S2G} - \gamma_{S2L}}{\gamma}\right), \quad (3.80)$$

where the indices $S1$ and $S2$ denote the left and right solid surfaces, respectively. If the external constraint is such that θ continues to increase, the triple line is suddenly de-pinned and the liquid is released and invades the lyophobic surface. On the right surface, the contact angle is the Young's contact angle θ_2 .

An interesting investigation of the pinning along a sinusoidal line has been done by Ondarçuhu [41] using the theory of elasticity of the interface by de Gennes et al. [1]. This approach is presented in Chapter 5 for the pinning of an interface on a jagged electrode boundary.

3.6.3 Droplet pinning on an edge

Pinning—or attachment—can also occur on an edge [42]. Suppose there is a straight edge, and the interface coming to contact this edge (Figure 3.77). The contact line on the angle stays fixed as long as the contact angle is not forced over the limit $\alpha + \theta$, where α is the angle between the two planes. The condition for pinning is then

$$\theta \leq \phi \leq \alpha + \theta, \quad (3.81)$$

where ϕ is the contact angle and θ is the Young's contact angle with the solid surfaces. In the case where the two planes have a different chemical surface, the

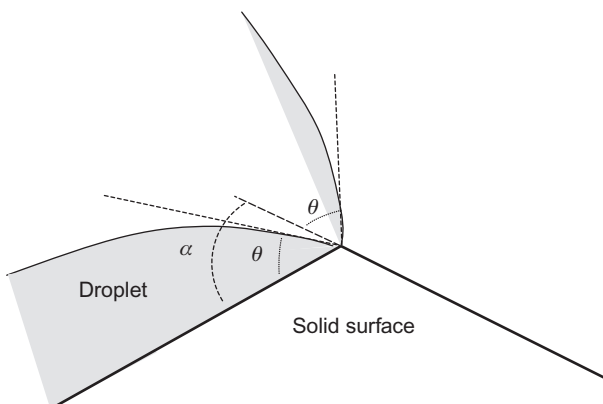
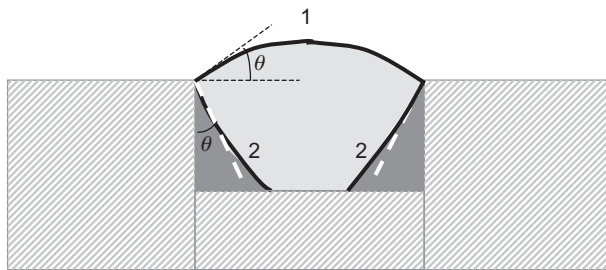


FIGURE 3.77

Droplet pinning on an edge: the droplet is pinned as long as the contact angle varies between the natural Young's contact angle θ to the value $\theta + \alpha$. Above this value, the interface moves over the right plane and the droplet is released.

**FIGURE 3.78**

Pinning of liquid in a groove: the interface stays attached to the rim as long as the volume of liquid is such that it is comprised between the two limits 1 and 2 defined by the continuous black lines.

Young's contact angles can be denoted θ_1 and θ_2 , and the condition (3.81) becomes

$$\theta_1 \leq \phi \leq \alpha + \theta_2.$$

We have already discussed the possible morphologies of liquid in a microgroove. Let us remark here that the interface of the liquid can stay pinned to the rim of the groove (Figure 3.78). Pinning occurs when, in a cross-section, the interface does not bulge above the limit imposed by the Young's contact angle of the top plane (limit 1 in Figure 3.78) or decreases below the wedge limit (limit 2 in Figure 3.78).

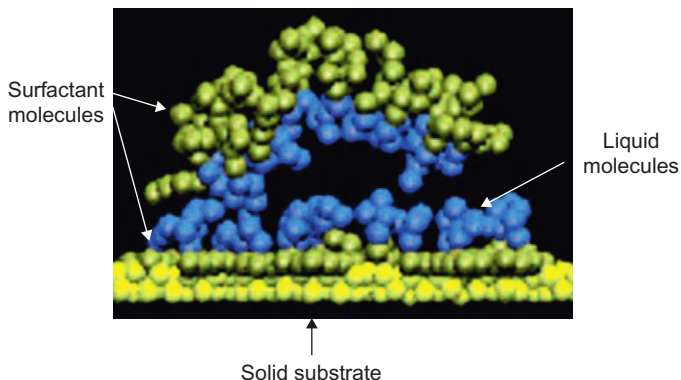
3.7 The effect of surfactants

3.7.1 Introduction

As we mentioned in Chapter 2, surfactants like Triton or Tween are often added to biological liquids to prevent the colloidal suspension contained in the droplet from sticking to the solid surfaces and aggregating. This adding of surfactants has the consequence of reducing the surface tension of the liquid with the air γ and also with the solid surface γ_{SL} . According to Young's law

$$\gamma \cos \theta = \gamma_{SG} - \gamma_{SL}.$$

At the same time, the surface tension γ and the contact angle θ are changed by the addition of surfactants. On the one hand, the surface tension γ is reduced by the migration of the surfactants to the interface which results in a reduction of the interfacial energy. On the other hand, the contact angle θ is reduced indirectly because of the deposition of surfactants on the solid surface changing the surface tension between the solid and the liquid γ_{SL} . Figure 3.79 results from a molecular dynamics simulation [43] and shows the two preferential locations of the surfactants.

**FIGURE 3.79**

Molecular dynamics simulation of a water droplet showing the surfactant molecules at the interface and on the substrate.

Source: Reprinted with permission from Ref. [43] © 2005, American Chemical Society.

Some surfactants reduce the contact angle by 10° or 20° but are not sufficient to obtain a complete wetting of the surface. Some others result in a total wetting of the liquid. The following section illustrates the effect of two types of surfactants: type 1 is linear chain molecules and type 2 is T-shape molecules.

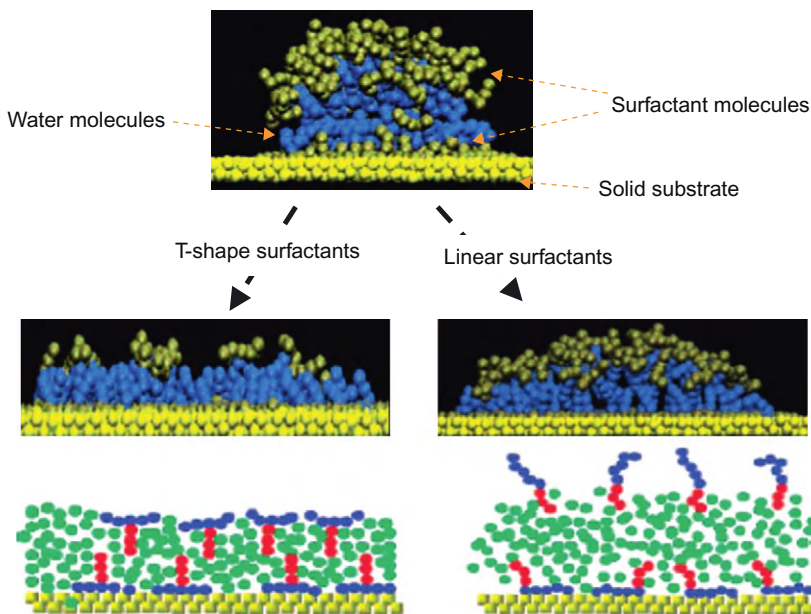
3.7.2 From partial wetting to total wetting

All surfactants are not equally effective in changing droplet wettability. The morphology of the surfactant molecule at the nanoscopic scale is determining. Shen et al. [43] have simulated the effect of flexible linear chain surfactants like alkyl chains, and rigid T-shape surfactants like trisiloxane (Figure 3.80).

T-shape surfactants work better than flexible linear surfactants because they facilitate the formation of a liquid film. As shown in Figure 3.80, at the bottom left corner, T-shape molecules rearrange between the liquid interface and the solid interface to form a “sandwich” laminating a water film.

3.8 Marangoni convection

Depending on the nature of the liquid, sitting droplets can be at rest with no internal convective motion, or can be agitated by internal motion, even if the external shape remains unchanged. High viscosity liquids and ionic liquids behave similarly to gels (see Chapter 7); they seldom show internal convection, at least when they are not moving on the substrate, whereas water droplets are often agitated by convective motions. There are two reasons for these motions: Marangoni

**FIGURE 3.80**

MD (molecular dynamics) numerical simulations of a droplet spreading on a substrate under the action of T-shape surfactants and flexible linear chain surfactants.

Source: Reprinted with permission from Ref. [43] © 2005, American Chemical Society.

convection and evaporation (the two phenomena might be linked, as we will see in [Section 3.9.4](#)).

In Chapter 2, we have seen that Marangoni convection is associated to a gradient of surface tension. This gradient of surface tension may be caused by temperature, concentration of surfactants, and even by an electric field. The general formulation proposed by Colin [44] uniting these three possible sources of surface tension gradient is

$$d\gamma = \frac{\partial\gamma}{\partial T} dT + \frac{\partial\gamma}{\partial c} dc + \frac{\partial\gamma}{\partial E} dE. \quad (3.82)$$

These three types of convective motions can be found in microfluidics systems.

3.8.1 Marangoni convection due to thermal nonuniformity

In Chapter 2, we have seen that surface tension depends on temperature. To the first order, this dependency is

$$\gamma = \gamma_0(1 + \alpha T), \quad (3.83)$$

where $\alpha = -1/T_C$ and T_C is the critical temperature in kelvin. The coefficient α being negative, the value of the surface tension decreases with temperature.

Very often the temperature of the solid substrate is not the same as that of the surrounding air. If the substrate is warmer than the air—which is the case, for example, during heating phases of polymerase chain reaction (PCR) reactions—the liquid droplet sitting on the substrate will experience a warmer region near the substrate and a cooler region near the apex of the droplet. Thus, the surface tension will be lower near the substrate and larger at the apex, resulting in a tangential force on the interface. If this tangential force is sufficient, it induces a circulation inside the droplet, as shown in [Figure 3.81](#). Thus, even if the external shape of the droplet does not change, there can be internal motions induced by a Marangoni effect. The internal motion is particularly strong near the interface.

Marangoni convection occurs if the variation of the surface tension force dominates the viscosity forces. A dimensionless number—the Marangoni number—determines the strength of the convective motion [\[45\]](#)

$$Ma = \frac{\Delta\gamma R}{\rho v \alpha}, \quad (3.84)$$

where R is the radius of the spherical cap, r is the density of the liquid, v is the kinematic viscosity, α is the thermal diffusivity, and $\Delta\gamma$ is the variation of surface tension on the interface. The Marangoni number represents the ratio between the tangential stress and the viscosity.

Thermal Marangoni convection in a droplet is numerically modeled with standard fluid mechanics approaches. First, because of the small dimensions of the droplet, the internal velocities are moderate (1 cm/s is an upper limit) and the capillary number defined by:

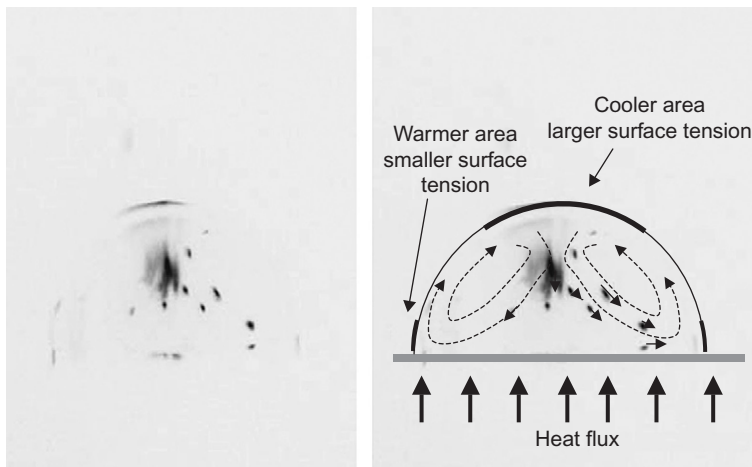
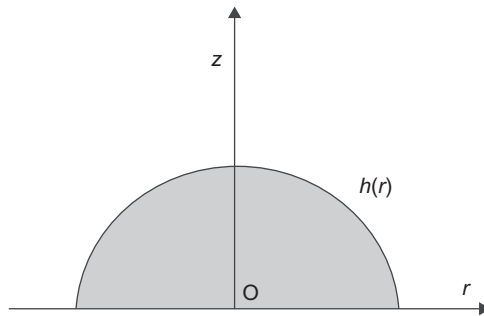


FIGURE 3.81

Observation of Marangoni convection in a sessile droplet obtained by heating an ionic liquid droplet from below.

Source: Photo Ph. Dubois, CEA/LETI.

**FIGURE 3.82**

A sessile spherical cap droplet on the substrate in an axisymmetrical coordinate system.

$$Ca = \frac{\mu \bar{u}}{\gamma} \quad (3.85)$$

is then small, much smaller than 1. In such a case, the shape of the droplet is not changed by the internal convective motions. Because the Bond number is also small, the droplet stays spherical all the time (Figure 3.82). Then, we can use an axisymmetric coordinate system to describe the geometry.

Suppose we have a steady-state regime. Neglecting the inertial terms, the equations governing this steady-state convective motion are the Stokes equations [46]

$$\begin{aligned} \frac{1}{r} \frac{\partial(r u_r)}{\partial r} + \frac{\partial u_z}{\partial z} &= 0 \\ \mu \left[\frac{\partial}{\partial r} \left(\frac{1}{r} \frac{\partial(r u_r)}{\partial r} \right) + \frac{\partial^2 u_r}{\partial z^2} \right] &= \frac{\partial P}{\partial r} \\ \mu \left[\frac{\partial}{\partial r} \left(\frac{1}{r} \frac{\partial(r u_z)}{\partial r} \right) + \frac{\partial^2 u_z}{\partial z^2} \right] &= \frac{\partial P}{\partial r} \end{aligned} \quad (3.86)$$

and the temperature field is determined by the energy equation

$$\rho C_p \vec{u} \cdot \nabla T + k \Delta T = 0. \quad (3.87)$$

At the substrate boundary, the velocity is zero $u_r = u_z = 0$. On the interface, we have the tangential stress condition

$$\tau|_{z=h} = \frac{d\gamma}{ds} = -\alpha \gamma_0 \frac{\partial T}{\partial s}, \quad (3.88)$$

where s is the curvilinear coordinate of the interface.

3.8.2 Marangoni convection due to concentration gradient

Surface concentration of macromolecules modifies locally the value of the surface tension. This is particularly true for surfactants. If the concentration reaches the CMC, the surface is uniformly saturated and there are no possible surface gradients. However, below the CMC threshold, the surface is not saturated; if the surface concentration in surfactants is not homogeneous, the surface tension is not uniform. The dependency of the surface tension on the concentration is given to the first order by:

$$\gamma = \gamma_0(1 + \beta_C) \quad (3.89)$$

inducing the tangential stress

$$\tau = \frac{d\gamma}{ds} = \beta\gamma_0 \frac{\partial C}{\partial s}.$$

A Marangoni effect may appear, assuming the Marangoni number defined by $Ma = \Delta\gamma R/\rho v D$ is large enough (D is the coefficient of diffusion). A schematic view of the Marangoni convection caused by surface concentration is shown in [Figure 3.83](#).

Unlike thermal convection, the concentration Marangoni convection is usually a transient phenomenon. As soon as the surface concentration becomes uniform, the motion stops.

An experimental observation of the concentration Marangoni convection has been made by Raccuit et al. [\[47,48\]](#). The authors used an electrowetting microdevice. A droplet with surfactants is initially at rest on an electrode. If suddenly the interface is increased by the actuation of a neighboring electrode, the newly created surface has a very low concentration in surfactants. A gradient of surface tension then appears and a Marangoni motion progressively equalizes the surface tension ([Figure 3.84](#)). The proof of the relaxing of the surface tension is the relaxing of the curvature of the interface.

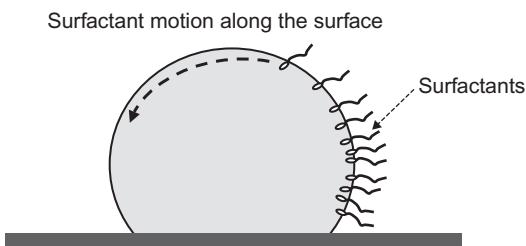
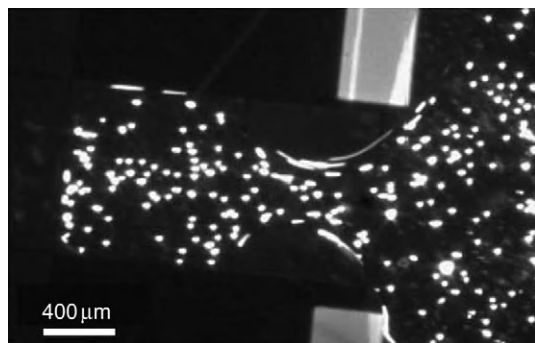


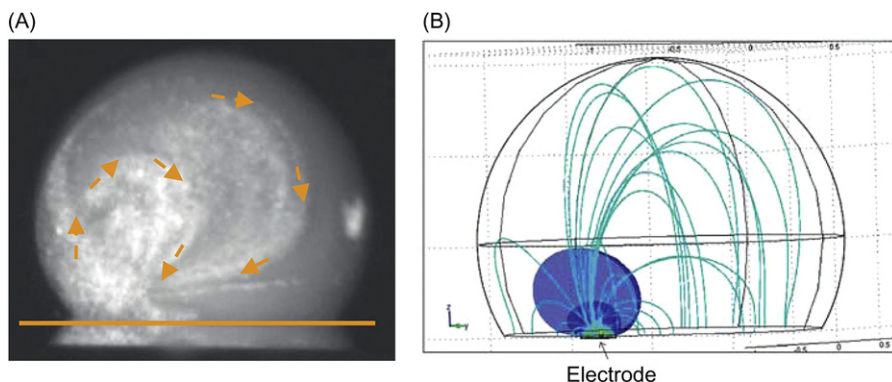
FIGURE 3.83

Schematic view of surfactant molecules moving along the surface from the regions of large surface concentration to the regions of smaller surface concentration.

**FIGURE 3.84**

Internal motion of the fluid during extrusion from a reservoir in an EWOD microsystem. First, an electrowetting motion transports very quickly a part of the droplet on the neighboring electrode. Then, a Marangoni motion starts and progressively uniformizes the surface tension. The motion is followed using fluorescent beads of $9\text{ }\mu\text{m}$ diameter.

Source: Photo O. Raccourt.

**FIGURE 3.85**

(A) Convective motion induced by an electric field applied in the droplet; (B) simulation of the electric field lines and isopotentials in the droplet (numerical program COMSOL).

3.8.3 Marangoni convection due to an electric field

The formula of Colin (Eq. (3.82)) introduces a variation of the surface tension as a function of the electric field, resulting in an electric Marangoni convection. This type of convection is currently the object of debate, and its effect on droplets is a subject of research. Strictly speaking, when an electric field is applied on an interface, it induces stresses on the interface. In a droplet, it has been observed that the tangential stress may be important and induces Marangoni-type

convection. Figure 3.85 shows the motion of fluorophores at a droplet interface when an electric field is actuated by an electrode located in the solid substrate below the droplet [48].

3.9 Evaporation

A drawback when working with aqueous droplets—or other volatile liquids—in a nonregulated atmosphere is evaporation. Since the volume of liquid in a droplet is very small, evaporation time is also small, and it is usual to see droplets rapidly vanishing. Of course, evaporation can be suppressed by controlling the ambient atmosphere; if the vapor content is set to maintain the atmosphere at dew (saturation) point, evaporation is suppressed. Note that the problem does not appear when using some organic liquids (silicone oil, etc.) or ionic liquids.

One would expect that the evaporation process of liquid droplets was described many years ago. Indeed, Wittaker, Morse, and Langmuir have set the basis for a theory in the 1910s; however, it is just recently that a more complete understanding of the evaporation process of microdrops has been announced.

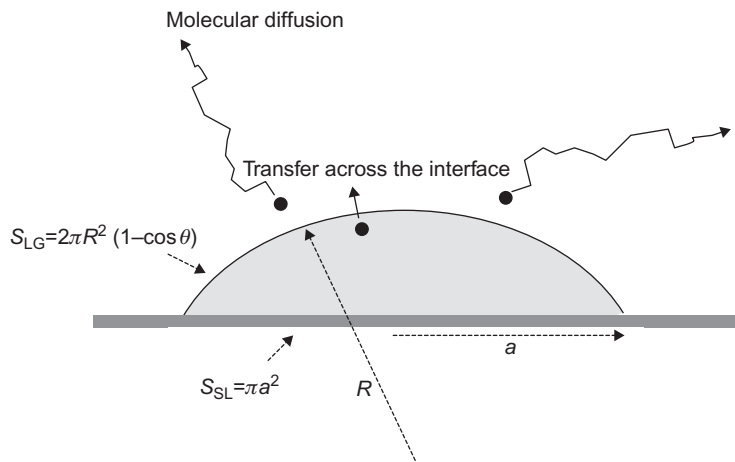
3.9.1 Evaporation of sessile droplets

In this section, we investigate evaporation of sessile droplets. We assume that there is no Marangoni-type convection inside the droplet and that the surrounding gas is at rest. Liquid evaporation is strongly associated with the diffusion of the vapor away from the liquid–gas interface (Figure 3.86). If the gas is saturated with vapor (dew point for water), evaporation is stopped.

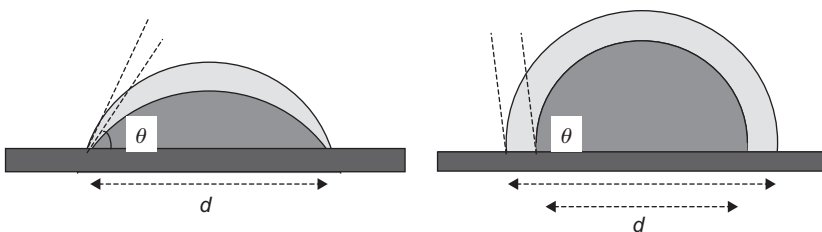
3.9.1.1 Experimental observations

It has been observed experimentally [49] that wetting and nonwetting droplets do not evaporate in the same way: in the case of a wetting droplet, the contact radius remains constant during the evaporation process—except at the very end, when the volume of liquid is vanishing; during the process, the contact angle decreases gradually. It is as if the contact line was pinned on the initial contact line. In the case of a nonwetting droplet, it is the contact angle that remains constant—except at the very end of the evaporation process (Figures 3.87–3.89); during the process, the contact radius decreases gradually.

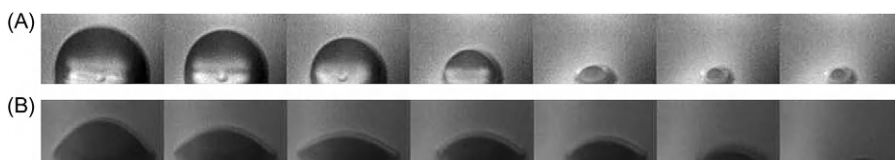
In both cases, the mass rate of liquid loss is proportional to the height of the drop [49–52]; in the case of a wetting substrate, the contact angle decreases linearly with time, whereas in the case of a nonwetting substrate, the droplet radius decreases as the square root of time [53]. In the following section, we derive expressions for the contact angle change with time in the wetting case, and for the contact radius change with time in the nonwetting case.

**FIGURE 3.86**

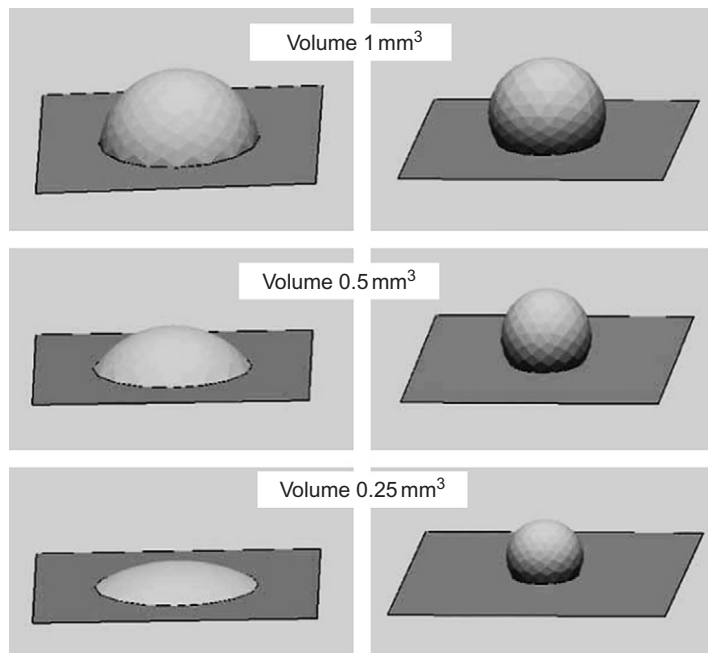
The two mechanisms during evaporation (assuming that there are no convective motions); evaporation is limited by diffusion in the gas phase rather than by the transfer rate across the interface.

**FIGURE 3.87**

The two schemes for sessile droplet evaporation [49] depending on the wettability of the surface.

**FIGURE 3.88**

Evaporation of a water droplet on silanized silicon (A) and on silicon oxide (B): recall that the silanization process makes the surface hydrophobic, whereas the silicon oxide is hydrophilic. In the first case (A), the contact angle remains constant; in the second case (B), the contact radius remains constant.

**FIGURE 3.89**

Evaporation of a water droplet on hydrophilic and hydrophobic surfaces using the Evolver numerical program: in the case of a hydrophilic contact, the triple contact line has been pinned and the base radius is constant; in the case of a hydrophobic contact, the contact angle is constant.

3.9.1.2 Theoretical model

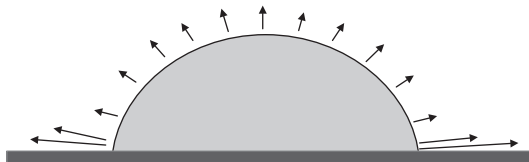
In the case of a complete sphere, i.e., a spherical droplet in space, the approach was done by Birdi et al. [54]; using Fick's law, they obtained the evaporation rate as

$$\frac{dm}{dt} = -D \int \nabla c \cdot d\vec{S}, \quad (3.90)$$

where D is the diffusion coefficient of the vapor and c its concentration. Equation (3.90) can be developed under the form

$$\frac{dm}{dt} = -D \int \frac{\partial c}{\partial n} dS. \quad (3.91)$$

Note that, due to the spherical isotropy, the gradient of vapor concentration is uniform and using the boundary conditions: $c = c_\infty$ as $r \rightarrow \infty$, and $c = c_0$ at $r = r_d$, where r_d is the radius of the liquid drop, and taking into account that the

**FIGURE 3.90**

Evaporation flux along the surface droplet according to Hu [60].

diffusion profile around a sphere varies as $1/r$, the concentration gradient can be approximated by [54]:

$$\frac{\partial c}{\partial n} = -\frac{c_0 - c_\infty}{r_d}. \quad (3.92)$$

The evaporation rate then becomes

$$\frac{dm}{dt} = 4\pi r_d D(c_0 - c_\infty) \quad (3.93)$$

showing that the rate of evaporation is proportional to the radius of the spherical drop. In the case of spherical cap geometry, Eq. (3.90) still applies

$$\frac{dm}{dt} = \rho \frac{dV}{dt} = -D \int \nabla c \cdot dS = -D \int \frac{\partial c}{\partial n} ds, \quad (3.94)$$

where ρ is the volumic mass of the vapor and the integral is taken on the surface of the spherical cap. It can be shown that the assumption of a radially constant gradient is not strictly verified, but only approximately. The evaporation flux is radially uniform except close to the triple line, as shown in Figure 3.90.

3.9.1.2.1 Wetting (lyophilic) case: $\theta < 90^\circ$

Using an alternative expression for the spherical cap surface,

$$S_{LG} = 2\pi R^2(1 - \cos \theta) = 2\pi Rh$$

the rate of reduction of volume due to evaporation can be approximated by:

$$\begin{aligned} \frac{dV}{dt} &= -\frac{D(c_0 - c_\infty)}{\rho} \int \frac{ds}{R} \\ &= -\frac{D(c_0 - c_\infty)}{\rho} \int_0^h \frac{2\pi R}{R} dh = -\frac{2\pi D(c_0 - c_\infty)}{\rho} h. \end{aligned} \quad (3.95)$$

Equation (3.95) can then be written under the form

$$\frac{dV}{dt} = -\lambda h, \quad (3.96)$$

where:

$$\lambda = -\frac{2\pi D(c_0 - c_\infty)}{\rho}.$$

Relation (3.96) shows that the rate of mass loss is proportional to the height of the droplet. Using the expression of the droplet volume as a function of the contact angle

$$V = \frac{\pi R^3}{3}(2 - 3 \cos \theta + \cos^3 \theta) = \frac{\pi r_b^3(2 - 3 \cos \theta + \cos^3 \theta)}{\sin^3 \theta},$$

we derive

$$\begin{aligned} \frac{dV}{dt} &= \frac{\partial V}{\partial \theta} \frac{d\theta}{dt} = \frac{\pi r_b^3}{3} \frac{d}{d\theta} \left[\frac{(2 - 3 \cos \theta + \cos^3 \theta)}{\sin^3 \theta} \right] \frac{d\theta}{dt} \\ &= \pi r_b^3 \frac{(1 - \cos \theta)^2}{\sin^4 \theta} \frac{d\theta}{dt}. \end{aligned} \quad (3.97)$$

After substitution in Eq. (3.95), using the relation $h = r_b \tan(\theta/2)$ and the trigonometric relation $\tan(\theta/2) = (1 - \cos \theta)/\sin \theta$, we obtain the following differential equation:

$$\frac{d\theta}{dt} = -\frac{\lambda h}{\pi r_b^3 ((1 - \cos \theta)^2 / \sin^4 \theta)} = -\frac{\lambda \sin^3 \theta}{\pi r_b^2 (1 - \cos \theta)}. \quad (3.98)$$

We can separate the variables in Eq. (3.98) to obtain

$$\frac{(1 - \cos \theta)}{\sin^3 \theta} d\theta = -\frac{\lambda}{\pi r_b^2} dt.$$

Integration of this differential equation gives

$$F(\theta) = \ln \left(\tan \left(\frac{\theta}{2} \right) \right) + \frac{(1 - \cos \theta)}{\sin^2 \theta} = -\frac{\lambda}{\pi r_b^2} (t - t_0), \quad (3.99)$$

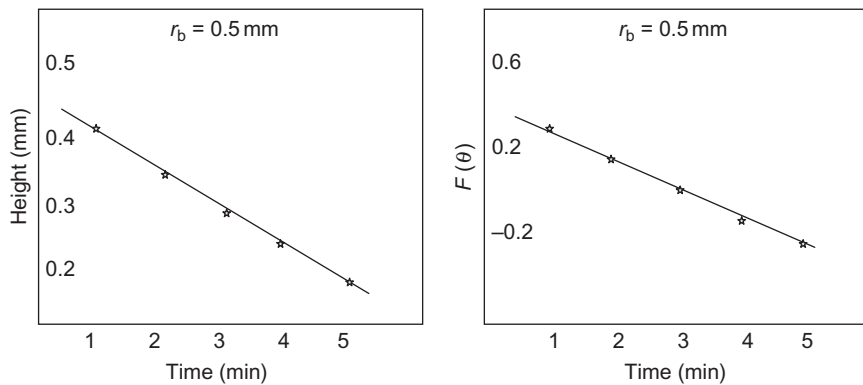
where t_0 is a constant of integration. Equation (3.99) is implicit; however, it has been shown that for a wetting angle in the interval $30^\circ < \theta < 90^\circ$, the function $F(\theta)$ is linear

$$F(\theta) = -1.592 + 1.632\theta. \quad (3.100)$$

Upon substitution of Eq. (3.100) in Eq. (3.99), we find a linear decrease of the contact angle with time during evaporation (λ is a positive number)

$$\theta = \theta_0 - \frac{\lambda}{1.632\pi r_b^2} (t - t_0).$$

This law fits the experimental data extremely well in the range $30^\circ - 90^\circ$, as shown in Figure 3.91.

**FIGURE 3.91**

(A) Time variation of the droplet height and (B) time variation of the function $F(\theta)$. Droplet radius of 0.5 mm.

Source: Data from Ref. [51].

3.9.1.2.2 Nonwetting (lyophobic) case: $\theta > 90^\circ$

This case has been studied by McHale et al. [53]. It can be shown that equation

$$\frac{dV}{dt} = -\lambda h$$

still holds. But from this point on, the treatment of the equation changes: this time the contact radius is not kept constant, but the contact angle remains approximately constant (Figure 3.92).

Then,

$$\frac{dV}{dt} = \frac{\partial V}{\partial r} \frac{dr}{dt} = -\lambda h.$$

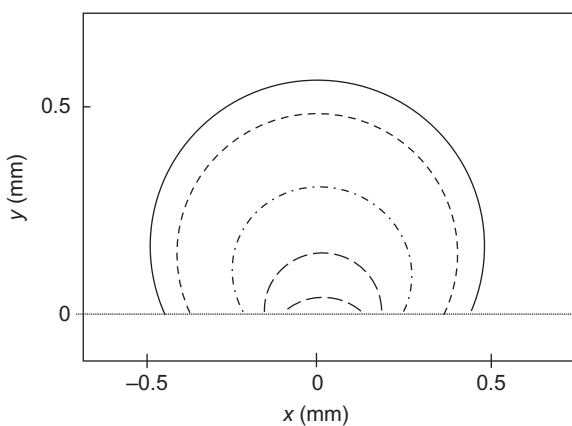
After some algebra, similar to that of the preceding case, we obtain the differential equation

$$r \frac{dr}{dt} = -\frac{\lambda \sin^2 \theta}{\pi(1 - \cos \theta)(2 + \cos \theta)} \quad (3.101)$$

which can be solved to give

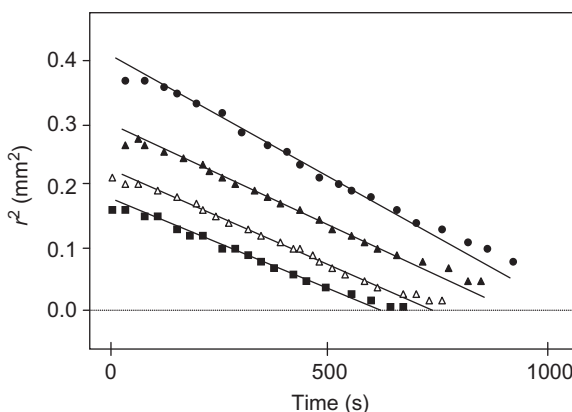
$$r^2 = r_0^2 - \frac{2\lambda \sin^2 \theta}{\pi(1 - \cos \theta)(2 + \cos \theta)} t. \quad (3.102)$$

Equation (3.102) shows that the square of the contact radius is proportional to the time. This is confirmed by McHale's experimental results (Figure 3.93).

**FIGURE 3.92**

Vertical profile of evaporating droplet; case of a lyophobic surface and an initial contact radius of 0.48 mm: the contact angle remains approximately constant except at the end of the evaporation process.

Source: Reprinted with permission from Ref. [53] © 1998, American Chemical Society.

**FIGURE 3.93**

Time variation of the contact radius r for water droplets on Teflon (hydrophobic case), showing the proportionality of r^2 with time except at the very end of the evaporation process.

Source: Reprinted with permission from Ref. [53] © 1998, American Chemical Society.

3.9.1.3 Discussion

In Eq. (3.99) or (3.102), the variation rate is related to the diffusion coefficient of vapor in the surrounding gas, through the coefficient λ . This can be used as a method for estimating the diffusion coefficient D . From the curves of Figure 3.92, one can estimate the diffusion coefficient as $2.32 \times 10^{-5} \text{ m}^2/\text{s}$, whereas the CRC

Handbook of Chemistry and Physics indicates a value of $2.56 \times 10^{-5} \text{ m}^2/\text{s}$ for the same conditions of temperature and pressure.

We have seen in the preceding paragraphs that the evaporation behavior of wetting and nonwetting droplets is quite different. There is no clear explanation for this difference at this time. According to McHale et al. [53], the difference could be attributed to the fact that, in the nonwetting case, there is a ring of saturated vapor trapped near the contact line, maintaining constant conditions and a constant Young's angle during the evaporation process. It is likely also that in the wetting case, impurities could gather in the sharp corner near the triple line, leading to the pinning of this contact line.

In the following section, we show that it is indeed the case for colloidal suspensions.

3.9.2 Evaporation rings

Most of the time, the microdrops we are interested in are laden with particles, macromolecules, or polymers. A typical feature of evaporation of these droplets is evaporation rings. Ring formation is well documented in the literature; it has been studied by numerous authors like Deegan [56,57], Zheng et al. [58], and Popov [59].

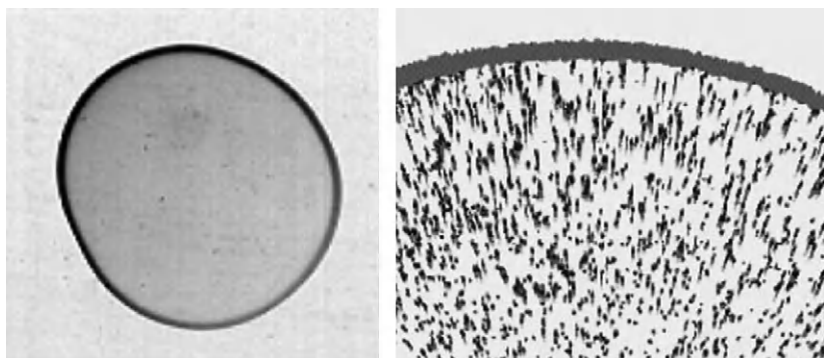
It seems that during the evaporation of a liquid droplet, the liquid at the edge of the droplet is “pinned” to the underlying surface by the deposited particles. This pinning prevents the droplet from shrinking. It implies that the footprint of the droplet remains constant. The evaporated liquid at the edge is replenished by liquid from the bulk of the droplet. This means that there is a flow of liquid moving toward the edge of the droplet. If the liquid droplet contains particles, like in a droplet of coffee, these particles will be transported outward by the flow and deposited near the contact line (Figure 3.94). Finally, when all the liquid has evaporated, the colloidal particles will form a ring of stain (Figure 3.95).

In DMF, these rings are a drawback. They modify locally the surface energy, and it becomes difficult to displace new droplets over these evaporation rings.



FIGURE 3.94

Sketch of an evaporating droplet: the two segments near the contact line represent the ring where colloidal particles are deposited. The evaporation rate is stronger near the contact line provoking a radial convective motion from the center toward the contact line. Here, it is supposed that there is no additional motion due to Marangoni convection [60].

**FIGURE 3.95**

Evaporation rings left by an evaporating droplet containing microparticles.

Source: From Ref. [56] © 2000, APS, reprinted with permission.

Careful—and sometimes difficult—washing of the surface is needed to restore the quality of the surface.

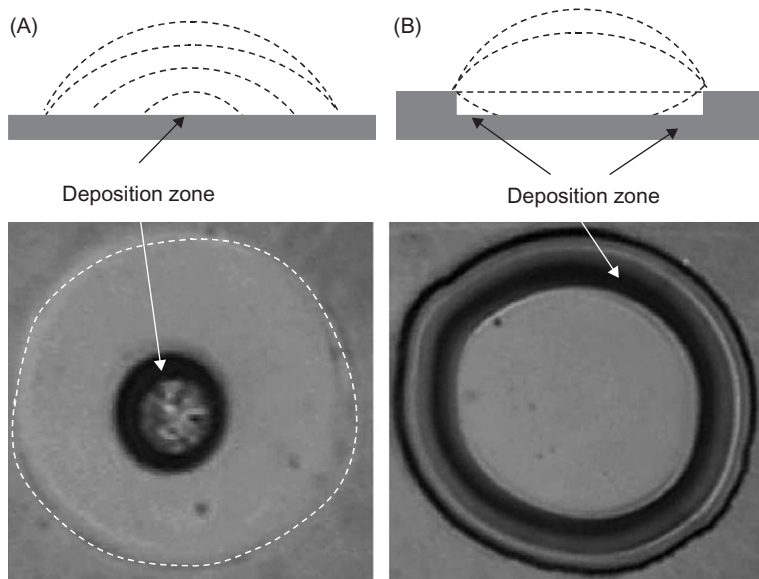
3.9.3 Evaporation stains

Evaporation rings are not a ubiquitous feature of droplet evaporation. Rings form only if the particles or macromolecules are sufficiently large to sediment or adhere to the solid surface in the corner near the triple line. If the molecules are very small, they are agitated by the convective motion and do not deposit in the corners. As a result, the center part of the droplet—the last region to dry—has more solute deposition than that of the border (Figure 3.96A). Chen et al. [61] have experimentally shown the difference between a droplet evaporating on a smooth horizontal plane and in a microwell. Due to pinning on the edges of the microwell, the last volume of liquid to evaporate is a ring adjacent to the rim of the well (Figure 3.96B).

3.9.4 Marangoni convection during evaporation

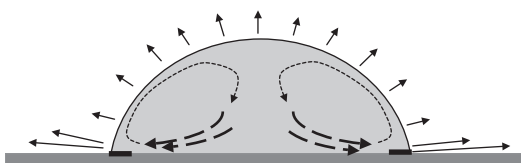
Besides the formation of rings or stains at the contact of the solid substrate during evaporation, another typical feature of droplet evaporation is Marangoni convection. One can distinguish two cases: that of a sessile droplet and that of a pendant droplet. In the first case, the evaporation rate is larger at the contact of the surface, resulting in a lower temperature of the interface and a larger surface tension. A stable Marangoni pattern forms in the droplet, as shown in Figure 3.97.

The case of a pendant drop is different [45]. There are no surface regions permanently at a lower temperature; it is a very unstable situation: when a cold spot forms on the surface, it is a focal point for convective motion; as soon as the temperature loss is compensated by the convective transport, the intensity of the

**FIGURE 3.96**

(A) Schematic of a drying droplet; the droplet sitting on a smooth horizontal plane reduces progressively to a small central region, whereas the droplet in a microwell reduces to a ring adjacent to the rim of the well. (B) Experimental view of the deposit.

Source: From Ref. [61] © 2006, Elsevier, reprinted with permission.

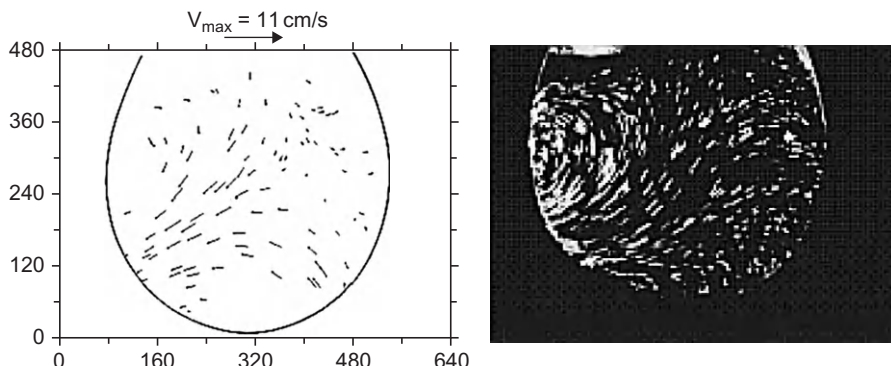
**FIGURE 3.97**

Schematic of the velocity field in an evaporating droplet when Marangoni convection superposes with the evaporating flow field [46].

Marangoni convection vanishes, and the same process appears again at a new cold spot. Figure 3.98 shows the Marangoni motion converging toward a hot spot.

3.9.5 The use of droplet evaporation in biotechnology, biology, and nanoassembly

Evaporation is a somewhat slow process compared to molecular motion, and the receding contact line is geometrically linear at the scale of a group of molecules.

**FIGURE 3.98**

Marangoni convection due to thermal instabilities at the surface of an evaporating droplet.

Source: From Ref. [45] © 1996, APS, reprinted with permission.

Thus, particles and molecules have time to rearrange during the receding of the triple line. This feature has been used for specific applications in modern biotechnology, biology, and nanoassembly.

In this section, we present some interesting applications of droplet evaporation.

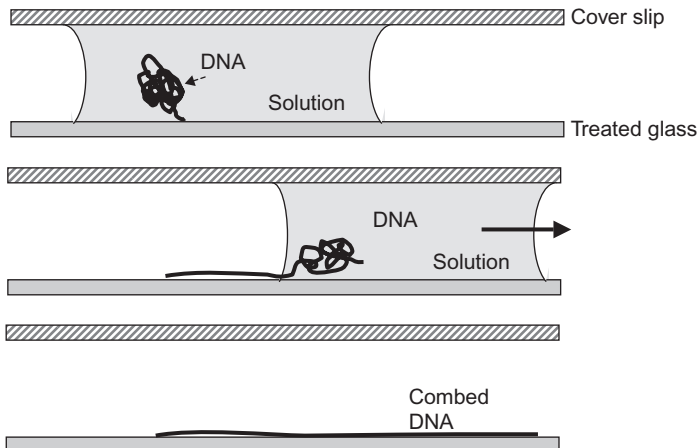
3.9.5.1 Drop evaporation as a tool for DNA stretching

In genomics—the study of the sequences, functions, and interactions of genes—DNA stretching is of great importance. Usually, DNA strands bunch up and stretching them is a necessary step before any observation of the DNA chain, and when very precise immobilization is needed [55,62]. This process is called molecular combing. One of the first methods—and still a very commonly used one—to comb DNA was proposed by Bensimon et al. [62]. This method takes advantage of liquid droplet evaporation (Figure 3.99). A DNA strand attached by one end to a glass surface stretches progressively as the gas–liquid interface retreats during evaporation. When all the liquid has vanished, the DNA strand forms a linear segment on the glass plate.

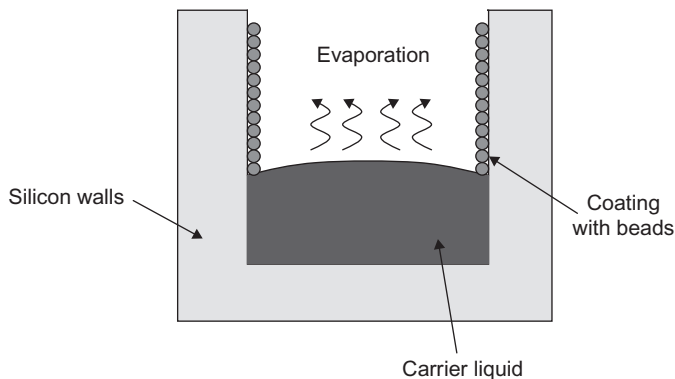
3.9.5.2 Drop evaporation as a tool for nanoassembly

Evaporation of a liquid in a microchannel is a process that is, at the same time, not too fast or too slow. It can be taken advantage of for coating the internal surfaces of microfluidic systems. Such coatings may be used to change the chemical composition of the walls, or to mask a boundary of wettability between two zones of the microsystem (composite microsystems).

If the volatile liquid is laden with the appropriate particles, the evaporating liquid deposits the particles in an ordered pattern along the solid walls of the microsystem. Vengallatore et al. [63] have shown how to coat the interior silicon walls of a microsystem with a layer of spherical polystyrene or silica beads

**FIGURE 3.99**

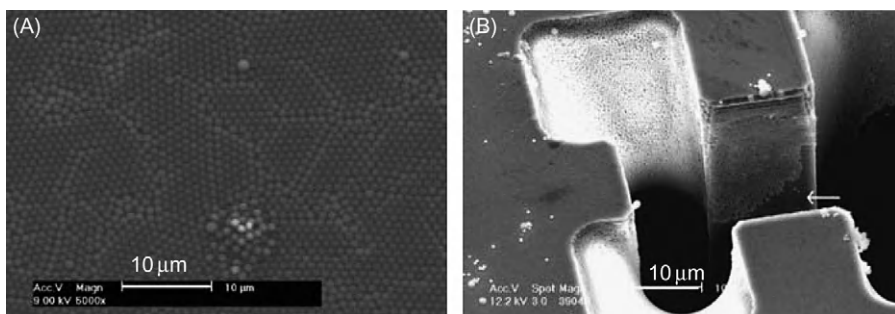
Combing DNA using droplet evaporation.

**FIGURE 3.100**

Schematic illustration of convective colloidal self-assembly: evaporation of the colloidal suspension leads to particle assembly on the internal surfaces.

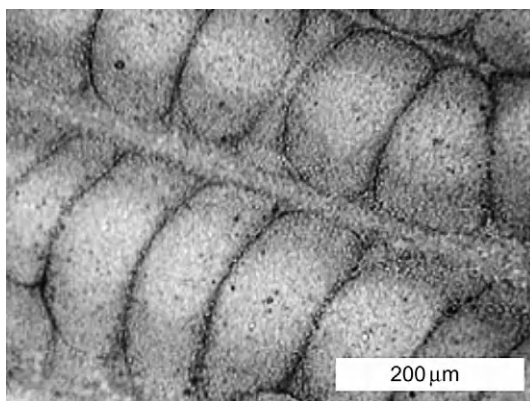
by evaporating the carrier fluid (Figure 3.100). An annealing treatment—heating of the coating for a brief moment—may be performed to stabilize the coating.

The result is shown in Figure 3.101. Particles predominantly assemble in hexagonal close-packed configurations, and, if sufficient precautions are taken, they can coat uniformly the internal walls of the microsystem.

**FIGURE 3.101**

(A) Coating of a surface with monodisperse polystyrene beads. (B) Nearly uniform coating of a microfabricated channel with monodisperse beads.

Source: From Ref. [63] © 2004, Elsevier, reprinted with permission.

**FIGURE 3.102**

Polymer coating of a quartz surface obtained by evaporation of a dichloromethane droplet containing PC (polycarbonate) polymers.

Source: From Ref. [64] © 2006, Elsevier, reprinted with permission.

3.9.5.3 Conclusion

Deposition of macromolecules or particles using droplet evaporation is of current interest. In the literature, there have been recent publications on this topic. Let us cite here the work of Bormashenko et al. [64] who used different polymer concentrations in an evaporating droplet of solvent to obtain patterned coating (Figure 3.102) and the publication of Schnall-Levin et al. [65] who showed the patterns made by the rearrangement of particles during evaporation.

3.10 Summary

This chapter has shown that droplet behavior shows very particular features, compared to usual fluid mechanics. At this scale, the interfacial forces are dominant and govern the shape and position of a droplet in a microsystem. These interfacial forces are dependent on the nature of the liquid, on the colloids that are present in this liquid, on the surface properties of the substrate, and on the geometry of the device.

Chapters 2 and 3 constitute the basis for the understanding of capillarity on microdrops. We have seen that capillarity by itself can be sufficient to displace droplets or to pin them. However, these capillary forces are fixed, and their intensity or location cannot easily be modified. Two types of forces can be relatively easily superposed on capillary effects in order to have a more flexible system: electric and acoustic forces. In the case of electric forces, we will speak of electrocapillarity or electrowetting. In the next chapters, we investigate the numerous applications where these forces are superposed to capillarity to handle droplets.

References

- [1] P.-G. de Gennes, F. Brochard-Wyart, D. Quéré, *Drops, Bubbles, Pearls, Waves*, Springer, New York, NY, 2004.
- [2] K. Brakke, The surface evolver, *Exp. Math.* 1 (1992) 141–165.
- [3] J.W. Harris, H. Stocker, *Handbook of Mathematics and Computational Science*, Springer, New York, NY, 1998. p. 107
- [4] J.G. Hocking, G.S. Young, *Topology*, Dover, New York, NY, 1988.
- [5] P. Concus, R. Finn, On the behavior of a capillary surface in a wedge, *Proc. Natl. Acad. Sci. U.S.A.* 63 (2) (1969) 292–299.
- [6] K. Brakke, Minimal surfaces, corners, and wires, *J. Geom. Anal.* 2 (1992) 11–36.
- [7] J.-C. Baret, M. Decré, S. Herminghaus, R. Seemann, Electroactuation of fluid using topographical wetting transitions, *Langmuir* 21 (2005) 12218–12221.
- [8] R. Seemann, M. Brinkmann, E.J. Kramer, F. Lange, R. Lipowsky, Wetting morphologies at microstructured surfaces, *Proc. Natl. Acad. Sci. U.S.A.* 102 (2005) 1848–1852.
- [9] R. Lipowsky, M. Brinkmann, R. Dimova, C. Haluska, J. Kierfeld, J. Shillcock, Wetting, budding, and fusion—morphological transitions of soft surfaces, *J. Phys. Condens. Matter.* 17 (2005) S2885–S2902.
- [10] C.C. Meek, P. Pantano, Spatial confinement of avidin domains in microwell arrays, *Lab Chip* 1 (2001) 158–163.
- [11] J. Berthier, P. Silberzan, *Microfluidics for Biotechnology*, Artech House Publishers, Norwood, MA, 2005.
- [12] H. Gau, S. Herminghaus, P. Lenz, R. Lipowsky, Liquid morphologies on structured surfaces: from microchannels to microchips, *Science* 383 (1999) 46–49.
- [13] P. Lenz, R. Lipowsky, Morphological transitions of wetting layers on structured surfaces, *Phys. Rev. Lett.* 80 (9) (1998) 1920–1923.

- [14] M. Brinkmann, R. Lipowsky, Wetting morphologies on substrates with striped surface domains, *J. Appl. Phys.* 92 (8) (2002) 4296–4306.
- [15] A. Klingner, F. Mugele, Electrowetting-induced morphological transitions of fluid microstructures, *J. Appl. Phys.* 95 (5) (2004) 2918–2920.
- [16] H. Gau, S. Herminghaus, P. Lenz, R. Lipowski, Liquid morphologies on structured surfaces: From microchannels to microchips, *Science* 283 (1999) 46–49.
- [17] Y. Fouillet, H. Jeanson, D. Jary, C. Vauchier, Moving droplets with microcatenaries, *Proceedings of MTAS 2003, Seventh International Conference on Micro Total Analysis Systems*, 5–9 October 2003, Squaw Valley, CA.
- [18] Th. Uelzen, J. Müller, Wettability enhancement by rough surfaces generated by thin film technology, *Thin Solid Films* 434 (2003) 311–315.
- [19] Seong H. Kim, Jeong-Hoon Kim, Bang-Kwon Kang, Han S. Uhm, Superhydrophobic CFx coating via in-line atmospheric RF plasma of He–CF₄–H₂, *Langmuir* 21 (2005) 12213–12217.
- [20] Liang Zhu, Yanying Feng, Xiongying Ye, Zhaoying Zhou, Tuning wettability and getting superhydrophobic surface by controlling surface roughness with well-designed microstructures, *Sens. Actuator, A Phys.* 130–131 (2006) 595–600.
- [21] J. Bico, U. Thiele, D. Quéré, Wetting of textured surfaces, *Colloids Surf. A Physicochem. Eng. Aspect* 206 (2002) 41–46.
- [22] J. Bico, C. Marzolin, D. Quéré, Pearl drops, *Europhys. Lett.* 47 (2) (1999) 220–226.
- [23] J. Bico, C. Tordeux, D. Quéré, Rough wetting, *Europhys. Lett.* 55 (2) (2001) 214–220.
- [24] N.A. Patankar, Transition between superhydrophobic states on rough surfaces, *Langmuir* 20 (2004) 7097–7102.
- [25] N.A. Patankar, Y. Chen, Numerical simulation of droplet shapes on rough surfaces, *Proceedings of the 2002 Nanotech Conference*, 21–25 April 2002, Puerto-Rico, pp. 116–119.
- [26] N.A. Patankar, On the modelling of hydrophobic contact angles on rough surfaces, *Langmuir* 19 (2003) 1249–1253.
- [27] T.N. Krupenkin, J.A. Taylor, T.M. Schneider, Shu Yang, From rolling ball to complete wetting: the dynamic tuning of liquids on nanostructured surfaces, *Langmuir* 20 (2004) 3824–3827.
- [28] L. Zhu, Y.Y. Feng, X.Y. Ye, Z.Y. Zhou, Tuning wettability and getting superhydrophobic surfaces by controlling surface roughness with well-designed microstructures, *Transducers'05, 13th International Conference on Solid-State Sensors, Actuators and Microsystems*, 5–9 June 2005, Seoul, Korea.
- [29] W. Barthlott, C. Neinhuis, Purity of the sacred lotus, or escape from contamination in biological surfaces, *Planta* 202 (1997) 1–8.
- [30] J.-G. Fan, X.-J. Tang, Y.-P. Zhao, Water contact angles of vertically aligned Si nanorod arrays, *Nanotechnology* 15 (2004) 501–504.
- [31] T. Onda, S. Shibuichi, N. Satoh, K. Tsujii, Super water-repellent surfaces, *Langmuir* 12 (9) (1996) 2125–2127.
- [32] S. Shibuichi, T. Onda, N. Satoh, K. Tsujii, Super water-repellent surfaces resulting from fractal structures, *J. Phys. Chem.* 100 (1996) 19512–19517.
- [33] N. Moumen, R.S. Subramanian, J. McLoughlin, Experiment on the motion of drops on a horizontal solid surface due to a wettability gradient, *Langmuir* 22 (2006) 2682–2690.

- [34] M.K. Chaudhury, G.M. Whitesides, How to make water run uphill, *Science* 256 (1992) 1539–1541.
- [35] D. Dos Santos, T. Ondarçuhu, Free-running droplets, *Phys. Rev. Lett.* 75 (16) (1995) 2972–2975.
- [36] S.M.M. Ramos, E. Charlaix, A. Benyagoub, Contact angle hysteresis on nanostructured surfaces, *Surf. Sci.* 540 (2003) 355–362.
- [37] H.A. Wege, J.A. Holgado-Terriza, J.I. Rosales-Leal, R. Osorio, M. Toledano, M.A. Cabrerizo-Vilchez, Contact angle hysteresis on dentin surfaces measured with ADSA on drops and bubbles, *Colloids Surf. A Physicochem. Eng. Aspect* 206 (2002) 469–483.
- [38] C.N.C. Lam, R. Wu, D. Li, M.L. Hair, A.W. Neumann, Study of the advancing and receding contact angles: liquid sorption as a cause of contact angle hysteresis, *Adv. Colloid Interface Sci.* 96 (2002) 169–191.
- [39] H. Tavana, A.W. Neumann, On the question of rate-dependence of contact angles, *Colloids Surf. A Physicochem. Eng. Aspect* 282–283 (2006) 256–262.
- [40] T. Cubaud, M. Fermigier, Advancing contact lines on chemically patterned surfaces, *J. Colloid Interface Sci.* 269 (2004) 171–177.
- [41] T. Ondarçuhu, Total or partial pinning of a droplet on a surface with chemical discontinuity, *J. Phys. (II)* 5 (1995) 227–241.
- [42] A. Buguin, L. Talini, P. Silberzan, Ratchet-like topological structures for the control of microdrops, *Appl. Phys. A* 75 (2002) 207–212.
- [43] Yangyang Shen, A. Couzis, J. Koplik, C. Maldarelli, M.S. Tomassone, Molecular dynamics study of the influence of surfactant structure on surfactant-facilitated spreading of droplets on solid surfaces, *Langmuir* 21 (2005) 12160–12170.
- [44] S. Colin, *Microfluidique*, Hermès Science, Paris, 2004.
- [45] J.J. Hegseth, N. Rashidnia, A. Chai, Natural convection in droplet evaporation, *Phys. Rev. E* 54 (2) (1996) 1640–1644.
- [46] Hua Hu, R.G. Larson, Analysis of the effects of Marangoni stresses on the microflow in an evaporating sessile droplet, *Langmuir* 21 (2005) 3972–3980.
- [47] O. Raccourt, J. Berthier, P. Clementz, Time dependant surface tension modification due to surfactant during electrowetting basic droplet operation, Euromech Colloquium 472 on Microfluidics and Transfer, 6–8 September 2005, Grenoble, France.
- [48] O. Raccourt, J. Berthier, Ph. Clementz, M. Borella, M. Plissonnier, On the influence of surfactants in electrowetting, *J. Micromech. Microeng.* 17 (2007) 1–7.
- [49] Jun Fukai, Hirotaka Ishizuka, Yosuke Sakai, Masayuki Kaneda, Masamichi Morita, Atsushi Takahara, Effects of droplet size and solute concentration on drying process of polymer solution droplets deposited on homogeneous surfaces, *Int. J. Heat Mass Transfer* 49 (2006) 3561–3567.
- [50] R.A. Meric, H.Y. Erbil, Evaporation of sessile drops on solid surfaces: pseudospherical cap geometry, *Langmuir* 14 (1998) 1915–1920.
- [51] S.M. Rowan, M.I. Newton, G. McHale, Evaporation of micro-droplets and the wetting of solid surfaces, *J. Phys. Chem.* 99 (1995) 13268–13271.
- [52] Hua Hu, R.G. Larson, Evaporation of a sessile droplet on a substrate, *J. Phys. Chem. B* 106 (2002) 1334–1344.
- [53] G. McHale, S.M. Rowan, M.I. Newton, M.K. Banerjee, Evaporation and the wetting of a low-energy solid surface, *J. Phys. Chem. B* 102 (1998) 1964–1967.

- [54] K.S. Birdi, D.T. Vu, A. Winter, A study of the evaporation rate of small water drops placed on a solid surface, *J. Phys. Chem.* 93 (1989) 3702–3703.
- [55] J.F. Allemand, D. Bensimon, L. Jullien, A. Bensimon, V. Croquette, pH-dependent specific binding and combing of DNA, *Biophys. J.* 73 (1997) 2064–2070.
- [56] R.D. Deegan, Pattern formation in drying drops, *Phys. Rev. E* 61 (1) (2000) 475–485.
- [57] R.D. Deegan, O. Bakajin, T.F. Dupont, G. Huber, S.R. Nagel, T.A. Witten, Capillary flow as the cause of ring stains from dried liquid drops, *Nature* 389 (1997) 827–829.
- [58] Rui Zheng, Y.O. Popov, T.A. Witten, Deposit growth in the wetting of an angular region with uniform evaporation, *Phys. Rev. E* 72 (2005) 046303.
- [59] Y.O. Popov, Evaporative deposition patterns: spatial dimensions of the deposit, *Phys. Rev. E* 71 (2005) 036313.
- [60] Hua Hu, R.G. Larson, Analysis of the microfluidic flow in an evaporating sessile droplet, *Langmuir* 21 (2005) 3963–3971.
- [61] Chin-Tai Chen, Fan-Gang Tseng, Ching-Chang Chieng, Evaporation evolution of volatile liquid droplets in nanoliter wells, *Sens. Actuators, A* 130–131 (2006) 12–19.
- [62] D. Bensimon, A.J. Simon, V. Croquette, A. Bensimon, Stretching DNA with a receding meniscus: experiments and models, *Phys. Rev. Lett.* 74 (1995) 4754–4757.
- [63] S. Vengallatore, Y. Peles, L.R. Arana, S.M. Spearing, Self-assembly of micro- and nanoparticles on internal micromachined silicon surfaces, *Sens. Actuators, A* 113 (2004) 124–131.
- [64] E. Bormashenko, R. Pogreb, A. Musin, O. Stanevsky, Y. Bormashenko, G. Whyman, et al., Self-assembly in evaporated polymer solutions: influence of the solution concentration, *J. Colloid Interface Sci.* 297 (2006) 534–540.
- [65] M. Schnall-Levin, E. Lauga, M. Brenner, Self-assembly of spherical particles on an evaporating sessile droplet, *Langmuir* 22 (2006) 4547–4551.

Electrowetting Theory^{*}

4

CHAPTER OUTLINE

4.1 Introduction	162
4.2 Theoretical background.....	164
4.2.1 Thermodynamic approach	164
4.2.2 Energy minimization approach.....	169
4.2.2.1 <i>Derivation of Young's law</i>	170
4.2.2.2 <i>Derivation of Lippmann–Young's law</i>	171
4.2.3 Electromechanical approach.....	172
4.3 Lippmann–Young's law and the electrocapillary equivalence	176
4.4 Saturation.....	179
4.4.1 Saturation of the electrowetting effect.....	179
4.4.2 Possible explanations for the saturation effect	180
4.4.2.1 <i>Trapping of charges</i>	180
4.4.2.2 <i>Zero surface-liquid energy limit</i>	184
4.4.2.3 <i>Electric resistance of the liquid</i>	185
4.4.2.4 <i>Other models and discussion</i>	188
4.4.3 Modified Lippmann–Young's law	189
4.5 Hysteresis	193
4.5.1 Introduction	193
4.5.2 Hysteresis and minimum actuation potential.....	194
4.5.2.1 <i>Introduction</i>	194
4.5.2.2 <i>Capillary and electrowetting forces</i>	195
4.5.2.3 <i>Minimum potential of actuation</i>	196
4.5.2.4 <i>Experiments—comparison with the numerical results</i>	201
4.6 Working range of EWOD devices	202
4.6.1 Maximum potential.....	202
4.6.2 Working range	204
4.6.3 Conclusion.....	206

*This chapter was written in collaboration with Hsueh-Chia Chang (Bayer Professor of Engineering, Department of Chemical and Biomolecular Engineering, University of Notre-Dame, Indiana, USA).

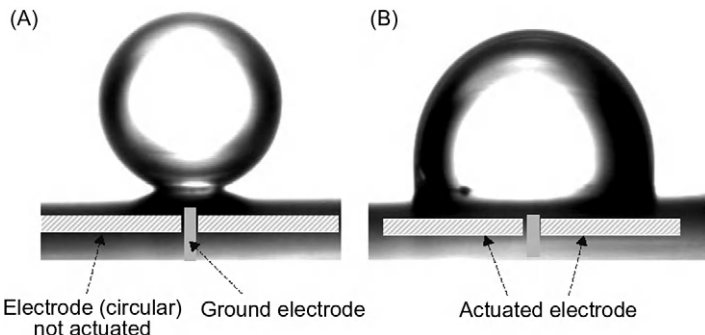
4.7 Materials and substrates	206
4.7.1 Capacitance	206
4.7.1.1 <i>Determination of the specific capacitance via the Lippmann–Young’s relation</i>	207
4.7.1.2 <i>Direct determination of the specific capacitance</i>	207
4.7.2 Dielectric breakdown	208
4.7.3 Materials	211
4.7.4 Existing substrates and their characteristics	213
4.8 Discussion: special substrates and new concepts	214
4.8.1 Low voltages	216
4.8.2 Electrowetting forces	216
4.8.3 Superhydrophobic microfabricated substrates	217
4.8.3.1 <i>Theoretical approach</i>	217
4.8.3.2 <i>Experimental approach</i>	218
4.8.4 Superhydrophobic droplets	220
4.9 Summary	222
References	222

4.1 Introduction

In the presence of a direct or alternating current electric field, electric charges gather at the interface between a conductive and a nonconductive (dielectric) material. The same electric field that induces these charges then couples with the interfacial electric charges to exert an interfacial force, and if the interface is deformable—like that of a conductive liquid and a nonconductive fluid or gas—this force can distort the interface. These induced interfacial electric forces are especially strong on a liquid–gas interface at the vicinity of the contact line, as the electric field often becomes singularly large at the sharp wedges near the contact line. The physics describing the electric forces on interfaces of conducting liquids and on triple contact lines is called “electrowetting.”

As early as 1857, Lippmann [1] observed a change in the capillary rise of mercury in the presence of electric charges (see Chapter 2 and Jurin’s law) and advanced the principle of electrocapillarity as described by an equation which is now called Lippmann’s law. This equation contains the principle of electrowetting, and more specifically EWOD, a technique aimed at activating and transporting liquid droplets on a solid substrate. This technique was pioneered by Berge in the 1990s [2,3] who combined Lippmann’s law with Young’s law to obtain the now-called Lippmann–Young’s law:

$$\cos \theta = \cos \theta_0 + \frac{C}{2\gamma_{LG}} V^2, \quad (4.1)$$

**FIGURE 4.1**

(A) In absence of electric charges, a droplet of water shows a very hydrophobic contact with the solid substrate. (B) The contact angle of the water with the substrate decreases when the electrode is actuated.

where C is the capacitance of the dielectric layer separating the bottom electrode from the liquid. Relation (4.1) predicts the change of contact angle of a sessile droplet with the intensity of the electric field, as shown in Figure 4.1.

A similar phenomenon occurs when considering the capillary rise of a liquid between two vertical plates (see Jurin's law in Chapter 2). We have seen that the capillary rise is given by

$$h_{\text{cap}} = \frac{2\gamma_{LG} \cos \theta_0}{\rho g D}, \quad (4.2)$$

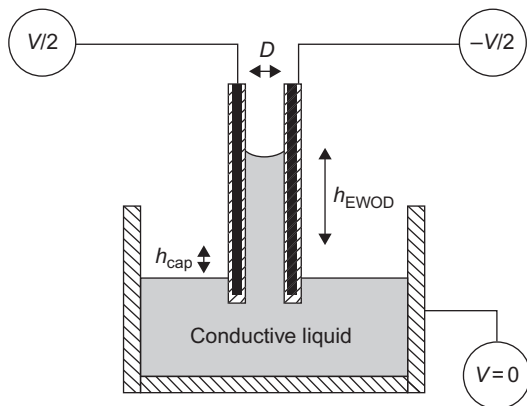
where D is the distance between the plates and ρ is the density of the liquid. If electrodes are embedded inside the two vertical plates (Figure 4.2), the liquid rise depends on the applied voltage. It can be shown that the "electrocappillary" rise, i.e., the additional vertical rise, is given by a similar expression

$$h_{\text{EDOW}} = \frac{2\gamma_{LG}(\cos \theta - \cos \theta_0)}{\rho g D} = \frac{C}{\rho g D} \left(\frac{V}{2} \right)^2, \quad (4.3)$$

where C is the capacitance of the dielectric layers.

As depicted in Figures 4.1 and 4.2, the electrowetting effect may seem like a simple physical phenomenon. We shall see in this chapter that the detailed physics of electrowetting is in fact quite complex. The interpretation of Lippmann's law is delicate and the causes of some phenomena—like saturation—are still debated. In this chapter, we present the theoretical background of electrowetting leading to the key relation also called the Lippmann–Young's law for static electrowetting.

Although it is not the only way to transport droplets—we shall see in Chapter 8 the principle of acoustic actuation—the electrowetting effect is quite effective when used to move, merge, mix, and separate droplets, and has been a major promoter of the recent developments of microsystems using DMF. The

**FIGURE 4.2**

Electrocapillary rise of a conductive liquid between two plates.

engineering aspects and applications of the electrowetting effect will be presented in Chapter 5.

4.2 Theoretical background

The derivation of Lippmann's law, i.e., the dependency of the contact angle according to the applied voltage, can be done by the following different approaches: the classical thermodynamic approach, the energy minimization approach, and the electromechanical approach. All these approaches are detailed by Mugele and Beret [4] in their review paper.

4.2.1 Thermodynamic approach

Although the interfacial tension in Lippmann's law is the gas–liquid interfacial tension, it is the solid–liquid interface that is relevant here—the electric field must penetrate this interface. We suppose a perfectly smooth solid surface at the contact of a conductive liquid or an electrolyte. We first follow the original Lippmann's approach: the solid is a metal directly in contact with the liquid and the potential difference is small enough so that no electric current is flowing through the liquid (no hydrolysis or any other Faradaic reaction at the metal surface). Upon applying an elementary electric field, an elementary potential difference builds up at the interface and an electric double layer forms in the liquid at the contact of the surface. Gibbs' interfacial thermodynamics which relates the normal force density to a gradient in the interfacial tension then yields

$$d\gamma_{SL}^{\text{eff}} = -\rho_{SL} dV, \quad (4.4)$$

where γ^{eff} denotes the effective surface tension at the liquid–solid interface, ρ_{SL} is the field-induced surface charge density in counterions, and V is the electric potential. If we make the Helmholtz simplifying assumption that the counterions are all located at a fixed distance d_{H} from the surface (d_{H} is of the order of a few nanometers), the double layer has a fixed specific capacitance (capacitance per unit area) in response to the charging by the normal electric field:

$$C_{\text{H}} = \frac{\varepsilon_0 \varepsilon_1}{d_{\text{H}}}, \quad (4.5)$$

where ε_1 is the relative permittivity of the liquid and ε_0 is the permittivity of vacuum: $\varepsilon_0 = 8.8541878176 \times 10^{-12} \text{ F/m}$. Direct integration of Eq. (4.4) yields

$$\begin{aligned} \gamma_{\text{SL}}^{\text{eff}}(V) &= \gamma_{\text{SL}} - \int_{V_{\text{pzc}}}^V \rho_{\text{SL}} \, dV \\ &= \gamma_{\text{SL}} - \int_{V_{\text{pzc}}}^V C_{\text{H}} V \, dV = \gamma_{\text{SL}} - \frac{C_{\text{H}}}{2} (V - V_{\text{pzc}})^2, \end{aligned} \quad (4.6)$$

where V_{pzc} is the potential at no charge: spontaneous charges appear at the surface of a solid when immersed into electrolyte solutions at zero voltage, and the potential at no charge is the voltage required to compensate this spontaneous charging. In assigning V in Eq. (4.6) to the voltage of the electrode relative to a distant reference electrode, we are assuming that most of the voltage drop occurs in the double layer and there is no Ohmic loss in the conducting liquid. This occurs when the double layer is fully charged and in the AC (alternating current) case, it stipulates that the AC frequency is lower than the inverse charging time of the double layer, $D/d_{\text{H}}^2 = \sigma/\varepsilon_0 \varepsilon_1$, where D is the ion diffusivity and σ is the conductivity of the liquid. Equation (4.6) is the original Lippmann's law for electrolytes in contact with a metal electrode. However, it should be emphasized that this derivation is truly valid only at an isolated solid–liquid interface and not at a contact line: nowhere in the reasoning does the contact line appear. It is also valid only for a metallic electrode surface. The analysis of the situation where a dielectric layer exists between the liquid and the electrode will be done later in this section. We have, in fact, estimated only the change in the electrode–liquid interfacial tension in the presence of an electric field. Nevertheless, using Young's law, we can translate the change in $\gamma_{\text{SL}}^{\text{eff}}$ to a change in the contact angle at a contact line. Young's law applied successively at zero potential and at potential V can be written as

$$\begin{aligned} \gamma_{\text{SG}} - \gamma_{\text{SL}} &= \gamma_{\text{LG}} \cos \theta_0 \\ \gamma_{\text{SG}} - \gamma_{\text{SL}}^{\text{eff}}(V) &= \gamma_{\text{LG}} \cos \theta, \end{aligned} \quad (4.7)$$

where θ , θ_0 are respectively the actuated and nonactuated contact angles. Upon subtraction of these two equations and substitution in Eq. (4.6), by assuming that

[Eq. \(4.6\)](#) derived for a bulk interface can be applied at the contact line, we obtain Lippmann–Young’s law [2]:

$$\cos \theta = \cos \theta_0 + \frac{C_H}{2\gamma_{LG}}(V - V_{pzc})^2. \quad (4.8)$$

[Equation \(4.8\)](#) shows that the contact angle decreases with an increase of the applied voltage. However, direct applications of Lippmann’s law to a conducting liquid contacting a metallic surface are of little use because of the limitation of the voltage due to hydrolysis phenomena. For water, $d_H \sim 2$ nm, $\varepsilon_l \sim 80$, $\gamma_{SL} \sim 0.040$ N/m, and the maximum voltage difference is of the order of 0.1 V, so that the relative change of the value of the surface tension is $\Delta\gamma_{SL}/\gamma_{SL} \sim 2\%$. In terms of contact angle, using $\gamma_{LG} = 0.072$ N/m, we find $(\cos \theta - \cos \theta_0) < 0.01$.

It is obvious that larger potentials are required to produce noticeable changes of the contact angle. In order to avoid hydrolysis, a thin dielectric layer can be used to insulate the liquid from the electrode [3]. In such a case, the former reasoning no longer applies, and we have to consider that the double layer is in series with the dielectric film. The specific capacitance is decreased by the presence of the dielectric (usually the electrolyte has a double layer capacitance much larger than that of the dielectric film). Because the capacitors are in series, it is the smaller dielectric layer capacitance that should now be used in Lippmann’s law. However, this smaller capacitance of the dielectric film is more than compensated by the much larger working voltages and a much larger contact angle distortion can be produced. This technique is called EWOD. In this new configuration, the electric double layer builds up at the surface of the insulator. The system now comprises two capacitors in series, namely the double layer at the solid surface—specific capacitance C_H —and the dielectric layer—specific capacitance C_D given by

$$C_D = \frac{\varepsilon_0 \varepsilon_D}{d}. \quad (4.9)$$

Comparing C_H —[Eq. \(4.5\)](#)—and C_D —[Eq. \(4.9\)](#)—we find

$$\frac{C_D}{C_H} = \frac{\varepsilon_D d_H}{\varepsilon_l d}.$$

This relation shows that $C_D \ll C_H$ because $d_H \ll d$ and $\varepsilon_D < \varepsilon_l$. Thus, the total capacitance C given by the relation

$$\frac{1}{C} = \frac{1}{C_D} + \frac{1}{C_H}$$

can be approximated by $C \approx C_D$ by neglecting the double layer capacitance. This relation shows that the voltage drop occurs within the dielectric layer (in comparison with the voltage drop in the double layer can be neglected), and [Eq. \(4.6\)](#) is replaced by

$$\gamma_{SL}^{\text{eff}}(V) = \gamma_{SL} - \frac{C}{2}V^2 = \gamma_{SL} - \frac{\varepsilon_0 \varepsilon_D}{2d}V^2, \quad (4.10)$$

where the potential at no charge V_{pzc} has been neglected assuming that the insulating layer does not give rise to spontaneous adsorption of charge. Using Young's law, we find Lippmann–Young's law for EWOD:

$$\cos \theta = \cos \theta_0 + \frac{C}{2\gamma_{\text{LG}}} V^2. \quad (4.11)$$

The last term on the right-hand side of Eq. (4.11) is dimensionless and is sometimes called the electrowetting number η :

$$\eta = \frac{C}{2\gamma_{\text{LG}}} V^2 = \frac{\varepsilon_0 \varepsilon_D}{2\gamma_{\text{LG}}} V^2. \quad (4.12)$$

For a dielectric like Teflon or parylene 1 μm thick and a droplet of water, the coefficient $\varepsilon_0 \varepsilon_D / 2\gamma_{\text{LG}}$ is of the order of 10^{-4} V^{-2} . In order to obtain a substantial change in contact angle, applied electric potentials should be of the order 30–80 V. We will see in Section 4.4 that the contact angle cannot go to zero by increasing the potential V , as predicted by Eq. (4.11), and that there is a limit (called saturation limit) above which an increase of potential does not result in a decrease of the value of the contact angle.

Equation (4.11) has been verified—for small to medium voltages—by using the experimental device of Figure 4.3. Once the actuation is switched on, the contact angle decreases and the drop changes to a more hydrophilic shape. The relation between the actuated contact angle and the applied voltage follows indeed the Lippmann–Young's equation, if the voltage is sufficiently far from the saturation value. Figure 4.3 corresponds to a droplet of water sitting on a 1 μm dielectric

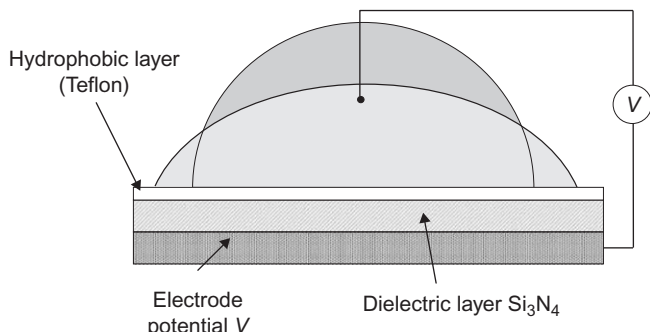
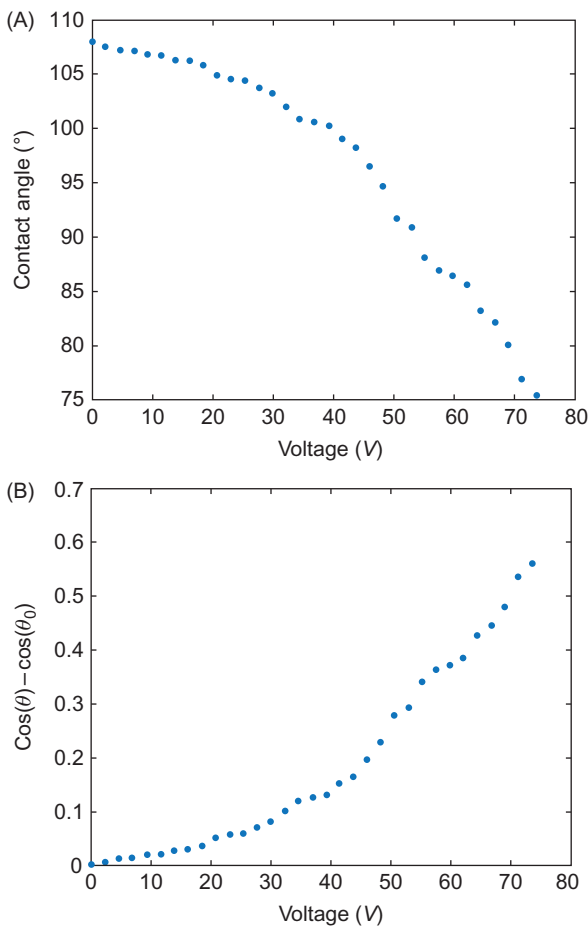


FIGURE 4.3

Scheme of the electrowetting setup used to verify Lippmann–Young's equation. The specific capacitance C of the system is the sum of the specific capacitances of the different layers between the electrode and the liquid. The zero potential electrode may be placed anywhere in the conducting drop. Upon actuation of a voltage V , the droplet spreads on the substrate. The value of the contact angle depends on the value of the actuation potential V .

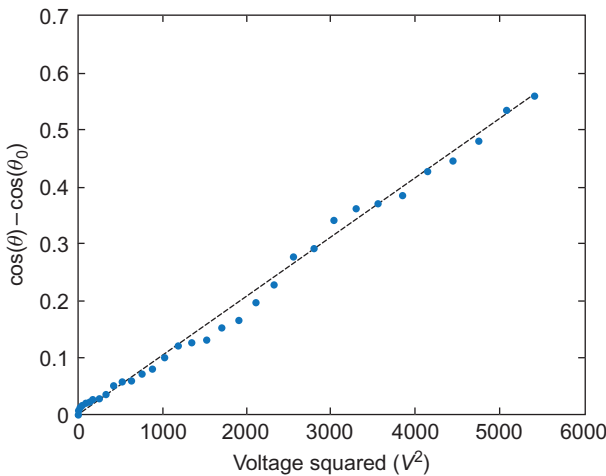
**FIGURE 4.4**

Lippmann–Young's relation between contact angle and applied voltage: (A) contact angle θ versus V and (B) $\cos \theta - \cos \theta_0$ versus V .

Source: Courtesy Dr. O. Raccourt, CEA/LETI.

coated with Teflon. The plot of Figure 4.4B shows the quadratic dependency of $\cos \theta - \cos \theta_0$ versus the voltage V : if we plot $\cos \theta - \cos \theta_0$ versus V^2 , the curve is well fit by a straight line, according to Lippmann–Young's law (Figure 4.5).

In this section, we have shown that the electrowetting effect can be viewed as a change of the value of the effective solid–liquid surface tension due to the apparition of electric charges either in the double layer or at the dielectric surface. This change in solid–liquid interfacial tension results in a change of the contact angle. The variation of the effective solid–liquid surface tension is proportional to the square of the potential drop between the electrode and the liquid, as stated

**FIGURE 4.5**

Linear dependency between $\cos \theta - \cos \theta_0$ and V^2 .

by Lippmann's law. Finally, using Young's law, we deduce Lippmann–Young's law representing the change in contact angle associated with an applied voltage.

In the following section, we present another approach based on energy minimization, leading directly to Lippmann–Young's equation. We show that the change of droplet contact angle results from a competition between dielectric energies which want to expand the liquid–solid area so as to decrease the charge concentration versus the surface tension energies which want to minimize the free surface of the droplet (see Section 2.10).

4.2.2 Energy minimization approach

Following the work of Shapiro and coworkers [5,6], this section presents an energy minimization approach to derive Young's law as well as Lippmann–Young's law. The derivation is rigorous and does not rely on an approach with forces, such as the Maxwell force at the interface, or the change in the liquid–solid surface tension. Instead, it uses an energy approach taking into account that the droplet remains spherical with a contact angle θ and a radius R (see Section 3.2). We are reminded that the drop has a spherical shape if the characteristic Bond number is much smaller than 1 corresponding to a situation where gravitational forces are unimportant (very small drop).

Mathematically, the energy of the droplet is a function $E = E(R, \theta; p)$, where R is the droplet radius, θ the contact angle, and p is a set of system parameters (such as the applied voltage, dielectric constants, ion concentrations, and temperature). Thus the energy depends on the geometry (R, θ) and system parameters.

First, note that the system assumes its equilibrium shape when the energy $E(R, \theta; p)$ is at a minimum. The derivative of the energy with respect to R and θ is then zero:

$$dE = \frac{\partial E}{\partial R}(R, \theta; p)dR + \frac{\partial E}{\partial \theta}(R, \theta; p)d\theta = 0. \quad (4.13)$$

However, R and θ are not independent since the droplet volume is constant. They are linked by

$$V(R, \theta) = \frac{\pi}{3}R^3(2 - 3\cos\theta + \cos^3\theta) = \pi R^3 \left(\frac{2}{3} - \frac{3\cos\theta}{4} + \frac{\cos 3\theta}{12} \right). \quad (4.14)$$

By putting $dV = 0$, we find

$$dR = RG(\theta)d\theta = R \left[-\frac{2\cos^2(\theta/2)\cot(\theta/2)}{2 + \cos\theta} \right] d\theta. \quad (4.15)$$

Substituting Eq. (4.15) in Eq. (4.13) yields

$$\frac{dE}{d\theta} = -R \left[\frac{2\cos^2(\theta/2)\cot(\theta/2)}{2 + \cos\theta} \right] \frac{\partial E}{\partial R} + \frac{\partial E}{\partial \theta} = 0. \quad (4.16)$$

Equation (4.16) constitutes the base for the derivation of Young and Lippmann–Young laws.

4.2.2.1 Derivation of Young's law

In this case, the only energy we consider is the interfacial energy. We have seen in Chapter 3 that the droplet interfacial energy is given by

$$E_{\text{int}} = \gamma_{LG}A_{LG} + (\gamma_{SL} - \gamma_{SG})A_{SL}, \quad (4.17)$$

where the subscripts S , L , and G denote solid, liquid, and gas phases, respectively. A denotes the interfacial area and γ the interfacial tension. The interfacial areas for a spherical cap have been derived in Chapter 3. We have

$$\begin{aligned} A_{LG} &= 2\pi R^2(1 - \cos\theta) \\ A_{SL} &= \pi R^2 \sin^2\theta. \end{aligned} \quad (4.18)$$

Finally, the interfacial energy can be cast under the form

$$E_{\text{int}} = \pi R^2[2\gamma_{LG}(1 - \cos\theta) + (\gamma_{SL} - \gamma_{SG})\sin^2\theta]. \quad (4.19)$$

Now, if we plug the expression of E_{int} given by Eq. (4.19) into Eq. (4.16):

$$\frac{dE_{\text{int}}}{d\theta} = -R \left[\frac{2\cos^2(\theta/2)\cot(\theta/2)}{2 + \cos\theta} \right] \frac{\partial E}{\partial R} + \frac{\partial E_{\text{int}}}{\partial \theta} = 0$$

we recover, after some algebra, the well-known Young's law:

$$\gamma_{LG}\cos\theta = \gamma_{SG} - \gamma_{SL}. \quad (4.20)$$

4.2.2.2 Derivation of Lippmann–Young’s law

Consider now the droplet of Figure 4.3. In Section 4.2.1, we found that almost all of the electric energy is located in the dielectric. Then, the electric energy for an elementary volume of the dielectric dv is given by

$$dE_{\text{diel}} = \frac{1}{2} (\vec{E} \cdot \vec{D}) dv, \quad (4.21)$$

where \vec{D} is the polarizability vector field, i.e., electric displacement vector. \vec{D} represents the induced dipole moment in the dielectric per unit volume. For an ideal dielectric, this moment is linearly related to the electric field:

$$\vec{D} = \varepsilon_0 \varepsilon_D \vec{E} \quad (4.22)$$

and the electric energy in the elementary volume is

$$dE_{\text{diel}} = \frac{1}{2} \varepsilon_0 \varepsilon_D |\vec{E}|^2 dv. \quad (4.23)$$

If we neglect the edge effect, i.e., the distortion of the electric field in the dielectric at the vicinity of the triple contact line (Figure 4.6), we have a uniform electrical field

$$\vec{E} = \{0, 0, -V/d\}. \quad (4.24)$$

This assumption is correct if the droplet is sufficiently large and might break down if the trend to miniaturizing the EWOD devices continues (at the present time, a typical dimension of a droplet in EWOD devices is 500 μm).

Using Eq. (4.24), we can integrate Eq. (4.23) to find the electric energy stored in the dielectric

$$E_{\text{diel}}(R, \theta) = \frac{1}{2} \varepsilon_0 \varepsilon_D \left(\frac{V}{d}\right)^2 A_{\text{SL}} d = \frac{\varepsilon_0 \varepsilon_D V^2}{2d} \pi R^2 \sin^2 \theta. \quad (4.25)$$

The total electric energy of the system is the difference between the electric energy stored in the dielectric and the energy in the external charging source [7].

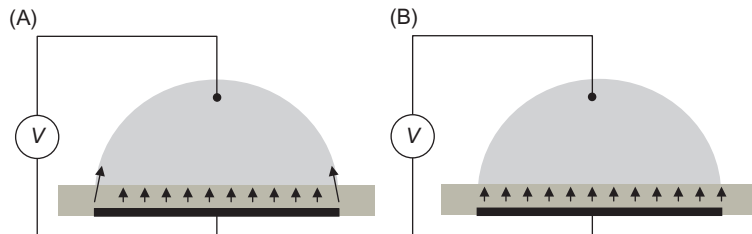


FIGURE 4.6

(A) The electric field is larger near the triple line due to edge effects. (B) If the contact surface of the liquid is sufficiently large, we can neglect the edge effect.

It can be shown that the energy stored in the external charging source is minus twice the energy stored in the dielectric. The basic reason is that every time the drop shape changes, the charged volume immediately under the solid–liquid contact area changes, and a packet of charge ΔQ must be received from or pushed back against the fixed voltage source. This requires a work $W = V \cdot \Delta Q = -E$. The energy stored in the charge source is then twice the energy stored in the dielectric but with an opposite sign. Hence, the total energy (surface plus electric energy) of the system is

$$E = R^2 \left[\left(\gamma_{SL} - \gamma_{SG} - \frac{\varepsilon_0 \varepsilon_D V^2}{2d} \right) \pi \sin^2 \theta + \gamma_{LG} 2\pi(1 - \cos \theta) \right]. \quad (4.26)$$

Upon substitution of Eq. (4.26) into Eq. (4.16), and observing that the derivation is similar to that of Eq. (4.19), replacing the term $(\gamma_{SL} - \gamma_{SG})$ by $(\gamma_{SL} - \gamma_{SG} - \varepsilon_D V^2 / 2d)$, we recover the Lippmann–Young’s equation

$$\cos \theta - \left(\frac{\gamma_{SL} - \gamma_{SL}}{\gamma_{LG}} + \frac{\varepsilon_0 \varepsilon_D V^2}{2\gamma_{LG} d} \right) = 0 \quad (4.27)$$

which can be equivalently expressed as

$$\cos \theta = \cos \theta_0 + \frac{\varepsilon_0 \varepsilon_D V^2}{2\gamma_{LG} d}. \quad (4.28)$$

This energy minimization approach explicitly considers the dielectric layer and the dielectric energy within it. However, like the thermodynamic approach of Section 4.2.1, it does not provide a physical picture of how the contact angle is reduced in mechanical terms. Whether such a distortion is solely due to a change in interfacial tension or some unique force at the contact line remains unresolved. While such a distinction may not be necessary for the contact angle, it becomes paramount when electrowetting dynamics needs to be scrutinized. With viscous effects, energy is not conserved and one cannot use the energy minimization approach. The actual force at the contact line must be captured. In the following section, we consider the electric forces exerted on the liquid explicitly, although we shall limit ourselves to static wetting problems.

4.2.3 Electromechanical approach

The two preceding approaches do not give any insight into the electric forces acting on the droplet, particularly why a Maxwell force at the solid–liquid interface has the same effect as reducing the gas–liquid interfacial tension. These two approaches only address the static problem. If one wants to address the dynamic problem, which would require the inclusion of viscous effects, the forces exerted by the electric field on the interface have to be explicitly determined. The electromechanical approach was introduced by Jones et al. [8,9], Kang [10], and recently reviewed by Zeng and Korsmeyer [11].

In the case of liquids, the body force density due to an electric field is given by the Korteweg–Helmholtz's relation:

$$\vec{f}_k = \sigma_f \vec{E} - \frac{\varepsilon_0}{2} E^2 \nabla \varepsilon_f + \nabla \left[\frac{\varepsilon_0}{2} E^2 \frac{\partial \varepsilon_f}{\partial \rho} \rho \right], \quad (4.29)$$

where ρ is the mass density of the liquid, ε_f is the permittivity of the liquid, and σ_f is the electric charges. The last term in Eq. (4.29) describes electrostriction and can be neglected here as the mass density of the liquid remains constant. The force acting on a volume element dV is obtained by integrating Eq. (4.29). It can be shown that it is equivalent to integrating the momentum flux density, i.e., the Maxwell stress tensor

$$T_{ik} = \varepsilon_0 \varepsilon \left(E_i E_k - \frac{1}{2} \delta_{ik} E^2 \right) \quad (4.30)$$

along the surface of dV in Eq. (4.30), the notation E^2 corresponds to $|\vec{E}|^2$ and δ_{ik} is the Kronecker delta function: $\delta_{ik} = 0$ if $i \neq k$ and $\delta_{ii} = 1$; and $i, k = x, y, z$. Surface integration of Eq. (4.30) is much easier than volume integration of Eq. (4.29). In general, the net force acting on the liquid volume element is

$$F_i = \oint_{\Omega} T_{ik} n_k dA, \quad (4.31)$$

where we use the Einstein summation convention (summation on the repeated indices). At the surface of a perfectly conducting liquid, on the gas side, the electric field is perpendicular to the surface (Figure 4.7), and related to the surface density of electric charges by Gauss' law

$$\sigma_s = \varepsilon_0 \vec{E} \cdot \vec{n}, \quad (4.32)$$

where \vec{n} is the outward unit normal vector. Moreover, the electric field vanishes in the conducting liquid. If we consider the x, y, z axis system such as the x -axis

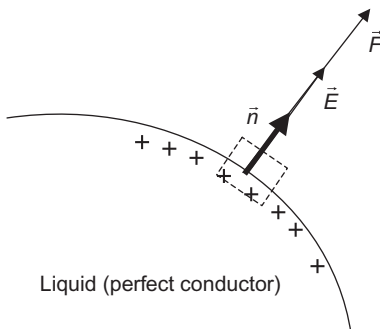


FIGURE 4.7

Electric force acting at the interface of a conducting liquid.

is aligned with n , the electric field is $E = (E_x, 0, 0)$ in the gas domain and $E = (0, 0, 0)$ in the liquid domain. In the gas domain, the Maxwell tensor is

$$[T] = \varepsilon \begin{pmatrix} \frac{1}{2}\varepsilon_0 E_x^2 & 0 & 0 \\ 0 & -\frac{1}{2}\varepsilon_0 E_x^2 & 0 \\ 0 & 0 & -\frac{1}{2}\varepsilon_0 E_x^2 \end{pmatrix} \quad (4.33)$$

and vanishes in the liquid domain

$$[T] = [0]. \quad (4.34)$$

We can now integrate Eq. (4.31); the cross terms xy , yz , and zx are all zero, the forces in the y (respectively z) direction cancel out, and we find that the only nonvanishing contribution is a force directed along the outward normal \vec{n} :

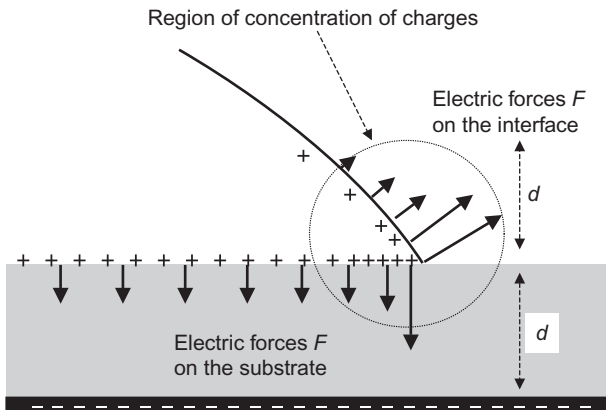
$$\frac{\vec{F}}{\delta A} = P_e \vec{n} = \frac{\varepsilon_0}{2} E^2 \vec{n} = \frac{\sigma_s}{2} \vec{E}, \quad (4.35)$$

where δA is an elementary surface area of the interface. In Eq. (4.35), P_e is the electrostatic pressure defined by $P_e = \varepsilon_0/2E^2$. The electrostatic pressure P_e acts on the liquid surface and brings a negative contribution to the total pressure within the liquid. The liquid interface is distorted by the electric forces acting on it, according to Eq. (4.35). They depend on the distribution of charges σ_f at the surface. Electric charges at the liquid–gas interface are located close to the triple contact line, as shown in Figure 4.8, within a distance equal to the dielectric thickness d .

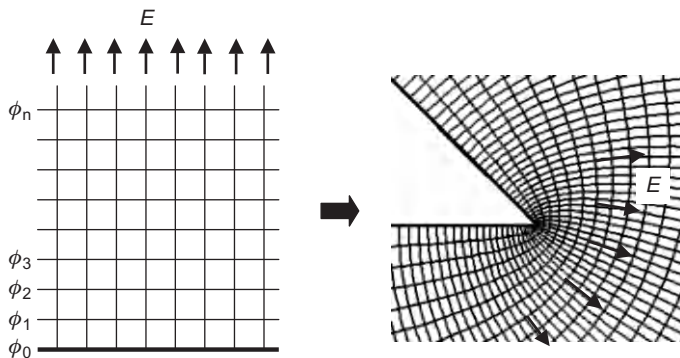
The problem of the surface distortion has been solved by Kang [10] and Vallet and Berge [12] using the Schwarz–Christoffel conformal mapping [13]. First, note that the electric potential ϕ satisfies the Laplace's equation $\nabla^2 \phi = 0$ and consequently is a harmonic function. The theory of analytic and harmonic functions shows that there exists a conformal mapping (the Schwarz–Christoffel mapping) that transforms the functions E and ϕ for a half plane into the same functions for a wedge (Figure 4.9). This mapping shows that the field and charges concentrate at the tip of the wedge. In fact, as is the case of any harmonic function near a geometric singularity, the electric field is singular at a wedge (see, e.g., Thamida and Chang [14]) but the Maxwell pressure is integrable and produces a finite Maxwell force at the contact line after Eq. (4.35) is integrated:

$$F_{\text{horizontal}} = \frac{\varepsilon_0 \varepsilon_D V^2}{2d} \quad (4.36)$$

$$F_{\text{vertical}} = \frac{\varepsilon_0 \varepsilon_D V^2}{2d} \frac{1}{\tan \theta}.$$

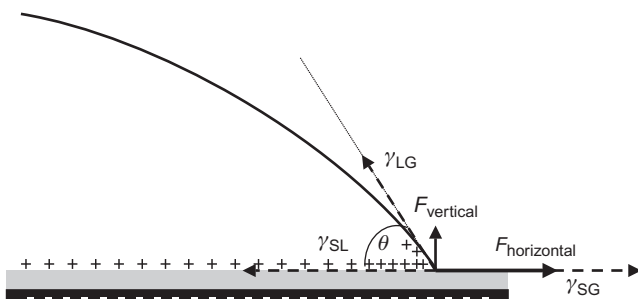
**FIGURE 4.8**

Schematic of the electric charge distribution in the vicinity of the triple contact line. Electric charges are located at the solid–liquid interface and at the liquid–gas interface, approximately within a distance d from the solid surface. In reality, this is a very simplified view since the liquid interface is distorted by the electric forces very close to the triple contact line.

**FIGURE 4.9**

Principle of the Schwarz–Christoffel conformal mapping. The two orthogonal fields E and ϕ are transformed from a simple half plane geometry (with an evident solution) to the geometry of a wedge. Remark the concentration of the electric field around the tip of the wedge.

We note first that the electric forces distribution on the liquid–gas interface caused by the Maxwell stress is limited to a very small region close to the triple line. At a macroscopic scale, we can picture the situation as in Figure 4.10 and assume that the forces are point forces acting on the triple line.

**FIGURE 4.10**

Resultant of the electric forces on the liquid–gas interface.

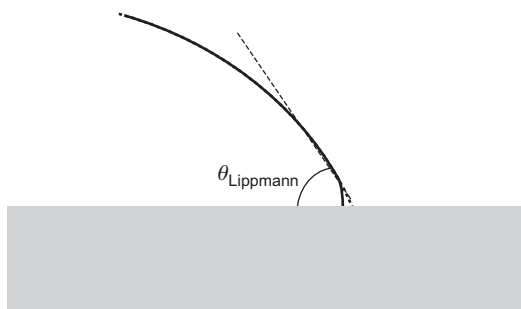
Second, using relation (4.36), we can make the balance of the forces—electric plus capillary—in the horizontal direction at the triple line, as has been done for deriving Young's equation, and we recover once again Lippmann's equation

$$\cos \theta = \cos \theta_0 + \frac{\varepsilon_D V^2}{2\gamma_{LG} d}. \quad (4.37)$$

The electromechanical approach shows that the Lippmann's term (electrowetting number η) comes directly from the Maxwell stress on the liquid–gas interface near the contact line, but its origin can be traced back to the thin solid dielectric layer and the wedge geometry of the liquid. In fact, since the liquid has a much higher permittivity (and conductivity) than the gas, it is the wedge shape of the gas phase that is responsible for distortion of the contact angle, as is clearly shown by the Schwarz–Christoffel transformation. The Lippmann term can also be called electrostatic pressure. Another consequence of Eq. (4.36) is that there is a vertical force on the liquid interface near the triple line. This vertical force increases quickly when the contact angle decreases. The theory even predicts that this force goes to infinity when the contact angle goes to zero. This could be an explanation for the phenomenon of the contact angle saturation (the contact angle cannot go to zero), usually accompanied by ejection of nanodrops (see Section 4.4). This could also be the reason why, extremely close to the solid surface, the shape of the interface is distorted [14], especially when the applied voltage is important (Figure 4.11).

4.3 Lippmann–Young's law and the electrocapillary equivalence

As seen from the previous sections, Lippmann's law has many physical interpretations. Although they all lead to the same mathematical formula, they often have

**FIGURE 4.11**

Deformation of the interface at high voltage [15].

different physical origins and have different physical implications. In the thermodynamic approach, Lippmann's law is related to a change in the solid–liquid apparent interfacial tension

$$\gamma_{\text{SL}}(V) = \gamma_{\text{SL},0} - \frac{C}{2} V^2 \quad (4.38)$$

and substitute Young's law

$$\begin{aligned} \gamma_{\text{SG}} - \gamma_{\text{SL},0} &= \gamma_{\text{LG}} \cos \theta_0 \\ \gamma_{\text{SG}} - \gamma_{\text{SL}}(V) &= \gamma_{\text{LG}} \cos \theta \end{aligned} \quad (4.39)$$

to obtain Lippmann–Young's law

$$\cos \theta = \cos \theta_0 + \frac{1}{2} \frac{C}{\gamma_{\text{LG}}} V^2. \quad (4.40)$$

Another slightly different way of writing Lippmann–Young's law, making the electric and capillary forces appear, is

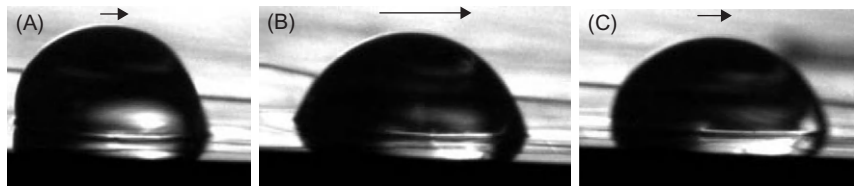
$$\gamma_{\text{LG}} \cos \theta - \gamma_{\text{LG}} \cos \theta_0 = \frac{1}{2} C V^2. \quad (4.41)$$

We see here that the voltage can be continuous or alternating. In the case of alternating voltage, the value of the voltage V in Eqs (4.40) and (4.41) should be the root mean square (rms) value:

$$V_{\text{rms}} = \frac{\sqrt{2}}{2} V$$

and

$$V_{\text{rms}}^2 = \frac{1}{2} V^2.$$

**FIGURE 4.12**

Photograph of a droplet during its motion: (A) phase 1, the droplet starts its motion; (B) droplet in full motion; and (C) end of motion.

Source: Courtesy R. Bavière, CEA/LETI.

The first interpretation of Lippmann–Young’s law stems from Eq. (4.40): when actuated, the contact angle of the droplet changes resulting in an “apparent” change of capillarity. It is very important here to note the word “apparent”: in reality, the contact angle at the wall is not the Lippmann’s contact angle (Figure 4.11) but still the Young’s contact angle; however, at some—not well defined—distance to the surface, the macroscopic contact angle has the value given by Lippmann–Young’s law [15]. Besides, one should be very careful with dynamic motion as viscous effects with other length scales and dynamic contact angle conditions would invalidate the current static theories. Indeed, the situation is quite different during rapid dynamic motion of droplets under EWOD actuation: the contact angles are not the equilibrium contact angles. For example, in Figure 4.12, we show the observed dynamic contact angles during the motion of a droplet under EWOD actuation [16]. So this interpretation is not formally rigorous, but it is very convenient in an engineering approach to explain many *static or quasi-static* phenomena occurring in EWOD microsystems [17–20]. For the first analysis of dynamic (or spontaneous) electrowetting, see Yeo and Chang [21], the review [22], and a related treatment of electrokinetic displacement of bubbles by Takhistov et al. [23].

The second, more rigorous interpretation of Lippmann–Young’s law stems from Eq. (4.38). In Chapter 2, we have seen that the capillary line force on a triple line with contact angle θ_0 is given by

$$f_{\text{cap}} = \gamma_{\text{LG}} \cos \theta_0. \quad (4.42)$$

This line force is directed in the solid plane perpendicularly to the triple contact line and oriented outward. Following Jones et al. [8,9], Kang [10], and Zeng and Korsmeyer [11], we have seen that the line tension electrostatic force is

$$f_{\text{EWOD}} = \frac{C}{2} V^2. \quad (4.43)$$

Lippmann–Young’s law—under the form (4.41)—can then be written as

$$f_{\text{tot}} = f_{\text{cap}} + f_{\text{EWOD}}. \quad (4.44)$$

**FIGURE 4.13**

Two different configurations for electrowetting experiments: (A) Static change in the macroscopic contact angle obtained using dielectric film coated planar electrodes. (B) Electrowetting effect produced using parallel line electrode configuration. The inset shows a schematic representation of the cross-section of the bulk drop and electrowetting film showing that the electric field lines are predominantly tangential to the interface.

Source: From Ref. [21] © 2006, APS, reprinted with permission.

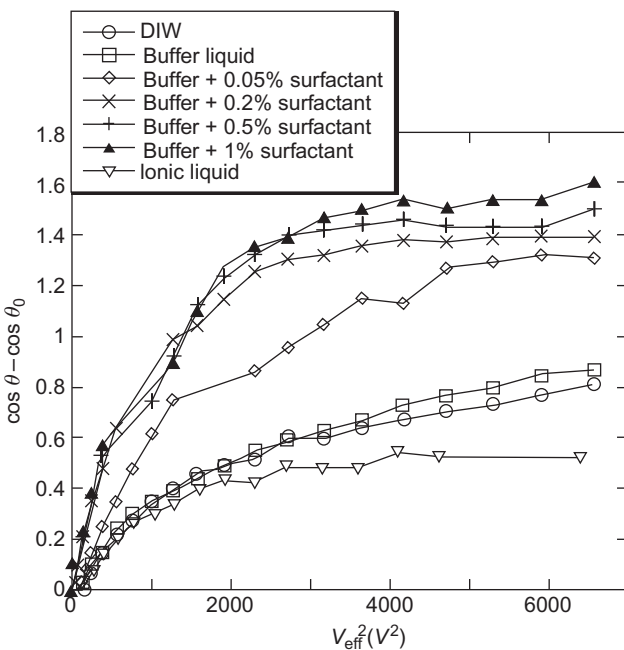
Under such a form, the electrowetting effect is to add an electric force to the capillary force on the triple line. A characteristic example of the interpretation of Lippmann–Young’s law by electric charge distribution and the Maxwell stress tensor has been pointed out by Yeo and Chang [21]: they showed that a droplet can be stretched using two parallel line electrodes, instead of planar electrodes (Figure 4.13). Clearly, in such a case, it is impossible to use the “apparent” contact angle interpretation.

4.4 Saturation

4.4.1 Saturation of the electrowetting effect

It has been observed that the domain of validity of the Lippmann–Young’s equation is limited to small and medium electric potentials. We have set up an experimental microdevice to explore the Lippmann–Young’s relations for different fluids (Figure 4.3). In this experimental setup, the zero potential electrode is located directly in the substrate below the droplet. Contact angles have been determined by image analysis of side views of the droplet using a Digidrop® analysis apparatus.

Relation (4.40) has been experimentally checked for different biological buffers (Figure 4.14) on an EWOD substrate consisting of a 300 nm Si_3N_4 dielectric layer and a 1 μm Teflon coating. The experimental results show that the Lippmann–Young’s relation is valid for electric potentials below 40–50 V; above this value there is a saturation effect and the contact angle does not decrease any more with the increasing voltage. Hence, there is an upper limit to the electrowetting force.

**FIGURE 4.14**

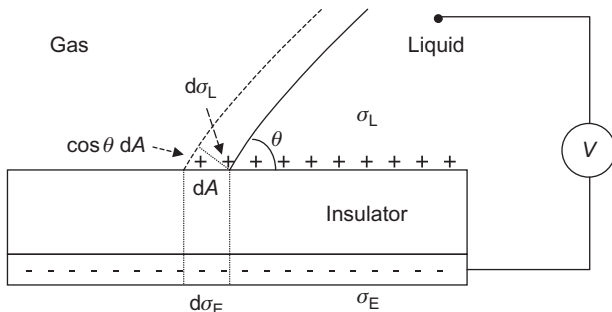
Plots of $(\cos \theta - \cos \theta_0)$ as a function of V^2 for different fluids (ionic liquid, DIW and buffers with 0%, 0.05%, 0.2%, 0.5%, and 1% surfactant). The drops are immersed in silicone oil.

4.4.2 Possible explanations for the saturation effect

At the present time, different explanations have been proposed for the saturation limit. We have already seen a possible explanation with Kang's formula for the electric force—Eq. (4.36). However, there is no consensus on the real cause of saturation, and the debate is still open. The saturation effect is important because it limits the electrowetting force acting on a droplet and constitutes a bottleneck for the development of scale down electrowetting devices. In the following sections, we present different explanations proposed for the saturation effect.

4.4.2.1 Trapping of charges

Verheijen and Prins [24] proposed a model of saturation based on the trapping of charges in the insulator when the voltage becomes sufficiently large. This trapping of charges reduces the density of charges at the solid–liquid surface and weakens the electrowetting effect. Saturation is obtained if, above the saturation voltage, the solid–liquid density of charges does not increase any more; in such a case the electric charges accumulate only in the dielectric.

**FIGURE 4.15**

Schematic of the electric charges during electrowetting. No trapped charges.

In order to investigate the effect of trapping of charges, we follow the approach of Verheijen and Prins which consists in using the virtual displacement principle to derive the expression of the free energy of the system. In the following, the development is done first in the case of no trapped charges, then in the case of charge trapping.

4.4.2.1.1 Virtual displacement: no charge trapping and Lippmann–Young’s equation

When an electric voltage is set between the electrode and the liquid, a charge density σ_L builds up in the liquid phase close to the liquid–solid interface. This charge density induces an image charge density σ_E on the metal electrode (Figure 4.15). An increase of surface charges provokes a displacement of the interface. Suppose there is an infinitesimal displacement dA . The free energy of the system can be written as

$$dE = \gamma_{SL} dA - \gamma_{SG} dA + \gamma_{LG} dA \cos \theta + dU - dW, \quad (4.45)$$

where U is the capacitive energy stored in the dielectric and dW the work performed by the voltage source. Note that Eq. (4.45) collapses to the Young’s equation in the absence of an externally applied voltage: at equilibrium, $dE/dA = 0$, and we have $0 = \gamma_{SL} - \gamma_{SG} + \gamma_{LG} \cos \theta$, which is Young’s equation.

The energy stored in the dielectric is derived in Section 4.2.2.2, Eq. (4.21):

$$\begin{aligned} \frac{dU}{dA} &= \frac{1}{2} dED = \frac{1}{2} d \left(\frac{V}{d} \right) (\varepsilon_0 \varepsilon_D E) \\ &= \frac{1}{2} d \left(\frac{V}{d} \right) \left(\varepsilon_0 \varepsilon_D \frac{V}{d} \right) = \frac{1}{2} d \left(\frac{V}{d} \right) \sigma L = \frac{1}{2} V \alpha_L. \end{aligned} \quad (4.46)$$

In Eq. (4.46), D is the electric displacement $D = \varepsilon_0 \varepsilon_D E$, and we have used Gauss's law to obtain $\varepsilon_0 \varepsilon_D E = \sigma_L$. Using the same argument as that of Section 4.2.2.2 [7], the energy of the voltage source is twice that of the dielectric:

$$\frac{dW}{dA} = V\sigma_L. \quad (4.47)$$

Upon substitution of Eqs. (4.46) and (4.47) into Eq. (4.45), and setting $dE/dA = 0$, we recover once again the Lippmann–Young's equation

$$\gamma_{LG} \cos \theta = \gamma_{SG} - \gamma_{SL} + \frac{\varepsilon_0 \varepsilon_D}{2d} V^2. \quad (4.48)$$

4.4.2.1.2 Trapping of charges and saturation effect

Suppose now that, at sufficiently high voltage, charges are pulled into the dielectric by electric forces. These charges may become trapped if the interactions of the ions with the solid are stronger than that with the liquid. Suppose for simplicity of the reasoning that these charges are trapped at a depth d_2 from the solid surface (Figure 4.16).

The work performed by the voltage source is still given by Eq. (4.47). However, the energy stored in the dielectric is different than that produced by Eq. (4.46) because the charges are not located at the same place and also because of the presence of trapped charges in the dielectric under the gas. If V_T denotes the potential at the level of the trapped charges on the gas side and V_T^L in the liquid side, we can write

$$\begin{aligned} \frac{dU_L}{dA} &= \frac{1}{2} d_1 E_1 D_1 + \frac{1}{2} d_2 E_2 D_2 = \frac{1}{2} d_1 \frac{V_T^L}{d_1} (\sigma_T + \sigma_L) + \frac{1}{2} d_2 \frac{V - V_T^L}{d_2} \sigma_L \\ &= \frac{1}{2} V_T^L \sigma_T + \frac{1}{2} V \sigma_L. \end{aligned} \quad (4.49)$$

On the gas side,

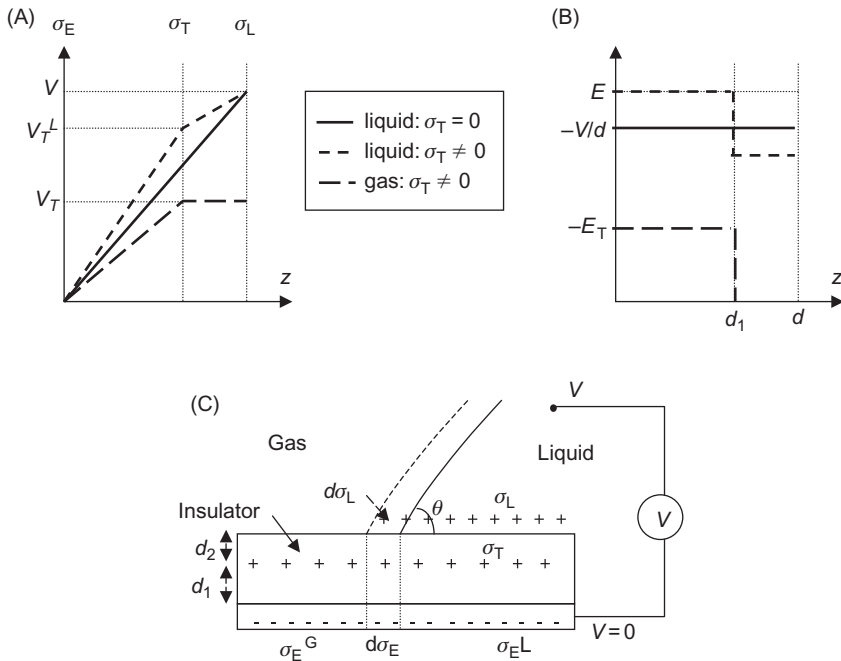
$$\frac{dU_G}{dA} = \frac{1}{2} d_1 \frac{V_T}{d_1} \sigma_T = \frac{1}{2} V_T \sigma_T. \quad (4.50)$$

Hence,

$$\frac{dU}{dA} = \frac{dU_L}{dA} - \frac{dU_G}{dA} = \frac{1}{2} V_T^L \sigma_T + \frac{1}{2} V \sigma_L - \frac{1}{2} V_T \sigma_T. \quad (4.51)$$

Setting $dE/dA = 0$, Eq. (4.45) becomes

$$\begin{aligned} \frac{dE}{dA} &= 0 \\ &= \gamma_{SL} - \gamma_{SG} + \gamma_{LG} \cos \theta + \frac{1}{2} V_T^L \sigma_T + \frac{1}{2} V \sigma_L - \frac{1}{2} V_T \sigma_T - V \sigma_L. \end{aligned} \quad (4.52)$$

**FIGURE 4.16**

Schematic of the electric charges during electrowetting with and without trapped charges: (A) potential profiles, (B) electric field, and (C) schematic of the trapped charges. Remark that the bottom electrode is at a zero potential and the liquid at the potential V .

Let us express V_T^L , σ_T and σ_L using Gauss' law:

$$V_T^L = V_T + \frac{d_1}{d} (V - V_T)$$

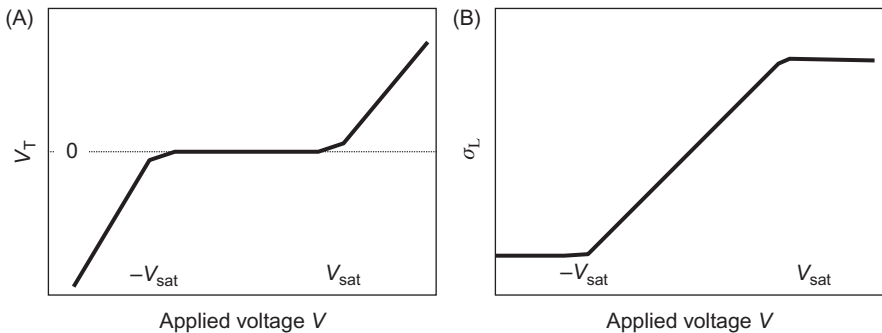
$$\sigma_T = \varepsilon_0 \varepsilon_D \frac{V_T}{d_1}$$

$$\sigma_L = \varepsilon_0 \varepsilon_D \frac{V - V_T^L}{d_2} = \varepsilon_0 \varepsilon_D \frac{V - V_T}{d}.$$

After substitution in Eq. (4.52), we obtain

$$\gamma_{LG} \cos \theta = \gamma_{SG} - \gamma_{SL} + \frac{\varepsilon_0 \varepsilon_D}{2d} (V - V_T)^2, \quad (4.53)$$

which is similar to the Lippmann–Young's law, except that the potential is $V - V_T$ instead of V . Let us remark here that V_T is a function of V . At saturation, i.e., for $V > V_{\text{sat}}$ (or $V < -V_{\text{sat}}$), the contact angle remains constant; from Eq. (4.53) we

**FIGURE 4.17**

(A) Trapped charge potential V_T as a function of applied potential V . (B) Surface charges σ_L as a function of the applied potential.

deduce that $V - V_T$ must be constant at saturation (hence $V_T = V + \text{cst}$); consequently the density of surface charges σ_L must also be constant at saturation. We then have Figure 4.17: the trapped potential V_T is proportional to V outside the interval $[-V_{\text{sat}}, V_{\text{sat}}]$ and vanishes inside this interval, whereas σ_L is constant outside the interval and proportional to V inside the interval.

Verheijen and Prins have experimentally observed that trapped charges exist, but they found that it was very difficult to find a quantitative estimate for V_T .

4.4.2.2 Zero surface-liquid energy limit

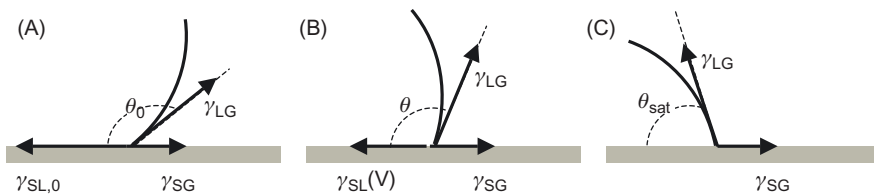
This model was pioneered by Peykov et al. [25], and Quinn et al. [26], and we will refer to it in the following by the abbreviation ‘‘PQRS model.’’ The PQRS model considers that the saturation phenomenon is a thermodynamic limit of stability. In Section 4.2.1, we presented the thermodynamic approach to the electrowetting effect; in this approach, the effective solid–liquid surface tension decreases with the voltage according to equation

$$\gamma_{\text{SL}}^{\text{eff}}(V) = \gamma_{\text{SL}} - \frac{1}{2}CV^2 \quad (4.54)$$

and the voltage dependent Young’s law can be cast under the form

$$\cos \theta(V) = \frac{\gamma_{\text{SG}} - \gamma_{\text{SL}}^{\text{eff}}(V)}{\gamma_{\text{LG}}} \quad (4.55)$$

Relation (4.55) is plotted in Figure 4.18 for different values of the applied voltage. For a zero voltage, the force balance is that defined by the classical Young’s law. As the voltage increases, the effective solid–liquid surface tension decreases, and the contact angle decreases according to Eq. (4.55). The lower limit for the effective solid–liquid surface tension is zero; at this point, the projection of γ_{LG} is equal and opposite to γ_{SG} . When this value is reached, the

**FIGURE 4.18**

Sketch of the different contact angles depending on the applied voltage: (A) at zero potential, the contact angle is determined by the classical Young's law, (B) the contact angle decreases when the applied voltage increases; and (C) the lower limit of the contact angle is obtained when the solid–liquid surface tension vanishes.

minimum contact angle is obtained. This minimum value is the saturation contact angle θ_{sat} .

According to Eq. (4.55), we have, at saturation,

$$\cos \theta_{\text{sat}} = \cos \theta(V_{\text{sat}}) = \frac{\gamma_{SG}}{\gamma_{LG}} \quad (4.56)$$

which is equivalent to

$$\theta_{\text{sat}} = \arccos \left(\frac{\gamma_{SG}}{\gamma_{LG}} \right). \quad (4.57)$$

Using Eq. (4.54), we derive

$$V_{\text{sat}} = \left(\frac{2\gamma_{SL,0}}{C} \right)^{1/2} = \left(\frac{2(\gamma_{SG} - \gamma_{LG} \cos \theta_0)}{C} \right)^{1/2}. \quad (4.58)$$

Formulas (4.57) and (4.58) require the knowledge of the solid surface tension γ_{SG} . We have seen in Chapter 2 that this surface tension is rather difficult to determine, except in the case of apolar surfaces for which Zisman's criterion produces a good approximation [27]. In the particular case of EWOD, the coating of the substrate is realized with apolar materials like Teflon, parylene, PET (polyethylene terephthalate), and PTFE (polytetrafluoroethylene), and we can reasonably use the value of the wetting surface tension (Zisman's criterion) for γ_{SG} in Eqs (4.57) and (4.58). The PQRS model predicts values of the saturation contact angle in reasonably good agreement with the experimental observations, although it is sometimes somewhat overestimated.

4.4.2.3 Electric resistance of the liquid

This approach has been proposed by Shapiro and coworkers [5,6]. In their model, the droplet liquid is not perfectly conducting; it presents a small electric resistance that depends on the shape of the droplet. When the droplet spreads under

the action of the applied electric potential, the resistance of the liquid increases: saturation is then seen as a geometrical effect.

The electrical diagram for the droplet-substrate system is shown in [Figure 4.19](#). In each domain (respectively liquid and dielectric), the electric potential ϕ is given by the equation

$$\nabla \cdot \vec{j} = \nabla(\sigma \vec{E}) - \nabla(\sigma \nabla \phi) = \nabla \left(\frac{1}{\rho} \nabla \phi \right) = 0, \quad (4.59)$$

where j is the electric current density, σ is the electric conductivity (S/m), and ρ is the electric resistivity (ρ /m). The boundary conditions are ([Figure 4.20](#))

- $\phi = V$ at the top electrode
 - $\phi = 0$ at the bottom electrode
 - $\nabla \phi \cdot \hat{n} = 0$ at the droplet surface,
- (4.60)

where \hat{n} is the normal unit vector.

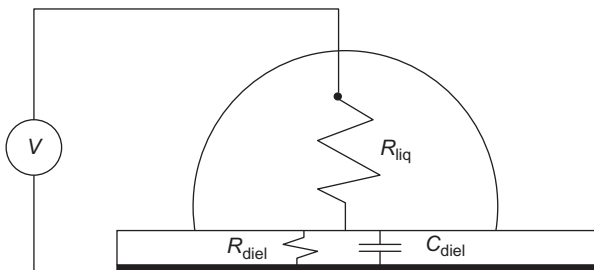


FIGURE 4.19

Electric diagram of the system showing a small amount of liquid resistance and a large dielectric solid resistance.

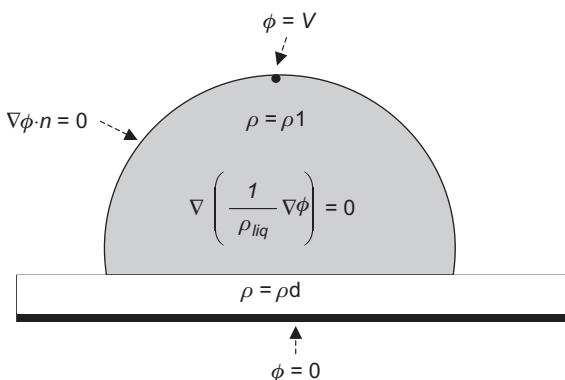
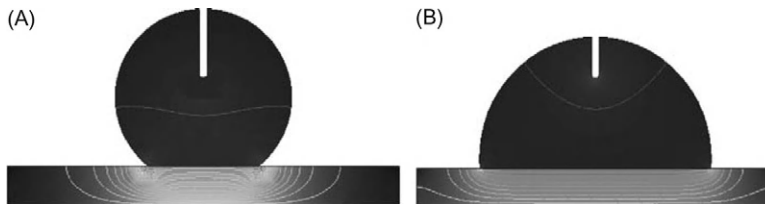


FIGURE 4.20

Boundary conditions and domain equations for the calculation of the electric potential in the slightly resistive droplet.

**FIGURE 4.21**

The amount of stored electrical energy decreases with the contact angle: (A) large contact angle and (B) smaller contact angle. The contour lines correspond to the electric potential (calculation performed with the COMSOL numerical software).

[Equation \(4.59\)](#) with boundary conditions [\(4.62\)](#) can easily be solved using a finite element technique ([Figure 4.21](#)). The results show that the strength of the electric field inside the solid dielectric, and thus the amount of stored electrical energy, decreases with the contact angle. As the droplet spreads, there is progressively a longer liquid path from the top electrode to the bottom electrode near the triple line. If there were no electric resistance in the liquid, the norm of the electric field would remain the same. Globally, the resistance of the droplet increases when the droplet spreads. Using Shapiro's energy approach, and by analogy with [Eq. \(4.26\)](#), it can be shown that the energy of the system can be cast under the form

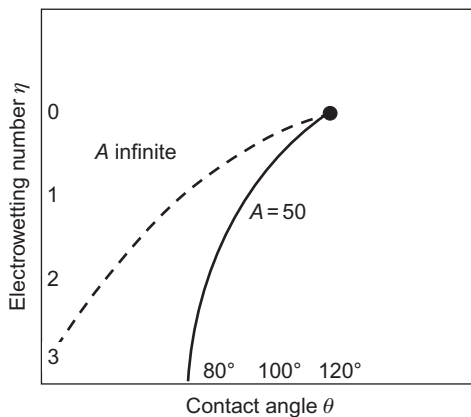
$$\frac{E(\theta)}{\gamma_{LG} R_0^2} = r(\theta)^2 \left[\left(\frac{\gamma_{SL} - \gamma_{SG}}{\gamma_{LG}} \right) \pi \sin^2 \theta + 2\pi(1 - \cos \theta) \right] - \frac{1}{2} \left(\frac{\varepsilon_D V^2}{\gamma_{LG} d} \right) r(\theta)^2 \frac{d}{R_0} F \left(\theta, \frac{\rho_l}{\rho_d}, \frac{d}{R_0} \right), \quad (4.61)$$

where R_0 is the initial radius, $r(\theta) = R(\theta)/R_0$, ρ_l and ρ_d the liquid and dielectric resistivity, and F a function that can be determined numerically. The problem depends now on three nondimensional parameters:

1. The surface tension coefficient $\Gamma = (\gamma_{SL} - \gamma_{SG})/\gamma_{LG}$
2. The electrowetting number $\eta = \varepsilon_D V^2 / (\gamma_{LG} d)$
3. The ratio of the solid to liquid resistivity $A = (\rho_d/\rho_l)(d/R_0)$.

The difference with [Section 4.2.3](#) is the supplementary term due to the resistivity of the liquid.

The function F contains the information on the decrease in energy when the contact angle decreases. It can be shown numerically, using formula [\(4.61\)](#), that the contact angle does not go to zero if the liquid has a sufficient resistivity ([Figure 4.22](#)). Above the saturation limit, the capacitive energy does not increase, and the increase in electric energy is balanced by the increase of the resistive

**FIGURE 4.22**

When the electrowetting number increases, the contact angle cannot go to zero if there is a sufficient resistivity of the liquid (A is the ratio $\rho_d d / \rho_l R_0$, A infinite corresponds to a perfectly conducting liquid).

loss. The saturation is then caused by the global resistance of the liquid when it spreads on the solid surface.

Shapiro's approach is very sensitive to the ratio of the resistivities. The latter has been used as a fitting parameter and is difficult to measure precisely.

4.4.2.4 Other models and discussion

All the preceding models neglect the “fringe effect,” i.e., the increase of the electric field near the triple line due to the discontinuity of material properties at the triple line. Papathanasiou and Boudouvis [15] have shown that the magnitude of the electric field increases up to 10 times in the dielectric at the level of the triple line for an external applied potential of the order of the saturation voltage (in their calculation, the liquid has been assumed to be perfectly conducting). Besides, the liquid interface is distorted by the action of the electric field in the vicinity of the contact line (Figure 4.23). Such an increase of the electric field results in the dielectric breakdown and charge leakage (see Section 4.6.2). In their view, saturation is closely associated to dielectric breakdown.

Vallet and Berge [12] have observed that, close to saturation, the luminescence of a region neighboring the triple line suddenly increases (Figure 4.24).

They remark that if the air is ionized, electrowetting stops working: the principle of electrowetting is that charges are adsorbed in the conducting liquid at the solid–liquid interface. These charges exert a lateral pressure outward on the wetting line, inducing the spreading of the drop. If air gets ionized, there is a leakage of the charges and the pressure on the triple line cannot increase with the applied voltage. The theory proposed by Vallet and Berge [12] assumes that the surrounding fluid is a gas. But what if the surrounding fluid is silicone oil, for instance?

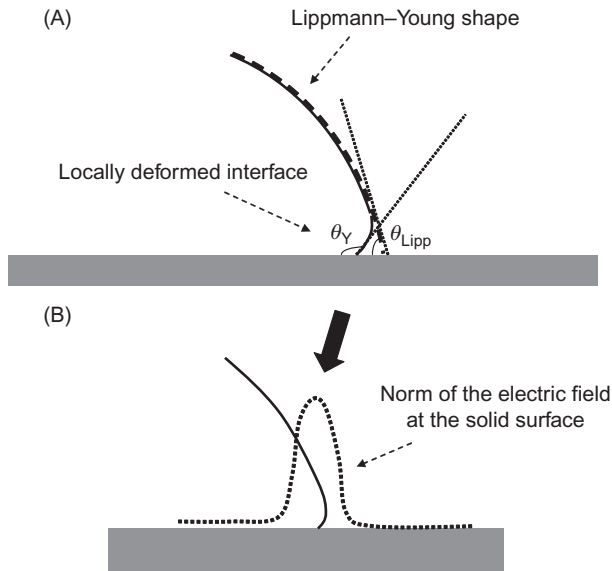


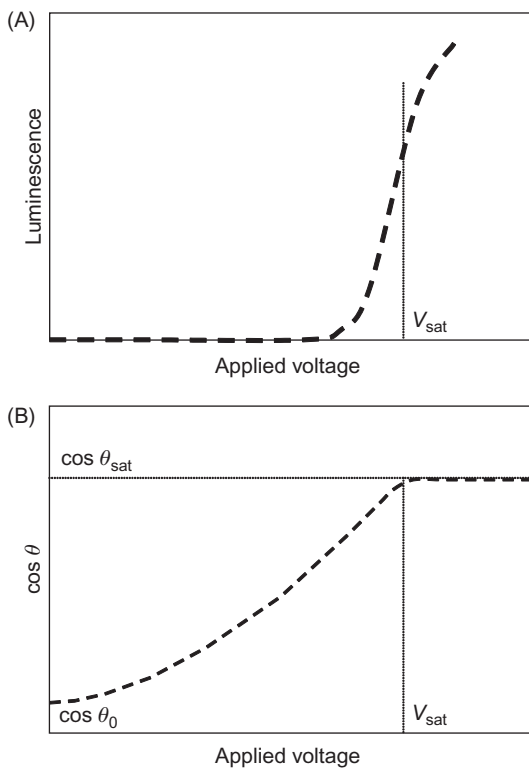
FIGURE 4.23

- (A) At high voltage, the liquid interface is distorted under the action of the electric field.
 (B) The magnitude of the electric field may be 10 times larger at the contact line at high voltage.

We have seen that many different explanations for the contact angle saturation for electrowetting have been proposed. These explanations are based on very different physical phenomena, like charge trapping, zero effective solid–liquid surface tension, increase of the liquid electric resistance, leakage due to dielectric breakdown, or air ionization near the triple line. Obviously, the saturation phenomenon is not yet clearly explained. However, independently of the physical explanation, we show in the next section that we can give a general analytical expression for the Lippmann–Young’s law taking into account the saturation phenomenon. This expression will be useful in the modeling of electrowetting.

4.4.3 Modified Lippmann–Young’s law

We have seen that, for low potentials, the relation between the contact angle θ and the applied voltage V is given by Lippmann–Young’s law. This law shows a linear dependence between $\cos \theta$ and V^2 . At large electric potentials, the contact angle has an asymptote. This situation is similar to that of paramagnetism where the induced magnetic moment is a linear function of the magnetic field $M = \chi H$, when the magnitude of the field is small and has a saturation limit when the magnitude of the field increases [19,20]. The work pioneered by Langevin in

**FIGURE 4.24**

(A) Luminescence versus applied voltage. (B) Saturation curve. The comparison of the two curves shows that luminescence is correlated to saturation.

the year 1905 has led to the definition of the so-called Langevin's, or sometimes Langevin–Debye's, function defined by

$$L(x) = \coth(3x) - \frac{1}{3x}. \quad (4.62)$$

Why is this function especially adapted to the situation? First, let us look at Langevin's function at the origin. Due to the term $1/3x$, we have to work out a Taylor's expansion at the origin. Remember that Taylor's expansions at the origin for hyperbolic sine and cosine are

$$\ch(3x) = 1 + \frac{(3x)^2}{2!} + \frac{(3x)^4}{4!} + O(x^6)$$

$$\sh(3x) = x + \frac{(3x)^2}{3!} + \frac{(3x)^5}{5!} + O(x^7).$$

Then, for $x \rightarrow 0$, the Langevin's function can be approximated by

$$L(x) \approx \coth(3x) - \frac{1}{3x} \approx \frac{1 + \frac{(3x)^2}{2!} + \frac{(3x)^4}{4!} + O(x^6)}{3x + \frac{(3x)^3}{3!} + \frac{(3x)^5}{5!} + O(x^7)} - \frac{1}{3x}.$$

After some algebra, we find

$$\begin{aligned} L(x) &\approx \coth(3x) - \frac{1}{3x} \approx \frac{1}{3x} \left[\frac{1 + \frac{(3x)^2}{2!} + \frac{(3x)^4}{4!}}{1 + \frac{(3x)^3}{3!} + \frac{(3x)^5}{5!}} - 1 \right] \\ &\approx \frac{1}{3x} \left[\left(1 + \frac{(3x)^2}{2!} \right) \left(1 - \frac{(3x)^2}{3!} \right) - 1 \right] \approx \frac{1}{3x} \left[(3x)^2 \left(\frac{1}{2} - \frac{1}{6} \right) \right] \approx x. \end{aligned}$$

Thus, when $x \rightarrow 0$, $L(x) \approx x$.

Note that there is no term in x_2 in the expansion of L ; the next term is $9 \times 3/4$. This is very important, because it means that the Langevin's function is very close to the linear function $L(x) = x$ at the origin. This is one of the reasons for the good fit of Langevin's law at the origin.

Next, let us look at the behavior of Langevin's function at infinity. The calculation is straightforward:

$$\lim_{x \rightarrow \infty} L(x) = \lim_{x \rightarrow \infty} \coth(3x) = \lim_{x \rightarrow \infty} \frac{e^{3x} + e^{-3x}}{e^{3x} - e^{-3x}} = \lim_{x \rightarrow \infty} \frac{e^{3x}}{e^{3x}} = 1.$$

In conclusion, Langevin's function is closely approximated by the linear relation $L(x) = x$ at the origin and has the asymptote $L(x) = 1$ when $x \rightarrow \infty$ (Figure 4.25).

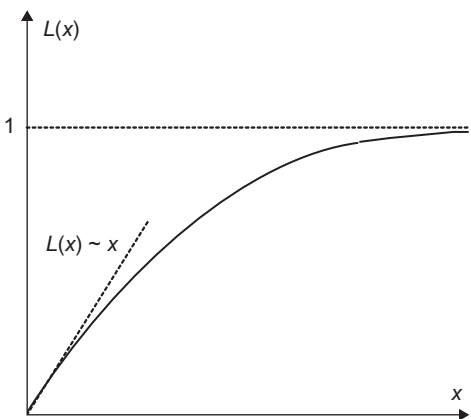
In the case of electrowetting, Lippmann–Young's law can be written under the form

$$\frac{\cos \theta - \cos \theta_0}{\cos \theta_S - \cos \theta_0} = \frac{CV^2}{2\gamma(\cos \theta_S - \cos \theta_0)}. \quad (4.63)$$

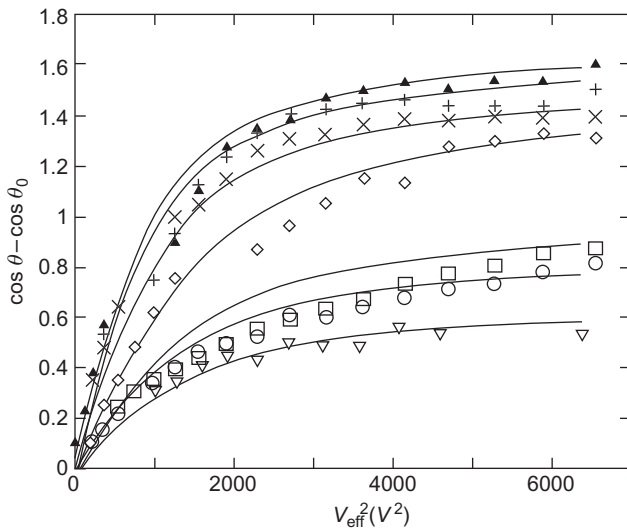
Hence, the law that takes into account the saturation can be written

$$\frac{\cos \theta - \cos \theta_0}{\cos \theta_S - \cos \theta_0} = L\left(\frac{CV^2}{2\gamma(\cos \theta_S - \cos \theta_0)}\right), \quad (4.64)$$

where L is the Langevin function $L(X) = \coth(3X) - 1/3X$ and θ_s the saturation angle. Equation (4.64) satisfies Eq. (4.63) for small and moderate values of the potential V . At large potentials, it also satisfies the saturation asymptote. Relation (4.64) may be called “modified” or “extended” Lippmann–Young's law. It has been verified that this function fits the experimental results [19]. Figure 4.26 shows the fit between the experimental points and the “modified” Lippmann's law.

**FIGURE 4.25**

Graph of the Langevin's function.

**FIGURE 4.26**

Fit of the experimental results for $\cos \theta - \cos \theta_0$ versus V^2 obtained by Langevin's functions. Note that in this particular case, we have considered the rms value of the voltage, because the electric alimentation was AC.

A plot of the capillary force $\gamma_{\text{LG}}(\cos \theta - \cos \theta_0)$ versus the electric potential squared is shown in Figure 4.27. At low voltage, all the theoretical curves and experimental points collapse on the line $CV^2/2$ showing the validity of the approach.

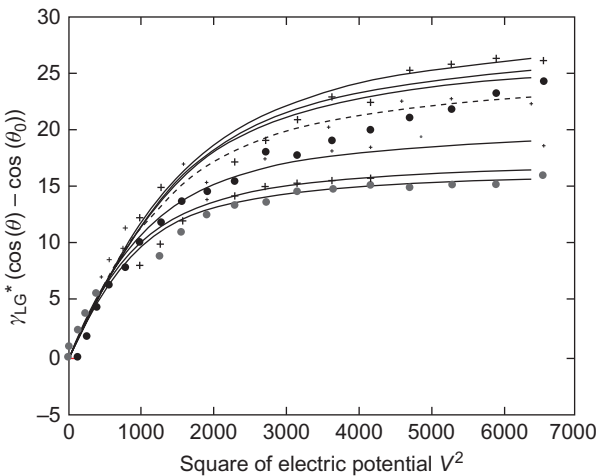


FIGURE 4.27

At low voltages, all curves collapse on the same straight line defined by its slope $C/2$. At high voltages, the curves separate to merge with their asymptote $\gamma_{LG}(\cos \theta_{sat} - \cos \theta_0)$. Continuous lines correspond to the modified Lippmann–Young’s law and dots to experimental observations.

Figure 4.27 shows that the different liquids—placed on the same EWOD microsystem—respond very differently to an electrowetting actuation. Indeed, Eq. (4.43) states that the electrowetting force is

$$f_{EWOD} = \frac{C}{2} V^2 \gamma_{LG} (\cos \theta - \cos \theta_0). \quad (4.65)$$

At saturation,

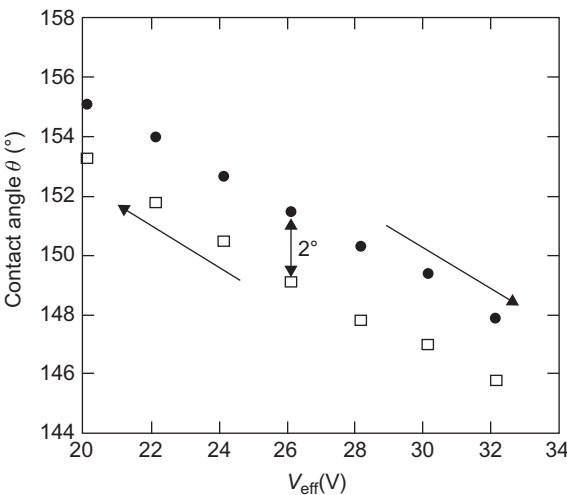
$$f_{EWOD,max} = \frac{C}{2} V_{sat}^2 = \gamma_{LG} (\cos \theta_{sat} - \cos \theta_0). \quad (4.66)$$

According to Figure 4.27, it is the saturation phenomenon that separates the different liquids regarding the electrowetting force, and there is a very important difference in the maximum electrowetting force between the different liquids. However, it seems that this observation has not yet been taken into account to give a supplementary insight into the saturation phenomenon.

4.5 Hysteresis

4.5.1 Introduction

Capillary hysteresis has been presented in Chapters 2 and 3. Hysteresis is defined as the deviation of the contact angle from its theoretical (and mean) value due to

**FIGURE 4.28**

Experimental evidence of electrowetting hysteresis. Case of a sessile droplet of DIW immersed in silicone oil (Brookfield) and contacting a SiOC substrate. The arrows show the advancing and receding phases.

Source: Courtesy Dr. O. Raccourt.

physical phenomena like microscopic surface defects and roughness. During dynamic motion of an interface, dynamic hysteresis refers to the advancing and receding contact angles.

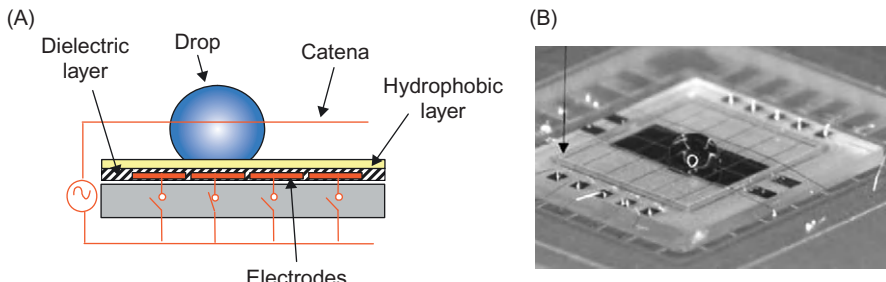
Hysteresis is also observed in electrowetting. When we established Lippmann–Young’s law in [Section 4.2](#), the value of the macroscopic contact angle was in reality the average between an advancing and a receding value. If we start with a nonactuated droplet and we increase the value of the voltage, the droplet spreads. The contact angle is then an advancing contact angle. Conversely, when the voltage decreases, the droplet regains its initial shape and the observed contact angles are the receding contact angles. The advancing and receding contact angles differ ([Figure 4.28](#)).

Another manifestation of electrowetting hysteresis occurs in EWOD microsystems, during the motion of a droplet on a line paved with electrodes (we present droplet motion in detail in the next chapter). Below a minimum actuation voltage V_{\min} , the droplet does not move. In the following section, we produce the relation between hysteresis and minimum actuation voltage.

4.5.2 Hysteresis and minimum actuation potential

4.5.2.1 Introduction

Let us consider the example of EWOD microsystems schematized in [Figure 4.29](#). It is observed that a droplet of conductive liquid does not move from one

**FIGURE 4.29**

(A) Principle of an open EWOD design. In the picture, the catena (zero potential) is placed above the substrate, but it can be also embedded into the substrate. (B) Prototype of open EWOD microsystem.

Source: From Ref. [28].

electrode to the next as soon as an electric actuation is applied. A minimum voltage threshold is required in order to obtain the motion of the drop [24]. This minimum electric potential—noted V_{\min} —depends on the nature of the liquid/fluid/solid triplet.

In this section, we relate the value of the minimum potential to the hysteresis contact angle. We show that the force balance on the droplet produces an implicit relation linking the minimum potential V_{\min} to the value of the hysteresis contact angle α .

Experiments have been conducted using different substrates (Teflon and SiOC) and different conductive liquids and surrounding gas/fluids (DIW in oil or air, biological buffers with surfactants in oil or air, ionic liquids in air). It will be shown that the results of the models are in meaningful agreement with the experimental results.

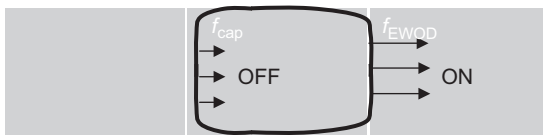
4.5.2.2 Capillary and electrowetting forces

Our starting point is Lippmann–Young’s law

$$\cos \theta - \cos \theta_0 = \frac{C}{2\gamma} V^2. \quad (4.67)$$

At the onset of the motion, there is no dynamic effect; hence, we will interpret Lippmann–Young’s law as a pseudocapillary effect, according to Section 4.3. A droplet starts to move under an “*apparent wettability gradient*” between an actuated and a nonactuated electrode. We remind here that the electrowetting line force density on a triple line is given by

$$f_{\text{EWOD}} = \frac{C}{2} V^2 = \gamma(\cos \theta - \cos \theta_0). \quad (4.68)$$

**FIGURE 4.30**

Sketch of a droplet starting to move toward the actuated electrode.

This line force acts on that part of the triple line located above the actuated electrode (Figure 4.30). On the part of the triple line located on the initial nonactuated electrode, the forces are just the capillary line forces. Usually, the substrate is hydrophobic, so the forces are exerted in the same direction as the electrowetting forces.

We recall that the capillary line force acts on the triple line in the plane of the substrate, perpendicularly to the triple line. In the case of a hydrophilic contact, $\cos \theta > 0$ and the line force points away from the liquid, whereas, in the case of hydrophobic contact, the line force is negative and points inside the droplet. The EWOD line force, as stated by Kang [10] (Section 4.2.3), acts on the triple line—at least extremely close to the triple line—and has a component located in the plane of the substrate, perpendicular to the triple line, and a vertical component.

If the surface were perfect, and using the pseudocapillary equivalence for the electrowetting force, the drop would immediately move as soon as the neighboring electrode is actuated [29,30]. However, experiments have shown that there is an electric potential threshold below which the droplet does not move, i.e., there is a pseudogradient of wettability below which the droplet does not move.

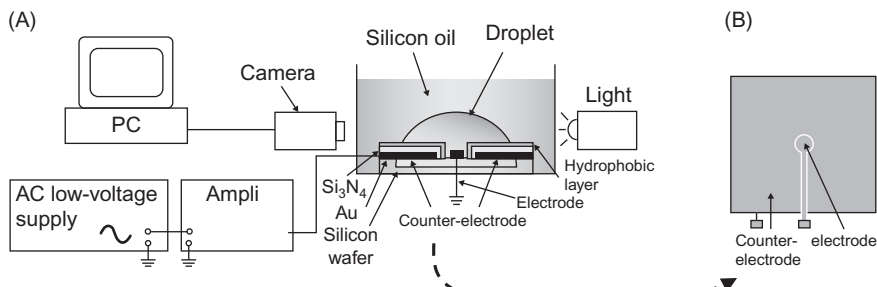
4.5.2.3 Minimum potential of actuation

4.5.2.3.1 Measure of hysteresis contact angle

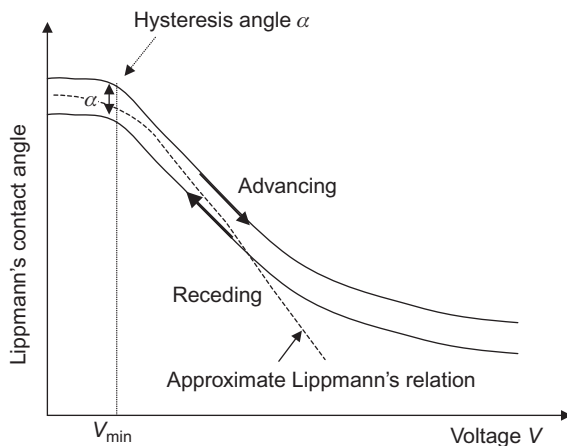
As we have seen in Chapter 3, a special experimental device is used to measure contact angle hysteresis [31]. Liquid is pumped in and out of the drop by a motorized syringe. The contact angle during each of the phases is observed by photographing the droplet from its side. The contact angle hysteresis is the difference of contact angle between the advancing and receding motion.

The particular case of electrowetting is still more difficult to comprehend. We have set up an experimental device similar to that of Tavana and Neumann [31]; however, in the case of electrowetting, liquid is not pumped in or out of the drop, but the contact line spreads or shrinks following an increase or a decrease of the actuation voltage. Figure 4.31 shows the experimental setup. The substrate is similar to a usual EWOD substrate, with electrodes, Si_3N_4 dielectric layer, and hydrophobic coating of SiOC or Teflon. The second counter-electrode is located in the middle of the chip.

Experiments have been performed using different liquids, substrates, and surrounding fluids. Figure 4.28 shows the experimental results for a microdrop of

**FIGURE 4.31**

Schematic view of the experimental set up. (A) View of the experimental setup with electronics and monitoring and (B) view of the electrowetting pad from top.

**FIGURE 4.32**

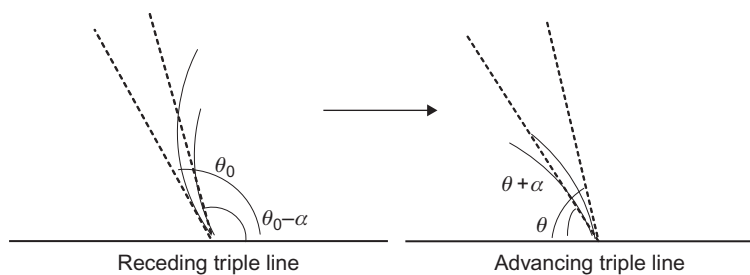
Sketch of the hysteresis curves. Actuated contact angles are not identical if the voltages are increasing or decreasing. Advancing and receding curves are approximately shifted by the hysteresis angle α .

DIW immersed in silicone oil and placed on a SiOC substrate. The contact angle is not the same when the droplet is spreading on the substrate (advancing) or receding from the substrate. After having performed different plots using different substrates and liquids, we have noticed that the plot of Figure 4.28 is typical. The vertical shift between the two curves defines the electrowetting hysteresis angle. A schematized view of the phenomenon is shown in Figure 4.32.

The notion of contact angle hysteresis is very approximate. In Figure 4.32, we have simplified somewhat the situation: in reality the shift between the two curves is not strictly constant. It shows some variations, not only when the electric

Table 4.1 Experimental Observations of the Hysteresis Angle

Liquids	Surrounding Fluid	Substrate	Hysteresis Angle
DIW	Air	Teflon	7–9°
Biologic buffer 0.01% Tween	Air	Teflon	4–5°
Ionic liquids [tmba][NTf ₂]	Air	Teflon	3–4°
Ionic liquids [C ₁₀ H ₂₃ NO ₃] [NTf ₂]	air	Teflon	3–4°
Ionic liquids [bmim][PF ₄]	Air	Teflon	6–7°
Ionic liquids [bmim][PF ₆]	Air	Teflon	7–8°
DIW	Silicone oil	SiOC	1.5–2°
Biologic buffer 0.01% Tween	Silicone oil	SiOC	1–1.5°
Biologic buffer 0.1% Tween	Silicone oil	SiOC	0.5–1°

**FIGURE 4.33**

Sketch of the advancing and receding contact angles with and without the hysteresis angle.

potential changes, but also with the experimental conditions, and between two similar chips. Observed values of the hysteresis contact angle are given in [Table 4.1](#).

4.5.2.3.2 Model

The analysis of the preceding section suggests that the contact angle may vary between its advancing and receding values ([Figure 4.33](#)). We assume here that the two contact angles are the actuated and nonactuated Young's contact angles plus or minus the hysteresis angle.

The static advancing and static receding limit contact angles are then $\theta + \alpha$ and $\theta_0 - \alpha$, where θ is the actuated contact angle and θ_0 the nonactuated contact angle. This notation stems from the Hoffman–Tanner's law [\[32\]](#) indicating that the advancing and receding contact angles are respectively larger and smaller

than their Young's values. The minimum actuation potential is then the potential required for obtaining a net positive electrocapillary force, i.e.,

$$\theta(V_{\min}) + \alpha \leq \theta_0 - \alpha. \quad (4.69)$$

This relation is illustrated in Figure 4.34.

Using Eq. (4.68), we calculate the forces on a droplet placed on a row of electrodes. We demonstrate first that the real shape of the droplet on the electrodes has no importance. Figure 4.35 shows different forms of contact lines. Suppose any form—even nonphysical—of the contact line of the droplet as shown in Figure 4.36.

The electrocapillary force in the direction x (unit vector i) on the hydrophilic electrode is given by

$$F_x = \int_L \gamma \cos \theta \, dl \, \vec{n} \cdot \vec{i}, \quad (4.70)$$

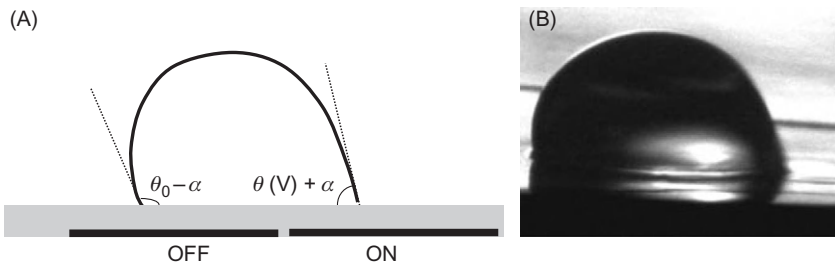


FIGURE 4.34

(A) Sketch of the droplet at onset of actuation. If $V > V_{\min}$, $\theta(V) + \alpha < \theta_0 - \alpha$ and the drop moves to the right under the action of capillary and electrocapillary forces. (B) Photograph of a droplet starting its motion.

Source: Courtesy Dr. R. Bavière.

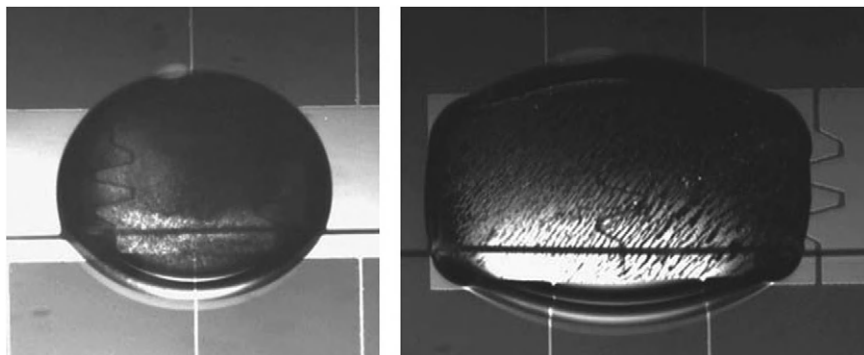
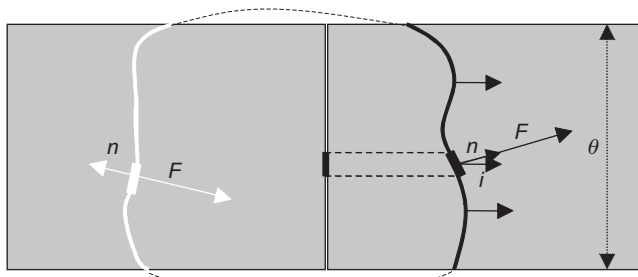


FIGURE 4.35

Different shapes of droplets on EWOD electrodes.

**FIGURE 4.36**

Sketch of the contact of a drop with the substrate.

where dl is a unit element of the contour line and n is the normal unit. [Equation \(4.70\)](#) can be integrated:

$$F_x = \gamma \cos \theta \int_L dl \vec{n} \cdot \vec{i} = e\gamma \cos \theta. \quad (4.71)$$

[Equation \(4.71\)](#) shows that the shape of the triple line above an electrode has no effect on the capillary force. If we observe that the x -direction force on the triple line outside the electrodes vanishes, we conclude that the x -direction capillary force on the droplet, whatever its shape, is

$$F_x = e\gamma(\cos \theta - \cos \theta_0). \quad (4.72)$$

This force remains constant during the motion of the droplet between two electrodes. Now, if we take into account the contact angle hysteresis, we obtain the advancing and receding capillary forces

$$\begin{aligned} F_{a,x} &= e\gamma \cos(\theta + \alpha) \\ F_{r,x} &= -e\gamma \cos(\theta_0 - \alpha). \end{aligned} \quad (4.73)$$

It is assumed that the contact angle hysteresis is small compared to the actuated and nonactuated contact angles. Because α is small compared to the Young's values of the contact angles, [Eq. \(4.73\)](#) can be rearranged

$$\begin{aligned} F_{a,x} &= e\gamma[\cos \theta - \alpha(\cos \theta + \sin \theta_a)] \\ F_{r,x} &= -e\gamma[\cos \theta_0 - \alpha(\cos \theta_0 - \sin \theta_0)]. \end{aligned} \quad (4.74)$$

The total capillary force is then

$$F_x = e\gamma[\cos \theta - \cos \theta_0] - e\gamma\alpha[\cos \theta + \sin \theta - \cos \theta_0 + \sin \theta_0]. \quad (4.75)$$

The first term on the right-hand side of [Eq. \(4.75\)](#) is the usual “Lippmann’s” force—[Eq. \(4.67\)](#). The second term is a resistance force depending on the value of the hysteresis contact angle. It can be shown that this second term is always negative, because $\cos \theta - \cos \theta_0 > 0$. A consequence is that hysteresis reduces the capillary force, in accord with the analysis of the first section.

Because the minimum potential corresponds to the linear part of the Lippmann–Young’s relation, the “Lippmann’s” force can be expressed using Eq. (4.67):

$$F_{\text{EWOD}} = \frac{eC}{2} V^2. \quad (4.76)$$

A criterion for drop displacement is then

$$\frac{eC}{2} V^2 - e\gamma\alpha[\cos\theta + \sin\theta - \cos\theta_0 + \sin\theta_0] > 0. \quad (4.77)$$

Without hysteresis ($\alpha = 0$), the drop would move even with an infinitely small electric actuation. Taking into account the hysteresis ($\alpha \neq 0$), condition (4.77) shows that the minimum electric potential is given by

$$V_{\min}^2 = \frac{2\gamma}{C} \alpha [\cos\theta(V_{\min}) + \sin\theta(V_{\min}) - \cos\theta_0 + \sin\theta_0]. \quad (4.78)$$

Using Lippmann–Young’s law, Eq. (4.78) can be cast under the form

$$\frac{2}{C\gamma} V_{\min}^2 = \frac{\alpha}{1-\alpha} [\sin\theta(V_{\min}) + \sin\theta_0]. \quad (4.79)$$

Equation (4.79) is somewhat cumbersome, because it is an implicit equation due to the fact that θ depends on V . Equation (4.79) can be solved numerically, taking into account that the term $\sin\theta(V_{\min})$ is obtained via the Lippmann–Young’s equation (4.68). In the case where V_{\min} and α are sufficiently small, Eq. (4.79) can be simplified

$$V_{\min} \approx 2\sqrt{\frac{\gamma\alpha \sin\theta_0}{C}}. \quad (4.80)$$

A large capacitance, a low liquid surface tension, a large (very hydrophobic) Young’s angle, and a small value of the hysteresis angle minimize the value of the voltage required to move droplets.

4.5.2.4 Experiments—comparison with the numerical results

Experiments have been performed on open EWOD systems using two types of substrates: a $1.2 \mu\text{m}$ hydrophobic layer of SiOC on top of a 400 nm dielectric layer of Si_3N_4 and a 400 nm Teflon layer on top of the same Si_3N_4 layer.

The values of V_{\min} have been obtained by increasing the potential by 0.5 V until the droplet starts to move. Measurements have been repeated on many electrodes of the same chip with back and forth motions. DIW, biologic buffers in air or silicone oil, and ionic liquids in air have been successively tested. However carefully one operates, there remains a discrepancy of about $2.5\text{--}5 \text{ V}$. Note that there is necessarily a small bias in the approach because the observed values of V_{\min} have been obtained on a different microsystem than that for the hysteresis angle, although the fabrication process is the same.

Table 4.2 Values of Thickness and Relative Permittivity for the Different Usual Materials

Material	Thickness	Relative Permittivity
SiOC	1.2 μm	3.36
Teflon	400 nm	1.9
Si ₃ N ₄	400 nm	7.8
Teflon	1000 nm	2.2
Water (electric double layer)	<30 nm	80

The capacitance C is defined by the relation

$$C = \frac{\varepsilon_0}{\sum_i d_i / \varepsilon_i},$$

where d_i is the thickness of the underlying layers (the layer of water may be neglected) and ε_i their relative electric permittivity. Using the values of Table 4.2, the capacitances of both systems have been calculated ($C_{\text{SiOC}} = 0.026 \text{ mF/m}^2$ and $C_{\text{Teflon}} = 0.045 \text{ mF/m}^2$).

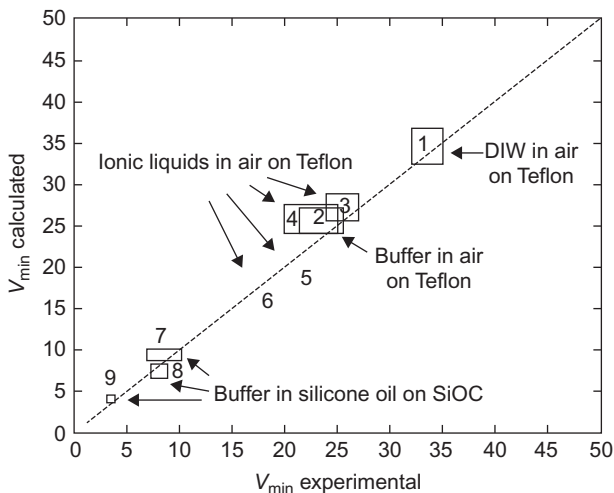
In Figure 4.37, we compare measured minimum actuation potentials with calculated ones. Calculated values have been obtained by solving Eq. (4.79) with the hysteresis values of Table 4.1. Because there are two limit values for the hysteresis angle α and an experimental range for V_{\min} , the corresponding values on the figures are contained in a rectangular box. Calculated values of the minimum potential agree rather well with the experimentally measured potentials.

It can be observed that high surface tension droplets like DIW surrounded by air require an important V_{\min} , of the order of 30–40 V, whereas lower surface tension liquids like ionic liquids require lower values of V_{\min} (15–25 V). Water and biologic buffers immersed in silicone oil have at the same time a low surface tension and a small hysteresis due to the oil film beneath the droplet, thus the corresponding minimum potential is quite small, of the order of 5 V. The results correspond to former observations described in the literature. The reduction of hysteresis due to a liquid film at the solid surface has already been reported [32,34]. The surface of the film is smooth and homogeneous, and the situation is close to that observed by Zisman [27] who found no hysteresis for polymer coated surfaces.

4.6 Working range of EWOD devices

4.6.1 Maximum potential

Equation (4.79) or (4.80) gives an expression of the minimum actuation that is required to move droplets [33]. However, there exists also a maximum actuation

**FIGURE 4.37**

Comparison between calculated and measured values of the minimum potential: biological buffers immersed in silicone oil have the smallest V_{\min} . 1: DIW; 2: biologic buffer $\text{NH}_4\text{HCO}_3 + 0.05\%$ Tween; 3: $[\text{bmim}][\text{PF}_6]$; 4: $[\text{bmim}][\text{BF}_4]$; 5: $[\text{C}_{10}\text{H}_{23}\text{NO}_3][\text{NTf}_2]$; 6: $[\text{tmba}][\text{NTf}_2]$; 7: DIW; 8: biologic buffer $\text{NH}_4\text{HCO}_3 + 0.05\%$ Tween; 9: biologic buffer $\text{NH}_4\text{HCO}_3 + 0.1\%$ Tween. For 1–6, the surrounding fluid is air and the substrate is Teflon. For 7–9, the surrounding fluid is silicone oil and the substrate is SiOC. The values of γ_C are 47 mN/m for Teflon/air and 20 mN/m for SiOC/silicone.

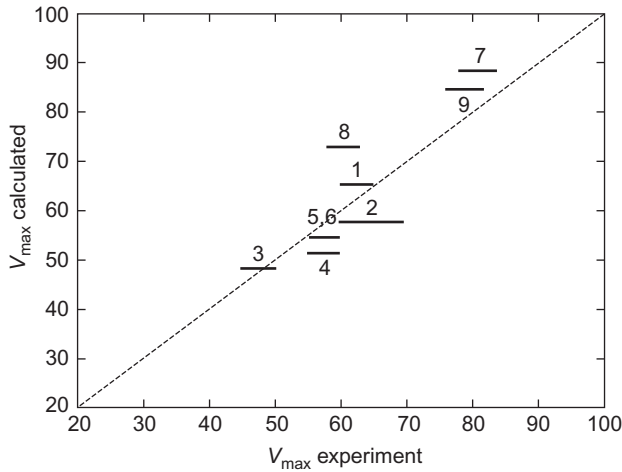
Source: From Ref. [33] © 2007, Elsevier, reprinted with permission.

voltage—noted V_{\max} —above which the electrocapillary force on a drop does not increase further due to saturation phenomenon (see Section 4.4). For the moment, we do not take into account dielectric breakdown voltage—which is closely related to saturation, according to Papathanasiou and Boudouvis; this point will be treated later in Section 4.8. Hence $V_{\max} = V_{\text{sat}}$. Thus, for a given type of EWOD microdevice [35–37] characterized by its capacitance C and its surface properties, and for a given electrically conductive liquid immersed in a surrounding nonconductive gas or fluid, the electrowetting principle will only be effective between the two limits V_{\min} and V_{\max} .

As we have seen in Section 4.4, different models are proposed for the saturation phenomenon. It is very convenient here to use the PQRS model to express V_{\max} as indicated in Eq. (4.58)

$$V_{\max} = \left(\frac{2\gamma_{SL,0}}{C} \right)^{1/2} = \left(\frac{2(\gamma_{SG} - \gamma_{LG} \cos \theta_0)}{C} \right)^{1/2}. \quad (4.81)$$

The advantage of this model is to produce an analytical relation for V_{\max} which, combined with the V_{\min} model, indicates the maneuverability interval for

**FIGURE 4.38**

Comparison for V_{\max} between experimental results (dashed line) and model. The numbers refer to the same data as in the preceding figure.

Source: From Ref. [33] © 2007, Elsevier, reprinted with permission.

any droplet in open EWOD systems. The maximum actuation potential depends on the microfabrication of the chip through the capacitance C and the surface tension of the substrate γ_c , and on the interfacial properties between the liquid and the surrounding fluid, through the term $\gamma \cos \theta_0$.

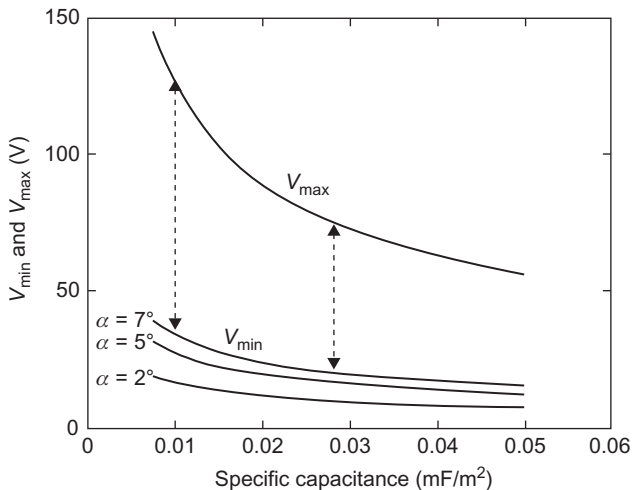
Using the same data as above, we have compared the calculated and experimental values of V_{\max} in Figure 4.38.

4.6.2 Working range

It is interesting to bring together Eqs (4.79) and (4.81) defining the values of V_{\min} and V_{\max} . The minimum potential corresponds to the potential required to overcome the contact angle hysteresis and displace drops by EWOD; the maximum potential is linked to the saturation limit. The domain for EWOD workability is then given by the following relation:

$$\frac{\alpha}{1-\alpha} \gamma [\sin \theta(V_{\min}) + \sin \theta_0] < \frac{CV^2}{2} < \gamma_c - \gamma \cos \theta_0. \quad (4.82)$$

At this stage, we note that the interval $[V_{\min}, V_{\max}]$ depends on the capacitance C as shown in Figure 4.39. Microdevices with thinner layers of dielectric have a larger capacitance and require lower level of actuation. There is a clear advantage in trying to increase the specific conductance of the dielectric layer: the actuation requires lower potentials as well for V_{\min} than for V_{\max} .

**FIGURE 4.39**

Interval $V_{\min} - V_{\max}$ as a function of the capacitance C .

Equation (4.82) can be equivalently written as

$$\begin{aligned} f_{\min} &= \frac{\alpha}{1-\alpha} \gamma [\sin \theta(V_{\min}) + \sin \theta_0] < f_{\text{EWOD}} < \gamma_C - \gamma \cos \theta_0 \\ &= f_{\max} \end{aligned} \quad (4.83)$$

showing the range of electrowetting force. The optimal solution would be the lowest possible f_{\min} and a largest possible f_{\max} . First, let us analyze the conditions for obtaining the smallest possible f_{\min} . The hysteresis angle α is usually small, and the left side of Eq. (4.83) can be approximated by $2\alpha\gamma \sin \theta_0$. For aqueous liquids, a very hydrophobic contact angle θ_0 is optimal for having a very low minimum force for droplet motion, because $\sin \theta_0 \sim (\pi - \theta_0) \sim 0$. On the other hand, the maximum electrowetting force is $f_{\max} = \gamma_{SLO}$. The hydrophobic substrate that maximizes γ_{SLO} is the most suitable. If we choose the most hydrophobic situation possible in order to satisfy the f_{\min} constraint, we have approximately $\cos \theta_0 \sim -1$, and the maximum force is $f_{\max} \sim \gamma_C + \gamma = \gamma_{SLO}$.

From an experimental standpoint, water droplets in silicone oil show a large working interval: on the one hand, they present a small minimum force to move droplets because the value of θ_0 is large and the contact angle hysteresis α is small, due to an oil liquid film between the droplet and the substrate. On the other hand, the value of γ_{SL} is increased due to the presence of the oil film separating the hydrophobic substrate and the liquid. The result can be generalized; aqueous liquids surrounded with silicone oil instead of air perform better in EWOD microsystems.

Using a typical value for the specific capacitance $C \sim 0.03 \text{ mF/m}^2$, relation (4.83) shows that the minimum electrocapillary forces lie in the range $1\text{--}20 \mu\text{N}$ and the maximum forces in the range $15\text{--}40 \mu\text{N}$.

4.6.3 Conclusion

We have presented a model for the minimum actuation potential in EWOD microsystems that incorporates contact angle hysteresis and produces the value of the threshold electric potential to displace drops. On the other hand, the maximum potential is approximately given by the zero interfacial tension criterion of the Peykov–Quinn–Ralston–Sedev model. These two values define the workability range of an EWOD-based microsystem for any combination of droplet liquid, surrounding fluid, and solid substrate.

Consequently, and in accordance with the experimental observations, it is shown why some triplets liquid/substrate/surrounding fluid are better adapted to EWOD technique than others. In the following chapters, we give examples of different liquids that can be displaced by EWOD (aqueous liquids, ionic liquids, blood, milk, etc.). As there is a growing interest in downsizing EWOD devices, particular attention should be given to reducing the minimum actuation potential. The model shows that the largest possible nonactuated (hydrophobic for aqueous liquids) contact angle is recommended for minimizing the working voltage. To this extent, superhydrophobic substrates are currently investigated [38–42]; we shall present these substrates later in Section 4.7.4.

So far, we have not considered the phenomenon of dielectric breakdown. In this section, the maximum voltage of actuation has been calculated on the base of the saturation effect. We will see in the next section that dielectric breakdown is a major concern in electrowetting and reinforce the importance of the choice of the substrate in EWOD microsystems.

4.7 Materials and substrates

In this section, we investigate the characteristics of the solid substrates regarding their specific capacitance and their dielectric breakdown limit. It will be seen that dielectric breakdown is a considerable limit to the electrowetting force in EWOD microsystems. We then examine some new concepts aimed at increasing the hydrophobic character of the substrate in order to reduce the actuation voltages.

4.7.1 Capacitance

The specific capacitance of a substrate can be deduced by two different approaches. First, we use the Lippmann–Young’s plots; second, we perform a direct calculation.

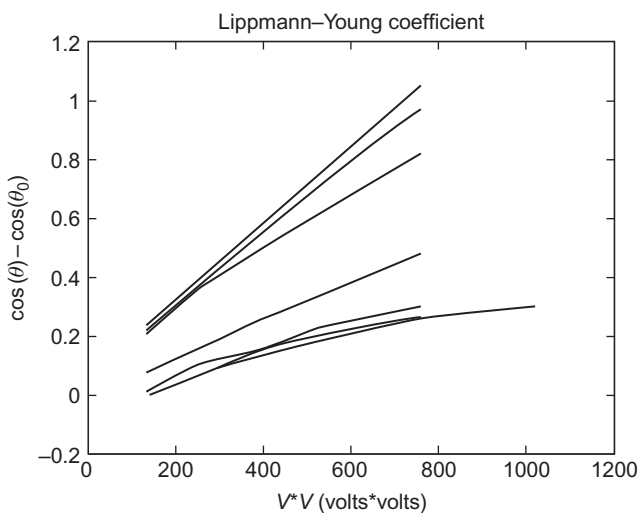


FIGURE 4.40

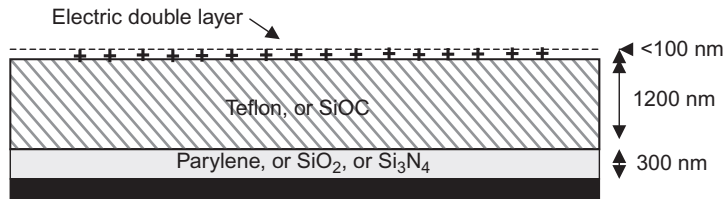
Linear part of the Lippmann–Young's plots for different liquids. The dotted line corresponds to DIW $\gamma_{LG} = 30 \text{ mN/m}$ immersed in silicone oil. The other surface tensions for biologic buffers are then 28.4, 19.9, 13.4, 10.7, and 9.9 mN/m. The surface tension for ionic liquid is 42.6 mN/m. The value of the capacitance is $C = 20 \mu\text{F}/\text{m}^2$.

4.7.1.1 Determination of the specific capacitance via the Lippmann–Young's relation

One important remark here is that the values of the coefficient $C/2\gamma$ are the slope of the linear part of the Lippmann–Young's plots at low voltage. Figure 4.40 shows the linear relations between $\cos(\theta) - \cos(\theta_0)$ and V^2 for different liquids on the same substrate. If we know at least one of the values of the surface tension γ , we can deduce the value of the capacitance C . Conversely, we can then deduce the values of the surface tensions of the other liquids. If we know the values of all the surface tensions, we obtain a set of consistent values for C , and the average value can be considered as the real specific capacitance.

4.7.1.2 Direct determination of the specific capacitance

In a vertical cross-section, the substrate comprises successively an electrode, a layer of dielectric, and a hydrophobic layer (Figure 4.41). In the horizontal plane, the electrodes are separated by an electrically insulating spacer. The dielectric layer guarantees the electric insulation; materials commonly used for dielectric are parylene, SiO_2 , Teflon, and Si_3N_4 . The hydrophobic layer contributes to increase the amplitude of the change of contact angle between nonactuated and actuated states. Hydrophobic layers are often made of Teflon and spread by spin coating; sometimes they are made of SiOC spread by plasma deposition.

**FIGURE 4.41**

Total capacitance includes the contribution of the dielectric layer (parylene, SiO₂, or Si₃N₄), the hydrophobic layer (Teflon, SiOC, etc.); the contribution of the electric double layer can be neglected.

From a general standpoint, the effective capacitance of n parallel layers is given by

$$\frac{1}{C} = \sum_{i=1,n} \frac{1}{C_i}. \quad (4.84)$$

If ε_i and d_i respectively denote the dielectric constant and thickness of the layer i , the capacitance of layer i is given by

$$C_i = \frac{\varepsilon_0 \varepsilon_i}{d_i}, \quad (4.85)$$

where ε_0 is the permittivity of vacuum, equal to 8.854×10^{-12} F/m (C²/Jm). Substitution of Eq. (4.85) into Eq. (4.84) yields

$$C = \frac{\varepsilon_0}{\sum_{i=1,n} d_i / \varepsilon_i}. \quad (4.86)$$

In Table 4.2, we have indicated approximate values of the dielectric constants for different materials frequently used in the composition of the substrate. The values of Table 4.2 indicate that the contribution of the electric double layer to the total capacitance is negligible. It is less than 3/1000. Hence, the double layer can be taken out of Eq. (4.86) and we obtain

$$\frac{1}{C} = \frac{1}{C_{\text{dielectric}}} + \frac{1}{C_{\text{hydrophobic}}}. \quad (4.87)$$

An order of magnitude of the capacitance of current EWOD microsystems is $C \sim 2.2 \times 10^{-5}$ F/m². According to Eq. (4.87), the capacitance is increased by reducing the thicknesses of the layers of the substrate. However, there is a limit to this reduction given by the dielectric breakdown limit. In the following section, we develop the notion of breakdown of a dielectric.

4.7.2 Dielectric breakdown

Breakdown of dielectric occurs when the electric field in the dielectric exceeds a limit value called the critical electric field, denoted here E_{BD} . Above this value,

Table 4.3 Values of the Breakdown Voltage for Some Usual Materials

Material	Paraffin	Oil	Teflon	Glass	Mica
Critical electric field E_{BD} (MV/m or V/ μ m)	10	15	59	100	197

Note that the values indicated here are given for perfect materials. Real values are usually less than that.

the material is disrupted. This threshold is also called the theoretical dielectric strength of a material. It is an intrinsic property of the bulk material. At breakdown, the electric field frees bound electrons. If the applied electric field is sufficiently high, free electrons may become accelerated to velocities that can liberate additional electrons during collisions with neutral atoms or molecules in a process called avalanche breakdown. Breakdown occurs quite abruptly (typically in nanoseconds), resulting in the formation of an electrically conductive path and a disruptive discharge through the material. For solid materials, a breakdown event severely degrades, or even destroys, its insulating capability. The detailed physical explanation of dielectric breakdown is not the subject of this book and is well documented in the literature [43]. For a dielectric of thickness d , the critical electric field E_{BD} is related to the dielectric breakdown voltage V_{BD} by

$$V_{BD} = dE_{BD}. \quad (4.88)$$

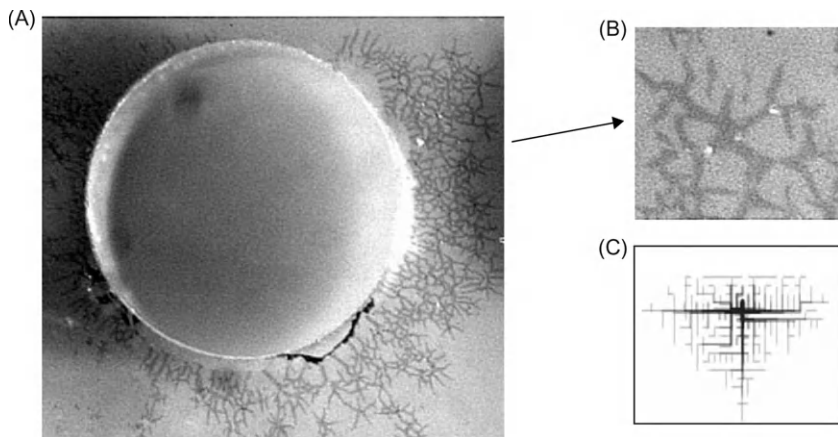
Indications of the value of the critical electric field are given in [Table 4.3](#) for some of the usual materials. In a preceding section, we developed the notion of saturation potential. Typically, saturation potentials are of the order of 80 V for a chip of capacitance $C \sim 2.2 \times 10^{-5}$ F/m², obtained with a total dielectric/insulating layer of Teflon of 1.5 μ m thickness, approximately. Thus the electric field at saturation is of the order of 55 V/ μ m. This value is just below the breakdown value of Teflon. In other words, these commonly used chips have been designed to function unto the saturation potential.

However, dielectric breakdown is sometimes observed at lower values of the potential, as shown in [Figure 4.42](#). What could be the reason for this breakdown? This is presently a subject of studies, but it seems that breakdown frequently occurs when there are defaults in the substrate surface or when objects like cells or proteins adhere to the substrate. A possible explanation could be the anomalous value of the electric field at the vicinity of geometrical inhomogeneities.

The contact of an object with the substrate is shown in [Figure 4.42](#).

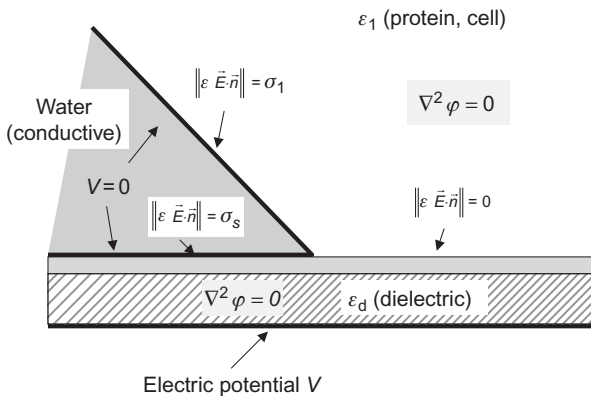
Assuming that the liquid is perfectly conductive and that the object is insulating—which is a coarse assumption in the case of a cell or a protein, and if ϵ_1 and ϵ_d denote the relative permittivity of the object and the solid dielectric, respectively, the electric potential in the domain defined in [Figure 4.43](#) is given by the Laplace's equation [10,15]

$$\epsilon_1 \nabla^2 \phi_1 = \epsilon_d \nabla^2 \phi_d. \quad (4.89)$$

**FIGURE 4.42**

(A) Dielectric breakdown at the vicinity of a spherical object; the breakdown is materialized by the formation of cracks having the shape of tree branches; (B) closeup on the “tree effect”; and (C) electrostatic breakdown model showing the growth of “failure tree” due to electron avalanche.

Source: From Ref. [43] © 2003, IOP, reprinted with permission.

**FIGURE 4.43**

Electric scheme of the contact of an object with the substrate.

From a theoretical point of view, the electric potential can be obtained through the Schwarz–Christoffel conformal mapping, in a similar mathematical approach as that of [Section 4.2.3](#). If the angle of the wedge is “mathematically” sharp, there is a pole of the transform at the tip of the wedge; using Cauchy’s theorem, the value of the potential field is theoretically infinite at the pole. However, sharp angles are not physical, and an electrostatic numerical calculation immediately

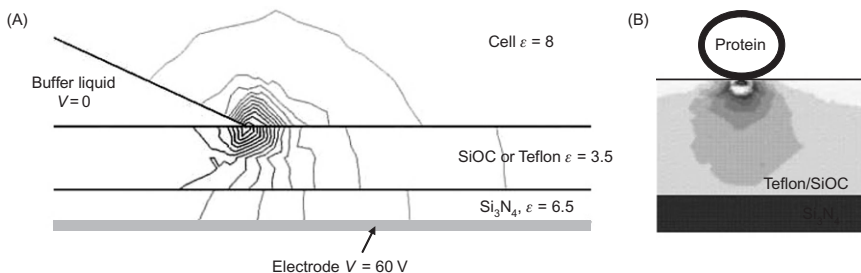


FIGURE 4.44

(A) Contour plot of the magnitude of the electric field in the vicinity of the contact of a cell with the substrate (Comsol software): the magnitude of the electric field shows a peak at the tip of the wedge. (B) Contour plot of the magnitude of the electric field below a protein sticking to the surface (Comsol software).

shows that there is local peak in the magnitude of the electric field at the tip of the wedge formed by the substrate, the conducting liquid, and the object, as shown in [Figure 4.44A](#). In our case, we have supposed the object perfectly insulating, which is an approximation. In reality, the peak will be less than that predicted by the preceding approach; nevertheless there will be an anomalous value of the magnitude of the electric field in the vicinity of the contact line.

This anomalous, localized value of the electric field may increase the voltage above the dielectric breakdown voltage [43]. This could be the explanation why dielectric breakdown is sometimes observed when cells or proteins adhere to the substrate ([Figure 4.44](#)), or when the surface gets crackled after a long period of use. Reinforcement of the level of the dielectric breakdown voltage, without raising the value of the capacitance, by using a more resistant material seems possible, or introducing a buffer layer in the substrate [44]; however, the introduction of a buffer layer in the dielectric is criticized by Kuiper and Hendriks [45]: their advice is that, if the dielectric is covered with a low dielectric constant hydrophobic top-coat, the field amplification in this topcoat may cause topcoat breakdown followed by dielectric breakdown. This question is presently debated and not yet solved.

4.7.3 Materials

In [Section 4.6](#), we have seen that the maximum electrowetting line force that we can obtain in an EWOD system is limited by the saturation effect. However, there is another limit: the dielectric breakdown limit. Once the dielectric has broken down, electric charges leak through the dielectric and the electrowetting effect vanishes.

It is quite easy to see that the condition brought by the DBV (dielectric breakdown voltage) requires that the dielectric thickness be larger than a minimum value. Suppose we want to obtain an electrowetting force corresponding to a

given $\Delta\cos\theta$ (smaller than $\Delta\cos\theta_{\text{sat}}$) for a droplet of water. Let us start from Lippmann–Young’s law written under the form

$$\cos\theta_a - \cos\theta_0 = \frac{1}{2\gamma} \frac{\varepsilon_0\varepsilon_D}{d} V^2$$

then the potential V can be expressed as a function of d :

$$V = \sqrt{\frac{2\gamma d}{\varepsilon_0\varepsilon_D} (\cos\theta_a - \cos\theta_0)}. \quad (4.90)$$

For a given Lippmann’s angle θ_a , the voltage V varies like the square root of the dielectric thickness d ; the corresponding graph has been plotted in Figure 4.45 (continuous line). This relation has been experimentally verified by Saeki et al. [46]. On the other hand, relation (4.88) has also been plotted in Figure 4.45 (dotted line). The two curves intersect at $d = d_{\min}$; the coordinates of the intersection point are [45]

$$d_{\min} = \frac{2\gamma(\cos\theta_a - \cos\theta_0)}{\varepsilon_0\varepsilon_D E_{\text{BD}}^2} \quad (4.91)$$

$$V_{\min} = \frac{2\gamma(\cos\theta_a - \cos\theta_0)}{\varepsilon_0\varepsilon_D E_{\text{BD}}}.$$

The dielectric thickness must then be larger than d_{\min} for the system to function with the specific requirements ($\cos\theta_a - \cos\theta$). Below this lower limit for the dielectric thickness, the voltage required to obtain the contact angle difference ($\cos\theta_a - \cos\theta$) will result in the breakdown of the substrate.

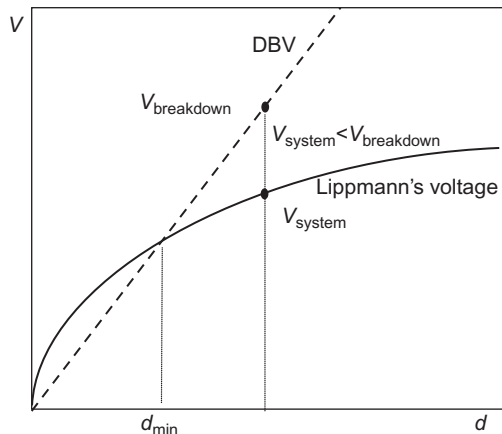


FIGURE 4.45

Minimum dielectric thickness: the working voltage must be smaller than the DBV; for a targeted $\Delta\cos\theta$ the minimum dielectric thickness must be larger than d_{\min} .

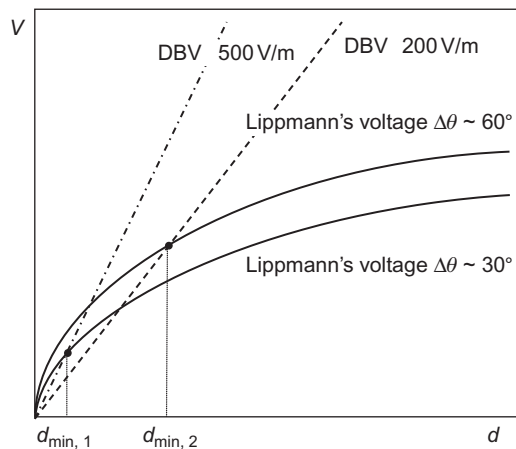


FIGURE 4.46

The minimum substrate thickness depends on the amplitude of the contact angle variation $\Delta \cos \theta$ (limited by $\Delta \cos \theta_{\text{sat}}$) and on the DBV of the substrate.

If we find a better dielectric withstanding a larger critical electric field E_{BD} , the slope of the DBV is then increased and the minimum thickness is reduced (Figure 4.46). The minimum dielectric thickness also depends on the desired amplitude of $\Delta \cos \theta$. If the system can function with a smaller $\Delta \cos \theta$, the dielectric thickness can be further reduced.

We have already noted that the thickness d of the dielectric is usually chosen so that the saturation voltage V_{sat} corresponds to the dielectric breakdown voltage V_{BD} . The explanation is straightforward: using the PQRS saturation model—Eq. (4.58)—we find

$$V_{\text{sat}} = \sqrt{\frac{2\gamma_{\text{SL0}}d}{\varepsilon_0 \varepsilon_D}} = \sqrt{\frac{2d\gamma_{\text{LG}}(\cos \theta_{\text{sat}} - \cos \theta_0)}{\varepsilon_0 \varepsilon_D}}. \quad (4.92)$$

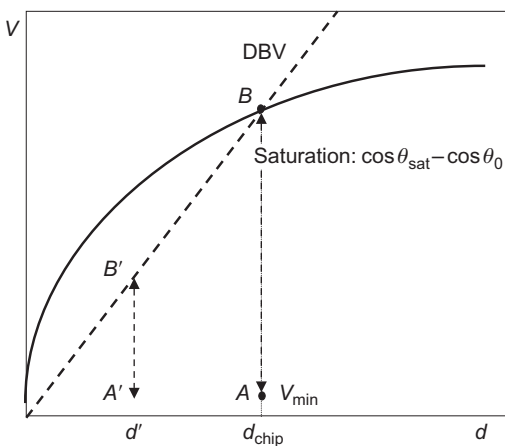
The right term of Eq. (4.92) is a direct consequence of the PQRS saturation model, in which the following relation yields

$$\gamma_{\text{SL0}} = \gamma_{\text{LG}} (\cos \theta_{\text{sat}} - \cos \theta_0).$$

We obtain the plot of Figure 4.47: the whole range of contact angles can be reached, unto the saturation limit. Note that we have not considered here the fringe effect described by Papathanasiou and Boudouvis [15] which results in a lower limit for the breakdown voltage (see Section 4.4.2.4).

4.7.4 Existing substrates and their characteristics

The different characteristics of substrates found in the literature are given in Table 4.4. At the present time, the usual EWOD microsystems use low voltages

**FIGURE 4.47**

The working interval for an EWOD microchip with a substrate thickness d_{chip} is the segment comprised between the points A and B . A corresponds to the voltage V_{\min} . If the thickness of the substrate was $d' < d_{\text{chip}}$, then the whole range ($\cos \theta_{\text{sat}} - \cos \theta$) could not be covered because of early breakdown of the dielectric. The optimal theoretical thickness is then d_{chip} .

(no more than 80 V) in order to reduce their electric power. In order to avoid fragility problems and the consequences of surface defects, and to achieve robustness, dielectric thickness is usually of the order of 1 μm .

Recently, there has been a trend toward using thinner dielectric layers in order to increase the specific capacitance. However, this trend has been limited by the dielectric breakdown. When the dielectric layer is very thin, any microfabrication defect leads to dielectric breakdown; besides a charge trapping mechanism could lead to electric charge leakage; finally the sensitivity to objects adhering to the substrate (proteins, cells in biology) is very high.

4.8 Discussion: special substrates and new concepts

At the end of this chapter, the question is: from the expression of the electrowetting law, what can we expect from EWOD microsystems? In other terms, what would be an optimal EWOD microsystem, keeping in mind that the trend is to scale down such microsystems to be able to handle smaller liquid volumes?

There are two possible answers depending on the specific applications: either we want to perform a list of operations and manipulations with the smallest possible electric supply—this is, for example, the case of portable systems in space or biotechnological applications, or we want to build the most effective system regardless of the cost of electric energy.

Table 4.4 Different Characteristics of Substrate Found in the Literature

Dielectric Material	Dielectric Thickness	Dielectric Relative Permittivity	Topcoat (Hydrophobic)	Topcoat Thickness	Topcoat Relative Permittivity	Maximum Voltage (V)	Maximum $\Delta\theta$	References
Parylene	20 μm	2.65	Teflon AF 1600	20 nm	2.2	250	60°	[36,46,47]
Parylene	10 μm	2.65	Teflon AF 1600	30 nm	2.2	250	60°	[24,46,47]
Teflon AF 1600	5.8 μm	2.2	–	–	–	200	60°	[45,47]
Si_3N_4	300 nm	7.8	Teflon AF 1600	1 μm	2.2	70	45°	[20,28]
Si_3N_4	300 nm	7.8	SiOC	1.2 μm	3.4	80	45°	[20,28]
Parylene	700 nm	2.65	Teflon AF 1600	200 nm	2.2	55	?	[47,48]
SiO_2	100 nm	4.0	Teflon AF 1600	20 nm	2.2	15	40°	[34,47]
BST (barium strontium titanate)	70 nm	?	Teflon	70 nm	2.2	10	35°	[36,47]

4.8.1 Low voltages

We investigate here the conditions for working with low voltages. The approximate value of the minimal voltage has been derived in [Section 4.5](#):

$$V_{\min} \approx 2\sqrt{\frac{\alpha\gamma \sin \theta_0}{C}}. \quad (4.93)$$

Hence, the smallest possible hysteresis contact angle α is a first requirement, a very hydrophobic surface is a second requirement, and a large capacitance is a third requirement, i.e., a very thin dielectric. However, there is a limit to the reduction of the thickness of the dielectric. If we want to be able to operate unto saturation angle, the maximum voltage is given by

$$V_{\max} = \min\{V_{DB}, V_{sat}\}. \quad (4.94)$$

Using the results obtained in this chapter, relation (4.94) can be written as

$$V_{\max} = \min\left\{dE_{DB}\sqrt{\frac{2\gamma_{SL0}}{C}}\right\}. \quad (4.95)$$

The minimum dielectric thickness is then

$$d = \frac{2\gamma_{SL0}}{\varepsilon_0 \varepsilon_D E_{DB}^2}. \quad (4.96)$$

Hence, a material with a large critical electric field E_{DB} is necessary to reduce the dielectric thickness.

4.8.2 Electrowetting forces

We consider now the electrowetting force; we will see in the following chapter that a large electrowetting force is needed to perform operations such as cutting droplets in two, dispensing of droplets from a reservoir, etc. Thus, we may want a system having the lowest possible minimum electrowetting force to displace droplets and the largest possible maximum electrowetting force.

The minimal force is

$$f_{\min} \approx 2\alpha\gamma \sin \theta_0. \quad (4.97)$$

Thus, a substrate with a low hysteresis and a superhydrophobic behavior is optimal. On the other hand, the maximum force is the minimum of two forces: the force corresponding to the DBV and the saturation force

$$f_{\max} = \frac{1}{2}C \min\{V_{DB}^2, V_{sat}^2\}. \quad (4.98)$$

Hence the maximum electric line force is

$$f_{\max} = \min \left\{ \frac{1}{2} \varepsilon_0 \varepsilon_D d E_{DB}^2, \gamma_{SL0} \right\}. \quad (4.99)$$

Again, a material with a large critical electric field is recommended.

4.8.3 Superhydrophobic microfabricated substrates

It has been shown in the preceding chapter that superhydrophobic substrates are advantageous, because for one thing, their hysteresis level is low: droplets can be moved and maneuvered at very low actuation potential. This is a very important point since nominal actuation levels should be far from the breakdown voltage; hence the durability of the chip is increased. Electrowetting on textured, superhydrophobic surfaces is currently the subject of many investigations.

4.8.3.1 Theoretical approach

We first focus on the theoretical approach, following Torkkeli's approach [38]. Suppose a droplet deposited on a superhydrophobic substrate, in a Cassie's regime (see Chapter 3). The fraction of the liquid in contact with the substrate is denoted f and the fraction in contact with the air trapped below is $1 - f$. When the electrode is actuated, an electrowetting force appears. According to the thermodynamic approach, the diagram of the forces exerted on the droplet is shown in Figure 4.48.

In the thermodynamical approach, the electrowetting effect results in a decrease of the apparent solid–liquid surface tension $\gamma_{SL} - \gamma'_{SL}(V)$. In the special case of superhydrophobic contact (Cassie regime), it affects only the wetted fraction f of the surface. We have seen before in this chapter

$$\gamma'_{SL}(V) = \frac{CV^2}{2}.$$

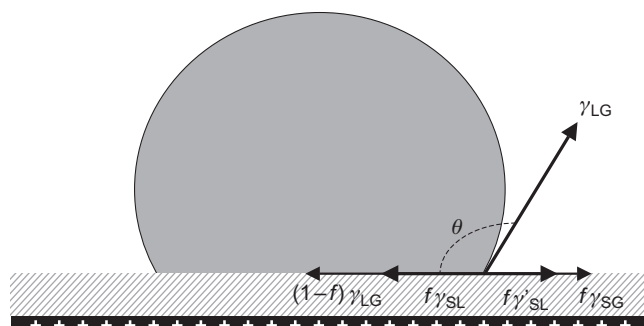


FIGURE 4.48

Schematic of the forces exerted on the droplet.

Let us write the force balance

$$\gamma_{LG} \cos \theta + (1-f)\gamma_{LG} + f\gamma_{SL} = f\gamma'_{SL}(V) + f\gamma_{SG} \quad (4.100)$$

which can be cast under the form

$$\cos \theta = (f - 1) + \frac{f\gamma'_{SL}(V)}{\gamma_{LG}} + f \frac{\gamma_{SG} - \gamma_{SL}}{\gamma_{LG}}.$$

Substitution of the Young's equation yields

$$\cos \theta = (f - 1) + \frac{f\gamma'_{SL}(V)}{\gamma_{LG}} + f \cos \theta_0.$$

And substitution of the Cassie–Baxter's equation yields

$$\cos \theta = \cos \theta_C + f \frac{CV^2}{2\gamma_{LG}}, \quad (4.101)$$

where θ_C is the Cassie's angle. In conclusion, the Lippmann–Young's equation can be transposed to superhydrophobic substrate under the condition to correct the electrowetting force by the contact factor f . This factor f is small for superhydrophobic substrate, so that the electrowetting force is reduced. But, on the other hand, hysteresis has been considerably reduced. The droplet moves more easily on the electrodes of the EWOD microsystem.

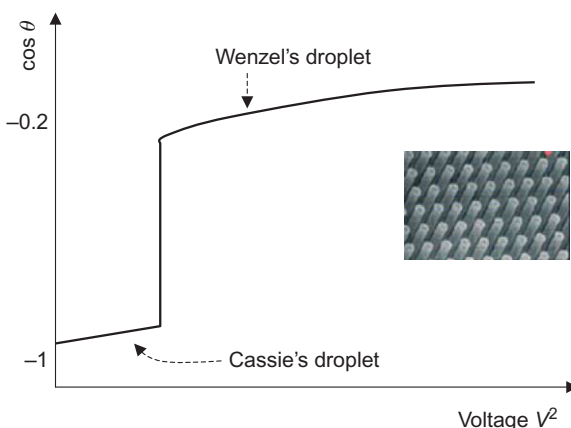
4.8.3.2 Experimental approach

We have seen in Chapter 3 that nanostructured surfaces, if they are correctly designed, have a superhydrophobic behavior. Krupenkin et al. [39] first experimented with such substrates for electrowetting.

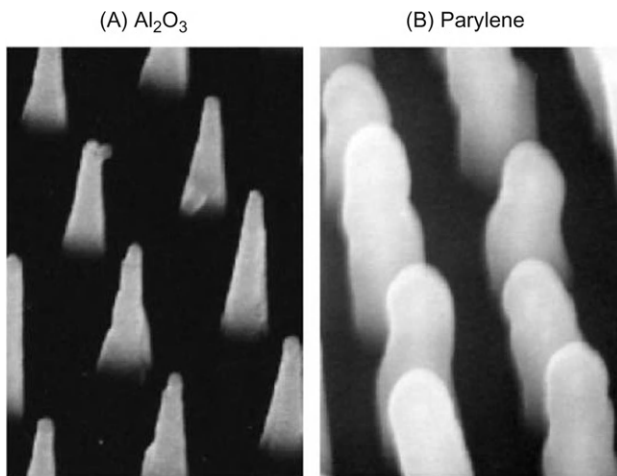
The electrowetting effect is observed on such substrates (Figure 4.49). However, the drawback is that there is no reversibility. In the initial state, or at a very low voltage, the droplet sits on top of the pillars in a Cassie's regime. When the voltage increases above some level, the droplet sinks between the pillars; the droplet is now in a Wenzel's regime. Decreasing the voltage does not bring the droplet back to its initial Cassie's shape.

More recently, Dhindsa et al. [40] have improved Krupenkin's design. They use carbon nanofibers (CNFs) coated with Al_2O_3 or parylene (Figure 4.50) to form the pillars.

A saline droplet surrounded by air has the behavior described by Krupenkin. However, reversibility is achieved if the droplet is immersed in dodecane. Figure 4.51 shows the dodecane or the air film between the droplet and the substrate. In both cases, when the voltage is actuated, the droplet sinks between the pillars. But when the voltage is switched off, the film of dodecane reconstitutes and the droplet regains its initial shape on the top of the pillars. Such a design seems interesting for applications in optics; however, for biotechnology and

**FIGURE 4.49**

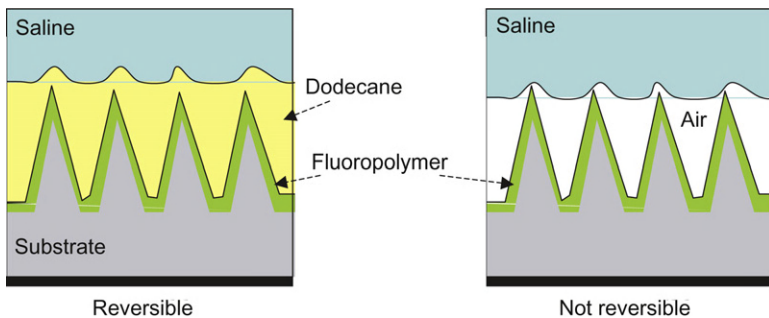
Electrowetting on superhydrophobic nanostructured substrate: the droplet has initially a nearly 180° contact angle and sits on the top of the pillars (Cassie's regime). For some value of the actuation voltage, the droplet sinks between the pillars (Wenzel's regime). The mechanism is not reversible.

**FIGURE 4.50**

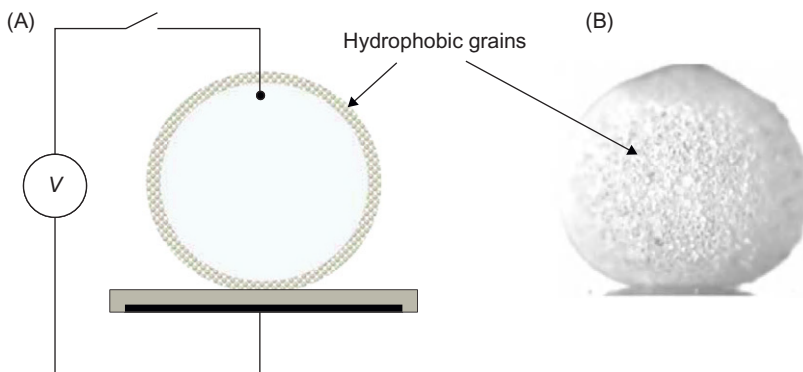
Vertically aligned CNFs covered with a layer of Al_2O_3 (A) and parylene (B).

Source: Reprinted with permission from Ref. [40] © 2006, American Chemical Society.

microchemistry, the drawback might be the contamination of the film by macromolecules initially contained in the saline solution. To avoid contamination, a recent proposal was to encapsulate the droplet [41] instead of nanostructuring the substrate. This is the topic of the next section.

**FIGURE 4.51**

Sketch of the film of dodecane or air below the droplet (at zero voltage).

**FIGURE 4.52**

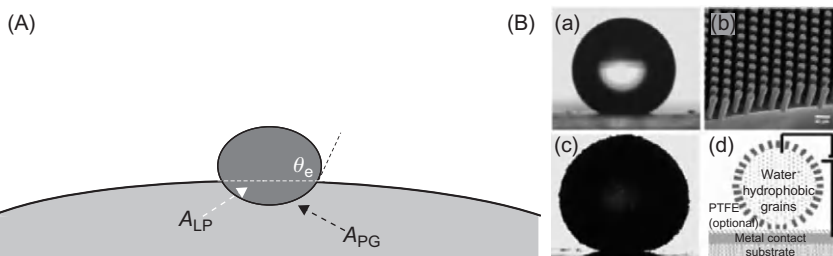
(A) Sketch of the electrowetting device, the aqueous droplet is coated with hydrophobic grains (lycopodium or silica). (B) A photograph of the droplet showing the granular coating of the interface.

Source: Reprinted with permission from Ref. [40] © 2007, American Chemical Society.

4.8.4 Superhydrophobic droplets

We have just seen that Krupenkin et al. [39] and Dhindsa et al. [40] have tested electrowetting on a substrate constituted of microfabricated pillars; however, reversibility is not always achieved by such systems. The originality of the work of McHale et al. [41] is the transposition of the idea of superhydrophobicity to the droplet itself (Figure 4.52). The starting point is that an aqueous droplet can be coated with hydrophobic particles. This can be shown theoretically by considering the surface energy of the droplet. Suppose we have a spherical grain at the surface of the liquid, as shown in Figure 4.53A. The surface area A_{LP} is given by

$$A_{LP} = \pi R_S^2 \sin^2 \theta_e, \quad (4.102)$$

**FIGURE 4.53**

(A) Schematic of the solid sphere on a liquid interface. (B) A droplet coated with hydrophobic particles can have a hydrophobic behavior similar to that of a droplet on nanostructured pillars.

Source: Reprinted with permission from Ref. [41] © 2007, American Chemical Society.

where R_S is the radius of the spherical grain and θ_e its Young's contact angle. On the other hand, the surface A_{PG} is

$$A_{PG} = 2\pi R_S^2(1 + \cos \theta_e). \quad (4.103)$$

From an energy point of view, when a spherical grain attaches to the liquid surface, it replaces the solid–air interface area of the particle A_{PG} by a same area solid–liquid interface, and the liquid–air interface loses a surface area A_{LP} . Hence, the net change in SFE is

$$\Delta E = 2\pi R_S^2(1 + \cos \theta_e)(\gamma_{SL} - \gamma_{SG}) - \pi R_S^2 \sin^2 \theta_e \gamma_{LG}. \quad (4.104)$$

Using Young's law,

$$\cos \theta_e = \frac{\gamma_{SG} - \gamma_{SL}}{\gamma_{LG}}$$

we obtain

$$\Delta E = -2\pi R_S^2 \gamma_{LG}(1 + \cos \theta_e)^2. \quad (4.105)$$

Relation (4.105) shows that ΔE is always negative or zero (zero only if $\theta_e = 180^\circ$). As a result, it is always energetically favorable that grains spontaneously attach to the liquid–vapor interface, even if they are hydrophobic. If R_g denotes the radius of the grain, the length of a grain protruding into air is

$$d_g = R_g(1 - \cos \theta_e). \quad (4.106)$$

Relation (4.106) shows that highly hydrophobic grains protrude substantially, enough to obtain a hydrophobic configuration similar to that of the nanostructure surface described in the preceding section (Figure 4.53B). It is shown that such an aqueous droplet coated with silica beads reacts to an electric actuation in the same manner as a simple water droplet on a superhydrophobic substrate, and that

the motion is reversible. In biotechnology, an advantage of such a system is the reduction of the possible contamination to the substrate.

4.9 Summary

In this chapter, we have dealt with the theory of static electrowetting. We have derived the fundamental law of electrowetting, i.e., the Lippmann–Young’s law for low voltages, and analyzed the phenomena of saturation and dielectric breakdown for high voltages. We have seen that, in appearance, Lippmann–Young’s law may seem easy to understand. However, the reality is much more complicated. In particular, the extension to dynamic wetting where the contact angle is a function of the wetting speed cannot be explained by this static law, unless the motion is very slow and a quasisteady approximation can be made. There is still little theory that can predict the dynamic behavior of droplets in EWOD-actuated systems. Nevertheless, electrowetting devices have been successfully developed, principally based on the static and quasi-static assumption when possible [20], and empirically, when dynamic effects are important.

In the following chapter, we show how the electrowetting effect can be used to move, merge, separate, and mix droplets. All these steps are essential components of the digital droplet platform for LOC.

References

- [1] G. Lippmann, Relations entre les phénomènes électriques et capillaires, *Ann. Chim. Phys.* 5 (1875) 494.
- [2] B. Berge, Electrocapillarity and wetting of insulator films by water, *Comptes rendus de l’Académie des Sciences, Séries II* 317 (1993) 157–163.
- [3] C. Quilliet, B. Berge, Electrowetting: a recent outbreak, *Curr. Opin. Colloid. Interface Sci.* 6 (2001) 34–39.
- [4] F. Mugele, J.-C. Baret, Electrowetting: from basics to applications, *J. Phys. Condens. Matter* 17 (2005) R705–R774.
- [5] B. Shapiro, H. Moon, R. Garell, C.J. Kim, Equilibrium behavior of sessile drops under surface tension, applied external fields, and material variations, *J. Appl. Phys.* 93 (2003) 5794–5811.
- [6] N. Fortner, B. Shapiro, Equilibrium and dynamic behavior of micro flows under electrically induced surface tension actuation forces, *Proceedings of the International Conference on MEMS, NANO and Smart Systems (ICMENS’03)*, IEEE Publishers, Piscataway, NJ, 2003.
- [7] R.P. Feynman, R.B. Leighton, M. Sands, *The Feynman Lectures on Physics II*, Addison-Wesley, Edmonton, Canada, 1977; Section 8-2.
- [8] T.B. Jones, J.D. Fowler, Young Soo Chang, Chang-Jin Kim, Frequency-based relationship of electrowetting and dielectrophoretic liquid microactuation, *Langmuir* 19 (2003) 7646–7651.

- [9] T.B. Jones, An electromechanical interpretation of electrowetting, *J. Micromech. Microeng.* 15 (2005) 1184–1187.
- [10] Kwan Hyoung Kang, How electrostatic fields change contact angle in electrowetting, *Langmuir* 18 (2002) 10318–10322.
- [11] J. Zeng, T. Kormeyer, Principles of droplet electrohydrodynamics for lab-on-a-chip, *Lab. Chip.* 4 (2004) 265–277.
- [12] M. Vallet, B. Berge, Limiting phenomena for the spreading of water on polymer films by electrowetting, *Eur. Phys. J. B* 11 (1999) 583.
- [13] T.A. Driscoll, L.N. Trefethen, *Schwarz–Christoffel Mapping*, Cambridge University Press, Cambridge, UK, 2002.
- [14] S. Thamida, H.-C. Chang, Nonlinear electrokinetic ejection and entrainment due to polarization at nearly insulated wedges, *Phys. Fluids* 14 (2002) 4315.
- [15] A.G. Papathanasiou, A.G. Boudouvis, A manifestation of the connection between dielectric breakdown strength and contact angle saturation in electrowetting, *Appl. Phys. Lett.* 86 (2005) 164102.
- [16] R. Bavière, J. Boutet, Y. Fouillet, Dynamics of droplet transport induced by electrowetting actuation, *Microfluid. Nanofluid.* (2007).
- [17] K. Adamiak, Numerical model for the contact angle in electrowetting, Fifth International Meeting on Electrowetting, Rochester, NY, 31 May–2 June, 2006.
- [18] Ilju Moon, Joonwon Kim, Using EWOD (electrowetting-on-dielectric) actuation in a micro conveyor system, *Sensor Actuator A Phys.* 130–131 (2006) 537–544.
- [19] J. Berthier, Ph. Clementz, D. Jary, O. Raccourt, P. Claustre, C. Peponnet, Y. Fouillet, Mechanical behavior of micro-drops in EWOD systems: drop extraction, division, motion and constraining, Proceedings of the Nanotech 2005 Conference, Anaheim, pp. 688–691, 8–12 May, 2005.
- [20] J. Berthier, Ph. Clementz, O. Raccourt, D. Jary, P. Claustre, C. Peponnet, Y. Fouillet, Computer aided design of an EWOD microdevice, *Sensor Actuator A Phys.* 127 (2006) 283–294.
- [21] L. Yeo, H.-C. Chang, Electrowetting films on parallel line electrodes, *Phys. Rev. E* 73 (2006) 011605-1–011605-16.
- [22] L. Yeo, H.-C. Chang, Static and spontaneous electrowetting, *Modern Phys. Lett. B.* 19 (2005) 549.
- [23] P. Takhistov, A. Indeikina, H.-C. Chang, Electrokinetic displacement of air bubbles in micro-channels, *Phys. Fluids* 14 (2002) 1.
- [24] H.J.J. Verheijen, M.W.J. Prins, Reversible electrowetting and trapping of charge: model and experiments, *Langmuir* 15 (1999) 6616.
- [25] V. Peykov, A. Quinn, J. Ralston, Electrowetting: a model for contact angle saturation, *J. Colloid. Polym. Sci.* 278 (2000) 789–793.
- [26] A. Quinn, R. Sedev, J. Ralston, Influence of the electrical double layer in electrowetting, *J. Phys. Chem. B.* 107 (2003) 1163–1168.
- [27] W.A. Zisman, Contact angle, wettability and adhesion, Advances in Chemistry Series, vol. 43, R.F. Gould (editor), American Chemical Society, Washington, DC, 1964. p. 1
- [28] Y. Fouillet, H. Jeanson, I. Chartier, A. Buguin, P. Silberzan, Déplacement de gouttes par un microcaténaire, Conférence SHF Microfluidique, Toulouse, France, décembre 2002, appeared in *La Houille Blanche*, Vol. 4, pp. 37–42, 2003.
- [29] M.K. Chaudhury, G.M. Whitesides, How to make water run uphill, *Science* 256 (1992) 1539–1541.

- [30] Subramanian, N. Moumen, J. McLaughlin, Motion of a drop on a solid surface due to a wettability gradient, *Langmuir* 21 (2005) 11844–11849.
- [31] H. Tavana, A.W. Neumann, On the question of rate-dependence of contact angles, *Colloids Surf. A: Physicochem. Eng. Aspects* 282–283 (2006) 256–262.
- [32] M. Fermigier, P. Jenffer, An experimental investigation of the dynamic contact angle in liquid–liquid systems, *J. Colloid. Interface Sci.* 146 (1990) 226–242.
- [33] J. Berthier, Ph. Dubois, Ph. Clementz, P. Claustre, C. Peponnet, Y. Fouillet, Actuation potentials and capillary forces in electrowetting based microsystems, *Sensor Actuator* 134 (2) (2007) 471–479.
- [34] E.B. Dussan, On the spreading of liquids on solid surfaces: static and dynamic contact lines, *Annual Rev. Fluid Mech.* 11 (1979) 371–400.
- [35] M.G. Pollack, R.B. Fair, D. Shenderov, Electrowetting-based actuation of liquid droplets for microfluidic applications, *Appl. Phys. Lett.* 77 (11) (2000) 1725–1726.
- [36] H. Moon, S.K. Cho, R.L. Garrell, C.-J. Kim, Low voltage electrowetting-on-dielectric, *J. Appl. Phys.* 92 (7) (2002) 4080–4087.
- [37] S.K. Cho, H. Moon, C.-J. Kim, Creating, transporting, and merging liquid droplets by electrowetting-based actuation for digital microfluidics circuits, *J. Microelectromech. Syst.* 12 (1) (2003) 70–80.
- [38] A. Torkkeli, Droplet microfluidics on a planar surface, Dissertation for the degree of Doctor of Science in Technology, 2003.
- [39] T.N. Krupenkin, J.A. Taylor, T.M. Schneider, Shu Yang, From rolling ball to complete wetting: the dynamic tuning of liquids on nanostructured surfaces, *Langmuir* 20 (2004) 3824–3827.
- [40] M.S. Dhindsa, N.R. Smith, J. Heikenfeld, P.D. Rack, J.D. Fowlkes, M.J. Doktycz, et al., Reversible electrowetting of vertically aligned superhydrophobic carbon nanofibers, *Langmuir* 22 (2006) 9030–9034.
- [41] G. McHale, D.L. Hebertson, S.J. Elliott, N.J. Shirtcliffe, M.I. Newton, Electrowetting of nonwetting liquids and liquid marbles, *Langmuir* 23 (2007) 918–924.
- [42] S.H. Kim, J.-H. Kim, B.-K. Kang, H.S. Uhm, Superhydrophobic CF_x coating via in-line atmospheric RF plasma of He–CF₄–H₂, *Langmuir* 21 (2005) 12213–12217.
- [43] S.J. Dodd, A deterministic model for the growth of non-conducting electrical tree structures, *J. Phys. D: Appl. Phys.* 36 (2003) 129–141.
- [44] S.M. Lebedev, O.S. Gefle, Y.P. Pokholkov, E. Gockenbach, H. Borsi, V. Wasserberg, et al., Influence of high-permittivity barriers on PD activity in three-layer dielectrics, *J. Phys. D Appl. Phys.* 37 (2004) 3155–3159.
- [45] S. Kuiper, B. Hendriks, Voltage reduction in electrowetting-on-dielectric, Fifth International Meeting on Electrowetting, Rochester, NY, 31 May–2 June, 2006.
- [46] F. Saeki, J. Baum, Hyejin Moon, C.J. Jeong-Yeol Yoon, Kim, R. Garrell, Electrowetting on dielectrics (EWOD): reducing voltage requirements for microfluidics, *Polym. Mater. Sci. Eng.* 85 (2001) 12.
- [47] Y.-W. Chang, D.Y. Kwok, Electrowetting on dielectric: a low voltage study on self-assembled monolayers and its wetting kinetics, Proceedings of the 2004 International Conference on MEMS, NANO and Smart Systems (ICMENS'04), EEE Publishers, Piscataway, NJ, 2004.
- [48] E. Seyrat, R.A. Hayes, Amorphous fluoropolymers as insulators for reversible low-voltage electrowetting, *J. Appl. Phys.* 90 (3) (2001) 1383–1386.

EWOD Microsystems^{*}

5

CHAPTER OUTLINE

5.1 Introduction	226
5.2 Open and covered EWOD microsystems	228
5.2.1 Open EWOD microsystems	228
5.2.1.1 <i>Systems with catenae</i>	229
5.2.1.2 <i>Systems without catenae</i>	230
5.2.2 Covered EWOD microsystems	231
5.3 Droplet motion	232
5.3.1 Principle of droplet motion—quasi-static aspects and departure from equilibrium	232
5.3.2 Dynamic aspect—velocity of motion	234
5.3.2.1 <i>Scaling numbers</i>	234
5.3.2.2 <i>Droplet velocity</i>	237
5.3.3 Shape of the electrodes: crenellated electrodes	242
5.3.3.1 <i>Electrowetting force</i>	244
5.3.3.2 <i>Theory of triple contact line elasticity</i>	244
5.3.3.3 <i>A criterion for the dimensions of the dents</i>	246
5.3.3.4 <i>Examples of jagged electrode designs</i>	248
5.3.3.5 <i>Discussion</i>	250
5.3.3.6 <i>Numerical simulation—analysis of the forces</i>	251
5.3.4 Motion from a covered to an open EWOD system	253
5.3.5 Effect of a catena	259
5.4 Division of droplets	260
5.4.1 Theoretical approach	260
5.4.2 Droplet division in open EWOD systems	261
5.4.3 Droplet division in covered EWOD systems	263
5.4.3.1 <i>Stretching</i>	263
5.4.3.2 <i>Stretching and pinching</i>	265
5.4.4 Experimental results	269
5.4.5 Droplet dispensing	271

*This chapter was written in collaboration with Hsueh-Chia Chang, Bayer Professor of Engineering, Department of Chemical and Biomolecular Engineering, University of Notre Dame, Notre Dame, IN.

5.4.5.1 Analysis of the dispensing mechanism	271
5.4.5.2 Insensitivity to the surface tension.....	273
5.4.5.3 Velocity field in the liquid during drop dispensing	274
5.4.6 Influence of the cutting electrode on drop volume and reproducibility	275
5.4.7 Centering electrode and shape of reservoir electrode.....	278
5.4.7.1 Centering electrode	278
5.4.7.2 Shape of reservoir electrode.....	279
5.5 Droplet merging and mixing	284
5.5.1 The difficulty of mixing in covered EWOD microsystems	284
5.5.1.1 Back and forth motion.....	284
5.5.1.2 Successive merging and divisions	286
5.5.1.3 Loop motion.....	286
5.5.2 Mixing in open EWOD systems.....	288
5.5.2.1 Mixing by Marangoni effects	288
5.5.2.2 The difficulty of mixing viscous fluids	289
5.6 Dilution	289
5.6.1 Dilution of solutes	289
5.6.2 Dilution of discrete particles.....	291
5.7 Magnetic beads in EWOD microsystems.....	292
5.8 Architecture of EWOD microsystems	294
5.8.1 General architecture	294
5.8.2 Multiplexing.....	295
5.9 Other EWOD microsystems	296
5.9.1 Electrowetting conveyor system	296
5.9.2 Extension of the electrowetting concept: electrowetting filament and open microfluidics	297
5.10 Summary	298
References	299

5.1 Introduction

Electrowetting microdevices have been conceived using the principle of electrowetting discussed in the preceding chapter. Architecture of such microdevices usually involves microfabricated electrodes embedded in a solid substrate, each electrode having roughly the characteristic size of a droplet ([Figure 5.1](#)). The electrode is coated by a dielectric layer covered by a hydrophobic layer in order to increase the electrowetting effect on the droplet.

Successive actuation of electrodes is used to digitally activate targeted droplets. Initially, droplets are dispensed from a reservoir, then moved from one electrode to the next, merged with other droplets in order to introduce specific biochemical

species for the desired reaction, then mixed for better reaction yield; after that, they are generally divided in order to regain the same initial volume and transported to the exit. All these operations are performed on a digital grid formed by electrodes that can be individually addressed, as shown in [Figure 5.2](#).

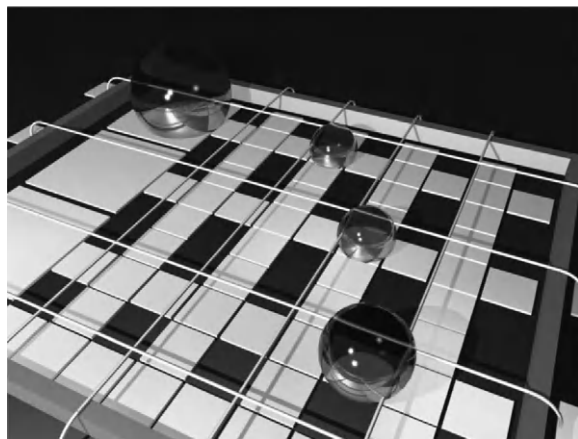


FIGURE 5.1

Schematic view of a DMF architecture.

Source: *Image CEA-LETI*.

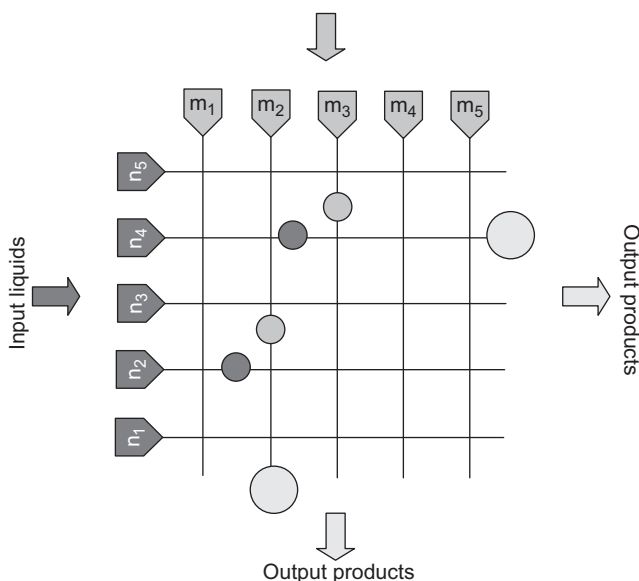


FIGURE 5.2

Schematic view of a DMF system designed to perform programmed operations on droplets.

In this chapter, we study how the basic operations like drop motion, merging, mixing, and division are performed. But first, we present the two types of EWOD microsystems, the “open” and “covered” EWOD microsystems.

5.2 Open and covered EWOD microsystems

DMF (digital microfluidics) is a promising way to manipulate biological targets like DNA, proteins, or cells in very small liquid volumes. The advantages of such devices are the use of lesser quantities of costly reagents, better biochemical reaction efficiency, and shorter operating times. DMF based on EWOD is a fast developing technology [1–3]. The basic manipulations of drops can be achieved in such microsystems [4,5].

Two different types of EWOD-based microsystems have been developed: open systems where the sessile droplet is sitting freely on a horizontal solid substrate and covered systems where the droplet is confined between two plates (Figures 5.1 and 5.2). Each of these systems has its own advantages. Drop dispense, motion, and splitting are easier in covered EWOD systems, whereas mixing and evaporation (for species concentration) are preferably performed in the open configuration. With some hybrid designs, these two types of EWOD are interfaced such that droplet motion between a covered and an open region is possible under electrowetting actuation [6].

5.2.1 Open EWOD microsystems

Historically, open EWOD systems have been first built with catenae (Figures 5.3 and 5.4); the potential difference for droplet actuation is thus established between the electrode embedded in the substrate and the catena, which is used as the reference electrode. Catenae are difficult to mount in the microsystem and need to be

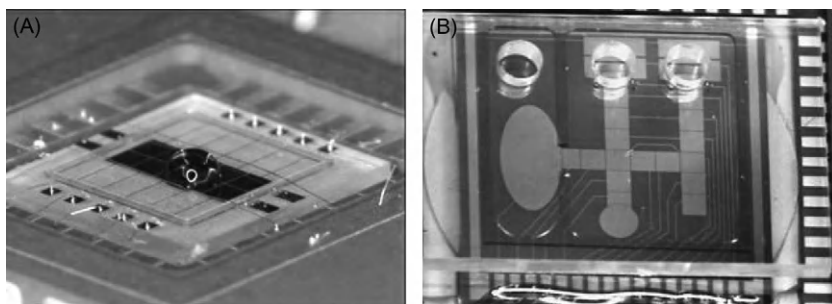


FIGURE 5.3

(A) Open EWOD microsystem [7]; the drop sits on an electrode paved substrate; (B) covered EWOD microsystem; the droplets are squished between two horizontal solid plates; the holes at the top of the picture are used for the injection of the liquid.

Source: Both photographs courtesy C. Peponnet and Y. Fouillet, CEA-LETI.

carefully aligned. New concepts of actuation have been recently developed, like “buried” catenae or even no catenae at all. In this section, we discuss both open EWOD systems, with and without catenae.

5.2.1.1 Systems with catenae

The catena has exactly the same role as the reference electrode contacting the liquid in the electrowetting test system ([Figure 5.4](#)). Its horizontal position, parallel to the surface of the substrate, allows for the droplet to move from one electrode to the next alongside the catena.

We have already introduced the capillary effect of a catena on a droplet in Chapter 3. We stress here that catenae should be carefully located, parallel to the substrate, aligned and centered with the electrode row; otherwise the motion could be blocked. Indeed, if there is an angle between the catena and the direction of the motion (direction of the electrode row) the droplet may be pinned. This is, for instance, the case of [Figure 5.5B](#). The spherical droplet cannot move past the change of direction of the catena.

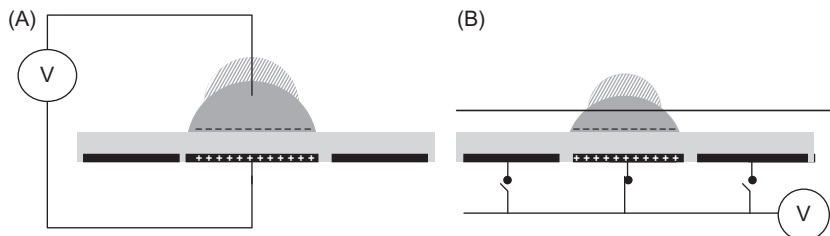


FIGURE 5.4

(A) Electrowetting test system described in Chapter 3; (B) open EWOD system with catenae. The figure shows the two positions of the droplet depending on the actuation of the electrodes.

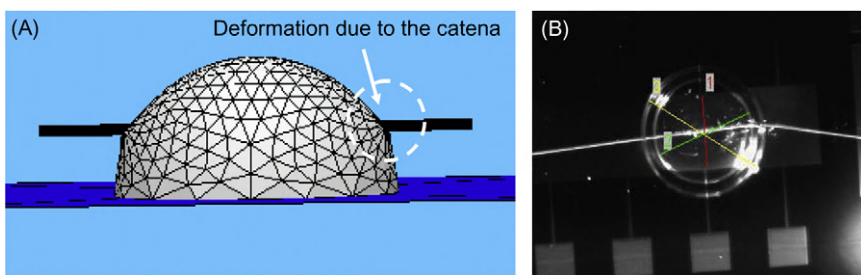


FIGURE 5.5

(A) Surface Evolver calculation of the shape of a droplet pierced by a hydrophilic catena [\[8\]](#); deformation stays localized to a small area close to the wire. (B) Experimental view confirming the negligible deformation caused by the catena.

Source: Photograph CEA-LETI.

However, if catenae are correctly placed, they do not substantially perturb the behavior of droplets (an exception may be very hydrophilic liquids like ionic liquids). Usual electrode sizes are in the range $500\text{ }\mu\text{m}$ – 1 mm . Studies are being conducted to reduce this size. In consequence, the droplets in EWOD microsystems have a Bond number $Bo = \Delta\rho g R^2/\gamma$ smaller than 0.05. Therefore, surface tension prevails over gravity, and sessile drops in open EWOD microsystems can be assumed spherical. They remain nearly spherical even if a catena is used as an electrode. Figure 5.5 shows the effect of a hydrophilic catena piercing the droplet (usually catenae are metallic wires—very often made of gold, and they have a hydrophilic contact with aqueous solutions).

5.2.1.2 Systems without catenae

Catenae bring complexity to the system: they must be connected to the electric source, and they must be carefully aligned with the electrodes. Two solutions are

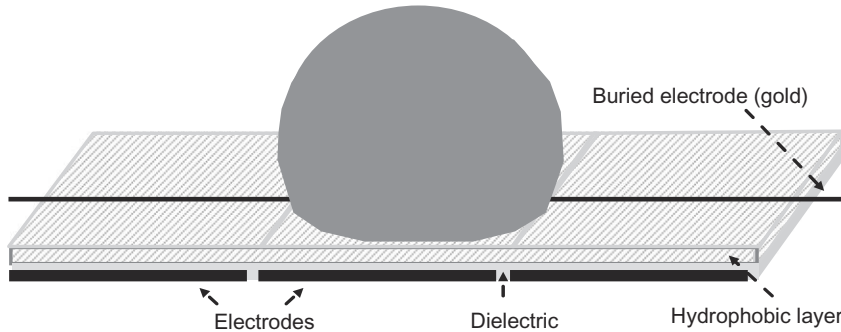


FIGURE 5.6

Principle of a buried reference electrode.

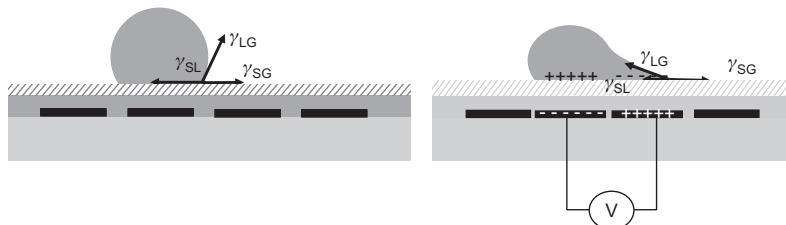


FIGURE 5.7

Electric charge distribution in the substrate and droplet when a potential difference is established between the droplet electrode and the next: the droplet spreads onto the two electrodes. Remark that we have adopted the notation where the effect of the electrowetting effect is translated in a decreased solid–liquid surface tension.

currently being developed: (i) “buried” catena, i.e., the catena is buried in the substrate, (ii) no catena at all, the next electrode being used as the reference electrode. The first case uses the same principle as that described in the preceding section ([Figure 5.6](#)); the droplet is at the same potential as the catena.

The second case uses a slightly different principle ([Figure 5.7](#)): the electric field is established between one electrode and the next. One electrode is at the potential $+V$, the other at potential 0. However, the potential of the droplet is a floating potential. More details concerning the way these designs act on droplets will be given in [Section 5.3](#).

5.2.2 Covered EWOD microsystems

In a covered EWOD system, the catena is replaced by a top plate covering the droplet ([Figure 5.8](#)). The free surface, i.e., the surface area between liquid and surrounding fluid (usually air, sometimes silicone oil), is reduced in this design. The substrate at the bottom is similar to that of open EWOD systems. The top plate is constituted by a plate electrode usually made of ITO coated with a thin layer of Teflon. Thus, without electric actuation, the contact is hydrophobic with both plates, as shown in [Figure 5.8](#).

In a covered EWOD system, the droplet follows closely the shape of the electrodes ([Figure 5.9](#)). In such a configuration, the vertical gap is very small compared to the horizontal dimension of the droplet, and the surface area of the free interface (liquid–air) is very small compared to that of the solid–liquid interface. Consequently, the energy of the liquid–air interface is much smaller than that of the solid–liquid interface and the droplet adopts the shape of the underlying electrode. This is why a droplet can adopt a nearly “square” shape.

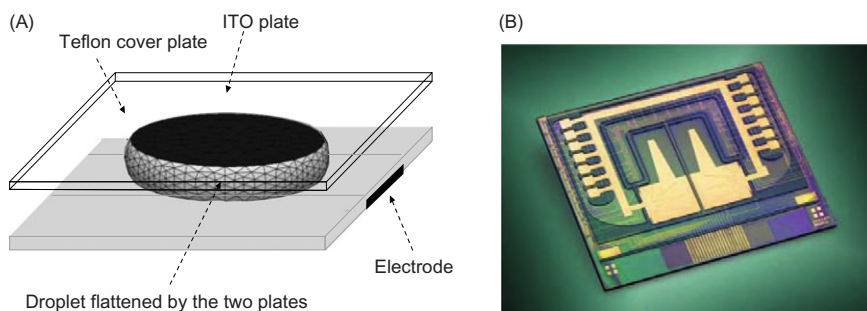
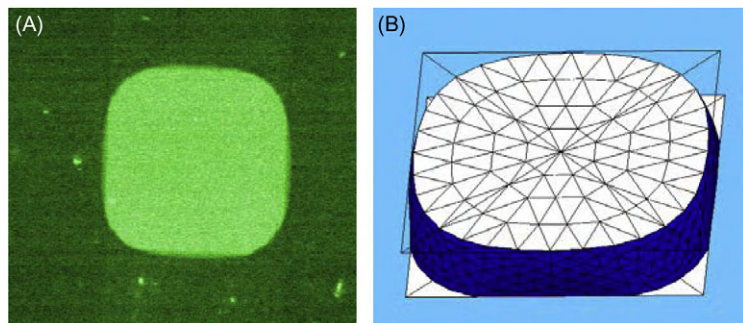


FIGURE 5.8

Schematic view of a covered EWOD microsystem: (A) droplet squished between two plates and (B) covered EWOD microsystem fabricated by the LETI.

Source: Courtesy C. Peponnet and Y. Fouillet, CEA-LETI.

**FIGURE 5.9**

(A) Photograph of a “square” droplet in a covered EWOD microchip and (B) the droplet simulated with Evolver software.

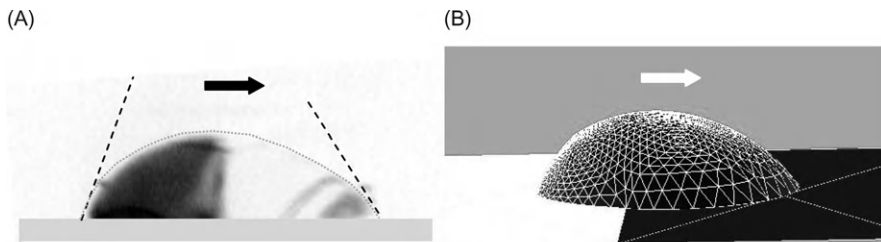
5.3 Droplet motion

In Chapter 4, we analyzed how EWOD produces forces on droplets. In this section, we show that these forces can be used to move droplets. First, we show how electrowetting actuation can force a droplet out of its equilibrium state; second, we present some dynamic aspects of droplet motion; and finally, we analyze the effect of different technological solutions on the motion of droplets.

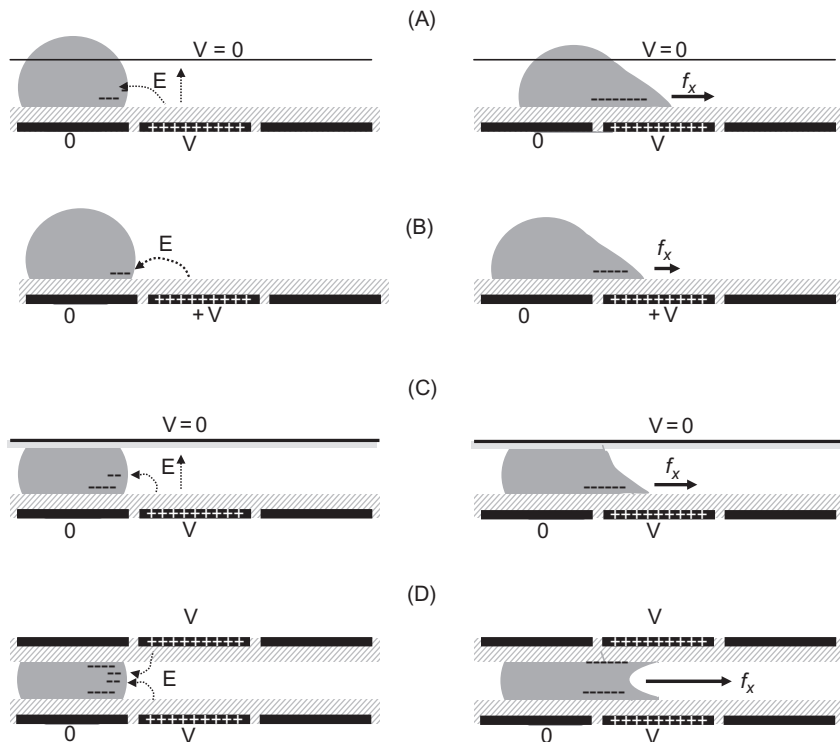
5.3.1 Principle of droplet motion—quasi-static aspects and departure from equilibrium

The principle of droplet motion due to a difference—or a gradient—of wettability is well known [9,10]. We showed in Chapter 3 that, when a droplet is located on the boundary between a lyophobic region and a lyophilic region, it moves to the lyophilic region, at least if hysteresis of contact angle is not too large. The situation is similar in the case of electrowetting (Figure 5.10). If a conductive droplet is located on the boundary between an actuated and a nonactuated electrode, an electrowetting force is applied on the contact line located above the actuated electrode, and a capillary force is exerted on the contact line located on the lyophobic surface. The resultant of the forces parallel to the surface is directed toward the electrically actuated region. The droplet is out of equilibrium, and if the resulting force is sufficient to overcome hysteresis, the droplet moves.

In the preceding section, we presented the usual EWOD designs: open EWOD with catenae, open EWOD without catenae, and covered EWOD systems. Figure 5.11 shows how the electric charges are induced at the liquid interface resulting in an electrowetting force acting on the droplet. Jones [11] has shown that the electrowetting force acting on a droplet positioned above different substrate

**FIGURE 5.10**

(A) View of a droplet of ionic liquid, moving to the right and (B) numerical simulation with Surface Evolver assuming a slow motion.

**FIGURE 5.11**

Electric scheme of the four different EWOD designs: (A) open EWOD with catena: an electrowetting force is exerted on the right boundary of the droplet; (B) open EWOD without catena: the neighboring electrode is the zero potential electrode; (C) covered EWOD: configuration similar to (A), the electrowetting force exerted on the right boundary of the droplet pulls the droplet onto the neighboring electrode; and (D) the electrowetting force can be doubled if the cover plate is fabricated and actuated in the same way as the bottom plate.

with specific capacitance C_i and a voltage difference between the electrode and the droplet V_i is

$$F_x = \sum_i \frac{\partial}{\partial x} \left(\frac{1}{2} C_i V_i^2 \right). \quad (5.1)$$

We can deduce the electrowetting force in the different configurations of [Figure 5.11](#). The electrowetting force divided by the width of the electrode F_x/e is

$$f_x = \frac{F_x}{e} = \frac{1}{2} CV^2 \quad (5.2)$$

for cases (a) and (c). In case (d), the force is twice that of case (c)

$$f_x = \frac{F_x}{e} = 2 \left[\frac{1}{2} CV^2 \right] = CV^2. \quad (5.3)$$

Note that case (d) requires twice the electric energy of case (a) or (c). Configuration (b) is more complex because the potential in the droplet is not fixed [\[12,13\]](#). We have approximately the relation

$$f_x = \frac{F_x}{e} \leq \frac{1}{4} CV^2 \quad (5.4)$$

showing that the electrowetting force is much smaller in this configuration.

5.3.2 Dynamic aspect—velocity of motion

5.3.2.1 Scaling numbers

In Chapter 3, we see that the balance between the gravity and the surface tension forces was characterized by the Bond number [\[14\]](#)

$$Bo = \frac{g \Delta \rho l^2}{\gamma}. \quad (5.5)$$

When a droplet is in motion, other forces, like electrowetting, viscous, and inertia forces are acting on the droplet. We have seen that the ratio of the electrowetting forces to the surface tension forces is given by the electrowetting number

$$\eta = \frac{CV^2}{2\gamma}. \quad (5.6)$$

Let us now consider the ratio between inertia and surface tension. It can be expressed by the nondimensional Weber number

$$We = \frac{\rho v^2 l}{\gamma}, \quad (5.7)$$

where v is the velocity of motion of the droplet, ρ its density, and l a characteristic length (in our case, the contact radius). If the Weber number is larger than the

critical Weber number ($We_{\text{crit}} = 1.1$), the droplet is very distorted by inertia forces and breakup may occur [15]. At a very low Weber number, inertia is negligible; for a moderate Weber number, inertia deforms the droplet without disrupting it. Next, we consider the nondimensional Ohnesorge number defined by

$$Oh = \frac{\mu}{\sqrt{\rho l \gamma}}, \quad (5.8)$$

where μ is the dynamic viscosity of the liquid. This number represents the ratio of viscous forces to the inertia forces times the surface tension forces. Above the critical value $Oh_{\text{crit}} = 0.03$ [16], viscosity plays an important role during the manipulation of the droplet, e.g., for droplet merging. The well-known capillary number represents the ratio of the viscous forces to the surface tension forces

$$Ca = \frac{\mu v}{\gamma}. \quad (5.9)$$

The capillary number is linked to the Weber and Ohnesorge numbers by the relation

$$Ca = Oh\sqrt{We}. \quad (5.10)$$

The Reynolds number of the droplet represents the ratio of the internal inertia forces to viscosity forces; it is expressed by

$$Re = \frac{\rho v l}{\mu} \quad (5.11)$$

assuming that the velocity of the droplet motion v is a satisfactory scale of the internal velocity of the droplet. The Reynolds number is also a function of Weber and Ohnesorge numbers

$$Re = \frac{\sqrt{We}}{Oh}. \quad (5.12)$$

For microdrops, the internal flow field is always laminar, i.e., the Reynolds number is always smaller than the critical Reynolds number. In conclusion, four independent nondimensional numbers characterize the droplet behavior: Bo , η , We , and Oh . Maximum values of the different dynamic nondimensional numbers are shown in Table 5.1; these values correspond approximately to the maximum measured velocities (largest possible values of η).

Analysis of the values of Table 5.1 shows two different behaviors in common EWOD systems (approximate electrode size 500–1000 μm). On one hand, water-based liquids have, in comparison with surface tension forces, very small viscous effects during their motion, and small to moderate inertia effects. On the other hand, ionic liquids show moderate to strong viscous effects (the Ohnesorge number may be larger than its critical value) and negligible inertia effects. In summary, most of the time, droplet motion in EWOD microsystems (of dimensions less than 1 mm) is essentially governed by surface tension forces and Young's constraints at

Table 5.1 Maximum Values of the Dynamic Nondimensional Numbers

	Surface Tension (mN/m)	Dynamic Viscosity (kg/m/s)	Density (kg/m ³)	Maximum Velocity (mm/s)	Typical Dimension (μm)	We	Oh	Ca	Re
Water	72	0.001	1000	100	1000	0.13	4×10^{-3}	0.0013	100
Water + surfactant	40	0.001	1000	100	1000	0.20	5×10^{-3}	0.0020	100
Ionic liquid	40	0.1	1200	20	1000	0.012	0.5	0.05	0.2

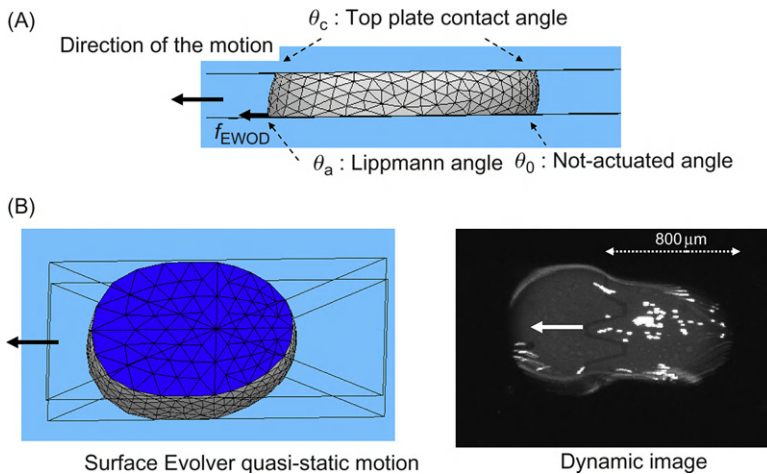


FIGURE 5.12

(A) Motion is triggered by dissymmetry of the electrocapillary forces on the triple lines.

(B) The quasi-static model of Surface Evolver is compared to the real dynamic image of the motion. Discrepancy is mostly due to inertial effects.

the contact of the solid surface. Note that this will be even more the case when the size of the electrodes is reduced. *Thus, the morphology of the electrodes is the key factor for the control of droplet motion and manipulation.*

Figure 5.12 shows the effect of the Weber number on the motion of a water droplet. If inertia was totally negligible, the motion could be described by the electrocapillary equivalence (see Chapter 4) and modeled using a quasi-steady-state approach (here, the Surface Evolver software). The reality shows that the droplet is slightly deformed by inertia forces. However, the discrepancy is not that important, and a model purely based on surface tension forces predicts correctly the possibility/impossibility of droplet motion, if not the accurate shape of the droplet during motion.

5.3.2.2 Droplet velocity

In DMF systems, a droplet moves from one location on the chip to the next incrementally. Because inertia forces are small, the droplet accelerates very quickly, reaches a nearly steady velocity, and decelerates abruptly. In this section, we focus on the “nearly steady state” velocity of the droplet.

Velocity depends on the strength of the electrocapillary forces. It is then expected that velocity of the droplet is directly related to this force. In reality, the motion of microdrops is a complex physical phenomenon involving surface tension, viscosity, dynamic contact angles, internal motion, etc., and is still a subject of research. In the following section, we present a very simple model proposed by Chen et al. [17] to make an estimate of the velocity of microdrops during their motion in EWOD microsystems.

5.3.2.2.1 Model

We consider a droplet of volume Vol either sandwiched between two plates (covered EWOD) or sitting on a flat surface (open EWOD), as shown in [Figure 5.13](#).

We can do the following simplified analysis: if the velocity of motion is constant, the electrowetting force balances the friction force due to viscous dissipation at portions of the wall in contact with the drop, assuming that the other resisting forces, such as contact-line resistance, are negligible compared to the viscous dissipation. Then, in the case of the covered system, the contact surface is assumed circular (which is not true in reality)

$$F_{\text{viscous}} \approx 2\pi r^2 \tau_w \approx \frac{12\mu\text{Vol}}{\delta^2} v_{\text{cov}}, \quad (5.13)$$

where v_{cov} is the global velocity and τ_w is the wall friction, approximated with the Poiseuille profile

$$\tau_w \approx \frac{6\mu v_{\text{cov}}}{\delta}. \quad (5.14)$$

Using the capillary equivalence, we can express the electrowetting force by

$$F_{\text{elec}} \approx 2r\gamma_{\text{LG}}(\cos \theta_a - \cos \theta_r) \quad (5.15)$$

and by equating [Eqs. \(5.13\)](#) and [\(5.15\)](#) we deduce the droplet velocity of motion

$$v_{\text{cov}} \approx \frac{\delta\gamma_{\text{LG}}}{6\pi\mu r}(\cos \theta_a - \cos \theta_r). \quad (5.16)$$

If the voltage is smaller than the saturation voltage, we can use the Lippmann–Young’s relation, and the velocity can be estimated by

$$v_{\text{cov}} \approx \frac{\delta}{12\pi\mu r} CV^2. \quad (5.17)$$

[Equation \(5.17\)](#) shows that the velocity of motion is proportional to the square of the electric potential.

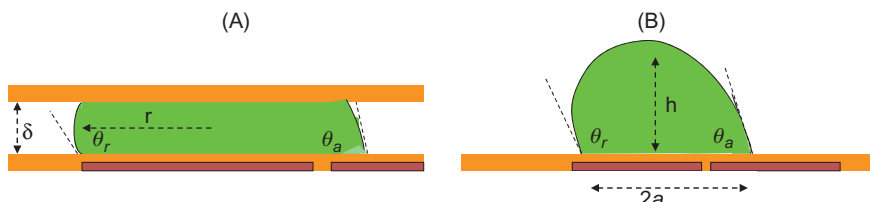


FIGURE 5.13

(A) Droplet moving in a covered EWOD configuration and (B) droplet moving in an open EWOD configuration.

In the case of the open EWOD system,

$$F_{\text{viscous}} \approx \pi a^2 \tau_w.$$

The shear stress τ_w can be approximately expressed by

$$\tau_w \approx \frac{5\mu v_{\text{open}}}{2h} \quad (5.18)$$

based on a peak velocity located at $2/5$ of the drop height, according to numerical simulations. Then,

$$F_{\text{viscous}} \approx \frac{5\pi\mu a^2}{2h} v_{\text{open}}. \quad (5.19)$$

The electrowetting force is

$$F_{\text{elec}} \approx 2a\gamma_{\text{LG}}(\cos \theta_a - \cos \theta_r) \quad (5.20)$$

and the droplet velocity is

$$v_{\text{open}} \approx \frac{4h}{5\pi\mu a} \gamma_{\text{LG}}(\cos \theta_a - \cos \theta_r). \quad (5.21)$$

In terms of voltage (far from the saturation limit), we have

$$v_{\text{open}} \approx \frac{2h}{5\pi\mu a} CV^2. \quad (5.22)$$

It is easy to see that the velocity of a droplet is larger in an open EWOD system. The velocity ratio $v_{\text{cov}}/v_{\text{open}}$ is given by

$$\frac{v_{\text{cov}}}{v_{\text{open}}} \approx \frac{5}{24} \frac{\delta a}{r h}. \quad (5.23)$$

In Eq. (5.23), the term a/h is of the order of 1, and $\delta \ll r$, showing that the velocity of motion is much larger in an open configuration. We note that this model assumes that the two dominant forces are the electrowetting and the friction forces, and supposes a Poiseuille flow inside the droplet. It neglects internal recirculation, the effect of the triple line, the deformation of the droplet during motion, etc. Much is still to be done to understand the motion of droplets under electrowetting actuation. Let us mention that the first numerical simulations of Dolatabadi et al. [18] agree on some points with Chen's model, but disagree about the effect of the vertical gap δ . However, it is a general observation, according to Eqs. (5.16) and (5.21), that the velocity of motion is proportional to the electrowetting force and inversely proportional to the viscosity.

5.3.2.2 Experimental results

The variation of the velocity with the square of the voltage predicted by the preceding model has been checked by Pollack et al. [19] for low to moderate

values of the applied voltage (Figure 5.14). Besides, there is a very interesting point in Pollack's publication: the velocity is the same when the dimensions are reduced homothetically, i.e., when the ratio δ/r is kept constant. This is exactly what is predicted by Eqs. (5.16) and (5.17).

At large voltages, the electrowetting force saturates and in consequence the velocity of motion is limited by an asymptote (Figure 5.15). Using the modified

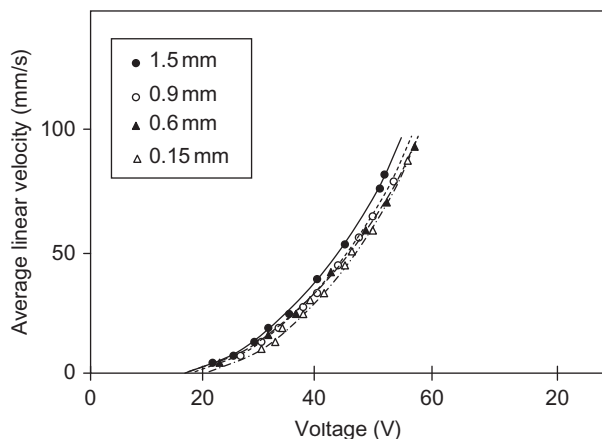


FIGURE 5.14

At low voltages, the velocity of motion varies as the square of the applied voltage. The size of the electrodes is indicated in the legend.

Source: From Ref. [19]; reproduced by permission of the Royal Society of Chemistry.

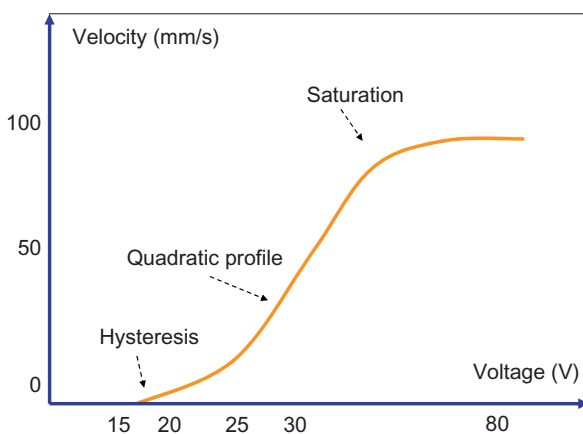


FIGURE 5.15

Relation between the velocity of motion and the voltage showing saturation for large actuation potentials.

Lippmann's law (see Section 4.4.3) based on the Langevin's function, Eq. (5.16) can be recast under the form

$$v_{\text{cov}} \approx \frac{\delta}{6\pi\mu r} \gamma_{\text{LG}} (\cos \theta_S - \cos \theta_0) L \left(\frac{CV^2}{2\gamma(\cos \theta_S - \cos \theta_0)} \right) \quad (5.24)$$

and Eq. (5.21) under the form

$$v_{\text{open}} \approx \frac{4h}{5\pi\mu a} \gamma_{\text{LG}} (\cos \theta_S - \cos \theta_0) L \left(\frac{CV^2}{2\gamma(\cos \theta_S - \cos \theta_0)} \right), \quad (5.25)$$

where L is the Langevin's function and θ_S is the saturation angle. These relations between the droplet velocity and the voltage then have the shape shown in Figure 5.15. There is a constant asymptote at high voltages that represents the upper bound of the velocity. In conclusion, velocity of motion in electrowetting devices is limited by the saturation of the electrowetting force and very high velocities cannot be expected. This upper limit on drop velocity is typically 15 cm/s.

Experimental observations confirm that the velocity is reduced when the viscosity increases (Figure 5.16). One expects that there is a viscous limit above which liquids cannot be moved in EWOD microsystems. In biology, viscous (even non-Newtonian) liquids are sometimes used, like polysaccharides, blood, or alginates. Their viscosity increases with the concentration in monomers, dimers, trimers, etc. [20]. In Chapters 6 and 7, we will discuss the maneuverability of biological or chemical fluids. For instance, in chemical applications, it has been observed that ionic liquids can be displaced on EWOD chips, but at a small velocity (bottom curve of Figure 5.16).

Let us finally analyze the effect of surfactants. Remember that in biology and biotechnology, surfactants are currently used for many reasons, the most important being to disperse aggregates and to reduce adhesion on the solid walls.

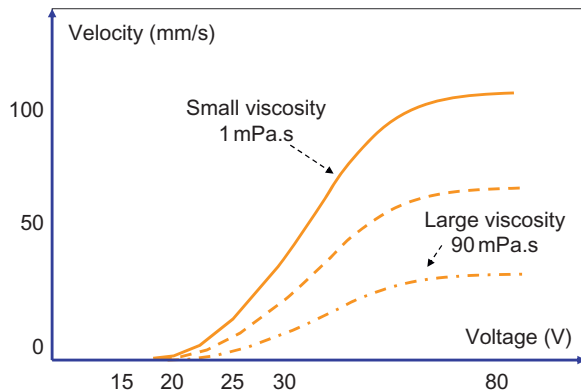
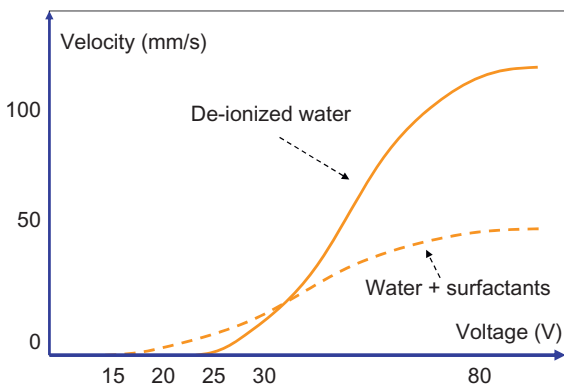


FIGURE 5.16

Droplet velocity is reduced by increasing the viscosity of the liquid.

**FIGURE 5.17**

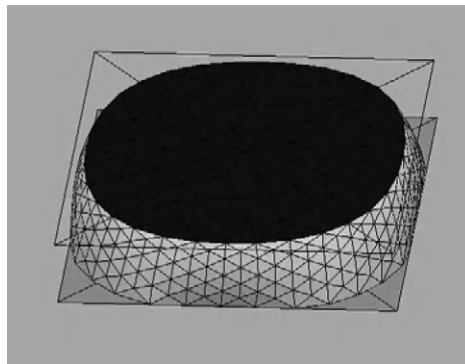
Observed velocities of a droplet as a function of applied voltage; velocities are higher when the surface tension is large, except at very low voltage.

A comparison of the droplet velocity between DIW and biologic buffer is shown in [Figure 5.17](#). We observed that hysteretic effects are reduced when surfactants are present in the solution, but the droplet motion is much slower. The reduction of the hysteresis threshold in the case of biologic buffers can be attributed to the reduction of the quantity $\gamma_{LG} \sin \theta_0$ (Section 4.5), and the reduction of the velocity is certainly due to a smaller value of the solid–liquid surface tension γ_{SL} .

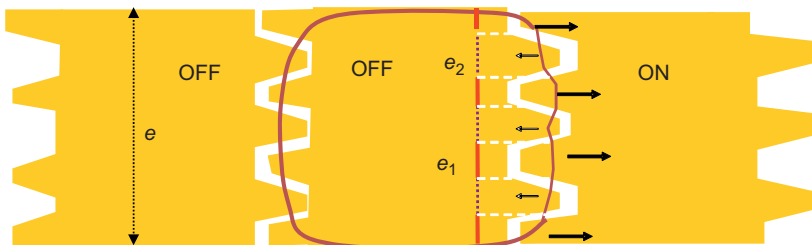
5.3.3 Shape of the electrodes: crenellated electrodes

We have seen in the preceding section that, in electrowetting microsystems, micro-drops are displaced “digitally” on rows of electrodes. However, the motion of a droplet from one electrode to the next is not straightforward. Microfabrication imposes a gap separating the electrodes. This gap is usually of the order of 10–30 μm , depending on the precision of the lithography process, compared to an electrode size of the order of 800 μm . This gap creates a permanent hydrophobic region between two neighboring electrodes. If the droplet has a volume such that it is “contained” or “limited” by the boundaries of the electrode as shown in [Figure 5.18](#), it cannot move to the next electrode when the latter is actuated.

This is frequently the case in covered EWOD microsystems where droplet volumes are carefully controlled, and the size of the electrodes determines the volume of liquid in each droplet within a margin of a few percent. In order to remedy the problem, jagged or crenellated electrodes have been designed as shown in [Figure 5.19](#). The idea behind such a design is that the droplet contact line with the electrode plane extends over onto the dents of the next electrode. As soon as the next electrode is actuated, electrocapillary forces act to produce the motion of the droplet. Such jagged electrodes require more complicated

**FIGURE 5.18**

Microdrop confined by the electrode boundaries in a covered EWOD microsystem. Surface Evolver simulation [8].

**FIGURE 5.19**

Sketch of the crenellated electrodes and position of the droplet. The force exerted by the neighboring electrode at the beginning of the displacement on the advancing contact line is symbolized by arrows.

microfabrication but are very efficient for droplet motion provided the geometry and dimension of the dents are correctly designed.

First, we show that, at the very beginning of the motion, the electrowetting force on a droplet is proportional to the length of the contact line located on the neighboring actuated electrode. This result proves that the electrode's jagged boundary plays a key role in electrowetting actuation, and that its design must be carefully considered for drop motion to commence. We then investigate in a second section the position of the contact line on a jagged electrode. From a theoretical standpoint, this position is related to the theory of partial/total pinning on wettability boundaries, pioneered by de Gennes et al. [21] and Ondarçuhu [22]. We first review the theory and then show how a criterion for determining the size of the dents can be derived.

5.3.3.1 Electrowetting force

In this section, we analyze the electrowetting force on the droplet at the very beginning of the motion. The electrowetting force is due to the Maxwell stress tensor [23–25] and, because the system is static at the onset of motion, can be translated as a capillary effect using Lippmann–Young’s law. It has been established [26] that the electrowetting force during full motion from one electrode to the next is given by

$$F_{e,\text{motion}} = e\gamma(\cos \theta_a - \cos \theta_{na}), \quad (5.26)$$

where e is the width of the electrode and θ_a and θ_{na} are the actuated and nonactuated contact angles, respectively. In Figure 5.19, we show the position of the contact line at the very beginning of the motion.

In this case, the electrowetting force is

$$F_{e,\text{start}} = e_1\gamma \cos \theta_a + e_2\gamma \cos \theta_{na} - e\gamma \cos \theta_{na}, \quad (5.27)$$

where e_1 and e_2 are the total cross dimensions corresponding to the part of the contact line on the actuated and nonactuated electrodes, respectively. The first term on the right-hand side of Eq. (5.27) is the pulling force exerted on the liquid by the actuated neighbor electrode, and the second term is the force on that part of the contact line located on the nonactuated electrode (usually $\cos \theta_{na} < 0$, so that the force is directed to the right). The last term of Eq. (5.27) corresponds to the receding contact line. Note that

$$e_1 + e_2 = e.$$

After substitution in Eq. (5.26), we find

$$F_{e,\text{start}} = e_1\gamma(\cos \theta_a - \cos \theta_{na}). \quad (5.28)$$

Comparison of Eqs. (5.28) and (5.26) shows that at the beginning of the motion, the force on the droplet is only

$$F_{e,\text{start}} = \frac{e_1}{e} F_{e,\text{motion}}. \quad (5.29)$$

We verify that if $e_1 = 0$, i.e., there is no part of the contact line overlapping on the neighboring electrode, no electrowetting force acts on the droplet. Relation (5.29) shows that it is important to have at rest a significant part of the contact line overlapping the next electrode.

5.3.3.2 Theory of triple contact line elasticity

The position and shape of an interface depend on two constraints: surface tension that tends to minimize the surface area and the Young’s contact angles acting directly on the contact line. For a wavy contact line, these effects act oppositely. This is the basis of the elasticity theory for the contact line proposed by de Gennes et al. [21] and applied by Ondarçuhu [22] to a sinusoidal contact line. Note that the elasticity theory differs from the line tension theory [27]:

the elasticity theory corresponds to a “macroscopic” effect of the interface, whereas the line tension acts at a nanoscopic scale. In the case of this study, line tension is negligible compared to interfacial elasticity.

We just reproduce here the results of Ondarçuhu. The sinusoidal contact line is given by the expression

$$y = \eta(x) = \eta \cos(qx), \quad (5.30)$$

where η is the amplitude and q is the wave vector. The results are obtained under the assumption that $\eta q \ll 1$. If the pinning is total, i.e., the contact line follows the sinusoidal boundary, the shape of the interface is obtained by solving the Laplace's equation with the condition that far from the surface, the contact angle is an average contact angle θ_0 . Then, the maximum and minimum contact angles θ_+ and θ_- can be derived. For the pinning to be total, these two values must be comprised in the interval $[\theta_1, \theta_2]$ corresponding to the contact angle with each surface (canthotaxis). It can be shown that four different morphologies of the contact line can be obtained. These morphologies are shown in Figure 5.20.

The two lines in Figure 5.20 are given by the relations

$$\begin{aligned} \eta q &< 1 - \frac{\theta_1}{\theta_0} \\ \eta q &< \frac{\theta_2}{\theta_0} - 1, \end{aligned} \quad (5.31)$$

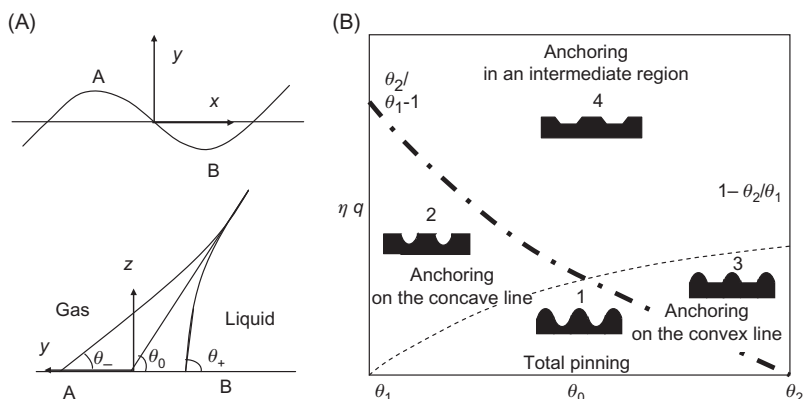


FIGURE 5.20

(A) Schematic of the contact line and its deformation; top: the contact line in the (x, y) plane; bottom: profile of the interface in the (y, z) plane. (B) The four different types of pinning on a sinusoidal boundary line. θ_0 is the contact angle far enough from the contact line, where the interface ignores the details of the contact line.

Source: From Ref. [22] © EDP 1995, reprinted with permission.

where θ_0 is the uniform average angle of the interface at some distance of the contact line θ_1 and θ_2 is the Young's contact angles with the two substrates. We note that in the case of total pinning, i.e., the contact line follows strictly the sinusoidal line, ηq is quite small.

5.3.3.3 A criterion for the dimensions of the dents

If we approach the crenellated boundary line by a sinusoidal function, as shown in Figure 5.21, the analysis of the preceding section applies. We note that the boundary line depends on the gap between the electrodes δ , so that the amplitude η is a function of the size of the “dents” λ and of the size of the gap δ . Approximately, we have

$$\eta \approx \frac{\lambda - \delta}{2}. \quad (5.32)$$

Relation (5.32) shows that if δ increases, the amplitude of the sinusoidal boundary line decreases. The sinusoidal function is then described by

$$\eta(y) = \eta \cos(qy) = \frac{\lambda - \delta}{2} \cos(qx), \quad (5.33)$$

where x is the horizontal coordinate and y is the vertical coordinate according to Figure 5.21.

In the case of electrowetting, we have to design the dents so that the contact line overlaps on the concave part of the sinusoidal curve. This allows the droplet to experience a capillary pull when the neighboring electrode is actuated. Referring to the preceding section, only domains 3 and 4 defined in Figure 5.20 are acceptable and the following relation must be satisfied

$$\eta q > \frac{\theta_2}{\theta_0} - 1. \quad (5.34)$$

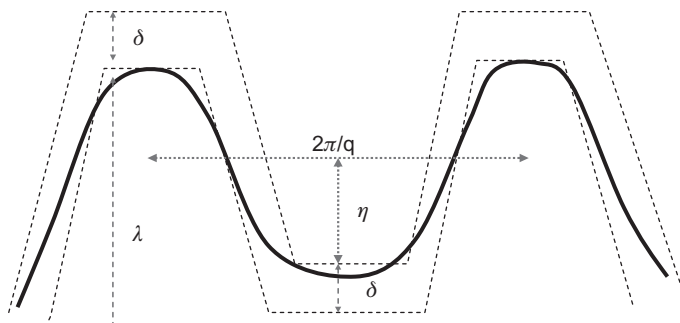


FIGURE 5.21

Crenellated electrodes can be approached by a sinusoidal boundary.

In Eq. (5.34), the exact value of θ_0 is not known. However, if we choose the nondimensional number ηq to be larger than

$$\eta q > \frac{\theta_2}{\theta_1} - 1, \quad (5.35)$$

we are assured that the contact line behavior lies within domain 4 describing the case of intermediate pinning. If we note e the electrode width and n the number of dents, we find the following relation for the dimensions of the crenellated electrodes [28]:

$$\frac{\lambda - \delta}{2} = \eta > \left[\frac{\theta_2}{\theta_1} - 1 \right] \frac{e}{2\pi n}. \quad (5.36)$$

Equation (5.36) can be written under the form

$$\lambda > \delta + \left[\frac{\theta_2}{\theta_1} - 1 \right] \frac{e}{\pi n}. \quad (5.37)$$

In dimensionless form

$$\frac{\lambda}{e} > \frac{\delta}{e} + \left[\frac{\theta_2}{\theta_1} - 1 \right] \frac{1}{\pi n}. \quad (5.38)$$

For aqueous liquids, typical values of the quantities appearing in Eq. (5.38) are: $\theta_1 = 80^\circ$, $\theta_2 = 110^\circ$, $e = 800 \mu\text{m}$, and $\delta = 20 \mu\text{m}$. The ratio λ/e as a function of the number of dents/peaks is given in Table 5.2.

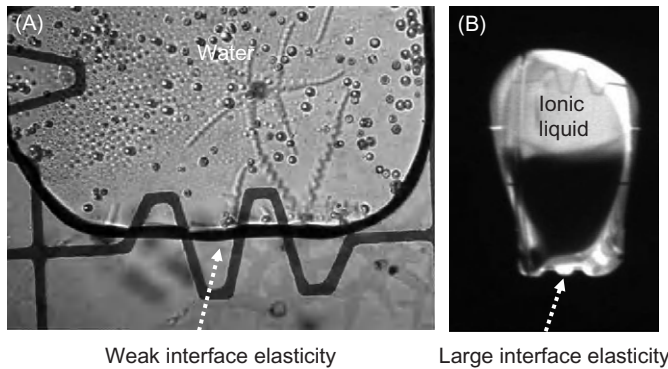
We note that the values of Table 5.2 are somewhat overestimated since we have considered the most unfavorable value $\theta_0 = \theta_1$. The reality is probably closer to $\theta_0 = (\theta_1 + \theta_2)/2$, so that Eq. (5.38) can be written as

$$\frac{\lambda}{e} > \frac{\delta}{e} + \left[\frac{\theta_2 - \theta_1}{\theta_2 + \theta_1} \right] \frac{1}{\pi n}. \quad (5.39)$$

Figure 5.22 shows the positions of the interface of a water droplet (A) and an ionic liquid droplet (B) on a jagged electrode. Ionic liquids are most of the time used in chemical applications, and the physical behavior of such liquids will be detailed in Chapter 10, dedicated to chemical applications of EWOD. In both cases, the interface location corresponds to domain 4 in Figure 5.20 (intermediate anchoring); in the case of water, the interface is slightly distorted by the

Table 5.2 Dimension of the Dents as a Function of the Number of Dents ($\theta_1 = 80^\circ$, $\theta_2 = 110^\circ$, $e = 800 \mu\text{m}$, and $\delta = 20 \mu\text{m}$)

Number of Dents	1	2	3	4	5	6
$\lambda (\mu\text{m})$	115	68	52	44	39	36
λ/e	0.14	0.08	0.06	0.05	0.045	0.04

**FIGURE 5.22**

(A) View of a water droplet interface on a jagged boundary showing a very rigid interface. The dimensions of the dents are approximately $130\text{ }\mu\text{m}$ for an electrode size of $800\text{ }\mu\text{m}$, which is largely above the threshold of $68\text{ }\mu\text{m}$ predicted by the elasticity theory and (B) view of an ionic liquid droplet: the interface at the bottom of the photograph is distorted by the presence of the dents showing a large elasticity of the interface.

Source: *Photograph courtesy Ph. Dubois, CEA-LETI.*

crenulated shape of the electrodes; this is not the case for ionic liquids, for which the interface is close to total pinning. The results of the theory can be extended to larger values of ηq because the only morphology of interest in our case is morphology 4 (Figure 5.20). For a given wave vector q , if the amplitude η is such that ηq satisfies Eq. (5.35) and $\eta q \ll 1$, a larger value of η will also produce a partial pinning situation.

5.3.3.4 Examples of jagged electrode designs

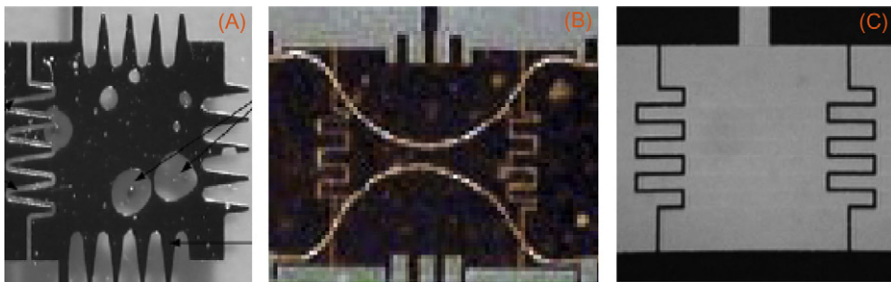
In the literature, many examples of crenulated electrodes can be found. We examine the value of the function

$$G(\lambda/e, \delta, n) = \frac{\lambda/e}{(\delta/e) + [(\theta_2/\theta_1) - 1](1/\pi n)} \quad (5.40)$$

which must be larger than 1 according to Eq. (5.38). We set the values of the contact angles $\theta_1 = 80^\circ$ and $\theta_2 = 110^\circ$ corresponding approximately to water on Teflon.

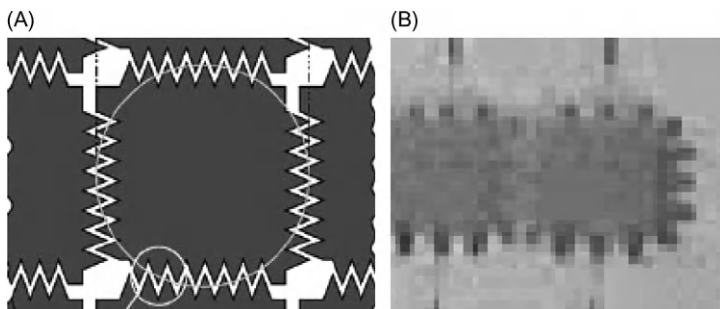
Our first example is that of the electrode design by Duke University [29] shown in Figure 5.23A. In this geometry, the peaks/dents are very pronounced and we have $\lambda/e \sim 0.25$, $\delta/e \sim 1/30$, and $n = 4$. Substituting these values in Eq. (5.40), we find $G \sim 3.2$.

The second example is that of the UCLA EWOD microsystem [4,30] shown in Figure 5.23B. In such a case, the value of the function $G \sim 1.5$. The third

**FIGURE 5.23**

Jagged electrode designs from Duke University (A), UCLA (B), and Pohang University (C).

Source: Reused with permission from Ref. [28] © 2005, American Institute of Physics.

**FIGURE 5.24**

Jagged electrode design from IMTEK (A) and IEMN (B).

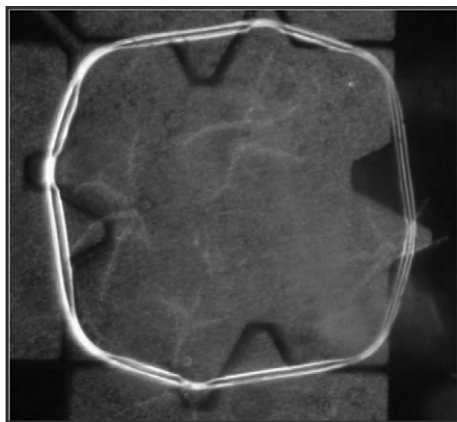
Source: Reused with permission from Ref. [28] © 2005, American Institute of Physics.

example is that of the Pohang University microsystem (Figure 5.23C) [13]; for this system, we find $G \sim 3.1$.

Another example is that of the EWOD microsystem of Figure 5.24 designed by IMTEK [31]. In this case, the value of the function G is approximately equal to $G \sim 1.4$. The design of IEMN [32] in Figure 5.24 corresponds to a value $G \sim 1.3$. We finally take the example of EWOD microsystems designed by LETI to displace biologic liquids and blood droplets (Figure 5.25) [33]. The values of the function G are approximately 3 and 1.4.

The values of G for the different systems are compared in Table 5.3. We verify that in all cases the function G is larger than 1, and condition (5.38) is satisfied.

Some of the values of G in Table 5.3 are close to 1. However, there is probably a safety margin due to the fact that the values in Table 5.3 would have been larger if we had used Eq. (5.39) instead of Eq. (5.38).

**FIGURE 5.25**

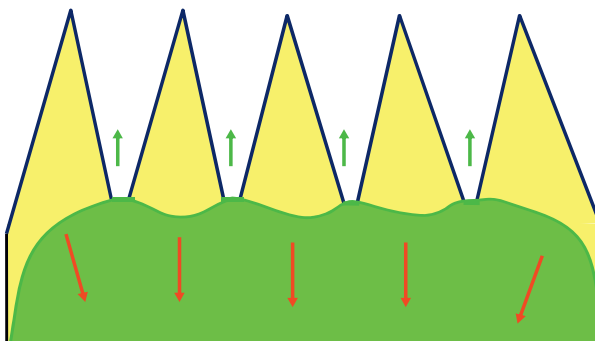
Jagged electrode design by the CEA/LETI.

Table 5.3 Approximate Values of the Function G for Different EWOD Microsystems

Institute	Value of G
Duke University	3.2
UCLA	1.5
Pohang University	3.1
IMTEK	1.4
IEMN	1.3
LETI 1	3
LETI 2	1.4

5.3.3.5 Discussion

The theory of elasticity of the triple line has been used to derive a geometrical condition for the dimensioning of the dents of jagged electrodes in EWOD microsystems. This condition states that the nondimensional ratio of the dent length to the dent width should be sufficiently large, larger than a threshold defined by the actuated and nonactuated contact angles. We have confirmed that this criterion is obeyed by the different electrode designs found in the literature. As a matter of fact, it was found that smaller dents would still have performed satisfactorily for water on Teflon. However, a safety margin is required for the use of combinations of liquids other than water/air systems, particularly for the case in which there is a larger difference between the actuated and equilibrium contact angles, e.g., water/oil or biological buffer/air systems.

**FIGURE 5.26**

Small overlapping of the contact line in the case of a large wave vector.

An interesting aspect of the geometrical condition derived here concerns the scale down of EWOD microdevices. The current approach is to homothetically scale down the size of the electrode and that of the dents; however, we anticipate that reducing the gap size by the same ratio as the reduction in electrode dimension will prove to be difficult. The condition derived here indicates that this effect could be partly compensated by increasing the numbers of dents. However, there is a limit to that increase: a large wave vector, i.e., a small wave length, is likely to result in a smaller length of the contact line overlapping the neighboring electrode (Figure 5.26); in such a case, according to Eq. (5.28), the electrowetting force at the onset of actuation may be small and not sufficient to overcome hysteresis and/or pinning.

As a consequence, the scale down of EWOD microsystems will require high performances of the microfabrication process in order to eliminate, as much as possible, the surface defects and to decrease the gap dimension.

5.3.3.6 Numerical simulation—analysis of the forces

As shown in the preceding section, the effect of jagged electrodes is to maintain a portion of the triple line overlapping the neighboring electrodes. Figure 5.27 shows a comparison between an experimental image of a droplet located on an actuated jagged electrode and the numerical modeling of the same droplet obtained with the numerical software Surface Evolver.

The action of the dents on the triple line appears clearly: the tips of the dents push the triple line outward, whereas the holes pull the triple line inward, resulting in an overlapping of the triple line on the neighboring electrodes. The interface adopts a position that minimizes the surface energy, so that the contact line seems to have a sort of tension that stretches it. This tension does not result from the line tension but on the constraints on the whole liquid–air interface. The numerical program Evolver, for instance, calculates the shape of the surface

according to the energy minimization principle and incorporating the Young's constraints on the contact line.

[Figure 5.27](#) corresponds to a completely static problem and [Figure 5.28](#) to a quasi-static problem (the motion of the droplet is just starting). In [Section 5.3.3.1](#), we have shown that the electrowetting force at the onset of motion is proportional to the transversal length of the triple line located on the actuated electrode. The portion of the contact in the actuated region pulls the contact line in the forward direction, whereas the portion on the nonactuated region pulls in

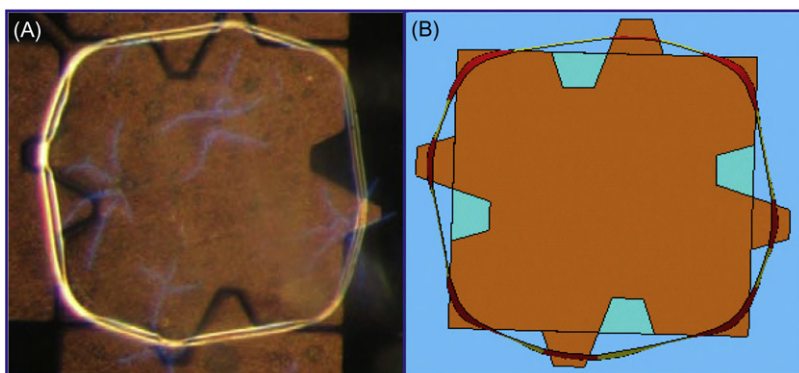


FIGURE 5.27

Comparison of the contour of the droplet between an experimental view (A) and a numerical simulation with Evolver software (B).

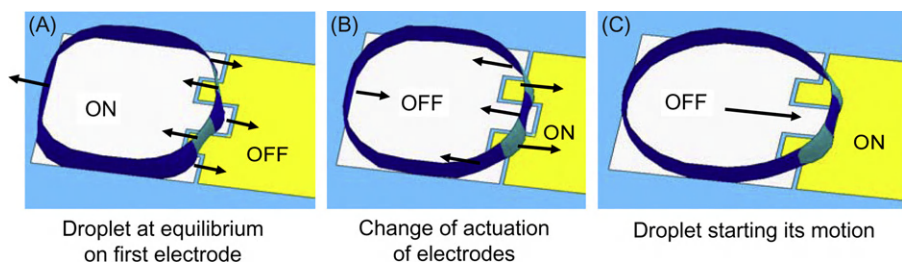


FIGURE 5.28

Numerical modeling of the motion of a droplet in a cover EWOD system with dented electrodes. The top cover has been dematerialized for clarity. (A) The droplet is at equilibrium, maintained on the first electrode. (B) The actuation has been shifted, and the resulting force on the droplet pulls the right triple line toward the second electrode. (C) The droplet accelerates its motion as soon as a large part of the triple line has reached the actuated electrode.

the other direction. The numerical simulation shows in detail how a droplet overlapping the neighboring jagged electrode starts its motion (Figure 5.28).

5.3.4 Motion from a covered to an open EWOD system

We have seen at the beginning of this chapter that two different types of EWOD microsystems have been developed: covered systems where the droplets are confined between two plates and open systems where the sessile droplet is sitting freely on a horizontal solid substrate. Each of these systems has its own advantages. We will show later that drop dispensing and splitting are easier in covered EWOD systems, whereas mixing and evaporation (for species concentration) are preferably performed in the open configuration [5,34]. Thus, the concept of a dual open/covered EWOD microsystem has been developed [6]. This concept relies on the fact that motion between a covered and open region—and backward—is possible under electrowetting actuation. In this section, we analyze the possibilities of such a motion. The approach is performed in three steps. First, we use the Surface Evolver software [8] to model the displacement of the droplet from one region to the other. This simplified model assumes that the capillary and electrowetting forces are dominant over inertial and viscous forces (i.e., the Weber and the Ohnesorge numbers are small). Second, from the Evolver results, and using Laplace's law, we deduce a very simple condition for droplet motion. Finally, we show a comparison between experimental results and the results of the model.

First, we note that the Weber and the Ohnesorge numbers are small. Hence, the electrowetting effect is considered equivalent to an electrocapillary effect according to Lippmann–Young's law

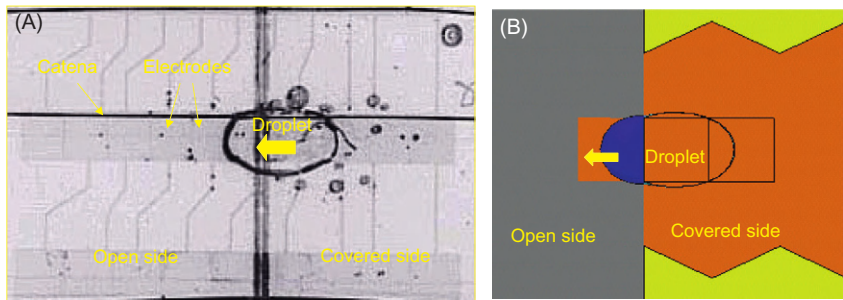
$$\cos \theta - \cos \theta_0 = \frac{C}{2\gamma_{LG}} V^2, \quad (5.41)$$

where C is the capacitance (per unit area) of the dielectric layers, V is the electric potential, and θ and θ_0 are the actuated and nonactuated contact angles, respectively.

It has been shown that the minimization theory correctly predicts microdrop behavior under electrowetting conditions [5]. As mentioned in Chapter 1, the Surface Evolver numerical program can be used to perform the minimization of the droplet surface energy under the Lippmann–Young's conditions [35]

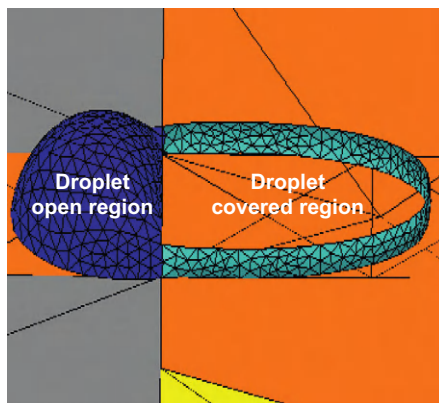
$$E = \gamma_{LG} S_{LG} - \gamma_{LG} \int_{S_{SL}} \int \cos \theta \, dA. \quad (5.42)$$

Typical features of water droplet motion calculated by the minimization approach are shown in Figure 5.29B and compared to experimental results (Figure 5.29A). A close-up view of the crossing of the covered/open boundary is shown in Figure 5.30.

**FIGURE 5.29**

(A) Experimental view of a droplet crossing the frontier between the covered region and the open region. The drop moves from right to left. (B) Same motion predicted by a quasi-static approach using Surface Evolver software.

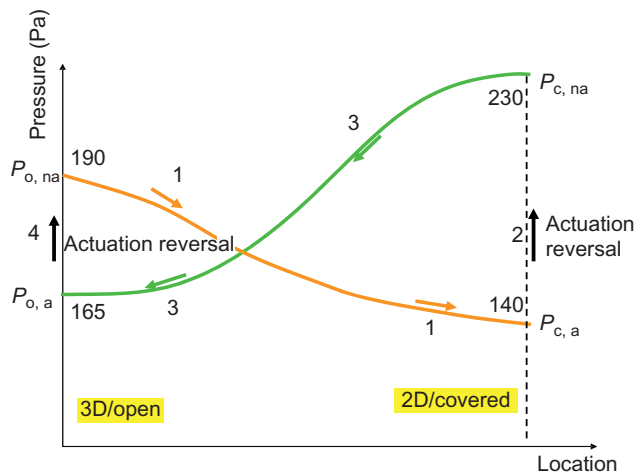
Source: From Ref. [6] © NSTI 2006, reprinted with permission.

**FIGURE 5.30**

Close-up view of the droplet crossing the covered/open boundary (the upper plate of the covered region has been dematerialized for clarity).

Source: From Ref. [6] © NSTI 2006, reprinted with permission.

Figure 5.41 shows the general pressure evolution in the droplet during a cycle. A cycle is defined by motion from the open region (noted 3D/open) to the covered region (noted 2D/covered) and back. Suppose that the droplet is initially in the 3D/open region (top left, Figure 5.31), with the electrodes in this region not actuated. Upon actuation of the electrodes in the 2D/covered region the droplet leaves its initial location and moves towards the 2D/covered region. When it has crossed the boundary and is located in the 2D/covered region (bottom right), the actuation is switched off and the droplet's internal pressure suddenly increases (top right). The actuation in the 3D/open region is then switched on and the

**FIGURE 5.31**

Droplet internal pressure during a cycle: the motion of the droplet corresponds to a decrease in pressure. Increase in pressure is obtained by suppressing the electric actuation when the droplet is on either side of the device. The two different curves correspond to the two configurations of covered EWOD devices, with or without electrodes in the upper cover.

droplet moves back to this latter region. When the droplet is entirely located in the 3D/open region (bottom right), the actuation is switched off and the droplet recovers its initial conditions.

This analysis leads to the conclusion that a motion from one region to the other is accompanied by a monotonous decrease in pressure. The condition for the motion from open to covered region is

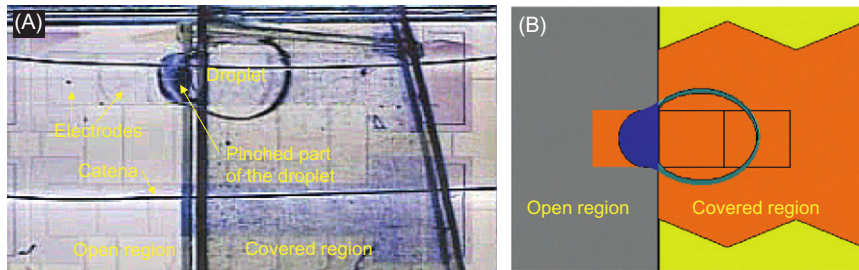
$$P_{\text{open,nonactuated}} > P_{\text{covered,actuated}} \quad (5.43)$$

and conversely, for the motion from covered to open region

$$P_{\text{covered,nonactuated}} > P_{\text{open,actuated}}. \quad (5.44)$$

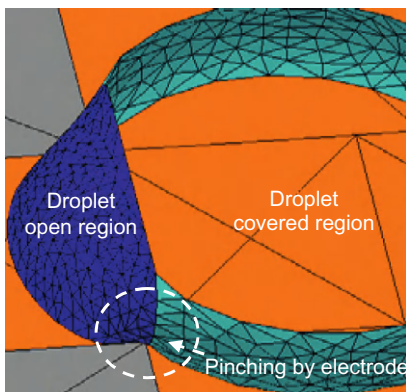
Note that if the covered region has electrodes embedded in its top and bottom plates, i.e., actuation can be switched on in both plates, the crossing toward the covered region is facilitated (dashed line in Figure 5.41).

However, there exists an exception to the rule stated by inequalities (Eqs. (5.43) and (5.44)). If the drop volume is too large compared to the electrode size, i.e., the droplet overfills the corresponding electrode volume, blockage of the drop due to a pinching effect may occur during the motion from covered to open configuration (Figures 5.32 and 5.33). This case corresponds to a non-monotonous pressure curve. This drawback can easily be avoided by increasing the width of the electrodes at the transition region.

**FIGURE 5.32**

(A) Experimental view of a droplet blocked on the covered/open boundary by pinching effect on the open region electrode. (B) Same situation predicted by Surface Evolver calculation.

Source: From Ref. [6] © NSTI 2006, reprinted with permission.

**FIGURE 5.33**

Close-up view of the droplet blocked the covered/open boundary due to a pinching effect provoked by a narrow electrode (the upper plate of the covered region has been dematerialized for clarity).

Source: From Ref. [6] © NSTI 2006, reprinted with permission.

Droplet pressure in each region can be calculated by using Laplace's law. First, for a drop of volume V , confined between two horizontal plates separated by a distance δ , internal pressure is given by

$$P_C = \gamma_c \left(\frac{-\cos \theta_t - \cos \theta_b}{\delta} + \sqrt{\frac{\pi \delta}{V}} \right), \quad (5.45)$$

where θ_t and θ_b are the contact angles with the top and bottom plates, respectively and γ_c the surface tension in the covered region—which can be different from

that of the open region γ_o depending on the surrounding fluid (oil or air). In Eq. (5.45), the first term of the right-hand side corresponds to the vertical curvature, and the second term to the horizontal curvature. For a sessile drop of same volume (3D/open configuration), we obtain, again using Laplace's law

$$P_O = 2\gamma_o \left(\frac{3V}{\pi(2 - 3 \cos \theta + \cos^3 \theta)} \right), \quad (5.46)$$

where θ is the contact angle with the substrate. We are then left with two conditions derived from Eqs. (5.43) and (5.44); the first one is for the motion from the open to covered region

$$P_O(\theta = \theta_0) - P_C(\theta_b = \theta_a) \geq 0.$$

So that

$$2\gamma_o \left(\frac{3V}{\pi(2 - 3 \cos \theta_0 + \cos^3 \theta_0)} \right)^{-\frac{1}{3}} - \gamma_c \left(\frac{-\cos \theta_a - \cos \theta_t}{\delta} + \sqrt{\frac{\pi \delta}{V}} \right) \geq 0. \quad (5.47)$$

And, the second one is for the opposite motion

$$P_C(\theta_b = \theta_0) - P_O(\theta = \theta_a) \geq 0$$

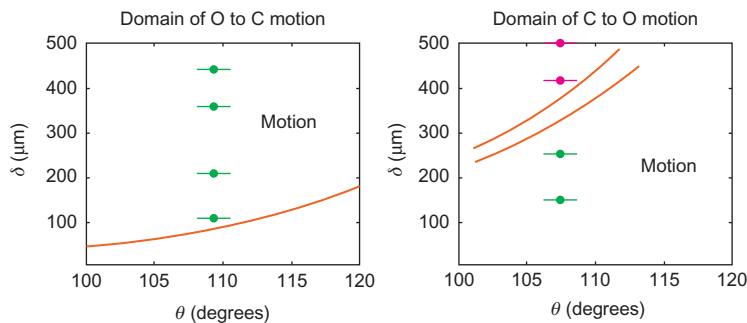
So that

$$2\gamma_o \left(\frac{3V}{\pi(2 - 3 \cos \theta_a + \cos^3 \theta_a)} \right)^{-\frac{1}{3}} - \gamma_c \left(\frac{-\cos \theta_0 - \cos \theta_t}{\delta} + \sqrt{\frac{\pi \delta}{V}} \right) \leq 0, \quad (5.48)$$

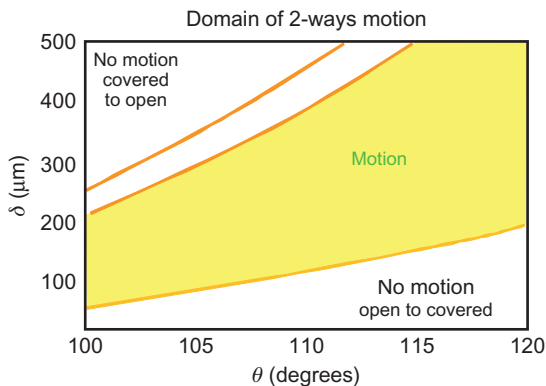
where θ_0 is the nonactuated contact angle with the solid substrate and θ_a the actuated contact angle.

Experiments have been performed on standard EWOD chips (Figures 5.29 and 5.32). The electrodes are $800 \mu\text{m} \times 800 \mu\text{m}$. Different conditions have been tested: the water droplet can be surrounded by air ($\gamma = 72 \text{ mN/m}$) or by silicone oil ($\gamma = 33 \text{ mN/m}$), and the height of the vertical gap in the covered region can take the values 110, 200, 360, or $450 \mu\text{m}$. The zero potential electrode is provided by a catena that runs all along the electrode row, just below the level of the upper plate. The nonactuated contact angle is close to 113° for water/air, and electric potential was chosen so that the actuated contact angle is 80° (potential value close to 60 V). It has been found that the contact angle on the upper plate of the covered region is a very important parameter of the problem, as shown in Figure 5.34.

Figure 5.34A shows that the motion from open to covered region is not possible if the vertical gap is too small: the counterpressure in the covered region is then too large and Eq. (5.47) is not satisfied. Motion in the reverse direction is not possible if the gap is too large, i.e., Eq. (5.48) is not satisfied because the driving pressure in the covered region is too small. There is a domain where both motions are always possible. This domain is shown in Figure 5.35. It appears immediately that this domain is sufficiently large to leave room to build a component where back and forth motions are possible.

**FIGURE 5.34**

(A) Conditions for water droplet motion (in air) from open to covered EWOD configuration.
 (B) Conditions for droplet motion from covered to open EWOD configuration. Vertical scale “Delta” is the vertical gap in the covered region and the horizontal scale is the contact angle θ_t on the upper plate in the covered region. Continuous lines correspond to the analytical model—[Eqs. \(5.47\) and \(5.48\)](#); they separate the domain where motion is possible from the domain where motion is impossible. Dots are the experimental results. Circle dots correspond to observed drop motion from one configuration to the other, while square dots signify that the motion was not obtained. The different continuous lines correspond to different nonactuated contact angle values θ_0 (bottom plate).

**FIGURE 5.35**

Superposition of the two previous figures: the domain for which the motion is possible both ways is the gray region comprised between the red lines. (For interpretation of the references to color in this figure legend, the reader is referred to the web version of this book.)

From this analysis, it has been shown that the motion from an open to a covered region of an EWOD microdevice—and conversely—is closely related to the difference of drop internal pressure between the departing and the arriving regions. Electrodes at the covered/open region boundaries must be adequately

designed in function of the liquid droplet volume; they should not be too narrow in order to avoid a pinching effect resulting in stopping the motion.

For a droplet of water in air, motion from open to covered region is possible provided that the vertical gap in the covered region is not too small, and motion from covered to open region is possible if the vertical gap is not too large. Contact angle with the upper plate θ_t is an important parameter of the motion; below 90° the droplet will have difficulties exiting the covered region toward the open region due to hydrophilic grip on the upper plate; above 120° , the motion toward the covered region will be increasingly difficult due to hydrophobic repulsion on the upper plate. There is an important dimension for a component where both motions are easily possible. A vertical distance of about $200\text{ }\mu\text{m}$ seems to work well for buffer liquid drops of $0.1\text{--}0.5\text{ }\mu\text{L}$ on Teflon substrate and electrodes of $800\text{ }\mu\text{m} \times 800\text{ }\mu\text{m}$.

5.3.5 Effect of a catena

The effect of a catena has been treated in Section 3.2.8. We just recall here that the catena is used as a zero potential contact for some open EWOD systems (Figure 5.36).

It has been observed that the catena modifies the behavior of the drop. In the case of a hydrophobic contact, the drop adopts a position tangential to the catena, and in the case of a hydrophilic contact, the drop wants to be positioned symmetrically on the catena. The explanation of this phenomenon is presented in Chapter 2. Figure 5.37 shows a droplet having a lyophobic contact with the catena. It is positioned tangentially to the wire. After adding surfactants, the contact becomes lyophilic and the drop moves to a position centered on the wire.

In conclusion, the position of the catena above the electrodes has to be carefully chosen depending on its wettability. A hydrophilic catena should be located above the median of the electrode row, whereas a hydrophobic catena is best located above the edge of the electrode row. A catena at a nonoptimized position can block the drop motion.

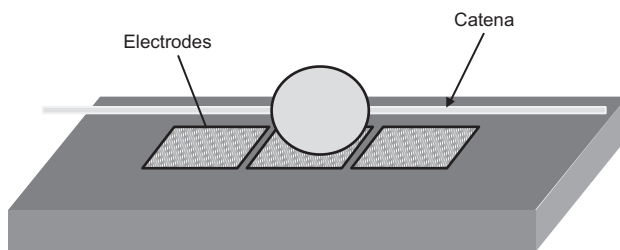
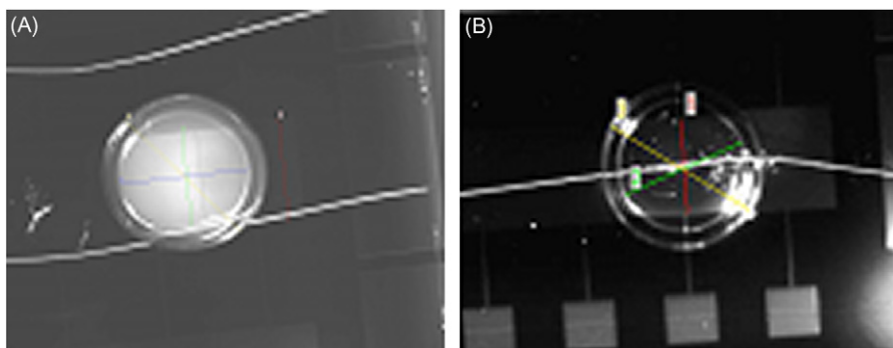


FIGURE 5.36

Schematic view of an open EWOD microsystem with catena.

**FIGURE 5.37**

(A) The microdrop is tangent to the catena due to a hydrophobic contact. (B) Catena intersects the drop in its middle when the contact is hydrophilic due to the addition of surfactants.

Source: Photograph Ph. Clementz.

5.4 Division of droplets

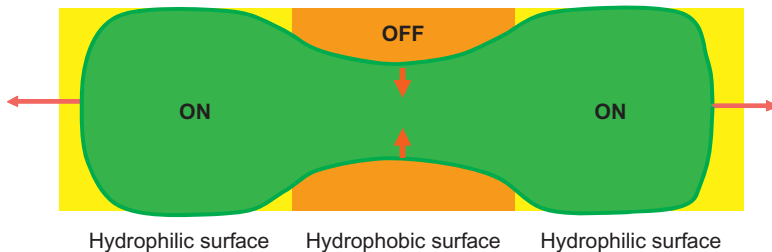
A very important operation for the digital manipulation of droplets in EWOD microsystems is the splitting, or cutting of droplets, i.e., the division of a droplet into two “daughter droplets.” This operation is needed because merging of droplets increases by two times the volume of liquid that the system must treat. Division in two half-volumes restores the possibilities of the system. Actually, together with drop dispensing this operation is the most challenging in EWOD devices.

5.4.1 Theoretical approach

The principle of droplet cutting/splitting/division is shown in Figure 5.38. The liquid is first stretched or elongated by two actuated electrodes at both ends of the droplet, creating two lyophilic (hydrophilic) areas with electrocapillary forces pulling in opposite directions. Second, the nonactuated lyophobic (hydrophobic) electrode exerts a pinching force on the triple contact line [4.5]. Depending on the force balance and the elasticity of the interface, the droplet can be—or not—cut in two.

Splitting a drop into two same daughter drops requires an energy input which is a function of the increase in free surface. The total drop energy is the sum of the surface energies

$$E = \gamma_{LG}S_{LG} + \gamma_{SL}S_{SL}. \quad (5.49)$$

**FIGURE 5.38**

Drop division: scheme of the forces on the contact line; the principle is to apply a stretching force in one direction combined with a pinching force in the other direction.

Considering a sessile drop of volume V and its division in two smaller sessile drops, it can easily be shown that the division of a spherical drop (open system) corresponds to the relative energy input of

$$\frac{\Delta E}{E} = 2^{1/3} - 1 \approx 0.26, \quad (5.50)$$

whereas the division of a drop of radius a , confined between two plates separated by a distance δ , requires a relative energy increase of

$$\frac{\Delta E}{E} \approx \frac{(\sqrt{2} - 1)}{\sqrt{2}(1 + (\gamma_{SL}a/\gamma_{LG}\delta))}. \quad (5.51)$$

Since $a \gg \delta$ and $\gamma_{SL} > \gamma_{LG}$, the denominator of Eq. (5.51) is much larger than 1, and we find that it requires much less energy to cut a droplet into the covered EWOD configuration

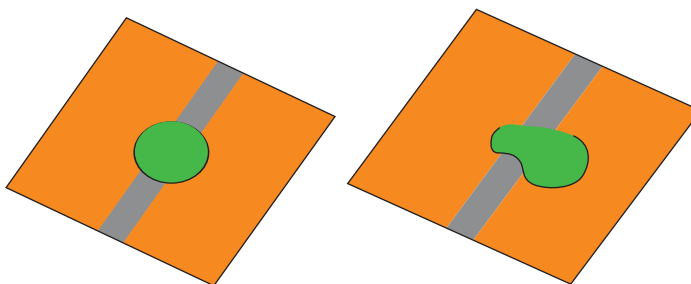
$$\left. \frac{\Delta E}{E} \right|_{\text{covered}} \ll \left. \frac{\Delta E}{E} \right|_{\text{open}}. \quad (5.52)$$

Indeed, it is experimentally checked that the division of a sessile water droplet is impossible by electrowetting actuation, whereas this operation is feasible in covered EWOD microsystems.

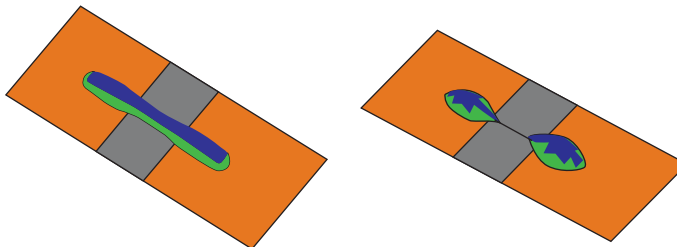
5.4.2 Droplet division in open EWOD systems

Numerical results confirm the experimental impossibility of splitting sessile water droplets with EWOD. The electrowetting forces are not large enough to elongate the droplet sufficiently. Figure 5.39 shows that the droplet does not elongate significantly and squirts randomly to the side.

Furthermore, numerical simulations show that, in an open EWOD configuration, a drop can be split if it has been previously elongated by other means (Figure 5.40).

**FIGURE 5.39**

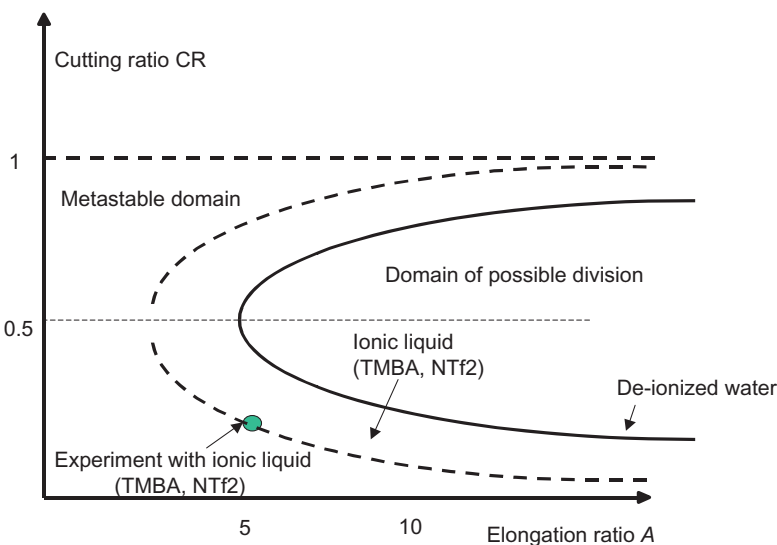
A spherical drop cannot be split; it just escapes to any one of the two hydrophilic regions.

**FIGURE 5.40**

Division of an initially stretched droplet predicted by the Evolver numerical software.

From all the liquid that we have tested, it appears that only ionic liquids may be split in an open system EWOD, because they have very small contact angles with the actuated electrodes and their elasticity is larger than that of aqueous liquids.

Drop division potentially depends on two dimensionless parameters: the initial elongation ratio A between drop length and drop width and the “cutting” ratio CR between pinching length and initial drop length. The domain of possible splitting is plotted in Figure 5.51 for two very different liquids. For the usual buffer liquid (continuous line), with a surface tension $\gamma_{LG} = 70 \text{ mN/m}$ and hydrophilic and hydrophobic contact angles of 70° and 115° , the optimal “cutting” ratio is $CR = \frac{1}{2}$ and the elongation required is $A > 5$. An “open” water droplet has to be stretched at least on five electrodes to be split by electrowetting. The domain where splitting is possible depends on the values of the contact angles and on the elasticity of the interface. In Figure 5.41, the dotted line corresponds to an ionic liquid with 60° and 93° contact angles.

**FIGURE 5.41**

Domain of possible drop division for open EWOD systems obtained by a series of Evolver calculations. Continuous line: DIW with contact angles 70° and 115° and surface tension 70 mN/m. Dotted line: ionic liquid with contact angles 60° and 93° and surface tension 40 mM/m.

5.4.3 Droplet division in covered EWOD systems

It has been experimentally and numerically checked that droplet division is easier in covered EWOD systems. We follow here the theoretical approach to droplet division in covered EWOD systems proposed in Ref. [36].

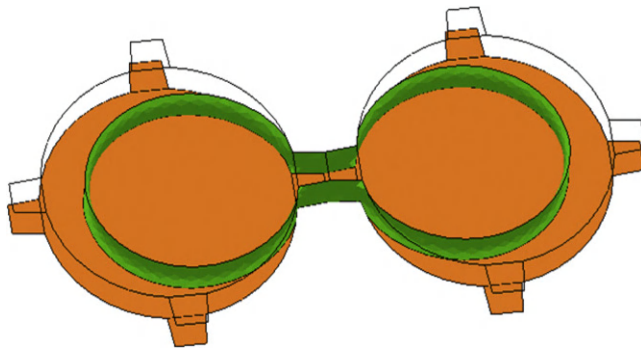
5.4.3.1 Stretching

The first idea that comes to mind is to stretch the droplet by capillary forces, in order to elongate a filament that will eventually break. Then, the question is reduced to: can a droplet be cut by exerting capillary traction forces on two ends?

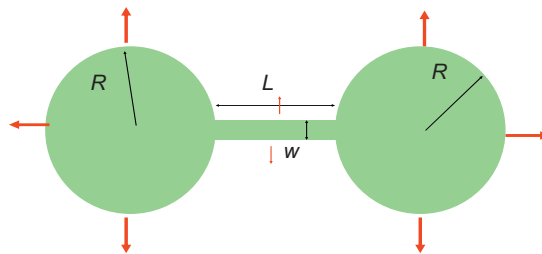
Let us start with the artificial situation where a partial splitting has already occurred, in order to facilitate the splitting. The droplet is then supposed divided in two regions linked by a large thread (Figure 5.42).

Because the liquid wets the two substrates (bottom and top plates), capillary forces are exerting traction on the wetted perimeter of the droplet, as shown in Figure 5.43.

Let us follow first a theoretical approach which makes use of the free energy: The total surface energy is given by Eq. (5.49).

**FIGURE 5.42**

Sketch of a droplet placed between wetting walls, “artificially” stretched in two regions. The cover plane has been dematerialized for visualization.

**FIGURE 5.43**

Schematic of the initial droplet.

Let us make the approximation that the free interfaces are flat. We have the notations shown in [Figure 5.43](#)

$$S_{SL} = 2(2\pi R^2 + Lw) \quad (5.53)$$

and

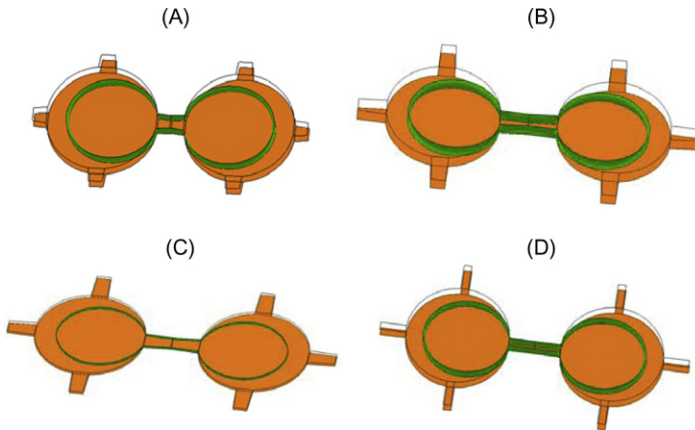
$$S_{LG} = 2h(2\pi R + L). \quad (5.54)$$

Moreover, the liquid volume is

$$\text{Vol} = hS_{SL}. \quad (5.55)$$

If there is no evaporation, [Eq. \(5.55\)](#) implies that

$$d\text{Vol} = h dS_{SL} = 0. \quad (5.56)$$

**FIGURE 5.44**

Splitting cannot be obtained by varying the different parameters: (A) small L , (B) longer L , (C) small h , and (D) small w .

Then, using Eq. (5.49)

$$dE = \gamma_{LG} dS_{LG}. \quad (5.57)$$

Using Eq. (5.54), and remarking that L is constant, we find

$$dE = 4\pi\gamma_{LG}h dR \quad (5.58)$$

and

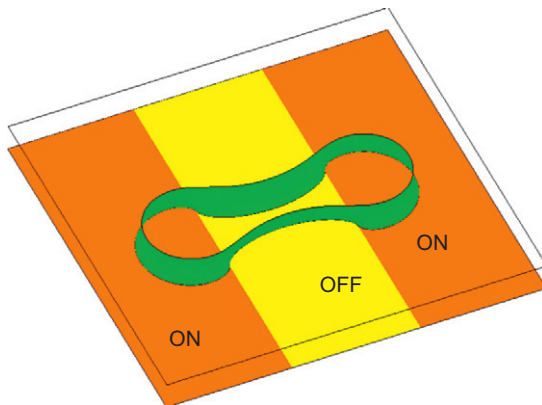
$$\frac{dE}{dR} = 4\pi\gamma_{LG}h > 0. \quad (5.59)$$

The droplet evolves to find its minimum energy morphology. Relation (5.59) indicates that the liquid filament cannot shrink—i.e., R cannot increase—because an increase of R would increase the energy E . Hence, the droplet cutting is not possible by exerting capillary forces on the two ends.

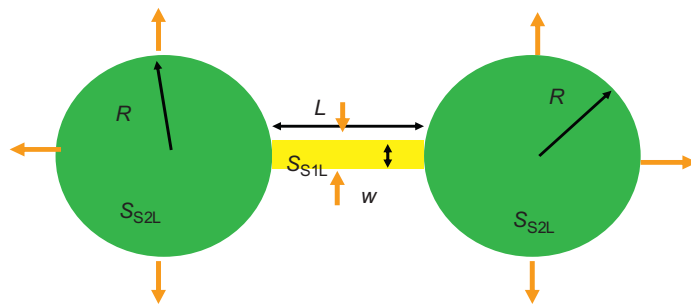
We have numerically checked this analysis with Surface Evolver. The starting point is a droplet split in two circular regions and linked by a thread (Figure 5.44). Using many different values of the parameters like h , L , w , or R cutting was never obtained.

5.4.3.2 Stretching and pinching

Stretching the droplet is not sufficient to achieve splitting. Let us consider now an additional capillary force which is the pinching of the droplet. The question is then: can a droplet be cut by exerting capillary traction forces on two ends and a pinching in the middle? Figure 5.45 represents a droplet placed between two horizontal

**FIGURE 5.45**

Sketch of the droplet pinched in the middle and stretched by the two ends. The cover plate has been dematerialized for visualization. Note that the cover plate is neutral ($\theta = 90^\circ$); hence, only the capillary forces on the bottom plate contribute to the splitting.

**FIGURE 5.46**

Schematic view of the droplet with the pinching in the thread region.

planes, with two hydrophilic (lyophilic) regions at both ends and a hydrophobic (lyophobic) region in the middle. In EWOD systems, such an action is obtained by actuating the two end electrodes and not actuating the middle electrode.

The sketch of the capillary forces is shown in [Figure 5.46](#). The hydrophilic regions tend to stretch the droplet, while the hydrophobic region pinches the middle of the droplet.

Let us follow a theoretical approach based on the free energy minimization. The total surface energy is

$$E = \gamma_{S1L} S_{S1L} + \gamma_{S2L} S_{S2L} + \gamma_{LG} S_{LG}, \quad (5.60)$$

using the same notations as above, and where the indices 1 and 2 denote respectively the pinched and rounded regions of the liquid. In the case of EWOD, the actuated solid–liquid surface tension is $\gamma_{S2L} = \gamma_{SL}^{\text{eff}}$. Let us make the approximation that the free interfaces are flat. We have the notations shown in [Figure 5.46](#)

$$S_{S1L} = 2Lw \quad (5.61)$$

and

$$S_{S2L} = 2(2\pi R^2). \quad (5.62)$$

However, the liquid–gas surface area is

$$S_{LG} = 2h(2\pi R + L). \quad (5.63)$$

Besides the liquid volume is

$$\text{Vol} = hS_{SL} = h(S_{S1L} + S_{S2L}). \quad (5.64)$$

If there is no evaporation, [Eq. \(5.64\)](#) implies that

$$d\text{Vol} = dS_{S1L} + dS_{S2L} = 0. \quad (5.65)$$

Differentiating [Eq. \(5.63\)](#) yields

$$dE = \gamma_{S1L} dS_{S1L} + \gamma_{S2L} dS_{S2L} + \gamma_{LG} dS_{LG}. \quad (5.66)$$

Using [Eq. \(5.65\)](#), we find

$$dE = (\gamma_{S2L} - \gamma_{S1L})dS_{S2L} + \gamma_{LG} dS_{LG} \quad (5.67)$$

and remarking that L is constant, but w and R vary,

$$dE = (\gamma_{S2L} - \gamma_{S1L})8\pi R dR + \gamma_{LG} 4\pi h dR. \quad (5.68)$$

And finally,

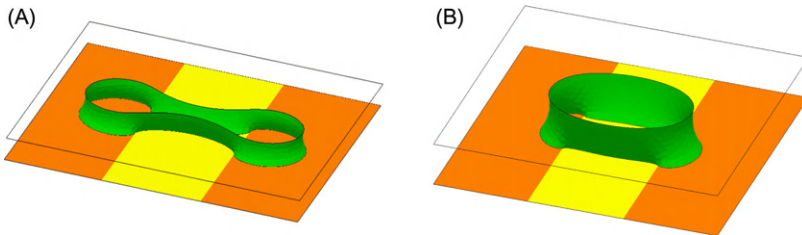
$$\frac{dE}{dR} = 4\pi [2R(\gamma_{S2L} - \gamma_{S1L})] + \gamma_{LG} h. \quad (5.69)$$

The comparison to [Eq. \(5.59\)](#) shows that there is now an additional term on the right-hand side of [Eq. \(5.69\)](#). This time, the sign of dE/dR can be positive or negative depending on the values of the parameters. In order to have splitting, the free energy E must decrease when the radius R increases: $dE/dR < 0$. The condition for splitting is then

$$h < \frac{2R(\gamma_{S1L} - \gamma_{S2L})}{\gamma_{LG}}. \quad (5.70)$$

Lipmann's law states that electrowetting changes the value of the solid–liquid surface tension $\gamma_{S2L} = \gamma_{S2L}^{\text{eff}}$ (see preceding chapter). Using the capillary equivalence for electrowetting, with region 2 actuated and region 1 not actuated,

$$\begin{aligned} \cos \theta_0 &= \frac{\gamma_{S1G} - \gamma_{S1L}}{\gamma_{LG}} \\ \cos \theta_a &= \frac{\gamma_{S2G} - \gamma_{S2L}^{\text{eff}}}{\gamma_{LG}}. \end{aligned} \quad (5.71)$$

**FIGURE 5.47**

Splitting is achieved when h is small (A) but not when h is sufficiently large (B).

By difference, and using the equality $\gamma_{S1G} = \gamma_{S2G}$, we obtain

$$\cos \theta_a - \cos \theta_0 = \frac{\gamma_{S1L} - \gamma_{S2L}^{\text{eff}}}{\gamma_{LG}}. \quad (5.72)$$

Substitution in the Berge–Lippmann–Young’s (BLY) equation yields the relation

$$\gamma_{S1L} - \gamma_{S2L}^{\text{eff}} = \frac{C}{2} V^2, \quad (5.73)$$

where C is the specific capacitance and V is the tension. Substituting back in Eq. (5.70) yields

$$h < 2R \frac{CV^2}{2\gamma_{LG}} = 2R\xi, \quad (5.74)$$

where ξ is the electrowetting number. Relation (5.74) shows that splitting can be achieved if the vertical gap is sufficiently small and/or the electrowetting number sufficiently high, and/or the radius R sufficiently large. The radius R being approximately of the order of the electrode dimension, EWOD systems with small vertical gaps and/or large electrodes require a smaller voltage to cut the droplet. The fact that a high value of the electrowetting number facilitates the cutting is obvious: the more the droplet is stretched at both ends while it remains pinched in the middle, the easier is the cutting.

Note that relation (5.74) can be rewritten under a nondimensional form as

$$\frac{h}{R} < 2 \frac{CV^2}{2\gamma_{LG}} = 2\xi \quad (5.75)$$

showing that the electrowetting number—in our case the voltage—can be progressively relaxed as R increases during the splitting. In other words, once the thinning of the liquid junction has started, the splitting is inevitable and goes to its end.

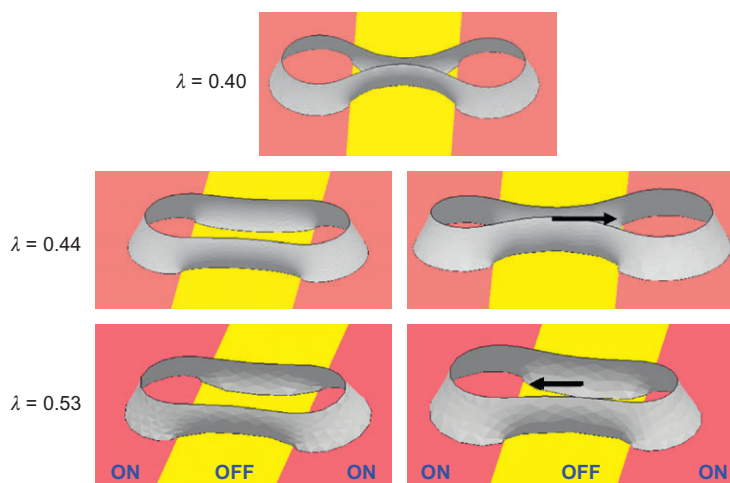


FIGURE 5.48

Division of a droplet is possible in a covered EWOD device if the ratio λ of the vertical gap and a characteristic dimension of the droplet (representing its volume) is small enough (the liquid is water and the contact angles are 80° , 120° , and 110° , respectively for the actuated, nonactuated electrodes, and cover plate). Note that for $\lambda > 0.50$ approximately, the droplet escapes laterally.

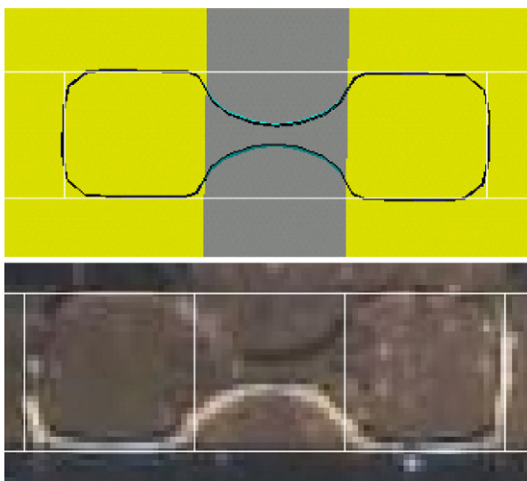
The numerical analysis confirms this theoretical approach ([Figure 5.47](#)). A droplet can be cut in two if the vertical gap between the two plates is sufficiently small. When the vertical gap h is large, no shrinking in the middle of the droplet can be achieved.

Note that if the droplet is initially located dissymmetrically relatively to the hydrophobic pinching region, the droplet can escape laterally instead of being cut, as shown in [Figure 5.48](#).

5.4.4 Experimental results

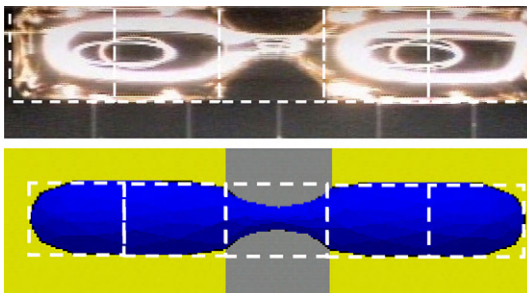
The simulation results of the preceding sections have been verified experimentally. First, for a covered EWOD microsystem ([Figure 5.49](#)) with $800 \mu\text{m} \times 800 \mu\text{m}$ electrodes and a vertical gap of $100 \mu\text{m}$, the drop is made of water and is immersed in silicone oil. At the beginning, the drop has a rounded shape and it evolves to the shape of [Figure 5.49](#) as soon as the electrodes to the left and to the right have been actuated; then the pinching process acts on the middle part of the drop until it is split into two identical “daughter drops.” Note the circular profiles in the “cutting” region due to surface energy minimization.

Second, we have used ionic liquids to show the principle of drop division after elongation in an open EWOD system. Ionic liquids have good wettability, do

**FIGURE 5.4**

Shape of drop comparison between experiment and Evolver calculation during an attempt of division of a confined drop (water in oil). In this case, the electric potential is 20 V and not sufficient to obtain drop splitting.

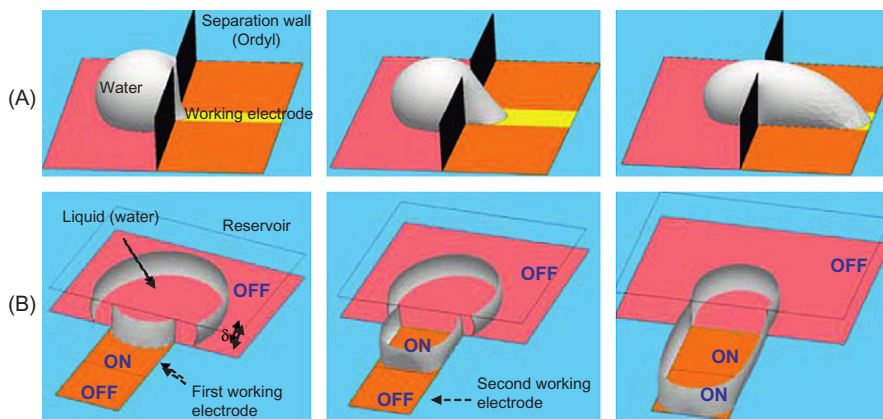
Source: From Ref. [5] © Elsevier 2006, reprinted with permission.

**FIGURE 5.5**

Comparison between experiment and Evolver calculation during the division of an ionic liquid droplet: the droplet can be sufficiently elongated and the splitting is effective.

Source: From Ref. [5] © Elsevier 2006, reprinted with permission.

not evaporate, and are used in microchemistry (see Chapter 10). The drop spreads easily on the five actuated electrodes and takes a rectangular shape, because the elasticity of the surface is large. Switching off the central electrode is sufficient to obtain the splitting of the drop (Figure 5.50).

**FIGURE 5.51**

(A) Water dispense from a reservoir is not achievable in open EWOD systems and (B) first step of drop dispense (formation of a rivulet) in a covered EWOD system. Calculations with Evolver.

5.4.5 Droplet dispensing

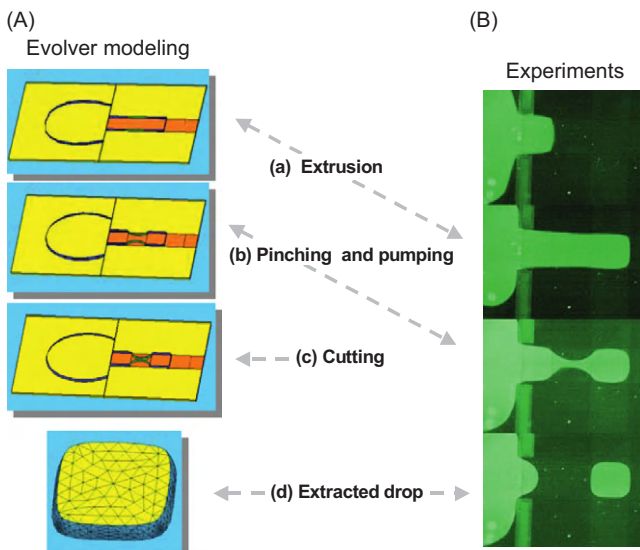
At the beginning of any EWOD process, microdrops have to be extracted from a reservoir. This step is called droplet dispensing [37–39]. In the following section, we investigate the conditions for satisfactory droplet dispensing [40].

5.4.5.1 Analysis of the dispensing mechanism

First, we observe that experimental and numerical simulations show that drop dispensing in an open EWOD system is not possible for the usual buffer fluids (aqueous solutions and biological buffers). As a consequence, we analyze the dispensing in a covered EWOD microsystem (Figure 5.51).

To be effective, dispensing is constituted by three steps:

1. Liquid extrusion from the reservoir onto the electrode row by applying an electric potential on the electrode row and by switching off the reservoir electrodes. Extrusion occurs because there is an electrowetting force driving the liquid onto the electrode row and a hydrophobic force pushing the liquid out of the reservoir.
2. A pinching effect shrinks the liquid filament at the level of the cutting electrode when the latter is switched off. This pinching effect has been analyzed in the preceding section. This pinching step is sometimes enough to separate a droplet from the reservoir, but it has been observed that a third step, called the “back pumping” step, was useful to easily extract well-calibrated droplets.

**FIGURE 5.52**

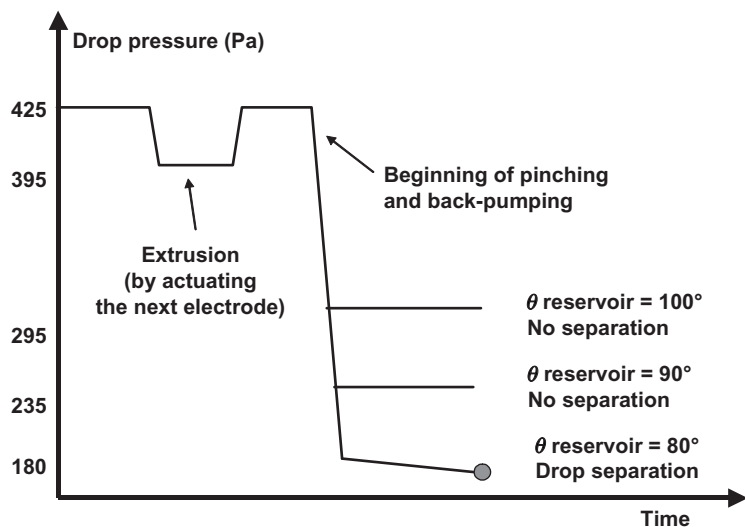
Comparison between the numerical and experimental results for drop dispensing in a closed EWOD microsystem. (A) Evolver model showing the liquid extrusion from reservoir, the pinching of the liquid rivulet, and the separation by back pumping. (B) Experimental view of the dispense.

Source: From Ref [5] © Elsevier 2006, reprinted with permission.

3. Final dispensing is obtained by “back pumping” the liquid into the reservoir after reactuation of the reservoir electrodes. The role of back pumping is to decrease the droplet pressure so that pinching becomes more effective.

It has been checked that the dispensing process is facilitated if the reservoir is separated from the processing electrodes by a solid wall made of plastic (e.g., Ordyl). Simulation results obtained with the Evolver software are very close to the experimental results (Figure 5.52) and confirm the key role of back pumping for drop dispensing. In fact, back pumping consists of switching the contact angle from a hydrophobic value—which results in pressurizing the drop—to a hydrophilic ($< 90^\circ$) or neutral ($90\text{--}95^\circ$) value in order to reduce the internal pressure. This decrease in pressure facilitates the pinching effect on the cutting electrode.

Figure 5.53 shows the time evolution of the drop internal pressure during the different phases of the extraction process. If the decrease in pressure due to back pumping is sufficient, the pinching effect on the cutting electrode becomes efficient and separation occurs.

**FIGURE 5.53**

Pressure evolution during drop dispense. Each time an electrode in the electrode row is actuated, internal pressure decreases and the drop spreads on the new electrode. When the reservoir electrode is actuated for back pumping with a contact angle of 80° , the pressure decreases to a level where the pinching effect becomes effective and drop separates ($\gamma_{LG} = 40 \text{ mN/m}$).

Table 5.4 Values of Contact Angles in the Reservoir to Obtain Dispense, as a Function of the Surface Tension

Liquids	Water + Surfactant/Oil	Water/Oil	Water/Air
Surface tension (mN/m)	20	36	72
Maximum contact angle in reservoir during back pumping ($^\circ\text{C}$)	95	94	93

Value of surface tension has nearly no effect on the dispensing.

5.4.5.2 Insensitivity to the surface tension

It is observed numerically and experimentally that the value of the surface tension has little influence on drop dispensing. Table 5.4 indicates the limit values of contact angle in the reservoir during back pumping to obtain drop dispense for different values of the surface tension, in the case of $800 \mu\text{m} \times 800 \mu\text{m}$

electrodes and a vertical gap of $100\text{ }\mu\text{m}$. The nonactuated contact angle on the cutting electrode is 120° , the value of the capacitance is $C = 20\text{ }\mu\text{F/m}^2$, and the reservoir volume is $0.9\text{ }\mu\text{L}$. The drop does not separate from the liquid of the reservoir if the contact angle is larger than the listed contact angle. The results of Table 5.4 show that, in this geometry, it is not always necessary to have hydrophilic contact angle for back pumping. Contact angles less than 94° are sufficient. However, it is best to have the smallest possible actuated contact angles if we want to dispense many drops until there remains only a very small volume of liquid in the reservoir.

The present results agree with the dispensing equation obtained in Ref. [40] linking the actuated contact angle θ_a to the dimensions and characteristics of the microsystem and showing that the surface tension does not affect the dispense possibility. We recall this equation because it bears the physics of the dispensing

$$\cos \theta_a - \cos \theta_0 = \frac{2\delta}{e} + \frac{\delta \sqrt{(\theta_w - \frac{\sin 2\theta_w}{2})}}{\sqrt{S_R}}, \quad (5.72)$$

where θ_w is the contact angle with the separation wall (Ordyl) and S_R is the contact surface of the drop in the reservoir. To the right-hand side of Eq. (5.72), the first term corresponds to the “pinching” effect and the second term to the “back pumping.” Equation (5.72) shows that the smaller the vertical gap δ , the easier the drop dispensing. It shows also that the dispensing becomes more difficult when the volume of liquid in the reservoir decreases.

5.4.5.3 Velocity field in the liquid during drop dispensing

Liquid motion during dispensing can be visualized by following the motion of particles dispersed in the liquid. Figure 5.54 shows the progression of the

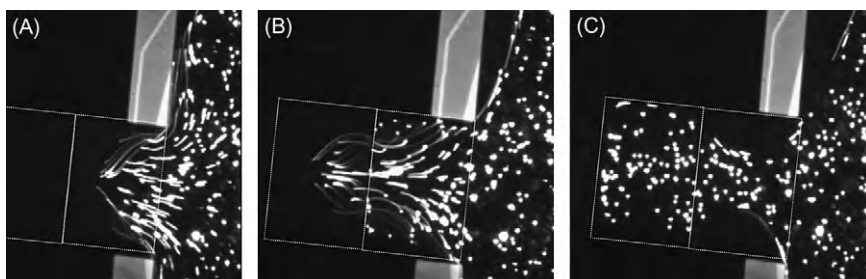


FIGURE 5.54

Visualization of the hydrodynamic motion during dispensing: the molecules in the vicinity of the interface move much faster than those in the bulk (A and B). The motion stops immediately when the extracted droplet reaches the boundaries of the actuated electrode, confirming that surface tension forces prevail on inertia (C). The dotted lines outline the electrode boundaries.

Source: Photographs courtesy D. Jary, CEA-LETI.

reservoir liquid (DIW) toward the electrodes. In photograph (A) the first electrode is actuated and the liquid moves to cover the electrode surface; we note that the velocity of the liquid is larger on the interface. After the liquid has invaded the first electrode, the next electrode is actuated (B). A similar motion starts again with higher velocities at the interface. It seems that the liquid invades the volume above the actuated electrode in the form of a thin layer near the droplet interface, the bulk of the reservoir being little affected. Note the shape of the interface in the reservoir; it does not contact the Ordyl wall, because of the curvature of the interface at the inlet corner. Motion stops abruptly when the electrode is invaded by the liquid, confirming that inertia is small compared to surface tension forces.

5.4.6 Influence of the cutting electrode on drop volume and reproducibility

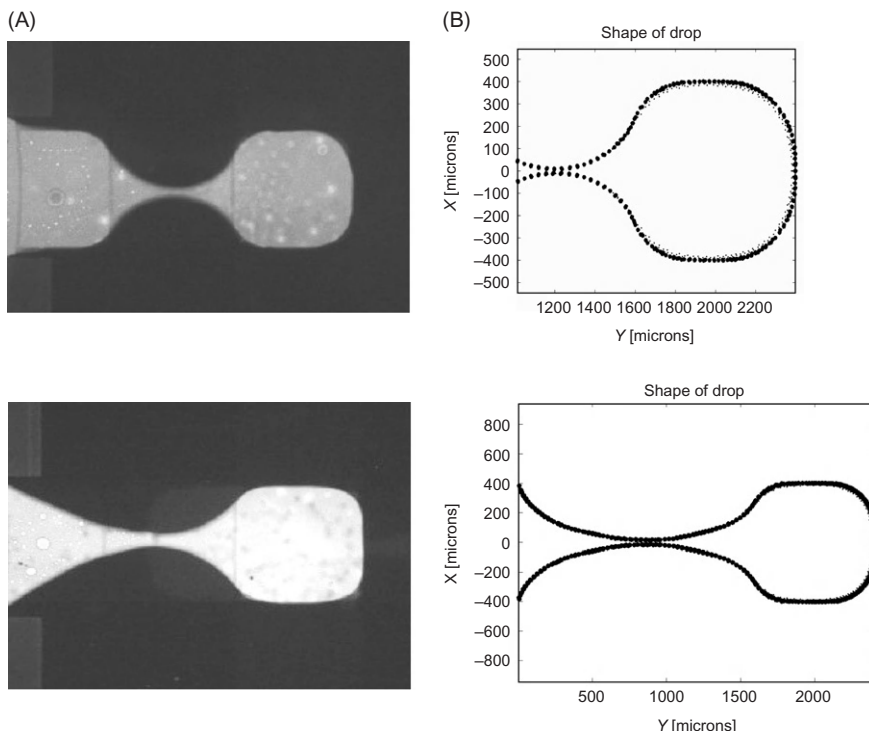
In biology and biotechnology, the extracted drops from the reservoir are used as biological units for the biological operations that take place in the biochip. It is then extremely important to control precisely the volume of the drops and to ensure their reproducibility.

It has been observed that the dispensing process described in the preceding section produces reproducible droplets. The model shows that the size of the cutting electrode closely controls the size of the final extracted drop. The reason is purely morphological as shown by the comparison between experiments and numerical simulations. It is the tail of the drop that retracts at the very moment of separation and adds to the drop volume ([Figure 5.55](#)). A limitation of the tail size results in a better controllability of the extracted drop volume. Hence, there is a definite advantage to reducing the size of the cutting electrode.

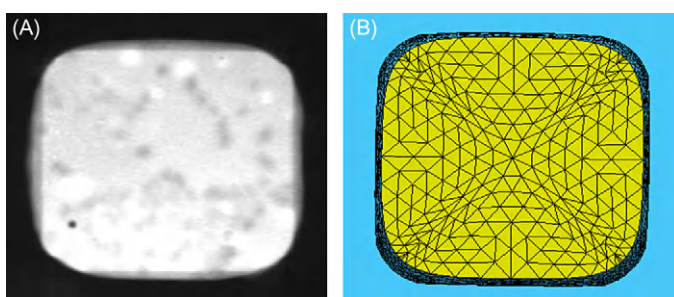
As we have seen in this chapter, depending on the surface tension, the shape of the drop follows more or less the shape of the underlying electrode ([Figure 5.56](#)). However, when retracting after separation, the tail forces a supplementary volume of liquid into the already formed droplet. It is this “tail” volume that may produce variability in the droplet volume. [Figure 5.57](#) shows two different configurations where different volumes of liquid are stocked above the electrode.

[Table 5.5](#) shows the final volume of the extracted drop depending on the size of the cutting electrode. Note that for a cutting electrode length less or equal to that of the standard electrode (here $800 \mu\text{m}$), the drop volume is less than the volume of $800 \times 800 \times 100 \mu\text{m}^3 = 0.064 \mu\text{L}$, and that for an electrode length of twice the electrode size, the liquid volume bulges out of the electrode (its volume is much larger than $0.064 \mu\text{L}$).

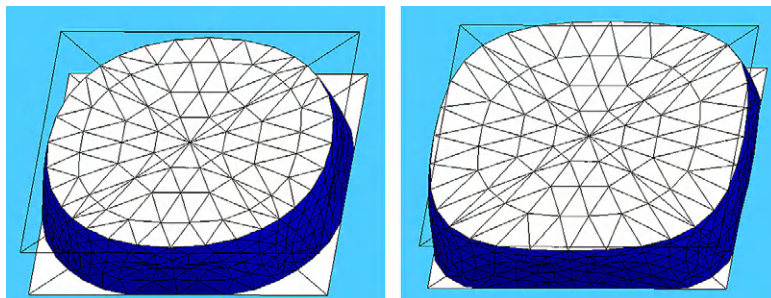
The calculated values of [Table 5.2](#) are close, but a little below the experimental values. Using a cutting electrode of the same size as that of the electrodes, we have obtained a very good reproducibility of the drop volume which fluctuates between 64.5 and 66.0 nL ([Figure 5.58](#)). It is a general rule that the reproducibility is satisfactory when the size of the cutting electrode is less than the size of the electrodes in the electrode row.

**FIGURE 5.55**

Extraction of a microdrop from the reservoir. (A) Experimental view of the extraction obtained by using one or two cutting electrodes and (B) numerical simulations with the numerical software Surface Evolver in the same conditions. Using a single cutting electrode produces more controllable volumes of droplets.

**FIGURE 5.56**

(A) Fluorescent microdrop observed with a binocular, blurred contour corresponds to the upper and lower contact line. (B) Microdrop on electrode calculated with Surface Evolver. The lower electrode being actuated, the contact angle is in the range 70° – 85° ; the upper plate being at zero potential, the contact angle is hydrophobic (110° – 115°).

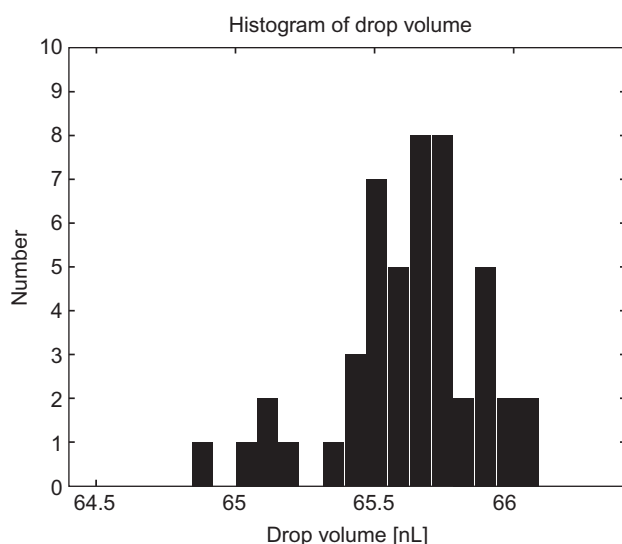
**FIGURE 5.57**

Two different shapes of a drop confined between two plates in a covered EWOD microsystem depending on the liquid volume “forced” into the droplet.

Table 5.5 Calculated Values of Extracted Drop Volume in Nanoliters versus Length of Cutting Electrode and Surface Tension

Surface Tension (mN/m)	Length of Cutting Electrode (μm)		
	600	800	1600
$\gamma = 40$	56	60	69
$\gamma = 20$	56	60	71
$\gamma = 8$	56	61	77

Note that below 600 μm , dispensing does not occur anymore because pinching becomes inefficient.

**FIGURE 5.58**

Volume reproducibility of extracted droplet: histogram of drop volume. The average volume is $\text{Vol} = 65.626 \text{ nL}$ —very close to the volume comprised between the lower and the upper electrodes (64 nL)—and the standard deviation is $\sigma = 0.26 \text{ nL}$ ($\text{CV} = 0.4\%$).

5.4.7 Centering electrode and shape of reservoir electrode

5.4.7.1 Centering electrode

Solid substrates of EWOD microsystems are microfabricated using extra care to make them as smooth as possible. We have seen in Chapter 3 that surface defects can lead to unwanted pinning, resulting in the malfunctioning of the microchip. But a consequence of the smoothness of the surface is that microdrops, if not anchored by a boundary line, may not always be positioned at the same location on the surface. They show an unstably positioned drop (Figure 5.59) that drifts until it finds an anchored position by pinning to a singular point or to a boundary line. To maintain a microdrop at a given location, star-shaped electrodes are used.

The principle of drop centering by star-shaped electrodes is intuitive; it stems from the analysis of the preceding section where opposite electrocapillary forces are created by using crenellated electrodes. When the star-shaped electrode is actuated, the resultant of the electrocapillary forces is zero provided that the droplet is positioned at the center of the electrode (Figure 5.60).

A numerical simulation using the Surface Evolver software confirms this analysis (Figure 5.61). A sessile droplet located on the plane is displaced toward the center by the actuation of the star-shaped electrode. After release of the actuation, it regains the same spherical shape but is now positioned at the center of the star-shaped electrode.

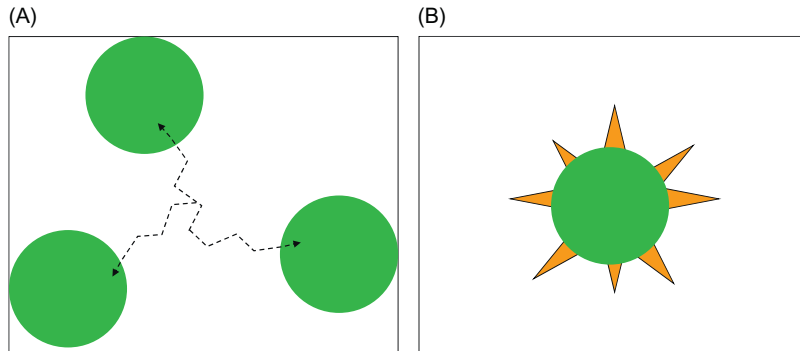


FIGURE 5.59

(A) On a smooth surface droplets drift until they are pinned on a boundary; the free energy of the droplet is the same for any of the shown locations and (B) a star-shaped electrode centers the droplet.

5.4.7.2 Shape of reservoir electrode

In the reservoir of EWOD microsystems, the volume of liquid decreases each time a microdrop is dispensed into the system. Thus, the large droplet of the reservoir progressively decreases. It is essential that this large droplet be positioned right in front of the first “working” electrode of the microsystem, or else dispensing liquid may be stalled.

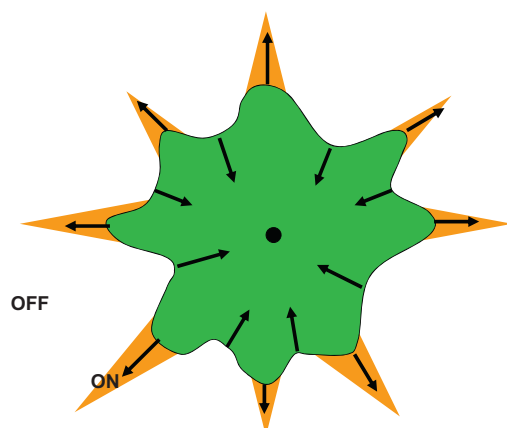


FIGURE 5.60

Droplet artificially pinned on a central position by the use of a star-shaped electrode. Any deformation of the triple contact line increases the free energy of the system.

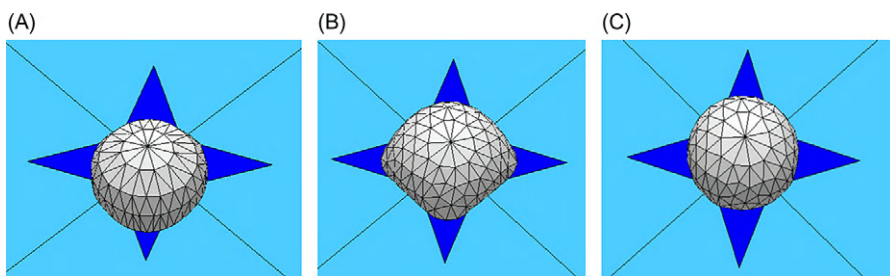


FIGURE 5.61

Surface Evolver simulation of a droplet on a star-shaped electrode. (A) The droplet is initially positioned arbitrarily on the plane; (B) when the star-shaped electrode is actuated, the droplet moves in such a way that it maximizes its contact surface on the actuated electrode; and (C) after the actuation is turned off, the droplet regains its spherical shape and is positioned at the center of the star-shaped electrode.

5.4.7.2.1 Centering electrode

We first show that, in the geometry of droplet dispensing, a spike-shaped electrode can be used to “center” the droplet in front of the “opening gate” in the vertical wall separating the reservoir from the “working” electrodes. In Figure 5.62, we have numerically simulated how a droplet at first not positioned

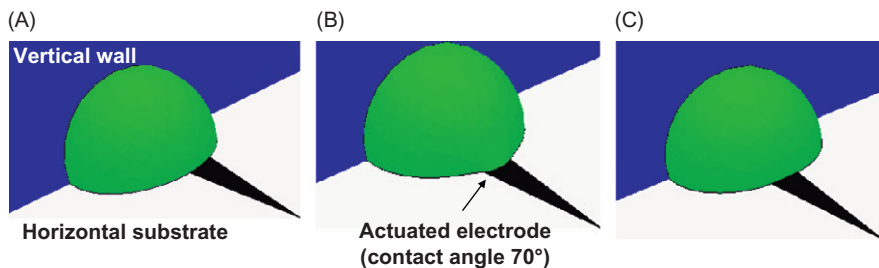


FIGURE 5.62

Simulation of a droplet being moved to the desired location by the successive actuation/deactuation of a spike-shaped electrode: (A) droplet “decentered,” (B) actuation of the spike electrode brings the droplet in the center, and (C) after deactuation of the electrode, the droplet regains its original shape. Operations (A), (B), and (C) are equivalent to a translation of the droplet along the vertical wall.

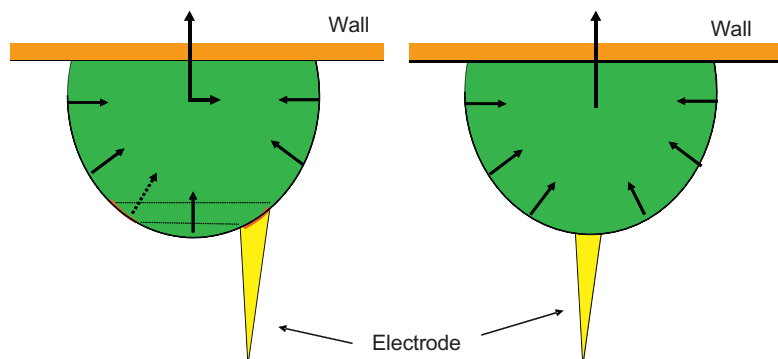


FIGURE 5.63

Sketch of the forces on the contact line: in a dissymmetrical position relative to the electrode, there is a resultant capillary force parallel to the vertical wall. In the symmetrical position, this resultant vanishes and the droplet is at equilibrium.

at the right location can be recentered by actuation followed by deactuation of a spike electrode.

From a physical standpoint, the effect of the spike-shaped electrode is schematized in [Figure 5.63](#). When the droplet has a dissymmetrical position relative to the electrode, there is a resultant of the capillary forces on the triple line parallel to the vertical wall. This force translates the droplet until its position becomes symmetrical and the resultant vanishes.

5.4.7.2.2 Star-shaped electrode

We have shown in the preceding section that a spike-shaped electrode centers the droplet in front of the opening gate. However, this is not the only constraint we want to put on the drop in the reservoir. We have seen in [Section 5.4.5.3](#) ([Figure 5.62](#)) that the liquid in the reservoir can move away from the opening gate after the dispensing of a droplet because of the curvature of the contact line imposed by the corner of the opening gate. In [Figure 5.64](#), we show that a half star-shaped electrode, when actuated exerts a force that brings the droplet back toward the “opening gate.” First, the long spike-shaped electrode centers the droplet; second, a resultant electrocapillary force is exerted on the liquid, due to the force on the triple contact line on the star-shaped electrode close to the “opening gate.” The liquid on the

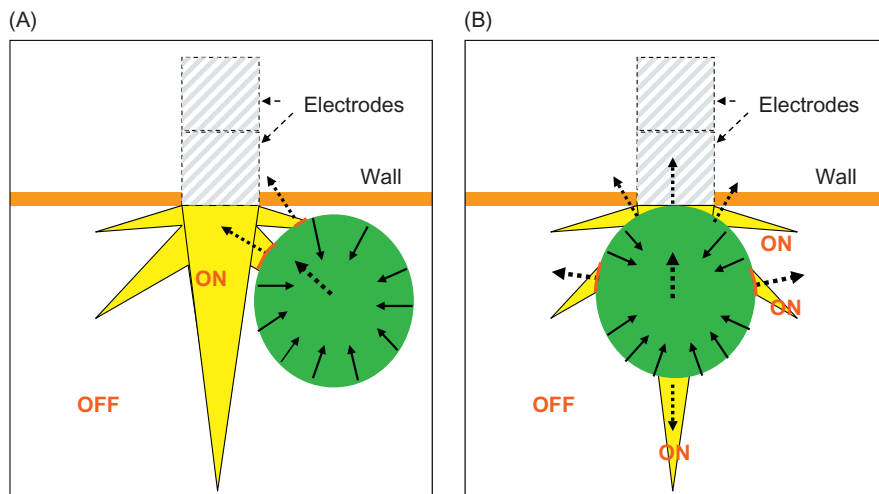
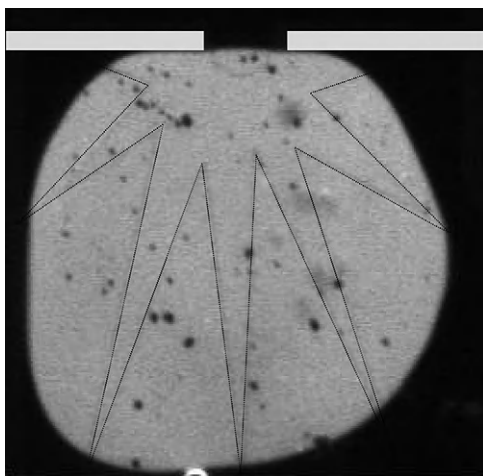


FIGURE 5.64

(A) Sketch of the resultant of the forces when the drop in the reservoir has moved away from the opening gate. (B) The star-shaped electrode brings back the liquid toward the opening gate.

**FIGURE 5.65**

Verification of the role of the star-shaped electrode: the droplet has been pulled back toward the Ordyl wall by actuation of the star-shaped electrode; then the star-shaped electrode is switched off and the system is ready for a new droplet dispensing.

Source: *Photograph Y. Fouillet, CEA-LETI.*

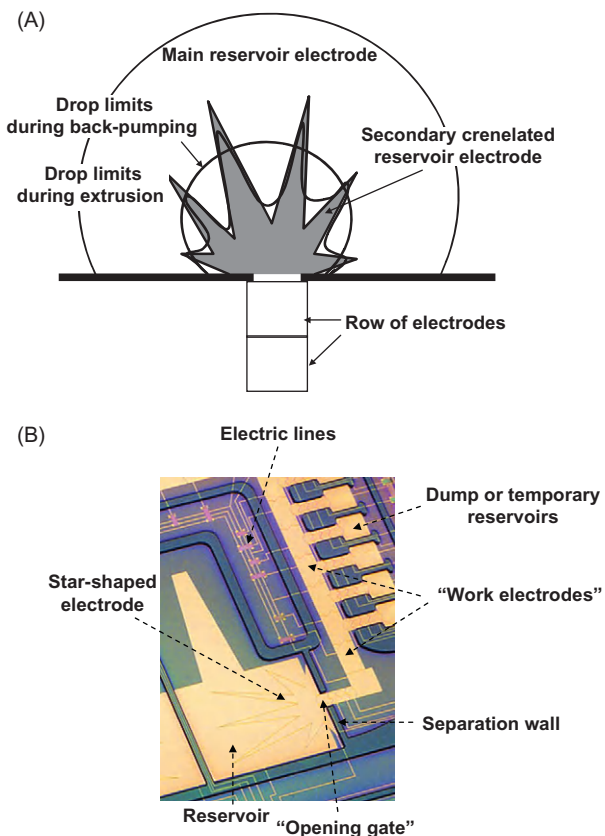
reservoir then is pushed toward the Ordyl wall and ready for a new droplet dispensing.

[Figure 5.65](#) shows the liquid in the reservoir positioned on the star-shaped electrode (after it has been deactuated). The liquid is correctly placed for the dispensing of the next droplet through the opening gate at the top.

5.4.7.2.3 Examples of reservoir designs

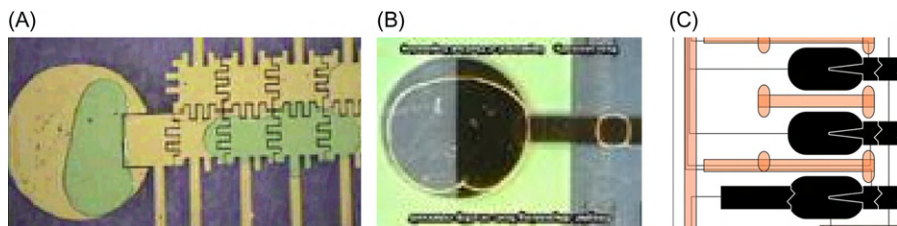
From the technological standpoint, it is easy to construct the reservoir with two electrodes: a primary electrode covering most of the surface of the reservoir and a secondary half star-shaped electrode ([Figure 5.66](#)). During the first phase of liquid extrusion onto the “working” electrode row, the main electrode is not actuated (OFF), resulting in a hydrophobic pushing force on the triple contact line, while the secondary star-shaped electrode is at first actuated (ON), resulting in a translation of the reservoir liquid toward the injection electrode. When the liquid is engaged at the working electrodes, the star-shaped electrode is switched off, increasing the pushing force toward the electrode row. When the liquid is sufficiently pulled by the capillary forces exerted by the “working” electrodes, the back pumping step is engaged, and the two reservoir electrodes are actuated again (ON), leading to droplet separation.

Other reservoir electrodes, less sophisticated, but somewhat easier to fabricate are described in the literature; they are shown in [Figure 5.67](#).

**FIGURE 5.66**

(A) Schematic view of the reservoir electrodes. (B) EWOD microsystem with reservoir and star-shaped electrode for dispensing.

Source: Photograph Y. Fouillet, CEA-LETI.

**FIGURE 5.67**

Schematic views of different reservoir electrodes: (A) circular electrode with an entrant working electrode from the University of Toronto, reprinted with permission from [41], © 2006, ACS; (B) circular reservoir with semi-circular centering electrode from Duke University (<http://microfluidics.ee.duke.edu/>), reprinted with permission by R.B. Fair; and (C) one spike electrode (LETI).

5.5 Droplet merging and mixing

Merging of two droplets is a straightforward operation. It suffices that the two droplets be displaced toward the same electrode (or the same couple of electrodes). Usually, the two drops contain aqueous liquids and their coalescence is immediate (except if the viscous effects characterized by the Ohnesorge number are dominating). However, mixing of the liquids of the two droplets is a complex process. As a matter of fact, mixing in fluids in their laminar state is a very complicated phenomenon. In this case, mixing is promoted by diffusion (which can be a very slow process, since the diffusion coefficients can be very small for macromolecules) and by stretching and folding of the streamlines [42] (Figure 5.68). For more insights, consult Ottino [43] on the concepts of chaotic mixing with laminar flow. Mixing inside droplets is even more complicated, because of “skin effects” that we will point out below. From a theoretical standpoint, mixing inside droplets has yet to be fully delineated, and we will only tackle the problem by an experimental approach.

5.5.1 The difficulty of mixing in covered EWOD microsystems

For a covered EWOD system, different actuation patterns can be thought of in order to increase the striation process. In the following, we present the results of three processes: (i) back and forth motion, (ii) successive division and merging operations, and (iii) loop motion. These operations are shown in Figure 5.69.

5.5.1.1 Back and forth motion

Mixing by a back and forth motion on a row of electrodes is shown in Figure 5.70. One droplet is marked with fluorescent dye, while the other is not marked. Efficiency of mixing is monitored by the diffusion of the fluorescent dye. It is interesting that the mixing is induced by two filaments of the liquid—which is located at the tail during the motion—moving along the free (liquid-air) interface (Figure 5.71). This pattern seems to be general and has

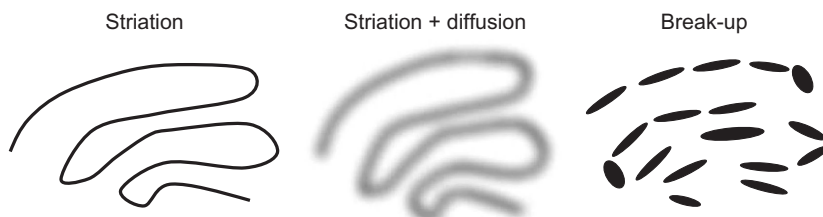
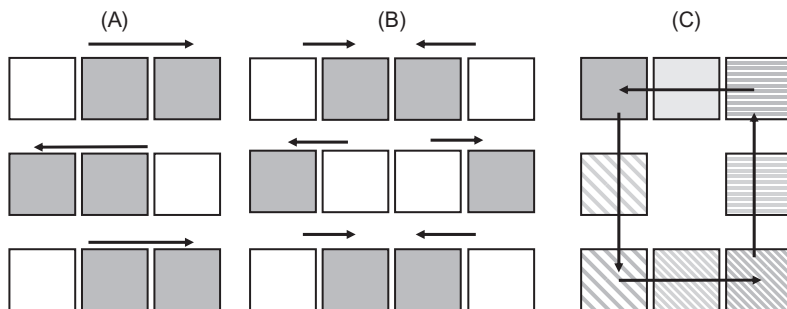
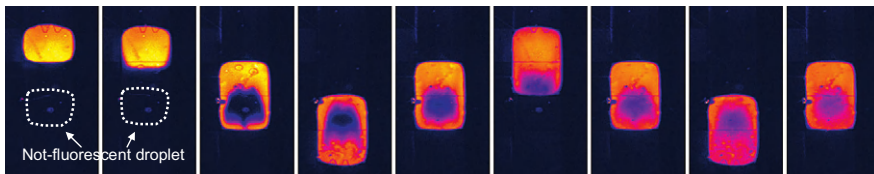


FIGURE 5.68

The different processes leading to mixing. Striation results from successive stretching and folding of the streamlines [43].

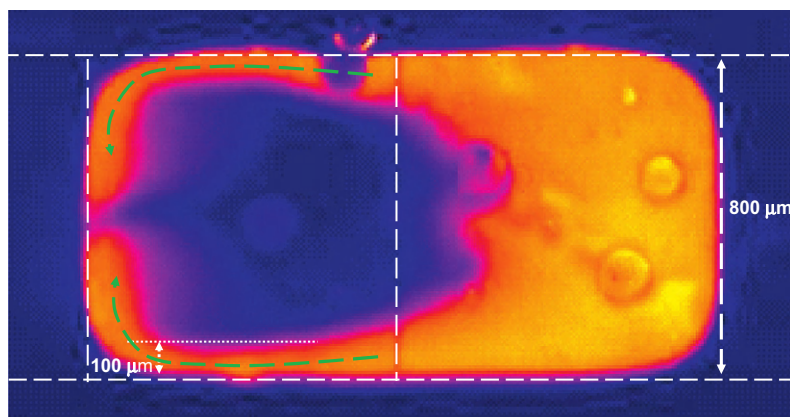
**FIGURE 5.69**

Three sequences of actuation for mixing droplets in EWOD microsystems: (A) back and forth motion, (B) successive merging and divisions, and (C) loop motion.

**FIGURE 5.70**

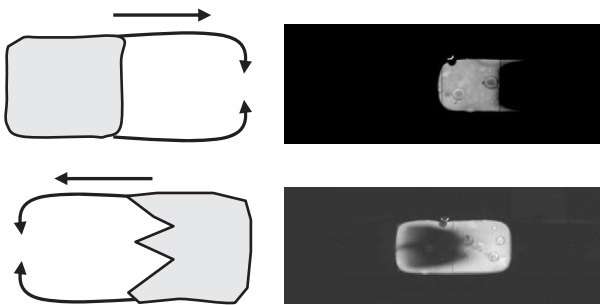
Images of the mixing of two droplets of water in a covered EWOD microsystem. One of the droplets is painted with fluorescent dye. Remark how the mixing is induced by a flow pattern alongside the liquid–air interface.

Source: *Photograph courtesy D. Jary, CEA-LETI.*

**FIGURE 5.71**

Detail of mixing pattern: the liquid in the tail of the merged droplet progresses very quickly along the edges of the electrodes, like a skin effect, probably under the action of electric forces.

Source: *Photograph courtesy D. Jary, CEA-LETI.*

**FIGURE 5.72**

Sketch of the mixing by back and forth motion.

also been observed by Paik et al. and Fowler et al. [44–46]. We note the similarity with Figure 5.48 where the particles close to the interface are moving much faster than those in the bulk. We interpret this result as an electric Marangoni effect (see Chapter 2) caused by the electric forces acting on the liquid–air interface. Intuitively, it is as if a liquid “skin” was pulled toward the newly created interface by the droplet motion.

The mixing is shown in Figure 5.72. We see that the back and forth motion of the liquid skin reduces the efficiency of mixing, the bulk of the two liquids staying separated for a long time.

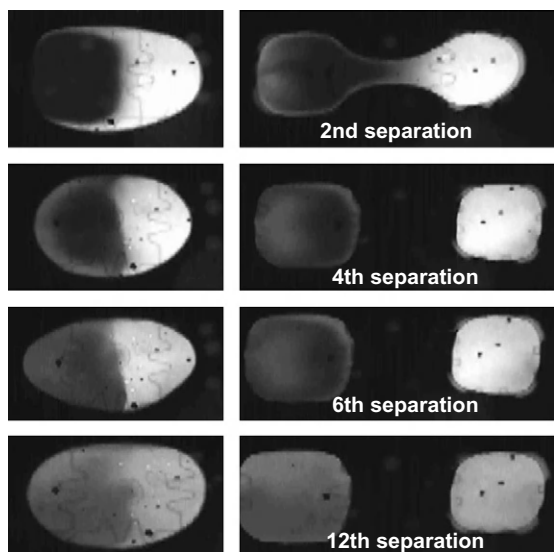
5.5.1.2 Successive merging and divisions

Another way to mix liquids from two droplets is to induce successive merging and divisions, as shown in Figure 5.73. We observe the same pattern as in the preceding section. The two droplets exchange their “liquid skin,” as is seen on the top right photograph, where a skin of bright liquid surrounds the dark droplet and conversely a skin of the black droplet surrounds the bright droplet. Again, mixing occurs slowly by diffusion of the liquid in the “skin.”

5.5.1.3 Loop motion

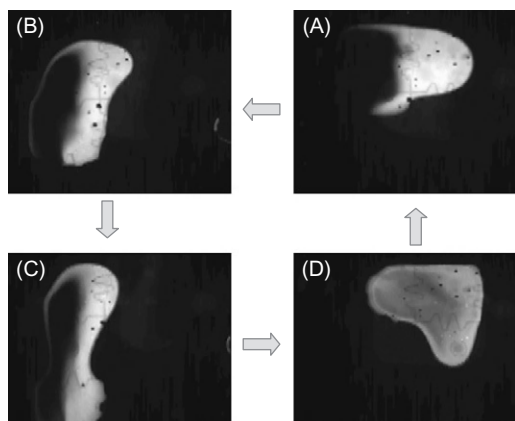
The two preceding mixing processes do not induce the stretching–folding pattern which is the best promoter for mixing [43]. In order to induce such a stretching–folding pattern, loop motions have been investigated. Figure 5.74 shows the mixing pattern obtained by a square loop motion.

We still observe the “skin” effect, but this time the bulk is stretched and folded at each corner leading to a much better mixing efficiency.

**FIGURE 5.73**

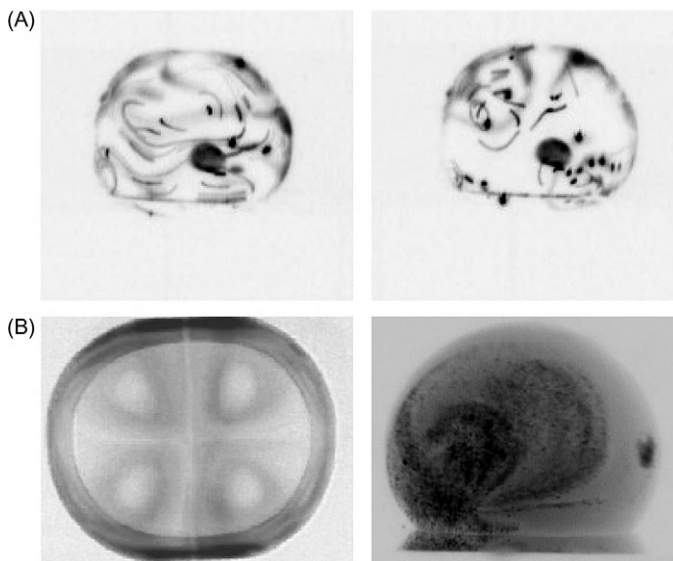
Mixing of droplets is a slow process: if the droplet follows cycles of division and merging, it takes many cycles before mixing is achieved. Mixing is due to diffusion of the “skin” toward the central regions, not by hydrodynamic mixing of the central regions.

Source: Photograph CEA-LETI.

**FIGURE 5.74**

Mixing droplets by a square loop motion. The motion starts at the upper right (A). Mixing is more efficient because of the stretching and folding of the droplet in the corners (image (C) in the bottom left corner). A single cycle on the eight electrodes loop is nearly enough to obtain the mixing of the two liquids.

Source: Photograph Y. Fouillet, CEA-LETI.

**FIGURE 5.75**

Marangoni flow in a sessile droplet: (A) thermal Marangoni convection: effect of evaporation; (B) electric Marangoni convection: effect of the electric field; left: recirculation rolls caused by the presence of two actuated electrodes; right: typical electric Marangoni flow in a droplet on an actuated electrode.

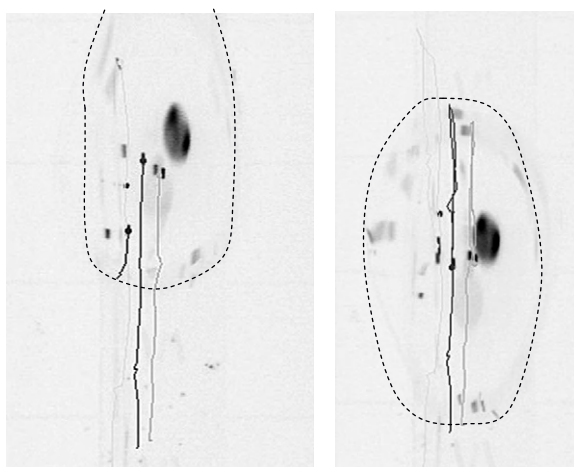
Source: *Photographs courtesy Ph. Dubois, Y. Ishida and O. Raccourt.*

5.5.2 Mixing in open EWOD systems

In this section, we investigate the mixing patterns in sessile droplets in open EWOD microsystems. We will see that mixing liquids in open EWOD systems is easier, at least for aqueous droplets because of their small viscosity.

5.5.2.1 Mixing by Marangoni effects

Marangoni convection is a ubiquitous feature in droplet microfluidics. In Chapters 2 and 3, we discuss the different types of Marangoni convection: thermal, concentration, and electric. Note that some authors do not favor the name of “electric Marangoni convection,” like Jones [11], because it is not formally rigorous; the term electroconvection is more appropriate; however, following Colin [47], it is convenient to use Gibbs’ approach and to use the notion of effective surface tension when electric charges are located close to the interface. Figure 5.75 shows two types of Marangoni flow in a sessile droplet: first, the well-known random motion due to evaporation (no actuation of

**FIGURE 5.76**

Straight line motion of markers in an ionic liquid sessile droplet moved back and forth in an open EWOD device.

Source: Photograph Ph. Dubois and J. Berthier, CEA-LETI.

electrodes); second, typical electric Marangoni—or electroconvective—patterns in a droplet whose interface is submitted to electric stresses [48].

The convective motions can be very active in water-based droplets and induce a very strong mixing.

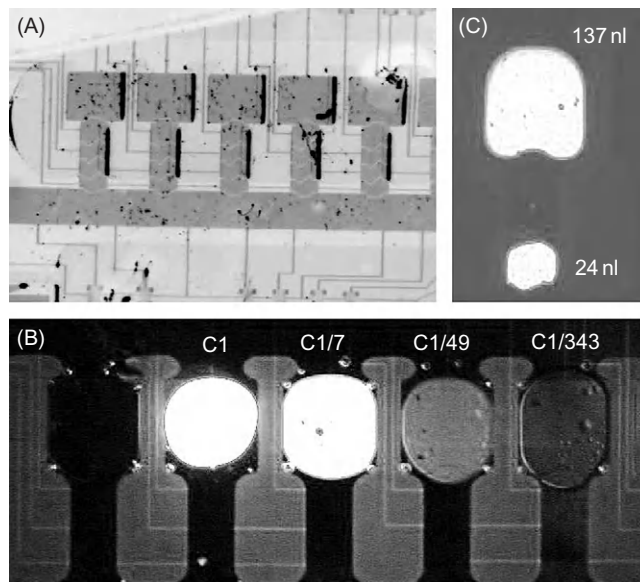
5.5.2.2 The difficulty of mixing viscous fluids

So far we have investigated the mixing of aqueous droplets, which have a small dynamic viscosity. The situation is somewhat different for highly viscous fluids, like ionic liquids. For such liquids, the Marangoni effect seems ineffective. In order to induce some mixing, back and forth motions on electrodes have been investigated. Markers in the liquid have been monitored (Figure 5.76) showing an extremely linear pattern. Hence, the mixing efficiency is very low in viscous fluids. Besides, these fluids behave like “gels”: their motion from one electrode to the next is approximately a translation of the whole droplet.

5.6 Dilution

5.6.1 Dilution of solutes

Controlling and monitoring the dilution of reactants is a very important operation in biology. Concentrations must be very accurately dosed to follow the biologic protocols. The difficulty of diluting reactants is often overlooked; traditionally in

**FIGURE 5.77**

(A) View of the EWOD architecture to perform dilution operations; (B) a liquid at a concentration C_1 in a biochemical species can be diluted 343 times in three successive dilution operations; and (C) dilution is based on extraction of $1/7$ of the initial droplet volume.

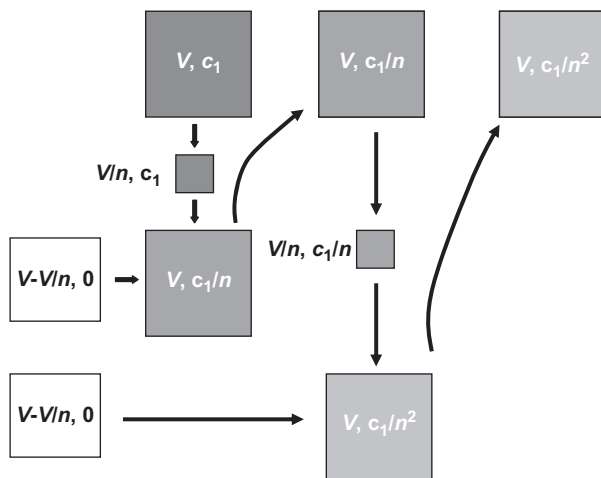
Source: Courtesy Y. Fouillet, CEA-LETI.

In biology, it is done using pipettes, but the control of the diluted concentrations is not very accurate. We have seen that EWOD can handle with precision tiny volumes of liquids. In this respect, EWOD is well adapted to dilution operations. As mentioned earlier, the size and shape of the electrodes determines precisely the volume of the droplet. In [Figure 5.77](#), we show how precise dilution can be realized on EWOD microchips.

The principle of EWOD dilution is the extraction of a fixed, well-determined volume of a liquid and the merging of this volume in a fresh droplet with a zero concentration, as shown in [Figure 5.78](#). Each step divides the concentration by a factor n equal to the ratio of the volume of the reservoir electrode and the working electrode

$$n = \frac{V_{\text{reservoir}}}{V_{\text{elec}}} \cong \frac{S_{\text{reservoir}}}{S_{\text{elec}}}. \quad (5.73)$$

Note that at each step a mixing operation must be performed in order to homogenize the solution. Homogenization is not always possible if the particles in the solution are large, discrete entities like polymers, macromolecules, etc., as we will show next.

**FIGURE 5.78**

Principle of dilution on EWOD microchips.

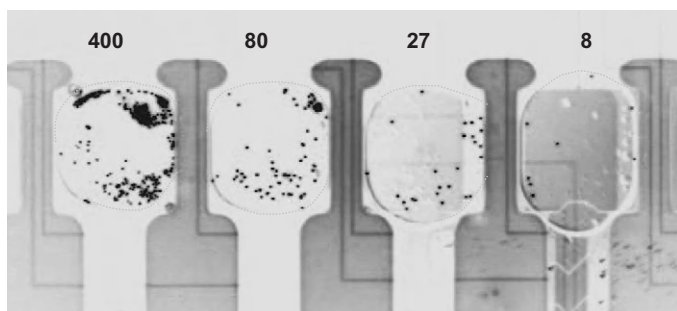
**FIGURE 5.79**

Photograph of an aqueous droplet containing cells.

Source: Photograph D. Jary, CEA-LETI.

5.6.2 Dilution of discrete particles

In the preceding section, the dilute species diffuse in the available volume, and the concentration homogenizes, given sufficient time, or efficient mixing. The situation is not quite the same if we consider discrete entities like particles, magnetic beads, cells, etc. Concentration of such particles is not homogeneous: the particles are submitted to body forces like gravity and to interaction forces (electrostatic, van der Waals, etc.) and Brownian motion, or even mixing, is not sufficiently efficient to disperse the particles and cannot homogenize the liquid. This is, for example, the case of cells in an aqueous droplet (Figure 5.79).

**FIGURE 5.80**

Dilution of concentration of particles on an EWOD-based microchip. The number on top of each reservoir is the number of particles.

Source: Courtesy D. Jary, CEA-LETI.

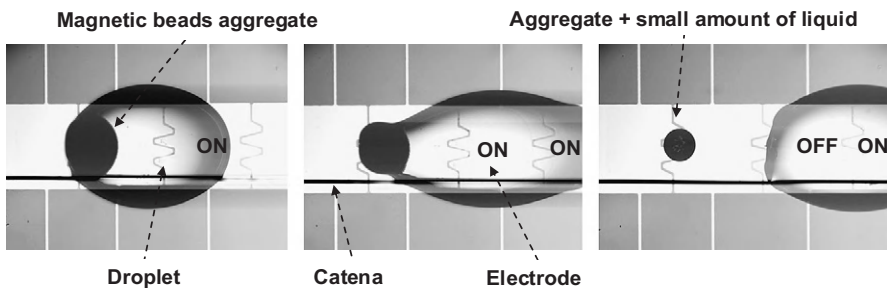
Figure 5.80 shows the dilution process of solid spherical particles in EWOD reservoirs: obviously, the concentration is not homogeneous in the reservoirs; hence, the dilution rate between two steps of dilution is not constant. This problem is fundamental in biology and biotechnology, when one wants to study “single cells.” This problem is presently being investigated in many laboratories around the world.

5.7 Magnetic beads in EWOD microsystems

In biotechnology, magnetic beads are often used for the transport of macromolecules [42,49,48]: super-paramagnetic beads are functionalized or labeled to recognize and bind to a specific molecule. Functionalization is achieved by coating the magnetic bead with molecules having a chemical affinity for the target molecules. Hence, when dispersed in a liquid, the labeled beads capture or bind to the target molecules, forming a composite macromolecule. In the absence of a magnetic field, the particles disperse in the liquid phase. In the presence of a magnetic field, they are attracted toward the magnetic pole; besides they aggregate together because of the formation of chains of magnetic dipoles [42].

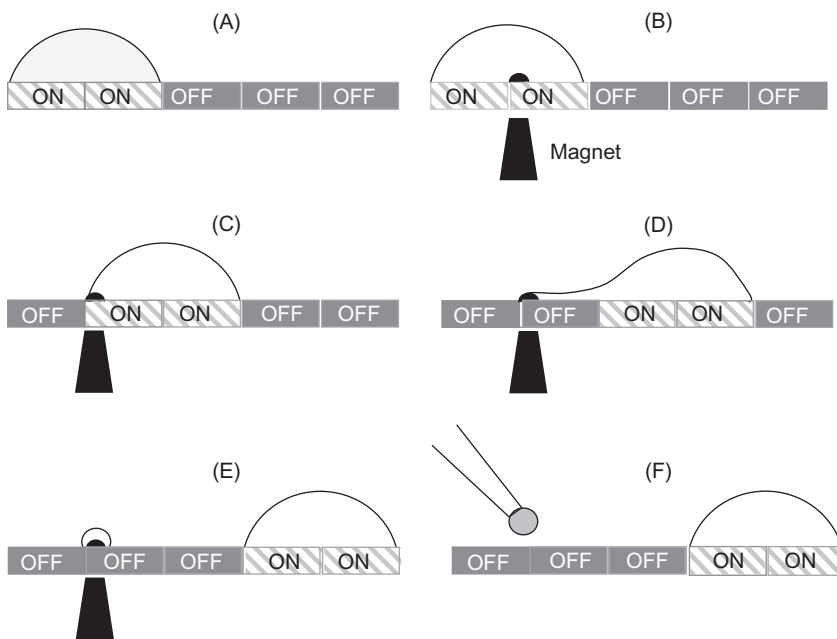
In biotechnology, it is thought that processes based on magnetic capture and concentration, similar to those using microflows, can be developed in DMF devices, with all the advantages of smaller liquid volumes, allowing more precise and sensitive recognition and/or bioanalysis. Figure 5.81 shows an open EWOD device (with catena) and a droplet containing magnetic beads aggregated by a mini magnet placed below the substrate. If the electrowetting forces are sufficient and if the magnetic forces are sufficient, the magnetic aggregate separates from the droplet.

Figure 5.82 demonstrates the principle of concentration of target molecules by paramagnetic labeled microbeads. First, the beads are dispersed in the droplet and

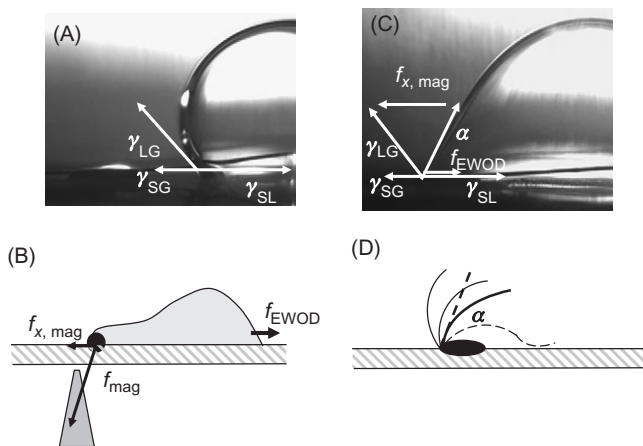
**FIGURE 5.81**

Combination of magnetic forces exerted on an aggregate of magnetic beads and electrowetting forces exerted on a conductive liquid droplet. In this case, the magnetic forces are sufficiently important to pin the aggregate and the electrowetting forces are sufficiently large to move the droplet, leaving behind the aggregate with a small amount of liquid.

Source: *Photograph courtesy N. Chiaruttini, CEA-LETI.*

**FIGURE 5.82**

Principle of extraction/concentration using a combination of electrowetting and magnetic beads. At the end of the process (F), the concentrated aggregate of magnetic beads attached to target molecules can be removed with a pipette.

**FIGURE 5.83**

Balance of forces on the receding contact line. (A) Young's law in absence of magnetic and electrowetting forces; (B) deformation of the droplet under the two actions of the magnetic and electrowetting forces; (C) balance of the forces at the rupture limit; and (D) if the electrowetting forces are sufficient for pulling the interface and decreasing the contact angle below its limit value, rupture inevitably occurs.

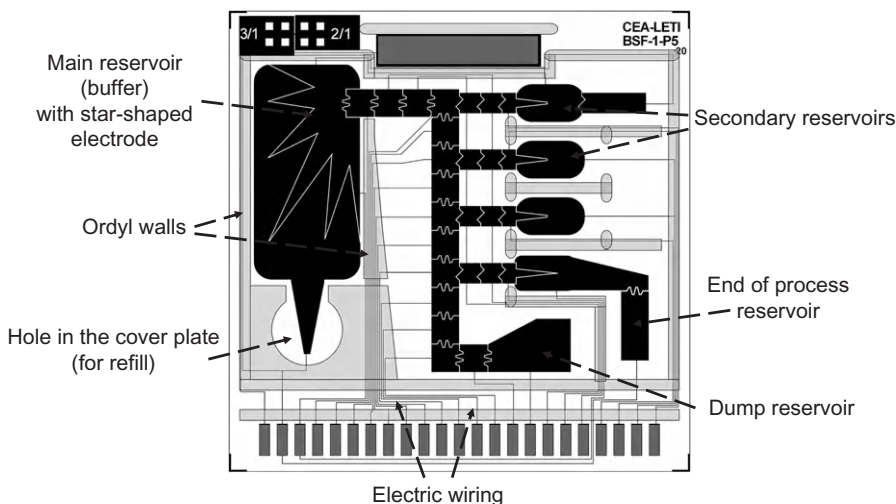
some capture the target molecules (A); then the beads are aggregated by using a mini magnet (B); the droplet is then motioned by electrowetting actuation (C and D); if the magnetic and electrowetting forces are sufficient, the droplet continues its motion, leaving behind the aggregate with a small amount of liquid (E). Target molecules are now concentrated in “nano” droplet.

[Figure 5.83](#) shows the balance of forces applied on the receding contact line. In the absence of magnetic and electrowetting forces, the balance of forces is given by the Young's law (A). The aggregate is blocked near the tip of the magnet; the shift in the horizontal direction of the magnetic aggregate produces a horizontal magnetic force $f_{x,mag}$; the equilibrium position is found to give the maximum force $f_{x,mag}$ (B). The limit angle α of the droplet is given by the diagram (C). If the electrowetting force is larger than the equilibrium force of diagram (C), the contact angle decreases under the value α , and the droplet separates from the magnetic aggregate (D).

5.8 Architecture of EWOD microsystems

5.8.1 General architecture

In the preceding sections, we have dealt with the basic manipulations of droplets in EWOD systems. These manipulations involved only a few electrodes. In this

**FIGURE 5.84**

Covered EWOD biochip from LETI.

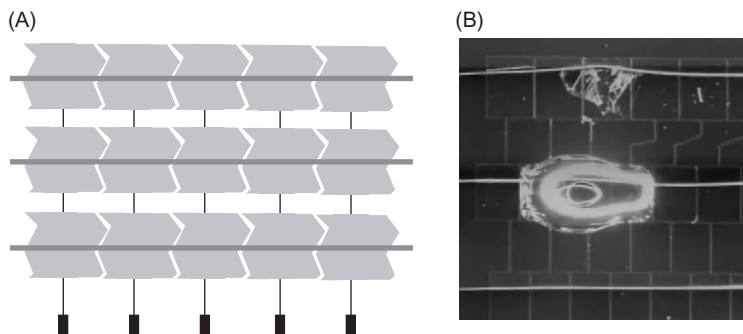
Source: Courtesy Y. Fouillet, CEA-LETI.

section, we give some insights into the more complex architecture of complete EWOD microdevices. Usually, EWOD biochips include a few reservoirs containing the different reagents and buffers, and a sufficient number of electrodes to perform the required biological and chemical operations.

Figure 5.84 shows a typical biologic EWOD chip with its main and secondary, dump reservoirs, and the electric wiring. The figure especially shows the complexity of the wiring. The electrodes are most of the time individually addressed. However, some electrodes are often difficult to connect to an electric line; besides it is very costly in terms of microfabrication to have two levels of wiring in the substrate. A technique called “multiplexing” is then used to address groups of electrodes without losing their individual functionality. We discuss this technique in the following section.

5.8.2 Multiplexing

We have seen that EWOD chips require a paving of the substrate with electrodes. Some EWOD applications require a large number of electrodes and reservoirs. Addressing each one of the electrodes individually is not always possible if the wires are all in the same plane inside the substrate. However, depending on the travel scheme of the droplets on the chip, some electrodes can be put on the same electric line [50]. Consider the design of Figure 5.85 [7]. The system comprises $M = 5$ electrodes in a row and $N = 3$ rows. Droplets can be individually handled if it is possible to switch the catenaries to the voltage 0 or V and

**FIGURE 5.85**

(A) Multiplexing scheme for an open EWOD system with catenae: number of electrodes in a row is $M = 5$, number of rows $N = 3$, number of electrical lines $M + N = 8$, total number of electrodes $N \times M = 15$. (B) EWOD system with multiplexing.

Source: *Photograph Ph. Dubois CEA-LETI*.

the electrodes to 0 or V . Hence, the $N \times M = 15$ electrodes require only $M + N = 8$ electric switches.

Multiplexing is very efficient for systems doing droplet manipulations in parallel. An example of such microsystems is that of Moon et al. [51]. It realizes the generation of multiple droplets from a reservoir and parallel in-line sample purification of a carrier fluid containing proteins.

5.9 Other EWOD microsystems

EWOD microsystems can be used to perform functions other than those presented above. A first functionality is a “conveyor system”; a second functionality is the “electrocapillary filaments.”

5.9.1 Electrowetting conveyor system

A particularly interesting use of EWOD has been proposed by Moon et al. [2]. The concept is that of a conveyor system moved by electrowetting actuation. The system is an open EWOD system without catena. The “carriage” is composed of a thin flat plate placed on four droplets (Figure 5.86). These four droplets are the “wheels” of the “carriage.” A first requirement is that the four droplets move in parallel and at the same speed on two electrode rows, constituting the “road.” A second requirement is that the plate placed upon the four droplets be hydrophobic, or else the droplets will merge together.

It has been observed that the moving plate can carry an important load and can be used as a moving frame for biological/chemical applications.

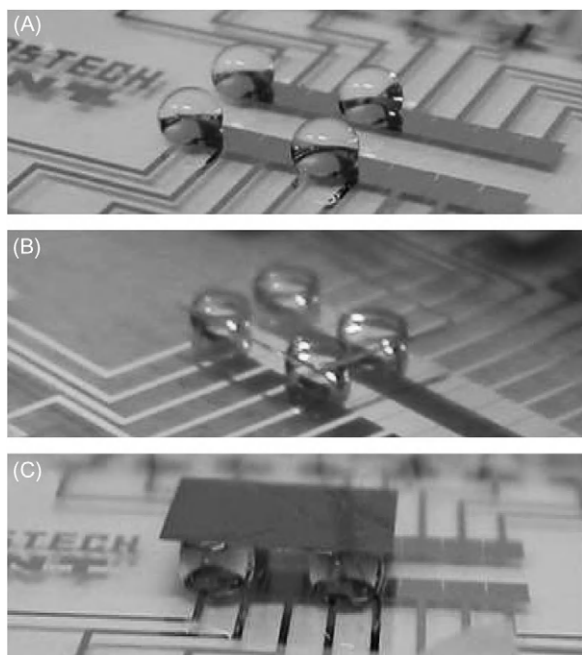


FIGURE 5.86

Conveyor belt constituted of four droplets on EWOD substrate (A) and a top pad made of glass (B) or silicon (C).

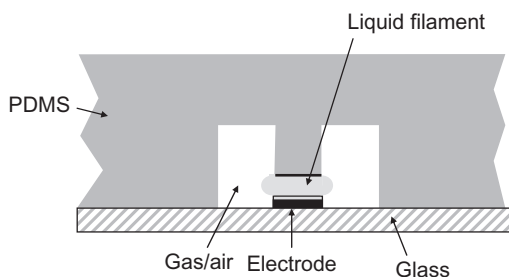
Source: Reused with permission from Ref. [2] © 2002, American Institute of Physics.

5.9.2 Extension of the electrowetting concept: electrowetting filament and open microfluidics

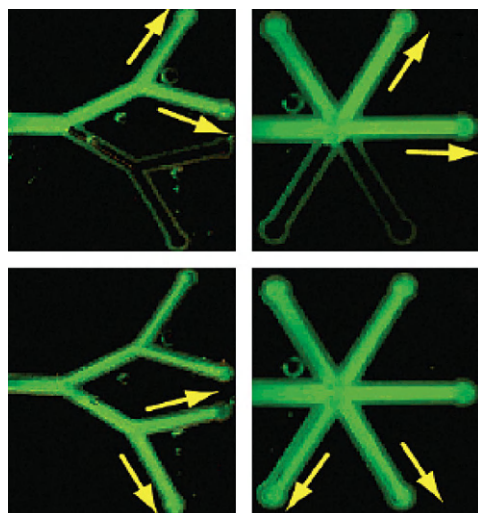
A very interesting use of electrowetting actuation is the ability to work with “liquid filaments” or “fingers” [52]. The principle is derived from that of space applications for microengines: a filament of liquid may move even if it is not totally enclosed between solid walls. It suffices that capillary forces maintain the free boundaries of the liquid. Such type of flow is sometimes called “open microfluidics.” It is clear that such flows cannot be motioned by pressure; however, if the filament is not too long, it can be moved by electrocapillary forces. Thus, Satoh and coworkers [52] have developed a microsystem based on electrowetting, which can move conductive liquid filaments. The cross-section of such a system is shown in Figure 5.87.

Figure 5.88 shows the extension of water filaments. The system does not need valves to orient the flow; it is done by the actuation of the proper electrodes.

An important advantage of such devices is the large interfacial area between the liquid and the gas. Typically, it could be very effective for chemical micro-reactions or to extract particles and molecules from the gas phase.

**FIGURE 5.87**

Cross section of the device: the lateral sides of the liquid filament are maintained by capillary forces.

**FIGURE 5.88**

Extension of liquid “fingers” by electrowetting actuation.

Source: Reprinted with permission from Ref. [52] © 2005, American Chemical Society.

5.10 Summary

In this chapter, we have presented the physical principles of open and covered EWOD microdevices. We have shown how and under what conditions droplets can be moved, merged, divided, mixed, and diluted in such devices. The basic operations combined with digital manipulation of droplets constitute the heart of EWOD microdevices. Assembling a complete biochip requires a complex

architecture with microfabricated electrodes, whose complexity is even more daunting if multiplexing is needed.

In Chapters 6 and 7, EWOD systems dedicated to biology, biochemistry, and chemistry are presented.

References

- [1] M.G. Pollack, R.B. Fair, D. Shenderov, Electrowetting-based actuation of liquid droplets for microfluidic applications, *Appl. Phys. Lett.* 77 (11) (2000) 1725–1726.
- [2] H. Moon, S.K. Cho, R.L. Garrell, C.-J. Kim, Low voltage electrowetting-on-dielectric, *J. Appl. Phys.* 92 (7) (2002) 4080–4087.
- [3] B. Shapiro, H. Moon, R.L. Garrell, C.-J. Kim, Equilibrium behavior of sessile drops under surface tension, applied external fields, and material variations, *J. Appl. Phys.* 93 (9) (2003) 5794–5811.
- [4] S.K. Cho, H. Moon, C.-J. Kim, Creating, transporting, and merging liquid droplets by electrowetting-based actuation for digital microfluidics circuits, *J. Microelectromech. Syst.* 12 (1) (2003) 70–80.
- [5] J. Berthier, Ph. Clementz, O. Raccourt, D. Jary, P. Claustre, C. Peponnet, Y. Fouillet, Computer aided design of an EWOD microdevice, *Sens. Actuators A Phys.* 127 (2006) 283–294.
- [6] J. Berthier, Ph. Clementz, J.-M. Roux, Y. Fouillet, C. Peponnet, Modeling microdrop motion between covered and open regions of EWOD microsystems, Proceedings of the 2006 Nanotech Conference, Boston, MA, 7–11 May 2006.
- [7] Y. Fouillet, H. Jeanson, D. Jary, O. Constantin, C. Vauchier, Moving droplets with microcatenaries, Proceedings of the 7th International Conference on Miniaturized Chemical and Biochemical Analysis Systems (μ TAS), Squaw-Valley, CA, 5–9 October 2003.
- [8] K. Brakke, The surface evolver, *Exp. Math.* 1 (1992) 141.
- [9] M.K. Chaudhury, G.M. Whitesides, How to make water run uphill? *Science* 256 (1992) 1539–1541.
- [10] R.S. Subramanian, N. Moumen, J. McLaughlin, Motion of a drop on a solid surface due to a wettability gradient, *Langmuir* 21 (2005), 11844–11849.
- [11] T.B. Jones, An electromechanical interpretation of electrowetting, *J. Micromech. Microeng.* 15 (2005) 1184–1187.
- [12] M. Washizu, Electrostatic actuation of liquid droplets for microreactor applications, *IEEE Trans. Ind. Appl.* 34 (4) (1998) 732.
- [13] I. Moon, J. Kim, Using EWOD (electrowetting-on-dielectric) actuation in a micro conveyor system, *Sens. Actuators A Phys.* 130–131 (2006) 537–544.
- [14] A.A. Darhuber, S.M. Troian, Principles of microfluidic actuation by modulation of surface stresses, *Annu. Rev. Fluid Mech.* 37 (2005) 425–455.
- [15] R.-Q. Duan, S. Koshizuka, Y. Oka, Two-dimensional simulation of drop deformation and break-up around the critical Weber number, *Nucl. Eng. Des.* 225 (2003) 37–48.
- [16] F. Blanchette, T.P. Bigioni, Partial coalescence of drops at liquid interfaces, *Nat. Phys.* 2 (2006) 254–257.

- [17] C.-Y. Chen, E.F. Fabrizio, A. Nadim, J.D. Sterling, Electrowetting-based microfluidics devices: design issues, 2003 Summer Bioengineering Conference, Sonesta Beach Resort in Key Biscayne, FL, 25–29 June 2003.
- [18] A. Dolatabadi, K. Mohseni, A. Arzpeyma, Behavior of a moving droplet under electrowetting actuation: numerical simulation, *Can. J. Chem. Eng.* 84 (2006) 17–21.
- [19] M.G. Pollack, A.D. Shenderov, R.B. Fair, Electrowetting-based actuation of droplets for integrated microfluidics, *Lab Chip* 2 (2002) 96–101.
- [20] T.P. Lodge, Reconciliation of the molecular weight dependence of diffusion and viscosity in entangled polymers, *Phys. Rev. Lett.* 83 (16) (1999) 3218–3221.
- [21] P.-G. de Gennes, F. Brochard-Wyart, D. Quéré, *Drops, Bubbles, Pearls, Waves*, Springer, New York, NY, 2004.
- [22] T. Ondarçuhu, Total or partial pinning of a droplet on a surface with chemical discontinuity, *J. Phys. II* 5 (1995) 227–241.
- [23] L.Y. Yeo, Hsueh-Chia Chang, Electrowetting films on parallel line electrodes, *Phys. Rev. E* 73 (2006) 011605.
- [24] T.B. Jones, J.D. Fowler, Young Soo Chang, C.-J. Kim, Frequency-based relationship of electrowetting and dielectrophoretic liquid microactuation, *Langmuir* 19 (2003) 7646–7651.
- [25] Jun Zeng, T. Korsmeyer, Principles of droplet electrohydrodynamics for lab-on-a-chip, *Lab Chip* 4 (2004) 265–277.
- [26] J. Berthier, Ph. Dubois, Ph. Clementz, P. Claustre, C. Peponnet, Y. Fouillet, Actuation potentials and capillary forces in electrowetting based microsystems, *Sens. Actuator* 134 (2007) 471–479.
- [27] R. Aveyard, J.H. Clint, D. Nees, Theory for the determination of line tension from capillary condensation, *J. Chem. Soc. Faraday Trans.* 93 (24) (1997) 4409–4411.
- [28] J. Berthier, C. Peponnet, A model for the determination of the dimensions of dents for jagged electrodes in EWOD microsystems, *BioMicrofluidics* 1 (2007) 014104-1–014104-10.
- [29] Fei Su, K. Chakrabarty, R.B. Fair, Microfluidics-based biochips: technology issues, implementation platforms and design-automation challenges, *IEEE Trans. Comput. Aided Des. Integrated Circ. Syst.* 25 (2) (2006) 211–223.
- [30] M. Armani, S. Walker, B. Shapiro, Modeling and control of electrically actuated surface tension driven microfluidic systems, Proceedings of the 13th Mediterranean Conference on Control and Automation, Limassol, Cyprus, 27–29 June 2005.
- [31] J. Lienemann, A. Greiner, J.G. Korvink, Modeling, simulation, and optimization of electrowetting, *IEEE Trans. Comput. Aided Des. Integrated Circ. Syst.* 25 (2) (2006) 234–247.
- [32] J. Carlier, S. Arscott, V. Thomy, J.C. Fourrier, F. Caron, J.C. Camart, et al., Integrated microfluidics based on multi-layered SU-8 for mass spectrometry analysis, *J. Micromech. Microeng.* 14 (2004) 619–624.
- [33] D. Jary, A. Chollat-Namy, Y. Fouillet, J. Boutet, C. Chabrol, G. Castellan, et al., DNA repair enzyme analysis on EWOD fluidic microprocessor, Proceedings of the 2006 Nanotech conference, Boston, MA, 7–11 May 2006.
- [34] P. Clementz, J. Berthier, J.M. Roux, R. Blanc, G. Castellan, C. Chabrol, et al., EWOD contribution to sample preconcentration: droplet geometrical transformation from drop formation to evaporation step, NanoBio Europe Conference, Münster, Germany, 22–24 September 2005.

- [35] N.A. Patankar, Y. Chen, Numerical simulation of droplets shapes on rough surfaces, Nanotech 2002; Technical Proceedings of the 5th International Conference on Modeling and Simulation of Microsystems, San Juan, Puerto Rico, USA, 22–25 April, 2002, pp. 116–119.
- [36] J. Berthier, K. Brakke, *The Physics of Microdroplets*, Scrivener-Wiley Publishing, Beverly, MA, 2012.
- [37] R. Ahmed, T.B. Jones, Dispensing picoliter droplets on substrates using dielectrophoresis, *J. Electrostatics* 64 (2006) 543–549.
- [38] K.-L. Wang, T.B. Jones, A. Raisanen, Dynamic control of DEP actuation and droplet dispensing, *J. Micromech. Microeng.* 17 (2007) 76–80.
- [39] C. Peponnet, EWOD actuated droplet microfluidics: from a fluidic function toolbox to biological validations, 8th LETI Annual Meeting, Grenoble, France, 29–31 May 2006.
- [40] J. Berthier, O. Raccourt, Ph. Clementz, D. Jary, P. Claustre, C. Peponnet, Y. Fouillet, An analytical model for the prediction of microdrop extraction and splitting in digital microfluidics systems, 8th Annual NSTI Nanotech 2005, Anaheim, CA, 8–12 May 2005.
- [41] M.W.L. Watson, M. Abdelgawad, G. Ye, N. Yonson, J. Trottier, A.R. Wheeler, Microcontact printing-based fabrication of digital microfluidic devices, *Anal. Chem.* 78 (2006) 7877–7885.
- [42] J. Berthier, P. Silberzan, *Microfluidics for Biotechnology*, Artech House Publishers, Norwood, MA, 2005.
- [43] J.M. Ottino, *The Kinematics of Mixing: Stretching, Chaos, and Transport*, Cambridge University Press, Cambridge, UK, 1989.
- [44] P. Paik, V.K. Pamula, R.B. Fair, Rapid droplet mixers for digital microfluidic systems, *Lab Chip* 3 (2003) 253–259.
- [45] P. Paik, V.K. Pamula, M.G. Pollack, R.B. Fair, Electrowetting-based droplet mixers for microfluidic systems, *Lab Chip* 3 (2003) 28–33.
- [46] J. Fowler, Hyejin Moon, C.J. Kim, Enhancement of mixing by droplet-based microfluidics, Proceedings IEEE Micro Electro Mechanical Systems, Las Vegas, Nevada, USA, 20–24 January, 2002, pp. 97–100.
- [47] S. Colin, *Microfluidique*, Hermès Science Publications, London, 2004.
- [48] O. Raccourt, J. Berthier, P. Clementz, M. Borella, M. Plissonnier, On the influence of surfactants in electrowetting systems, *J. Micromech. Microeng.* 17 (2007) 1–7.
- [49] U. Häfeli, W. Schütt, J. Teller, M. Zborowski, *Scientific and Clinical Applications of Magnetic Carriers*, Plenum Press, New York, 1997.
- [50] S.-K. Fan, C. Hashi, C.-J. Kim, Manipulation of multiple droplets on NxM grid by cross-reference Ewod driving scheme and pressure-contact packaging, 17th IEEE International Conference on Micro Electro Mechanical Systems MEMS 2004, Maastricht, the Netherlands, 25–29 January 2004.
- [51] H. Moon, A.R. Wheeler, R.L. Garrell, J.A. Loob, C.-J. Kim, An integrated digital microfluidic chip for multiplexed proteomic sample preparation and analysis by MALDI-MS, *Lab Chip* 6 (2006) 1213–1219.
- [52] W. Satoh, H. Hosono, H. Suzuki, On-chip microfluidic transport and mixing using electrowetting and incorporation of sensing functions, *Anal. Chem.* 77 (2005) 6857–6863.

Introduction to Liquid Dielectrophoresis*

6

CHAPTER OUTLINE

6.1 Introduction	303
6.2 DEP and the manipulation of particles	304
6.2.1 Theoretical basis—the dielectrophoretic force	304
6.2.2 The Clausius–Mossotti's factor	306
6.2.3 The crossover frequency	308
6.2.4 Conclusions	308
6.3 Liquid dielectrophoresis	309
6.3.1 Introduction—experimental approach	309
6.3.2 Basis of LDEP	311
6.3.3 LDEP modeling	314
6.3.4 LDEP and EWOD—critical frequency	317
6.3.5 LDEP devices for water nanodroplet formation	318
6.3.6 Applications to single DNA molecule isolation	321
6.4 Conclusions	322
References	323

6.1 Introduction

From a general standpoint, digital microfluidic systems can be divided into two groups: EWOD and liquid dielectrophoresis (LDEP). It is recalled here that many advantages such as the low power consumption, small volume, no pumps, and no valves are offered in digital microfluidic systems.

So far, in this book, we have not much considered the frequency of the actuating voltage. In this chapter, we focus on the effect of AC electric fields in microfluidic devices. It has been shown that EWOD and LDEP actuation are related by

*This chapter has been written with the collaboration of Raphaël Renaudot and Vincent Agache, CEA-LETI.

frequency [1,2]. It will be shown that EWOD and LDEP actuation are, respectively, the low- and high-frequency responses of a conducting or slightly conducting liquid (usually aqueous) to a nonuniform electric field.

As we have seen in the preceding chapter, EWOD is an electrowetting phenomenon on dielectric-coated electrodes, which originates from the electrostatic force acting near meniscus. DC or low-frequency AC voltage, typically less than 100 V, is employed. For EWOD, the electric fields in the liquid are close to zero, the water itself serves as a moving, deformable electrode.

LDEP is a dielectrophoretic effect on liquid media originated from the ponderomotive force on dielectrics [3]. AC voltage, of the order of 200–300 V_{rms} at 50–200 kHz, is employed. For LDEP, the electric fields in the liquid are not zero; a bulk liquid is polarized to move toward regions of high electric field strength under a nonuniform electric field.

In this chapter, we first shortly present dielectrophoresis (DEP) because it bears the theoretical basis, then we focus on LDEP, investigate its links with electrowetting, and show its applications to the generation of picoliter droplets.

6.2 DEP and the manipulation of particles

DEP is an electric method widely used to manipulate biologic objects in microsystems. Except for some special cases, DEP is not a transport technique; it is rather a micromanipulation tool. Based on a contrast between the polarizabilities of the particle and the medium, it can be used on any kind of particle charged or not. In this section, we present the theoretical basis of DEP and analyze the two different cases of the positive and negative DEP.

6.2.1 Theoretical basis—the dielectrophoretic force

Although the physics of DEP has been known and characterized for a long time, this effect has recently regained some interest in the biology–biotechnology community mainly because of its potential when coupled to microstructures. By definition, DEP is the motion induced by *nonuniform* electric fields and is due to a contrast of polarizabilities between the particle and its solvent. For the interested reader, there are some good textbooks that provide a more detailed description than this introduction [4,5]. From a theoretical standpoint, we recommend the article by Jones [6] where the main assumptions for the derivation of the DEP force are clearly stated.

Let us consider a small particle in a solvent in the presence of an electric field. Because of this field, charges accumulate nonuniformly at the interface with the surrounding medium. This charge distribution creates a dipole that interacts with the electric field. If the field is not homogeneous—different on both sides of the particle—a net force acts upon it that drives it toward the high electric field areas

if its polarizability is higher than that of the medium and in the other direction in the opposite case.

More quantitatively, the basic Maxwell equations predict that a particle of polarizability α , and of radius a experiences a force F in the presence of an external electric field E given by

$$\vec{F} = \frac{2}{3}\pi a^3 \alpha \nabla |\vec{E}|^2. \quad (6.1)$$

The particles we are interested in are “lossy dielectrics.” This means that, on top of the intrinsic permittivity of the particles, one has to also consider their conductivity and the energy dissipated via this ionic conduction. In this framework, expressing the polarizability in Eq. (6.1) leads to

$$F = 2\pi a^3 \varepsilon_0 \varepsilon_{r,1} \operatorname{Re}(f_{CM}) \nabla E^2, \quad (6.2)$$

where ε_0 is the vacuum permittivity, $\varepsilon_{r,1}$ is the relative permittivity of the solvent, f_{CM} is the so-called Clausius–Mossotti’s factor, and $\operatorname{Re}(f_{CM})$ is given by

$$f_{CM} = \frac{\varepsilon_p^* - \varepsilon_l^*}{\varepsilon_p^* + \varepsilon_l^*}, \quad (6.3)$$

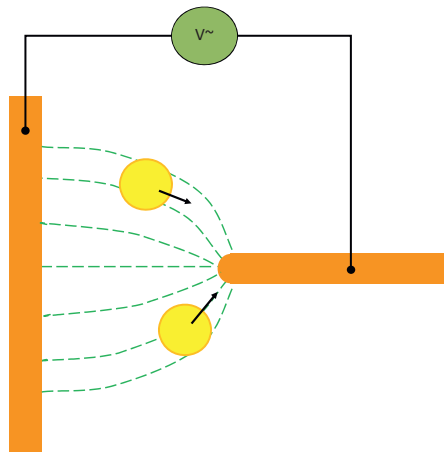
where ε_p^* and ε_l^* are, respectively, the complex permittivities of the particle and the liquid

$$\varepsilon^* = \varepsilon_0 \varepsilon_r - j \frac{\sigma}{\omega}, \quad (6.4)$$

where ε_r is the relative permittivity, σ is the conductivity, and ω is the frequency of the electric field. We also note $\varepsilon_l = \varepsilon_0 \cdot \varepsilon_{r,l}$ and $\varepsilon_p = \varepsilon_0 \cdot \varepsilon_{r,p}$.

Let us examine relation (6.2). First, the direction of the force exerted on the particle depends on the sign of the real part of the Clausius–Mossotti’s factor: if $\operatorname{Re}(f_{CM}) > 0$, the particle is attracted to the regions where the field is maximum (as illustrated in Figure 6.1), this case is called positive DEP. In the other case, the particle is repelled from these areas (actually, it is the solvent that is attracted to these areas forcing the particles to be repelled from them): it is the negative DEP case where the particles appear to be driven toward the low electric field areas.

Second, the DEP force is proportional to the gradient of the square of the electric field $F \approx \nabla E^2$. This dependence implies that DEP can be used with DC or AC fields. In the first case, however, electrophoresis will compete with DEP in the motion of the particles. The use of high-frequency AC fields is particularly interesting because it suppresses electrolysis or, more generally, electrochemistry at the surface of the electrodes. Because the DEP force depends on the gradient of the electric field, intensity particle transport over large distances is difficult. It would be necessary to maintain a large gradient over such distances which require large electric fields (and thus high voltages) in the macroscopic world. However, large local gradients are more easily created in microstructures (small scales).

**FIGURE 6.1**

Polarizable particles attracted toward high electric field region in positive DEP regime.

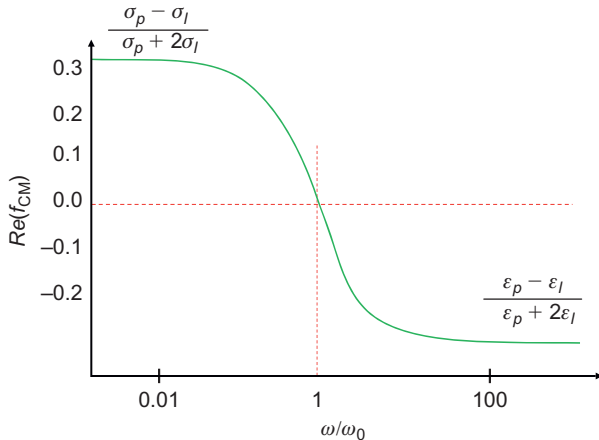
This explains why, with the development of microfabrication and its use in life science, this effect has been effectively rediscovered recently to manipulate, characterize, or sort particles. However, to transport them over large distances remains a challenge.

6.2.2 The Clausius–Mossoti’s factor

If we want to go one step further in the calculation of the force induced by the electric field, we have to expand the Clausius–Mossoti’s factor. This discussion is very different whether we deal with low or high frequencies.

At low frequencies (lower than 10 kHz), there is some dispersion of the dielectric constant of the particle. That is, ϵ_p is actually a function of the frequency of the electric field [7]. This dispersion is mainly due to the relaxation time of the polarization of the double layer surrounding the particle (this time depends on the radius of the particle and on the Debye length). The situation is quite complex and there is no satisfactory model that fully describes all the observed phenomena [8].

At higher frequencies, the counterions of the double layer do not have enough time to move and the particle is basically nondispersive meaning that ϵ_p and σ_p are independent of the frequency. The polarization is then only due to the contrast in dielectric constants between the particle and its surrounding medium. This interfacial polarization (Maxwell–Wagner’s effect [4]) is described by a unique relaxation time τ that depends only on the permittivities and conductivities of the particle and the medium.

**FIGURE 6.2**

Evolution of the real part of the Clausius–Mossoti’s factor with the frequency. The point $\omega = \omega_0$ is the crossover frequency.

We can then express the real part of the Clausius–Mossoti’s factor as

$$\text{Re}(f_{\text{CM}}) = \frac{(\varepsilon_p - \varepsilon_l)\omega^2\tau^2}{(\varepsilon_p + 2\varepsilon_l)(1 + \omega^2\tau^2)} + \frac{(\sigma_p - \sigma_l)}{(\sigma_p + 2\sigma_l)(1 + \omega^2\tau^2)}, \quad (6.5)$$

where

$$\tau = \frac{\varepsilon_p + 2\varepsilon_l}{\sigma_p + 2\sigma_l} \quad (6.6)$$

in this case, $\text{Re}(f_{\text{CM}})$ varies monotonously with the electric field frequency between the extreme values

$$\frac{\sigma_p - \sigma_l}{\sigma_p + 2\sigma_l} \quad (\text{for } \omega \rightarrow 0) \quad (6.7)$$

and

$$\frac{\varepsilon_p - \varepsilon_l}{\varepsilon_p + 2\varepsilon_l} \quad (\omega \rightarrow \infty) \quad (6.8)$$

as shown in Figure 6.2. There remain however some discrepancies between this expression and the forces quantitatively measured in diluted colloidal suspensions. It becomes important to take into account the ionic double layer that effectively modifies the conductivity of the particles. Some authors have treated this problem by considering an infinitely thin conductive layer on the surface of the particle. Empirically, one then adds a surface

conductivity λ_s to the particle conductivity σ_p . The total effective conductivity then becomes

$$\sigma'_p = \sigma_p + 2 \frac{\lambda_s}{a} \quad (6.7)$$

The behavior of the particles is then well described by using σ'_p rather than σ_p .

We have plotted in [Figure 6.2](#), the expression of $\text{Re}(f_{\text{CM}})$ in this high-frequency regime. The low-frequency regime down to DC behavior cannot be described by this curve. Below typically 1–10 kHz, $\text{Re}(f_{\text{CM}})$ decreases and the particles may even take a negative DEP behavior.

6.2.3 The crossover frequency

From [Eq. \(6.5\)](#) and as is illustrated in [Figure 6.2](#), the behavior of the particles switches from positive to negative DEP when the frequency of the applied field varies. This frequency is called the crossover frequency and is a particularly convenient—although far from complete—way to characterize particles. For instance, a crossover frequency spectrum for different conditions such as variable solvent conductivities characterizes the dielectric constant and conductivity of the considered particle or complex bioparticles [9].

This frequency is easily calculated by solving the equation $\text{Re}(f_{\text{CM}}) = 0$ and its solution is then given by

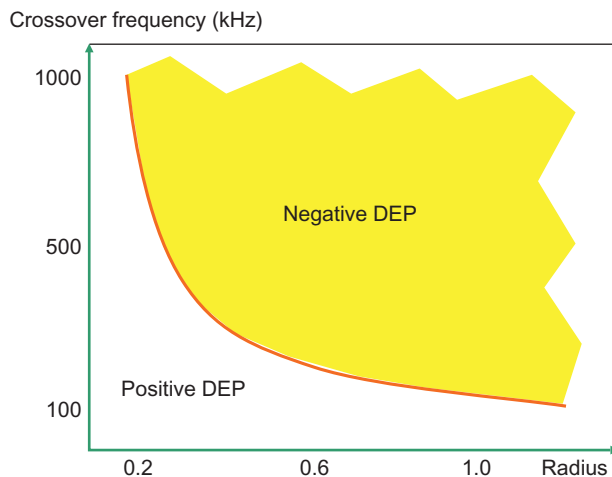
$$f_0 = \frac{1}{2\pi} \sqrt{\frac{(\sigma'_p + 2\sigma_l)(\sigma'_p - \sigma_l)}{(\varepsilon_p + 2\varepsilon_l)(\varepsilon_p - \varepsilon_l)}}, \quad (6.8)$$

where σ'_p is given by [Eq. \(6.7\)](#). A fit of such spectra gives an accurate description of some characteristics of the particle.

The coefficient σ'_p is also a function of the particle's radius. [Equation \(6.8\)](#) has been tested for identical particles of various radii ([Figure 6.3](#)). The excellent agreement between theory and experiments is a good way to determine the surface conductivity of these particles.

6.2.4 Conclusions

DEP is a vast domain, which includes sophisticated physics, such as interaction between particles and electric field, dipolar or multipolar attractions, double layers, and so on. Electrode designs have been the subject of much research. Materials and microfabrication have also been the topic of many investigations. At the present time, the number of publications pertaining to DEP is larger than 2000. Applications are many and still evolving, in domains such as mineral separation, micropolishing, manipulation and dispensing of fluid droplets, and manipulation and assembly of microcomponents. An interesting review on the state of the art of DEP has been written by Pethig [[10](#)].

**FIGURE 6.3**

Crossover frequency between positive and negative DEP for polystyrene latex beads of different radii in pure water.

6.3 Liquid dielectrophoresis

6.3.1 Introduction—experimental approach

In the previous section, we have focused on the manipulation of lossy dielectric particles by DEP. In this section, we focus on liquid droplets in electric fields. Nonuniform electric fields induce a DEP force on polarizable media, including liquids such as water or dielectric liquids. With properly designed electrodes, the DEP effect may be exploited to control and manipulate small liquid volumes. This principle is called LDEP.

The first physicist to observe LDEP was Pellat [11] during the year 1895. Pellat's experimental setup, as shown schematically in Figure 6.4, is comprised of a pair of parallel electrode plates separated by a gap s , partially immersed in a reservoir of dielectric liquid of density ρ and permittivity ε .

Upon the application of a voltage V across the electrodes, the dielectric liquid between the electrodes, due to nonuniform field effects, rises vertically upward (covering regions of higher electric field) and attains a new equilibrium height h given by

$$h \approx \frac{(\varepsilon - \varepsilon_0)E^2}{2\rho g}, \quad (6.9)$$

where

$$E = \frac{V}{s}. \quad (6.10)$$

In Pellat's experiment, the liquid is oil. In 1971, Jones et al. [12] developed a dielectric siphon based on the same principle. These experiments have demonstrated that liquid interface can be moved under the action of electric fields. These experiments however were at the macroscale. The first microscale LDEP systems were developed recently at the beginning of the twenty-first century [13]. The most interesting aspect of LDEP for micro- and nanotechnologies is probably

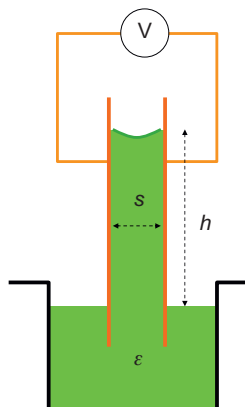


FIGURE 6.4

Pellat's experiment showing the rise of a liquid (insulating oil) between two parallel electrodes [11].

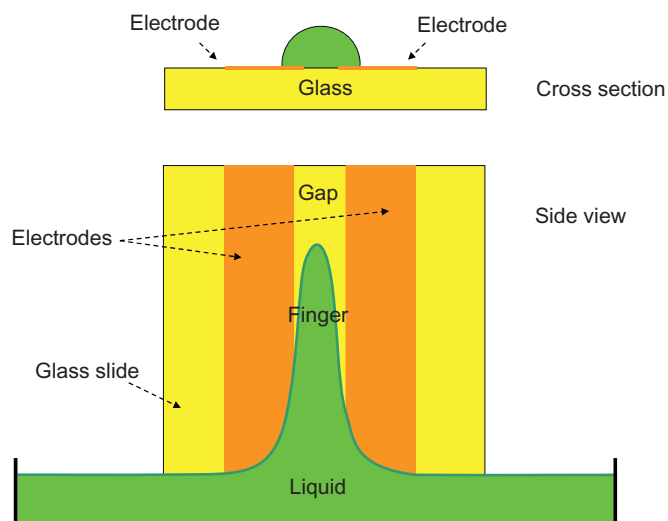


FIGURE 6.5

Liquid fingering by LDEP ($\epsilon/\epsilon_0 = 2.4$, $\rho = 900 \text{ kg/m}^3$, $V = 200 \text{ V}$, and $f = 60 \text{ Hz}$).

the formation and manipulation of small volumes of liquids (fingerlike configuration or droplets). The technique is based on the “liquid fingering” phenomenon, which is described next.

Pellat and Melcher’s experiments have shown that liquid interfaces can be displaced by AC electric fields. An interesting LDEP microdevice consisting of two parallel planar electrodes was proposed by Jones [14]; this device is shown in [Figure 6.5](#). Upon actuation of the electrodes with an AC voltage— $V \sim 200 \text{ V}_{\text{rms}}$ at 60 Hz—the liquid (insulating transformer oil) rises along the electrodes. This phenomenon is called liquid fingering.

In the following section, we analyze the physical principles that explain the motion of the liquid interface.

6.3.2 Basis of LDEP

Pohl [4] originally defined DEP as the attraction of uncharged but polarizable particles into regions of higher electric field intensity. DEP liquid actuation is not concerned with particles inside the liquid. Rather, it exploits the force to manipulate liquid masses. LDEP is phenomenologically similar to particulate DEP in that polarizable liquids also are drawn into regions of stronger electric field intensity.

Consider the system depicted in [Figure 6.6](#), closely related to the liquid fingering configuration, with an insulating liquid. Using the virtual work theorem, the ponderomotive force is given by

$$F^e = -\frac{\partial W_e}{\partial x} \Big|_{V=cste} = -\partial \frac{\frac{1}{2}CV^2}{\partial x}. \quad (6.11)$$

Upon introduction of the expression for the total capacitance C , the ponderomotive force is

$$F^e = -\frac{(\varepsilon_r, \text{liq} - 1)\varepsilon_0 w V^2}{2D}, \quad (6.12)$$

where w is the width of the electrodes, ε_0 is the permittivity of vacuum, and ε_r is the relative permittivity.

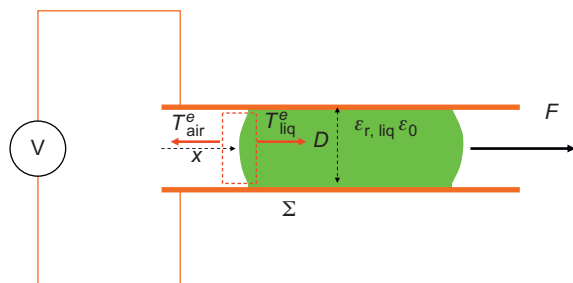


FIGURE 6.6

Sketch of a liquid moved by a ponderomotive force.

Another approach to the same problem can be made using Maxwell tensor

$$T^e = -\frac{1}{2}\varepsilon_r\varepsilon_0 E^2. \quad (6.13)$$

In this case

$$F_x^e = (T_{\text{liq}}^e - T_{\text{air}}^e)wD = -\frac{1}{2}(\varepsilon_r - 1)\varepsilon_0 E^2 wD = -\frac{w}{2D}(\varepsilon_r - 1)\varepsilon_0 V^2, \quad (6.14)$$

which is identical to [Eq. \(6.12\)](#). The utilization of the Maxwell tensor on a symbolic surface surrounding the interface explains the liquid rise in the Pellat's experiment ([Figure 6.7](#))

$$T_z^e = T_{\text{air}}^e - T_{\text{liq}}^e \quad (6.15)$$

and

$$T_z^e = -\frac{1}{2}(\varepsilon_{r,\text{liq}} - \varepsilon_{r,\text{air}})\varepsilon_0 E^2 \quad (6.16)$$

where $E = V/s$. The interface stabilizes when

$$T_z^e = P_{\text{air}} - P_{\text{liq}} = -\rho g h. \quad (6.17)$$

The liquid elevation is then given by

$$h = \frac{1}{2\rho g}(\varepsilon_{r,\text{liq}} - 1)\varepsilon_0 \frac{V^2}{s^2}. \quad (6.18)$$

This is the same expression as the historic Pellat's expression [\(6.9\)](#).

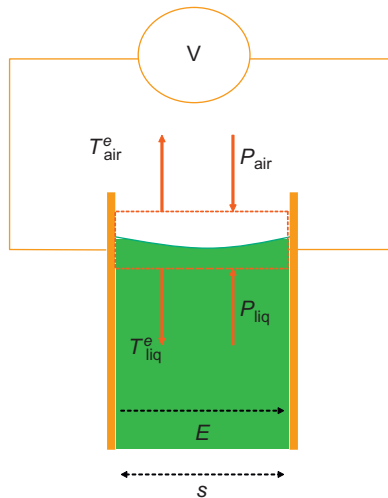


FIGURE 6.7

Ponderomotive force in the Pellat's experiment.

In all the preceding analysis, the capillary forces have been neglected. Note that at very small scale, a capillary rise can be observed depending on the contact angle and the distance between the two plates [15]. In the present case, we assume that the contact angle is close to 90° . A more strict approach requires the taking into account of capillarity. However, such an approach is still to be done.

An interpretation of the force on the interface is shown in Figure 6.8: the electric charges in the liquid exert an electric force on the interface resulting in the motion of the liquid.

Note that the ponderomotive force is proportional to $(\epsilon_r - 1)$. The relative permittivity is then a determining element in the ponderomotive effect. In Table 6.1, we indicate the values of the relative permittivity of some useful liquids.

In the previous developments, liquids were considered electrically insulating. However, one of our aims is to use LDEP for poorly to slightly conducting liquids, such as DIW. In order to avoid spurious phenomena like hydrolysis and Joule effect, it is best to coat the electrodes with a dielectric layer. In such a case, the preceding reasoning is still valid if we take the precaution to introduce the dielectric capacitance. It is also often the case that the dielectric layer be coated with a hydrophobic layer, as it is in EWOD devices. Hence, in the preceding analysis capacitances of the dielectric and hydrophobic layers have to be introduced. In the following section, we develop the theory of LDEP in the case of passivated electrodes.

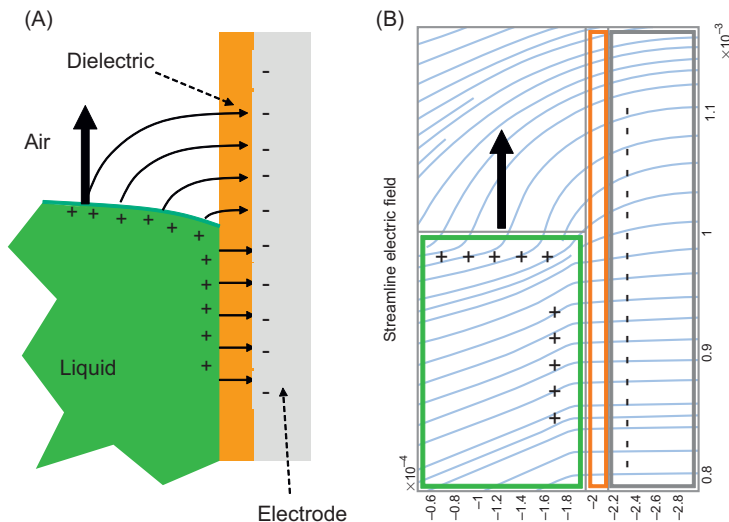


FIGURE 6.8

Coulombic interpretation: the locally intense electric field acts on the surface charges:
 (A) sketch of interface and wall and (B) electric streamlines calculated with COMSOL (<http://www.comsol.com/>) taking into account copper electrode, alumina dielectric, and liquid ethanol.

Table 6.1 Relative Permittivity of Some Liquids

Liquid	Temperature (°C)	Relative Permittivity
Acetone	20	20.7
Ethanol	25	24.3
Methanol	20	33.1
Ammonia	20	16.5
Chloroform	20	4.8
Glycerol	20	42.5
Heptane	20	1.9
Hexanol	25	13.3
Mercury	146	1
Oil (olive)	20	3.1
Phenol	10	4.3
Water	20	80.4

6.3.3 LDEP modeling

As for EWOD, LDEP systems can be in a so-called open or covered configuration. In open systems, a sessile rivulet is elongated by electric forces. In the case of covered LDEP system, a (hydrophobic) dielectric and a grounded electrode are placed on top of the device, and the rivulet is elongated by the electric forces. Basically, the reasoning for deriving the LDEP force is the same in both cases; only the expression of the liquid capacitance and impedance changes.

A usual approach of the problem is to make a lumped decomposition of the system [16–19]. The two (open or covered) configurations are shown in Figure 6.9. For simplicity, we restrict ourselves to the case of covered systems [18] for which the calculation is much easier than open systems [19,20].

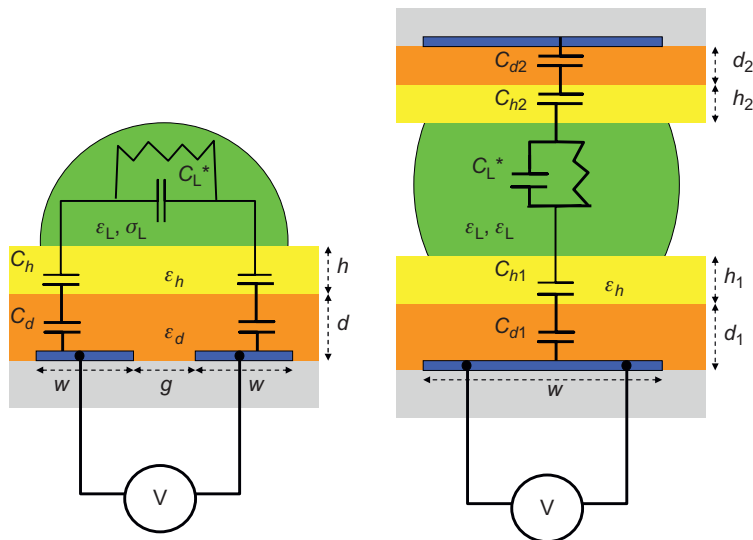
Following a very common approach, we use the virtual work theorem for calculating the LDEP force

$$F = \frac{\partial U}{\partial y}, \quad (6.19)$$

where the direction of the motion is along the y -axis. The energy of the system (neglecting the surface tension) is given by

$$U = \sum_i \frac{1}{2} C_i \Delta V_i^2, \quad (6.20)$$

where ΔV_i is the voltage drop between the boundary of each layer. Note that the indices i include all the layers in the liquid side as well as the air side because Eq. (6.20) is the electric energy of all the system. Below we respectively note, for

**FIGURE 6.9**

Two configurations for LDEP: (A) open LDEP and (B) covered (or two plates) LDEP.

Source: From Ref. [19].

simplicity, i and i^* the indices in the liquid and air side. These voltages are related to the layer impedances by

$$\Delta V_i = \frac{Z_i}{\sum_j Z_j} V. \quad (6.21)$$

Formerly, Eq. (6.21) can be substituted in Eq. (6.20) to yield

$$U = \frac{1}{2} V^2 \sum_i C_i \left(\frac{Z_i}{\sum_j Z_j} \right)^2. \quad (6.22)$$

Note that the capacitances and impedances are functions of the location of the moving interface. The capacitances in the air side can be expressed as

$$C_i^* = \frac{\varepsilon_{r,i} \varepsilon_0 W (L - y)}{d_i} = A_i (L - y), \quad (6.23)$$

where y is the direction of the motion, W is the total width of the system ($W = 2w + g$), d_i is the depth of the layer, $\varepsilon_{r,i}$ is the relative permittivity, and L is the total length of the electrodes. In the liquid side, the expressions for capacitances are

$$C_i = \frac{\varepsilon_{r,i} \varepsilon_0 W y}{d_i} = A_i y. \quad (6.24)$$

In the case of a dielectric layer, the electric equivalent scheme is a pure capacitance, while for a conductive media the electric equivalent scheme is a pure

resistance. In between, for a poorly to moderately conductive liquid, the equivalent scheme is a capacitance in parallel with a resistance. The impedances of the different layers are given by

$$Z_i = \frac{1}{j\omega C_i} \quad (6.25)$$

for dielectric layers, and for the liquid

$$Z_{\text{liq}} = \frac{1}{R_{\text{liq}} + j\omega C_{\text{liq}}}, \quad (6.26)$$

where $\omega = 2\pi/f$, f being the frequency. Using the virtual work theorem (6.20), and substituting Eq. (6.22), the electric force is then

$$F = \frac{1}{2} V^2 \sum_i \frac{\partial}{\partial y} \left[C_i(y) \left(\frac{Z_i(y)}{\sum_j Z_j(y)} \right)^2 \right], \quad (6.27)$$

where the summation index i refers to the liquid side as well to the air side. If we decompose the system as shown in Figure 6.10, we can express the different terms inside the parenthesis in the right-hand side of Eq. (6.27) as functions of the properties of the materials and geometrical dimensions.

In the case of “open” LDEP system, the theoretical developments have been conducted by Renaudot and colleagues [19].

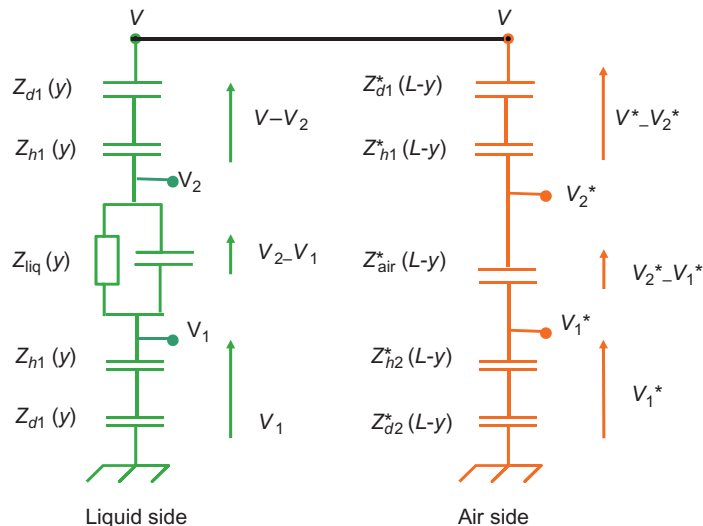


FIGURE 6.10

Sketch of the impedances and voltages.

6.3.4 LDEP and EWOD—critical frequency

Expression (6.26) for the LDEP electromechanical force is similar to that of the EWOD force. In both cases, the expression is of the form

$$F = \frac{1}{2} \tilde{C} V^2. \quad (6.28)$$

The difference comes from the expression of the term \tilde{C} which is a different function of the capacitances. In order to be more explicit, let us develop the expression (6.20) for the electric energy. Upon substitution of the different capacitances, we find

$$U = \frac{1}{2} \left[C_{\text{top}}(y)(V - V_2)^2 + C_{\text{top}}(L - y)(V - V_2^*)^2 + C_{\text{liq}}(y)(V_2 - V_1)^2 + C_{\text{air}}(L - y)(V_2^* - V_1)^2 + C_{\text{bot}}(y)(V_1)^2 + C_{\text{bot}}(L - y)(V_1^*)^2 \right], \quad (6.29)$$

where C_{top} and C_{bot} are the equivalent capacitances of the top cover and bottom plate. The electromechanical force being the derivative of U with respect to y , and using Eqs. (6.23) and (6.24) for calculating the capacitances, we find

$$F = \frac{1}{2} \left[A_{\text{top}}(V - V_2)^2 - A_{\text{top}}(V - V_2^*)^2 + A_{\text{liq}}(V_2 - V_1)^2 - A_{\text{air}}(V_2^* - V_1)^2 + A_{\text{bot}}(V_1)^2 - A_{\text{bot}}(V_1^*)^2 \right]. \quad (6.30)$$

Expression (6.30) states that the total electromechanical force is the sum of three terms, two electrowetting forces (on top and bottom) and an LDEP force

$$F = F_{\text{EW,top}} + F_{\text{LDEP}} + F_{\text{EW,bot}}. \quad (6.31)$$

More specifically

$$\begin{aligned} F_{\text{EW,top}} &= \frac{1}{2} A_{\text{top}} [(V - V_2)^2 - (V - V_2^*)^2] \\ F_{\text{LDEP}} &= \frac{1}{2} [A_{\text{liq}}(V_2 - V_1)^2 - A_{\text{air}}(V_2^* - V_1)^2] \\ F_{\text{EW,bot}} &= \frac{1}{2} A_{\text{bot}} [V_1^2 - V_1^{*2}]. \end{aligned} \quad (6.32)$$

It has been shown that, depending on the AC frequency, these three terms do not have the same importance. A critical frequency f_c [16–18] can be defined as

$$f_c = \frac{1}{2\pi} \frac{g_L}{(C_D + C_L)}, \quad (6.33)$$

where g_L is the conductance of the liquid layer (product of the electric conductivity by the depth of the liquid layer), C_D is the total capacitance of the dielectric layers (top and bottom plates), and C_L is the capacitance of the liquid layer. Note that nearly always $C_D \gg C_L$. Note that the air capacitance does not contribute to

the evaluation of the critical frequency because of the absence of any resistive element.

When $f \ll f_c$, the liquid behaves as a pure conductor; the voltage drop occurs across the dielectric layer; and the electromechanical force is an electrowetting force. However, if $f \gg f_c$, the liquid is purely insulating. The voltage drop occurs across the liquid, and the DEP force causes the liquid motion.

If the liquid is totally insulating, the critical frequency is zero and no EWOD effect can be found. If the liquid is poorly conductive, the critical frequency is small and a weak electrowetting force exists below this critical frequency [21,22]. In the case of the Pellat's experiment, there are no dielectric layers and the liquid is poorly conductive: the critical frequency is low, and LDEP is observed at low frequency (50 Hz). A conductive liquid has a high critical frequency. Frequencies above 500 kHz are used for LDEP with DIW. Biological samples are highly conductive, and EWOD forces dominate in a very large range of frequencies.

6.3.5 LDEP devices for water nanodroplet formation

The formation of picoliter droplets by LDEP using parallel coplanar electrodes has been pioneered by Ahmed and Jones [23] and recently extensively investigated [2,24]. The concept of the device directly stems from the fingering effect described earlier. It consists of two long, coplanar, and parallel electrodes placed horizontally, penetrating on one side in a reservoir. Three different types of devices have been successively designed (Figure 6.6).

The first device—noted (A) in Figure 6.11—is directly derived from the liquid fingering effect. When actuated, a liquid finger progresses along the electrodes to

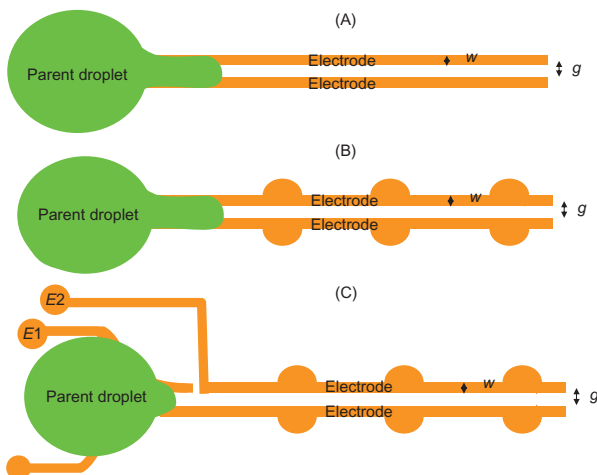


FIGURE 6.11

Different LDEP devices: (A) straight electrodes, (B) electrodes with bumps, and (C) electrodes with bumps and backflow valve.

become a long rivulet. A few milliseconds are sufficient to displace the liquid along the electrodes unto their extremity. After removing the actuation, the liquid rivulet breaks up under the action of Plateau–Rayleigh instabilities [25–27]. The Plateau–Rayleigh theory addresses the breakup of inviscid cylindrical liquid jets. Let us recall that if R is the initial radius of the jet, then all wavelengths longer than $\lambda_{\text{crit}} = 2\pi R$ are unstable, and the harmonic disturbances at wavelength

$$\lambda^* = 9.016R \quad (6.34)$$

are growing fastest. λ^* is called the most unstable wavelength. The viscosity of the liquid has only a small influence on the most unstable wavelength, as was shown by Weber [28]. The viscosity-corrected expression of λ^* is

$$\lambda^* = 2\pi R \sqrt{2 + 6(Oh/2)^{0.5}} \quad (6.35)$$

where Oh is the dimensionless Ohnesorge number [29] defined by

$$Oh = \frac{\rho\nu^2}{\gamma R}, \quad (6.36)$$

where ρ , ν , and γ are, respectively, the liquid density, kinematic viscosity, and surface tension. Interestingly, it has been demonstrated by Davis [30] that the most unstable wavelength was nearly the same for free jets and for sessile rivulets: the influence of the substrate wettability on the breakup is small as shown by Schiaffino and Sonin [31]. In the case of rivulet LDEP and assuming that the rivulet is nearly semicylindrical ($R = 2w + g$), the most unstable wavelength for the breakup of water rivulet is then

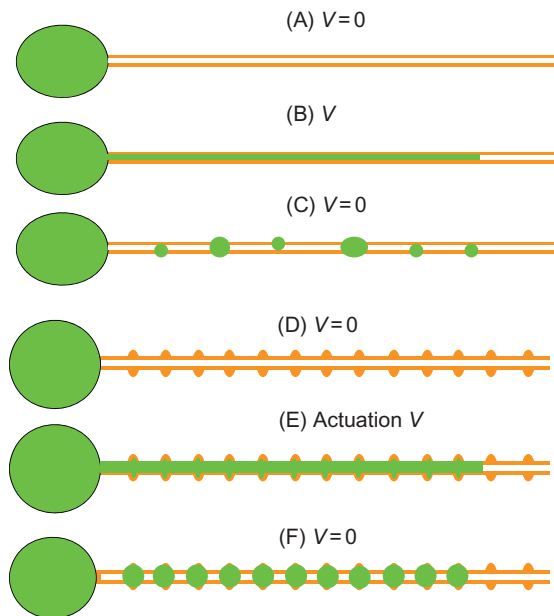
$$\lambda^* = 9.016(2w + g). \quad (6.37)$$

If the breakup droplets were all at a distance λ^* , their volume would be

$$\text{Vol} = \pi R^2 \frac{\lambda^*}{2}. \quad (6.38)$$

However, it is observed that the droplet spacing is not uniform, and the breakup-droplet volume is irregular (Figure 6.12A–C). This phenomenon is attributed to the retraction of the rivulet toward the parent drop—retraction that occurs under the action of the surface tension of the liquid, in order to minimize its free energy.

As often in fluid mechanics, one would like to take advantage of instabilities, and at the same time control them. This is the case of flow focusing devices that will be presented later in the book. Hence, from this notion of most unstable wavelength stemmed the idea of forcing the instabilities to develop at predefined locations, using local protrusion or “bumps,” as shown in Figure 6.11B. It has been shown in Ref. [23] that if the bumps are spaced at a distance λ^* , the breakup droplets will form exactly on the bumps, as shown in Figure 6.12D–F. However, if the bumps are spaced at $\lambda^*/2$, the droplet distribution is irregular.

**FIGURE 6.12**

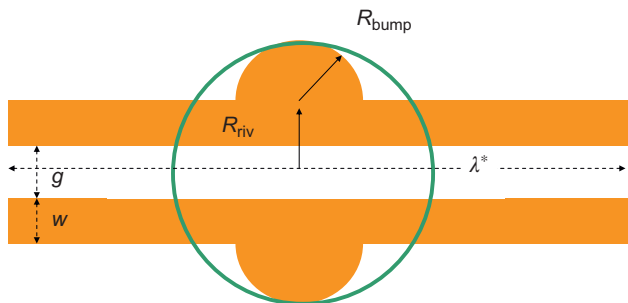
Droplet formation by LDEP: (A–C) device without bumps; (A) at time $t = 0$, the liquid is confined in the large reservoir at the left; (B) upon actuation (~ 150 V), a liquid rivulet extends between the electrodes; (C) after stopping the actuation, the liquid finger retracts and breaks up by Plateau–Rayleigh’s instabilities. (D–F) Device with bumps regularly spaced at λ^* ; (D) at time $t = 0$, the liquid is confined in the large reservoir at the left; (E) upon actuation (~ 150 V), a liquid rivulet extends between the electrodes; (F) after stopping the actuation, the liquid finger retracts, breaks up by Plateau–Rayleigh’s instabilities and leaves droplets in the protrusions, sketched from Refs. [22–24].

Finally, if the bumps are spaced at $2\lambda^*$, satellite droplets appear between the bumps. So, the spacing at λ^* is essential to obtain regularly spaced droplets.

In order to control still more the situation, an antiretraction design has been proposed (Figure 6.11C) [23]. The interruption of one electrode line acts as a backflow valve. Upon actuation, the liquid “jumps” over the gap; when the voltage is shut off, the liquid cannot retract toward the parent droplet.

A question remains: what is the volume of the breakup droplets? Let us analyze the problem by the sketch of Figure 6.13. Assuming a contact angle of 90° , the droplet volume is that of a hemisphere of radius $R_{\text{bump}} + R_{\text{riv}}$, and also the initial elongated volume

$$\text{Vol} = \frac{2\pi}{3}(R_{\text{bump}} + R_{\text{riv}})^3 \approx \pi R_{\text{riv}}^2 \frac{\lambda^*}{2} + \frac{2\pi}{3}R_{\text{bump}}^3. \quad (6.39)$$

**FIGURE 6.13**

Close-up view of a bump: the radius of the droplet is $R_{\text{bump}} + R_{\text{riv}}$, where $R_{\text{riv}} = w + g/2$.

As stated in Eq. (6.37), λ^* as a function of R_{riv} : $\lambda^* = 9.016R_{\text{riv}}$. Hence, Eq. (6.39) is a relation between R_{bump} and R_{riv} . The terms in R_{bump}^3 cancel out, and we are left with a quadratic expression. The solution is

$$R_{\text{bump}} \approx 0.98R_{\text{riv}}. \quad (6.40)$$

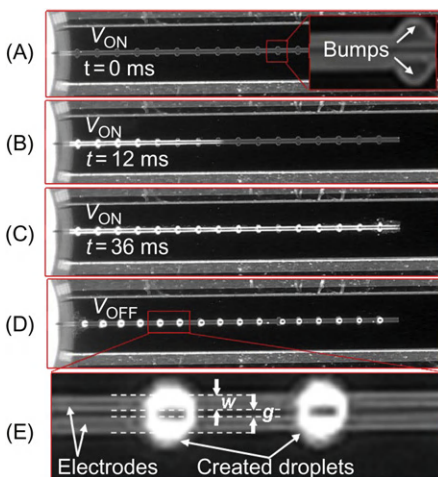
Already, the dimensions of LDEP systems have been reduced in order to produce even smaller droplets. Figure 6.14 shows a rivulet effect at a very small scale (electrode width 7 μm and gap 4 μm).

6.3.6 Applications to single DNA molecule isolation

Developments of LDEP systems are very recent. Even if the first experiment by Pellat is rather ancient, the principle of microscale LDEP is new. Applications are just starting to appear. We relate here a few recently published applications.

Wee and colleagues [32] have used the LDEP system described above to isolate single strands of DNA. Nanotweezers are then utilized to manipulate the DNA molecule. The principle is simple, once the principle of rivulet LDEP system is established: consider a long rivulet LDEP system and a parent drop with a very low concentration in DNA molecules. The formation of a long rivulet and the following breakup of the rivulet leaves small, isolated droplets, some with a single strand of DNA. The DNA strands can be further manipulated using nanotweezers.

Kaler and Prakash [33] managed to fabricate giant unilamellar vesicles (GUVs) using LDEP. It is recalled that GUVs can serve as interesting models for mimicking biological membranes and furthermore can be usefully leveraged in drug delivery and biosensor applications. In Kaler and Prakash's [33] paper, it is shown how LDEP can be used to assemble and precisely position GUVs over a range of diameter 30–100 μm .

**FIGURE 6.14**

(A–D) Evolution of a DIW liquid finger while applying a 250 ms alternative signal pulse of $236 \text{ V}_{\text{rms}}$ at 100 kHz. The dielectric layers are composed of 300 nm SiN and 300 nm SiOC. (E) The electrode width w is $7 \mu\text{m}$, while the gap g is $4 \mu\text{m}$. The picoliter droplets are created by the breakup of the capillary instability at semicircular profiles positions called bumps.

Source: Photographs courtesy V. Agache and R. Renaudot, CEA-LETI.

Another application pertains to microfluidic resonators [34–36]. It consists in patterning LDEP electrodes on the MEMS oscillator mass sensors to directly convey analyte solutions atop of the sensitive platform, instead of immersing it in the solution to be analyzed [37]. This configuration has the advantage of preserving the Q factor of the MEMS (in particularly for in-plane mode oscillators) while performing the measurements in the presence of liquid [38]. Many applications are presently in the developing process.

6.4 Conclusions

In this chapter, the principle of DEP has been recalled. Extension to LDEP has been presented. It has been shown that electrowetting and LDEP are the two facets of the same electromechanical approach.

A very interesting application of LDEP is the microconveyor device which dispenses picoliter liquid droplets at precise locations. Such a system could be used as a “common rail” for delivering droplets to EWOD devices. At the present time, other applications are just starting to be developed.

References

- [1] T.B. Jones, K.L. Wang, Frequency-dependent electromechanics of aqueous liquids: Electrowetting and dielectrophoresis, *Langmuir* 20 (7) (2004) 2813–2818.
- [2] S.-L. Tsai, J.-L. Hong, M.-K. Chen, L.-S. Jang, Experimental study of dielectrophoresis and liquid dielectrophoresis mechanisms for particle capture in a droplet, *Electrophoresis* 32 (2011) 1337–1347.
- [3] H.A.H. Boot, R.B.R.-S. Harvie, Charged particles in a non-uniform radio-frequency field, *Nature* 180 (1957) 1187.
- [4] H.A. Pohl, *Dielectrophoresis*, Cambridge University Press, Cambridge, UK, 1978.
- [5] T.B. Jones, *Electromechanics of Particles*, Cambridge University Press, Cambridge, UK, 1995.
- [6] T.B. Jones, Basic theory of dielectrophoresis and electrorotation, *IEEE Eng. Med. Biol. Mag.* 22 (2003) 33–42.
- [7] C. Ballario, A. Bonincontro, C. Cametti, Dielectric dispersions of colloidal particles in aqueous suspensions with low ionic conductivity, *J. Colloid Interface Sci.* 54 (3) (1976) 415–423.
- [8] K.R. Foster, F.A. Sauer, H.P. Schwan, Electrorotation and levitation of cells and colloidal particles, *Biophys. J.* 63 (1) (1992) 180–190.
- [9] M.P. Hughes, *Nanoelectromechanics in Engineering and Biology*, CRC Press, Boca Raton, FL, 2003.
- [10] R. Pethig, Review article—dielectrophoresis: status of the theory, technology, and applications, *Biomicrofluidics* 4 (2010) 022811.
- [11] H. PELLAT, Mesure de la force agissant sur les diélectriques liquides non électrisés placés dans un champ électrique, *C. R. Acad. Sci.* 119 (1895) 691–693.
- [12] T.B. Jones, M.P. Perry, J.R. Melcher, Dielectric siphons, *Science* 174 (1971) 1232–1233.
- [13] T.B. Jones, Liquid dielectrophoresis on the microscale, *J. Electrostat.* 51–52 (2001) 290–299.
- [14] T.B. Jones, M. Gunji, M. Washizu, M.J. Feldman, Dielectrophoretic liquid actuation and nanodroplet formation, *J. Appl. Phys.* 89 (2001) 1441.
- [15] J. Berthier, K. Brakke, *The Physics of Microdroplets*, Scrivener Publishing, Beverly, MA, 2012.
- [16] T.B. Jones, On the relationship of dielectrophoresis and electrowetting, *Langmuir* 18 (2002) 4437–4443.
- [17] T.B. Jones, J.D. Fowler, Y.S. Chang, C-J Kim, Frequency-based relationship of electrowetting and dielectrophoretic liquid microactuation, *Langmuir* 19 (2003) 7646–7651.
- [18] D. Chatterjee, H. Sheperd, R.L. Garrell, Electromechanical model for actuating liquids in a two-plate droplet microfluidic device, *Lab Chip* 9 (2009) 1219–1229.
- [19] R. Renaudot, V. Agache, B. Daunay, P. Lambert, M. Kumemura, Y. Fouillet, et al., Optimization of liquid dielectrophoresis (LDEP) digital microfluidic transduction for biomedical applications, *Micromachines* 2 (2011) 258–273.
- [20] B. Daunay, P. Lambert, L. Jalabert, M. Kumemura, R. Renaudot, V. Agache, H. Fujita, Effect of substrate wettability in liquid dielectrophoresis (LDEP) based droplets generation: theoretical analysis and experimental confirmation, *Lab Chip* 12 (2012) 361.

- [21] V. Srinivasan, V.K. Pamula, R.B. Fair, An integrated digital microfluidic lab-on-a-chip for clinical diagnostics on human physiological fluids, *Lab Chip* 4 (2004) 310–315.
- [22] D. Chatterjee, B. Hetayothin, A.R. Wheeler, D.J. King, R.L. Garrell, Droplet-based microfluidics with nonaqueous solvents and solutions, *Lab Chip* 6 (2006) 199–206.
- [23] R. Ahmed, T.B. Jones, Dispensing picoliter droplets on substrates using dielectrophoresis, *J. Electrost.* 64 (2006) 543–549.
- [24] K.V.I.S. Kaler, R. Prakash, D. Chugh, Liquid dielectrophoresis and surface microfluidics, *Biomicrofluidics* 4 (2010) 022805.
- [25] L. Rayleigh, *The Theory of Sound*, Cambridge University Press, Cambridge, UK, 2011 (vol. 2, 1945, reissued)
- [26] D.T. Papageorgiou, On the breakup of liquid threads, *Phys. Fluid.* 7 (7) (1995) 1521.
- [27] J. Eggers, Nonlinear dynamics and breakup of free-surface flows, *Rev. Mod. Phys.* 69 (3) (1997) 865.
- [28] C. Weber, Zum zerfall eines flüssigkeitsstrahles, *Z. Angew. Math. Mech.* 11 (1931) 135.
- [29] J. Berthier, P. Silberzan, *Microfluidics for Biotechnology*, second edition, Artech House Publishing, Norwood, MA, 2010.
- [30] S.H. Davis, Moving contact lines and rivulet instabilities. Part 1. The static rivulet, *J. Fluid Mech.* 98 (1980) 225.
- [31] S. Schiaffino, A.A. Sonin, Formation and stability of liquid and molten beads on a solid surface, *J. Fluid Mech.* 343 (1997) 95–110.
- [32] B. Wee, M. Kumemura, D. Collard, H. Fujita, Isolation of single DNA molecule in a picoliter-sized droplet formed by liquid dielectrophoresis, Twelfth International Conference on Miniaturized Systems for Chemistry and Life Sciences, 12–16 October 2008, San Diego, CA.
- [33] K.V.I.S. Kaler, R. Prakash, Dispensing and bio-functionalization of giant unilamellar vesicles on a chip, 13th International Conference on Electrostatics, Journal of Physics: Conference Series, Bangor, Wales, UK, vol. 301, 2011, p. 012015.
- [34] S. Son, W.H. Grover, T.P. Burg, S.R. Manalis, Suspended microchannel resonators for ultralow volume universal detection, *Anal. Chem.* 80 (2008) 4757–4760.
- [35] P.-S. Lee, J.H. Lee, N.Y. Shin, K.-H. Lee, D.K. Lee, S.M. Jeon, et al., Microcantilevers with nanochannels, *Adv. Mater.* 20 (2008) 1732–1737.
- [36] M. Godin, F.F. Delgado, S. Son, W.H. Grover, A.K. Bryan, A. Tzur, et al., Using buoyant mass to measure the growth of single cells, *Nat. Methods* 7 (2010) 387–390.
- [37] V. Agache, P. Caillat, P. Puget, Method and microsystem for detecting analytes which are present in drops of liquid, Patent No. PCT/EP2011/052025, 11/02/2011.
- [38] V. Agache, M. Cochet, R. Blanc, F. Baleras, P. Caillat, High Q factor plate resonators for ultrasensitive mass sensing applications, Proceedings of Transducers 2009, Denver, CO, 21–25 June 2009, pp. 1630–1633.

Electrowetting on Curved Surfaces

7

CHAPTER OUTLINE

7.1 Introduction	325
7.2 Theory of curved electrowetting.....	325
7.2.1 EWOD on a spherical surface.....	327
7.2.2 EWOD on a cylindrical surface.....	329
7.2.3 Conclusions	330
7.3 Electrowetting on a wavy surface.....	330
7.4 Electrowetting on a rod	332
7.4.1 Introduction	332
7.4.2 Electrowetting on a wire	334
7.5 Electrowetting on a sphere	335
7.6 Conclusion	336
References	337

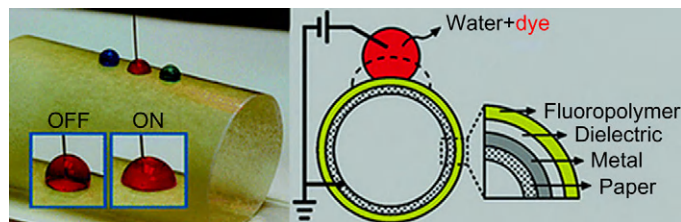
7.1 Introduction

Historically, the development of DMF has been done using planar surfaces. To point out the contrast with the conventional three-dimensional channel microfluidics, DMF has also been called “planar microfluidics.” Recently, it has been found that the planar requirement was not needed for electrowetting devices ([Figure 7.1](#)). This evolution of the technique is opening the way to new concepts.

In this chapter, the theory of electrowetting on curved surfaces is presented first, and then some examples of applications to different curved surfaces—wavy, cylindrical, and spherical surfaces—are analyzed.

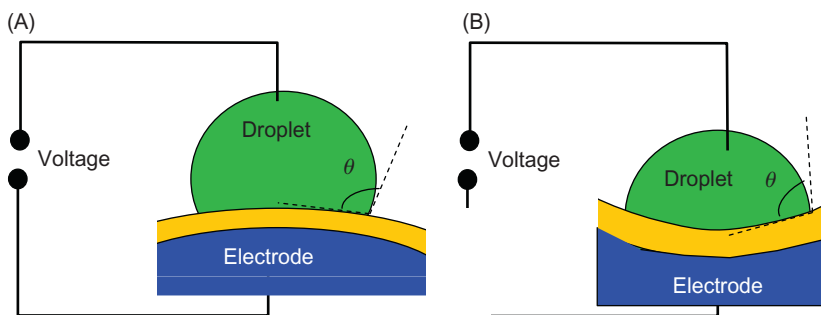
7.2 Theory of curved electrowetting

Theoretically, the assumption of a flat, planar surface is not a prerequisite for electrocapillarity or electrowetting. The same type of physical phenomena

**FIGURE 7.1**

Kim and Steckl [1] demonstrated that paper can be used as a flexible material for an electrowetting device.

Source: Reprinted with permission from Ref. [1] © ACS 2000.

**FIGURE 7.2**

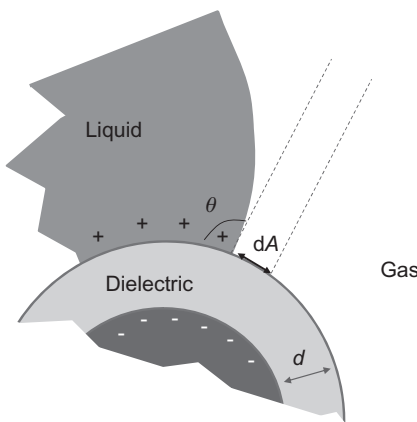
Sketch of a droplet on a curved surface: (A) convex and (B) concave surfaces.

should take place whether the surface is flat or curved. Figure 7.2 shows the two configurations of EWOD on a curved surface: the surface can be concave or convex.

The first experiments performed by Kim and Steckl [1] with flexible paper substrate, and Fan and colleagues [2] with “droplets-on-a-wristband” concluded that the curvature of the surface had no noticeable influence on the required driving voltages. However, the recent works of Wang and Zhao and Abdalgawad and coworkers [3,4] led to a more detailed analysis. We present here the approach followed by Wang and Zhao.

Consider the change of free energy of the system E with the actuation of an electric potential (Figure 7.3). The droplet spreads with the actuation and we have

$$dE = \gamma_{SL} dA - \gamma_{SG} dA + \gamma_{LG} \cos \theta dA + dU - dW_B, \quad (7.1)$$

**FIGURE 7.3**

Sketch of the contact of the droplet on the EWOD substrate.

where A is the droplet base area, U is the electric energy, and W_B is the work that the voltage source performs.

The equilibrium position is that of minimum free energy

$$\gamma_{SL} - \gamma_{SG} + \gamma_{LG} \cos \theta + \frac{dU}{dA} - \frac{dW_B}{dA} = 0. \quad (7.2)$$

The actuated contact angle θ is derived from Eq. (7.2) as soon as the terms dU/dA and dW_B/dA are known. According to electromagnetics, U is given by

$$U = \frac{1}{2} \varepsilon E^2 dv, \quad (7.3)$$

where E is the electric field intensity and v is the volume filled by the electric field. The predominant effect is the distribution of the electric field which depends on the geometry. If we assume that the triple line fringe effect is small, i.e., the droplet is not extremely small, an average value of the two terms dU/dA and dW_B/dA can be derived according to the local geometry. In the following sections, a spherical is considered first, and then a cylindrical geometry.

7.2.1 EWOD on a spherical surface

In the case of a spherical surface with a radius R , and dielectric thickness d , the term dv is given by

$$dv = \int_R^{R+d} \frac{dA}{(R+d)^2} r^2 dr, \quad (7.4)$$

where r is the radius of the sphere between the dielectric metal surface and dielectric gas surface. Using Eqs. (7.3) and (7.4), the term dU/dA is given by

$$\frac{dU}{dA} = \int_R^{R+d} \frac{\langle \varepsilon E^2 \rangle}{2} \frac{r^2}{(R+d)^2} dr, \quad (7.5)$$

where the brackets denote the average value over the thickness r . Geometrical considerations lead to

$$A_r = 2\pi r^2 (1 - \cos \beta), \quad (7.6)$$

where β is the half-spherical angle that encompasses the contact of the droplet with the sphere (Figure 7.4).

The average electric field is then

$$\langle E(r) \rangle = \frac{Q}{\varepsilon A_r} = \frac{Q}{2\pi\varepsilon r^2 (1 - \cos \beta)}, \quad (7.7)$$

where Q is the electric charge. Then,

$$V = \int_R^{R+d} \langle E(r) \rangle dr = \frac{Q}{2\pi\varepsilon (1 - \cos \beta)} \left(\frac{1}{R} - \frac{1}{R+d} \right). \quad (7.8)$$

Substitution of Eq. (7.7) in Eq. (7.8) yields

$$\langle E(r) \rangle = \frac{R(R+d)}{dr^2} V. \quad (7.9)$$

And we obtain the expression of dU/dA

$$\frac{dU}{dA} = \frac{\varepsilon V^2}{2d} \frac{R}{R+d} \quad (7.10)$$

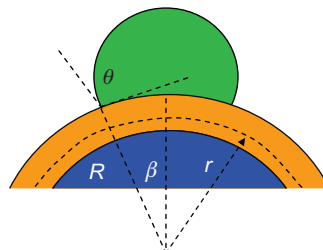


FIGURE 7.4

Sketch of the droplet on the sphere.

and the expression of the work dW_B/dA done by the voltage source to redistribute the charge can be written

$$\frac{dW_B}{dA} = V\sigma = V\varepsilon E(R + d) = \frac{\varepsilon V^2}{d} \frac{R}{R + d} \quad (7.11)$$

for a convex spherical surface, where σ is the charge. After substitution of Eqs. (7.10) and (7.11) in Eq. (7.2), and using Young's equation, we find

$$\cos \theta(V) = \cos \theta_0 + \frac{\varepsilon V^2}{2d\gamma_{LG}} \frac{1}{1 + (d/R)}. \quad (7.12)$$

In the case of a concave surface, the actuated contact angle is

$$\cos \theta(V) = \cos \theta_0 + \frac{\varepsilon V^2}{2d\gamma_{LG}} \frac{1}{1 - (d/R)}. \quad (7.13)$$

When $R \rightarrow \infty$ both Eqs. (7.12) and (7.13) converge toward the usual BLY law.

7.2.2 EWOD on a cylindrical surface

In the cylindrical case, for a convex cylinder, the expression of dU/dA is found to be

$$\frac{dU}{dA} = \frac{\varepsilon V^2}{2} \frac{1}{(R + d)\ln(R + d/d)} \quad (7.14)$$

and

$$\frac{dW_B}{dA} = V\sigma = V\varepsilon E(R + d) = \frac{\varepsilon V^2}{(R + d)\ln(R + d/d)}. \quad (7.15)$$

After substitution of Eqs. (7.14) and (7.15) in Eq. (7.2), and using Young's law, we find

$$\cos \theta(V) = \cos \theta_0 + \frac{\varepsilon V^2}{2d\gamma_{LG}} \frac{1}{(1 + (d/R))\ln(R + d/d)}. \quad (7.16)$$

In the case of a concave cylinder, the actuated contact angle is

$$\cos \theta(V) = \cos \theta_0 + \frac{\varepsilon V^2}{2d\gamma_{LG}} \frac{1}{(-1 + (d/R))\ln(R - d/d)}. \quad (7.17)$$

In this case again, when $R \rightarrow \infty$ both Eqs. (7.16) and (7.17) converge toward the usual BLY law. This is probably why the first researchers developing EWOD on curved surfaces did not notice any difference with the BLY law.

7.2.3 Conclusions

In the conventional approach of EWOD on planar surfaces, the change in contact angle is given by the BLY law which read dimensionlessly

$$\cos \theta(V) = \cos \theta_0 + \xi(V), \quad (7.18)$$

where ξ is the dimensionless electrowetting number

$$\xi(V) = \frac{\varepsilon V^2}{2d\gamma_{LG}}. \quad (7.19)$$

The curvature modifies the expression of the electrowetting number. For a spherical substrate, the curvature-modified electrowetting number is

$$\xi(V) = \frac{\varepsilon V^2}{2d\gamma_{LG}} \frac{1}{1 \pm (d/R)}. \quad (7.20)$$

A very interesting conclusion is that convex and concave surfaces do not behave similarly because of the antisymmetric terms $1 + d/R$ and $1 - d/R$. The hypothesis that the fringe effects are negligible does not allow for the curvature radius to be too small ($R \rightarrow 0$); besides, the ratio between the dielectric thickness and the surface curvature radius d/R is usually small. However, for nonnegligible ratios d/R , Eq. (7.20) implies that

$$\xi(V)_{\text{concave}} > \xi(V)_{\text{convex}}. \quad (7.21)$$

In consequence, using Eq. (7.20), the contact angle on a concave surface changes faster than that on a convex surface. As a result, it is easier to move a droplet by EWOD on a hollow part of the surface than on a rounded ridge.

In the following sections, we give examples of electrowetting on curved surfaces.

7.3 Electrowetting on a wavy surface

A typical example of electrowetting on curved surfaces is the “all-terrain droplet actuation (ATDA)” microsystem developed by Wheeler’s group [4]. In ATDA, a thin, flexible substrate is bent to form one of a wide variety of device shapes, which enables straightforward integration of distinct physicochemical environments on a monolithic platform (Figure 7.5). Of course, such a device uses open microfluidics device configuration, instead of the more common enclosed (covered) configuration which would not be feasible in this case.

In this particular case, motion of droplets by EWOD will be possible if

$$F_E > F_F + F_G, \quad (7.22)$$

where F_E is the electrowetting force, F_F is the friction force, and F_G is the gravity force. Tests have been realized to check the steepest angle that a droplet can climb under electrowetting actuation (with a particular substrate design). Figure 7.6 shows

that a droplet with a volume less than 5 μL can climb up a vertical plane under the action of electrowetting forces. Incidentally, the horizontal asymptote shows that a very large droplet (3 mm base) can be moved by EWOD on a flat surface.

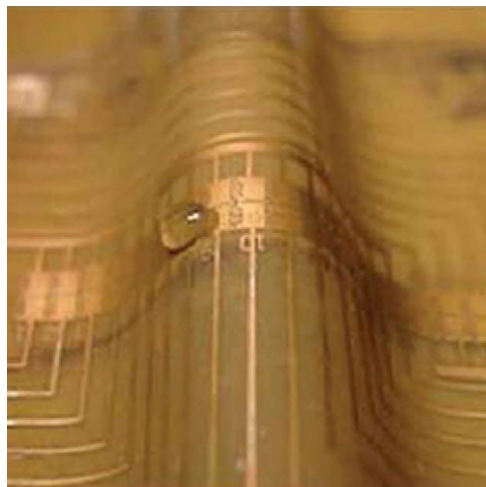


FIGURE 7.5

Electrowetting droplet climbing up a ridge [4], showing that electrowetting forces can overcome gravity for a small droplet.

Source: Reprinted with permission from Ref. [4] © RCS 2008.

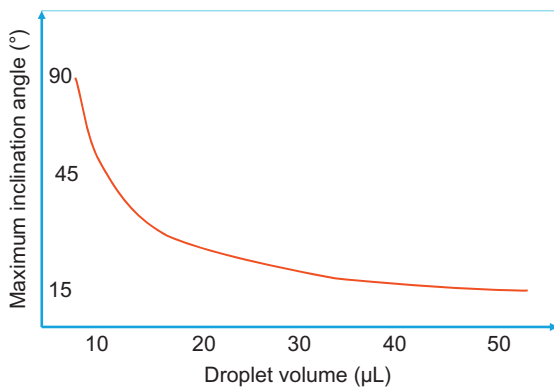


FIGURE 7.6

Maximum inclination angle versus droplet volume.

7.4 Electrowetting on a rod

7.4.1 Introduction

In this section, we present the morphological change of a droplet on a horizontal rod with the changing of the contact angle.

It is well known that droplets on a horizontal wire take different shapes depending on their volume, rod diameter, and contact angle [5]. In the case where the droplet is sufficiently small, gravity does not play any role in the shape of the droplet, and if the rod is lyophilic, the droplet has a so-called “barrel” shape. Mathematically speaking, the surface is an unduloid [6] (Figure 7.7).

A droplet has still a “nearly barrel” shape if the droplet is “small enough” and the contact “sufficiently lyophilic.” Two nondimensional numbers characterize the droplet volume and the rod diameter relatively to the effect of gravity: first the Gouyer or wire Bond number [7–9]

$$Go = \frac{r}{\kappa^{-1}} = \sqrt{\frac{\rho g r^2}{\gamma}}, \quad (7.23)$$

where $\kappa^{-1} = \sqrt{\gamma/\rho g}$ is the capillary length and r is the radius of the wire (Figure 7.7), or equivalently

$$Bo = \frac{r^2}{\kappa^{-2}} = Go^2. \quad (7.24)$$

An additional scaling number—a length scale—is then used to take into account the droplet volume

$$\mathfrak{R} = \frac{D'}{D}, \quad (7.25)$$

where D and D' are, respectively, the wire and droplet diameter (Figure 7.8).

When these two nondimensional numbers are small before unity, the shape of the droplet is not affected by gravity. In such a case, the droplet adopts a symmetrical shape. When the contact angle is small (less than 30°), one can speak of a “barrel shape” (Figure 7.9).

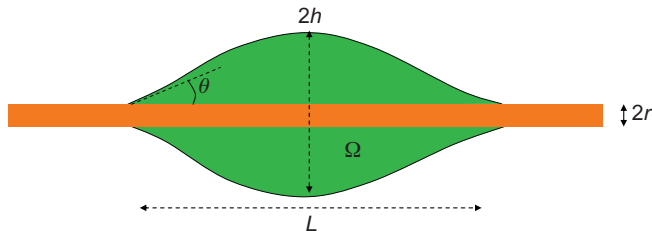
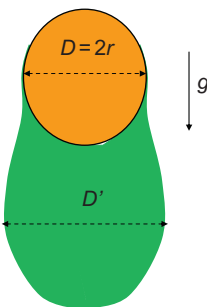
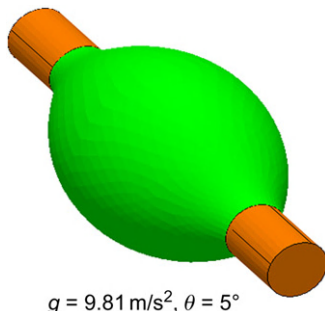


FIGURE 7.7

No-gravity droplet on a wetting, horizontal rod.

**FIGURE 7.8**

Sketch of a droplet suspended on a wire.

**FIGURE 7.9**

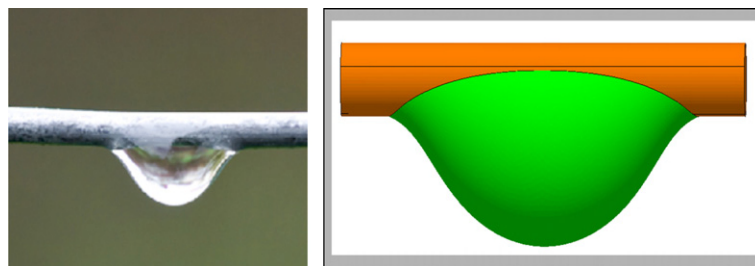
Simulation of a droplet on a rod obtained with the numerical program Evolver showing an unduloidal shape [6].

Just for completion, remark that the overpressure ΔP in the case of an unduloid has been calculated by Carroll [7]

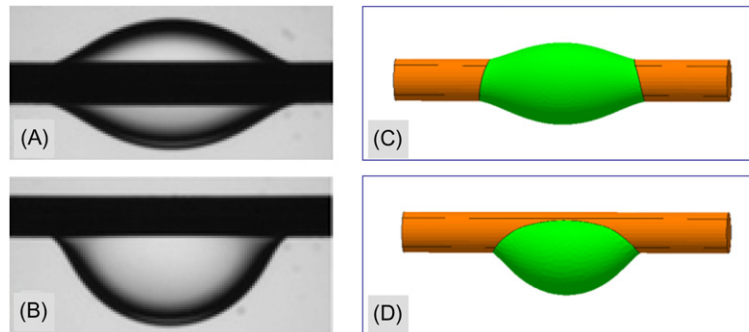
$$\Delta P = \frac{2\gamma}{r+h}. \quad (7.26)$$

This formula is consistent with the geometry of a fiber: when the volume of the drop tends to zero (i.e., $h \rightarrow r$), ΔP is equal to γ/r , the Laplace's pressure inside a cylinder of radius r . However, if the radius of the fiber tends to zero for a drop of given volume, we find $\Delta P = 2\gamma/h$, the overpressure in a sphere of radius h .

The other characteristic shape that a droplet on a rod can adopt is called “clamshell.” [Figure 7.10](#) shows a typical asymmetrical clamshell shape. This case occurs for large droplet volume and/or high contact angle. Eral and colleagues [10] have investigated the conditions for a clamshell shape.

**FIGURE 7.10**

Clamshell shape of a droplet on a horizontal rod.

**FIGURE 7.11**

Evolver calculation of the different shapes of the droplet by changing the value of the contact angle: (A) barrel shape; (B) clamshell shape; (C) barrel shape corresponding to a small contact angle (5°), note that a small effect of gravity can be seen by the inclination of the contact lines with the rod; and (D) clamshell shape corresponding to a contact angle of 35° .

Source: Reprinted with permission from Ref. [4] © RCS 2011.

7.4.2 Electrowetting on a wire

We have seen that the value of the contact angle deeply affects the position of the droplet on the wire. Depending on this value, the droplet can have a barrel shape or a clamshell shape. This property has been shown by Eral and colleagues [10] by using electrowetting to modify the value of the contact angle (Figure 7.11). In their experiment, Eral and colleagues [10] have used an oil droplet immersed in water. When actuation is turned off, the contact angle is small and the drop has a “barrel” shape; when the actuation is turned on, the contact angle increases and the droplet adopts a “clamshell” shape.

7.5 Electrowetting on a sphere

Everyone has remarked on the nature of the shape of a liquid droplet attached to a solid sphere. This is for example illustrated by a rain droplet pending on a spherical piece of fruit (Figure 7.12). A numerical example of a droplet—with gravity—attached to a sphere is shown for comparison in the same figure.

The morphology of a droplet L attached to a sphere S in presence of a gas G —or another immiscible liquid—depends on the three surface tensions γ_{LG} , γ_{SL} , and γ_{SG} as shown in Figure 7.13 [5].

Eral and coworkers [11] have used electrowetting actuation to change the morphology of a liquid droplet attached to a sphere and investigate the conditions for total engulfment. Lippmann's equation states that electrowetting actuation modifies the value of the effective solid–liquid surface tension γ_{SL} . It has the consequence of changing the contact angle θ between the liquid droplet and the solid sphere. Figure 7.14 shows a simulation performed with the numerical software Evolver with two different values of the solid–liquid surface tension (water droplet in air).

For the experimental realization of a drop on a sphere, a water drop in an oil bath is placed on a metal sphere coated with a dielectric layer. In their experiment, Eral and coworkers [11] used a 1.5 mm metallic sphere. They did not see a noticeable deviation from the BLY law probably because of this relatively large curvature radius—the ratio d/R of Eq. (7.12) is of the order of 0.00—and the deviation predicted by Wang and Zhao is hidden in the experimental noise.

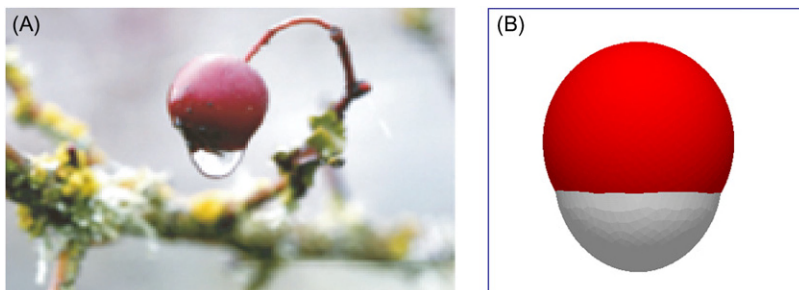
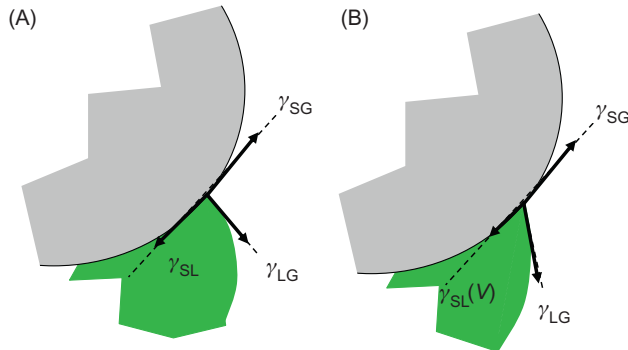


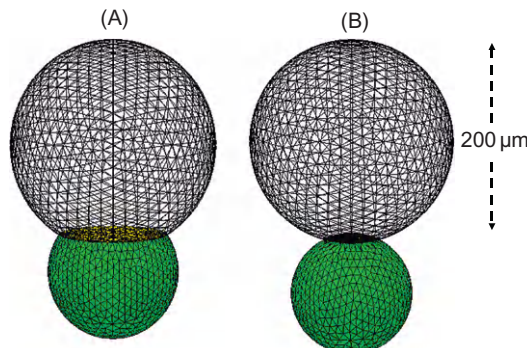
FIGURE 7.12

(A) Water droplet on a spherical piece of fruit and (B) simulation with Evolver.

Source: Reprinted with permission from Ref. [11] © ACS 2011.

**FIGURE 7.13**

Sketch of the contact of a liquid droplet attached to a solid sphere: (A) the contact angle results from the balance between the three surface tensions and (B) electrowetting actuation changes the contact angle.

**FIGURE 7.14**

Evolver calculation of a liquid droplet attached to a solid sphere: (A) $\gamma_{SL} = 0.002 \text{ mN/m}$ and (B) $\gamma_{SL} = 0.042 \text{ mN/m}$ ($\gamma_{LG} = 50 \text{ mN/m}$ and $\gamma_{SG} = 30 \text{ mN/m}$).

7.6 Conclusion

This chapter was dedicated to electrowetting on nonplanar surfaces. Historically, the developments of EWOD (electrowetting on dielectric) and EWD (electrowetting device) have been performed on planar surfaces. However, it has been

recently remarked that the planar geometry was not a requirement. New EWOD systems on curved surfaces have appeared and others are being presently developed, allowing for a broader scope of applications.

References

- [1] D.Y. Kim, A.J. Steckl, Electrowetting on paper for electronic paper display, *ACS Appl. Mater. Interfaces* 2 (2010) 3318–3323.
- [2] S.-K. Fan, H. Yang, W. Hsu, Droplet-on-a-wristband: Chip-to-chip digital microfluidic interfaces between replaceable and flexible electrowetting modules, *Lab Chip* 11 (2011) 343–347.
- [3] Y. Wang, Y.-P. Zhao, Electrowetting on curved surfaces, *Soft Matter* 8 (2012) 2599–2606.
- [4] M. Abdelgawad, S.L.S. Freire, H. Yang, A.R. Wheeler, All-terrain droplet actuation, *Lab Chip* 8 (2008) 672–677.
- [5] J. Berthier, K. Brakke., *The Physics of Microdrops*, Scrivener-Wiley Publishing, Beverly, MA, 2012.
- [6] K. Brakke, The surface evolver, *Exp. Math.* 1 (2) (1992) 141–165.
- [7] B.J. Carroll, The equilibrium of liquid drops on smooth and rough circular cylinders, *J. Colloid Interface Sci.* 97 (1) (1984) 195–200.
- [8] G. McHale, M.I. Newton, Global geometry and the equilibrium shapes of liquid drops on fibers, *Colloids Surf. A* 206 (103) (2002) 79–86.
- [9] E. Lorenceau, D. Quéré, Drops on a conical wire, *J. Fluid Mech.* 510 (2004) 29–45.
- [10] H.B. Eral, R. Ruiter, J. Ruiter, J.M. Oh, C. Semprebon, M. Brinkmann, F. Mugele, Drops on functional fibers: from barrels to clamshells and back, *Soft Matter* 7 (2011) 5138–5143.
- [11] H.B. Eral, G. Manukyan, J.M. Oh, Wetting drop on a sphere, *Langmuir* 27 (9) (2011) 5340–5346.

Biological Applications of EWOD*

8

CHAPTER OUTLINE

8.1 Introduction	340
8.2 Biological liquids and physiological samples compatible with EWOD devices	340
8.2.1 Physiological liquids.....	340
8.2.2 Proteins and biofouling	342
8.2.3 Cells.....	342
8.2.4 Conclusion.....	344
8.3 Sample collection and analysis on an LOC platform	344
8.4 PCR on DMF systems	346
8.4.1 Introduction	346
8.4.2 Architecture of a PCR–EWOD microsystem	347
8.4.3 Thermal analysis	348
8.4.3.1 Single thermal region—single Peltier device	349
8.4.3.2 Two thermal regions—two Peltier devices.....	351
8.4.3.3 Conclusions.....	352
8.4.4 Experimental realization of PCR and results.....	352
8.4.4.1 Experimental conditions.....	352
8.4.4.2 On-chip PCR results.....	353
8.4.4.3 Conclusions.....	354
8.5 DNA repair microprocessor.....	357
8.6 Protein analysis coupled with mass spectrometry	360
8.7 Cell-on-a-chip microsystems: example of a cell concentrator	362
8.8 Summary	364
References	365

*This chapter was written in collaboration with Christine Peponnet (Director of the Biochip Laboratory at the CEA-LETI).

8.1 Introduction

The preceding chapters were dedicated to the physics of the digital microfluidics chip (DMC). In the following chapters, concrete applications of such microsystems are presented. At the present time, applications are found in the domains of biology and biotechnology, chemistry, and optics. This chapter is devoted to biological and biotechnological applications. In these fields, applications are principally related to the development of biosensors (LOC, immunoassays), and, to a lesser extent, of cell-on-a-chip.

First of all, let us ask the question: What would be an ideal on-site biochemical analysis system? An ideal sensor is required to be inexpensive, fast, robust, sensitive, and reliable, to have low power consumption, a high degree of automation and integration, a high throughput, to use small reagent volumes, and to cover a wide spectrum of samples and biological parameters. With all these requirements, it is clear that the ultimate biochemical sensor is still a long way ahead. The complexity of such systems and the technological problems to solve are huge. However, as we shall see in this chapter, considerable progress is being made in the domain of sample collection and preparation, DNA analysis, DNA repair, protein recognition, and cell sorting. In this chapter, we present examples illustrating these applications. A preliminary step is to determine which biological and physiological liquids are compatible with EWOD-based microsystems, i.e. which liquids can successfully be displaced and maneuvered in such microsystems.

8.2 Biological liquids and physiological samples compatible with EWOD devices

We have seen in the preceding chapters that a condition for a liquid to be maneuvered on EWOD-based microsystems is that the liquid is electrically conductive. However, we do not know if this condition is sufficient. Examples corresponding to DIW, buffers, and ionic liquids have been shown. By extrapolation of these results, it is logical to presume that human physiological liquids, which are electrically conductive due to their salt content, might be compatible with EWOD-based microsystems. In this section, we investigate the compatibility of usual biological liquids with EWOD-based microsystems.

8.2.1 Physiological liquids

Srinivasan et al. [1], Lei Li et al. [2], and Jeong-Yeol et al. [3] have shown that physiological liquids, like blood, sweat, tears, serum, and milk can be moved on EWOD-based microsystems, although not always so easily as DIW or buffers. A convenient method to assess the maneuverability of a liquid on an EWOD chip

is to measure the maximum switching frequency as a function of the applied voltage. The method consists of observing if a back-and-forth motion of a droplet between two neighboring electrodes can be obtained by switching the actuation of these two electrodes. If the switching of actuation between the two electrodes is too fast, motion does not occur. Hence, the maximum switching frequency is the maximum rate at which a droplet can be moved across adjacent electrodes (Figure 8.1). This is a measure of the aptitude of a droplet to move on a DMF device. It takes into account at the same time the electric force exerted on the droplet and the resistance to motion due to the viscous forces (friction on the substrate).

An interesting observation stemming from Figure 8.1 is that serum (blood plasma) is more easily transportable than whole blood. This is not surprising since whole blood is constituted of serum plus red and white blood cells which make it much more viscous and give it a non-Newtonian rheological behavior. This property is general: carrier fluids are moved at lower voltages than the same carrier fluids transporting biological macromolecules, proteins, and cells. We will come back to the motion of proteins and cells in the next section. It is especially interesting to know that whole blood is compatible with EWOD-based systems, since many applications are linked to blood analysis. Figure 8.2 shows that whole blood obeys the general Lippmann–Young’s law and can be displaced on EWOD electrodes.

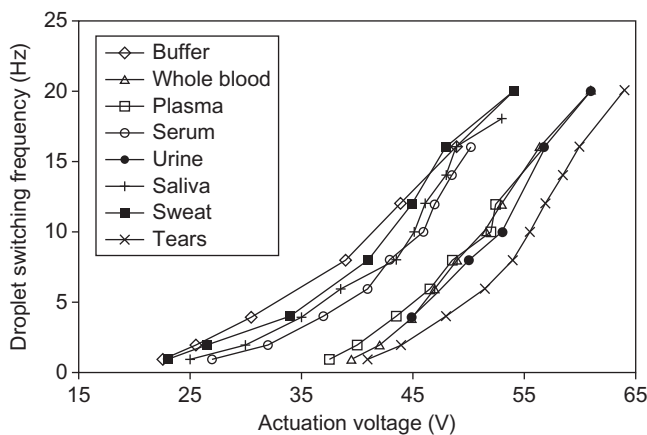
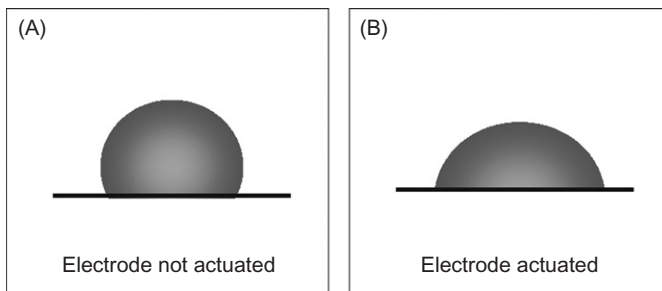


FIGURE 8.1

Transportability of different human physiological liquids: maximum droplet switching frequency as a function of the applied voltage; the maximum switching frequency is the maximum rate at which a droplet can be moved across adjacent electrodes, it is a measure of the transportability of a droplet in an EWOD-based microsystem. The droplet volume is $1.12 \mu\text{L}$ and the surrounding media is silicone oil.

Source: From Ref. [2]; reproduced by permission of the Royal Society of Chemistry.

**FIGURE 8.2**

Droplet of blood on an electrode; the contact angle varies with the applied voltage according to Lippmann–Young’s law.

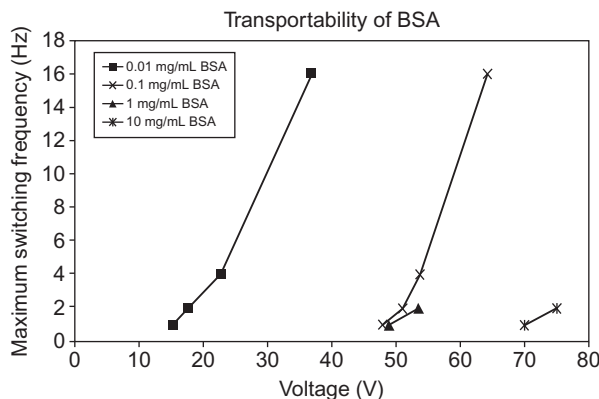
8.2.2 Proteins and biofouling

The situation is more complex with fluids containing enzyme-laden reagents, proteins, and cells. These liquids pose several challenges. By necessity, EWOD surfaces are hydrophobic, and most proteins adsorb irreversibly to hydrophobic surfaces. This phenomenon is called biofouling. Proteins adsorbed to the surface prevent the correct functioning of the chip by rendering the surface hydrophilic [4] and by inducing droplet pinning and even dielectric breakdown (see Chapter 4). In order to avoid—or reduce—biofouling, silicone oil is widely used. The effect of silicone oil is to maintain a film between the droplet and the solid surface. The effect of an oil film regarding electrowetting has been studied in Chapter 4.

Often a protein called bovine serum albumin (BSA)—or other proteins like casein—are added to biological reagents to reduce adhesion of enzymes and proteins to solid surfaces [5]. Advantages of BSA—or casein—are their biocompatibility with most biological reactions and their low cost. However, they adsorb to solid surfaces. The aptitude of a droplet containing BSA to be maneuvered on EWOD devices depends on the initial concentration in BSA. Figure 8.3 shows that a droplet containing a buffer with BSA (surrounded by oil) is maneuverable on an EWOD-based device if the concentration in BSA is less than 0.01 mg/mL [6]. Above this limit, the required voltages are large, and the saturation limit or the breakdown level is quickly reached.

8.2.3 Cells

One of the applications expected from DMF systems is the precise handling of cells. The first step is to verify that cells can be moved by electrowetting forces on EWOD-based microchips. Evidently there is a size limit above which the cells cannot be moved. For small- to medium-sized cells ($<70\text{ }\mu\text{m}$), the challenge is

**FIGURE 8.3**

Transportability of droplets on EWOD-based microsystems decreases quickly when the concentration of BSA increases.

Source: Reprinted with permission from Ref. [6] © 2004, SPIE.

**FIGURE 8.4**

Jurkat cells transported by a droplet on an EWOD-based microsystem. The cell size is approximately 50 μm .

Source: Photograph D. Jary, CEA-LETI.

that the cells involved must be maintained alive and that, with the cells, a nutrient solution must also be moved. To prevent adherence on the solid surfaces, surfactants must be added to the carrier liquid. However, the usual surfactants, like Tween, are not biocompatible; they usually kill the cells. We have seen in the preceding section that BSA can be used only at very low concentration. Usually it is not enough for cells. In the literature, specific surfactants have been studied and found to be biocompatible. This is the case of Pluronic [7,8]. Let us mention that Pluronic is a poloxamer, i.e., an amphiphilic copolymer composed of a central hydrophobic chain of polyoxypropylene (polypropylene oxide) flanked by two hydrophilic chains of polyoxyethylene (polyethylene oxide). Figure 8.4 shows a cell-laden droplet on an EWOD-actuated chip.

8.2.4 Conclusion

Many physiological liquids are compatible with the EWOD mode of transportation, opening a wide range of biological applications to these systems. Some care must be taken with enzymes, proteins, and cells to prevent them from adsorbing to the solid surfaces. To this extent, the use of biologically adapted surfactants is a major improvement. In the following sections, we present some applications of EWOD-based microsystems to sample collection, DNA analysis, DNA repair, protein recognition, and cell concentration.

8.3 Sample collection and analysis on an LOC platform

The following example [9,10] describes a system to collect and analyze airborne particles using microdroplets circulating in an EWOD chip. This microdevice prefigured the DMF systems that are being developed to address environmental problems with the detection of the chemical and biochemical composition of aerosol; it is also a good illustration of the integration in the same device of different physical phenomena already encountered and analyzed in this book.

The collection, preconcentration, and analysis of the target particles are realized in four steps: (i) the first step consists of collecting airborne particles by impinging a jet on the surface of an open EWOD chip. During this phase, the particles adsorb on the surface. (ii) The airstream is blanked off and a scanning droplet is moved as fast as possible on the surface (velocities of 10 cm/s can be reached in open EWOD-based systems). In order to increase the velocity of motion and to reduce evaporation, the water droplet is clad in a thin oil film. The surface is scanned in a few seconds and the droplet does not have time to evaporate. Figure 8.5 shows the

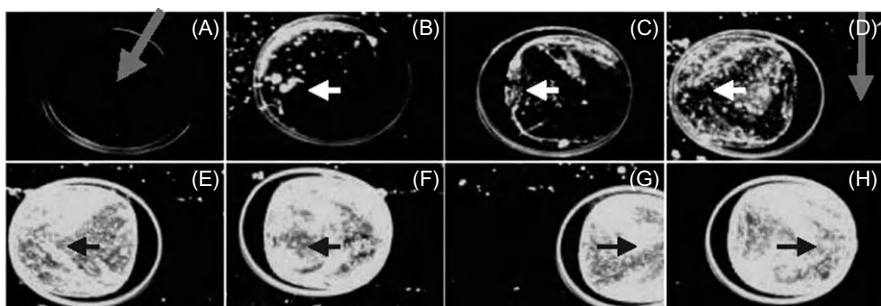


FIGURE 8.5

Photographs of a droplet sweeping a solid surface and collecting the particles initially adsorbed on the surface. (A) Initial droplet; (B) droplet scans over beads; (C) beads collected in drop; (D) the surface is cleaned along the droplet trajectory; (E and F) more beads are collected; and (G and H) the droplet returns to its initial location over a cleaned surface.

Source: Reprinted with permission from Ref. [9] © 2004, SPIE.

scanning phase and particle collection by the droplet. During this phase, the collected particles are concentrated in the moving droplet. (iii) The droplet is then transferred to a covered EWOD region filled with silicone oil. The conditions of transfer from open to covered EWOD-based systems have been analyzed in Chapter 5. **Figure 8.6** illustrates such a transfer. In the new covered environment, the droplet cannot evaporate. In this region, the droplet is mixed with specific reagents that produce colored reaction products. (iv) The concentration of the analyte is quantitatively determined by measuring adsorption at specific wavelengths using a simple light emitting diode and photodiode setup.

Applications include sampling of airborne contaminants—such as sulfates, nitrates, and ammonium—bioagents, and also of nitroaromatic explosive particles such as TNT (trinitrotoluene). Very low detection limits are achieved due to the efficiency of the concentration in the droplet. If the absorption of the impinging particles is total, following Ref. [9], the concentration in the droplet c_w is related to that in the air c_a by the relation

$$c_w = \frac{c_a Q_a t}{V_w}, \quad (8.1)$$

where V_w is the volume of the water droplet, Q_a is the air flow rate, and t is the collection time. In terms of limit of detection (LOD), **Eq. (8.1)** yields

$$\text{LOD}_a = \frac{\text{LOD}_w V_w}{Q_a t}. \quad (8.2)$$

Formula (8.2) shows that the detection level is proportional to the detection level on the chip times the extraction volume and divided by the sampling flow rate. Due to the very small value of the drop volume, a very low detection limit in air can be achieved in a short time (1 mn). Of course, the reasoning assumes

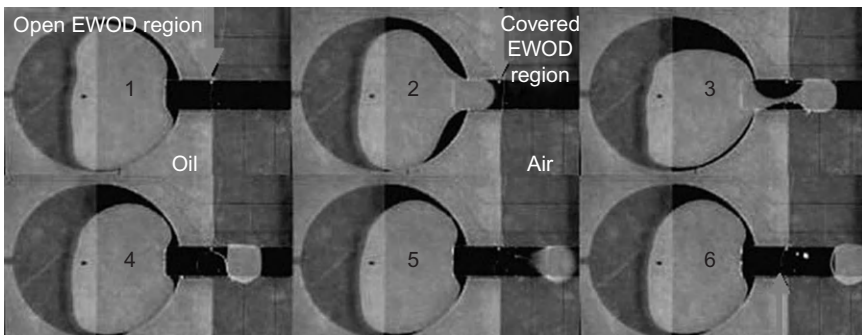


FIGURE 8.6

Droplet motion from an open EWOD region to a covered EWOD region. In the open region, droplet is surrounded by silicone oil, whereas it is surrounded by air in the covered region.

Source: Reprinted with permission from Ref. [9] © 2004, SPIE.

that the capture of the impinging particles is total and that the scanning by the droplet is extremely efficient.

8.4 PCR on DMF systems

8.4.1 Introduction

Most of the time, biologic samples only contain a very small number of DNA strands; bioanalysis of DNA for the detection of viruses, hereditary diseases, or genotyping requires a sufficiently large number of strands. Hence, the initial DNA strands must be replicated—or amplified—in a sufficiently large number. PCR is the most used *in vitro* method to amplify DNA sequences, because it amplifies exponentially the sequences via enzymatic replication. It is not the purpose of this book to go into the details of biological processes like PCR [11,12]. We shall just mention here the information needed for the comprehension of the design and functioning of a PCR digital system. A PCR requires a PCR mix containing several basic components, such as the primers, which are complementary to the DNA regions at the 5' and 3' ends of the DNA region that is to be amplified, a DNA polymerase used to synthesize a DNA copy, deoxynucleotide triphosphates from which the DNA polymerase builds the new DNA, and a buffer solution, which provides suitable chemical environment for optimum activity of the DNA polymerase.

Basically, a PCR requires 20–30 cycles, each cycle doubling the number of DNA sequences. Each cycle comprises three steps: the first step is a denaturation step during which the double-stranded DNA is separated in two single DNA strands. Denaturation requires a temperature of 94–96°C. Denaturation is followed by the annealing step. In this step, the reaction temperature is lowered to 55–64°C: the primers and the DNA strands bind together if their sequence is complementary. A relatively low temperature (lower than the fusion temperature) is needed for attachment. The annealing step is followed by an extension/elongation step during which the DNA polymerase synthesizes new DNA strands complementary to the DNA template strands. The temperature at this step depends on the DNA polymerase used. Usually, a temperature of 70–74°C is optimum.

Hence, the reaction mix must be submitted to multiple temperature cycles. The duration of the cycles depends on the uniformity of the temperature and the volume of liquid. In microsystems, the time required for a temperature cycle is much shorter than for conventional systems. Assuming perfect conditions and perfect mixing, the denaturation step requires a stabilization time of a few seconds, approximately 10 s is needed for the annealing step, and the elongation process is nearly instantaneous. One of the advantages of microsystems is the ability to work with very small volumes of liquid, for which temperature homogeneity and diffusion efficiency are higher than that of macrosystems. However, the thermal cycles induce constraints on the system, especially regarding evaporation and bubble formation.

In the next section, we first present the architecture of a PCR–EWOD microsystem; then we analyze the thermics of a PCR digital microsystem, and finally we show PCR results in DMF systems.

8.4.2 Architecture of a PCR–EWOD microsystem

In order to achieve the PCR, the following operations must be successively performed: (i) dispensing of the sample mix, (ii) merging of the droplet with another droplet containing the PCR mix (primers, polymerase, triphosphates), (iii) mixing the components, (iv) submitting the droplet to the temperature cycles, and (v) detecting the reaction results. The three first steps have already been detailed in the preceding chapter. We now focus on steps (iv) and (v).

Conceptually, the thermal regulation can be performed using two different approaches: either there is only one region of thermal heating/cooling and the droplet is at rest in this region (Figure 8.7), or the droplet alternately moves from a region maintained at 64°C to a region maintained at 95°C (Figure 8.8). These two categories are just the translation to DMF of the “stationary-chamber micro-PCR chips” and the “continuous flow micro-PCR chips” that have been

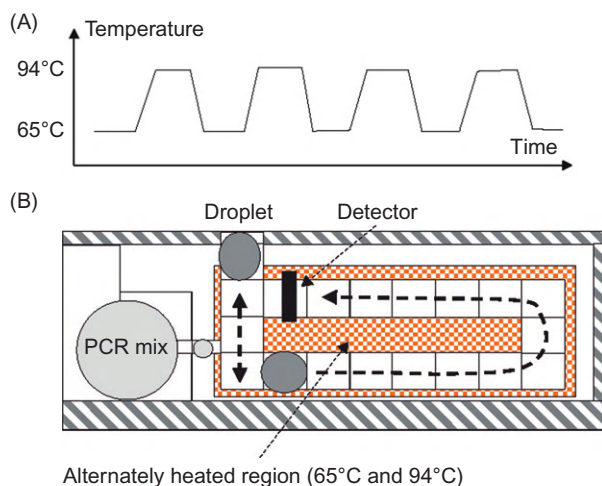
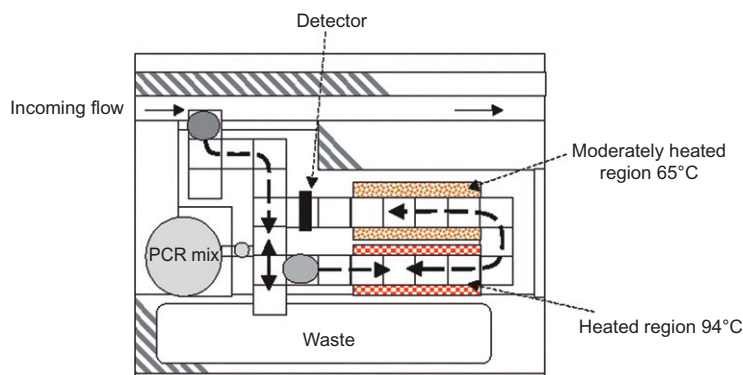


FIGURE 8.7

(A) Temperature cycles (between 65°C and 94°C) that the liquid must observe for the PCR to be effective; the temperature is monitored by a Peltier device located below the substrate. (B) Schematic view of a PCR chip (one zone of thermal regulation). The incoming droplet is merged with a droplet of PCR mix, then is mixed by back-and-forth motion; the droplet is then moved step by step toward the detector. At each step, a thermal cycle is performed to achieve the duplication of the DNA strands. The liquid is progressively enriched in target DNA and eventually reaches the detector.

Source: Sketch Y. Fouillet CEA-LETI.

**FIGURE 8.8**

Schematic of a PCR–EWOD microsystem with two zones of thermal regulation: the droplet is extracted from a flowing liquid, then transported on the EWOD chip; there, it merges with a droplet of PCR mix. After mixing by back-and-forth motion, the droplet is moved alternately from the heated to moderately heated regions. After approximately 20 cycles, the droplet is directed toward the detector.

Source: Sketch Y. Fouillet CEA-LETI.

developed for conventional microfluidic systems, depending if the samples are stationary or moving inside the channels.

In the following section, we analyze the temperature control of PCR–EWOD devices.

8.4.3 Thermal analysis

Mini-Peltier devices are often used in microsystems for temperature regulation. Peltier devices are based on the thermoelectric effect [13]. In 1821, J.T. Seebeck discovered that dissimilar metals that are connected at two different locations (junctions) will develop a microvoltage if the two junctions are held at different temperatures. This effect is known as the “Seebeck effect”; it is the basis for thermocouple thermometers. A little later, in 1834, J. Peltier discovered the inverse of the Seebeck effect, now known as the “Peltier effect”: a temperature difference builds up at the junction between two dissimilar metals or semiconductors when a voltage is applied. This results in a small heat pump, also known as a thermoelectric cooler (TEC). The advantages of Peltier devices are numerous: they can be miniaturized (their size varies from a few millimeters thick by a few millimeters to a few centimeters square), they can be used as well as cooling or heating devices (one junction cools off while the other heats up), they have no moving parts, they need no Freon refrigerant, they induce no vibrations, they have a long lifetime and a good precision on the temperature control; besides, they do not require large voltages for miniaturized systems.

For a system with a unique thermal region regulating the temperature cycles, a unique mini-Peltier device is used. For two regions of different temperatures, two mini-Peltier devices are needed.

8.4.3.1 Single thermal region—single Peltier device

The conception and design of the PCR–EWOD chip necessitates the knowledge of the transfer function between the Peltier and the EWOD system, and the thermal response of the system. In the following, we use a numerical approach [14] to determine the temperature field in the system. The equation governing the thermal behavior of the chip is simply the heat conduction equation

$$\frac{\partial T}{\partial t} = \frac{k}{\rho C_p} \nabla^2 T \quad (8.3)$$

with the adequate boundary conditions. In Eq. (8.3), T is the temperature in kelvin, k is the heat conductivity ($\text{W}/\text{m}/\text{K}$), ρ is the density (kg/m^3), and C_p is the specific heat capacity ($\text{J}/\text{K}/\text{kg}$). We investigate the cases of a covered EWOD system with an insulating cover and of an open EWOD system with an oil cover. Figures 8.9 and 8.10 show the temperature field in the system during the annealing step (liquid temperature 65°C), with the two different cover conditions. In both cases, there is approximately a 3°C temperature difference between the Peltier device and the droplet. The droplet temperature is extremely uniform in the case of a covered system—and sufficiently uniform in the case of an oil cover—to ensure an adequate annealing. Similar results are obtained for the denaturation phase.

Concerning temperature transient, the response of the system is very fast (Figure 8.11). The droplet temperature follows the temperature transient of the Peltier device without any time shift.

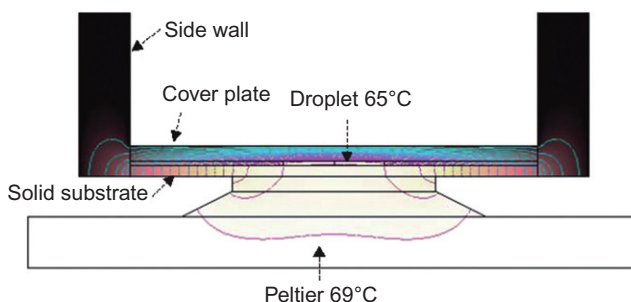
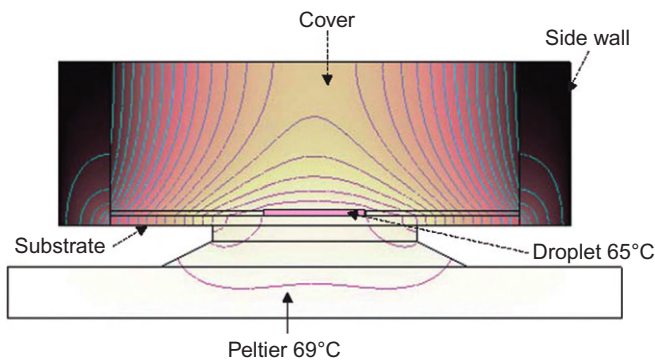
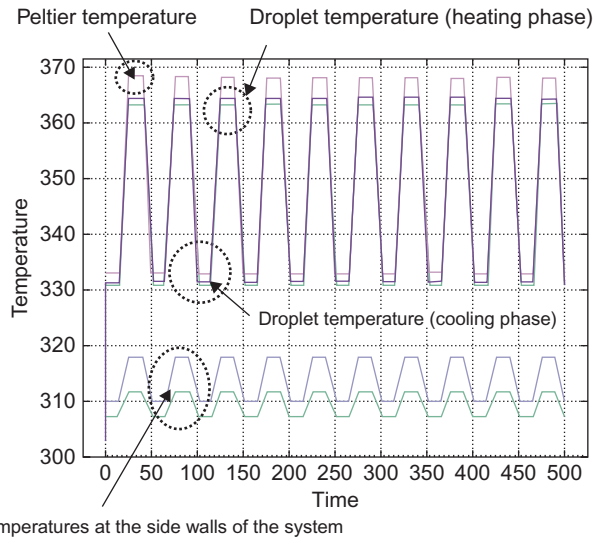


FIGURE 8.9

Covered EWOD system: the temperature field in the droplet is homogeneous within a 0.5°C margin. The side walls are made of plastic to reduce lateral heat loss. Calculation made with the COMSOL numerical software [14].

**FIGURE 8.10**

Open EWOD system with a droplet immersed in oil: the temperature field in the droplet is homogeneous within a 1°C margin. The relatively thick layer of oil reinforces the thermal insulation.

**FIGURE 8.11**

Heating phase: even for an open EWOD system, temperatures are very homogeneous inside the droplet. Temperature transient inside the droplet follows perfectly that of the Peltier, showing no time shift.

8.4.3.2 Two thermal regions—two Peltier devices

A two-region EWOD–PCR device is shown in Figure 8.12. In order to function correctly, the two regions must be maintained at a right, stable temperature. But, if the substrate is thermally conductive, like silicone or glass, there is a temperature leakage through the substrate. This temperature leakage prevents a uniform temperature in the droplet. The solution is to insert an insulating separation in the substrate (Figure 8.13). This separation blocks the heat flux through the substrate and the two regions are thermally homogeneous.

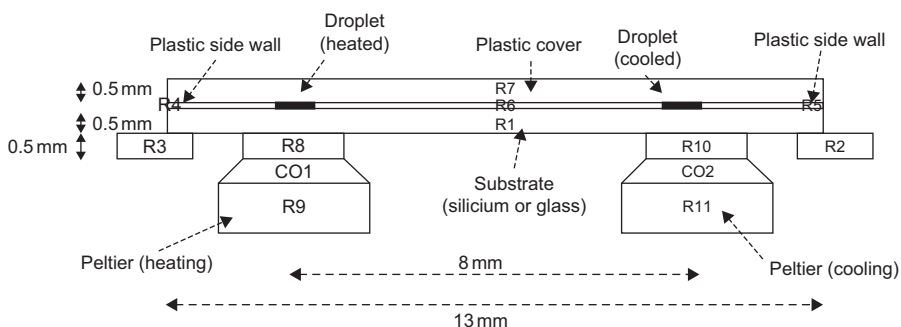


FIGURE 8.12

Schematic of a PCR–EWOD system with two temperature control regions: the two Peltier devices are separated by approximately 8 mm. The calculation was performed with the COMSOL numerical software.

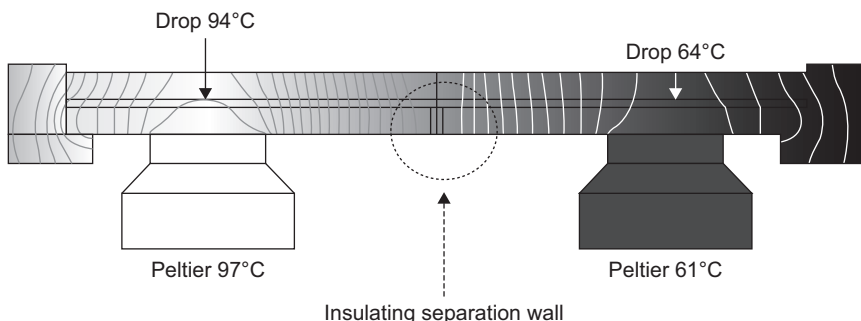


FIGURE 8.13

Temperature control is achieved by two Peltier devices, one heated to 97°C, one cooled to 61°C. The droplet temperatures are very homogeneous at 94°C in the heated zone and at 64°C in the cooled zone. Calculation made with the COMSOL numerical software [14].

8.4.3.3 Conclusions

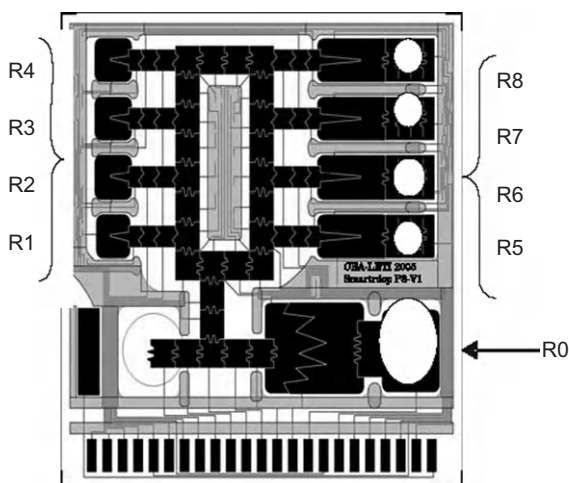
In conclusion, droplet microsystems present many advantages over conventional systems for thermal heating/cooling and thermal cycling of liquids. On the one hand, the temperature of the liquid is highly homogeneous and can be very precisely tuned, under the condition that the oil layer—or the cover layer—and the side walls are sufficiently insulated. On the other hand, thermal transients are very fast, due to the small amount of liquid. The only drawback of miniaturization is the confinement of the temperature to a very small region around the droplet. A separation wall constituting a thermally insulating barrier can be incorporated into the substrate to enhance the confinement but requires a more complicated fabrication process.

8.4.4 Experimental realization of PCR and results

8.4.4.1 Experimental conditions

The demonstration of the feasibility of PCRs in DMF systems has already been made by Yi-Hsien Chang et al. [15] for the dengue II virus and by Pollack et al. [16] for single nucleotide polymorphisms or SNPs. We present here the results of SNP–PCR amplification performed in the LETI laboratories. First, let us recall that SNPs are DNA sequence variations that occur when a single nucleotide (A, T, C, or G) in the genome sequence is variable. For example, an SNP is the possibility of finding in the population a position in the genome where two different cases can be found such as the DNA sequences ACGGCTAA and ATGGCTAA. For a variation to be considered an SNP, it must occur in at least 1% of the population. SNPs, which make up about 90% of all human genetic variation, occur every 100–300 bases along the 3-billion-base human genome. Two of every three SNPs involve the replacement of cytosine (C) with thymine (T). SNPs can occur in both coding (gene) and noncoding regions of the genome. Many SNPs have no effect on cell function, but scientists believe others could predispose people to disease [17]. Hence, identification of SNPs is a major issue in biology.

As we mentioned earlier, the biologic protocol for a PCR is complex, and we only mention here its main features. As the aim is to reproduce conventional PCR reactions performed in tubes, the protocol is directly derived from that of a tube PCR. The primers are the same, and the polymerase is also a Taq-polymerase [12]. A small concentration (0.08 µg/µL) of BSA is added to the mix to prevent polymerase adsorption on the solid substrate; this is needed since the surface/volume ratio is very high. The human placenta DNA to be analyzed is introduced in a reservoir on the chip, and a negative control is realized by the use of a water droplet in another reservoir. The DNA concentration is the same as that of the conventional test of 0.01 mg/µL corresponding

**FIGURE 8.14**

EWOD microchip for the realization of SNP-PCR. The white dots are the holes drilled into the upper cover used to introduce the liquids. R0 is the main reservoir (for DNA sample), and R1–R8 are 8 auxiliary reservoirs; R5–R8 are directly accessible for loading with the different PCR mix. A length scale is given by the small electrodes which are $800 \times 800 \mu\text{m}^2$.

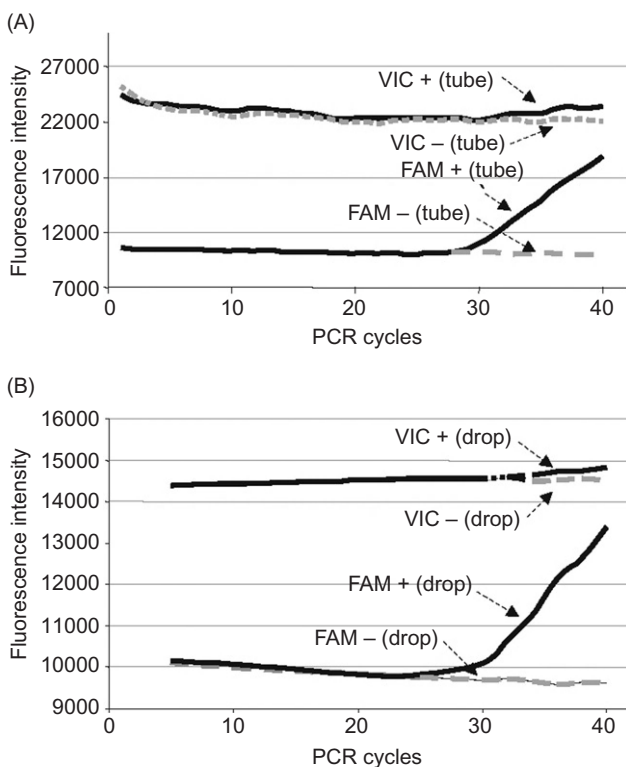
Source: Photo Y. Fouillet CEA-LETI.

to only 25 copies (i.e., initial DNA strands) for a 64 nL droplet and 4200 copies for a 10 μL tube reaction.

The EWOD chip used for this PCR test is covered (covered EWOD) and initially filled with mineral oil (Figure 8.14). Just after oil filling, the chip is placed under vacuum for 10 mn to avoid potential air trapping (air/gas bubbles prevent the correct functioning of the reaction). Thermal cycling occurs in a temperature plateau of 10 mn at 94°C, followed by 40 cycles of 30 s at 65°C and 30 s at 94°C. A dedicated two-color fluorescent detector is used to measure the fluorescence level of the PCR reactions at each PCR cycle. Fluorescence detection is adapted to the FAM™ (carboxyfluorescein) and VIC® fluorophores—one label for each allele—with excitation wavelengths of 488 and 520 nm, respectively, and emission wavelengths of 510 and 555 nm.

8.4.4.2 On-chip PCR results

Experimental results are very satisfactory: Figure 8.15 shows the comparison between in-tube and on-chip PCR results. The fluorescent time profiles are very similar. In both cases, the fluorescent level of the FAM marker rises quickly after approximately 27 cycles. At the end of the reaction (after 40 cycles), the PCR

**FIGURE 8.15**

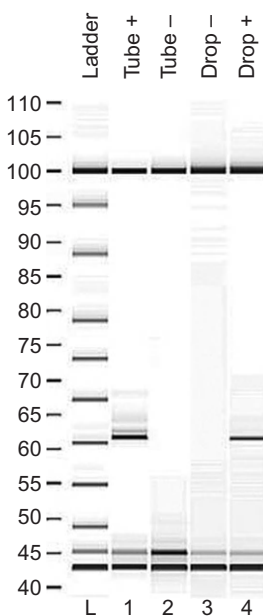
SNP-PCR results: (A) conventional test in tube and (B) test on EWOD-based microsystem. Both cases have similar results and FAM signal shows a sharp turn after 27 cycles.

Source: Courtesy A-G Brachet, CEA-LETI.

product is quantified by capillary electrophoresis (Bioanalyzer, AgilentTM). Comparable yields were obtained for droplets and tube reactions, as shown in Figure 8.16.

8.4.4.3 Conclusions

On-chip EWOD-PCRs present some very interesting advantages. First, on-chip PCRs can be really fast. Thermal cycling was reduced to cycles of 2 s at 94°C and 10 s at 60°C and were found to give satisfactory results. The total time for 40 cycles is then only 8 mn. Second, only a very small quantity of PCR mix is needed compared to the same reaction in-tube. Third, the signal-to-noise ratio is much better in a droplet PCR than that in a tube

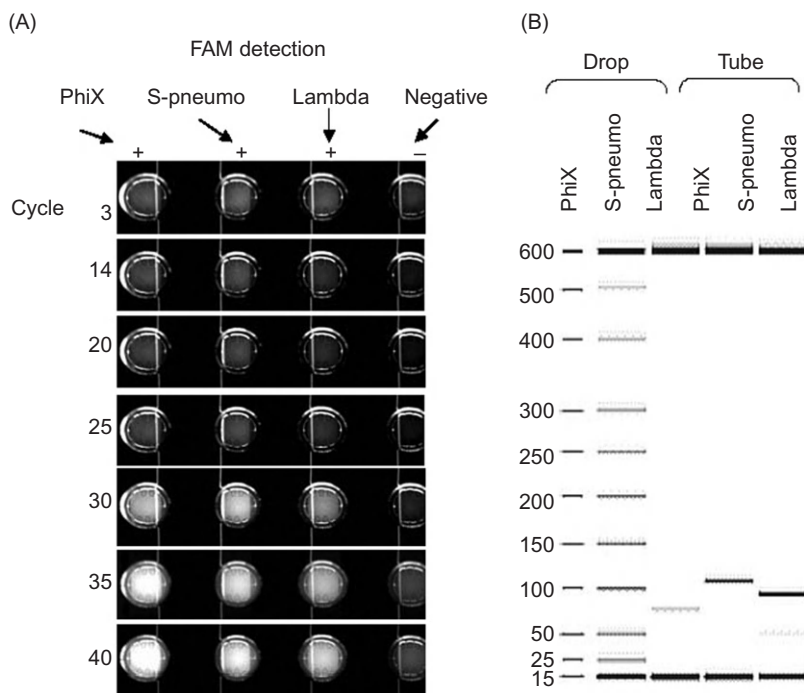
**FIGURE 8.16**

Comparison of PCR yields and specificity: the same DNA sequence is amplified by the conventional in-tube method and the EWOD method.

Source: Courtesy A-G Brachet, CEA-LETI.

PCR, resulting in an increased sensitivity of the assay. Indeed, the number of PCR cycles required to amplify a certain number of copies depends on the concentration. Thus, in a smaller volume, PCR amplification is detected more readily than in a large tube reaction. Finally, PCRs can be easily run in parallel on the same chip. [Figure 8.17](#) shows the results of three DNA sequence amplifications (corresponding to PhiX, S-pneumoniae, and lambda DNA sequences) obtained in parallel on the same chip, compared with in-tube conventional analysis realized in three different tubes.

However, digital PCRs present some difficulties. First, we must be assured that there is no cross contamination between the different drops. Cross contamination could happen through the oil phase or by biofouling, i.e., adsorption/desorption on the solid surface. On their EWOD-based system, Pollack et al. [16] found no substantial cross contamination on 15,000 transfer opportunities between a droplet with and without DNA ([Figure 8.18](#)). In our case, we did not find any contamination through the oil phase and, like Pollack, no contamination of sample DNA; however, PCR products were found to

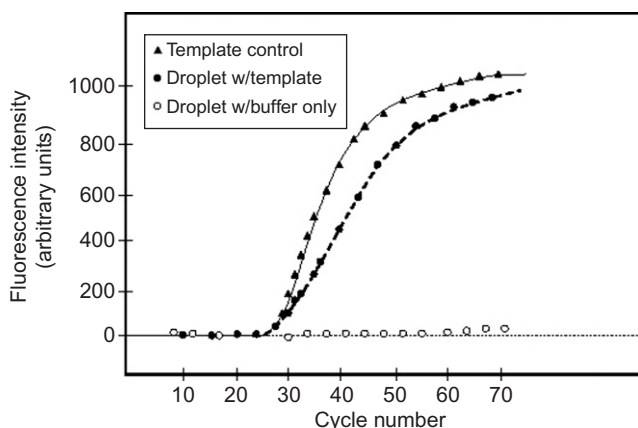
**FIGURE 8.17**

(A) Fluorescence control of the four droplets at the same cycle number (the fourth droplet is a droplet without DNA for differential imaging). (B) Analysis by gel electrophoresis after the 40th cycle. Again the in-tube and on-chip results are similar.

Source: Courtesy A-G Brachet, CEA-LETI.

cause some contamination due to adsorption/desorption on the solid surfaces. This could result in a problem if the PCR chips are used several times for PCR amplification. An important remark is that one should be cautious with the new superhydrophobic substrates that are being developed to increase the electrowetting force (see Chapter 4), when these substrates present rugosities; cross contamination and biofouling could become an important issue in such a case.

Second, gas bubbles are prone to form due to the relatively high temperatures (94°C). Bubbles are a serious caveat in the functioning of EWOD-based chips. They might lead to dielectric breakup and chip deterioration. Degassing precautions should be used to avoid bubble formation.

**FIGURE 8.18**

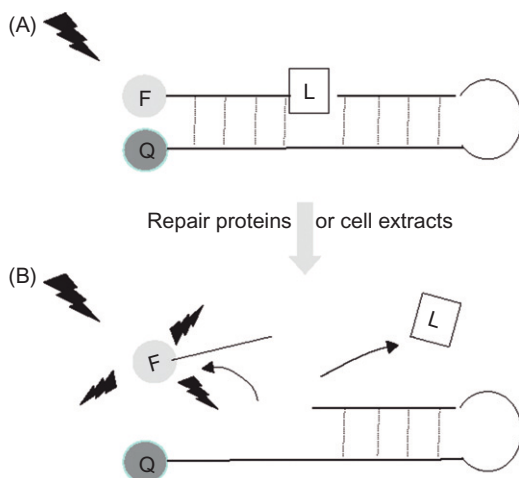
Cross-contamination results: droplets both with and without DNA were collected after 15,000 intersecting transfers, added as the template component to a PCR mixture and amplified in a commercial real-time PCR system [17].

8.5 DNA repair microprocessor

DNA repair activity tests have a large field of diagnostic applications: diseases associated with DNA repair deficiencies, identification of cancer predisposition, prediction of individual response to chemo- or radiation therapy, and finally high-throughput screening of DNA repair enzymes. A generic challenge is to test in parallel various enzymatic activities with a very limited amount of cellular extracts. A promising way is to run biological tests allowing the DNA repair activity to be monitored by real-time fluorescence measurement on an EWOD-based microchip [18].

Quantification of enzymatic repair activities is made by using a DNA molecular beacon in which a specific lesion has been inserted, as shown in Figure 8.19. The test consists of monitoring the DNA repair enzyme activity contained in the cell extracts; these enzymes excise the DNA lesion by fragmenting the DNA strand at the location of the lesion. As soon as the excision is performed, the fluorescent energy transfer (FRET) between the fluorophore and the quencher is canceled and there is an emission of fluorescence due to DNA breakage.

In the assay described here, the molecular beacon contains an 8-oxo-guanine lesion, and the DNA repair enzyme is a fapy glycosylase (Fpg). Incubation buffer is constituted by a solution of 25 mM Tris (pH 7.6), 2 mM EDTA, and 50 mM NaCl. All experiments were simultaneously performed on a chip using a 120 nL droplet and in an Eppendorf tube containing a 6 μ L volume, on a real-time PCR instrument (Stratagene MX 3500P). The on-chip experiment consists in

**FIGURE 8.19**

Principle of FRET-based DNA repair assay using DNA molecular beacon (F = fluorescent marker, Q = quencher) with a lesion (L). The presence of the quencher next to the fluorescent marker prevents the emission of light by the fluorophore (A). Once the DNA lesion L is cut out of the DNA strand, fluorescence is restored (B).

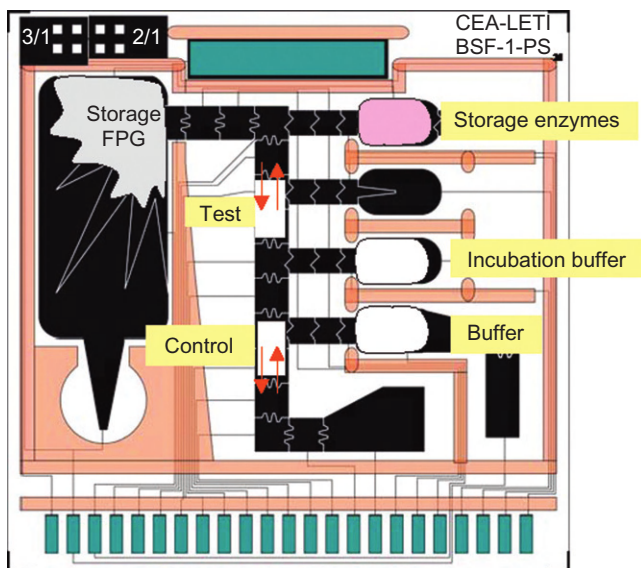
Source: Reprinted with permission from Ref. [18] © 2006, NSTI.

dispensing two 64 nL droplets of enzyme and substrate reagents, mixing them, and incubating at 37°C for 30 mn. A negative control droplet with no enzyme is located next to the incubating droplet in order to make a differential measure of the fluorescence (Figure 8.20).

Two different comparisons with in-tube reference were made: first, with a fixed repair enzyme concentration $[Fpg] = 1 \mu\text{M}$ and various concentrations of substrate ranging from 0.25 to 1.2 μM ; second, with a fixed substrate concentration $[8\text{-oxoGua}] = 1 \mu\text{M}$ and an enzyme concentration ranging from 200 nM to 1 μM . The results are shown in Figure 8.21 where the initial velocity of the reaction is plotted versus concentrations of enzymes or substrate. The results show that the on-chip tests compare very well with the in-tube conventional tests.

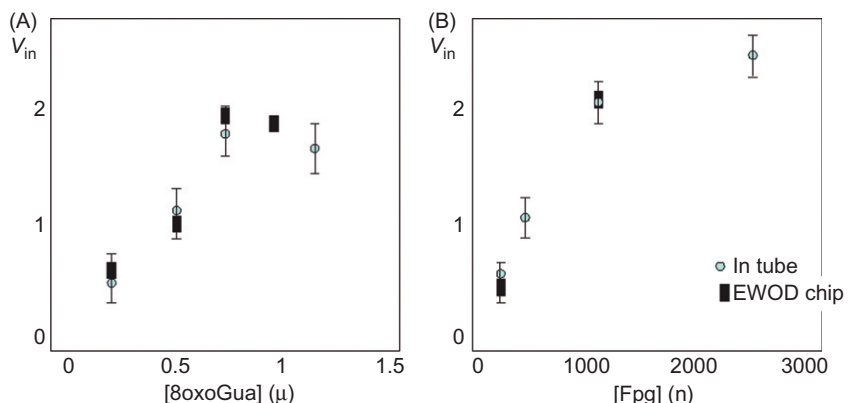
On the other hand, reaction kinetics are compared in Figure 8.22 for a fixed concentration of GFP (green fluorescent protein) and three different concentrations of 8-oxo-guanine. Here again, the kinetics of reactions are similar.

In conclusion, the EWOD-based assay performs quite well, a sensitivity of 5 nM of GFP was found, and no loss of activity due to volume size reduction was detected. A clear advantage is the use of tiny volumes of costly enzymes, compared to in-tube assays. However, cell extracts have not yet been used; only an enzyme has been tested. More systematic tests need to be developed to assess the validity of the approach on EWOD microprocessors.

**FIGURE 8.20**

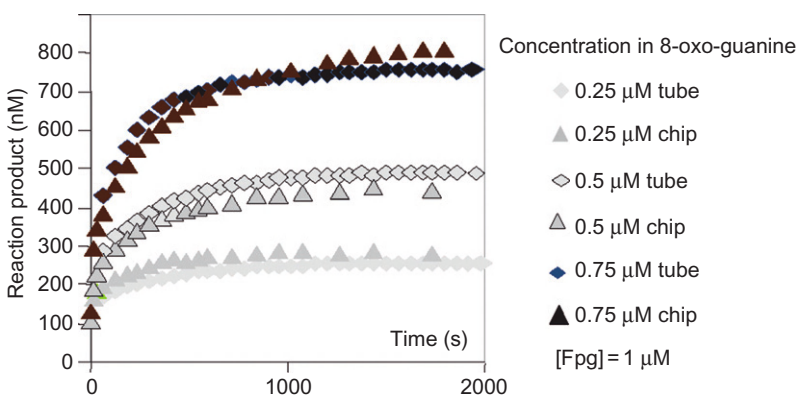
Covered EWOD chip for DNA repair activity test. Light emission from the test droplet is compared to a negative control droplet.

Source: Reprinted with permission from Ref. [18] © 2006, NSTI.

**FIGURE 8.21**

(A) Experimental results for a $1 \mu\text{L}$ concentration of Fpg. (B) Same for a $1.2 \mu\text{L}$ concentration of 8-oxo-guanine.

Reprinted with permission from Ref. [18] © 2006, NSTI.

**FIGURE 8.22**

Comparison of kinetics between in-tube and on-chip reactions.

8.6 Protein analysis coupled with mass spectrometry

Protein analysis has become a major issue in biology. Proteins are linked to gene expression; they are essential parts of all living organisms and participate in every process within cells. Many proteins are enzymes that catalyze biochemical reactions and are vital to metabolism. The analysis and classification of proteins is a major challenge. Microsystems now contribute to this search. The first integrated systems are being developed using microflow technology [19,20]. However, because there is a huge amount of a protein in liquid samples, it is advantageous to reduce as much as possible the analyzed volume, in order to be more specific. To this extent, DMF can bring a solution. However, an integrated DMF system is yet to be developed. At this time, the first systems being developed combine a DMF system and a conventional analysis system. They use a DMF system to transport the carrier fluid droplets, extract the proteins, and perform the enzymatic reactions; then the liquid is transferred onto a special plate which is incorporated in a conventional MALDI-MS device. Let us recall briefly that MALDI-MS or MALDI-TOF-MS stands for matrix-assisted laser desorption ionization time-of-flight mass spectrometry. This complicated device can identify large biomolecules, over 300,000 Da, in the time they take to traverse a region submitted to an electric field. First, the biomolecules are accelerated by an electric field; the kinetic energy acquired by the biomolecule is given by

$$E_c = \frac{1}{2}mv^2 = ze \nabla Es, \quad (8.4)$$

where m is the mass of the ion, v is the velocity of the ion, z is the number of charges, e is the charge on an electron in coulombs, ∇E is the electric field gradient, and s is the distance of the ion source region. The time taken by the

biomolecule to cross a region of constant electric field is recorded. This time depends on the ratio m/z of the biomolecule and identifies this molecule.

Figure 8.23 shows the principle of protein characterization microdevice, realized by coupling an EWOD-based microsystem with a MALDI-MS conventional apparatus.

Now, let us come back to the DMF system itself. The principle is based on soft printing and is shown in Figure 8.24.

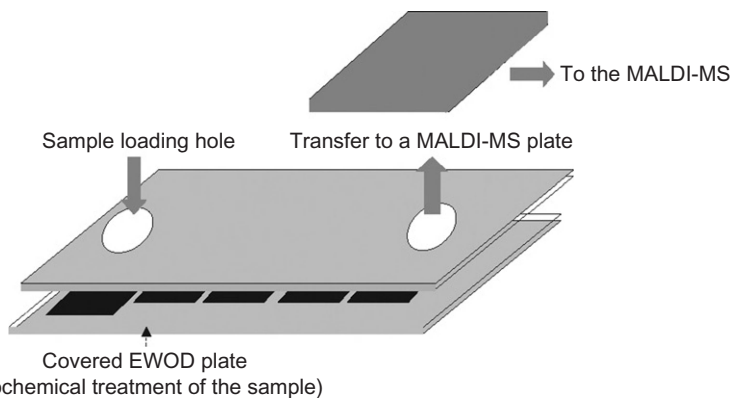


FIGURE 8.23

Schematic of a covered EWOD system coupled to a MALDI-MS [21].

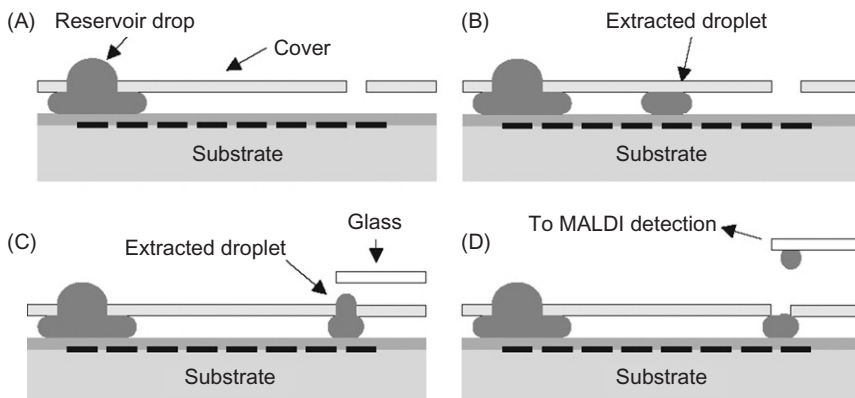
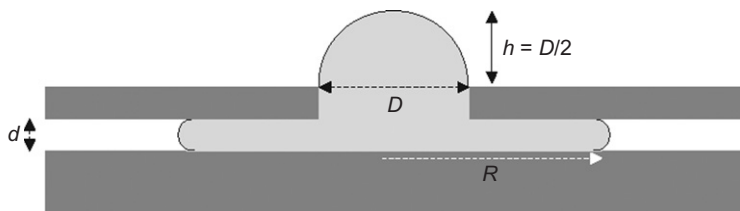


FIGURE 8.24

Soft printing process to a glass plate: (A) sample loading; (B) creating and transporting discrete droplets; (C) droplet bulging in the outlet port, approach of a glass plate; and (D) contact with the glass plate, moving away the glass plate with the droplet.

**FIGURE 8.25**

Sketch of a droplet bulging in the outlet port.

Let us examine here the conditions for optimal droplet bulging through the hole. We showed in Chapter 3 that the maximum bulging is obtained when the droplet shape is a half-sphere. The pressure of the droplet is given by Laplace's law

$$P = \frac{4\gamma}{D}, \quad (8.5)$$

where γ is the surface tension of the interface and D is the diameter of the hole (Figure 8.25). The droplet pressure can also be derived from the droplet shape between the two plates:

$$P = \gamma \left(\frac{-2 \cos \theta}{d} + \frac{1}{R} \right). \quad (8.6)$$

Relations (8.5) and (8.6) determine the value of R and consequently the size of the droplet in the covered EWOD system:

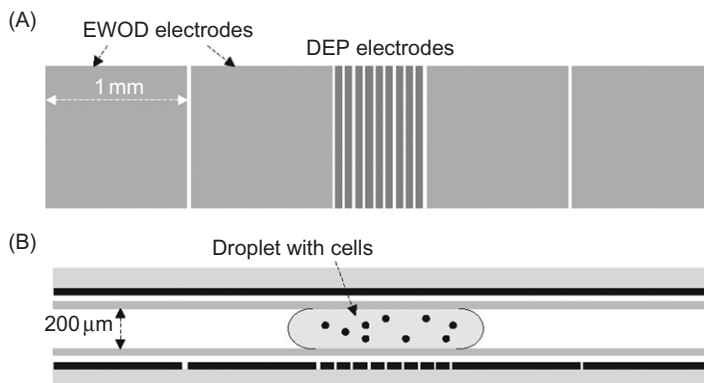
$$\frac{R}{d} = \frac{1}{2} \frac{1}{((2d/D) + \cos \theta)}. \quad (8.7)$$

The orifice diameter D should not be too large, because the interface would spread over onto the upper cover (because the pressure in the dome would be small compared to the pressure of the liquid between the two plates, and there would be no equilibrium possible), nor too small, because the volume of liquid bulging out would be too small ($h = D/2$).

In conclusion, the principle of a microsystem for protein analysis using DMF has been proposed. However, there is still a long way to go to obtain a prototype, and an integrated microdevice is still to be developed.

8.7 Cell-on-a-chip microsystems: example of a cell concentrator

We have seen that cells can be moved on EWOD-based chips—with the conditions that they are sufficiently small and that adequate surfactants are used.

**FIGURE 8.26**

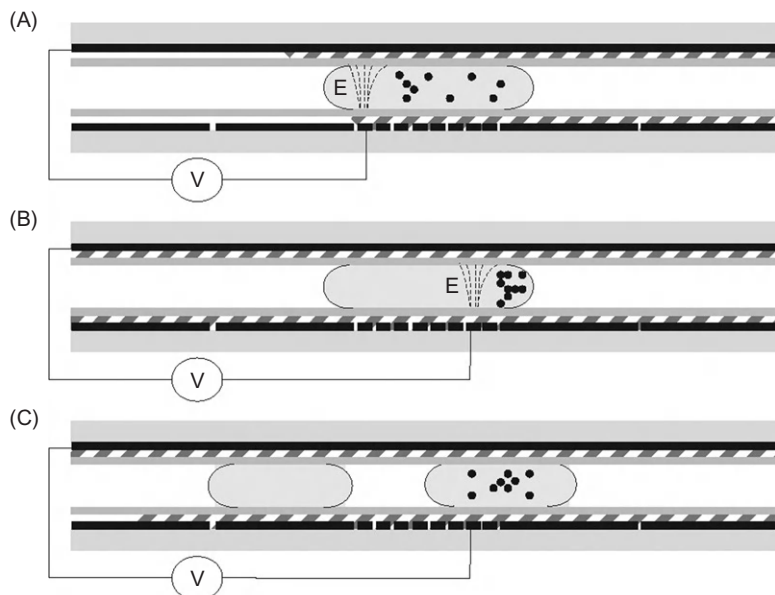
(A) View from top of the device with the EWOD electrodes—for droplet motion—and the DEP electrodes—for cells manipulation. (B) Side view of the device showing the top cover and the droplet.

The presence of electrodes in the chip makes it convenient to combine the electrowetting effect—for transporting droplets containing the cells—to a dielectrophoretic effect—for the manipulation of the cells [22]. It is noteworthy to mention that electrowetting is primarily a contact line phenomenon and refers to electric field-induced interfacial tension changes between a liquid and a solid conductor—as was shown in Chapter 4. On the other hand, DEP is a bulk phenomenon caused as a result of polarization induced in a dielectric liquid by a nonuniform electric field. Combining the two effects leads to very interesting applications, like that of the cell concentrator microsystem developed by Po-Weng Huang et al. [23]. Their device is schematized in Figure 8.26.

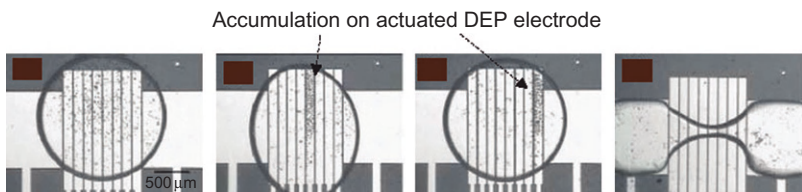
First, the EWOD electrodes are used to move the droplet containing the cells on the DEP electrodes. Then, the DEP electrodes are successively actuated in order to progressively confine—by negative DEP—the cells to an extremity of the droplet (Figure 8.27). Note that DEP can produce an attraction or repulsion effect on cells and particles depending on the actuation frequency; negative DEP corresponds to repulsive forces [22]. Finally, the droplet is cut in two by EWOD actuation. As a result, the cells are concentrated in a smaller droplet.

We note that the mechanism presented here is the opposite of that presented in Chapter 5 for the dilution of particulate solutions. Figure 8.28 shows the concentration of neuroblastoma cells contained in a solution of 3% PBS (phosphate-buffered saline) with a concentration of 280 nM of isotonic sucrose. In this case, a high-frequency positive DEP was used because the low-frequency negative DEP is not sufficient to displace the cells due to the screening of the dielectric layer.

This example shows that combining EWOD and DEP effects could lead to interesting technological solutions for cell manipulation. It is noteworthy that the voltages used for each effect do not alter the viability of the cells.

**FIGURE 8.27**

Principle of cell concentration by EWOD and DEP effects. (A) Negative DEP repels the cells to the right. (B) By successively displacing the actuation to the right, the cells are progressively confined in the right corner of the droplet. (C) The droplet is cut in two by EWOD actuation; the cells are concentrated in the right droplet.

**FIGURE 8.28**

Photograph of progressive concentration of neuroblastoma cells by positive DEP, followed by an EWOD splitting of the droplet. DEP was produced by a 60 V_{rms} voltage at a frequency of 2 MHz, whereas electrowetting splitting was obtained with a voltage of 84 V_{rms} at a frequency of 1 kHz.

Reprinted with permission from [23] © 2006, IEEE.

8.8 Summary

The development of DMF for biotechnological and biological applications is just at its beginning. These microsystems are not yet at the industrial stage but rather

are laboratory prototypes. The first results are promising and the potential of DMF seems important: necessary volumes of biologic samples are extremely reduced, volumes of costly reagents are also minute, sensitivity is expected to be very high, time of reaction/detection is short, and efficient parallelization can be achieved.

It is expected that DMF systems will follow the same evolution as that of conventional microflow systems. However, there are considerable remaining difficulties to overcome, like fabrication, integration, and portability.

References

- [1] V. Srinivasan, V.K. Pamula, R.B. Fair, An integrated digital microfluidic lab-on-a-chip for clinical diagnostics on human physiological fluids, *Lab Chip* 4 (2004) 310–315.
- [2] Lei Li, Huan Hu, Hong Lin, Da-Tian Ye, Electrowetting of the blood droplet on the hydrophobic film of the EWOD chips, in: Proceedings of the 27th Annual Conference of the IEEE Engineering in Medicine and Biology, Shanghai, China, 1–4 September, 2005, EMBS (Engineering in Medicine & Biology Society) Piscataway, NJ.
- [3] Jeong-Yeol Yoon, R.L. Garrell, Preventing biomolecular adsorption in electrowetting-based biofluidic chips, *Anal. Chem.* 75 (2003) 5097–5102.
- [4] http://en.wikipedia.org/wiki/Bovine_serum_albumin. Bovine serum albumin, wikipedia.
- [5] V. Srinivasan, K. Pamula, M.G. Pollack, R.B. Fair, A digital microfluidic biosensor for multianalyte detection, *Tech. Digest IEEE MEMS* (2003) 327–330.
- [6] V. Srinivasan, V. Pamula, P. Paik, R. Fair, Protein stamping for MALDI mass spectrometry using an electrowetting-based microfluidic platform, in: *Lab-on-a-Chip: Platforms, Devices, and Applications*, Conference 5591, SPIE Optics East, Philadelphia, 25–28 October, 2004.
- [7] L. Gan, X. Xiong, R. Wang, J.B. Power, M.R. Davey, Plant regeneration from cell suspension protoplasts of *Actinidia deliciosa*, in: ISHS Acta Horticulturae, V International Symposium on Kiwifruit, vol. 610, 2003.
- [8] J.H. Jeong, Y.M. Moon, S.O. Kim, S.S. Yun, H.I. Shin, Human cartilage tissue engineering with pluronic and cultured chondrocyte sheet, *Key Eng. Mater.* 342–343 (2007) 89–92.
- [9] R.B. Fair, A. Khlystov, V. Srinivasan, V.K. Pamula, K.N. Weaver, Integrated chemical/biochemical sample collection, pre-concentration, and analysis on a digital microfluidic lab-on-a-chip platform, in: *Lab-on-a-Chip: Platforms, Devices, and Applications*, Conference 5591, SPIE Optics East, Philadelphia, 25–28 October, 2004.
- [10] Yuejun Zhao, Sung Kwon Cho, Microparticle sampling by electrowetting-actuated droplet sweeping, *Lab Chip* 6 (2006) 137–144.
- [11] K.B. Mullis, F. Ferré, R.A. Gibbs, *The Polymerase Chain Reaction*, Birkhäuser, Boston, MA, 1994.
- [12] PCR. <<http://www.britannica.com/eb/article-9002524/polymerase-chain-reaction>>. Encyclopedia Britannica, PCR.

- [13] http://en.wikipedia.org/wiki/Peltier-Seebeck_effect. Thermoelectric effect, wikipedia.
- [14] COMSOL Reference Manual. COMSOL, Inc., Palo Alto, CA. <<http://www.comsol.com>>.
- [15] Yi-Hsien Chang, Gwo-Bin Lee, Fu-Chun Huang, Yi-Yu Chen, Jr-Lung Lin, Integrated polymerase chain reaction chips utilizing digital microfluidics, *Biomed. Microdevices* 8 (2006) 215–225.
- [16] M.G. Pollack, P.Y. Paik, A.D. Shenderov, V.K. Pamula, F.S. Dietrich, R.B. Fair, Investigation of electrowetting-based microfluidics for real-time PCR applications, in: Proceedings of the 2003 MicroTas Conference, Squaw-Valley, CA, Oak Ridge National Laboratory. 5–9 October, 2003.
- [17] <http://www.ornl.gov/sci/techresources/HumanGenome/faq/snps.shtml>.
- [18] D. Jary, A. Chollat-Namy, Y. Fouillet, J. Boutet, C. Chabrol, G. Castellan, et al., DNA repair enzyme analysis on EWOD fluidic microprocessor, in: Proceedings of the NSTI-Nanotech Conference, vol. 2, 2006, Boston, 7–11 May.
- [19] N. Sarrut, S. Bouffet, O. Constantin, J. Garin, F. Mittler, J. Sudor and F. Vinet, Comparison of hydrodynamic versus electroosmotic driven flows for enzymatic protein digestion in a microreactor, in: Proceedings of the MicroTas 2004 Conference, 26–30 September, 2004, RSC Publishing.
- [20] Fabien Sauter-Starace, C. Pudda, C. Delattre, H. Jeanson, C. Gillot, N. Sarrut, et al., in: W. Menz, S. Dimov, B. Fillon (Eds.), *Lab-on-a-chip: Advances in Packaging for MEMS and Lab-on-a-chip. Multi-Material Micro Manufacture*, Elsevier, Amsterdam, 2006.
- [21] U.-C. Yi, C.-J. Kim, Soft printing of droplets pre-metered by electrowetting, *Sens. Actuator A* 114 (2–3) (2004) 347–354.
- [22] J. Berthier, P. Silberzan, *Microfluidics for Biotechnology*, Artech House Publishers, Norwood, MA, 2005.
- [23] Po-Weng Huang, Tsu-Te Wang, Sheou-Wei Lin, Yu-Chi Chang, Shih-Kang Fan, Dielectrophoretic cell concentrator on EWOD-based chips, in: Proceedings of the First IEEE International Conference on Nano/Micro Engineered and Molecular Systems, Zhuhai, China, 18–21 January, 2006, Institute of Electrical and Electronics Engineers, Washington DC.

Cell Manipulations in EWD

9

CHAPTER OUTLINE

9.1 Introduction	367
9.2 Cells in EWOD devices	368
9.2.1 Motion of droplets laden with cells.....	368
9.2.2 Viability	370
9.3 DMF for cell-based arrays.....	370
9.4 Virtual microwells.....	371
9.4.1 Introduction	371
9.4.2 Theoretical approach	372
9.4.3 Cancer cell culture in an EWOD microdevice.....	376
9.4.4 Electrowetting device for dried blood spot analysis	378
9.5 Hydrogel disks for DMF	379
9.6 Concentration of immune cells in blood.....	383
9.7 Conclusion	384
Acknowledgment.....	384
References	385

9.1 Introduction

The development of biotechnological microsystems has been initially triggered by DNA detection and recognition. Still today, the miniaturization of such systems is continuing. Progressively microchips for the analysis of proteins have been developed. But it has been recognized that the study of DNA and proteins—even how important they were—could not furnish all the data needed by the biologists and the applications envisioned by the pharmaceutical industry. Progressively microsystems for the analysis of cells have been imagined and are gaining momentum. It is based on the fact that a cell is the irreducible element of life and is often studied as a living model of complex biological systems. Today the development of cell chips constitutes the vast majority of publications in the field of

biotechnology in scientific journals. New denominations like cellomics or cytomics appeared, referring to the functional analysis of cells [1]. It is now certain that the understanding of the intracellular mechanisms and of the communication between cells is fundamental, not only in the field of biology but also in medicine and pharmacology.

Conventionally, cell-based assays are using in well plates that enable simultaneous analysis of multiple cell types or stimuli. For such multiplexed analyses, cells in well plates are often evaluated using microplate readers, which can be integrated with fluid handling and other miscellaneous equipment in a robotic analysis platform. A major drawback of such systems is the expense of the instrumentation and the experimental consumables (e.g., plates, pipette tips, reagents, and cells). The latter is a particular disadvantage for cell-based assays as they are generally more complex and require larger amounts of reagents than cell-free assays.

More recently, microfluidics has been investigated as a convenient means for the development of cell-based assays. The first solutions investigated have been using microflows. In order to compensate for sedimentation, it was found necessary to operate with larger carrier fluid velocities; hence, “inertial microfluidics” has been invented, using larger flow velocities, presenting a nonnegligible inertia and capable of transporting larger biological objects like cells and bacteria [2–4]. Dean flows, pinched flow fractionation, flow focusing devices (FFD), recirculation microchambers, and deterministic lateral displacement have been developed to transport, separate, or capture cells [5–10]. All these functionalities are aiming to the functional study of cells. Once transported, separated, sorted, and immobilized, the biologic functionalities can be addressed, such as cellular culture, the communication between cells, the response of a cellular culture to some concentration of chemical species, cell differentiation, cellular mechanobiology, and so on [11–14].

However, a drawback of the use of microflows is the lack of specificity due to a poor confinement of the cells and different reagents. It has been found useful to isolate cell cultures in a small and closed environment. This concern is especially important in the case of single cell study [15]; it is also important to have the ability to deliver to a cell culture a precisely controlled amount of reagents [16,17].

The same arguments that prevailed for the development of DMF apply again, and it has been found of interest to investigate how DMF—especially EWOD devices—could be helpful as cellomic microsystems. The main difficulty stems from the fact that electrowetting forces are not very powerful. In this chapter, we present different approaches to use DMF for cell culture and analysis.

9.2 Cells in EWOD devices

9.2.1 Motion of droplets laden with cells

Many different kinds of biological liquids can be manipulated in EWOD devices. A first condition is that they must be electrically conductive, but this is not a

major restriction since body fluids are aqueous solutions with ions (like Na^+Cl^- for example). Another condition is that they must not be too viscous, which would considerably slow down the motion of droplets. It has been observed that body fluids like blood, sweat, and tears can be handled by EWOD (Figure 9.1).

However, the behavior of nonhomogeneous biological fluids in EWOD devices is more complicated: the ability to move cells with EWOD depends on the type of cells. Very large or adherent cells are difficult to transport with the relatively small electrowetting forces. In particular, this is the case of Langerhans islets (pancreatic cells) that easily adhere to the walls and which size is in the range 50–300 μm . Such cells are better handled by droplet microfluidics (see Chapter 14). But many other cells can be transported by electrowetting droplets. Figure 9.2 shows the dispensing of an aqueous droplet containing Jurkat T cells (human leukemia lymphocytes) [17]. HeLa and MCF-7 cells for example can also be manipulated in EWOD devices [18]. When dealing with cells that are difficult to manipulate because they tend to stick to the surface of the device, causing contact line pinning,

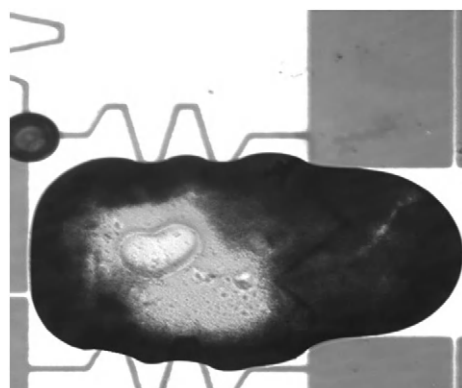


FIGURE 9.1

Droplet of blood in an EWOD device.

Source: Courtesy CEA-LETI.

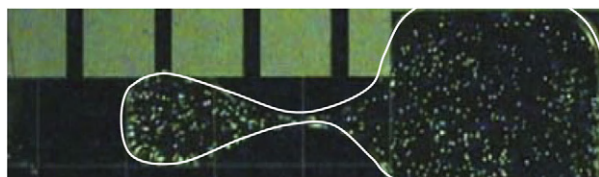


FIGURE 9.2

Dispensing of a droplet with Jurkat T cells [17]. The outline of the droplet has been painted with a white line for better visualization. A droplet is extracted by electrowetting force from the reservoir, carrying Jurkat cells.

Source: Reprinted with permission from Ref. [17] © RCS 2008.

one generally uses a nonionic surfactant, pluronic F68. This surfactant—used as a solution additive—facilitates actuation of suspensions of cells in liquids.

9.2.2 Viability

A concern when using electric methods with cells is the viability. In other words, are the cells affected by the electric field? A first remark is that the magnitude of the electrowetting electric field is small in EWOD devices compared to DEP, and even in the case of DEP viability can be maintained if precautions are taken [19]. Many studies have been done and it has been observed that electrowetting electrical field has no major effect on the cells, and do not lead to cell apoptosis [20–22].

Because cell manipulations spread over a long period of time (a few hours to a few days), evaporation must be taken into account and the cell culture must not dry. Usually, a controlled atmosphere with a constant concentration in vapor is maintained around the device.

9.3 DMF for cell-based arrays

A typical EWOD system for cell-based assay is shown in Figure 9.3. This example has been proposed by Barbulovic-Nad and coworkers [17]. The view is schematic, but it contains the principle: cells are transported from a reservoir to the working zone paved with the electrodes. In this particular case, the system is used to perform cytotoxicity assay on Jurkat T cells exposed to different concentrations of the surfactant Tween 20 (from 0.002% to 0.5%). The dye is used to

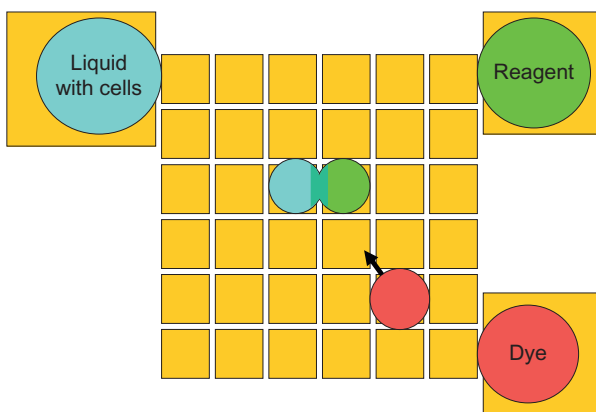
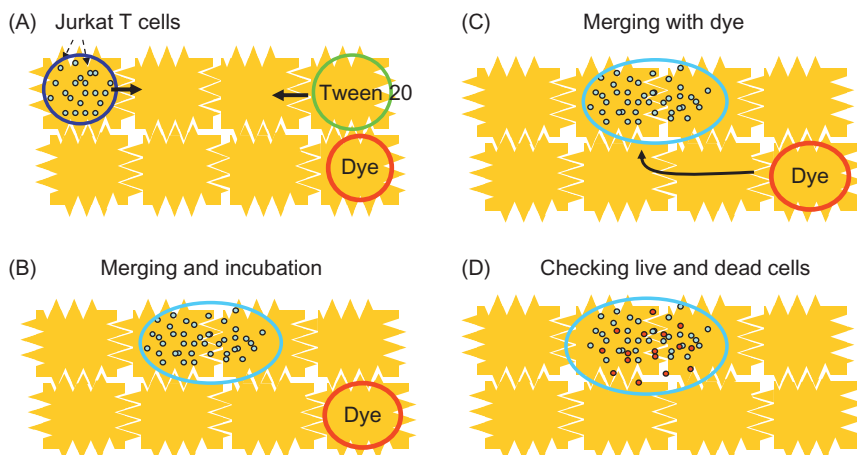


FIGURE 9.3

Sketch of a DMF chip for cell-based assay: the sample liquid contains the Jurkat T cells, and the reagent is a solution containing a determined concentration of Tween 20. The dye marks fluorescence the cells [17].

**FIGURE 9.4**

Protocol for the determination of the cytotoxicity of Tween 20 on Jurkat T cells.

mark the cells: it is a mix of calcein AM that stains the live cells and ethidium homodimer-1 that stains the dead cells.

The assay protocol is indicated in [Figure 9.4](#). Such an assay has proved to be much more sensible than traditional well devices because the count of live and dead cells is much more precise. It was found that conventional wells assays overestimate Tween 20 toxicity 15-fold.

9.4 Virtual microwells

9.4.1 Introduction

It has been found that the introduction of surface inhomogeneities in EWOD devices would add many new applications to the already existing panel, such as cell culture and cell analysis. These inhomogeneities are either patches of hydrophilic coating deposited on the hydrophobic EWOD substrate [\[18,23,24\]](#), or punched disks of paper [\[25\]](#).

These inhomogeneities have been called virtual microwells (VM) by Eydelnant and colleagues [\[26\]](#) and Chen et al. [\[27\]](#) to point out the trapping of liquid droplets by these hydrophilic patches on a hydrophobic substrate. The wells are called virtual because they are not confined on the sides like traditional wells but are defined by surface properties on the bottom and top plates.

In this section, we analyze the physical mechanisms for a droplet transported over a VM, especially since the microwell is hydrophilic, the possibility to remove the droplet from the well. Then, we present some characteristic applications of such designs.

9.4.2 Theoretical approach

In order to be efficient, microwells must not block droplet motion. This is the key point. As a matter of fact, the transported aqueous droplet easily invades the patch—because the patch is hydrophilic; but it is more difficult to remove the droplet away from the patch for the same reason. Indeed, in the first case, the electrowetting force can be approximately by

$$F_a \approx (e - d)\gamma \cos \theta_a + d\gamma \cos \theta_{d,a} - e\gamma \cos \theta_0, \quad (9.1)$$

where e is the electrode width, d the diameter of the patch, γ the surface tension, θ_a the actuated EWOD contact angle, θ_0 the nonactuated contact angle, and $\theta_{d,a}$ the (actuated) patch contact angle. Denoting by

$$F_0 \approx e\gamma \cos \theta_a - e\gamma \cos \theta_0 \quad (9.2)$$

the usual EWOD force, the expression for the advancing electrowetting force in presence of the patch is

$$F_a \approx F_0 + d\gamma(\cos \theta_{d,a} - \cos \theta_a). \quad (9.3)$$

Remarking that the actuated patch contact angle $\theta_{d,a}$ is smaller than the actuated EWOD contact angle θ_a —because the nonactuated contact angles are already in this order $\theta_d < \theta_0$, where θ_d is the (nonactuated or natural) patch contact angle, Eq. (9.3) yields

$$F_a > F_0. \quad (9.4)$$

Hence, the droplet easily covers the patch. Conversely, the receding electrowetting force can be expressed as

$$F_r \approx e\gamma \cos \theta_a - d\gamma \cos \theta_d - (e - d)\gamma \cos \theta_0. \quad (9.5)$$

Using F_0 again,

$$F_r \approx F_0 - d\gamma(\cos \theta_d - \cos \theta_0). \quad (9.6)$$

We remark in Eq. (9.6) that $\theta_d < 90^\circ$ because the patch is hydrophilic, and $\theta_0 > 90^\circ$ because the Teflon substrate is hydrophobic. Hence,

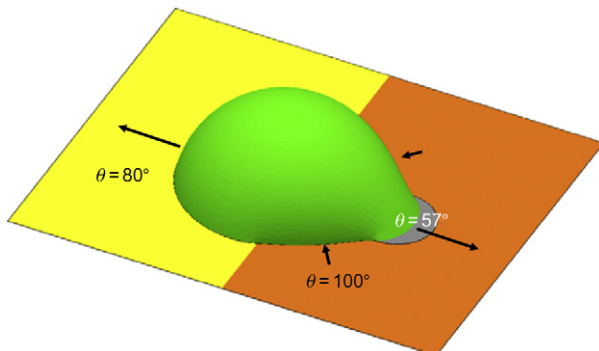
$$F_r < F_0. \quad (9.7)$$

The difficulty is then to remove the droplet out of the patch area. If we assume that the hydrophilic patch contact angle is of the same order of magnitude as the actuated EWOD contact angle, Eq. (9.7) yields

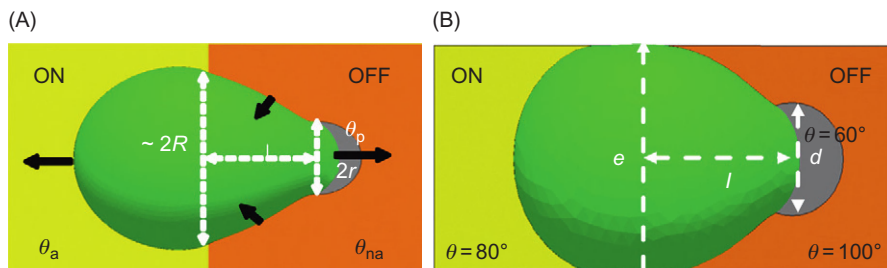
$$F_r \approx F_0 - \frac{d}{e}F_0 = F_0 \left(1 - \frac{d}{e}\right). \quad (9.8)$$

Equation (9.8) shows that by decreasing the patch diameter, the receding force F_r increases. There is a patch size above which the droplets will remain attached to the disk.

A more detailed analysis can be done by analyzing the shape of a droplet at the onset of leaving the patch for an “open” EWOD device (Figures 9.5 and 9.6).

**FIGURE 9.5**

Picture of a droplet at equilibrium between the electrowetting forces (on the left), the hydrophobic forces (on the right), and the hydrophilic force of the disk, obtained with the Evolver numerical software. The droplet volume is 0.125 μL , the distance between the electrode boundary and the disk is 500 μm , and the disk radius is 200 μm .

**FIGURE 9.6**

Sketch of the forces acting on the droplet: (A) droplet not bounded laterally and (B) droplet laterally bounded by the electrodes.

We can approximate the different capillary and electrocapillary forces acting on the droplet. The capillary force on the triple line located inside the disk is

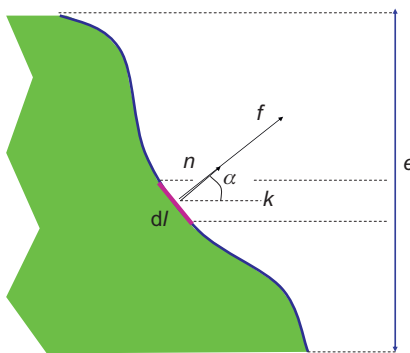
$$F_d \approx 2r\gamma \cos \theta_d. \quad (9.9)$$

The electrowetting force can be approximated by

$$F_e \approx 2R\gamma \cos \theta_a. \quad (9.10)$$

The hydrophobic force acting on the triple line inside the nonactuated electrode and outside the disk can be calculated by integrating the capillary force along the triple line [28]. It suffices to remark that

$$F_{na} \approx \gamma \cos \theta_0 \int_A^B \vec{n} \cdot \vec{k} \, dl = \gamma e \cos \theta, \quad (9.11)$$

**FIGURE 9.7**

Sketch of the triple line with the local capillary force per unit length f .

where e is the projected length of the triple line (Figure 9.7). In our particular case,

$$e \approx 2(R - r). \quad (9.12)$$

We obtain

$$F_{\text{na}} \approx 2(R - r)\gamma \cos \theta_0. \quad (9.13)$$

Equilibrium occurs when

$$F_a - F_{\text{na}} = F_d \quad (9.14)$$

or

$$R\gamma \cos \theta_a - (R - r)\gamma \cos \theta_0 = r\gamma \cos \theta_d. \quad (9.15)$$

Simplification of Eq. (9.15) leads to

$$R(\cos \theta_a - \cos \theta_0) \approx r(\cos \theta_d - \cos \theta_0). \quad (9.16)$$

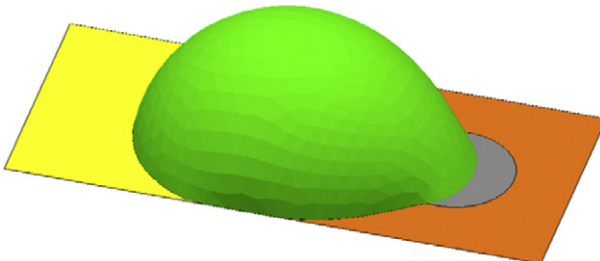
Note that if $r = R$, Eq. (9.16) collapses to $\theta_d = \theta_a$. The droplet can be extracted from the patch when

$$F_a - F_{\text{na}} > F_d, \quad (9.17)$$

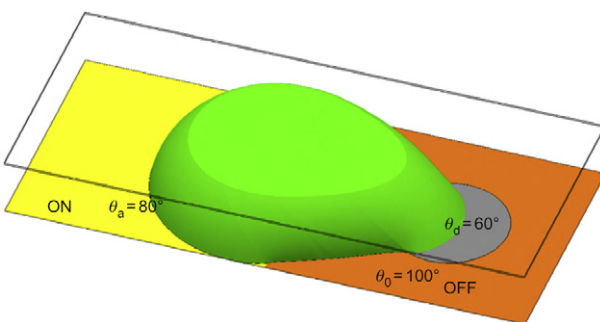
which leads to

$$\frac{r}{R} < \frac{\cos \theta_a - \cos \theta_0}{\cos \theta_d - \cos \theta_0}. \quad (9.18)$$

when r is sufficiently small, e.g., the patch is small compared to the electrode size, the droplet can leave the patch. This is in agreement with the observation made in Eq. (9.8). If the droplet is limited laterally by the electrode

**FIGURE 9.8**

Droplet blocked by a hydrophilic patch in an actuated ON/OFF EWOD system as produced by the Surface Evolver numerical software.

**FIGURE 9.9**

Equilibrium for a droplet in a closed EWOD device: the ratio $d/e = 0.5$ and the ratio $(\cos \theta_a - \cos \theta_0)/(\cos \theta_d - \cos \theta_0) = 0.51$ (Surface Evolver calculation).

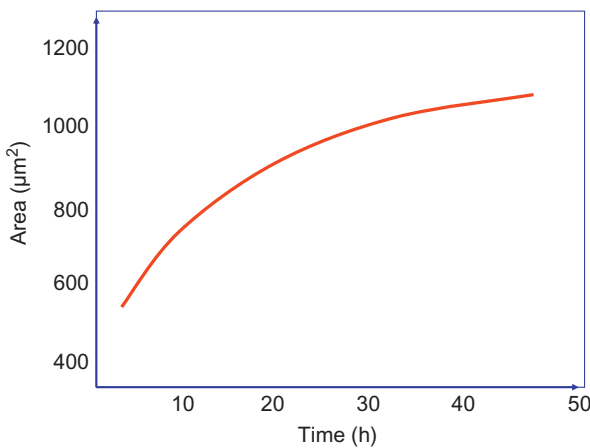
boundary—which is the general case, then $e = 2R$, and recalling that $d = 2r$ (Figures 9.6B and 9.8), Eq. (9.18) becomes

$$\frac{d}{e} < \frac{\cos \theta_a - \cos \theta_0}{\cos \theta_d - \cos \theta_0}. \quad (9.19)$$

The same relation (9.19) applies for a closed EWOD geometry, because the contact angle with the top cover is the same everywhere, and the integral of the capillary forces on the top cover is then null. Figure 9.9 shows an equilibrium condition in a closed EWOD geometry (for the same values of contact angles as for the open EWOD in Figure 9.6).

Note that relation (9.19) can be cast under the form

$$\xi > \frac{d}{e}(\cos \theta_d - \cos \theta_0), \quad (9.20)$$

**FIGURE 9.10**

Area occupied by a culture of HeLa cells measured by Bogojevik et al. [24].

where ζ is the electrowetting number defined by

$$\zeta = \frac{CV^2}{2\gamma_{LG}} = \cos \theta_a - \cos \theta_0. \quad (9.21)$$

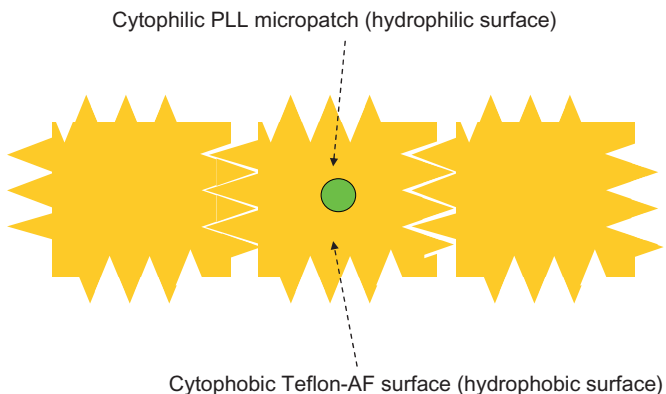
Relation (9.20) shows another way of interpreting Eq. (9.19): the electrowetting number (i.e., the voltage) has to be sufficient to de-pin the droplet from the hydrophilic patch.

In conclusion, the ratio of the diameter of the patch to the electrode width must not be too large for obtaining the droplet motion over the patch. But it is good to keep in mind that cells require a sufficient surface area to proliferate. For example, a typical spreading of HeLa cells culture is shown in Figure 9.10. In such a case, the diameter of the patch should be of the order of $40 \mu\text{m}$. Hence, the electrode dimensions cannot be too small and must respect relation (9.19).

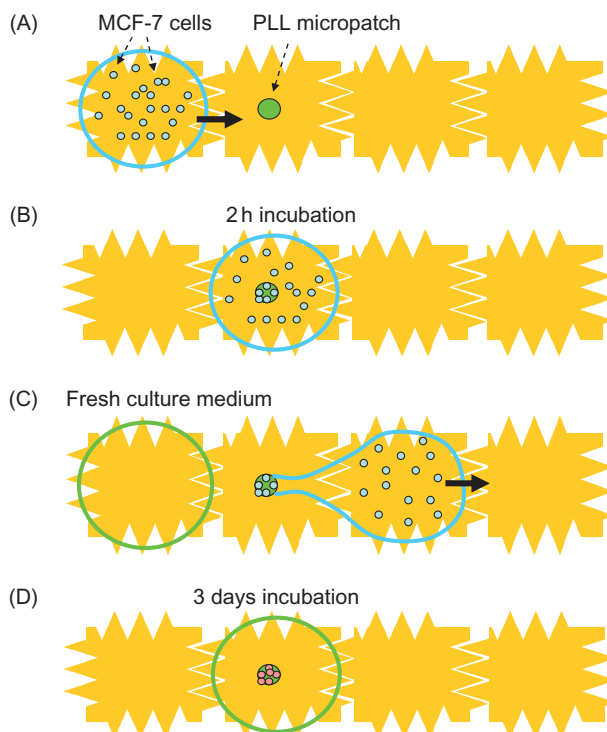
9.4.3 Cancer cell culture in an EWOD microdevice

A typical example of VM is the EWOD microsystem for the culture of cells developed by Vergauwe and colleagues [18]. They have created cytophilic poly-L-lysine (PLL) micropatches on EWOD hydrophobic Teflon-AF surfaces where cells can easily adhere (Figure 9.11). These patches are not too large compared to the electrode size, so that their hydrophilic property does not prevent EWOD operations. But they are sufficiently large for allowing cell proliferation.

On chip culture of MCF-7 cells (human breast cancer cells) the following protocol can be done (Figure 9.12): first a carrier droplet containing a certain number of MCF-7 cells is moved on the chip until it surrounds the PLL patch.

**FIGURE 9.11**

Sketch of a cytophilic PLL micropatch on an EWOD surface.

**FIGURE 9.12**

MCF-7 breast cancer cell culture in an EWOD device: (A) transport of the initial cell population; (B) cell adhesion on the PLL patch and first incubation; (C) removal of the initial drop and introduction of a cell culture medium; and (D) 3 days of incubation leading to the proliferation of the cells [18].

The MCF-7 cells adhere to the patch and incubate for 2 h (at 37°C). The droplet is moved out of the system and a fresh cell culture medium is brought in and cells incubate for 3 days at 37°C. Using fluorescence, it is checked that the cells are viable and proliferating.

9.4.4 Electrowetting device for dried blood spot analysis

Using the idea of VM, Jebral and colleagues [25] have developed an EWOD device for the analysis of blood by placing a paper disk in an open EWOD device. Remarking that dried blood spot (DBS) samples stored on filter paper were very easy to obtain, but that direct analysis of paper was difficult, they have proposed to introduce the paper patches in an EWOD device in order to perform the desired analysis (Figure 9.13).

Punched 3 mm diameter filter papers bearing dried blood are first positioned on the EWD surface. The fluidic operative mode is the following (Figure 9.14): first an extraction solvent—used to lyse the cells—is moved onto the electrode where the DBS has been placed; then after the time needed for the extraction, the liquid extract is moved onto a neighboring electrode and allowed to dry. A droplet of derivatization solvent is then moved onto the dried extract and left to evaporate. A dried derivatized extract is obtained.

In order to achieve the biological protocol, the derivatized extract has to be analyzed by a mass spectrometer. This process is done by coupling the EWOD chip to a microfluidic channel that exits through a nozzle in the mass spectrometer. The device has been successfully used to test for amino acid metabolism disorders in newborn patients—namely for the quantification of methionine, phenylalanine, and tyrosine.

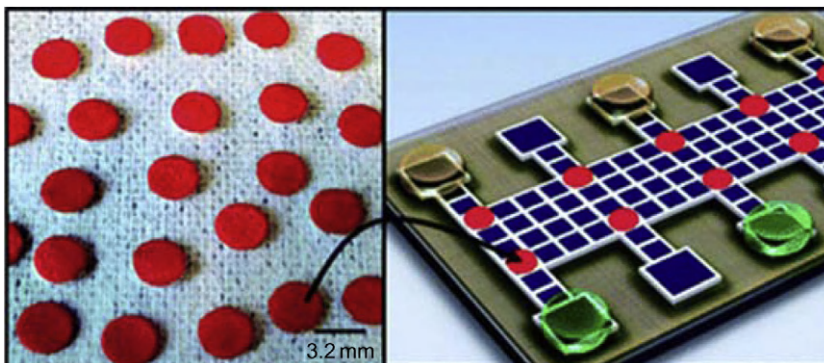
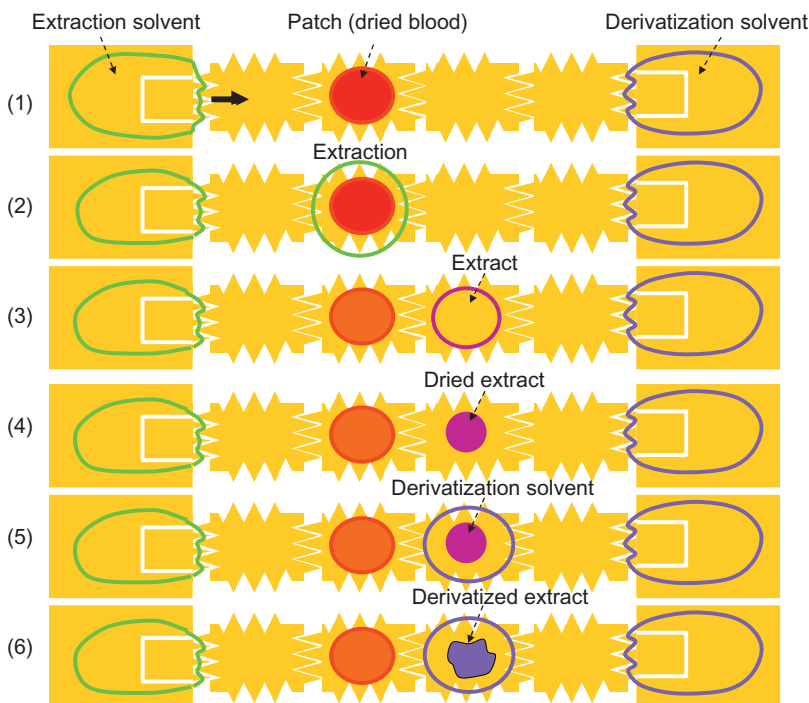


FIGURE 9.13

Principle of DMF device for DBS analysis.

Source: Reprinted with permission from Ref. [25] © RCS 2011.

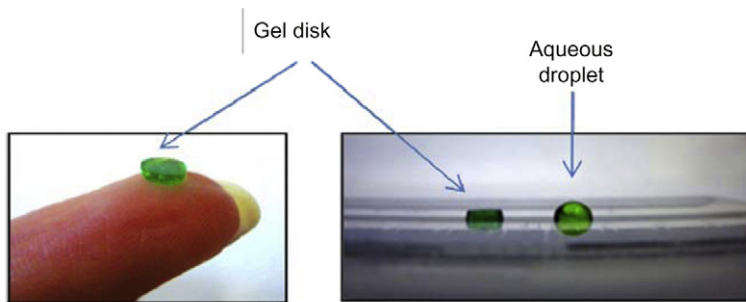
**FIGURE 9.14**

Functional diagram for dried blood analysis.

9.5 Hydrogel disks for DMF

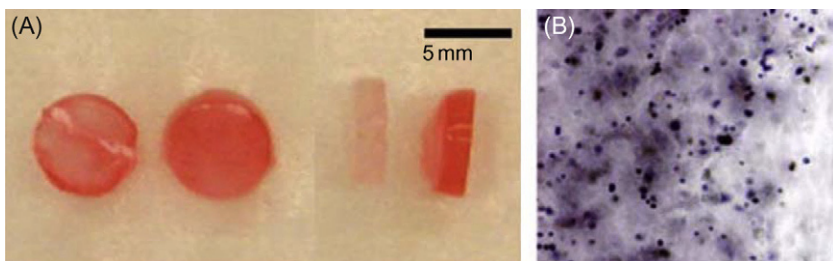
The concept of VM has been extended to pseudovirtual microwells by Aaron Wheeler's group. Progressively VM have incorporated paper patches, and finally porous disks. The use of hydrogel disks in EWD was first evoked by Fair and colleagues [29], but only recently practical developments have been achieved [16]. From a general standpoint, hydrogels are hydrophilic polymers swollen with water. They are useful for a wide range of applications in biology and biotechnology because their pores serve as stable sites for immobilizing proteins and cells. Hydrogel disks are especially interesting for 3D cell culture [30] (Figures 9.15 and 9.16). Usual sizes of hydrogel disks are in the range of 50 μm –5 mm.

Conventionally, hydrogels are placed in microflows that transport nutrients or reagents which in time diffuse inside the polymeric matrix. Nutrients promote cell culture or cellular response; reagents are often used to trigger enzymatic reactions with proteins.

**FIGURE 9.15**

View of a hydrogel disk.

Source: Reprinted with permission from Ref. [16] © AIP 2012.

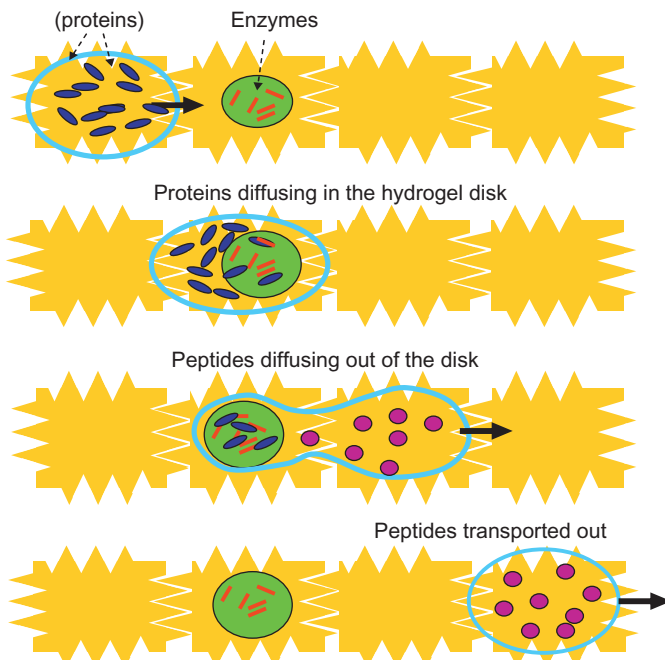
**FIGURE 9.16**

PEG-based hydrogel disks containing cells: (A) hydrogel is crosslinked to take the shape of a disk and (B) cells are suspended within the crosslinked hydrogel.

Source: Photographs by courtesy of Jenifer Elisseeff, Johns Hopkins University.

It has been recently demonstrated by Fiddes et al. [16] that hydrogel disks can be placed inside EWOD microsystems. Droplets can be transported to the hydrogel disks placed on an electrode by electrowetting actuation, where they can dispense the chemical species to the biologic objects immobilized inside the disks, and then can be removed away from the disk, again using electrowetting actuation (Figure 9.17). The advantage of using EWOD is to control precisely the amount of species delivered to the targets inside the disks.

So far, only an experimental demonstration has been presented. Let us investigate under what conditions the liquid droplet can be removed from the disk electrode to continue its motion further on the EWOD system. In this case also, the numerical program Evolver can be used because first, the capillary equivalence of electrowetting applies, and second, the viscous and inertial forces are small compared to the capillary effect.

**FIGURE 9.17**

Sketch of a proteomic reaction performed in an EWOD system using a hydrogel disk.

[Figure 9.18](#) shows the mechanics of the droplet separation from the disk.

Let us perform an analysis of the energy of the system in the state where the droplet surrounds the disk and in the state where the droplet has detached from the disk ([Figure 9.19](#)).

The surface energy in the first configuration (not actuated) is

$$E_1 = \gamma_{LG} h 2\pi R_1 + \gamma_{SL} h 2\pi R_0 + \gamma_{SL} 2\pi(R_1^2 - R_0^2) + \gamma_{SG} 2(A - \pi R_1^2), \quad (9.22)$$

where A is the surface of the solid substrate (or cover plate). The surface energy in the second state (still not actuated) is

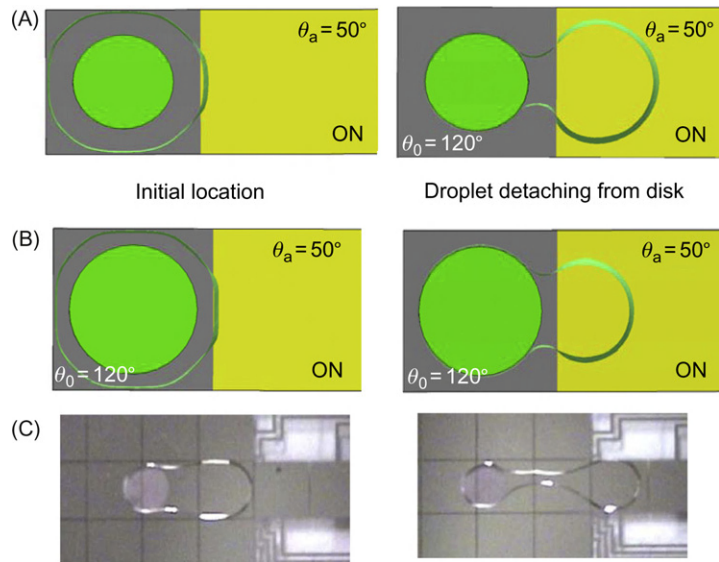
$$E_2 = \gamma_{LG} h 2\pi R_2 + \gamma_{LG} h 2\pi R_0 + \gamma_{SL} h 2\pi R_0 + \gamma_{SL} 2\pi R_2^2 + \gamma_{SG} 2(A - \pi R_2^2 - \pi R_0^2). \quad (9.23)$$

[Equation \(9.23\)](#) assumes that there is a very thin liquid layer remaining attached to the disk. Remarking that the liquid volume is constant

$$\text{Vol} = h\pi R_2^2 = h(\pi R_1^2 - \pi R_0^2), \quad (9.24)$$

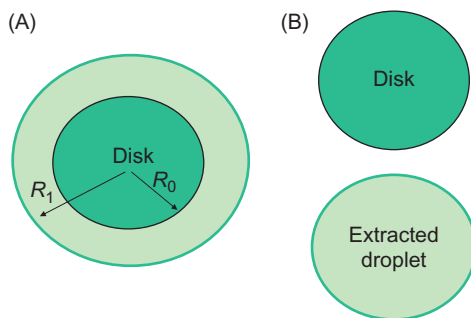
we find

$$R_2^2 = R_1^2 - R_0^2 \quad (9.25)$$

**FIGURE 9.18**

(A) Droplet surrounding a hydrogel disk and extracted from the disk area by electrowetting force; (B) same as (A) with a larger disk. Note that the cover plate has been dematerialized for visualization; and (C) experimental view by Fiddes et al. [16].

Source: Reprinted with permission from Ref. [16] © AIP 2012.

**FIGURE 9.19**

(A) Initial location of the liquid around the disk and (B) droplet detached from disk.

Using Eqs. (9.25), (9.23), and (9.22), we deduce

$$\Delta E = E_2 - E_1 = \gamma_{LG} h 2\pi (R_2 - R_1 + R_0) \quad (9.26)$$

which represents the energy that should be furnished by the electrowetting process to extract the droplet from its first energy level to its second energy level. Approximating the electrowetting energy by

$$\Delta E = \frac{CV^2}{2} e^2, \quad (9.27)$$

where e is the square electrode size, we finally obtain the electrowetting number that is necessary for removing the droplet

$$\xi = \frac{CV^2}{2\gamma_{LG}} > 2\pi \frac{h(R_2 - R_1 + R_0)}{e^2}. \quad (9.28)$$

Substituting Eq. (9.25) in Eq. (9.28) yields

$$\xi = \frac{CV^2}{2\gamma_{LG}} > 2\pi \frac{h\left(R_2 - \sqrt{R_2^2 + R_0^2} + R_0\right)}{e^2}. \quad (9.29)$$

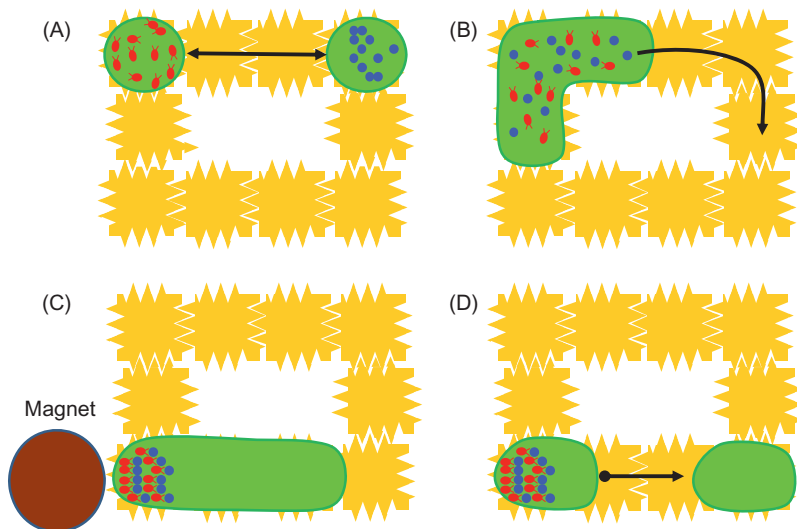
We verify that if $R_0 \rightarrow 0$, then an extremely small electrowetting actuation is enough to move the droplet (as if there were no disk). This remark is similar to that already done for virtual walls.

9.6 Concentration of immune cells in blood

Immune cells in human blood participate in the body's reaction to viral and bacterial infections. Hence, it is important to be able to determine the concentration of immune cells in blood. An interesting approach for the determination of CD8+ T-lymphocytes in human blood using DMF has been proposed by Shah et al. [31] at UCLA. In this particular case, the aim is twofold: cytotoxic (CD8+) T-lymphocytes in the human blood (from 2 to 8×10^5 cells/mL) act as key effectors of the cellular immune response against infections [32], but also pose clinical challenges, such as rejection of transplanted organs [33].

The basic idea that has guided Kim's approach is that if CD8+ lymphocytes could be isolated from other peripheral blood components and then lysed, the concentration of these cells and their associated proteins could be measured for a noninvasive diagnosis.

The device is constituted by a conventional EWOD system and a magnet. First, a diluted blood sample (to which a nonionic surfactant has been added) is merged with a droplet containing antibody-conjugated magnetic beads (MB-Abs). The two components are mixed by a rotating motion of the droplet, as shown in Figure 9.20, enhancing the binding between the magnetic beads and the targeted lymphocytes. The magnet is then introduced to concentrate the captured CD8+.

**FIGURE 9.20**

(A and B) Merging the CD + with the blood sample, the binding is enhanced by rotating motion; (C and D) concentration of the cells with the help of a magnet.

The operation is repeated—with rinsing sequences—in order to improve the purity of the extracted sample. This sample is then merged with a lysing agent and detection is performed.

This work exemplifies the use of EWOD systems to achieve sorting and separation of targets from a carrier fluid.

9.7 Conclusion

This chapter was devoted to the cellular applications of EWOD systems. EWOD microsystems have adapted to new functionalities that are required by today developments of biotechnology, i.e., the culture of cells and all the peripheral operations on these cultures. Concepts like VM and hydrogel disks have considerably increased the functionalities of DMF systems.

Acknowledgment

I would like to thank Ken Brakke for his help with the numerical software Surface Evolver (<http://www.susqu.edu/brakke/evolver/evolver.html>).

References

- [1] R.W. Smith, D.T. Clark, The Hitchhiker's Guide to inner (cellular) galaxies: cytology, cytometry, cytomics, cellomics and kinomics, *Microsc. Microanal.* 11 (2005) 252–253.
- [2] D. Di Carlo, D. Irimia, R.G. Tompkins, M. Toner, Continuous inertial focusing, ordering, and separation of particles in microchannels, *Proc. Natl. Acad. Sci. USA.* 104 (48) (2007) 18892–18897.
- [3] D. Di Carlo, Inertial microfluidics, *Lab Chip* 9 (21) (2009) 3038–3046.
- [4] S.K. Mitra, S. Chakraborty, *Microfluidics and Nanofluidics Handbook: Chemistry, Physics, and Life Science Principles*, Taylor and Francis Publishing, Boca Raton, FL, 2011.
- [5] M. Lavine, Microfluidics: streams swirled by Dean, *Science* 312 (2006) 1279–1281.
- [6] M. Yamada, H. Nakashima, M. Seki, Pinched flow fractionation: continuous size separation of particles utilizing a laminar flow profile in a pinched microchannel, *Anal. Chem.* 76 (2004) 5465–5471.
- [7] M.J. Kennedy, S.J. Stelick, S.L. Perkins, L. Cao, C.A. Blatt, Hydrodynamic focusing with a microlithographic manifold: controlling the vertical position of a focused sample, *Microfluid. Nanofluid.* 7 (4) (2009) 569–578.
- [8] J. Atencia, D.J. Beebe, Controlled microfluidic interfaces, *Nature* 437 (2005) 648–655.
- [9] J.P. Shelby, D.S.W. Lim, J.S. Kuo, D.T. Chiu, High radial acceleration in micro-vortices, *Nature* 425 (2003) 38.
- [10] L.R. Huang, E.C. Cox, R.H. Austin, J.C. Sturm, Continuous particles separation through deterministic lateral displacement, *Science* 304 (2004) 987–990.
- [11] J. El-Ali, P.K. Sorger, K.F. Jensen, Cells on chips, *Nature* 442 (2006) 403–411.
- [12] R. Gunawan, J. Silvestre, H.R. Gaskins, L.B. Schook, P.J.A. Kenis, D.E. Leckband, Cell migration and polarity on microfabricated gradients of extracellular matrix proteins, *Langmuir* 22 (2006) 4250–4258.
- [13] S. Kakaç, B. Kosoy, D. Li, A. Pramuanjaroenkij, *Microfluidics Based Microsystems*, Springer, New York, 2009.
- [14] J. Rajagopalan, M. Taher, A. Saif, MEMS sensors and microsystems for cell mechanobiology, *J. Micromech. Microeng.* 21 (2011) 054002.
- [15] A. Rival, C. Delattre, Y. Fouillet, C. Chabrol, G. Castellan, F. Bottausci, et al., EWOD Digital Microfluidic Device for Single Cells Sample Preparation and Gene Expression Analysis, from LabAutopedia Lab Automation 2010 Conference, Palm Springs, CA, January 2010.
- [16] L.K. Fiddes, V.N. Luk, S.H. Au, A.H.C. Ng, E. Kumacheva, A.R. Wheeler, Hydrogel discs for digital microfluidics, *Biomicrofluidics* 6 (2012) 014112.
- [17] I. Barbulovic-Nad, H. Yang, P.S. Park, A.R. Wheeler, Digital microfluidics for cell-based assays, *Lab Chip* 8 (2008) 519–526.
- [18] N. Vergauwe, D. Witters, F. Ceyssens, S. Vermeir, B. Verbruggen, R. Puers, J. Lammertyn, A versatile electrowetting-based digital microfluidic platform for quantitative homogeneous and heterogeneous bio-assays, *J. Micromech. Microeng.* 21 (2011) 054026.
- [19] S.V. Puttaswamy, S. Sivashankar, R.-J. Chen, C.-K. Chin, H.-Y. Chang, C.H. Liu, Enhanced cell viability and cell adhesion using low conductivity medium for

- negative dielectrophoretic cell patterning, *Biotechnol. J. Special Issue: Focus: Chromatography and cell patterning* 5 (10) (2010) 1005–1015.
- [20] D. Witters, N. Vergauwe, S. Vermeir, F. Ceyssens, S. Liekens, R. Puers, J. Lammertyn, Biofunctionalization of electrowetting-on-dielectric digital microfluidic chips for miniaturized cell-based applications, *Lab Chip* 11 (2011) 2790–2794.
 - [21] M.G. Pollack, V.K. Pamula, V. Srinivasan, A.E. Eckhardt, Applications of electrowetting-based digital microfluidics in clinical diagnostics, *Expert Rev. Mol. Diagn.* 11 (4) (2011) 393–407.
 - [22] S. Srigunapalan, I.A. Eydelnant, C.A. Simmos, A.R. Wheeler, A digital microfluidic platform for primary cell culture and analysis, *Lab Chip* 12 (2012) 369.
 - [23] I. Barbulovic-Nad, S.H. Au, A.R. Wheeler, A microfluidic platform for complete mammalian cell culture, *Lab Chip* 10 (2010) 1536–1542.
 - [24] D. Bogojevik, M.D. Chamberlain, I. Barbulovic-Nad, A.R. Wheeler, A digital microfluidic method for multiplexed cell-based apoptosis assays, *Lab Chip* 12 (2012) 627–634.
 - [25] M.J. Jebrail, H. Yang, J.M. Mudrik, N.M. Lafrenière, C. McRoberts, O.Y. Al-Dirbashi, et al., A digital microfluidic method for dried blood spot analysis, *Lab Chip* 11 (2011) 3218–3224.
 - [26] I.A. Eydelnant, U. Uddayasankar, B. Li, M.W. Liao, A.R. Wheeler, Virtual micro-wells for digital microfluidic reagent dispensing and cell culture, *Lab Chip* 12 (2012) 750–757.
 - [27] T.-H. Chen, C.-M. Su, H.-C. Chih, C.-T. Yang, Selective wettability assisted nanoliter sample generation via electrowetting-based transportation, ASME 2007 5th International Conference on Nanochannels, Microchannels, and Minichannels (ICNMM2007) June 18–20, 2007, Puebla, Mexico, pp. 147–153.
 - [28] J. Berthier, P. Dubois, P. Clementz, P. Claustre, C. Peponnet, Y. Fouillet, Actuation potentials and capillary forces in electrowetting based microsystems, *Sens. Actuators A* 134 (2007) 471–479.
 - [29] R.B. Fair, A. Khlystov, T.D. Tailor, V. Ivanov, R.D. Evans, P.B. Griffin, et al., Chemical and biological applications of digital-microfluidic devices, *IEEE Des. Test Comput.* 24 (2007) 10–24.
 - [30] S. Lee, D.T. Eddington, Y. Kim, W. Kim, D.J. Beebe, Control mechanism of an organic self-regulating microfluidic system, *J. Microelectromech. Syst.* 12 (6) (2003) 848–856.
 - [31] G.J. Shah, J.L. Veale, Y. Korin, E.F. Reed, H.A. Gritsch, C.J. Kim, Specific binding and magnetic concentration of CD8 + T-lymphocytes on electrowetting-on-dielectric platform, *Biomicrofluidics* 4 (2010) 044106.
 - [32] M. Toner, D. Irimia, Blood-on-a-chip, *Annu. Rev. Biomed. Eng.* 7 (2005) 77–103.
 - [33] M. Barry, R.C. Bleackley, Cytotoxic T lymphocytes: all roads lead to death, *Nat. Rev. Immunol.* 2 (2002) 401.

Chemical Applications^{*}

10

CHAPTER OUTLINE

10.1 Introduction	388
10.1.1 Continuous flow systems	388
10.1.2 Digital microfluidic.....	390
10.2 Nonaqueous solvents on EWOD chips	393
10.2.1 Volatile organic solvents.....	393
10.2.1.1 <i>Displacement in closed systems</i>	393
10.2.1.2 <i>Dispensing of volatile organic solvent</i>	396
10.2.1.3 <i>Mixing in closed systems</i>	396
10.2.1.4 <i>The problem of evaporation</i>	397
10.2.2 Displacement of ionic liquids	398
10.2.2.1 <i>Definition of ionic liquids</i>	398
10.2.2.2 <i>Static behavior</i>	399
10.2.2.3 <i>Motion of ionic liquids</i>	401
10.2.2.4 <i>Working potentials</i>	402
10.2.2.5 <i>Ionic liquid dispensing</i>	403
10.2.2.6 <i>Cutting ionic liquid droplets</i>	404
10.2.2.7 <i>Mixing of ionic liquids on an opened system</i>	405
10.3 Chemical synthesis in droplets in EWOD-based systems	407
10.3.1 Synthesis in aqueous media	407
10.3.2 Synthesis in VOSs	409
10.3.3 Synthesis in ionic liquids	410
10.4 Conclusions and perspectives.....	415
References	416

*This chapter was written with the collaboration of Gilles Marchand (CEA/Leti-Minatec, Department of Technology for Biology and Health, 17 rue des Martyrs 38054 Grenoble, France), Philippe Dubois (CEA/Leti-Minatec, Department of Technology for Biology and Health, 17 rue des Martyrs 38054 Grenoble, France; University of Rennes 1, UMR CNRS 6510, 263 avenue du Général Leclerc, 35042 Rennes France), and Michel Vaultier (University of Rennes 1, UMR CNRS 6510, 263 avenue du Général Leclerc, 35042 Rennes France).

10.1 Introduction

In the last decade, LOC dedicated to chemical applications have seen a growing interest [1–5]. Many reasons are similar to those already mentioned in the preceding chapters, namely, reduction of the volume of reagents, optimization of the reactions leading to faster production of desired products with a greater yield and purity, portability of the systems, and reduction of waste production; in the case of chemical applications, another advantage of miniaturization is related to the increase in security during the dangerous synthesis by an efficient dissipation of heat generated by exothermic reaction owing to the high surface-area-to-volume ratios. Furthermore, microsystems offer a unique approach to the spatial and temporal control of chemical reactions [6].

10.1.1 Continuous flow systems

Most microsystems described in the literature are continuous flow systems. These consist of a network of micrometer-sized channels embedded into a solid substrate such as glass [6,7], silicon [8], polymers [9], steel or stainless steel [10], and ceramics [11]. In most of these microsystems, liquids and suspended solids are transported in channels from one location to another using generally hydrodynamic (pressure) pumping (Figure 10.1A). However, in a pressure-driven flow, the velocity profile in a cross-section is quadratic (approximately a paraboloid if the channel is rectangular), and the mean flow rate depends on the channel cross-sectional area. This shape generates unwanted diffusion; Watts and Haswell [12] reported a new kind of microreactor in borosilicate glass, as shown in Figure 10.1B, based on electro-osmotic flow (EOF) [13]. EOF offers significantly less unwanted dispersive effects than pressure-driven flow and, with appropriate application of electric potentials, its valve-less control of fluid flow is a convenient high-performance sample separation technique. In an ideal EOF, the velocity profile will be flat—except very close to the walls—and the mean velocity is independent of the cross-sectional area due to the very small thickness of the electric double layer. However, EOF in microfluidic devices can be difficult to control due to many complex factors such as solid surface material, buffer characteristics, and hydrodynamic effects.

A range of chemical reactions such as Suzuki coupling [14], Wittig reaction [15], Michael addition [16], nitration of benzene, or tripeptide synthesis (Figure 10.2) have been carried out to demonstrate the advantages that microreactors offer in terms of stereo-selective product control [15,17], multistep synthesis [18], reaction kinetics, or conversion rate [6]. For example, the time necessary for Suzuki coupling [6] has been reduced from 8 h to 6 s with the same conversion rate.

In spite of many advantages, microreactors suffer from several drawbacks such as the presence of large dead volume, the frequent obstruction of the channels, the difficulty of maintaining a constant hydrodynamic pressure, especially for viscous liquids, and the control of surface charges when electro-osmotic

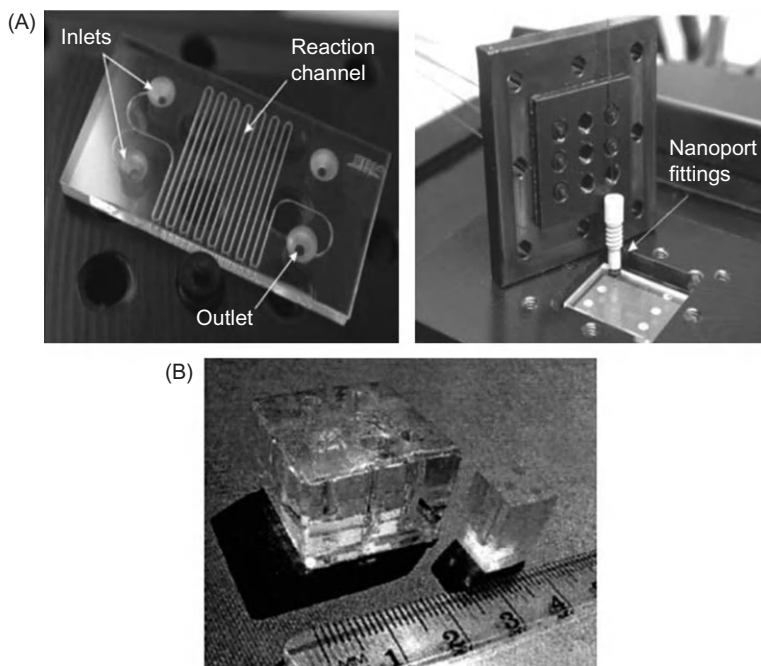


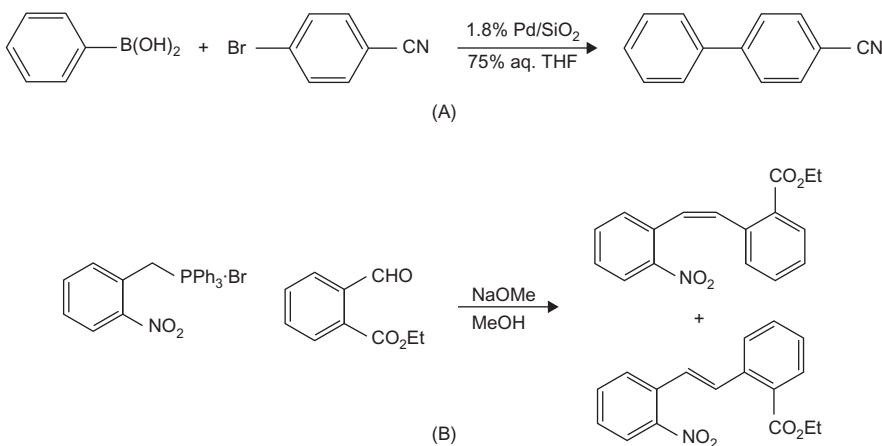
FIGURE 10.1

(A) View of the device etched in borosilicate glass. The on-chip reactions were carried out in a 197 mm long, 200 μm wide, 100 μm deep microchannel under pressure-driven flow [7]. (B) The device consists of a borosilicate glass base plate containing an etched channel network and a top block with 3 mm drilled holes to introduce the reagent into the reservoirs. Thermal bonding of the two layers results in a sealed microreactor with typical dimensions in the range of 2.5 cm \times 2.5 cm \times 2.0 cm. Transport under EOF.

Source: (A) From Ref. [7]. (B) From Ref. [6]. Reproduced by permission of the Royal Society of Chemistry. © 2002, Elsevier; reprinted with permission.

pumping is used. For this last actuation mode, the requirement of electric charges on the solid surface limits the choice of materials.

In an attempt to avoid these problems, a continuous flow microfluidic system in which droplets are separated by immiscible liquid spacers (Figure 10.3) has been proposed [19] (more details on droplet microfluidics are given in Chapter 9). The system consists of a series of nanoliter plugs of many different aqueous reagents, separated and surrounded by a fluorinated carrier fluid and spaced by gas bubbles inside a hydrophobic glass or plastic capillary. Reactant filled droplets may be issued from the emulsification process of a multiple fluid co-flow immersed in an immiscible carrier fluid [20]. This three-phase liquid/liquid/gas system was preferred to a two-phase system, since it enhances reliability in the manipulation and transport of these plugs. Indeed, in a two-phase system, plugs may coalesce during

**FIGURE 10.2**

Examples of reaction performed in a microreactor. Schematic representation of the Suzuki coupling (A) and Wittig reaction (B) described by Watts and Haswell [12].

subsequent use if the viscosity of the carrier fluid is very different from that of the plugs or if the viscosities within plugs vary significantly. Air bubbles can be used for actuation of steady microfluidic flow [21].

However, although the droplet format resolves many problems existing with liquids in flow, complex protocols are relatively difficult to perform with this system, and for the moment, only a few validations [22,23] have been reported for aqueous solvents which are often not suitable for chemical synthesis and one for octadecene [24].

10.1.2 Digital microfluidic

DMF is an alternative approach to droplet microfluidic systems (see Chapter 1). In such microsystems, droplets containing reagents, samples, etc. are manipulated on 2D planar chips—contrary to microfluidic channels. Such devices have several advantages, such as no dispersion due to diffusion—the droplet interface limits the extension of diffusion—no or negligible cross-mixing, and simplified fluidic manipulation. This very interesting concept allows easy programming of displacements and merging of droplets containing different reagents ($A_1 \dots A_x, B_1 \dots B_x$) on a chip. Thus, the concept of DMF opens the way to multistep reactions and parallel or combinatorial synthesis (Figure 10.4).

Several fluidic actuators have been reported such as chemical [25–27] or thermal gradient, acoustic waves [28–30], and electrical methods. DEP [31] and EWOD [32] are the most common electrical methods (Figure 10.5). These electrical methods are based upon the micromanipulation of droplets by an

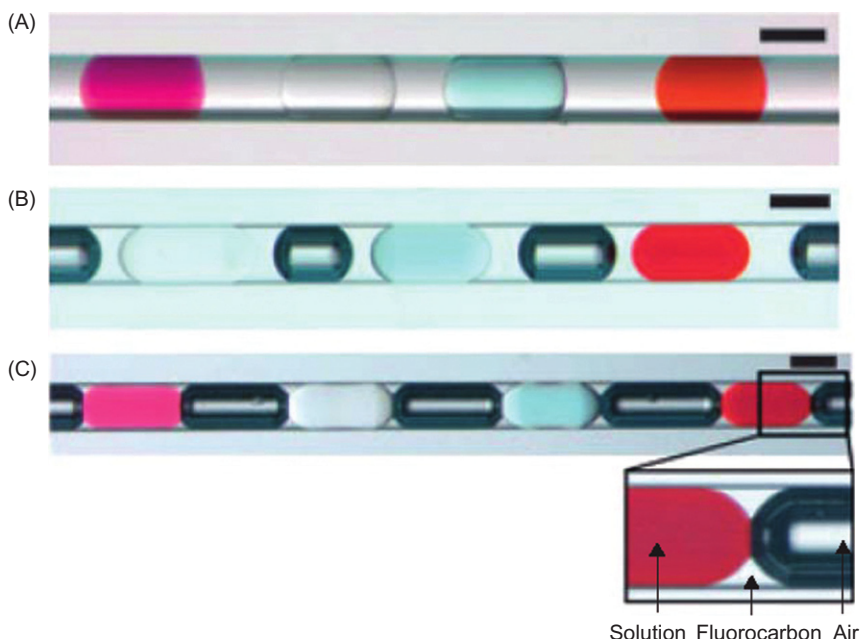
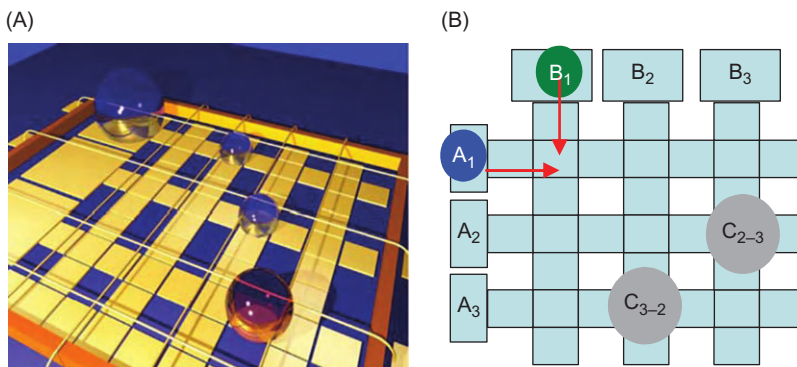


FIGURE 10.3

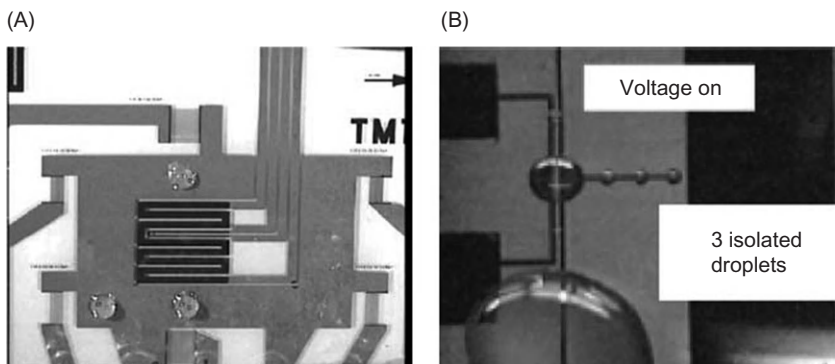
(A) Array of plugs of four different reagents in a capillary. The flow contains KMnO_4 (purple), NaCl (colorless), CuSO_4 (blue), and $\text{Fe}(\text{SCN})_3$ (red) plugs, respectively. The carrier fluid is fluorocarbon. (B and C) An array of plugs of different reagents transported by a fluorocarbon flow and separated by air bubbles (dark) in a capillary. In (B) the aqueous plugs are separated from the air bubbles by a layer of fluorocarbon, thereby preventing cross contamination between plugs. (For interpretation of the references to color in this figure legend, the reader is referred to the web version of this book.)

Source: From Ref. [19] © 2005 Wiley, reprinted with permission.

individually addressable electrode array via a programmed external electric field. They offer the possibility of performing elementary fluidic functions without any moving parts or pressure actuation. Hence, these electrical methods open the way to digital LOC requiring elementary operations like dispensing of droplets containing reagents from reservoirs, displacement of these droplets in the LOC, mixing, cutting, and merging of the droplets leading to a biological, biochemical, or chemical reaction. Some biological [34] and chemical [35] applications using DEP were reported. However, DEP requires high frequencies to displace droplets (AC voltage >50 kHz) raising the problem of electrical connection and heating of the solution. Conversely, EWOD requires only low frequencies (1–5 kHz), and, even better, can be used with DC voltage. Moreover, EWOD heating of

**FIGURE 10.4**

Principle of a DMF system: (A) droplets on a planar chip and (B) design of a multiplexed chip allowing the performing of combinatorial synthesis.

**FIGURE 10.5**

(A) Photograph of aqueous droplets on a planar LOC displaced by acoustic waves. (B) View of water droplet formation with DEP.

Source: From Ref. [33] © 2003, Elsevier; reprinted with permission. (B) Reused with permission from Ref. [31] © 2001, American Institute of Physics.

droplets is negligible even with high ionic strength solutions [36]. Therefore, EWOD appears to be applicable for a wider matrix of samples than DEP.

This chapter deals with droplets displaced by EWOD actuation and used as microreactors for chemical applications. First, the validation of elementary fluidic functions with different solvents is reported. Then examples of chemical synthesis performed in water, organic solvents, and ionic liquids are described. Finally, the possible perspectives of droplet microreactors are investigated.

10.2 Nonaqueous solvents on EWOD chips

Most applications of EWOD-based microsystems are found in biotechnology, with reactions such as PCR [37,38] or DNA reparation [39], performed in aqueous solvents (see preceding chapter). Consequently, the displacement, merging, mixing, and dispensing of aqueous solutions have been widely studied. However, even if some specific organic synthesis can be performed in water, chemical synthesis usually requires nonaqueous solvents. The use of nonaqueous solvents—more adapted to organic synthesis—in EWOD-based microsystems [40–42] has been developed recently.

10.2.1 Volatile organic solvents

10.2.1.1 Displacement in closed systems

We have seen in Chapters 4 and 5 that closed EWOD systems were more favorable for moving droplets than open EWOD systems, and that the motion of aqueous liquids was easier in oil. However, not all liquids are immiscible with oil. The possibility of using DMF to move and split droplets of pure organic solvents and solutions *under air* in a closed microsystem has been reported by Chatterjee et al. [40]. The EWOD microsystems used for these experiments are constituted of a microfabricated substrate including an array of conductive gold electrodes, a dielectric layer (SiO_2 or parylene-C), hydrophobic Teflon-AF coating, and a top plate with a single ITO electrode laminated on a glass substrate and coated with a Teflon-AF layer. The gap between the electrode array and the top plate is in the range 100–300 μm . Solvent droplets (0.1–0.6 μL for moderate to high boiling point liquids and up to 2 μL for low boiling point liquids) are sandwiched between the two plates (Figure 10.6).

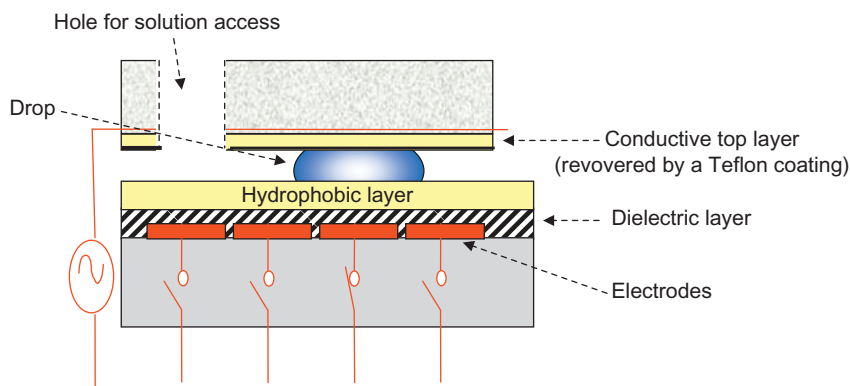


FIGURE 10.6

Scheme of a closed digital microsystem.

Operations on droplets are performed by applying $90V_{\text{rms}}$ AC potentials at 10 Hz to 8 kHz between the electrode in the top plate and the appropriate electrodes in the bottom plate. It was demonstrated that a wide range of organic solvents can be manipulated *under air* in such a system. Table 10.1 gives the voltage-induced contact angle changes and the movabilities of the organic solvents and solutions in comparison with water.

Many solvents can be actuated, and motion is not always correlated with either a high liquid surface tension or an electrically induced change in the liquid–solid contact angle. For example, ethanol and chloroform can be actuated and moved. Ethanol presents a low surface tension (22×10^{-3} N/m) and a contact angle change

Table 10.1 Movability of Organic Solvents and Solutions in EWOD Systems

Liquid	ϵ_r	σ (S/m)	γ (mN/m)	$\Delta\Theta$ (deg)	Movable
Fornamide	111	3.5×10^{-3}	57	16.1	Y
Water	80	8.7×10^{-4}	72	30.0	Y
Formic acid	51.1	7.0×10^{-3}	37	26.3	Y
DMSO	47.2	3.0×10^{-5}	43	15.3	Y
DMF	38.3	3.2×10^{-5}	37	6.9	Y
Acetonitrile	36.6	1.9×10^{-5}	29	9.8	Y
Methanol	33.0	1.7×10^{-4}	22	9.8	Y
Ethanol	25.3	7.4×10^{-5}	22	10.5	Y
Acetone	21.0	5.0×10^{-7}	23	6.4	Y
Piperidine	4.3	1.0×10^{-5}	29	8.9	Y
1-Pentanol	15.1	8.0×10^{-7}	25	12.8	Y ($d < 100 \mu\text{m}$)
1-Hexanol	13.0	1.6×10^{-5}	26	14.6	Y ($d < 100 \mu\text{m}$)
Dichloromethane	8.9	1.0×10^{-7}	27	3.7	Y ($d < 100 \mu\text{m}$)
Dibromomethane	7.8	2.6×10^{-6}	39	7.3	Y ($d < 100 \mu\text{m}$)
THF	7.5	5.0×10^{-8}	26	4.9	Y ($d < 100 \mu\text{m}$)
Chloroform	4.8	7.0×10^{-8}	27	0.5	Y ($d < 100 \mu\text{m}$)
65% toluene, 35% 1-hexanol	3.7	3.0×10^{-8}	28	6.1	Y ($d < 100 \mu\text{m}$)
4.7 mM TBATFB in toluene	2.3	1.8×10^{-7}	28	5.6	Y ($d < 100 \mu\text{m}$)
Toluene	2.4	8×10^{-14}	28	0.2	N
Carbon tetrachloride	2.2	4×10^{-16}	26	1.0	N
Cyclohexane	2.0	7×10^{-16}	25	0.2	N

Source: From Ref. [40].

of 10.5° , while chloroform has a surface tension of 27×10^{-3} N/m and nearly no voltage-induced contact angle changes. Remember that even if there is no change of apparent contact, an electrowetting force can exist (Chapter 4). Generally, polarizable liquids with dielectric constants greater than 3 and/or conductivities greater than 10^{-9} S/m are movable. The mixture of unmovable liquids and movable liquids can be moved as long as the mixture has a dipole moment, a dielectric constant, and/or conductivity above the threshold. Furthermore, liquids having conductivities ranging from 10^{-8} to 1 S/m can be actuated in the same device. Hence, most of hydrocarbon and apolar solvents of which the conductivities were near 10^{-14} – 10^{-16} S/m cannot be actuated or displaced on EWOD devices. This impossibility will limit the use of some essential solvents, and then, it will reduce the scope of the possible chemical reactions in droplets.

Additionally, it is observed that solvents become more movable if the AC voltage frequency is decreased (the limit being a DC actuation). Because the properties of Table 10.1 do not depend on the frequency, it was suggested that the frequency-dependent permittivity ε^* be used to predict if a droplet can be moved:

$$\varepsilon^* = \varepsilon_0 \left(\varepsilon_r - j \frac{\sigma}{\omega \varepsilon_0} \right), \quad (10.1)$$

where ε_0 is the permittivity of vacuum, ε_r the dielectric constant (relative permittivity), σ the conductivity, and ω the angular frequency. Figure 10.7 shows this correlation. For instance, on the microsystem used in Ref. [40], authors noted that solutions with $|\varepsilon^*|$ greater than 2×10^{-9} F/m can always be moved, whereas solutions with $|\varepsilon^*|$ lower than 8×10^{-11} F/m were never movable. Solutions with

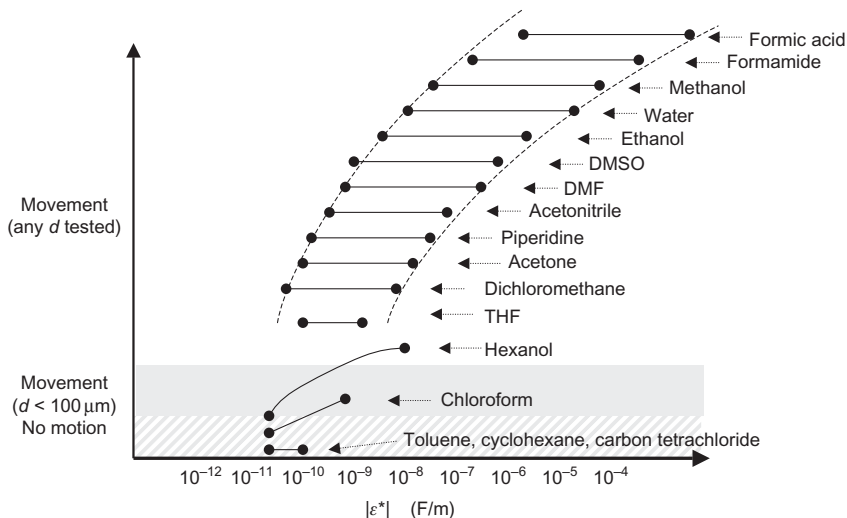


FIGURE 10.7

Maneuverability of different chemical species on covered EWOD chip. The left and right points correspond respectively to an actuation frequency of 8 and 0.01 kHz.

an intermediate value of $|\varepsilon^*|$ require a smaller vertical gap d between the array of electrodes and the top plate to be displaced by electrowetting.

10.2.1.2 Dispensing of volatile organic solvent

The potential to move a droplet on an EWOD-based chip is a necessary criterion, but it is not sufficient in itself to ensure a satisfactory functioning of the chip. An important point in chemistry, essentially in combinatorial chemistry or in parallel synthesis, is the possibility to split the solvent droplets containing different reagents or to generate droplets from a reservoir. The mechanisms of droplet dispensing and splitting have been investigated in Chapter 5 [43]. Droplet volume is approximately defined by the dispensing electrode surface multiplied by the gap value between the microstructured substrate and the cover plate (with a bias due to the shape of the free interfaces).

Garrell and coworkers [40] have reported EWOD dispensing of ethanol (Figure 10.8), but no information was given for the other organic solvents.

10.2.1.3 Mixing in closed systems

Due to the very small dimension of a droplet, internal recirculating flow inside a droplet is laminar. Mixing is then a diffusional phenomenon, enhanced by the process of stretching and folding (see Chapter 3). Stretching and folding is much easier in low viscosity fluids, so mixing in droplets is then closely associated with the viscosity of the liquid. As given in Table 10.2, viscosities of volatile organic solvents (VOSs) are comparable to those of aqueous solutions.

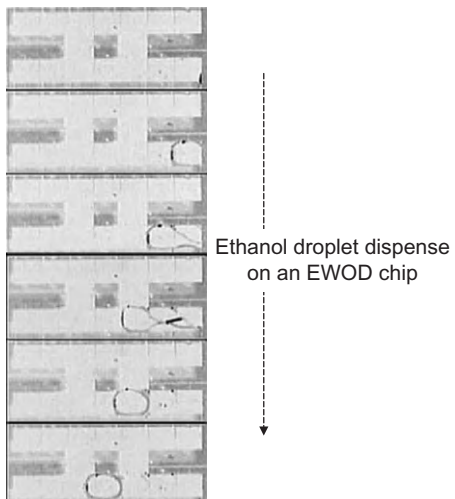


FIGURE 10.8

Dispense of ethanol droplet on a covered EWOD device.

Source: From Ref. [40], reproduced by permission of the Royal Society of Chemistry.

Therefore, the mixing in VOS droplets is similar to that of aqueous solutions. EWOD-actuated mixing in aqueous droplets has been detailed in Chapter 5. Let us recall that back-and-forth linear motions are not the most effective way to enhance mixing in droplets [45], and that loop motions are more effective because they create more successive stretching and folding of the fluid filaments [46].

10.2.1.4 The problem of evaporation

VOS displacement, dispensing, and mixing are currently investigated in order to assess their adaptability to EWOD-based microsystems. However, tiny droplets of VOSs evaporate very rapidly, even if some of these solvents have high boiling points. Evaporation constitutes a serious drawback for most chemical synthesis. Indeed, many organic reactions necessitate heating and/or pressurization during several hours of incubation. A solution consists in manipulating the VOS droplets in covered microsystems and under oil [47] or orthogonal solvent. However, this way of proceeding introduces other problems such as complexity of the fluidic connections—which are similar to that of microchannel systems, cross contaminations, and eventual miscibility between oil or orthogonal solvent and droplet solvent, and expulsion of smaller droplets due to the instability of the liquid contour [48]. Furthermore, in the case of covered microsystems in air, the evaporation of low boiling solvents (e.g., chloroform, dichloromethane, and acetone) cannot be avoided. When the size of the droplet becomes smaller than an electrode, maneuverability is lost. This difficulty explains why chemical synthesis examples in the literature in VOSs are scarce. Non-VOSs such as ionic

Table 10.2 Viscosities of Common VOSs and Aqueous Solutions [44]

Solvents	Temperature (°C)	$10^3 \times \eta$ Viscosity (Pa s)
Acetone	0	0.399
	15	0.316
	30	0.295
Acetonitrile	0	0.442
	15	0.375
	25	0.345
Ethanol	0	1.773
	10	1.466
	30	1.003
Ethylacetate	0	0.582
	10	0.512
	30	0.400
Water	0	1.787
	10	1.307
	30	0.7975
NaCl solution (1% wt)	20	1.004

liquids are now preferred for chemical synthesis on EWOD-based microsystems. In the following section, we present the characteristics of such liquids and their properties on EWOD-based microdevices.

10.2.2 Displacement of ionic liquids

10.2.2.1 Definition of ionic liquids

The term “ionic liquid” is usually used to refer to an organic salt with a melting point less than 100°C. Often, this melting point is even lower than in room temperature; therefore, ionic liquids are free flowing at room temperature, hence the generic term, room temperature ionic liquids (RTILs) [49,50]. An ionic liquid usually consists of an organic cation (e.g., ammonium, imidazolium, phosphonium, pyrrolidinium, and guanidinium) and an inorganic anion (e.g., tetrafluoroborate, hexafluorophosphate, bis(trifluoromethylsulfonyl)imide, and nitrate). Figure 10.9 represents typical ionic liquids like [tmbo] [NTf₂] and [bmim] [NTf₂]. Some ionic liquids are in a dynamic equilibrium where at any time more than 99.99% of the liquid is constituted of ionic rather than molecular species.

The main characteristics of ionic liquids are:

- negligible vapor pressure which makes them very easy to contain, manipulate, transfer, and allows their use under high vacuum or heating conditions; thus they are considered “environment-friendly” alternatives to VOSs;
- intrinsic conductivity (Coulombic fluids);

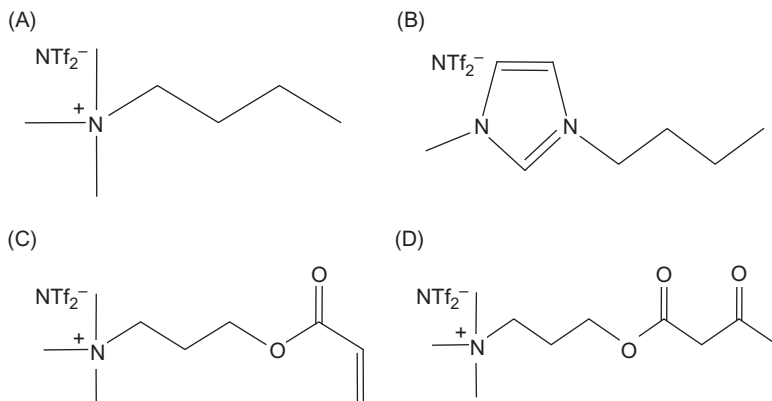


FIGURE 10.9

Examples of ionic liquids: RTILs (A and B) and TSILs (C and D). (A) *N*-trimethyl-*N*-butylammonium bis(trifluoromethylsulfonyl)imide [tmbo][NTf₂]; (B) 1-butyl-1-methyimidazolium bis(trifluoromethylsulfonyl)imide [bmim][NTf₂]; (C) (3-acryloyloxypropyl)-trimethylammonium bis(trifluoromethylsulfonyl)imide; and (D) (3-acetoacetoxypropyl)-trimethylammonium bis(trifluoromethylsulfonyl)imide.

- nonflammability associated with the low vapor tension;
- thermal stability (some of them can be heated up to 400°C without degradation which is much greater than most classical organic solvents);
- wide liquid range (by simply adjusting the substitution pattern around a central core structure for the cation or varying the anion);
- solvating properties for a wide range of organic [51], inorganic, and organometallic compounds [49].

The drawback to the use of ionic liquids is their high viscosities (from 30 to 400 cP compared to 0.89 cP for water at 25°C) [52], which limits their continuous microfluidic use.

Because of their properties, ionic liquids attract great attention in many fields, including organic chemistry, electrochemistry, catalysis, physical chemistry, and engineering. Moreover, a subclass of ionic liquids called task-specific ionic liquids (TSILs) has widened the utilization scope of ionic liquids [53–55]. Their functional groups covalently linked to the cation, the anion, or both, confer additional properties to these salts, thereby expanding their potential applications far beyond those of conventional ionic liquids. Moreover, TSILs and RTILs can be combined in solutions. Hence, supported synthesis in a homogeneous solution can be achieved which represents a major advantage [56,57]. Indeed, the reaction can thus occur on a supported phase (easy purification) in solution (no limitation of the kinetics and yields), and the final product can be easily purified since starting reagents and by-products can be eliminated by a simple washing with diethyl ether.

10.2.2.2 Static behavior

Several authors [40–42] have dealt with the static behavior of ionic liquids under EWOD, more specifically to their ability to spread on a surface under electric actuation [58,59]. The authors found that the electrowetting curves are very similar to the electrowetting curves recorded for aqueous solutions (water or buffer) on a hydrophobic surface. They observed that the Lippmann–Young’s relation is valid at low voltage (linear relation between the cosine of the contact angle and the square of the voltage, with a slope equal to $C/2\gamma$), and, at high voltage, the saturation threshold was observed [60] whatever be the sign of the potential [24]. According to the developments detailed in Chapter 4, we have represented in Figure 10.10 the Lippmann–Young’s relation for ionic liquids under the form

$$\gamma(\cos \theta - \cos \theta_0) = \frac{C}{2} V^2. \quad (10.2)$$

We observe that the saturation phenomenon for voltages is larger than approximately $60V_{rms}$. In Chapter 4, we have shown that the Langevin’s function [61] given by Eqs. (10.3) and (10.4) could be used to fit the electrowetting curves of water and biological buffers with surfactants. We observe that this same function

also fits the ionic liquid curves; our conclusion is that ionic liquids and aqueous solutions are ruled by the same constitutive law:

$$\frac{\cos \theta - \cos \theta_0}{\cos \theta_S - \cos \theta_0} = L\left(\frac{CV^2}{2\gamma(\cos \theta_S - \cos \theta_0)}\right), \quad (10.3)$$

where L is the Langevin's function defined by

$$L(X) = \coth(3X) - 1/3X \quad (10.4)$$

and

$$X = CV^2/2\gamma(\cos \theta_S - \cos \theta_0).$$

However, despite the same constitutive law, the efficiency of electrowetting for ionic liquids is lower than aqueous salt solutions. In Figure 10.10, we observe that the electrowetting force $\gamma(\cos \theta - \cos \theta_0)$ is lower for ionic liquids. On the other hand, contrary to Millifiorini [41] who concludes that the nature of the anion is not of such a crucial importance with respect to electrowetting, it has been shown that both anion and cation have an influence on electrowetting curves. Indeed, the same cation bmim^+ with three different anions (PF_6^- , BF_4^- , NTf_2^-) leads to three different behaviors in terms of saturation level. Thus, electrowetting forces of 40, 36, and 18 mN were observed for $[\text{bmim}][\text{PF}_6]$, $[\text{bmim}][\text{BF}_4]$, and $[\text{bmim}][\text{NTf}_2]$, respectively. On the other hand, for the same anion NTf_2^- with four different cations, only two distinct behaviors were observed. This could be explained by, first, the relatively similar structures of the cations bmim^+ and tmbo^+ (Figure 10.9A and B) and, second, the strong similarity of structure between the cations $\text{C}_{10}\text{H}_{20}\text{NO}_3^+$ and $\text{C}_{9}\text{H}_{17}\text{NO}_2^+$ (Figure 10.9C and D).

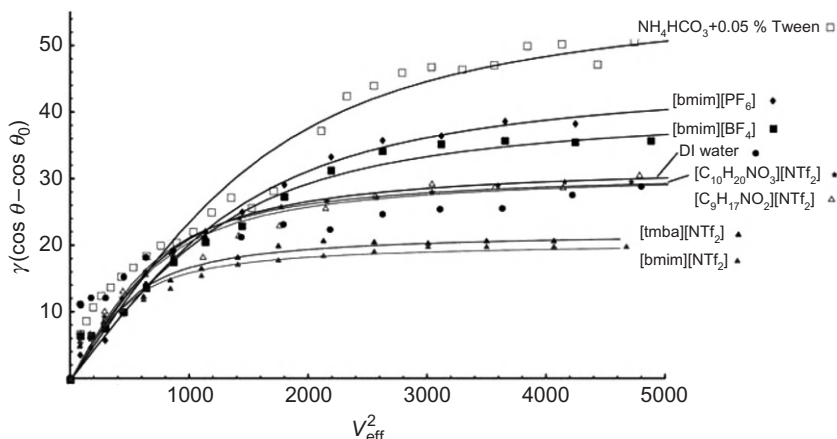


FIGURE 10.10

Representation of the relation $\gamma(\cos \theta - \cos \theta_0) = C/2V^2$ and Langevin's function for various ionic liquids, DIW, and NH_4HCO_3 25 mM + 0.05% Tween 20 buffer.

Source: From Ref. [61] © 2006, NSTI, reprinted with permission.

10.2.2.3 Motion of ionic liquids

As ionic liquids respond to electrowetting actuation, their displacement on a matrix of electrodes has been tested. Garrell and coworkers [40] demonstrated that [bmim][BF₄] and [bmim][PF₆] can be moved in a covered system under an oil layer. Dubois et al. [42,62] explored the possibility of moving ionic liquids on an open system under air. A gold wire (25 µm diameter) was used as a catena (Figure 10.11). This design presents the advantage of simplicity as it allows direct access to droplets (Chapter 4).

The motion of DIW droplets was observed on such systems; a maximum motion speed of 125 mm/s was obtained [42]. Typical velocities of ionic liquids on EWOD-based microsystems are comprised between 1 and 10 mm/s. However, the comparison of the nature of motion of DIW droplet with a quick camera and ionic liquids does not show a significant difference. It is reasonable to attribute this difference between the maximum motion speed of DIW and ionic liquids to the difference in viscosity between the two species. Indeed, as previously described, ionic liquids present viscosities 30–400 times more important than water. Nonetheless they are movable on EWOD-based microsystems. Two nondimensional numbers illustrate the importance of viscous forces in the dynamic behavior of ionic liquids in EWOD systems. The Ohnesorge (*On*) number illustrates the ratio between the viscous forces and surface tension, and the Reynolds (*Re*) number represents the ratio between the inertia forces and the viscous forces. They are given by

$$On = \frac{\eta}{\sqrt{\rho D \gamma}} \quad (10.5)$$

and

$$Re = \frac{uD}{v}, \quad (10.6)$$

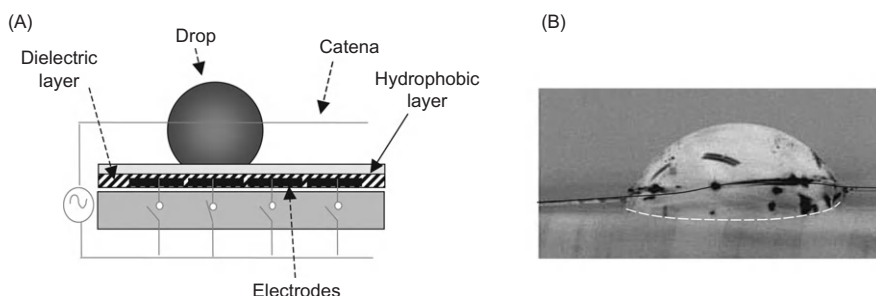


FIGURE 10.11

(A) Sketch of an open digital microsystem with catena. (B) Photograph of a drop of ionic liquid pierced by a gold catena.

Source: Photograph Ph. Dubois, CEA/LETI.

where ρ is the density of the liquids, u the maximum motion speed of the droplet, D the diameter of the droplet, γ the liquid/air surface tension of the liquid, ν the cinematic viscosity of the liquid, and η the dynamic viscosity of the liquid.

Both numbers show large differences between DIW and ionic liquid, as is given in [Table 10.3](#). Ionic liquids have a large Ohnesorge and a small Reynolds number, whereas it is the opposite for water. Thus we can establish the following rules:

- For ionic liquids: *viscous forces > surface tension forces > inertia*.
- For water: *surface tension forces > inertia > viscous forces*.

The velocity of the digital displacement of droplets on EWOD devices is related to the electrowetting force (driving force) and the viscosity of the liquid (resistive force) [\[63\]](#). A high electrowetting force and a low viscosity correspond to the larger velocities. To this extent, water and ionic liquids are at the two extremes of the scale. Note that the electrowetting force is governed by the saturation limit, and for both types of liquids, the velocity of motion saturates when the electric saturation is reached.

10.2.2.4 Working potentials

It is observed that a droplet of conductive liquid does not move from one electrode to the next as soon as an electric actuation is applied. A minimum voltage threshold is required in order to obtain the motion of the drop. This minimum electric potential—noted V_{\min} —depends on the nature of the liquid/fluid/solid triplet. On the other hand, a maximum actuation voltage—noted V_{\max} —exists above which the electrocapillary force on a drop does not increase any more, only the risk of dielectric breakdown increases [\[64–68\]](#). Moreover above V_{\max} , there is no more gain in the motion speed of a droplet. It has been shown in Chapter 4 that V_{\min} is proportional to $2\sqrt{\alpha\gamma \sin \theta_0}$ and V_{\max} to $\sqrt{\gamma_{SL} - \gamma_{LG} \cos \theta_0}$.

Table 10.3 Ohnesorge and Reynolds Nondimensional Numbers for RTIL and Water

Liquid	ρ^a	u^b	D^c	γ^d	ν^e	η^f	On	Re
[tmba][NTf ₂]	1.43	1.3	1.3	34.5	58.0	82.9	1×10^3	3×10^{-2}
[bmim][BF ₄] ^g	1.17	4.0	1.1	46.3	71.8	84.0	1×10^3	6×10^{-2}
[bmim][PF ₆] ^g	1.38	1.3	1.1	43.7	210.3	290.2	4×10^3	7×10^{-3}
DIW	1.00	120	1.2	72.5	0.9	0.9	1×10^1	2×10^2

^aDensity (g/cm^3).

^bMotion speed (mm/s).

^cDroplet diameter (mm).

^dSurface tension (mN/m).

^eCinematic viscosity (mm^2/s).

^fDynamic viscosity (cP).

Consequently, for defining the functioning range of the microsystem, it is necessary to know the two limits given by the potentials V_{\min} and V_{\max} . The working potential was determined for several ionic liquids and water-based solutions [42]. Table 10.4 gives the working potentials for different ionic liquids in air on a Teflon-covered substrate. In air, ionic liquids show a wider working interval than water. Indeed, the minimum potential to move ionic liquid droplets (18–30 V) is lower than that of water (40 V), whereas the saturation threshold is similar for both. In Chapter 4, an estimate of the working potentials, i.e., of the values of the minimum and maximum potentials V_{\min} and V_{\max} have been derived based respectively on an analysis of the hysteresis phenomenon for V_{\min} and on a saturation correlation for V_{\max} (PQRS model) [68]. Figure 10.12 shows that the estimates of the minimum and maximum potentials are still valid for ionic liquids. Note that the minimum actuation potential V_{\min} for ionic liquids and that of a biological buffer containing 1% of Tween 20 are similar.

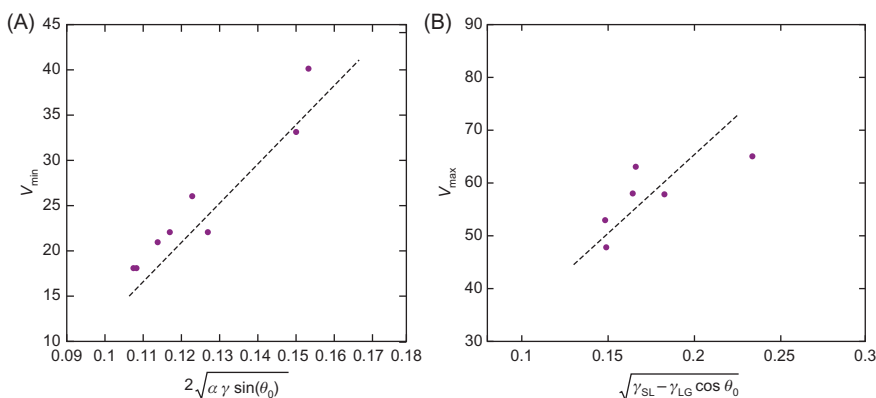
10.2.2.5 Ionic liquid dispensing

An important point in the design of EWOD chips is related to the dispensing of liquid from a reservoir located on the chip. If liquids can be directly dispensed from an on-chip reservoir, it will avoid the use of a syringe pump or spotting

Table 10.4 Physical Characteristics of Ionic Liquids in Comparison with Water

Liquids	γ (mN/m)	θ_0	θ_s	V_{\min}	V_{\max}
[tmba] [NTf ₂]	34.5	77.0	30–45	18	48
[bmin] [BF ₄]	46.3	94.2	40–45	22	58
[bmin] [PF ₆]	43.6	94.8	30–40	26	58
[bmin] [NTf ₂]	33.9	76.5	30–35	18	53
[teba] [NTf ₂]	—	76.5	30–32	18	48
[emin] [NTf ₂]	—	81.1	35–40	23	58
[C ₈ H ₁₉ BrN][NTf ₂]	—	85.7	30–35	27	48
[C ₇ H ₁₆ NO ₂][NTf ₂]	—	89.5	31–36	30	58
[C ₂₅ H ₅₄] [OTf]	—	79.5	30–35	22	53
[C ₆ H ₁₆ NO][NTf ₂]	—	89.1	30–35	28	58
[C ₉ H ₁₇ NO ₂][NTf ₂]	37.4	85.1	28–30	21	63
[C ₁₀ H ₂₀ NO ₃][NTf ₂]	39.4	86.6	33–40	22	58
DIW water	72.5	110.0	85–90	40	63
NH ₄ HCO ₃ 25 mM + 0.05% Tween 20	65.7	98.0	50–55	23	65
NH ₄ HCO ₃ 25 mM + 1% Tween 20	38.0	81.0	—	20	—

All measurements were made at room temperature. Surface tensions (mN/m) were measured with the pendant drop method on a Drop Shape Analysis System G10/DSA10. All contact angles were measured with a commercial Digidrop GBX system, with droplets of 1 μ L. V_{\min} : minimum actuation voltage (V_{ms}) to displace a droplet of 0.4 μ L on a row of $800 \times 800 \mu\text{m}^2$ electrodes. V_{\max} : saturation voltage (V_{ms}). For buffer +1% Tween 20, evaporation and very long equilibration time makes it impossible to obtain meaningful data

**FIGURE 10.12**

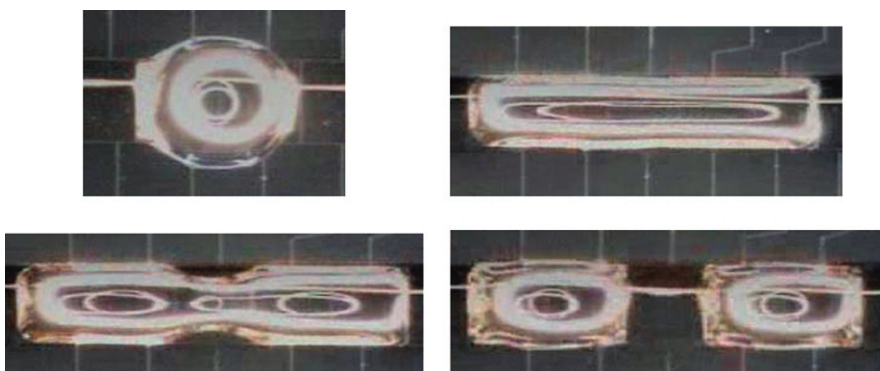
(A) Plot of V_{\min} as a function of $2\sqrt{\alpha\gamma \sin(\theta_0)} \sin(\theta_0)$ based on the values of [Table 10.4](#).
 (B) Plot of V_{\max} as a function of $\sqrt{\gamma_{SL} - \gamma_{LG} \cos \theta_0}$, based on the values of [Table 10.4](#).

robot. Such a feature renders the chip portable and allows for chemical reactions of combinatorial chemistry.

Generation of ionic droplets from a reservoir in covered EWOD-based microsystems is similar to that described in [Section 10.2.1.2](#) for VOS [40]. In such covered microsystems, it has been shown that ionic liquids can be distributed from a reservoir with a 100 μm gap while applying a 55 V_{rms} voltage [69]. Thus, ionic liquid droplets with volumes less than 100 nl may be delivered. However, addition of perfluorous solvent was needed to reduce the wettability of ionic liquids on the polymer walls of the reservoir. Moreover, it has been checked that drops of ionic liquid can be transported easily from a closed system to an open one (see [Section 5.3](#)).

10.2.2.6 Cutting ionic liquid droplets

Cutting a droplet into two has been recognized as a very important operation. Most studies in this area deal with water [70], showing the necessity of performing the splitting in a covered system. Experiments with ionic liquids have shown that splitting ionic liquids by EWOD is possible, even in open systems, as shown in [Figure 10.13](#). A drop of ionic liquid [tmaba][NTf₂] is stretched on five electrodes by successive actuation of the electrodes; the switch off of the central electrode leads to the generation of two droplets of the same size. At the present time, it is not clearly established why ionic liquid droplets are much easier to cut than aqueous droplets. The most striking aspect is the possibility of stretching ionic liquid droplets. We tend to associate this phenomenon with the large elasticity of ionic liquid interfaces that we analyzed in Chapter 5 [69,71].

**FIGURE 10.13**

Splitting $[\text{tmbo}][\text{NTf}_2]$ droplet in an open EWOD system. A $0.8 \mu\text{L}$ droplet was deposited on a chip. By successive actuations of electrodes ($V = 55 V_{\text{rms}}$), the droplet was stretched on five electrodes; cutting is then obtained by switching off the central electrode.

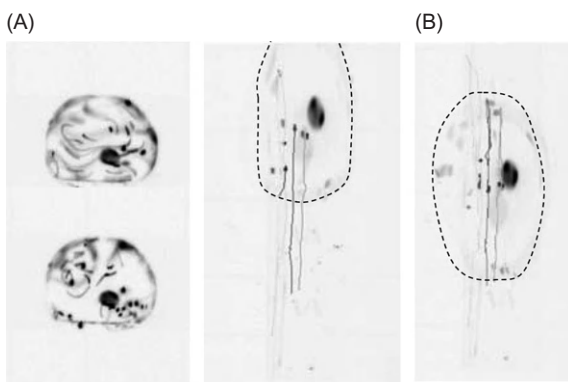
Source: Photograph Ph. Dubois.

10.2.2.7 Mixing of ionic liquids on an opened system

Homogeneous mixing of components—biomolecules, chemical species—inside a droplet is essential for obtaining an optimal bio- or chemical reaction. Insufficiently mixed liquids have poor reaction rates. We have already analyzed the mixing of aqueous solutions on EWOD substrates (Chapter 5) [72]. In this section, we focus on ionic liquids. In order to follow the convective movement inside a droplet, fluorescent beads are added to the liquid (Figure 10.14).

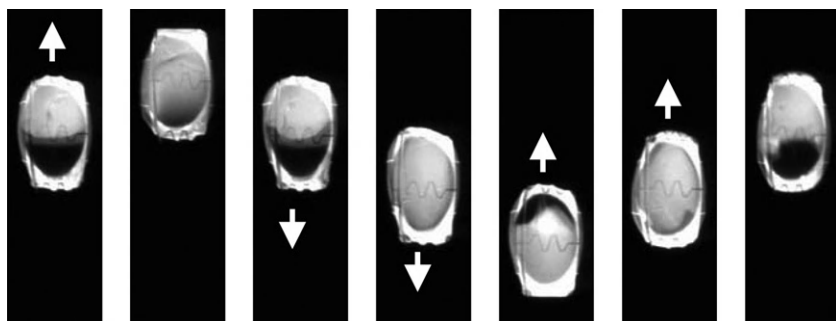
Two different types of motion can be induced inside a droplet: first convective motions triggered by external conditions: a thermal gradient induces a Marangoni convective effect, mass transfer to the air by evaporation induces convection [73], and an electric field imposes tangential constraints resulting in an electroconvective effect [74]. The second type of motion is that triggered by the motion (displacement) of the droplet itself on the solid substrate. This case has been illustrated in Chapter 5, where we showed what pattern of motion was the most effective to induce mixing inside the droplet.

Whatever the cause of the internal motion, an important difference of behavior between water and ionic liquids was observed. Fluorescent beads draw circular trajectories showing strong convection inside a water droplet. This is not the case for ionic liquids where beads draw linear trajectories coming back near their initial position after back-and-forth motion on a row of aligned electrodes. It appears that ionic liquids behave similarly to gels. Ionic liquid high values of viscosity (up to 300 times more viscous than water) can shut off the electroconvection effects observed in a water droplet. Thus, in the absence of additional mixing factors, mixing occurs only by diffusion in ionic liquids. No local recirculation occurs inside droplets during motion, resulting in a very slow mixing of two ionic

**FIGURE 10.14**

Internal motion tracked by fluorescent beads inside droplet: (A) DIW ($0.8 \mu\text{L}$ to $70V_{\text{rms}}$) during evaporation and (B) ionic liquid $[\text{bmim}][\text{BF}_4]$ ($0.4 \mu\text{L}$ to $70V_{\text{rms}}$) during back-and-forth motion on a row of electrodes; edges are indicated by a dotted line.

Source: Photograph Ph. Dubois.

**FIGURE 10.15**

Pictures of the mixing of a fluorescent droplet of $[\text{tmBa}][\text{NTf}_2]$ by back-and-forth displacement on a row of aligned electrodes. See how the last photograph is like the first one.

Source: Photograph Ph. Dubois.

components in a droplet. This fact has been confirmed by another experiment with fluorescent molecules. After the merging of fluorescent droplets, and back-and-forth displacement on the chip, the fluorescent droplet recovers its original position (Figure 10.15); homogenization of the solution required many back-and-forth motions, taking a total time of 6 min. This poor mixing can be predicted by the Reynolds number (Re) as given in Table 10.3. The Reynolds number obtained with $[\text{tmBa}][\text{NTf}_2]$ is around 3×10^{-2} . This very low Reynolds number indicates a very laminar flow which is disadvantageous for a quick mixing.

The preceding analysis shows that mixing in ionic liquid droplets is not easy and mixing enhancement solutions must be developed. Solutions using thermal heating to decrease the viscosity or acoustic actuation to increase the convective forces are currently being investigated.

The high value of viscosity in ionic liquids renders them very cumbersome to use in microchannel-based systems. The driving pressure would be too important for the microfabricated components. Again, thermal heating of the liquid is a solution [75].

10.3 Chemical synthesis in droplets in EWOD-based systems

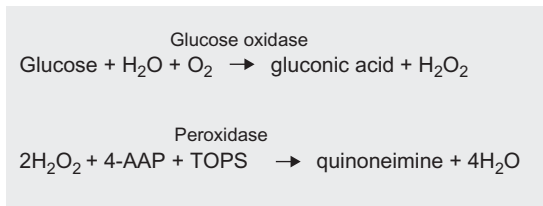
In the following section, examples of synthesis performed in droplets handled by EWOD-based systems are reported. The section is divided into three parts, one for each media: first water or aqueous solutions, second VOSs, both types of liquid requiring a covered EWOD-based systems, and finally ionic liquids, allowing the use of an opened EWOD-based system. Advantages and drawbacks of all these systems are discussed.

10.3.1 Synthesis in aqueous media

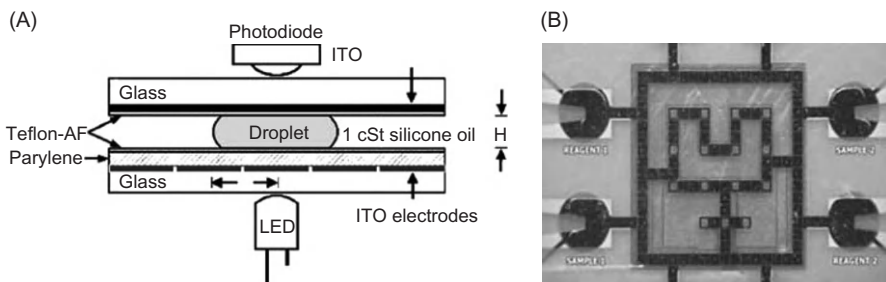
Aqueous solutions are generally reserved for biological reactions, and only some very specific chemical reactions can be performed in such media. On the other hand, water, more precisely buffer, is an ideal medium to perform biochemical synthesis. For example, a biocatalytic reaction is described in Refs [37,76], which demonstrates the feasibility of a bioassay in a covered system. A calorimetric enzyme-kinetic method based on the Trinder's reaction [77] has been used for the determination of glucose concentrations (Figure 10.16). In this system, two droplets of aqueous solutions containing respectively glucose oxidase, peroxidase, 4-aminoantipyrinidin, and *N*-ethyl-*N*-sulfopropyl-*m*-toluidine in one droplet and glucose in the second one, were sandwiched between two plates, in air or in any other immiscible liquid (Figure 10.17A). After merging the two droplets together, the glucose is enzymatically oxidized to gluconic acid in the presence of glucose oxidase. The hydrogen peroxide then reacts with 4-amino antipyrine and *N*-ethyl-*N*-sulfopropyl-*m*-toluidine in the presence of peroxidase to form violet colored quinoneimine which exhibits an absorbance maximum at 545 nm.

The LOC used for the reaction of a multiplexed bioassay is shown in Figure 10.17B. Sample injection holes, reservoirs, fluidic pathways, mixing areas, and optical detection sites are all located on the same substrate.

No chemical reaction in water droplet displaced under EWOD actuation has been reported in the literature. However, aqueous media were used with DEP actuation, which is the other possible electrical method for displacement of

**FIGURE 10.16**

Schematic representation of the Trinder's reaction.

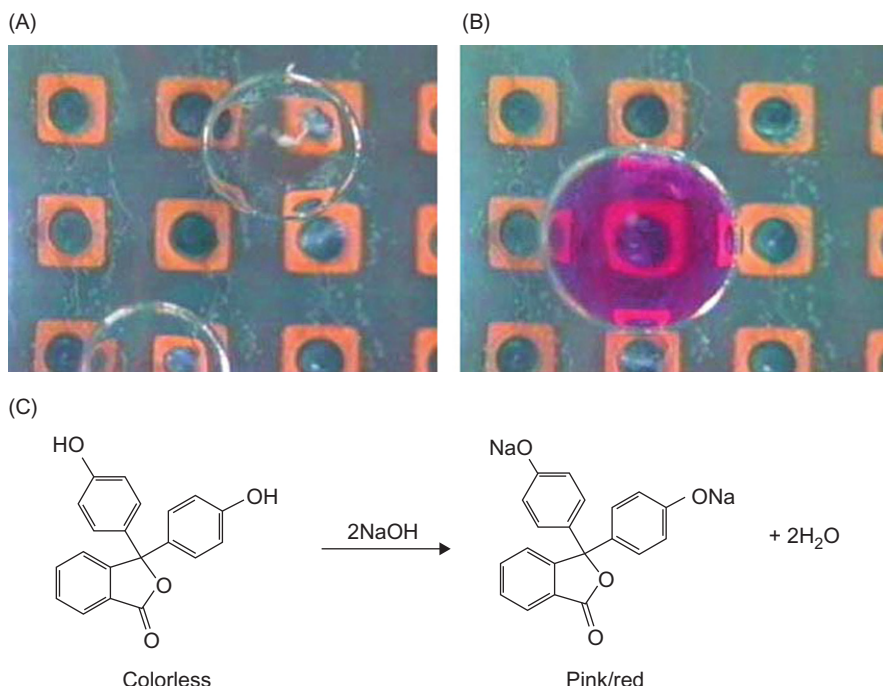
**FIGURE 10.17**

(A) Vertical cross-section of the electrowetting chip showing the detection device. (B) Microfabricated EWOD chip used for multiplexed bioassay (glucose detection).

Source: From Ref. [37], reproduced by permission of the Royal Society of Chemistry.

droplets in LOC. A first demonstration of a chemical reaction performed in a droplet is the alkalization of phenolphthalein [78] which has been realized in an oil environment to prevent evaporation. This reaction was performed by coalescence of two water droplets containing respectively NaOH (1 mM) and phenolphthalein under DEP actuation. The red color taken by the liquid is an indicator of the reaction (Figure 10.18). In this reaction, phenolphthalein, a pH indicator, is deprotonated by NaOH. The two phenol functions are then transformed in two phenolate functions favoring the electronic delocalization on the conjugated backbone.

Even if some reactions can be performed in aqueous solutions [79], these examples are not very numerous and limited to some types of chemical reactions. Indeed, despite the fact that water is the cheapest, safest, and most nontoxic solvent known, most of the time the presence of water is not compatible with the reaction and is eliminated by drying of substrates and solvents. The use of water as a medium for organic reactions is, therefore, one of the latest challenges for modern organic chemists.

**FIGURE 10.18**

(A) Picture of the droplets containing NaOH (right) and phenolphthalein (left). (B) After merging, the droplet takes a red color indicating that the reaction has taken place.

(C) Schematic representation of the reaction between phenolphthalein and soda.

(For interpretation of the references to color in this figure legend, the reader is referred to the web version of this book.)

Source: From Ref. [78], reproduced by permission of the Royal Society of Chemistry.

10.3.2 Synthesis in VOSs

Chemical syntheses in VOS are not very widespread due to their relatively high volatility necessitating a cover plate or an oil layer that has to be immiscible with the VOS. Among the few examples reported in the literature, the very simple reaction between nitroaromatic compounds and potassium hydroxide (KOH) can be mentioned. This reaction allows the detection of trinitroaromatic compounds, the most commonly used class of explosives. To perform this reaction in droplet format, Pamula et al. [80] have dissolved in dimethyl sulfoxide (DMSO) 2,4,6-trinitrotoluene (TNT) or 2,4-dinitrotoluene (DNT) and KOH in a water/DMSO (1:2000) mixture. Droplets of TNT and KOH were dispensed manually by a pipette under a silicone oil layer on an electrowetting chip and the two droplets are coalesced by applying voltages (50 V) between appropriate electrodes. The droplet is then further mixed by shuttling it across four

electrodes for 30 s. The mixing should be complete in less than 30 s for this pattern of mixing [46]. The reaction between TNT/DNT and KOH leads to colored Jackson–Meisenheimer complexes [81] which can easily be detected on chip by UV–visible measurements. These complexes are produced by reaction between an arene carrying electron-withdrawing groups and a nucleophile (Figure 10.19). These salts have been identified as reactive intermediates in nucleophilic aromatic substitution but stable and isolated.

As shown above, chemistry in droplets of water or VOSs is possible in EWOD-covered systems. However, evaporation of tiny droplets is a major drawback for most chemical syntheses. Moreover, many reactions necessitate heating, pressure, and/or several hours in incubation. To avoid evaporation, some authors suggest using a surrounding oil environment. Certainly it stops evaporation, but, as previously noted, this approach brings other problems such as fluidic connections and liquid/liquid cross contamination between droplets through the surrounding solvent.

10.3.3 Synthesis in ionic liquids

Dubois et al. [42,62] have recently reported experiments using droplets of RTILs and TSILs as stable microreactors displaced by EWOD in chemical applications. The approach consists of using an open DMF chip coated with Teflon, ionic liquid droplets containing different reagents, and EWOD actuation for moving and merging the droplets. This concept takes advantage of the negligible vapor pressure of ionic liquids allowing the handling of very small liquid volumes ($<1\text{ }\mu\text{L}$) on open microsystems, thus simplifying the experimental approach, facilitating direct access to the droplets and avoiding cross contamination induced by the presence of oil. Chemical syntheses with minute amounts of reagents (especially useful for potentially explosive or expensive reactions) can be

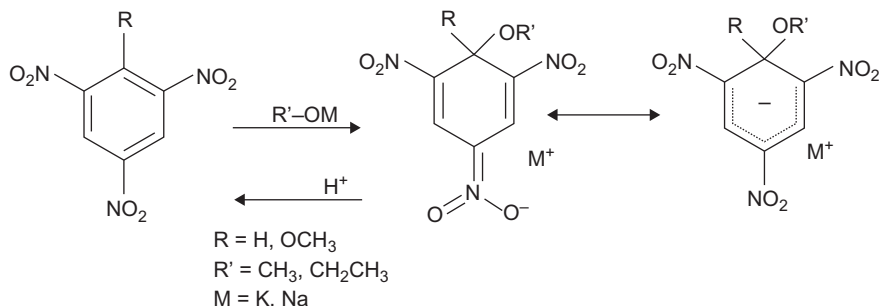


FIGURE 10.19

Schematic representation of the reaction between an arene and a nucleophile leading to a Jackson–Meisenheimer complex.

completely achieved in solution using ionic liquid matrices such as RTILs or on soluble supports using TSILs or task-specific onium salts in solution in RTILs. In this last case, the excess of reagents and by-products could be eliminated at the end of the reaction by simply washing or heating the droplets.

The demonstration of ionic liquid droplet displacement in EWOD microsystems has opened the way to performing on-chip multicomponent chemical reactions. A tetrahydroquinoline synthesis via a well-known three-component reaction described by Grieco and coworkers [82–84] has been chosen for several reasons: (i) tetrahydroquinolines are an important class of biologically active compounds [85], (ii) the reaction is a relatively complex reaction (a good model for proof of feasibility), and (iii) this reaction occurs rapidly at room temperature with a quantitative yield and has been demonstrated on solid supports [86]. In this reaction, aniline reacts with an aldehyde in the presence of an electron-rich olefin and an acidic catalyst (trifluoroacetic acid, TFA) to produce tetrahydroquinolines at room temperature (Figure 10.20). The first step of this reaction is the imine formation followed by an Aza Diels–Alder reaction ($[4 + 2]$ -cycloaddition) [87]. The electron-withdrawing effect of the nitrogen atom and the activation of the dienophile by the acidic catalysts allows for the reaction to occur very rapidly at room temperature contrary to the classical Diels–Alder reactions.

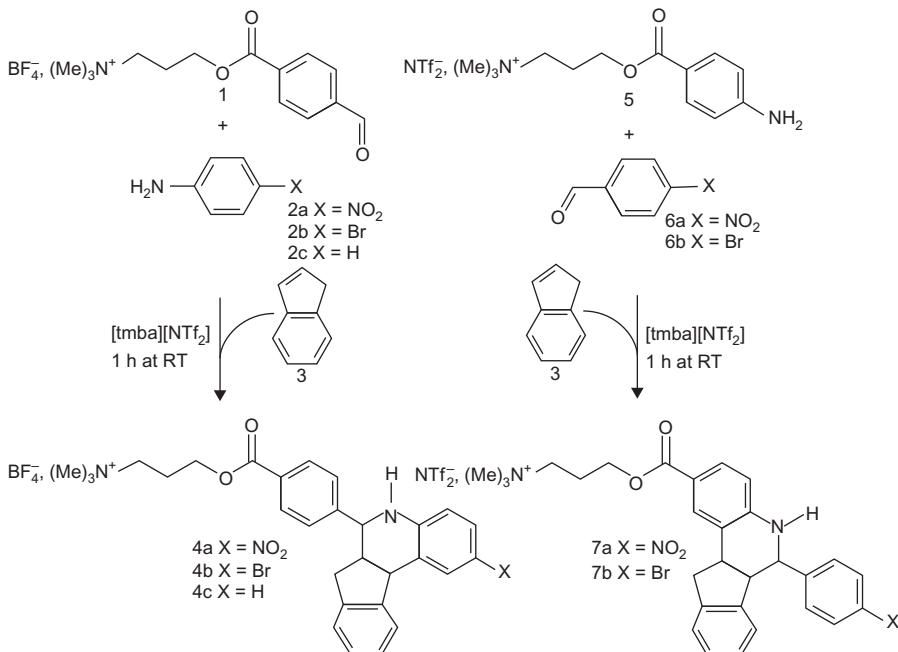


FIGURE 10.20

Schematic representation of Grieco's reaction in a droplet microreactor.

A similar reaction was run in an EWOD microsystem, using TSILs in solution in [tmba][NTf₂]. In a more detailed way, a 0.2 μL droplet of [tmba][NTf₂] containing a TSIL containing either an aldehyde function (1) or an aniline function (5) and 10 equivalents of TFA was deposited manually on the chip. The droplet was approached from a second droplet of [tmba][NTf₂] containing the derivate 2 or 6. After coalescence, the first step of the reaction takes place and the activated imine starts to be generated. Next, the resulting droplet was merged with a third droplet containing an excess of indene. The reaction was then incubated within 1 h at room temperature. At the end of the reaction, the final product was analyzed off- and online (Figure 10.21).

This approach seems to be very promising for low-volume organic synthesis in solution. Indeed, ionic liquids enable the use of open systems, simple to use and avoiding the cross contamination induced by the use of a secondary fluid. Moreover, the combination of RTILs and TSILs (or task-specific onium salts) allows a fast separation of the expected final product and the starting reagents or by-products. Thus, complex protocols can be achieved on this system due to the easy displacement of droplets by EWOD. However, some difficulties occur in such an approach which can limit its significance.

The first difficulty is the evaporation of the nonsupported species through the droplet of ionic liquids. Indeed, even if the ionic liquids have a negligible volatility, because of the high surface/volume ratio, volatile reagents can diffuse through the droplet and evaporate at its surface. For instance, to perform fully the Grieco reaction described in Figure 10.20, 10 equivalents of TFA are needed in the droplet format, whereas one equivalent is enough in a flask. Solutions to this problem exist. First, TFA can be replaced by a TSIL containing an acid function. Second, in the wide range of components available for organic chemistry, a solid reagent, with the same physical and chemical properties, can be used instead of the volatile compound. For instance, if TFA is replaced by trichloroacetic acid (TCA), which is solid at ambient temperature, a 100% conversion rate is obtained with only two equivalents. Third, a saturated atmosphere can prevent the full evaporation of the volatile compound, which should also be a possible way to introduce volatile reagents inside droplets.

The second difficulty arises from the large surface/volume ratio offered by a digital microsystem. This large surface/volume ratio can boost unwanted reactions, such as oxygen quenching or hydrolysis. In the particular case of RTIL, we have to keep in mind the high hydroscopic capacity of ionic liquids. Therefore, high hydrophobic RTIL, e.g., the ones with NTf₂⁻ or fluorinated anions, have to be preferred. A dry atmosphere which surrounds the chip can protect from such unwanted reactions. One should note that covered EWOD systems also suffer from this drawback.

Finally, reactions in open digital microsystems suffer from the poor mixing of ionic liquids. Indeed, the high viscosities of ionic liquids prevent reagents from a quick diffusion through the droplets [88]. Thus, at room temperature, after the merging of two droplets, around 40 min are needed to obtain a total

conversion (whereas 5 min were needed in a stirred beaker). In this case, reagents are only mixed by a passive way, i.e., by diffusion. Therefore, an active, faster process is required. Back-and-forth displacement of droplets on the chip has been investigated, but as previously noted, it was found to be not very efficient for

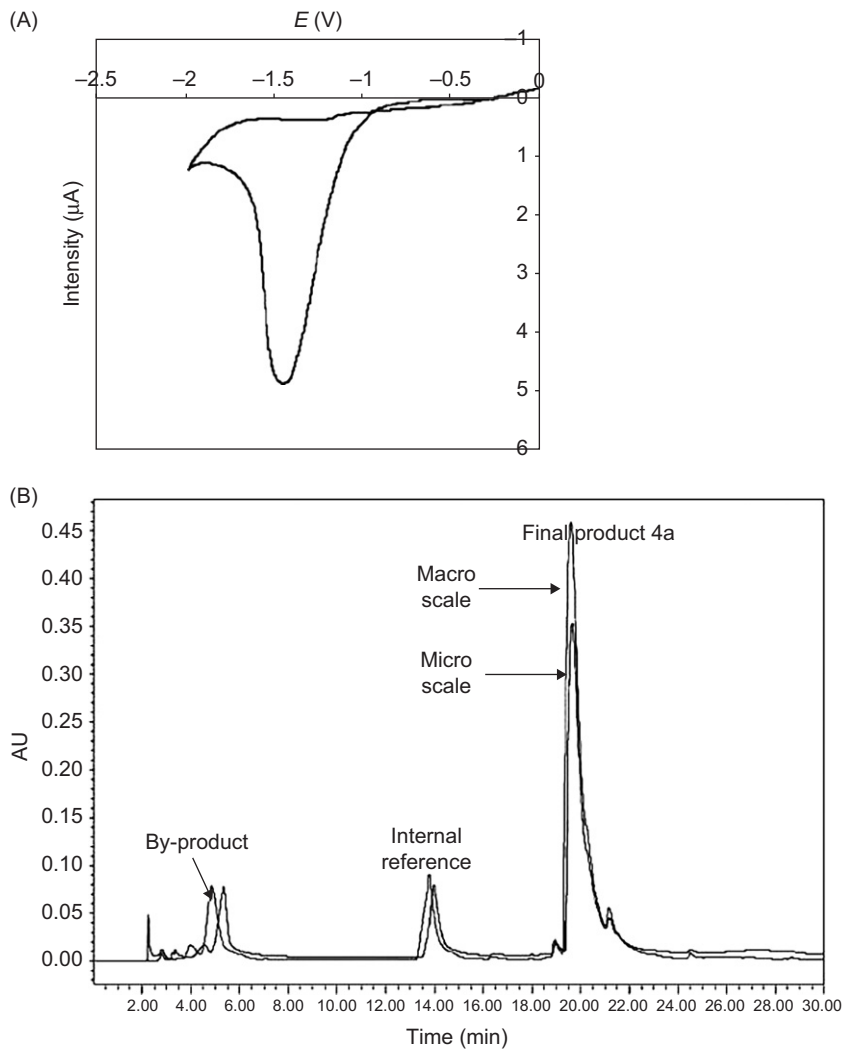


FIGURE 10.21

(A) Online detection: cyclic voltammogram of 7a in [tmaba][NTf₂] at a gold electrode ($\phi = 25 \mu\text{m}$ and $V = 50 \text{ mV/s}$). (B) Off-line detection: comparison of the chromatograms of the macro- and microscale reactions after the reaction of 1 with 2a and 3. The observed by-product in this chromatogram corresponds to a residual protonated *p*-nitroaniline. The numbers 7a, 1, 2a, and 3 correspond to Figure 10.20.

ionic liquids. In order to enhance internal convective motions, droplets have been heated from below. In this case, mixing is promoted by two effects. First, the viscosity of the ionic liquids decreases which facilitates internal motion. Second, internal convection appears due to a Marangoni effect (see Section 2.8). Heat related mixing of droplets of RTIL was investigated and a strong effect was observed (Figure 10.22A). Consequently, the Grieco reaction was performed at a higher temperature and it was observed that the rate enhancement was clearly improved. One may object that the improvement of the kinetic rate is due to the favorable thermodynamic effect of temperature on Grieco reaction and not to the improvement of the droplets mixing. However, the Grieco reaction is already really fast at ambient temperature in the bulk scale, which indicates a low thermodynamic barrier. Besides, at 80° and 120°C, the time needed for full mixing is identical; and we have observed only a small difference in the kinetic rate (Figure 10.22B).

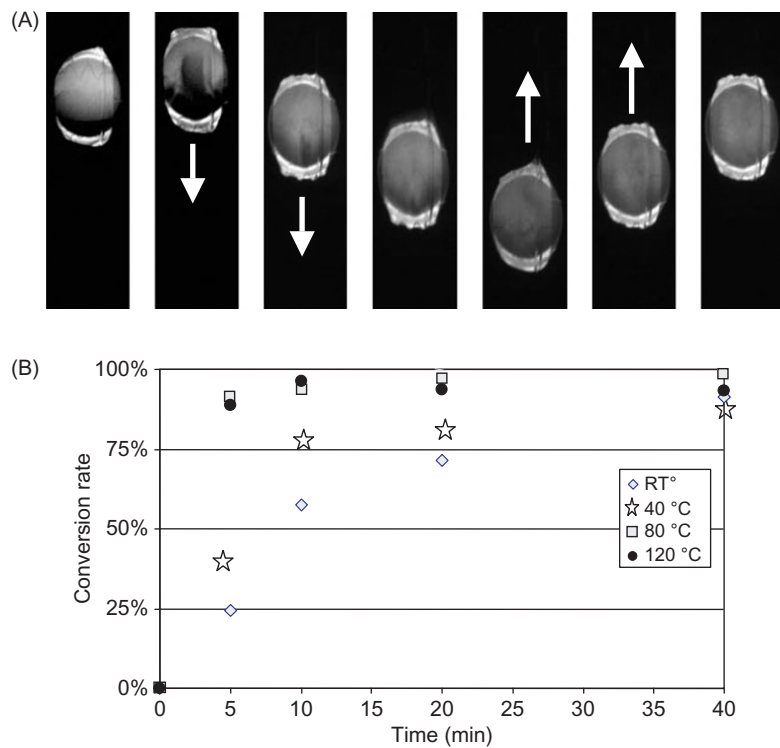


FIGURE 10.22

(A) Photographs of the mixing of a fluorescent droplet of $[\text{tmbo}][\text{NTf}_2]$ with another nonmarked droplet with heating from below (120°C) after one back-and-forth motion. (B) Improvement of kinetic rate with the temperature increase.

10.4 Conclusions and perspectives

Compared to traditional batch reactions, digital chemical microreactor technology is showing definite advantages. These types of microreactors produce outputs with higher yield and purity, in a shorter time, with safer conditions, and using smaller amounts of reagents. As mentioned above, microflow devices exhibit a number of drawbacks associated with the nature of the technology itself. The development of droplet-based microreactors, although still in its infancy, is bringing in promising new possibilities in this area, especially because it avoids the problems associated with continuous microflow systems.

We have shown in this chapter that droplets of a number of molecular solvents or ionic solvents, e.g., RTILs, can be moved on planar microsystems by EWOD technique. It is interesting to note that the walls of the microreactors have become the interface between the liquid and the ambient atmosphere. In order for the microreactor to have a sufficient lifetime to be useful, it is necessary that the liquid constituent of the droplet does not evaporate too fast. Molecular solvents, even the ones with a high boiling point, evaporate, introducing a severe limitation as to their use for such devices. Solutions to these problems have been proposed, but they introduce important limitations. These limitations disappear when using RTILs which have extremely low vapor pressures and therefore do not evaporate. The developments of the chemistry in ionic liquids are becoming so numerous that it opens up a very large number of possibilities for DMF reactors. This is even more the case since the discovery that ionic liquids can be functionalized, thus conferring to the liquid and consequently to the droplet-specific chemical, physical, and spectroscopic properties. It is important to keep in mind that ionic liquid droplet microreactors can be functionalized by solubilization of onium salts bearing one or several functional groups in a nonfunctionalized ionic liquid matrix. This opens up the field of homogeneous catalysis via onium salt supported catalysts, and the field of solution phase chemistry via soluble supports immobilized in ionic liquids matrixes, offering new possibilities for combinatorial chemistry. Multiplexing has been shown to make possible the handling of a large number of droplets (Chapter 5). Therefore, DMF reactors are a promising tool for future developments in the combinatorial chemistry area. For example, they can be used for the search of new active molecules or scaffolds. One can also envision the use of this technology for process intensification. Since droplets can be merged and also can be dispensed from a 3D reservoir, it is reasonable to predict that these systems will be used for automated multistep synthesis. A proper functionalization of the onium salt should also open the way to intelligent droplet microreactors which are able to act as microsensors and/or micropipes. The capacity of online detection must be added to these devices in order to make the digital microreactors an even more attractive technology.

Among the foreseen applications, the ones using enzymes are especially interesting: enzymes can be dissolved in ionic liquids; it has been shown that their

catalytic efficiency and thermal stability are increased in such an environment. This could lead to the design of digital microreactors with enzyme activity aimed at organic synthesis, analytical purposes, and molecular biology. It may be safe to say that applications of this technology are only limited by the capacity to imagine new applications, keeping in mind that there are still a number of technical problems waiting to be solved.

References

- [1] Y. Kikutani, H. Hisamoto, M. Tokeshi, T. Kitamori, Micro wet analysis system using multi-phase laminar flows in three-dimensional microchannel network. *Lab Chip* 4 (2004) 328–332.
- [2] D.M. Ratner, E.R. Murphy, M. Jhunjhunwala, D.A. Snyder, K.F. Jensen, P.H. Seeberger, Microreactor-based reaction optimization in organic chemistry—glycosylation as a challenge. *Chem. Commun.* (2005) 578–580.
- [3] G.N. Doku, W. Verboom, D.N. Reinhoudt, A. van den Berg, *Tetrahedron* 61 (2005) 2733–2742.
- [4] S. Taghavi-Mogadam, A. Kleemann, K.G. Golbig, Microreaction technology as a novel approach to drug design, process development and reliability. *Org. Proc. Res. Develop.* 5 (2001) 652–658.
- [5] D.A. Snyder, C. Noti, P.H. Seeberger, F. Schael, T. Bieber, G. Rimmel, W. Ehrfeld, Modular Microreaction Systems for Homogeneously and Heterogeneously Catalyzed Chemical Synthesis. *Helv. Chim. Acta* 88 (2005) 1–9.
- [6] P.D.I. Fletcher, S.J. Haswell, E. Pombo-Villar, B.H. Warrington, P. Watts, S.Y.F. Wong, X. Zhang, Micro reactors: principles and applications in organic synthesis, *Tetrahedron* (2002) 4735.
- [7] M. Brivio, R.E. Oosterbroek, W. Verboom, M.H. Goedbloed, A. van den Berg, D.N. Reinhoudt, Surface effects in the esterification of 9-pyrenebutyric acid within a glass micro reactor. *Chem. Comm.* (2003) 1924–1925.
- [8] K.F. Jensen, Microreaction engineering—is small better? *Chem. Eng. Sci.* 56 (2001) 293–303.
- [9] D.C. Duffy, J.C. McDonald, O.J.A. Schueller, G.M. Whitesides, Rapid Prototyping of Microfluidic Systems in Poly(dimethylsiloxane). *Anal. Chem.* 70 (1998) 4974.
- [10] K. Jähnisch, V. Hessel, H. Löwe, M. Baerns, Chemistry in microstructured reactors. *Angew. Chem. Int. Ed.* 43 (2004) 406–446.
- [11] C.M. Mitchell, D.-P. Kim, P.J.A. Kenis, Ceramic microreactors for on-site hydrogen production. *J. Catal.* 241 (2006) 235–242.
- [12] P. Watts, S.J. Haswell, The application of micro reactors for organic synthesis. *Chem. Soc. Rev.* 3 (2005) 235–246.
- [13] P.D. Fletcher, S.J. Haswell, V.N. Paunov, Theoretical considerations of chemical reactions in micro-reactors operating under electroosmotic and electrophoretic control. *Analyst* 124 (1999) 1273.
- [14] G.M. Greenway, S.J. Haswell, D.O. Morgan, V. Skelton, P. Styring, The use of a novel microreactor for high throughput continuous flow organic synthesis. *Sensor Actuator B* 63 (2000) 153.

- [15] V. Skelton, G. Greenway, S.J. Haswell, P. Styring, D.O. Morgan, B.H. Warrington, S.Y.F. Wong, The Preparation of a Series of Nitrostilbene Ester Compounds Using Micro Reactor Technology. *Analyst* 126 (2001) 7.
- [16] C. Wiles, P. Watts, S.J. Haswell, E. Pombo-Villar, Addition of enolates to α and β -unsaturated ketones within a micro reactor. *Lab Chip* 2 (2002) 62–64.
- [17] C. Wiles, P. Watts, S.J. Haswell, E. Pombo-Villar, Stereoselective alkylation of an Evans auxiliary derivative within a pressure driven micro reactor. *Lab Chip* 4 (2004) 171–173.
- [18] P. Watts, C. Wiles, S.J. Haswell, E. Pombo-Villar, P. Styring, The synthesis of peptides in micro reactors, *Chem. Commun.* (2001) 990.
- [19] B. Zheng, R.F. Ismagilov, A microfluidic approach for screening submicroliter volumes against multiple reagents by using preformed arrays of nanoliter plugs in a three-phase liquid/liquid/gas flow. *Angew. Chem. Int. Ed.* 44 (2005) 2520–2523.
- [20] G. Cristobal, L. Arbouet, F. Sarrazin, D. Talage, J.-L. Brunel, M. Joanicot, L. Servant, On-line laser Raman spectroscopic probing of droplets engineered in microfluidic devices. *Lab Chip* 6 (2006) 1140–1146.
- [21] P. Marmottant, S. Hilgenfeldt, A bubble-driven microfluidic transport element for bioengineering. *Proc. Natl. Acad. Sci. U.S.A.* 101 (2004) 9523.
- [22] I. Shestopalov, J.D. Tice, R.F. Ismagilov, Multi-step synthesis of nanoparticles performed on millisecond time scale in a microfluidic droplet-based system. *Lab Chip* 4 (2004) 316–321.
- [23] Z. Nie, S. Xu, M. Seo, P.C. Lewis, E. Kumacheva, Polymer particles with various shapes and morphologies produced in continuous microfluidic reactors. *J. Am. Chem. Soc.* 127 (2005) 8058–8063.
- [24] E. Chan, A. Alivisatos, R.A. Mathies, Temperature microfluidic synthesis of CdSe nanocrystals in nanoliter droplets. *J. Am. Chem. Soc.* 127 (2005) 13854–13861.
- [25] R. Yamada, H. Tada, Manipulation of droplets by dynamically controlled wetting gradients. *Langmuir* 21 (2005) 4254–4256.
- [26] E. Raphaël, C.R. Acad. Sci. Ser. II 306 (1998) 751.
- [27] M.K. Chaudhury, G.M. Whitesides, How to make water run uphill. *Science* 256 (1992) 1539.
- [28] F. Brochard, Motions of droplets on solid surfaces induced by chemical or thermal gradients. *Langmuir* 5 (1989) 432.
- [29] A. Wixforth, C. Strobl, Ch. Gauer, A. Toegl, J. Scriba, Z. Guttenberg, Acoustic manipulation of small droplets. *Anal. Bioanal. Chem.* 379 (7–8) (2004) 982–991.
- [30] Z. Guttenberg, H. Müller, H. Habermüller, A. Geisberg, J. Pipper, J. Felbel, et al., Planar chip device for PCR and hybridization with surface acoustic wave pump. *Lab Chip* 5 (2005) 308–317.
- [31] T.B. Jones, M. Gunji, M. Washizu, M.J. Feldman, Dielectrophoretic liquid actuation and nanodroplet formation. *J. Appl. Phys.* 89 (2001) 1441–1448.
- [32] J. Gong, S.-K. Fan, C.-J. Kim, Portable Digital Microfluidics Platform with Active but Disposable Lab-On-Chip, Tech. Dig., 17th IEEE International Conference on Micro Electro Mechanical Systems, Maastricht, The Netherlands, 25–29 January, 2004, p. 355–358.
- [33] A. Wixforth, Acoustically driven planar microfluidics. *Superlattices Microstruc.* 33 (2003) 389–396.

- [34] J. Schwartz, J.V. Vykoukal, P. Gascoyne, Droplet-based chemistry on a programmable micro-chip. *Lab Chip* 7 (2004) 11–17.
- [35] J. Millman, K. Bhatt, B. Prevo, O.D. Velev, Anisotropic particle synthesis in dielectrophoretically controlled microdroplet reactors. *Nat. Mater.* 4 (2005) 98.
- [36] M.G. Pollack, A.D. Shenderov, R.B. Fair, Electrowetting-based actuation of droplets for integrated microfluidics. *Lab Chip* 2 (2002) 96–101.
- [37] V. Srinivasan, V.K. Pamula, R.B. Fair, An integrated digital microfluidic lab-on-a-chip for clinical diagnostics on human physiological fluids. *Lab Chip* 4 (2004) 310–315.
- [38] Y. Fouillet, D. Jary, A.G. Brachet, C. Chabrol, J. Boutet, P. Clementz, et al., Design and validation of a complex generic fluidic microprocessor based on EWOD droplet for biological applications. *Micro Total Anal. Syst.* (Boston, MA), 2005, pp. 59–69.
- [39] D. Jary, A. Chollat-Namy, Y. Fouillet, J. Boutet, C. Chabrol, G. Castellan, et al., Nanotech 2006, Boston 7–11 May, 2006.
- [40] D. Chatterjee, B. Hetayothin, A.R. Wheeler, D.J. King, R.L. Garrell, Droplet-based microfluidics with nonaqueous solvents and solutions. *Lab Chip* 6 (2006) 199–206.
- [41] S. Millifiorini, A.H. Tkaczyk, R. Sedev, J. Efthimiadis, J. Ralston, Electrowetting of ionic liquids. *J. Am. Chem. Soc.* 128 (2006) 3098–3101.
- [42] P. Dubois, G. Marchand, Y. Fouillet, J. Berthier, T. Douki, F. Hassine, et al., Ionic liquid droplet as a microreactor. *Anal. Chem.* 78 (2006) 4909–4917.
- [43] Y. Fouillet, D. Jary, A.G. Brachet, J. Berthier, R. Blervaque, L. Davous, et al. EWOD digital microfluidics for lab on a chip. International Conference on Nanochannels, Microchannels and Minichannels, 19–21 June, Limerick, Ireland, 2006.
- [44] Handbook of Chemistry and Physics, 70th ed., CRC Press, Taylor and Francis, Boca Raton, FL, 1989–1990.
- [45] P. Paik, V.K. Pamula, M.G. Pollack, R.B. Fair, Electrowetting-based droplet mixers for microfluidic systems. *Lab Chip* 3 (2003) 28–33.
- [46] P. Paik, V.K. Pamula, R.B. Fair, Rapid droplet mixers for digital microfluidic systems. *Lab Chip* 3 (2003) 253–259.
- [47] P.R.C. Gascoyne, J.V. Vykoukal, J.A. Schwartz, T.J. Anderson, D.M. Vykoukal, K.W. Current, et al., Dielectrophoresis-based programmable fluidic processors. *Lab Chip* 4 (2004) 299–309.
- [48] M. Vallet, B. Berge, L. Vovelle, Electrowetting of water and aqueous solutions on poly(ethylene terephthalate) insulating films. *Polymer* 37 (1996) 2465–2470.
- [49] P. Wasserscheid, T. Welton, *Ionic Liquids in Synthesis*, Wiley CH, Weinheim, Germany, 2003.
- [50] T. Welton, Room-temperature ionic liquids. Solvents for synthesis and catalysis. *Chem. Rev.* 99 (1999) 2071–2083.
- [51] R.D. Rogers, K.R. Seddon, Ionic liquids - solvents of the future? *Science* 302 (2003) 792–793.
- [52] A. Bagno, C. Butts, C. Chiappe, F. D'Amico, J.C.D. Lord, D. Pieraccini, F. Rastrelli, The effect of the anion on the physical properties of trihalide-based N,N-dialkylimidazolium ionic liquids. *Org. Biomol. Chem.* 3 (2005) 1624–1630.
- [53] J. Fraga-Dubreuil, J.-P. Bazureau, Grafted ionic liquid-phases supported synthesis of small organic molecule. *Tetrahedron Lett.* 42 (2001) 6097–6100.

- [54] S.T. Handy, M. Okello, Homogeneous supported synthesis using ionic liquid supports: Tunable separation properties. *J. Org. Chem.* 70 (2005) 2874–2877.
- [55] J.H. Davies, Sweet success: ionic liquids derived from non-nutritive sweeteners. *Chem. Lett.* 33 (2004) 1072–1077.
- [56] M. Vaultier, S. Gmouh, Compositions containing ionic liquids and uses thereof, especially in organic synthesis. French Patent, FR 2845084 application no. 2002-11910, WO 2004 029004.
- [57] M. Vaultier, S. Gmouh, F. Hassine, Use of functionalized onium salts as a soluble support for organic synthesis. French Patent, FR 2857360 application 2003-8413, WO 2005 005345.
- [58] E. Colgate, H. Matsumoto, An investigation of electrowetting-based microactuation. *J. Vac. Sci. Technol. A* 8 (1990) 3625–3633.
- [59] M. Washizu, Electrostatic actuation of liquid droplets for microreactor applications. *Proc. IEEE Trans. Ind. Appl.* 34 (1998) 732–737.
- [60] F. Muggele, J.-C. Baret, Electrowetting: from basics to applications. *J. Phys. Condens. Matter.* 17 (2005) R705–R774.
- [61] J. Berthier, O. Raccourt, P. Clementz, D. Jary, C. Peponnet, Y. Fouillet, An analytical model for the prediction of microdrop extraction and splitting in digital microfluidics systems. Nanotechnology Conference and Trade Show, Anaheim, CA, 8–12 May, 2005, pp. 664–667.
- [62] P. Dubois, G. Marchand, Y. Fouillet, C. Peponnet, C. Chabrol, J. Berthier, M. Vaultier, Ionic liquid droplet as microreactor displaced by electrowetting on dielectric. *Proc. Micro. Total Anal. Syst.* 1 (2005) 412–414.
- [63] R. Bavière, J. Boutet, Y. Fouillet, Dynamics of droplet transport induced by electrowetting actuation. SHF-Microfluidics, 12–14 December 2006, pp. 287–294, Toulouse, France.
- [64] V. Peykov, A. Quinn, J. Ralston, Electrowetting: a model for contact-angle saturation. *Colloid Polymer Sci.* 278 (2000) 789–793.
- [65] A. Quinn, R. Sede, J. Ralston, Contact angle saturation in electrowetting. *J. Phys. Chem. B.* 109 (2005) 6268–6275.
- [66] M. Vallet, M. Vallade, B. Berge, Limiting phenomena for the spreading of water on polymer films by electrowetting. *Eur. Phys. J. B* 11 (1999) 583–591.
- [67] H.J.J. Verheijen, M.W.J. Prins, Contact angles and wetting velocity measured electrically. *Langmuir* 15 (20) (1999) 6616–6620.
- [68] J. Berthier, Ph. Dubois, Ph. Clementz, P. Claustre, C. Peponnet, Y. Fouillet, Actuation potentials and capillary forces in electrowetting-based microsystems. *Sensor Actuator A Phys.* 134 (2) (2007) 471–479.
- [69] J. Berthier, Ph. Clementz, O. Raccourt, D. Jary, P. Claustre, C. Peponnet, Y. Fouillet, Computer aided design of an EWOD microdevice. *Sensor Actuator A* 127 (2006) 283–294.
- [70] P.K. Wong, T.H. Wang, J.H. Deval, C.M. Ho, Electrokinetics in micro devices for biotechnology applications. *Transactions Mechanotron.* 9 (2004) 366–376.
- [71] S.K. Fan, C. Hashi, C.J. Kim, Manipulation of multiple droplets on NxM grid by cross-reference EWOD driving scheme and pressure-contact packaging. *IEEE Conference on MEMS*, Kyoto, Japan, January, 2003, p. 694–700.
- [72] E. Dussan, On the spreading of liquids on solid surfaces: Static and dynamic contact lines. *Annu. Rev. Fluid. Mech.* 11 (1979) 371–400.

- [73] J.J. Hegseth, N. Rashidnia, A. Chai, Natural convection in droplet evaporation. *Phys. Rev. E.* 54 (1996) 1640–1644.
- [74] G.I. Taylor, Disintegration of water droplets in an electric field. *Proc. Roy. Soc. CCLXXX* (1964) 501–509.
- [75] A.J. de Mello, M. Habgood, N.L. Lancaster, T. Welton, R.C. Wooton, Precise temperature control in microfluidic devices using Joule heating of ionic liquids. *Lab Chip* 4 (2004) 417–419.
- [76] V. Srinivasan, V.K. Pamula, R.B. Fair, Droplet-based microfluidic lab-on-a-chip for glucose detection. *Anal. Chim. Acta* 507 (2004) 145–150.
- [77] P. Trinder, *Ann. Clin. Biochem.* 6 (1969) 24–25.
- [78] T. Taniguchi, T. Torii, T. Higuchi, Droplet formation in a microchannel network. *Lab Chip* 2 (2002) 19–23.
- [79] U.M. Lindström, Stereoselective organic reactions in water. *Chem. Rev.* 102 (2002) 2751–2772.
- [80] V.K. Pamula, V. Srinivasan, H. Chakrapani, R.B. Fair, E.J. Toone, A droplet-based lab-on-a-chip for colorimetric detection of nitroaromatic explosives. *Proc. IEEE 2005, 18th International Conference on Micro Electro Mechanical System*, January 30–February 03, 2005, pp. 722–725.
- [81] G.A. Artamkina, M.P. Egorov, I.P. Beletskaya, Some aspects of anionic σ -complexes. *Chem. Rev.* 82 (1982) 427–459.
- [82] P. Grieco, A. Bahas, Role reversal in the cyclocondensation of cyclopentadiene with heterodienophiles derived from aryl amines and aldehydes: Synthesis of novel tetrahydroquinolines. *Tetrahedron Lett.* 29 (1988) 5855–5858.
- [83] P. Grieco, S.D. Larsen, Iminium ion-based Diels–Alder reactions: N-benzyl-2-azanorbornene. *Org. Synth.* 68 (1990) 206.
- [84] P. Grieco, S.D. Larsen, Iminium ion-based Diels–Alder reactions: N-benzyl-2-azanorbornene 2-azabicyclo[2.2.1]hept-5-ene, 2-(phenylmethyl)-]. *Org. Synth. Coll.* 8 (1993) 31.
- [85] A.R. Katritzky, S. Rachwal, B. Rachwal, Recent progress in the synthesis of 1,2,3,4-tetrahydroquinolines. *Tetrahedron* 52 (1996) 15031–15070.
- [86] A. Kiselyov, R.W. Armstrong, Solid support synthesis of tetrahydroquinolines via the Grieco three component condensation. *Tetrahedron Lett.* 38 (1997) 6163–6166.
- [87] V. Jurcik, R. Wilhelm, Imidazolinium salts as catalysts for the aza-Diels–Alder reaction. *Org. Biomol. Chem.* 3 (2005) 239–244.
- [88] P. Dubois, G. Marchand, S. Gmouh, M. Vaultier, Reaction Rates as a Function of Scale within Ionic Liquids: Microscale in Droplet Microreactors versus Macroscale Reactions in the Case of the Grieco Three-Component Condensation Reaction. *Chem. A Eur. J.* 13 (19) (2007) 5642–5648.

DMF for Optofluidic Microdevices^{*}

11

CHAPTER OUTLINE

11.1 Introduction	421
11.2 Electrowetting screen display	422
11.2.1 Principle.....	423
11.2.2 Pixel actuation and dewetting.....	424
11.2.3 Virtual confinement and Laplace's barriers.....	426
11.2.4 Perspectives	426
11.3 Tunable lens.....	427
11.3.1 Introduction.....	427
11.3.2 Principle.....	428
11.4 Electrowetting-actuated micromirrors	433
11.5 Polymer dispersed liquid crystals	436
11.6 Conclusion	437
References	437

11.1 Introduction

Optofluidics is a research field at the intersection of microfluidics and optics [1]. In reality optofluidics is a vast domain that spans from the observation of phenomena occurring in microflows, to optical devices actuated by microfluidics, and to active actuation of microsystems using light emission.

Optofluidics can be divided into two main categories: (1) the action of light (laser for example) on microflows and objects transported by microfluidic means and (2) the use of microfluidics to build new optical devices.

In the first category, a characteristic example is the optical tweezer. In this case, the use of a highly focused laser beam provides an attractive or repulsive

*This chapter has been written with the collaboration of Kenneth A. Brakke.

force depending on the refractive index mismatch to hold or move dielectric objects [2].

Typical examples of the second category are liquid lenses and screen displays [3–5]; in such cases, microfluidic actuation acts on the liquid to adopt a morphology that provides desired optical functions, such as a particular lens shape or the opening/closing of a colored pixel.

In this chapter, we focus on the use of DMF, especially electrowetting, for optofluidics. As we will see in some examples, electrowetting is a technique well adapted to optical applications. This approach is sometimes called optoelectrowetting (OEW). The reasons are the very small energy requirement of electrowetting optofluidic systems, the rapidity of the liquid interface displacement, and the very small size of the droplets which agrees well with that of light beams.

In this chapter, we successively present screen displays, tunable liquid lenses, tunable micromirrors, and LCs actuation, all of these applications using electro-wetting techniques.

11.2 Electrowetting screen display

Electrowetting display was imagined as early as the year 1981 by Beni and Hackwood [6]. Figure 11.1 sketches their first display. Since that time, the evolution of electrowetting displays has been very fast, in phase with the development of EWOD techniques. For example, the approach of Beni and Hackwood has

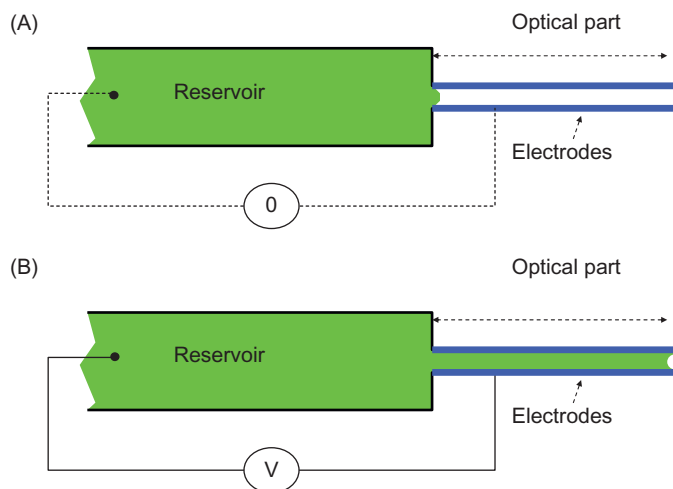


FIGURE 11.1

Sketch of the first electrowetting display proposed by Beni and Hackwood [6]. (A) When electric actuation is turned off, the water is confined to the reservoir and (B) when actuation is turned on, water penetrates the optical channel, changing the optical properties.

been revisited by Shamai and colleagues [7,8] and Heikenfeld and colleagues [4] to build an electrowetting display (Figure 11.2). Electronic screen display using electrowetting is now in a mature state and the commercial applications are beginning to appear on the market for mobile phones and laptop screens [9].

In this section, we present the general principle of electrowetting display and we analyze in detail the microfluidic behavior occurring in each pixel upon electric actuation.

11.2.1 Principle

In this section, we focus on the most widely known Liquavista® electrowetting screen display. This screen display is constituted by a matrix of pixels. Each pixel is filled by two immiscible liquids.

Let us now follow the demonstration of Zhou and colleagues [10], and consider first the principle of reverse electrowetting, described in Figure 11.3A and B. In the absence of electric actuation the oil droplet spreads on the hydrophobic (lyophilic) substrate. The Young's contact angle oil–water–dielectric is small; however, the water–oil–dielectric contact angle θ_Y is large. When the electrode is actuated, the contact angle decreases and the colored oil droplet contact with the solid substrate becomes small.

If the initial oil droplet is limited by a hydrophobic grid, the initial shape of the oil droplet is nearly an oil film limited by the grid (Figure 11.3C). When actuated, the oil recedes in the corners near the hydrophobic grid, and the pixel is now mostly covered by water. If the oil is tainted, the pixel changes color upon electrowetting actuation. Using a stack of superposed pixel, a complete set of colors can be reproduced.

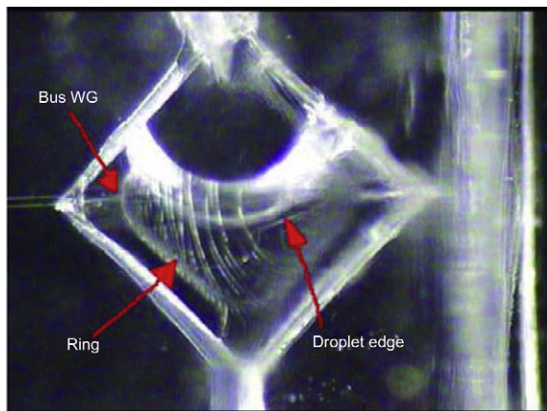
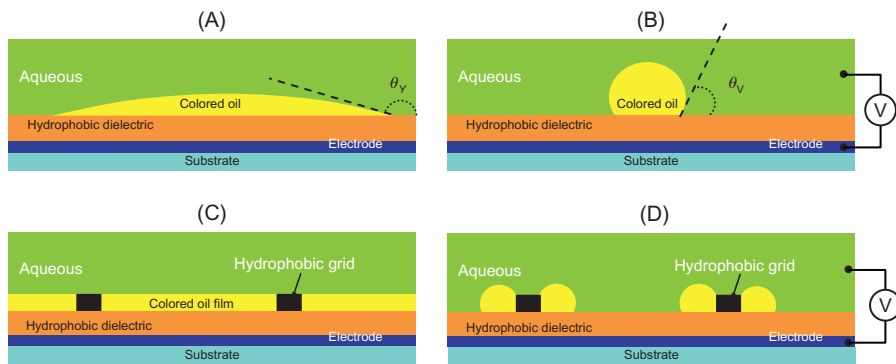


FIGURE 11.2

A modern approach of principle of Figure 11.1. The liquid penetrates the optical part upon electrowetting actuation, changing the transmission spectrum.

Source: Reprinted with authorization from Ref. [7]; © 2008 Optical Society of America.

**FIGURE 11.3**

(A) A colored oil droplet spreads on the hydrophobic dielectric; (B) after actuation of the electrode, the contact angle of water with the substrate decreases and the oil droplet takes a lyophobic shape (reverse electrowetting); (C) the presence of hydrophobic grid leads to the formation of an oil film; and (D) upon actuation, the film is broken and the oil is pushed toward the hydrophobic grids. Sketch inspired by the work of Zhou and colleagues [10].

11.2.2 Pixel actuation and dewetting

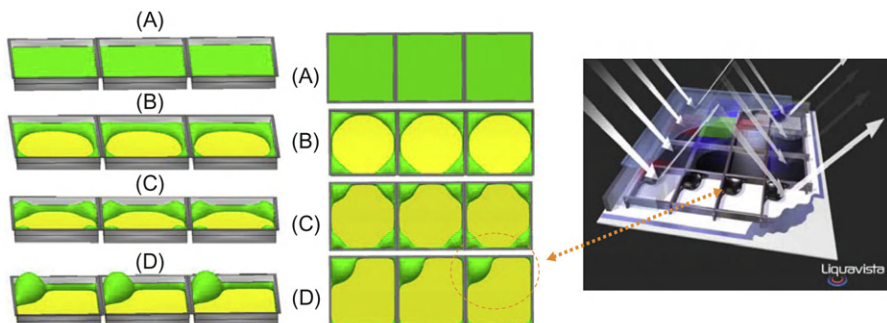
The wetting/dewetting mechanism can be investigated with Evolver [11], even if this numerical program does not treat dynamics. In fact, the capillary adjustment of an interface—governed by the capillary time, also called Tomotika time—is extremely fast, of the order of 10^{-6} s, and the volume of liquid so small that a quasi-static approach can be used.

Let us recall that the capillary time characterizes the time taken by a distorted interface to regain its equilibrium shape by the action of surface tension working against viscosity [12]. It is given by the ratio

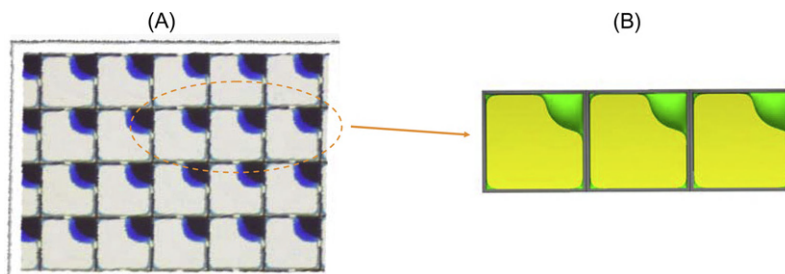
$$\tau_{\text{capillary}} = \frac{\eta R}{\gamma}, \quad (11.1)$$

where η is the fluid viscosity, R a characteristic dimension of the surface—in our case the pixel dimension—and γ the surface tension. Using an oil viscosity value of $\eta = 10 \cdot 10^{-3}$ Pa s, a typical pixel dimension of $10 \mu\text{m}$; and a surface tension between water and oil $\gamma = 30 \cdot 10^{-3}$ N/m, we obtain $\tau_{\text{capillary}} < 3 \cdot 10^{-6}$ s.

Figure 11.4 shows the behavior of the system upon actuation. Once the actuation is turned on, the electric field bends the oil–water surface and water contacts the hydrophobic dielectric. The water–oil–dielectric actuated contact angle is such that water repels the oil which recedes toward the four sides of the box, and further to the four corners. However, capillary stability is not achieved when liquid oil is pushed back in the four corners. A Laplace’s pressure effect

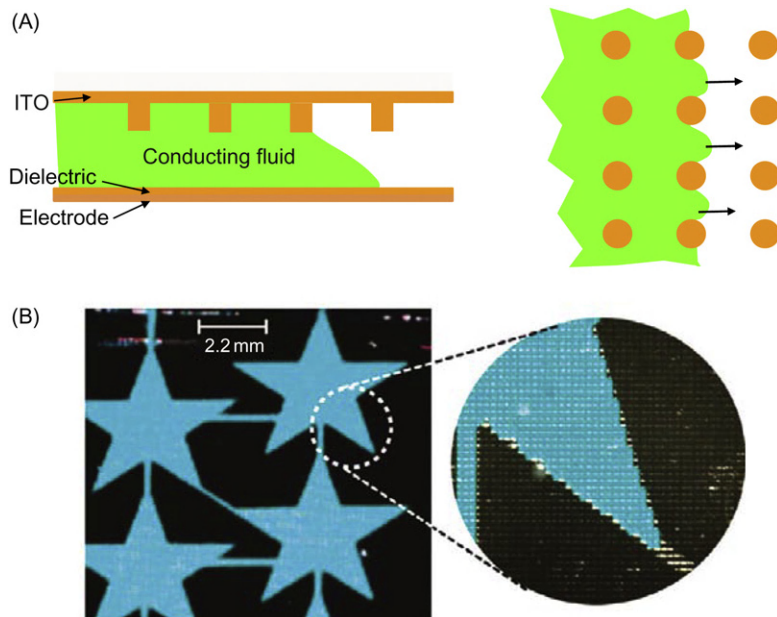
**FIGURE 11.4**

Left and middle: modeling of pixel dewetting with Evolver: (A) not actuated state; (B) immediately upon actuation dewetting starting; (C) liquid oil is expelled to the corners; and (D) in the numerical model, liquid oil is drained alongside the walls toward a unique corner due to Laplace's law (the corner droplet of larger size has the smallest pressure). Right: a view from Liquavista® showing the bulging shapes of the droplets after actuation.

**FIGURE 11.5**

(A) Sketch of the pixel matrix from Liquavista® and (B) modeling of three pixels with the Surface Evolver numerical program. The oil film remaining in the opposite corners to the droplet can be seen in the calculation as well as in the experimental view.

occurs because liquid oil bridges remain along the sides linking the four blobs in the corners. The situation is unstable. Any small amount of pressure or volume variation in a blob destabilizes the metastable equilibrium of the system: for example, if a blob has a slightly larger volume, its Laplace's pressure is lower than the neighboring liquid blobs and oil is flowing from these neighboring blobs toward the low pressure blob. Finally, an oil droplet forms in a corner, with a ring of oil remaining around the pixel walls. This slowly draining oil film can be seen in [Figure 11.5](#). Note that in the numerical modeling, the destabilizing effect is triggered by any slight difference in the shapes of the four initial blobs linked to the numerical noise.

**FIGURE 11.6**

(A) Principle of Laplace's barriers. The post, partially blocking the channel stabilizes the liquid interface. (B) The liquid interface follows any shape, even with sharp or reentrant angles.

Source: Reprinted with permission from Ref. [13] © RCS 2010.

11.2.3 Virtual confinement and Laplace's barriers

Another kind of display has been developed by Jason Heikenfeld's group [13,14]. Their approach is based on the “virtual confinement” concept based on the so-called Laplace's barriers. The principle of Laplace's barriers is shown in Figure 11.6. The underlying idea is to combine capillarity and electrowetting to force the liquid to adopt the desired shapes, even if these shapes have sharp reentrant angles (Figure 11.7).

To our mind, the combination of electrowetting and capillarity is a promising development, and not only for optofluidics.

11.2.4 Perspectives

It is expected that electrowetting-based screen displays (ESD) are going to be currently used for many electronic instrument displays, such as mobile phones, kindles, and laptops. Such devices have many advantages: first they operate at a very low level of electric power, and this is a determining advantage for portable, autonomous devices working on batteries. A second advantage is the brightness

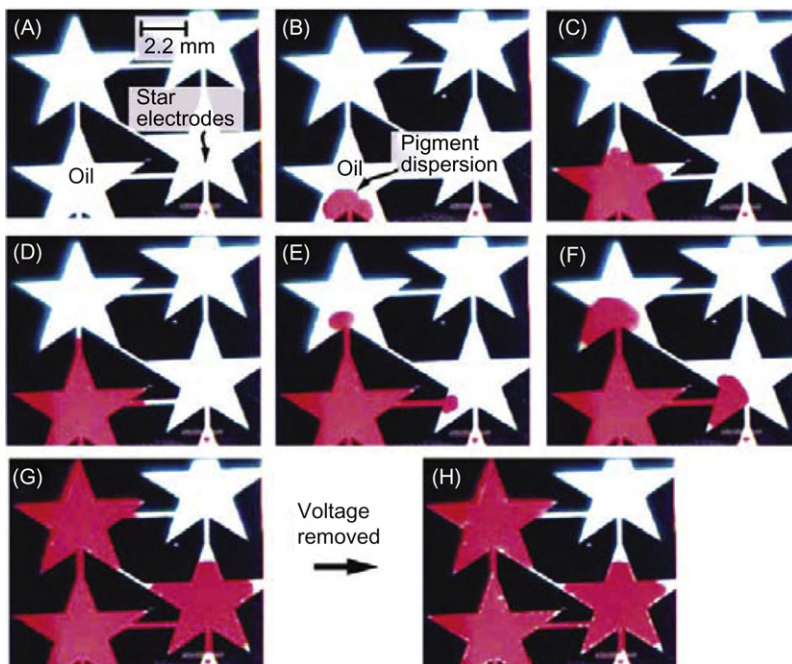


FIGURE 11.7

Star electrode filling on an arrayed ridge device in nonpolar oil: (A) unfilled device; (B–G) time lapse of device filling; and (H) voltage removed. The liquid stays in place after the shut-off of the actuation. Images obtained with a light-field microscope.

Source: Reprinted with permission from Ref. [13] © RCS 2010.

of the display: the screen can be seen even in a bright environment. With the development of EWOD on curved surface (see Chapter 7), electrowetting-based displays are going to be adapted to flexible surfaces, leading to many new applications, some even unforeseen at the present time. Finally, the speed at which the interfaces can relocate is very high and display can be extremely fast.

11.3 Tunable lens

In this section, we show how electrowetting has been used to build tunable liquid lenses.

11.3.1 Introduction

It is a common observation that droplets focus light as liquid lenses. Droplets deposited on book paper—or close to the surface—enlarge the writing behind (Figure 11.8). As early as the seventeenth century, the English scientist

**FIGURE 11.8**

A water drop in air can focus light like a lens.

Source: From Ref. [5], photograph Gady Fishel.

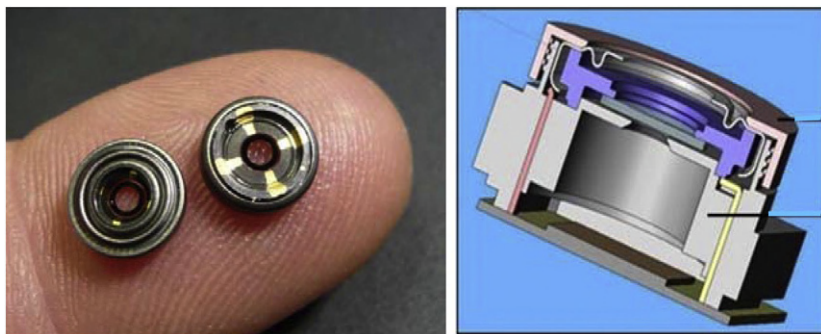
Stephen Gray used a water drop as a lens for a microscope he built. In 1696, he published an article in the Philosophical Transactions of the Royal Society describing an instrument called the “Water Microscope” [15]. This instrument was one of the earliest experimental microscopes using materials other than glass to make a microscope lens.

This smart invention was however very unpractical. The modern micro- and nanotechnologies have revived Stephen Gray’s approach to build liquid-based tunable lenses, using the principle of electrowetting. In this section, we present the principles of electrowetting-based tunable lenses.

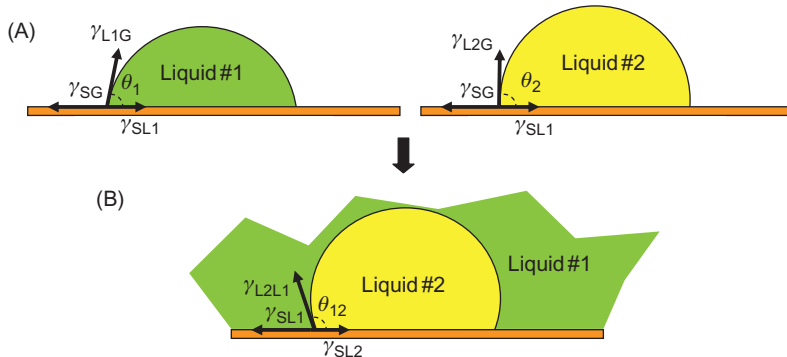
11.3.2 Principle

Bruno Berge, one of the founders of EWOD with the so-called BLY equation, is one of the pioneers of the development of tunable liquid lenses [16] (Figure 11.9). In such a device, a droplet of liquid oil is placed in a sealed chamber filled with water. Two thin, parallel, flat glass plates sandwich the microchamber. A similar design has been investigated by Ren and Wu [17].

The system is directly based on the electrowetting principle with an aqueous, conductive phase and an organic, non conductive phase. The equation derived from Young’s law that predicts the contact angle between two immiscible liquids is called the Bartell–Osterhof’s equation [18]. This equation is obtained by considering first the Young’s law for each liquid separately and then the Young’s

**FIGURE 11.9**

Miniaturized tunable liquid lenses for medical applications by Varioptics®.

**FIGURE 11.10**

(A) Contact of droplets of liquid 1 and liquid 2 surrounded by air or gas. (B) Contact of a droplet of liquid 2 immersed in liquid 1.

law for the two liquids. A combination of the three equations produces the liquid–liquid–solid contact angle (Figure 11.10).

Young's law for the first liquid is

$$\gamma_{L1,G} \cos(\theta_{L1,G,S}) = \gamma_{S,G} - \gamma_{S,L1} \quad (11.2)$$

and for the second liquid

$$\gamma_{L2,G} \cos(\theta_{L2,G,S}) = \gamma_{S,G} - \gamma_{S,L2}. \quad (11.3)$$

The difference of Eqs. (11.2) and (11.3) yields

$$\gamma_{L1,G} \cos(\theta_{L1,G,S}) - \gamma_{L2,G} \cos(\theta_{L2,G,S}) = \gamma_{S,L2} - \gamma_{S,L1} \quad (11.4)$$

If liquid 2 is immersed into liquid 1, Young's law yields

$$\gamma_{L1,L2} \cos(\theta_{L1,L2,S}) = \gamma_{S,L1} - \gamma_{S,L2}. \quad (11.5)$$

From Eqs. (11.4) and (11.5), we deduce the Bartell–Osterhof's relation

$$\cos(\theta_{L1,L2,S}) = \frac{\gamma_{L2,G} \cos(\theta_{L2,G,S}) - \gamma_{L1,G} \cos(\theta_{L1,G,S})}{\gamma_{L1,L2}}. \quad (11.6)$$

Surface tensions can easily be measured (by the pendant drop method for example), and if the two contact angles in air $\theta_{L1,S,G}$ and $\theta_{L2,S,G}$ are known—or measured with a goniometer—the contact angle $\theta_{L1,L2,S}$ is given by

$$\theta_{L1,L2,S} = \arccos \left[\frac{\gamma_{L2,G} \cos(\theta_{L2,G,S}) - \gamma_{L1,G} \cos(\theta_{L1,G,S})}{\gamma_{L1,L2}} \right]. \quad (11.7)$$

A graphical interpretation of the Bartell–Osterhof's equation has been simultaneously proposed in Refs. [12] and [19].

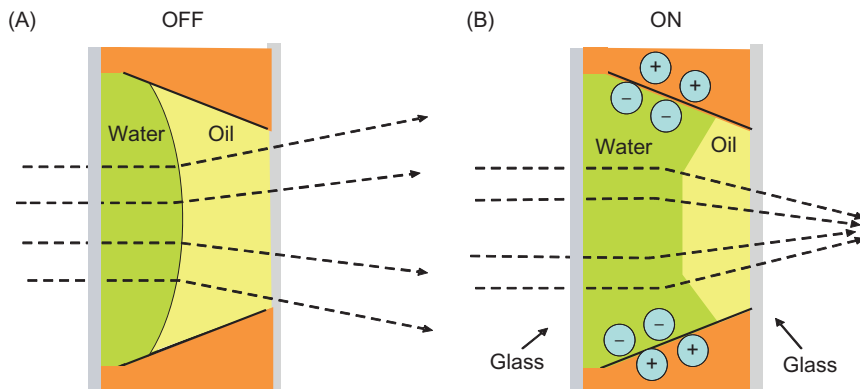
When not actuated, because the surface of the electrodes is coated by a hydrophobic dielectric layer, the oil phase wets partially the electrodes and the interface between oil and water is concave (relative to the oil phase). When actuated, the contact angle of the water with the electrodes decreases—conversely that of oil increases—and the interface shape changes progressively with the magnitude of the actuation voltage. Above a certain voltage, the interface becomes convex (relative to the oil phase), and the focal point can be adjusted by tuning the magnitude of the applied voltage (Figure 11.11).

Another interesting potentiality of the system is the orientation of the focalization of a beam (Figure 11.12). An asymmetric configuration can be obtained by using an independent set of electrodes, resulting in a tilted water–oil interface. Depending on the actuation voltage, the tilt can be adjusted and the focalization changed.

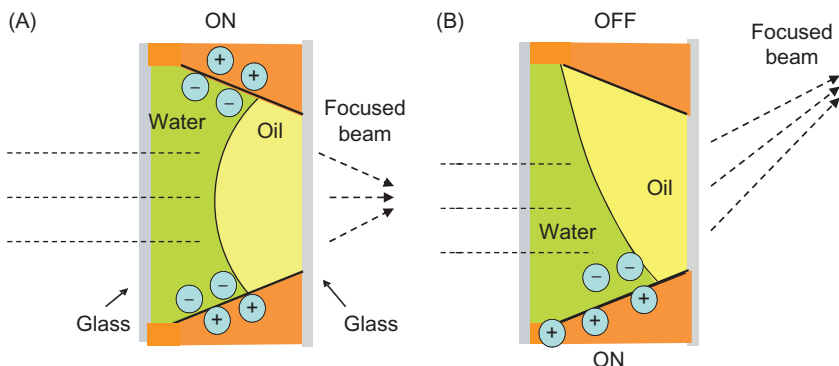
Finally, the system can be reversed, with the oil phase toward the incoming light beam (Figure 11.13). Depending on the actuated electrodes, the beam can be deflected upward or downward.

These different configurations of liquid lens can be modeled with the Evolver. Figures 11.14 and 11.15 show the results of the modeling of water–liquid interface for different contact angles.

Note that the tilting of the water–oil interface by an asymmetric actuation induces auxiliary problems: the Evolver predicts that a stable nonsymmetric configuration requires the pinning of the interface to stop the continuous

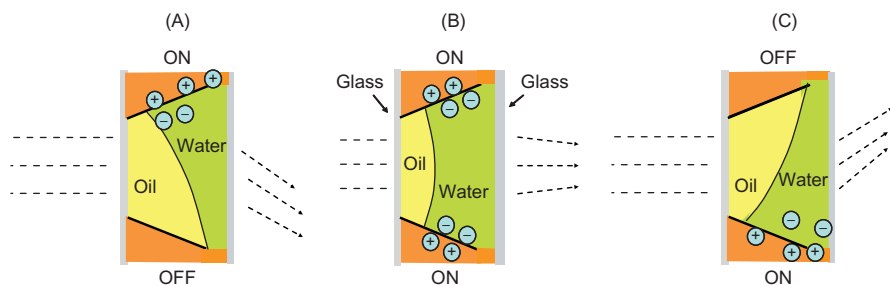
**FIGURE 11.11**

(A) The electrodes are not actuated and the interface has its natural concave shape (respectively to the oil phase) and (B) the electrodes are actuated and the interface adopts a convex shape (respectively to the oil phase).

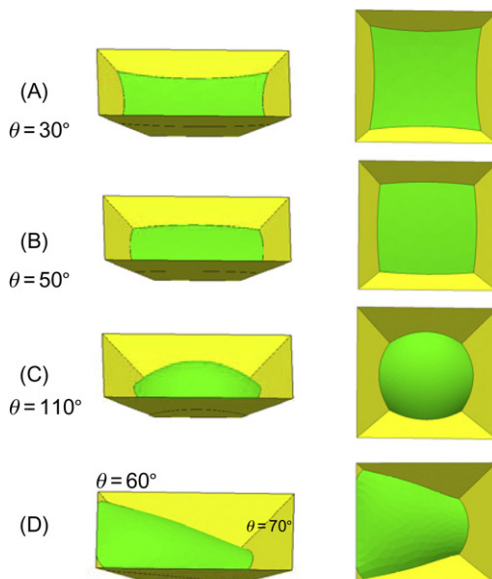
**FIGURE 11.12**

(A) Symmetrically actuated liquid lens focusing light on the central axis; (B) asymmetrical liquid lens switching the focus point laterally.

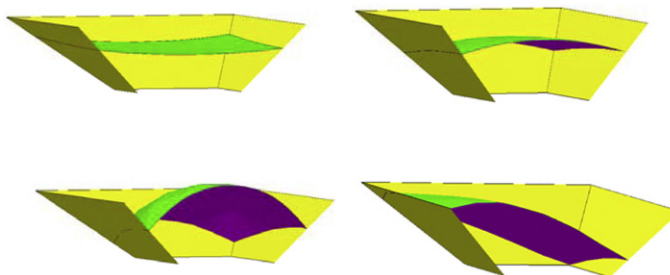
motion that would be triggered by the unequal contact angles. In the real device, this pinning is achieved by the presence of a sharp ridge. The numerical results presented above very closely agree with the experimental observations of Krogmann and colleagues [3] for the same geometry, as shown in Figure 11.16.

**FIGURE 11.13**

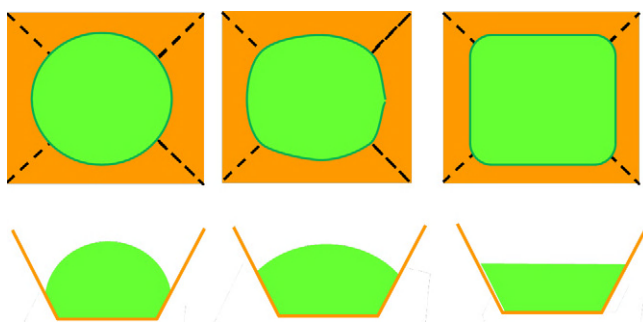
Reversed use of the liquid lens: (A) the light beam is deflected downward; (B) is not deflected; (C) is deflected upward, depending on the actuation of one or two electrodes.

**FIGURE 11.14**

(A–C) Three different shapes of the water–oil interface depending on the contact angle (i.e., electric actuation). The interface switches from a concave shape when there is no electrical actuation to a convex shape which becomes more accentuated with the increase in the oil–wall contact angle. (D) An asymmetrical actuation results in a slanted lens shape. In order to obtain a stable interface, a pinning (on an angle for example) of the interface is required, else the liquid motion after actuation would not stop. (All figures are obtained with the Surface Evolver numerical program.)

**FIGURE 11.15**

Slice of the liquid lens showing the different curvatures of the interface; the calculations correspond to the four different cases of the preceding figure.

**FIGURE 11.16**

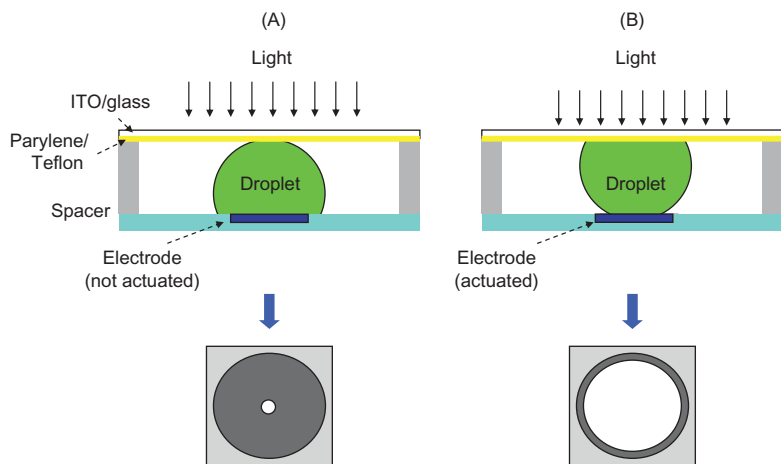
Different shapes of the liquid lens observed by Krogmann and colleagues.

Source: Reprinted with permission from Ref. [3] © IEEE/ASME 2008.

11.4 Electrowetting-actuated micromirrors

Microoptical systems and micromirrors are essential for optical switching, scanning, modulating, and imaging. It has been found that the electrowetting effect was well adapted to the actuation of micromirrors [20,21]. The following example illustrates this remark: consider a liquid metal droplet—like mercury, with a high surface tension and no evaporation—placed in a closed EWOD device (Figure 11.17).

The system is designed so that, when the actuation is shut off, the contact of the droplet with the upper ITO plate is minimal. In other words, the contact angle of the mercury with the parylene-coated ITO is of the order of 150° , while the contact angle of the mercury with the bottom substrate is of the order of 85° , and the droplet volume is carefully adjusted to minimize the contact with the cover plate—without suppressing it. In such a case, the incoming light is not reflected and the micromirror is OFF.

**FIGURE 11.17**

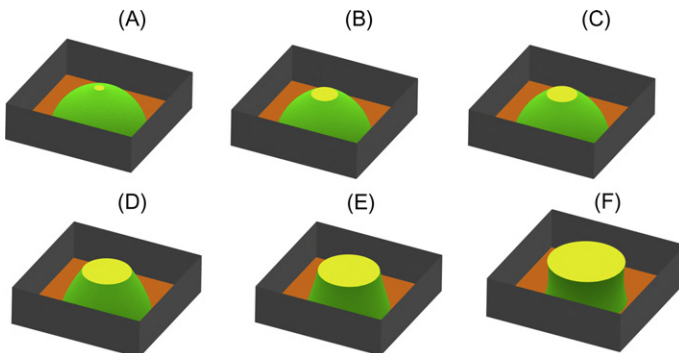
Principle of electrowetting actuated micromirrors [20]: (A) when the electrode is not actuated, the droplet is sitting on the bottom substrate and just touching the upper plate (ITO cover coated with a thin layer of parylene) and (B) after actuation the contact angle with the parylene decreases and the droplet moves up to wet the ITO–parylene cover plate.

When the actuation is turned on, the contact angle with the cover plate decreases—to $\sim 80^\circ$ —because of the electrowetting effect. The droplet then contacts the top cover reflecting the incoming light. The micromirror is ON, reflecting the incoming light.

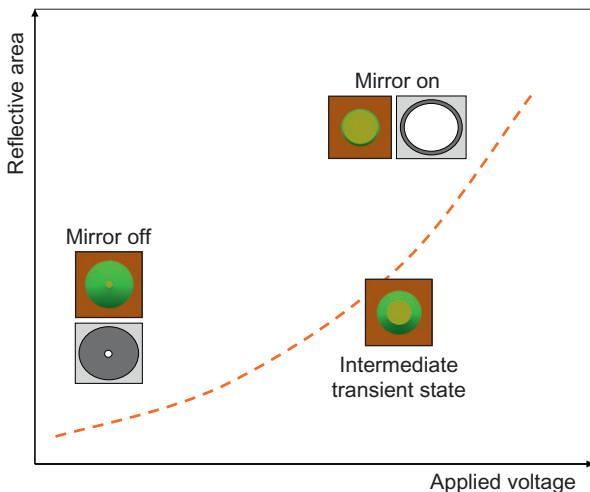
A model for the droplet can be done with the numerical program Evolver. Figure 11.18 shows the different shapes of the droplet depending on the contact angle. The influence of gravity cannot be neglected here because the density of mercury is large ($13,500 \text{ kg/m}^3$), and the closed form relations proposed by Berthier and Brakke [22] cannot be used in this particular case.

The contact area of the droplet with the cover plate varies nonlinearly with the contact angle: it increases rapidly at the beginning with the decreasing contact angle; then the increase rate progressively slows down. This is in agreement with the experiment. Figure 11.19 sketches the reflective area versus the applied voltage, according to Ref. [21]. Images from the numerical program Surface Evolver have been superposed to show the liquid contact with the cover plate. According to the observations of Wan and colleagues [21], less than $1/3 \text{ ms}$ is required to switch from a closed to open mirror configuration. Note that the capillary time (Tomotika time) for liquid mercury for a $100 \mu\text{m}$ radius droplet is

$$\tau = \frac{\eta R}{\gamma} \approx \frac{0.05 \cdot 10^{-4}}{0.49} \approx 10^{-5} \text{ s.} \quad (11.8)$$

**FIGURE 11.18**

Different droplet shapes with varying actuation contact angle. The contact angle at the bottom is 75° in all cases, and the vertical distance between the plates is $300\ \mu\text{m}$. The contact angle with the cover plate (dematerialized in the figure) is (A) 152° , (B) 145° , (C) 140° , (D) 120° , (E) 100° , and (F) 80° .

**FIGURE 11.19**

Reflective area as a function of the applied voltage: the mirror is off at low voltages, while it is on at higher voltages (80 V). The sketches on the figures have been obtained with the Evolver.

Hence, the switch time is limited by the electrowetting actuation system (0.2 ms), not by the capillary adjustment. In order to have a more usable system, gallium indium tin droplets are presently being substituted to mercury.

11.5 Polymer dispersed liquid crystals

Fan and colleagues have found that EWOD can be selected for their optical properties (Figure 11.20). For example, an EWOD layer could be a PDMS layer loaded with LCs [23]. They called such a matrix PDLC, standing for polymer dispersed LC.

On the one hand, from an EWOD standpoint, all the usual droplet manipulations can be performed on such structures: transport, merging, and splitting of droplets have been proved to be working (at 1 kHz and 100 V_{rms}). On the other hand, the materials are inherently transparent to light: it is the case of the Teflon layer (if the layer is thin enough), of the glass substrate, ITO electrode, and water. The only switchable material is constituted by the LCs.

Inside an LC droplet in the nematic phase, the configuration of the directors (long axes) of the LC molecules is determined by the LC droplet shape and size, the anchoring condition to the polymer matrix at the LC droplet surfaces, the applied electric field, and the elastic constant of the LC [24].

Before voltage application, the directors between individual LC droplets are random. The incident light is strongly scattered and the transmittance of the layer is reduced. The media is then opaque to light.

When sufficient voltage is applied between the top probe and the PDLC-covered bottom electrode, the directors of the LC droplets covered by the water droplet are reoriented parallel to the direction of the electric field. The PDLC becomes highly transparent along the direction of the electric field.

In summary, PDLC thin films can serve as a dielectric layer in electrowetting devices. When applying a voltage across the PDLC thin film, its surface wettability and transmittance are simultaneously changed. Basic liquid lens functions and droplet manipulations are then compatible.

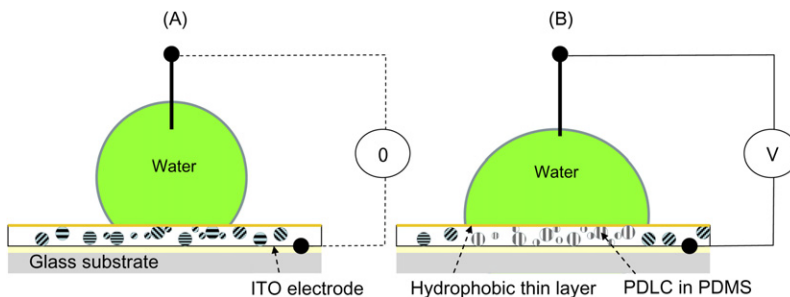


FIGURE 11.20

Sketch of a PDLC dielectric layer for electrowetting: (A) in absence of actuation, no electric charges are present in the solid layers and the LCs are oriented randomly; the PDLC-PDMS solid layer is opaque; (B) when the actuation is turned on, electric charges accumulate at the liquid–solid surface, the LCs are oriented parallel to the electric field, the substrate is then transparent to light.

11.6 Conclusion

This chapter is dedicated to the applications of DMF—especially EWOD—for optics. The domain of EWOD-operated optofluidics is wide and only a few typical examples have been given in this chapter.

EWOD technology is particularly well adapted to optics because the reconfiguration time of the droplet is extremely short—often less than 10^{-6} s—and the size of the droplet is small enough for miniaturized optical applications. Besides the electric energy requirement for operating such optical systems is very low; it is a definite advantage for portable and autonomous systems for which the autonomy of the batteries is a key issue. Citing Psaltis et al. [1], “the synergy between optics and fluids is particularly rich.”

References

- [1] D. Psaltis, S.R. Quake, C. Yang, Developing optofluidic technology through the fusion of microfluidics and optics, *Nature* 442 (2006) 7101.
- [2] A. Ashkin, Acceleration and trapping of particles by radiation pressure, *Phys. Rev. Lett.* 24 (4) (1970) 156–159.
- [3] F. Krogmann, W. Mönch, H. Zappe, Electrowetting for tunable microoptics, *J. Microelectromech. Syst.* 17 (6) (2008) 1501.
- [4] J. Heikenfeld, K. Zhou, E. Kreit, B. Raj, S. Yang, B. Sun, et al., Electrofluidic displays using Young–Laplace transposition of brilliant pigment dispersions, *Nat. Photonics* 3 (2009) 292–296.
- [5] R. Shamai, D. Andelman, B. Berge, R. Hayes, Water, electricity, and between...On electrowetting and its applications, *Soft Matter*. 4 (2008) 38–45.
- [6] G. Beni, S. Hackwood, Electro-wetting displays, *Appl. Phys. Lett.* 38 (1981) 207–209.
- [7] R. Shamai, U. Levy, On chip tunable micro ring resonator actuated by electrowetting, *Opt. Express* 17 (2009) 1116–1125.
- [8] Y. Fainman, L.P. Lee, D. Psaltis, C. Yang, Optofluidics: Fundamentals Devices, and Applications, McGraw-Hill, 2010.
- [9] R.A. Hayes, B.J. Feenstra, Video-speed electronic paper based on electrowetting, *Nature* 425 (2003) 383–385.
- [10] K. Zhou, J Heikenfeld, K.A. Dean, E.M Howard, M.R. Johnson, A full description of a simple and scalable fabrication process for electrowetting displays, *J. Micromech. Microeng.* 19 (2009) 065029.
- [11] K. Brakke, The surface evolver, *Exp. Math.* 1 (2) (1992) 141–165.
- [12] J. Berthier, P. Silberzan, Microfluidics for Biotechnology, second ed., Artech House, Norwood, MA, 2012.
- [13] E. Kreit, M. Dhindsa, S. Yang, M. Hagedon, K. Zhou, I. Papautsky, et al., Laplace barriers for electrowetting thresholding and virtual fluid confinement, *Langmuir* 26 (23) (2010) 18550.
- [14] E. Kreit, B.M. Mognetti, J.M. Yeomans, J. Heikenfeld, Partial-post Laplace barriers for virtual confinement, stable displacement, and $>5\text{ cm s}^{-1}$ electrowetting transport, *Lab Chip* 11 (2011) 4221.

- [15] S. Gray, A further account of the water microscope, *Philos. Trans. Royal Acad. Sci.* 19 (1696) 121.
- [16] B. Berge, J. Peseux, Variable focal lens controlled by an external voltage: an application of electrowetting, *Eur. Phys. J. E* 3 (2000) 159.
- [17] H. Ren, S.-T. Wu, Variable-focus liquid lens, *Opt. Express* 15 (10) (2007) 5931.
- [18] F.E. Bartell, H.H. Zuidema, Wetting characteristics of solids of low surface tension such as talc, waxes and resins, *J. Am. Chem. Soc.* 58 (1936) 1449.
- [19] M. Maillard, J. Legrand, B. Berge, Two liquids wetting and low hysteresis electrowetting on dielectric applications, *Langmuir* 25 (11) (2009) 6162–6167.
- [20] H. Zeng, A.D. Feinerman, Z. Wan, P.R. Patel, Piston-motion micromirror based on electrowetting of liquid metals, *J. Microelectromech. Syst.* 14 (2) (2005) 285.
- [21] Z. Wan, H. Zeng, A. Feinerman, Area-tunable micromirror based on electrowetting actuation of liquid-metal droplets, *Appl. Phys. Lett.* 89 (2006) 201107.
- [22] J. Berthier, K. Brakke, *The Physics of Microdroplets*, Scrivener Publishing, Beverly, MA, 2012.
- [23] S.-K. Fan, C.-P. Chiu, J.-W. Lin, Electrowetting on polymer dispersed liquid crystal, *Appl. Phys. Lett.* 94 (2009) 164109.
- [24] J.H. Erdmann, S. Zumer, J.W. Doane, Configuration transition in a nematic liquid crystal confined to a small spherical cavity, *Phys. Rev. Lett.* 64 (1990) 1907.

Droplet on Deformable Surfaces—Elasto-Capillarity and Electro-Elasto-Capillarity 12

CHAPTER OUTLINE

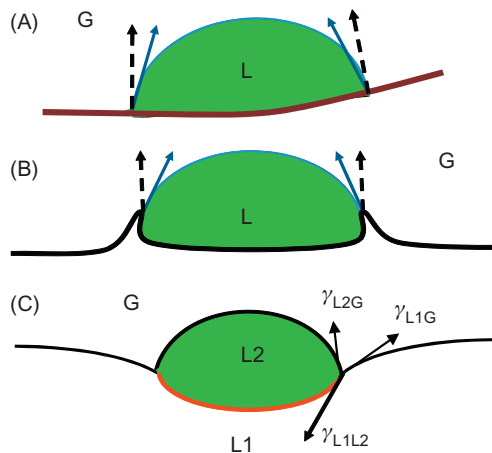
12.1 Introduction	439
12.2 Neumann's construction	440
12.3 Sessile droplet on a deformable substrate	441
12.4 Example of a cantilever	443
12.5 Elasto-capillarity and capillary origami	445
12.6 Electro-elasto-capillarity	447
12.7 Droplet at a liquid interface.....	448
12.7.1 Introduction: the difference between liquid droplets and rigid spheres at an interface.....	449
12.7.2 Behavior of a droplet on an immiscible liquid surface	450
12.7.3 Spreading and engulfment	452
12.7.4 Engulfment with gravity	453
12.8 Conclusion	455
References	455

12.1 Introduction

Young's law is currently used in droplet and interface microfluidics. However, one does not always realize that Young's law has been derived for a liquid contacting a solid nondeformable substrate. It is a balance of the projections on the substrate plane of the surface tension forces, namely for a solid–liquid–gas contact

$$\gamma_{LG} \cos \theta = \gamma_{SG} - \gamma_{SL}, \quad (12.1)$$

where indices S, L, and G stand for solid, liquid, and gas. In the case of a deformable substrate, the problem becomes more complex. This is the aim of this chapter.

**FIGURE 12.1**

Neumann's construction: (A) a sessile droplet bends a sensitive cantilever beam; (B) a sessile droplet deforms the surface of a viscoelastic medium (gel, for example); and (C) a droplet deposited on the surface of an immiscible liquid (G stands for gas, L for liquid).

The starting point is to remark that the surface tension force balance should also be valid on a normal to the surface. This problem was first examined by Neumann [1] in the year 1894; the equilibrium condition requires that

$$\vec{\gamma}_{L1L2} + \vec{\gamma}_{L1G} + \vec{\gamma}_{L2G} = \rightarrow 0. \quad (12.2)$$

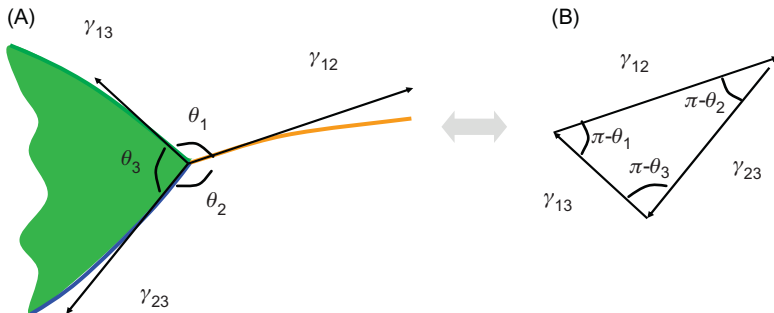
This relation—also called Neumann's construction—is a vector relation. **Figure 12.1** shows how the local morphology adapts to obtain the balance of the vertical projections of the surface tensions.

In this chapter, we first give some details about the Neumann's relation, and then we investigate the problem of a sessile droplet on a deformable substrate, taking the example of the microcantilever. Next, it is shown that, when the substrate is a thin elastic sheet, a capillary “origami” is obtained. Then, we show that electric forces can contribute to the deformation of the substrate. Finally, the problem of droplets at interfaces is presented.

12.2 Neumann's construction

Neumann's relation (12.2) is best seen for the contact of three immiscible fluids. **Figure 12.2** corresponds to such a case. The vector sum of the surface tensions must be zero, as shown in the right part of **Figure 12.2** [2].

The surface tensions between components 1, 2, and 3 can be assumed to be known quantities; at least they can be measured. The problem concerns the determination of

**FIGURE 12.2**

Neumann's construction: (A) the three surface tensions at the junction of three immiscible fluids; (B) Neumann's triangle.

the contact angles. It is only in the case of a rigid substrate that Young's law provides an easy way to determine the contact angle. In the case of immiscible liquids and/or deformable solids, such as gels, the determination of the contact angles requires numerical modeling [3]. Just an analytical relation between the contact angles θ_1 , θ_2 , and θ_3 exists; it is obtained by basic geometry using the triangle heights

$$\frac{\gamma_{12}}{\sin \theta_3} = \frac{\gamma_{23}}{\sin \theta_1} = \frac{\gamma_{31}}{\sin \theta_2}. \quad (12.3)$$

12.3 Sessile droplet on a deformable substrate

We examine first the problem of a sessile droplet on a deformable substrate. Figure 12.3 sketches the deformation of the substrate—with exaggeration for better visualization—at the contact of the droplet.

Let us follow the reasoning of Roman and Bico [4]. The normal force per unit length exerted by the droplet is

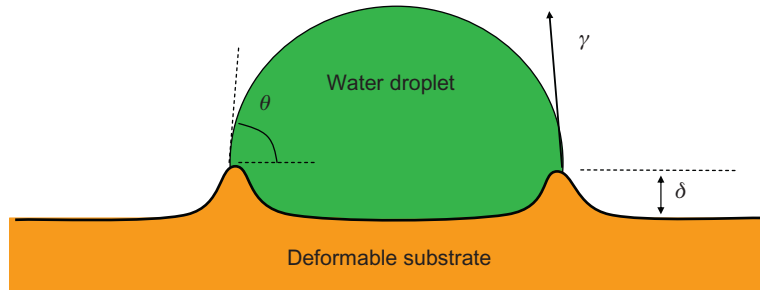
$$f \approx \gamma \sin \theta. \quad (12.4)$$

This force pulls up the deformable substrate along the contact line [5]. However, if δ is the typical amplitude of deformation of the pinched region, the corresponding force per unit length is of the order of

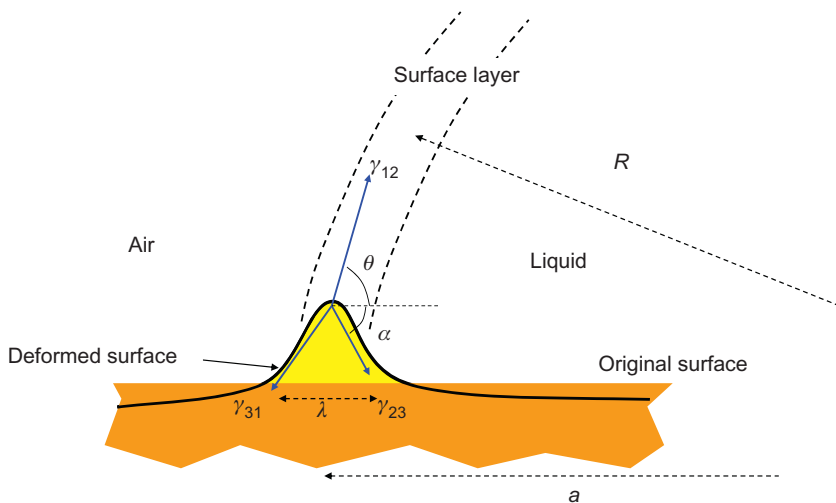
$$f \approx E\delta, \quad (12.5)$$

where E is the Young's modulus of the substrate [6]. Combining Eqs. (12.4) and (12.5) yields

$$\delta \approx \frac{\gamma \sin \theta}{E}. \quad (12.6)$$

**FIGURE 12.3**

Sketch of a sessile droplet deposited on a deformable substrate.

**FIGURE 12.4**

Sketch of the interface and deformation of the surface.

In the case of a water droplet on a glass substrate, $\gamma = 72 \text{ mN/m}$, and $E \sim 70 \text{ GPa}$, so that $\delta \sim 10^{-12} \text{ m}$, which is not observable. However, if the substrate is a rubbery solid, the Young's modulus is of the order of 70 kPa , and the deformation $\delta \sim 1 \mu\text{m}$, which is noticeable.

Lester [2] has followed an interesting analysis—requiring complicated algebra—resulting in an extended Young's formula. The schema for the reasoning is shown in Figure 12.4 for a liquid–liquid–air system. The substrate is pulled upward by the action of the surface tensions along a ring of width λ .

The equations derived by Lester are:

$$\begin{aligned}\gamma_{12} \cos \theta &= (\gamma_{13} - \gamma_{23}) \cos \alpha \\ \gamma_{12} \sin \theta &= (\gamma_{13} + \gamma_{23}) \sin \alpha \\ \alpha &= \arctan \frac{4\gamma_{12}(1 - \nu^2)}{\pi(\lambda/a)ER}\end{aligned}\quad (12.7)$$

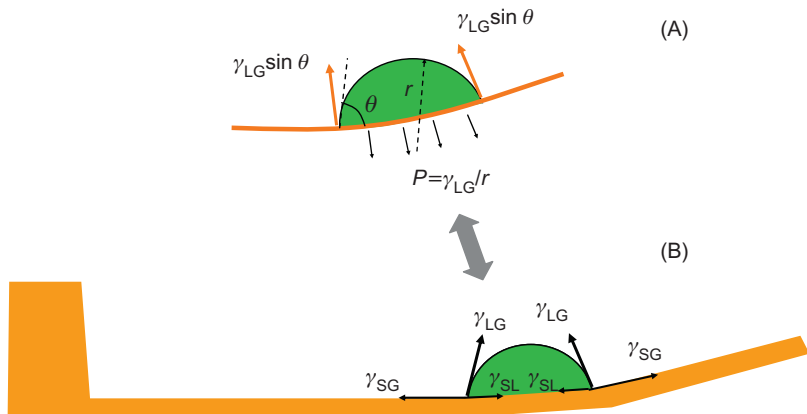
Remark that if the Young's modulus of the substrate E is large, then $\alpha \sim 0^\circ$, $\cos \alpha \approx 1$, $\sin \alpha \approx 0$, and Young's law is retrieved with the first equation in the system in Eq. (12.7). The same remark applies if the droplet radius R is large or if the air–liquid surface tension γ_{12} is small: this could be expected since the normal force (per unit length) is $f \approx \gamma \sin \theta$ and the resultant force along the whole triple line is $F \approx 2\pi a \gamma \sin \theta$: a large radius R and/or a large surface tension $\gamma = \gamma_{12}$ contribute to a large deformation. Note that the quantity $\gamma_{12}/E = \gamma/E$ —which has the dimension of a length—appears in Eq. (12.7) as well as Eq. (12.6). When this quantity is large, the deformation is important.

12.4 Example of a cantilever

Microcantilevers are extremely sensitive devices to measure minute amounts of mass [7,8]. Detection is made by detecting a change of oscillation frequency [9]. The presence of a droplet on a cantilever creates a small bending down of the beam due to the droplet weight, and an upward deflection triggered by the vertical component of the capillary forces along the triple line (Figure 12.5). In this section, we assume that the droplet weight is negligible and we focus on the upward deflection.

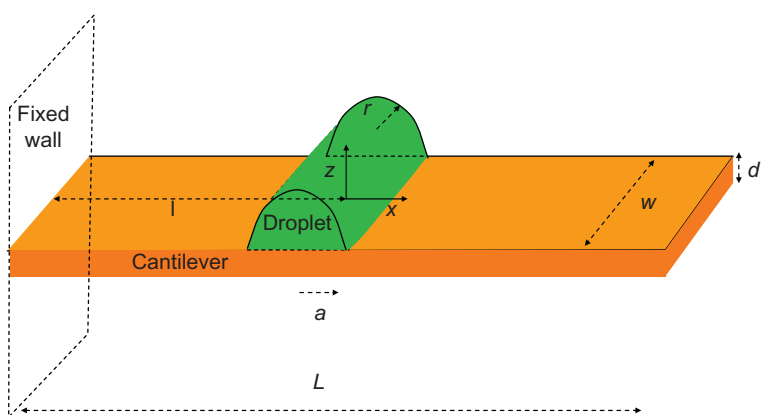
Let us follow the reasoning of Yu and Zhao [10]: On the one hand, there is a normal force (per unit length) on the triple line which is expressed by $f \approx \gamma \sin \theta$ (Eq. (12.4)). On the other hand, the Laplace's pressure of the drop $P = \gamma_{LG}/r$ results in a downward uniform force per unit surface on the beam under the droplet (r is the curvature radius of the droplet). At equilibrium, the two types of forces balance. However, a torque remains. By looking at Figure 12.5A, one can imagine a similarity with a “bow” where the pressure would be the archer's arm, and the force at the two ends, the “string.” Hence, a curvature appears.

For simplicity, let us assume that the droplet is sufficiently large to adopt a cylindrical shape, as shown in Figure 12.6 (2D assumption). In such a case, the wetted area is $A = 2wa = 2wr \sin \theta$, and the Laplace's force is $F = PA = 2w\gamma \sin \theta$. This is of course a gross approximation since the real shape has been obtained with Evolver (see Chapter 3). However, this approximation has the advantage to permit an analytical calculation.

**FIGURE 12.5**

Cantilever deformed by the presence of a water droplet.

Source: From Ref. [10].

**FIGURE 12.6**

Sketch of the droplet on the cantilever.

The torque induced by the droplet is determined by

$$M(x) = \begin{cases} 0 & x \leq -a \\ \gamma w \sin \theta \frac{a^2 - x^2}{2a} & -a \leq x \leq a \\ 0 & x \geq a \end{cases} \quad (12.8)$$

Using the relation between torque and deflection

$$M(x) = EI \frac{d^2z}{dx^2}, \quad (12.9)$$

where I is the second moment of area: $I = wd^3/12$ (for a rectangular beam). Substitution of Eq. (12.8) in Eq. (12.9) produces a differential equation of second order, which can be integrated twice to yield

$$z = \frac{\gamma w \sin \theta}{24EIa} (-x^4 + 6a^2x^2 + 8a^3x + 3x^4) \quad (12.10)$$

for $-a < x < a$. The deflection at $x = a$ is then

$$z(x = a) = \frac{8\gamma a^3 \sin \theta}{Ed^3} \quad (12.11)$$

and at the free end of a beam of length L

$$z(x = L - l) = \frac{8\gamma a^2 \sin \theta}{Ed^3} (L - l). \quad (12.12)$$

Note that the deflection increases when the droplet is placed closer to the fixed wall (the distance l decreases, while L is constant). It increases also with the total length of the beam L . Note also that the width w logically does not appear in Eq. (12.12). Finally, the deformation is again proportional to γ/E , which coincides with a former remark.

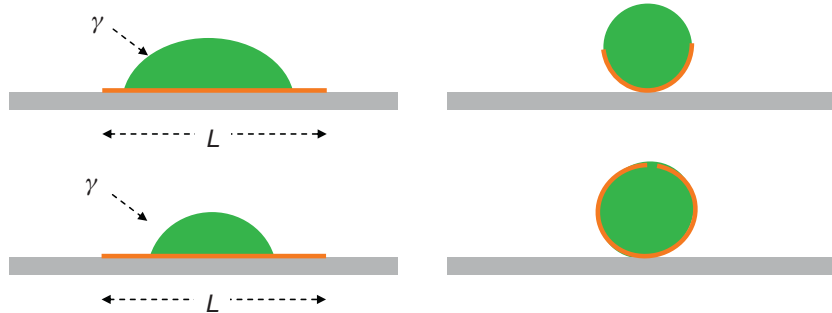
12.5 Elasto-capillarity and capillary origami

In the preceding section, we have seen how a soft, deformable substrate is deformed by the contact of a liquid droplet. In the case where the substrate is not a massive solid, but an elastic sheet, the presence of the droplet bends the underlying sheet in the case where the liquid is sufficiently wetting (Figure 12.7). This phenomenon is called elasto-capillarity, and a good review of the problem has been done by Roman and Bico [4].

A special case occurs when the sheet completely wraps the liquid. This configuration has been denoted “capillary origami” by Py and colleagues [11]. The physical analysis is the following [12]: On the one hand, the deformed sheet reduces the contact area between the droplet and the air; the surface energy is then decreased by the approximate quantity

$$\Delta E \approx \gamma L^2, \quad (12.13)$$

where L is a characteristic length of the deformable sheet and γ is the liquid–air surface tension. On the other hand, the energy is increased by the surface energy of the liquid with the deformable sheet and the bending energy of the sheet. The first contribution is small because the liquid wets the deformable sheet,

**FIGURE 12.7**

Sketch of the droplet and the elastic sheet. Depending on the liquid volume and the length of the elastic sheet, the elastic sheet may completely wrap the liquid to form a “capillary origami.”

i.e., γ_{LS} is small. The second contribution is related to the Young’s modulus E and Poisson ratio ν of the sheet. The bending stiffness of the plate B is defined by

$$B = \frac{Eh^3}{12(1-\nu^2)}, \quad (12.14)$$

where h is the thickness of the sheet. If κ is the curvature of the sheet, the bending energy per unit surface is

$$B \frac{\kappa^2}{2} = \frac{Eh^3}{12(1-\nu^2)} \frac{\kappa^2}{2}. \quad (12.15)$$

When the sheet wraps the droplet, the curvature is approximately

$$\kappa \approx \frac{1}{L}. \quad (12.16)$$

Spontaneous wrapping occurs when the reduction in surface energy is larger than the increase in bending energy

$$\gamma L^2 > B \frac{1}{2L^2} L^2 = \frac{B}{2}. \quad (12.17)$$

And the characteristic length of the problem is the elasto-capillary length defined as

$$L_{EC} = \sqrt{\frac{B}{\gamma}} \quad (12.18)$$

If the characteristic length of the sheet L is large compared to the elasto-capillary length $L \gg L_{EC}$, the sheet spontaneously wraps the droplet.

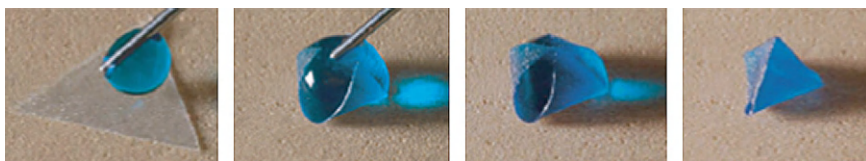


FIGURE 12.8

Wrapping of a droplet of water with a triangular PDMS sheet, resulting in a pyramid.

Source: Reprinted with permission from Ref. [11] © APS 2007.

For instance, in the work of Py and colleagues [11], triangular sheets of side L were experimentally found to form pyramids for $L > 11.9L_{EC}$ (Figure 12.8). Moreover, Guo and colleagues [13] have shown that a thin PDMS film is able to wrap a droplet.

12.6 Electro-elasto-capillarity

Elasto-capillary bending occurs when the decrease in surface energy is larger than the increase in bending energy. It has been found that the use of electric energy can control the folding and unfolding of the thin elastic membrane [14,15]. This mechanism is usually called electro-elasto-capillarity (EEC). A typical example is shown in Figure 12.9. The elastic membrane wrapping the droplet to form a capillary origami can be unfolded by electric forces. It suffices that electric forces counteract surface tension.

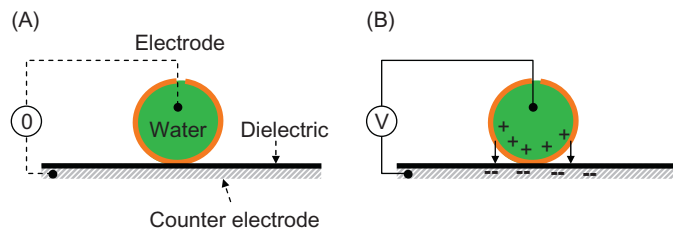
By approximating the system with the parallel plate assumption, the electric energy E_e is [16]

$$E_e = \frac{\varepsilon L^2 V^2}{2(d+h)}, \quad (12.19)$$

where ε , d , and V are, respectively, the dielectric constant and thickness of the insulating layer, and voltage. Both the dielectric and the membrane have the same dielectric constant in this formulation. Using Eqs. (12.13) and (12.19), we find that the electric energy can compensate for the surface tension if the voltage is larger than the critical voltage V_{crit} defined by

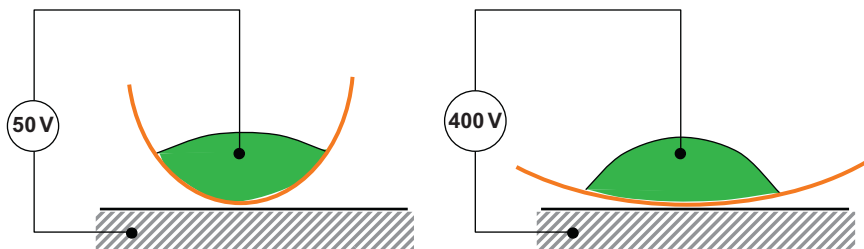
$$V_{crit} \approx \sqrt{\frac{2\gamma(d+h)}{\varepsilon}}. \quad (12.20)$$

Considering a dielectric constant $\varepsilon \sim 4 \cdot 10^{-1}$ F/m, a surface tension $\gamma \sim 70$ mN/m, and dielectric and membrane thickness of a few microns, one finds a critical voltage V_{crit} of the order of 100–200 V. In reality, paraphrasing Wang and colleagues [15], the phenomena sketched in Figure 12.9 could be called “electrowetting on a moving substrate.” This denomination is still clearer in the

**FIGURE 12.9**

EEC: (A) wrapping of the droplet by elasto-capillarity and (B) unfolding the membrane under the action of an electric field.

Source: From Ref. [14].

**FIGURE 12.10**

Bending of a PDMS film with the applied voltage.

Source: From Ref. [15].

sketch of Figure 12.10, taken from [15], where the different positions of a PDMS membrane are shown as a function of the voltage.

Applications of EEC are envisioned for reversible droplet encapsulation and for actuation of microelectromechanical devices.

12.7 Droplet at a liquid interface

We examine now the case of a droplet deposited on an immiscible liquid interface. Let us denote with the index D the droplet and with the index L the liquid, the gas being referred by the index G . Even if the density of the droplet is somewhat larger than that of the liquid, the droplet may float on the surface. The droplet may also be engulfed in the liquid substrate, or spread on its surface. In this section, we investigate the conditions for stable floatation, spreading, or engulfment.

12.7.1 Introduction: the difference between liquid droplets and rigid spheres at an interface

In this section, we follow the approach of Berthier and Brakke [3]. Even if the Neumann's force balance always applies at a triple line, there is a considerable difference between a deformable liquid droplet and a nondeformable body at an interface. In the first case, the vertical profile of the droplet has a singularity at the intersection of the triple line, i.e., the vertical profile is a continuous but not differentiable function at the intersection with the triple line (Figure 12.11A). In this case, Neumann's law has to be used to characterize the contact. However, a rigid body—for example a rigid sphere—behaves as a solid planar surface and Young's law can be used to define the contact at the triple line (Figure 12.11B).

In the case of a rigid body, a question is unanswered: what is the effect of the nonzero resultant perpendicular to the surface? In the case of a spherical rigid body placed at the surface of a liquid, the answer is straightforward: the normal resultants along the triple line cancel out by symmetry (Figure 12.12)

$$\int_{\Gamma} (\vec{\gamma}_{DG} + \vec{\gamma}_{DL} + \vec{\gamma}_{LG}) \cdot \vec{n} = 0. \quad (12.21)$$

In the case of a particle of random shape, the particle will rotate until it finds an equilibrium position where the resultants of the normal components of the surface tensions cancel out. An interesting investigation of the equilibrium position of orthorhombic particles at an interface has been performed by Morris and colleagues [17]. They have numerically shown that the shape of the particle, especially its aspect ratio, modifies the equilibrium position of the floatation.

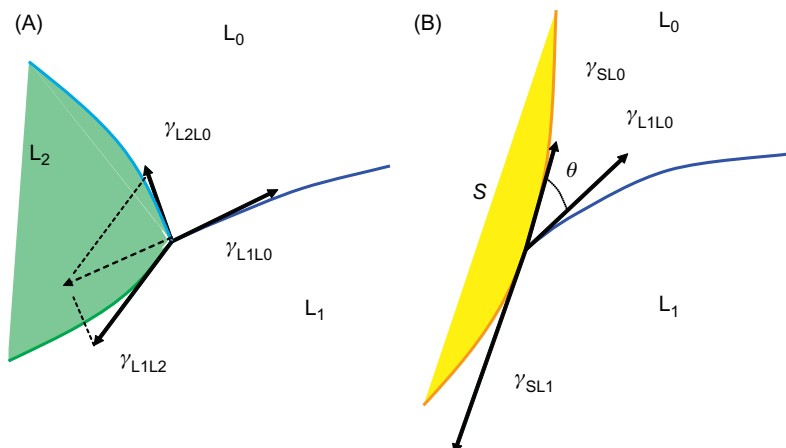
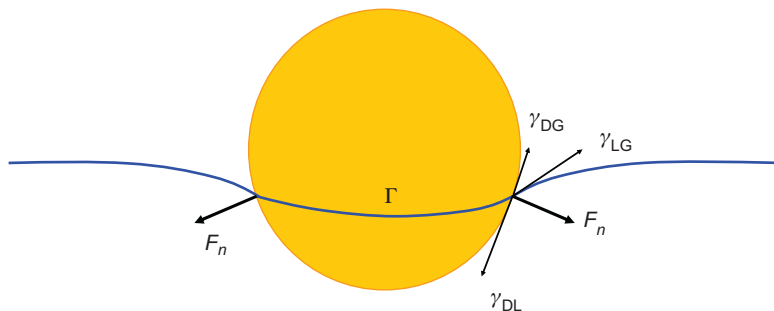


FIGURE 12.11

Sketch of a triple contact: (A) triple contact line between two liquids and a gas and (B) triple contact line between a solid, a liquid, and a gas.

**FIGURE 12.12**

In the case of a sphere, the normal resultants cancel out by symmetry (the index D corresponds to the “rigid droplet”).

12.7.2 Behavior of a droplet on an immiscible liquid surface

On the one hand, the relative position of the droplet at the interface is governed by the relative importance of the three surface tensions. On the other hand, if the droplet has sufficiently small dimensions or is buoyancy neutral, the gravitational effect is negligible. This behavior corresponds to the case where the Bond number is much smaller than 1

$$Bo = \frac{\Delta\rho g R^2}{\gamma} \ll 1, \quad (12.22)$$

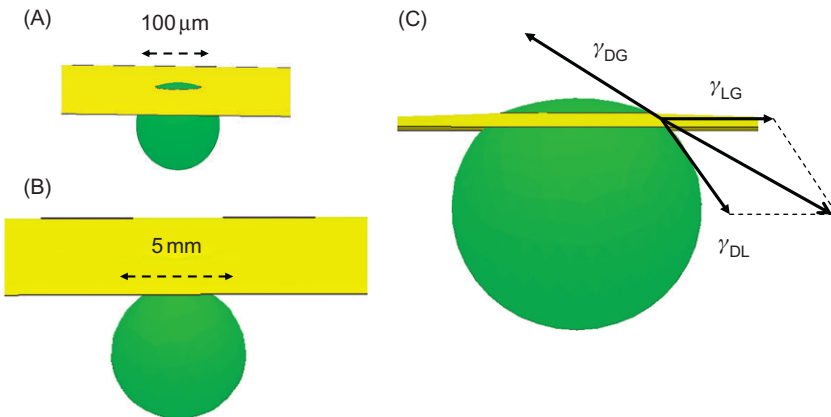
where $\Delta\rho$ is the density difference between the droplet and the liquid and R is the equivalent radius defined by

$$\text{Vol} = \frac{4}{3}\pi R^3. \quad (12.23)$$

Consider first a water droplet initially placed on top of an oil bath (Figure 12.13). If the Bond number is very small, the gravity effect is negligible and the water droplet finds an equilibrium position at the interface where most of the droplet volume lies below the interface (Figure 12.13A). Moreover, the oil surface remains nearly flat. A detailed analysis of the forces at the triple line is shown in Figure 12.13C.

In the case of a larger droplet, for which the gravity (floatability) force is not negligible, the interface is deformed, and the droplet falls into the oil bath if its relative weight is sufficient (Figure 12.13B).

Figure 12.14 shows some typical sketches of very small floating droplets obtained by numerical simulation with the Surface Evolver software for an equivalent radius $R = 200 \mu\text{m}$.

**FIGURE 12.13**

Water droplet deposited on oil: (A) a small water droplet stays at the surface, which remains nearly flat; (B) a large water droplet traverses the interface under the action of gravity; and (C) detail of a gravity-free water droplet at the oil interface: Neumann's construction at the triple line. Calculation preformed with the Evolver numerical software [18] using the values: $\gamma_{DL} = 45 \text{ mN/m}$, $\gamma_{LG} = 72 \text{ mN/m}$, $\gamma_{DG} = 30 \text{ mN/m}$.

The first case in [Figure 12.14A and B](#) corresponds to the spreading of an oil droplet on the water surface: $\gamma_{DL} = \gamma_{WO} = 45 \text{ mN/m}$, $\gamma_{LG} = \gamma_{WG} = 72 \text{ mN/m}$, $\gamma_{DG} = \gamma_{OG} = 30 \text{ mN/m}$. In this case

$$\gamma_{LG} > \gamma_{DL} \approx \gamma_{DG}. \quad (12.24)$$

The second case ([Figure 12.14C and D](#)) is an image of a pre-gelled droplet of alginate at an oil–water interface (oil on top of water). In such a case, the alginate–water surface tension is small compared to the two other surface tensions

$$\gamma_{DL} < \gamma_{DG} \approx \gamma_{LG}. \quad (12.25)$$

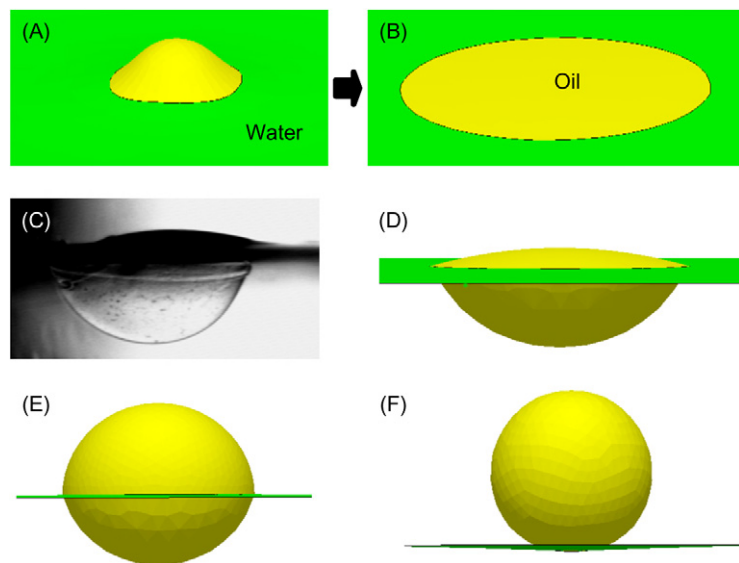
The third case ([Figure 12.14E](#)) corresponds to the case of a small surface tension between the droplet liquid and the air in comparison with the two other surface tensions

$$\gamma_{DG} < \gamma_{DL} \approx \gamma_{LG}. \quad (12.26)$$

This is for instance the case of a small droplet of mercury. The fourth case ([Figure 12.14F](#)) is an example of a very high drop-liquid surface tension

$$\gamma_{DL} > \gamma_{LG} \approx \gamma_{DG}. \quad (12.27)$$

The values of the three surface tensions determine the position of the droplet at the interface. There exist limit cases where three-phase equilibrium of surface tensions cannot be reached: these cases are spreading and engulfment.

**FIGURE 12.14**

Different configurations for a droplet at an interface: (A) a droplet of oil initially deposited at the surface of water spreads at the surface of water (B); (C) and (D) a droplet can adopt a nonsymmetrical shape depending on the values of the three surface tensions, here the drop liquid surface tension is small compared to the two others, corresponding to the case of a pre-gelled alginate droplet (with a core still liquid) at an oil–water interface; (E) sketch of a droplet when the surface tension between the liquid and the air is small before the two others; (F) a droplet can “float” on an interface, nearly like a hydrophobic droplet on a plane, if the surface tension between droplet and underlying liquid is very large compared to the two others.

Source: (D) Photograph courtesy P. Dalle.

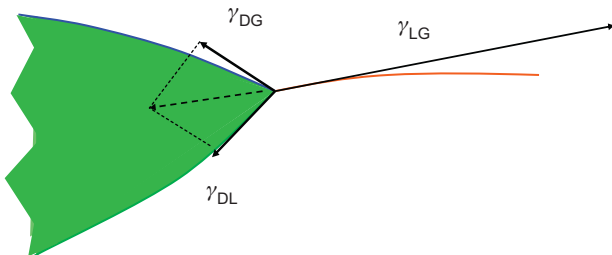
12.7.3 Spreading and engulfment

In the preceding section, we have seen that the relative value of the three surface tensions determines the position of the droplet. Now let us ask the following questions: under which condition a droplet completely spreads, and under which condition a droplet is totally engulfed in a liquid?

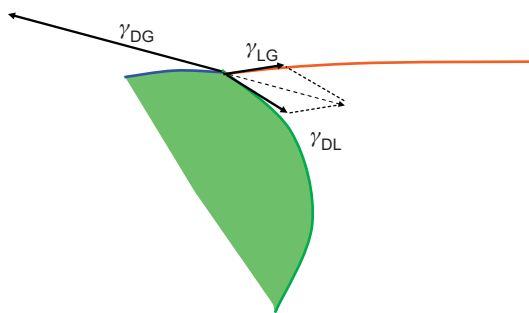
We have seen that, when the liquid–air surface tension is large compared to the two other surface tensions, the droplets have a tendency to spread. Assume now a liquid–air surface tension larger than the sum of the two others:

$$\gamma_{LG} > \gamma_{DG} + \gamma_{DL}. \quad (12.28)$$

In such a case, there cannot be a Neumann’s balance of the three surface tensions (Figure 12.15) and the droplet completely spreads at the surface of the liquid.

**FIGURE 12.15**

Sketch of an impossible balance of the surface tension forces leading to spreading.

**FIGURE 12.16**

Sketch of an imbalanced surface tension forces leading to droplet engulfment in the liquid phase.

A similar argument can be used for engulfment. Let us assume that the droplet liquid surface tension is larger than the sum of the two other surface tensions:

$$\gamma_{DG} > \gamma_{DL} + \gamma_{LG}. \quad (12.29)$$

In such a case, the Neumann's balance of the surface tension forces at the interface cannot be met ([Figure 12.16](#)) and the droplet is engulfed in the liquid.

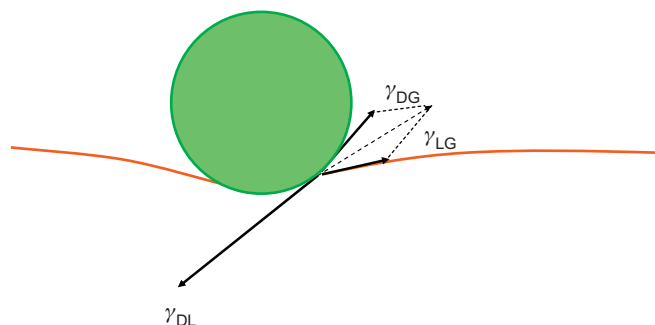
However, note that if

$$\gamma_{DL} > \gamma_{DG} + \gamma_{LG} \quad (12.30)$$

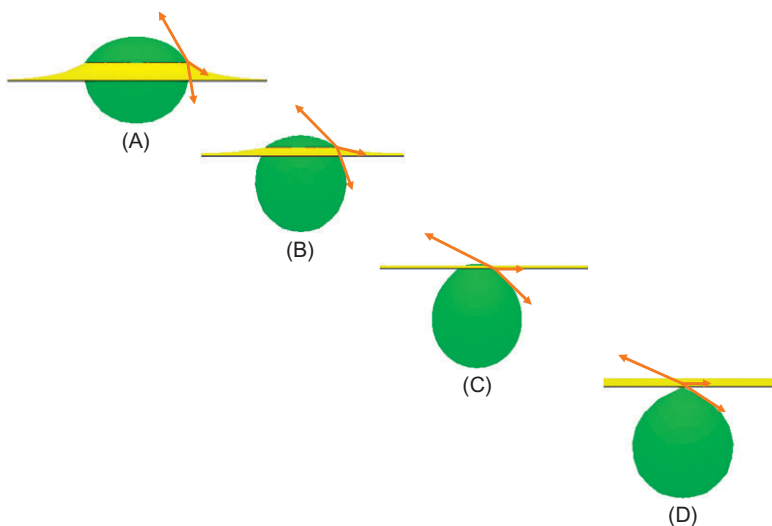
the droplet will not penetrate in the liquid, as sketched in [Figure 12.17](#).

12.7.4 Engulfment with gravity

In the case of a horizontal interface, and a sufficiently heavy droplet, engulfment may occur even if condition (12.29) is not exactly satisfied. Let us consider a

**FIGURE 12.17**

Sketch of a droplet that cannot penetrate in the liquid.

**FIGURE 12.18**

Progressive descent of a droplet into an immiscible liquid: the motion is slow and governed by capillary and gravity forces. Note the progressive change of the directions of the different surface tension forces. Calculation performed with the Evolver.

locally flat interface and a droplet with sufficient weight and/or sufficient capillary forces for crossing the interface: $R = 5\text{ mm}$, $\Delta\rho = 150\text{ kg/m}^3$, $\gamma_{DL} = 45\text{ mN/m}$, $\gamma_{LA} = 30\text{ mN/m}$, and $\gamma_{DA} = 72\text{ mN/m}$. With such values of the surface tension, the condition (12.29) is not exactly met, but engulfment occurs as shown in Figure 12.18. Note that the shape of the droplet is considerably modified by the crossing of the interface. This behavior is closely linked to the Neumann's construction—which predicts that the triple line is a singularity line.

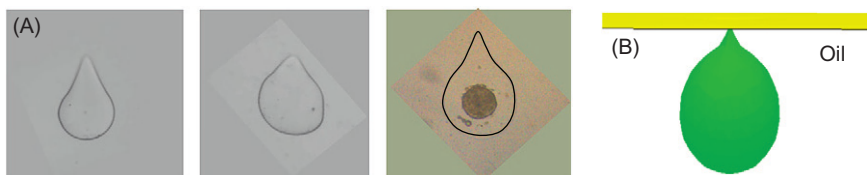


FIGURE 12.19

(A) Alginate droplet after having crossed an oil layer (this shape has been later freezed by polymerization in an aqueous layer of calcium located below); the last image on the right shows a pancreatic cell encapsulated in the alginate droplet and (B) modeling of a liquid aqueous droplet traversing an air–oil interface.

Source: Photograph P. Dalle, CEA-LETI.

The deformation of a droplet crossing an interface can be experimentally observed. Let us take the example of an alginate droplet gently dropped on an oil layer (Figure 12.19). The droplet adopts a “pear” shape during the crossing of the interface between oil and air; this shape can be easily observed after polymerization (gelling).

12.8 Conclusion

This chapter was devoted to the study of the interaction between a droplet and different substrates: microcantilever, elastic membranes, and immiscible liquid. In such cases, it is the Neumann’s construction which has to be used to determine the shape of the deformable substrate. The problem is much more complex than that of rigid substrate for which Young’s law applies. Closed form solutions for the deformation are seldom, and numerical approaches are essential.

References

- [1] F. Neumann, Vorlesungen über die Theorie der Capillarität, Teubner, Leipzig, 1894.
- [2] G.R. Lester, Contact angles of liquids at deformable solid surfaces, *J. Colloid Sci.* 16 (1961) 315–326.
- [3] J. Berthier, K. Brakke., *The Physics of Microdroplets*, Scrivener-Wiley Publishing, Beverly, MA, 2012.
- [4] B. Roman, J. Bico, Elastic-capillarity: deforming an elastic structure with a liquid droplet, *J. Phys. Condens. Matter* 22 (2010) 493101.
- [5] A.W. Adamson, A.P. Gast, *Physical Chemistry of Surfaces*, sixth ed., Wiley-Interscience, New York, 1997.
- [6] E.R. Shanahan, A. Carré, Viscoelastic dissipation in wetting and adhesion phenomena, *Langmuir* 11 (1995) 1396–1402.

- [7] S.K. Vashist, A review of microcantilevers for sensing applications, *AZojono, J. Nanotechnol.* (2007) [Online].
- [8] A. Vasudev, Microcantilever-based sensors, *Mechanical Devices, 2006 Research Accomplishments* (2006) 98.
- [9] H. Yu, X. Li, Bimalyte mass detection with a single resonant microcantilever, *Appl. Phys. Lett.* 94 (2009) 011901.
- [10] Y.-S. Yu, Y.-P. Zhao, Deformation of PDMS membrane and microcantilever by a water droplet: comparison between Mooney–Rivlin and linear elastic constitutive models, *J. Colloid Interface Sci.* 332 (2009) 467–476.
- [11] C. Py, P. Reverdy, L. Doppler, J. Bico, B. Roman, C.N. Baroud, Capillarity induced folding of elastic sheets, *Eur. Phys. J. Special Topics* 166 (2009) 67–71.
- [12] J. Bico, B. Roman, L. Moulin, A. Boudaoud, Elastocapillary coalescence in wet hair, *Nature* 432 (2004) 690.
- [13] X.Y. Guo, H. Li, B.Y. Ahn, E.B. Duoss, K.J. Hsia, J.A. Lewis, R.G. Nuzzo, Two and three-dimensional folding of thin film single-crystalline silicon for photovoltaic power applications, *Proc. Natl. Acad. Sci. U.S.A.* 106 (2009) 20149–20154.
- [14] M. Piñeirua, J. Bico, B. Roman, Capillary origami controlled by an electric field, *Soft Matter* 6 (2010) 4491–4496.
- [15] Z. Wang, F.-C. Wang, Y.-P. Zhao, [published online] Tap dance of a water droplet, *Proc. R. Soc. A*, 2012.
- [16] F. Mugele, J.C. Baret, Electrowetting: from basics to applications, *J. Phys. Condens. Matter* 17 (2005) R705–R774.
- [17] G. Morris, S.J. Neethling, J.J. Cilliers, An investigation of the stable orientations of orthorhombic particles in a thin film and their effect on its critical failure, *J. Colloid Interface Sci.* 361 (2011) 370–380.
- [18] K. Brakke, The surface evolver, *Exp. Math.* 1 (2) (1992) 141–165.

Acoustic Methods for Manipulating Droplets*

13

CHAPTER OUTLINE

13.1 Introduction	458
13.2 Digital microfluidics	459
13.2.1 Acoustic streaming	460
13.2.1.1 <i>SAWs on a solid</i>	461
13.2.1.2 <i>Elastic waves in a solid</i>	463
13.2.1.3 <i>Rayleigh waves</i>	465
13.2.1.4 <i>SAW excitation</i>	466
13.2.2 Internal streaming	468
13.2.3 Droplet actuation	471
13.3 Example 1: Acoustic mixing	473
13.4 Example 2: Acoustic droplet actuation	475
13.5 Applications	478
13.5.1 Microarray hybridization (biological application)	478
13.5.2 Polymerase chain reaction	479
13.5.3 Cell adhesion	484
13.5.3.1 <i>Blood flow on a chip</i>	484
13.5.3.2 <i>Proteins in a microflow</i>	486
13.5.3.3 <i>Cell–cell interactions on a chip</i>	486
13.5.3.4 <i>Advanced applications</i>	487
13.6 Summary	489
Acknowledgments	490
References	491

*This chapter was written by Thomas Frommelt, Matthias Schneider (Chair for Experimental Physics I, University of Augsburg, D-86519 Augsburg, Germany) and Achim Wixforth (Advalytix AG, D-85649 Brunnthal, Germany).

13.1 Introduction

The recent development of microfluidic systems in some sense marks a rebirth of the old discipline of hydrodynamics, however, on a much smaller scale than the one we are familiar with in our daily lives. Hence, the laws of hydrodynamics still apply but need to be adjusted to the changed physical environment of the microscale. The regime for microfluidics is governed by strong interactions between the fluid and the outer world, be it containers, tubes, or trenches. Here, surface effects like wettability, surface tension, adhesion and cohesion, and others lead to a completely different fluid behavior than the one we are used to. Usually, this new behavior is physically described by the ratio of inertial terms and viscous terms in the equations of motion of a fluid volume element. This ratio is usually referred to as Reynolds number. Flow at low Reynolds numbers in the macro world is usually restricted to very viscous fluids, like ice in a glacier, for example. Low Reynolds numbers are related to laminar flow and the absence of turbulence which has enormous consequences for chemical and biochemical reactions. Interestingly, the microscale behavior of fluids and particles is not that unusual, even in our macroscopic world, taking the fact that the vast majority of living species on our planet has a size of only a few micrometers, namely bacteria. They live in a world where the classical laws of hydrodynamics are not really applicable. In a famous paper, Purcell [1] describes the fate of such microbes in a microfluidic environment, describing all the obstacles these creatures experience as compared to an average size fish, but also outlining the strategies life developed to still be comfortable in the microworld.

Microfluidic systems miniaturize chemical and biological laboratory processes to a submillimeter scale. Reducing the dimensions of macroscopic biological or chemical laboratories is advantageous, as the small scale allows for the integration of various processes on one chip analogous to integrated microelectronic circuitry. Also, the required reagent volumes are reduced which saves material costs and allows the reactions to be carried out at high sample concentrations. These high concentrations drive the reactions toward the products' side and accelerate the kinetics. Finally, miniaturization results in enhanced precision by providing homogeneous reaction conditions.

Several approaches to realize microfluidic systems have been reported in the literature. In this context, the term LOC has emerged, already outlining the use and typical applications of such systems. In most cases, the reagents are transported in channels or capillaries with typical diameters ranging from 10 to 500 μm . These channels can be fabricated by deep etching processes on appropriate substrates such as glass, quartz, or silicon [2]. Alternatively, hot embossing is used to structure polymer substrates. The channels are capped by anodic bonding or glue processes. Generally, these systems do not allow the reagents to be handled separately, as the channels need to be completely filled in order for the fluidics to work properly. Therefore, the application of these systems is restricted to continuous flow processes rather than batch processes as found in macroscopic laboratories.

The number of different pumping mechanisms is even greater than the number of substrate materials employed in microfluidics. Some pumping units are not an integral part of the chip and must be linked with appropriate tubes or pipes. They use, for example, piezoelectric actuation or mechanically moving parts to drive the reagents through the channels. Others take advantage of the small dimensions of the microfluidic channel itself [3]. The chemical potentials of the channel walls and that of the liquid inside differ considerably, and a space charge region forms at the interface. A voltage applied along the channel induces a flow at the space charge region which drags along the liquid closer to the center of the channel. This electrokinetic effect works only for narrow channels and relatively high voltages. Fluidic motion can also be induced by spatially modulating the wetting properties of a substrate. For aqueous solutions, this can be achieved by patterning the substrate with hydrophobic and hydrophilic regions. The techniques used to realize such a modulation of the wetting properties include microcontact printing [4], vapor deposition, and photolithography [5,6]. Aqueous solutions tend to cover the hydrophilic regions and avoid the hydrophobic areas. A guided flow can be achieved [7] by changing the wetting properties with time. For example, illumination can induce a guided motion of liquids as the free energy of the surface changes locally under illumination [8]. Other pumping mechanisms include peristaltic pumps based on thin membrane [9] or polymer films [10] with a controlled deformation creating a guided flow along microchannels [11].

In this chapter, we present a novel approach of miniaturized liquid handling which does not displace the reagents in channels but rather on the surface of piezoelectric substrates. In our case, interdigital transducers (IDTs) excite surface acoustic waves (SAWs) which transfer momentum to liquids placed on the chip. The reagents can be manipulated either as discrete droplets or by streaming patterns induced in macroscopic volumes. The technology allows both batch and continuous processes to be carried out at high speed. The most important feature, however, is the programmability of the chip as different assay protocols can be realized with the same chip layout.

13.2 Digital microfluidics

Watching a “typical” chemist or biologist do laboratory work, the first thing that strikes the observer is that they usually operate discrete fluid volumes. They pipette a small amount of a fluid reagent from a reservoir, load a test tube or a beaker with it, pipette a second reagent volume, add it to the first one, stir it, heat it, etc. Unlike the fluid handling in a chemical plant, nearly all the fluid handling is done in a “digital” fashion. The reason is obvious. Closed volumes connected by tubes and hoses (“analog fluidics”) are much more difficult to meter, and cross contamination, intermixing, interdiffusion, and similar difficulties are easily avoided. Moreover, the flow resistance in tubes strongly depends on the liquids actually used, making the precise pumping and dispersion of the liquid a

cumbersome task in many cases. A multiple connected network of tubes and hoses represents a complex, very nonlinear system, where changes at one end of the network have a notable impact and crosstalk to the fluid/pressure behavior at the other end. For this reason, many LOC microfluidic applications have emerged, where the small amounts of fluids are defined as small, independent quantities.

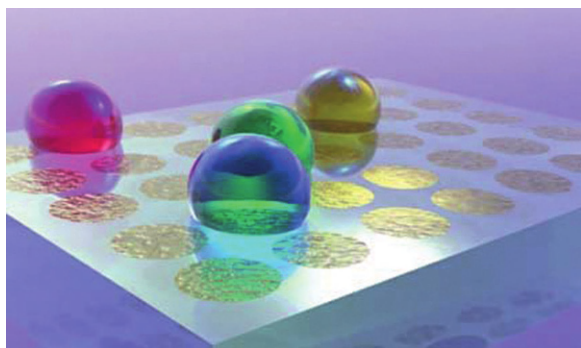
At this point, droplet-based fluidic systems enter the scene. Once we have a platform at hand that is able to control the movement and the handling of small fluid volumes in the form of droplets, and we find a way to deliberately actuate these droplets, we have a system that can be truly regarded as a miniaturized version of a macroscopic laboratory. Small droplets serve as microtest tubes and reactor vessels, being completely independent from each other and hence reducing the risk of cross contamination and intermixing to a minimum. These droplets, if small enough, do not need any containers, as surface tension acts as a potential well holding the fluid in place.

The next task on the route toward a laboratory on a chip is the fluid actuation. To be able to perform complicated experiments involving different reagents, some patterned surfaces are needed on the chip. This includes the flat world analog of channels, tubes, reservoirs, mixing chambers, and similar building blocks usually employed to guide, contain, or process liquids in a fluidic network. Hence, we need areas on the chip along which liquids can be moved in a predetermined manner (Figure 13.1). By a chemical modification of parts of the chip surface (i.e., silanization employing an octa-decyl-trichlorosilane, OTS-based surface chemistry), we are able to create patterns of preferred wettability (hydrophilic regions), being separated by regions of surface chemistry, where fluids are repelled (hydrophobic areas). Employing lithographic techniques borrowed from semiconductor microelectronics, we thus can create completely flat, 2D fluidic networks, where liquids are confined to virtual tracks, reservoirs, and reaction chambers by surface tension alone.

In Figure 13.2, we depict some of such self-assembled virtual potential wells for fluids on a surface. Photolithographic techniques have been employed to create “containers” for the smallest amounts of liquid, having shapes like a hexagon (Figure 13.2A) or a “tube” with a narrowing (acting as a pressure-driven valve). Given this surface functionalization, either closed fluid volumes or single droplets may be acoustically guided along predetermined pathways along the surface of the chip.

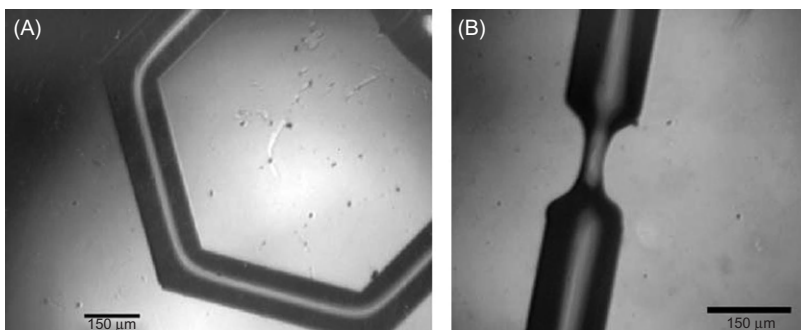
13.2.1 Acoustic streaming

In this chapter, we introduce the basics that are necessary to understand the acoustic actuation scheme for fluid manipulation on a chip. We start with a short and comprehensive description of SAWs on a solid, as we employ SAW to interact with a fluid, induce internal acoustic streaming, or supply enough force to actuate a droplet as a whole. This SAW–fluid interaction is presented in the following sections, with special emphasis given on the internal acoustic streaming in a small amount of fluid and droplet actuation, on the other hand.

**FIGURE 13.1**

Droplets on a patterned chip surface: if the droplets are small enough and the surface consists of areas of preferred wettability (hydrophilic anchors), surrounded by hydrophobic regions, the droplets are stabilized at a predetermined volume. They act as individual “virtual test tubes” for microscale laboratories.

Source: Courtesy Advalytix.

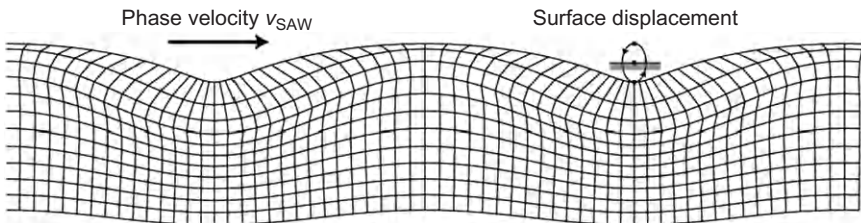
**FIGURE 13.2**

Photolithographically defined surface modification to modulate its wettability. This way, virtual fluidic tracks are created to confine small amounts of liquid to predetermined geometries or to guide an SAW-driven droplet along a predetermined path on the chip surface.

Source: From Ref. [12] © 2003, Elsevier, reprinted with permission.

13.2.1.1 SAWs on a solid

In a crystal, or more generally spoken in a solid, optical and acoustic lattice vibrations are observable. Both types of lattice vibrations in solids are distinguished from each other according to their vibrational modes. Optical vibrations show a dispersed motion of individual atoms and, in case each individual atom carries a charge of opposite sign, such vibrations can couple to electromagnetic waves, i.e., light. In acoustic modes, atoms move commonly as in the acoustic sound waves

**FIGURE 13.3**

Sketch of an SAW propagating on a piezoelectric substrate. Typical wavelengths are in the micrometer range, typical amplitudes less than a nanometer. Note the elliptically polarized displacement of the surface.

Source: Courtesy T. Frommelt.

of long wavelength in air. Another major difference between optical and acoustic modes is their dispersion. Acoustic phonons exhibit a linear dispersion close to the zone center. At the zone boundary, the group velocity vanishes such that lattice vibrations do not propagate and standing waves occur. Propagating lattice vibrations generate waves, which can be typically bulk waves or surface waves, depending on the boundary conditions [13]. The special case of SAWs was theoretically described in 1885 by Rayleigh from the perspective of seismology [14].

Meanwhile, reduced to the significantly smaller nanoscale, acoustic waves found their way into much friendlier fields: SAW devices are widely used for radio frequency (RF) signal processing and filter applications, and became a huge industry in mobile communication [15]. SAW devices have been around for years in communication circuitry—every cell phone has filters using the effect. An electrical signal fed into the so-called transducers on the surface of a piezoelectric chip is converted into a deformation of the crystal underneath. Given the right frequency of the signal, a mechanical wave is launched across the chip. In Figure 13.3, we sketch a snapshot of an SAW propagating on a solid.

In the recent past, SAWs have also been used to act in a completely different way than for filtering and signal processing, just by converting electrical signals into mechanical vibrations and vice versa. Excited on piezoelectric substrates, they are accompanied by large electric fields. Those electric fields are traveling at the speed of sound of the substrate (~ 3000 m/s) having the same spatial and temporal periodicity as their mechanical companions. Charges at or close to the surface are coupling to these electric fields, and currents are induced within a conducting layer. Nearly 20 years ago, SAW was introduced to study the dynamic conductivity $\sigma(\omega, k)$ of low-dimensional electron systems in high magnetic fields and at low temperatures. It turns out that the interaction between an SAW and the mobile charges in a semiconductor is strongest for very low sheet conductivities as they are observed, e.g., in the regime of the quantum Hall effect [16]. However, SAW can not only be used to probe the properties of quantum systems but also be used to deliberately alter some of them as SAW represents a spatially modulated strain and stress field accompanied

by strong electric fields in a solid and propagates at the speed of sound. Such an interaction between SAW and the optical properties of a semiconductor quantum well led us to the discovery that photogenerated electron hole pairs in a semiconductor quantum well can be spatially separated under the influence of an SAW mediated electric field. This in turn has an enormous impact on the photoluminescence (PL) of the semiconductor. We were able to show that the PL not only is quenched under the influence of an SAW, but also can be reestablished at a remote location on the sample and after a certain delay time [17]. Further studies include the acoustic charge transport and the creation of dynamically induced electron wires, as well as the study of nonlinear acoustic interactions with low-dimensional electron systems in semiconductors [18].

However, as will be outlined below, the piezoelectric effect is usually only a small contribution to the elastic properties of a solid: Most of the energy propagating in an SAW (usually more than 95%) is of mechanical nature. Hence, not only electrical interactions as described above, but also mechanical interactions are a possible scope for experimental investigations. Having wavelengths of a few micrometers and amplitudes of about only a nanometer, however, the forces and electric fields within the nano-quake are sufficient to have a macroscopic effect. Any piece of matter at the surface along the way of an SAW experiences its vibrating force: viscous materials like liquids absorb a lot of their energy. It turns out that the interaction between an SAW and a liquid on top of the substrate surface induces an internal streaming, and, as we will point out below, at large SAW amplitudes this can even lead to a movement of the liquid as a whole.

13.2.1.2 Elastic waves in a solid

Imagine an isotropic and homogeneous medium (density ρ) without external forces and piezoelectricity. An infinitesimal volume element $dV = dx_1 dx_2 dx_3$ experiences only the forces exerted by neighboring volume elements. Those forces can be described in terms of the symmetrical strain tensor T_{ij} [19]. Here, the T_{ii} are describing strain or stress forces, and $T_{ij,i \neq j}$ represents the shear forces in the system. Neglecting gravity, the equation of motion for such an infinitesimal volume element can be written as

$$\rho \frac{\partial^2 u_i}{\partial t^2} = \frac{\partial T_{ij}}{\partial x_j}. \quad (13.1)$$

Here, as throughout this chapter, the so-called Einstein sum convention has been used, indicating summation over double indices. In Eq. (13.1), u_i is the mechanical deformation in the direction x_i . The actual deformation of an infinitesimal volume element dV is described by the symmetrical deformation tensor S_{kl} [15]:

$$S_{kl} = \frac{1}{2} \left(\frac{\partial u_k}{\partial x_l} + \frac{\partial u_l}{\partial x_k} \right). \quad (13.2)$$

Strain and deformation are as usual connected via the elastic constants c_{ijkl} :

$$T_{ij} = c_{ijkl} S_{kl}. \quad (13.3)$$

This is the 3D version of Hooke's law, which for the case of a piezoelectric crystal has to be extended by an additional term in the strain, expressing the piezoelectricity. Together with the equation describing the dielectric displacement D , this results in the equations of constitution for a piezoelectric crystal:

$$\begin{aligned} T_{ij} &= c_{ijkl} S_{kl} - p_{kij} E_k \\ D_i &= p_{ijk} S_{jk} + \varepsilon_{ij} E_j \end{aligned} \quad (13.4)$$

Here, E denotes the electric field strength, p the piezoelectric tensor, and ε the dielectric tensor for the material under consideration.

The symmetric nature of T_{ij} and S_{kl} requires that $c_{ijkl} = c_{jikl}$ and $c_{ijkl} = c_{ijlk}$. From energy conservation, it can moreover be shown that $c_{ijkl} = c_{klji}$ [15]. Given these symmetry relations, it turns out that there are 21 independent elastic constants remaining for an arbitrary crystal structure. As can be seen from the above, the piezoelectric properties of a given material are also influenced by electromagnetic quantities as described by Maxwell's equations. However, it turns out that this purely electromagnetic influence is only weak; hence it is in most cases justified to approximate the electric field by the gradient of a scalar potential $E_i = -\partial\phi/\partial x_i$. Using this approximation, the constituting equations (13.4), the definition of the deformation tensor (13.2), the equation of motion (13.1), and Maxwell's equation $\operatorname{div} D = 0$, we finally end up with a system of four wave equations for the three components of the mechanical elongations u_i and the electrical potential ϕ :

$$\begin{aligned} \rho \frac{\partial^2}{\partial t^2} - c_{ijkl} \frac{\partial^2 u_k}{\partial x_i \partial x_l} - p_{kij} \frac{\partial^2 \phi}{\partial x_i \partial x_k} &= 0 \\ p_{ikl} \frac{\partial^2 u_k}{\partial x_i \partial x_l} - \varepsilon_{ik} \frac{\partial^2 \phi}{\partial x_i \partial x_k} &= 0 \end{aligned} \quad (13.5)$$

In general, this results in three different wave modes for an infinite crystal: one longitudinal mode and two orthogonally polarized transversal modes (shear waves). For the special case of a plane bulk wave in an infinitely large yz -cut LiNbO₃ crystal, the materials being discussed here, the equations further simplify. If the propagation direction is denoted by $x_3 = z$, one obtains for the longitudinal mode

$$\begin{aligned} \rho \frac{\partial^2 u_z}{\partial t^2} - c_{33} \frac{\partial^2 u_z}{\partial z^2} - p_{z3} \frac{\partial^2 \phi}{\partial z^2} &= 0 \\ p_{z3} \frac{\partial^2 u_z}{\partial z^2} - \varepsilon_{zz} \frac{\partial^2 \phi}{\partial z^2} &= 0 \end{aligned} \quad (13.6)$$

Elimination of ϕ results in the following wave equation:

$$c_{33} \left(1 + \frac{p_{z3}^2}{\varepsilon_{zz} c_{33}} \right) \frac{\partial^2 u_z}{\partial z^2} = \rho \frac{\partial^2 u_z}{\partial t^2}. \quad (13.7)$$

For the simpler case of a nonpiezoelectric material, Eq. (13.7) reduces to

$$c_{33} \frac{\partial^2 u_z}{\partial z^2} = \rho \frac{\partial^2 u_z}{\partial t^2} \quad (13.8)$$

which makes it obvious to express the effect of the piezoelectricity in terms of an *effective* elastic constant

$$c_{33}^* = c_{33} \left(1 + \frac{p_{z3}^2}{\varepsilon_{zz} c_{33}} \right) = c_{33}(1 + K^2) \quad (13.9)$$

K^2 in Eq. (13.9) is the so-called electromechanical coupling coefficient, in general a tensor of fourth rank. From the above it becomes clear that the effect of piezoelectricity “stiffens” a material of given elasticity by the amount of K^2 . The reason for this “piezoelectric stiffening” is additional restoring forces apart from the elastic forces, caused by a charge separation under deformation of a piezoelectric material. These additional restoring forces lead to an increase of the sound velocity for a piezoelectric medium, if compared to the corresponding non-piezoelectric substrate

$$v^* = \sqrt{\frac{c_{33}^*}{\rho}} = \sqrt{\frac{c_{33}(1 + K^2)}{\rho}} \approx v \left(1 + \frac{K^2}{2} \right), \quad (13.10)$$

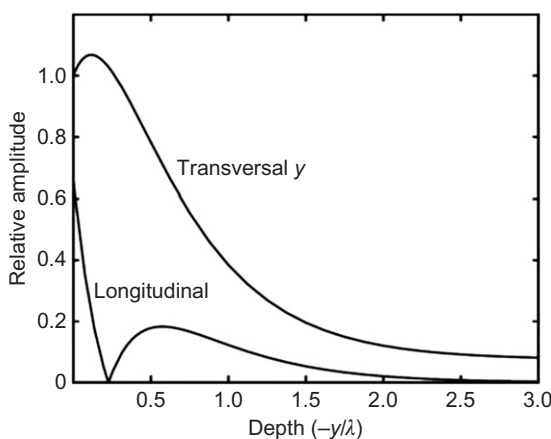
where $u = \sqrt{c_{33}/\rho}$. This characterizes the role and the definition of the electromechanical coupling coefficient K^2 :

$$K^2 \approx 2 \frac{\Delta v}{v} \quad (13.11)$$

Here, $\Delta v = v^* - v$ denotes the renormalization of the sound velocity if piezoelectricity is taken into account. The electric field related terms in Eq. (13.4) can be strongly modified if the substrate is, for example, covered by a thin conducting metal film. A varying conductivity at or close to the surface on which an SAW is propagating strongly influences both the amplitude of the SAW and its sound velocity. The difference in sound velocities of a “free” and a “shortened” surface is then given by $K^2/2$. This leads to the interactions between an SAW and quantum systems shortly described above.

13.2.1.3 Rayleigh waves

So far, we have only discussed the case of volume or bulk waves. The special case of an SAW can be obtained from the above calculations if the boundary conditions of a stress-free surface are considered: $T_{31} = T_{32} = T_{33} = 0$ for $x_3 = 0$. Here, the components of the stress normal to the surface vanish. The important case of the Rayleigh wave is visualized in Figure 13.4, where we depict the surface elongations along a cut through the substrate (y -cut LiNbO_3 in this case). As can be seen, both elongation components decay in a specific

**FIGURE 13.4**

Normalized surface elongations for a Rayleigh SAW on y -cut LiNbO_3 [20].

Source: Courtesy T. Frommelt.

manner with depth into the material. The exact shape of the decay, however, depends on the actual material, crystal cut, and anisotropy of the substrate under consideration.

A Rayleigh SAW thus exhibits an elliptically polarized particle movement directly at the surface of the crystal (see Figure 13.3). The motion of a volume element is *retrograde*, i.e., moving against the direction of SAW propagation and within the sagittal plane. As it turns out, the interaction between the SAW and a fluid on top of the substrate surface is governed by the transversal elongation of the surface, whereas the interaction between an SAW and an electrically conducting layer at the surface is mainly governed by the lateral fields [16].

13.2.1.4 SAW excitation

Rayleigh SAW on a piezoelectric solid can be excited in a particularly simple way: a lithographically designed electrode system in the shape of an interdigitated grating is deposited on top of the surface, using semiconductor technology. The period of the fingers determines the frequency of the SAW, which depends on the SAW velocity of the given crystal orientation and cut, respectively. There are many different designs for such IDTs for special purposes in high-frequency signal processing or sensor applications. We only want here to give an idea of their operation and restrict ourselves to the simplest cases. For a fixed frequency operation, IDTs consist of a comb-like metal structure where every second metal finger is connected. Application of an RF signal to the transducer causes a periodic crystal deformation underneath, via the inverse

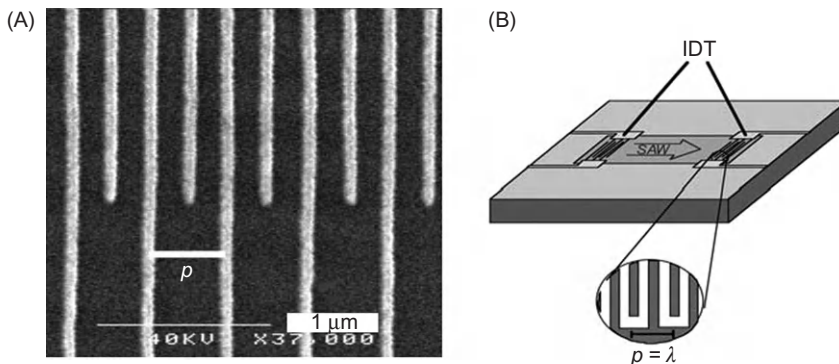


FIGURE 13.5

- (A) SEM micrograph of an IDT on a piezoelectric substrate. The surface acoustic wavelength λ is given by the periodicity p of the IDT and the SAW velocity v , respectively.
 (B) A delay line formed by two IDT on a piezoelectric substrate.

piezo effect. In first order, the resonant frequency of such an IDT is then given by:

$$f = \frac{v_{\text{SAW}}}{p}, \quad (13.12)$$

where p denotes the periodicity of the IDT, as sketched in Figure 13.5A. If two such transducers are deposited onto the same substrate, a so-called delay line is formed. Here, an RF signal fed into one of the transducers is converted into an SAW, propagating across the substrate and, at the second transducer, is reconverted into an RF signal via the piezoelectric effect. As the IDT and the delay line represent a resonant device, it exhibits a specific frequency response which is heavily exploited for RF signal processing. The bandwidth Δf of a delay line is basically given by the IDT layout and the number of finger pairs.

As can be suspected from the sketch presented in Figure 13.5, an SAW delay line is extremely sensitive to surface contamination. Both the transmitted SAW amplitude and the frequency response of the device are easily disturbed by any change of the boundary conditions at the free surface. This is true for all disturbances able to interact with the SAW. Most prominent, of course, is a mechanical load of the surface by contamination with a fluid, dust, or the like.

This is why the SAW device industry puts a lot of effort into proper sealing of SAW devices to avoid time unstability and deterioration. Any piece of matter at the surface along the way of an SAW experiences its vibrating force: viscous materials like liquids absorb a lot of energy, which indicates a strong interaction between the fluid and the SAW. This interaction induces internal streaming and eventually droplet actuation.

13.2.2 Internal streaming

The interaction between an SAW and a fluid on the surface of the substrate on which the SAW is propagating represents a delicate, though extremely interesting hydrodynamical problem. To approach it, we start from the Navier–Stokes equation, describing the flow in a hydrodynamic system. It is a nonlinear equation in the velocity components, reading

$$\rho \frac{\partial \vec{v}}{\partial t} + \rho(\vec{v} \cdot \text{grad}) \vec{v} = -\text{grad} p + \eta \Delta \vec{v} + \vec{f} \quad (13.13)$$

Here, \vec{v} is the velocity field of the flow, η the viscosity, and ρ the mass density of the fluid. p denotes the pressure that a fluid element experiences from its surroundings and \vec{f} is an externally applied body force driving the flow. The term $\rho(\vec{v} \cdot \text{grad}) \vec{v}$ describes the inertia of the fluid element and $\eta \Delta \vec{v}$ marks the viscous term. In microfluidics, the nonlinear term in the Navier–Stokes equation is often much smaller than the viscous term and can therefore be neglected. The validity of this approximation depends on the ratio of inertial forces and viscous forces, which is known as the dimensionless Reynolds number Re :

$$Re = \frac{\rho v^2 l^2}{l \eta v} = \frac{\rho v l}{\eta}. \quad (13.14)$$

In this definition, l denotes a typical length scale in the system under consideration, e.g., the channel diameter. For a microfluidic system, Re is usually a small number, indicating the little importance of inertia in the problem. The most prominent consequence thereof and hence the most important difference to a macroscopic fluid volume is the lack of turbulent flows in a microfluidic system. The transition between turbulent and laminar flow usually occurs at a threshold Reynolds number $Re \approx 2000$. For a typical microfluidic system, given $l \approx 10 \mu\text{m}$, $v \approx 100 \mu\text{m/s}$, and the material parameters of water ($\rho = 10^3 \text{ kg/m}^3$, $\eta = 10^{-3} \text{ kg/m/s}$), we end up with $Re \approx 0.001$. Solutions of the Stokes equations exhibit several remarkable properties. First, the flow is laminar and reversible. The streamlines of a laminar flow are locally straight and parallel. The global streamline pattern, however, may be complicated. Material lines of the fluid, when evolved together with the flow, may fold into even more complicated structures. If the sign of the flow is reversed, however, the complicated material lines will be restored into their initial shape. This behavior is due to the linearity of the Stokes equations and has grave implications for the ability of small living organisms trying to propel themselves through the fluid [1].

For an LOC application, this usually causes severe problems. For instance, mixing of two fluids or stirring a liquid to enhance homogeneity or to speed up a chemical reaction is a very difficult task for a purely laminar flow system. Also, pumping of a low Reynolds fluid is difficult, as the interaction of the fluid with the vessel walls is predominant. We will show that many of these obstacles can be overcome by employing acoustic methods.

To model the interaction between an SAW and a fluid, we treat the SAW as an array of point sources f_i of force, acting on a volume element of the fluid above the surface. This view is again justified, as it turns out [1] that the fluid flow for the given length and velocity scales is found to be over-damped. If the driving force f_i is switched off, then the flow ceases nearly immediately.

Acoustic streaming in classical, macroscopic systems has been treated in detail by several authors in the past, and for a detailed description of it, we wish to refer the reader to the works by Eckart [21] and Nyborg [11] as a starting point. The general framework of their theories on acoustic streaming is the following: The effect takes place on two separate timescales. On the short timescale, which in our case is the timescale of the SAW, the motion of the interface between the substrate and the fluid is resolved. On this scale, water does not perform an incompressible flow but has to be described by the equations of compressible fluid dynamics which consider the mass density of the fluid not as a constant but as part of the problem. Compared to the stress tensor in the previously formulated Navier–Stokes equations, the stress then contains an additional term accounting for the compressibility. It is this compressibility which gives rise to higher order terms in the pressure and velocity, finally leading to a DC term in the pressure distribution and the acoustic streaming. They further rely on conservation of mass and relate density and pressure. The SAW, which is a wave on the substrate surface only, then causes a longitudinal sound wave propagating from the substrate into the fluid. This sound wave is subject to viscous damping along its path in the fluid. Furthermore, the nonlinear terms in the compressible Navier–Stokes equation give rise to higher harmonic pressure and velocity fields, which oscillate with all multiples of the initial frequency. In a simple, 1D representation, the sound-induced pressure is given by

$$p(x, t) = p_{\max} \cos[\omega(t - x/v)] + 2\omega \cos^2[\omega(t - x/v)] + p_0. \quad (13.15)$$

Here, ω denotes the frequency of the SAW, v the sound velocity in the fluid, and p_0 a static pressure. The time average of the first and last terms in Eq. (13.15) equals zero, but the \cos^2 term results in a time-independent pressure. If attenuation is taken into account, this leads to a pressure gradient and the streaming velocity field which is observed in the experiment.

It turns out that due to phase matching arguments, the longitudinal sound wave in the fluid is obeying a diffraction law similar to the ones known from ray optics, leading to a diffraction of the wave from the parallel motion along the surface (SAW) to an oblique entrance into the fluid above the surface. The angle of diffraction turns out to be given by the different sound velocities in the substrate and the fluid, respectively:

$$\sin(\theta_R) = \frac{v_{\text{fluid}}}{v_{\text{SAW}}}. \quad (13.16)$$

The diffraction effect can be observed in an experiment, where an SAW generating IDT is placed directly underneath a fluid reservoir, containing water and a

small amount of ink to visualize the acoustic streaming in the container. In Figure 13.6, we depict the result of such an experiment.

Figure 13.7 shows a similar experiment performed in a small droplet. Here, a small amount of fluorescent dye was deposited on the surface of the chip, then a small droplet (~ 50 nL) was pipetted onto this dye spot. An SAW impinging from the left quickly dissolves the dye and distributes it throughout the droplet. Apart from the beauty of these pictures, the experiment has an enormous impact for future biochips, as it indicates the possibility of dissolving chemical reagents in a small virtual test tube by virtue of an SAW. This would enable the manufacturer of the chip to ship it preloaded with reagents. Only a suitable buffer needs to be applied to the chip and the SAW-driven fluidics do the rest.

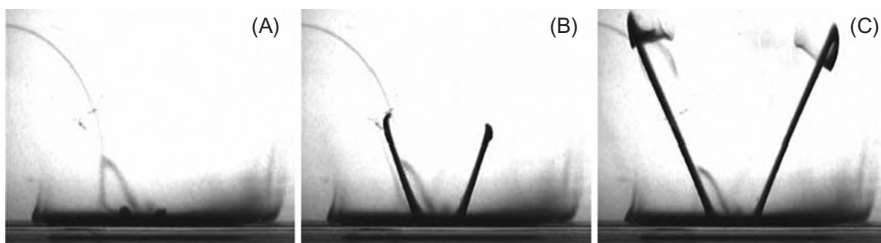


FIGURE 13.6

Fluid jets are caused by the actuation of an IDT at the bottom of a well covered by a small amount of dye. The fluid is contained in a cusp; the part shown in the pictures is approximately 18 mm wide. Between the snapshots, time spans of 0.16 and 0.48 s have elapsed. The long and thin shape of the colored fluid fingers indicate the direction in which the SAW acts on the fluid.

Source: Courtesy Advalytix.

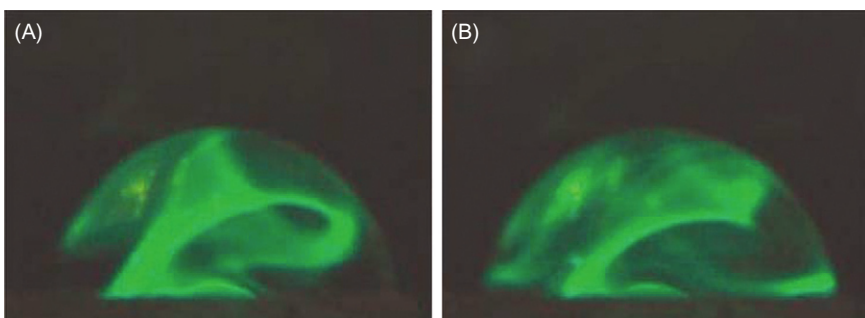


FIGURE 13.7

SAW-induced internal acoustic streaming in a small droplet. To visualize the streaming, prior to the droplet deposition, a small amount of fluorescent dye had been deposited on the chip surface. The SAW impinging from the left quickly dissolves this dye.

Source: From Ref. [12] © 2003, Elsevier, reprinted with permission.

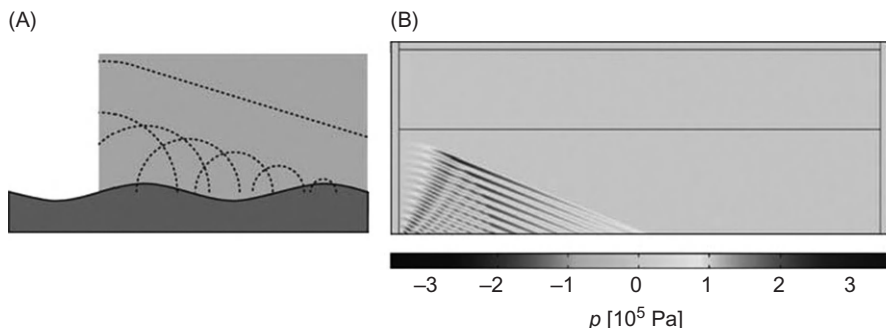


FIGURE 13.8

Finite element calculations of the pressure distribution in a substrate–fluid system (B) and the simple Huygens model (A).

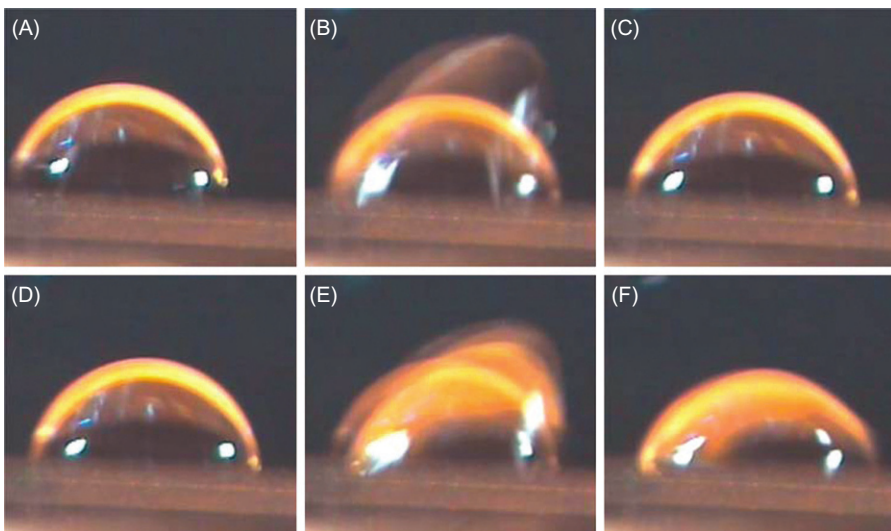
Source: Courtesy T. Frommelt.

This typical fingerprint of the SAW-driven acoustic streaming can also be theoretically understood and visualized when we look at a finite element simulation of the pressure distribution in an SAW-driven fluid. If the SAW is modeled as an array of point sources for the forces f_i , being damped in the direction of SAW propagation into the fluid reservoir, a Huygens like superposition leads to plane waves in the fluid (Figure 13.8). Phase matching results in a Rayleigh angle θ_R as given in Eq. (13.16).

SAW-induced acoustic streaming can be exploited for efficient pumping of closed fluid volumes on microfluidic chips, as well as for efficient stirring. The pumps in this case are integrated to the chip, have no moving parts, and are electrically addressable.

13.2.3 Droplet actuation

For high SAW amplitudes, not only internal acoustic streaming within a small fluid volume is observed, but an actuation of a droplet as a whole can be achieved. This SAW-driven droplet actuation if combined with a surface modification resulting in “virtual tracks” or lateral confinement of the droplet by an appropriate shaping of the SAW wave front opens a wealth of applications for an LOC system. A typical example for SAW-driven droplet actuation is shown in Figure 13.9. In this figure, we show a series of snapshots, where a small (~ 50 nL) droplet of water sitting on a chip surface is viewed from the side. An intense SAW is impinging from the left, being pulsed at a certain time sequence. Once the SAW pulse enters the droplet, violent internal streaming within the droplet is observed (cf. Figure 13.7; not visible in Figure 13.9) which is accompanied by a dynamic deformation of the droplet. Here, too, a relic of the Rayleigh diffraction angle can be observed.

**FIGURE 13.9**

A “jumping” droplet containing 50 nL water, on a flat substrate. The snapshots are taken at consecutive times. In the center pictures (B and E), a powerful pulsed SAW hits the droplet from the left, leading to a severe deformation. When the SAW is turned off, the droplet relaxes into its initial spherical shape at a shifted downwind position to the right.

Source: From Ref. [12] © 2003, Elsevier, reprinted with permission.

The theoretical description of this droplet actuation represents a particular challenge, as we obviously have to deal with extremely complex boundary conditions in this case. The fluid volume is finite and is only confined by surface tension effects, except for the base on which it is resting. Very recently, however, the problem has been solved leading to a beautiful agreement between theory and experimental observations [22]. In this last reference, a finite element algorithm for computing free surface flows driven by arbitrary body forces is presented.

Schindler et al. [22] represent the free surface shape by the boundaries of finite elements that move according to the stress applied by the adjacent fluid. Additionally, the surface is modeled to minimize its free energy and by adapting its curvature to balance the normal stress at the surface. The numerical approach consists of the iteration of two alternating steps: the solution of a fluidic problem in a prescribed domain with slip boundary conditions at the free surface and a consecutive update of the domain driven by the previously determined pressure and velocity fields. For a Stokes problem the first step is linear, whereas the second step involves the nonlinear free surface boundary condition. This algorithm is justified by both physical and mathematical arguments. It is tested in two dimensions for two cases that can be solved analytically. For the details of this nice piece of calculation, we again refer the reader to the original publication. However, the results are worth being summarized in Figure 13.10.

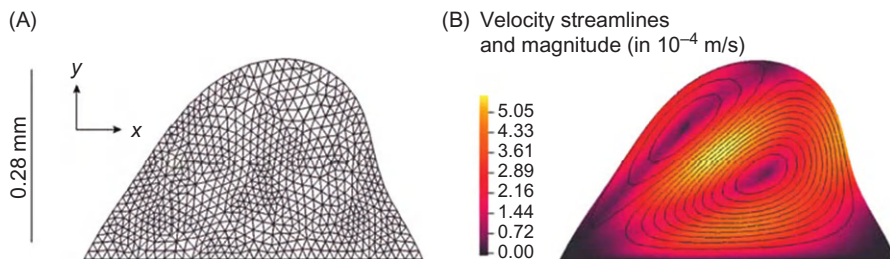


FIGURE 13.10

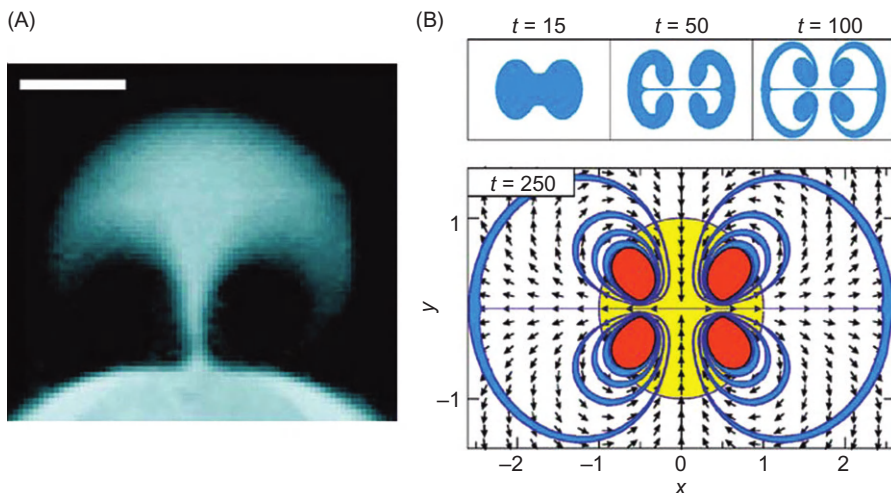
Finite element calculation of an SAW-driven droplet deformation and acoustic streaming within [22]. Note the similarity of the resulting streaming pattern to the one experimentally observed in Figure 13.7.

Source: Reused with permission from Ref. [22] © 2006, American Institute of Physics.

13.3 Example 1: Acoustic mixing

Efficient mixing of small amounts of fluid is probably the most challenging task for microfluidic devices. For liquids confined to small volumes, interaction between the fluid and the walls of the container become dominant, as the surface-to-volume ratio becomes very large. In general, this increased liquid–wall interaction is parameterized by Reynolds number, usually being a small quantity in microfluidic systems. A low Reynolds number, however, is equivalent to an increase in the apparent viscosity. As turbulent streaming only occurs at high Reynolds numbers, this in turn leads to slow mixing in microfluidic systems, in which only laminar flow processes are possible. Hence, the only way for small fluid volumes to mix effectively is by diffusion. Here, the smallness of the system is in favor of the diffusion limited timescales, as the respective length scales are equally small. However, for many applications, especially microarray-based assays [12,23,24], a deliberate and controlled agitation of the fluid under investigation would be of great importance. This is because diffusion-driven mixing is effective only on a short range. Microarray hybridization, however, requires transport of molecules in the fluid over large distances, and agitation is mandatory.

There are many different approaches for mixing in microfluidics. Many rely on external means like pumping through connections to the microfluidic chips. Other approaches rely on the flow geometry. Duct flows have recently received particular interest and many concepts for mixing the channel throughput exist [25]. Either the diffusion path is decreased by hydrodynamic focusing [26,27] or the contact surface is increased by multilamination [28,29]. Parabolic velocity profiles are used to mix by Taylor–Aris dispersion in ring channels [30,31]. Even chaotic advection can be induced within a channel, e.g., by patterning the walls [32], resulting in a meandering channel [33], or active flow disturbances [34–36]. Many or most of the above approaches, however, require either a sophisticated channel layout or external means which make the actual application difficult.

**FIGURE 13.11**

(A) A dye jet pumped by an SAW transducer, shortly after switching the RF power. In the center of the transducer, the fluid is pumped upward; on both sides the fluid is sucked in. The white scale bar is 0.5 mm. (B) Results of the theoretical modeling of this capillary gap flow profile (view from above). The inset shows the temporal evolution of the dye distribution.

Acoustically induced internal streaming seems to offer a path out of this dilemma. The same SAW that is used to actuate the fluid on a chip or in a closed volume can be employed to induce complex streaming patterns. Moreover, SAW can be modulated in frequency as well as in time, this being electrically activated.

A recent approach is related to the folding of material flow lines by modulated SAW-induced streaming. Here, an SAW of a given frequency and direction with respect to the fluid volume is modulated either in space (trajectory) or in time. Each SAW induces a (stable) streaming pattern like the one shown in Figures 13.6 or 13.7. The streaming pattern changes according to the SAW direction, frequency, or amplitude. Such SAW modulations can easily be achieved by switching the excitation parameters of the IDT.

One example for SAW mixing in a thin capillary gap formed between the SAW chip and a cover slip on top of it is shown in Figure 13.11. The plot shows an experimentally obtained micrograph of an SAW spread dye in a capillary gap together with a theoretical calculation of the flow profile for the same geometry [37]. The experimental picture represents a snapshot some time after the SAW has been turned on; the inset on Figure 13.11B shows the time evolution of the shape as extracted from our model calculation. The lower part of Figure 13.11B exhibits a snapshot of the material folding or flow line after some time. Similar but different flow lines are obtained if, for example, the direction of the SAW is

changed. The resulting material (dye in this case) distribution then represents a superposition of the single quasi-static cases. If this procedure is repeated several times, a homogeneous distribution of the dye is obtained.

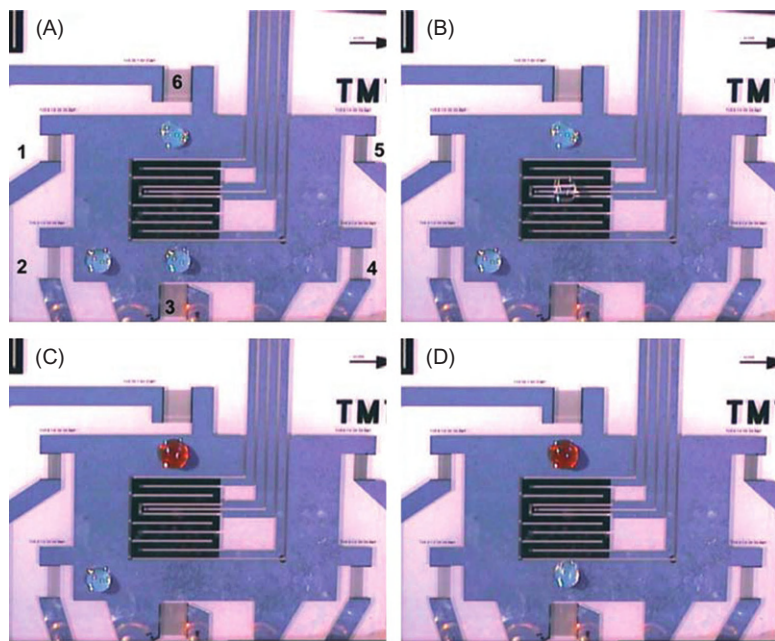
More recently, SAW-induced mixing in closed channels has been observed [38], triggering chaotic advection in a microfluidic system. The optimum SAW propagation parameters have been determined to achieve perfect mixing after the shortest possible times.

13.4 Example 2: Acoustic droplet actuation

The possibility that we can deliberately steer very small fluid volumes across a microfluidic chip, dissolve predeposited reagents, and mix and stir together with additional functional elements being integrated on the same chip, offers a wealth of applications for a miniaturized laboratory. The fact that the experiments or assays are operated in a batch mode, meaning that each step is independent from the other, makes the SAW-driven microfluidic system an ideal candidate to provide a programmable microfluidic processor. The same hardware can be used for completely different protocols, with computer software monitoring the different steps of the process. The pumps, mixers, and dissolvers are SAW driven and can easily be combined with heaters, sensors, etc. on the same chip. The technology to produce the chips is well established and borrowed from semiconductor technology. The chips can be produced in a few mask steps on whole wafers, making them so cheap that they can be used as consumables.

One example of such an acoustically driven, programmable microfluidic processor is shown in Figure 13.12. The figure shows a series of four snapshots of a chip, where three different chemicals in the form of little droplets are actuated, merged, and mixed. The chemicals in this case have been chosen such that each merger results in a color change of the output. The chip in this case is equipped with six different transducers, arranged around the circumference of the chip. Each transducer can be operated independently, two of each facing each other forming a delay line. The corresponding sound paths are patterned with a surface functionalization, leaving a hydrophilic virtual track behind, along which the droplets are guided (not visible, as monolayer chemistry). In the center of the chip, additional elements like heaters and a thermometer can be seen, all being produced by planar technology.

The whole area of the chip is about $1 \times 1 \text{ cm}^2$; the droplets used in this experiment are about 100 nL of volume. Application of a suitable RF signal to one of the transducers induces SAW-driven actuation of the desired droplet in its sound path. Interestingly, a second droplet being located in the lee side of the actuated one is not affected by the SAW (Figure 13.12A and D). The reason is that the SAW is strongly attenuated by the first droplet, leaving not enough amplitude behind it to actuate a second one. This remarkable feature makes individual actuation of individual droplets possible. Once two droplets merge, they are mixed

**FIGURE 13.12**

An SAW-driven microfluidic processor: three droplets (~ 100 nL each) are moved independently and remotely controlled by six acoustic nanopumps. (A–D) represent a series of subsequently taken snapshots to visualize the movement, and the chemical reactions occurring when the droplets are merged and mixed by the action of the surface wave. The chip not only contains the acoustic nanopumps and the fluidic environment but also additional systems like sensors and heaters.

Source: From Ref. [12] © 2003, Elsevier, reprinted with permission.

instantaneously, leading to a nearly immediate homogeneous chemical reaction as visualized by the respective color change. Control experiments, where the two droplets were carefully brought into contact by slightly pushing them with a pipette tip toward each other, revealed a very slowly moving reaction front within the resulting droplet. Without being able to estimate the time difference between the SAW mixed reaction and the diffusion-driven one, the SAW-driven reaction is definitely at least two orders of magnitude faster.

A very similar chip has been used to test a completely computer controlled feedback system, enabling the software to actually determine the position of a droplet on the chip. As the SAW actuation depends on many parameters like wetting angle, precise droplet size, quality of the surface functionalization, defects, or particle contaminations along the fluidic track, there is no reliable way to predict the position of a droplet from the excitation parameters alone. Instead, we make use of the fact that an SAW is strongly attenuated by a liquid droplet in its way.

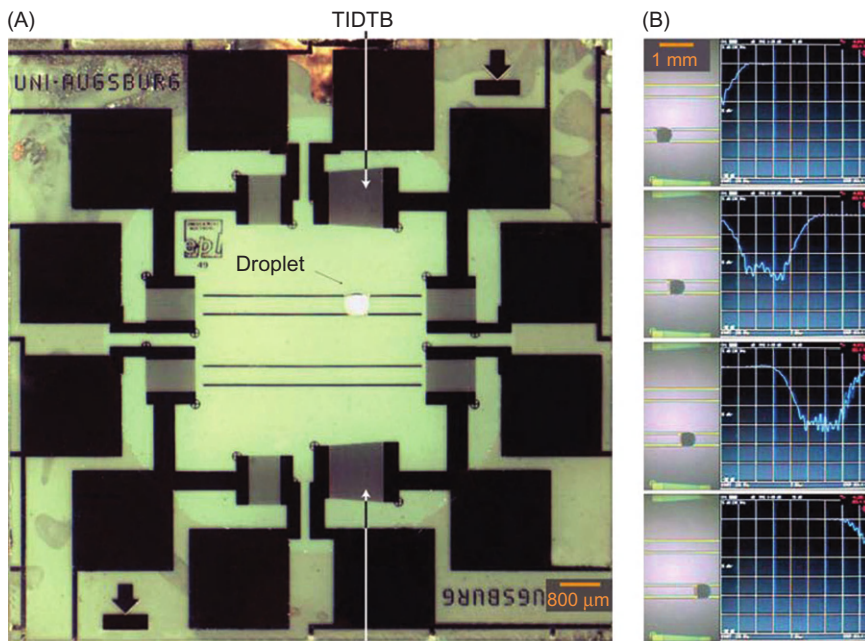


FIGURE 13.13

SAW-driven microfluidic chip with means to determine the actual droplet position on the chip. One set of IDT (A, B) is used to actuate the droplet; a second delay line (TIDTA, TIDTB) is employed to measure its position. Here, the SAW transmission between TIDTA and TIDTB is monitored as a function of the droplet's position. Strong attenuation is observed, once the droplet resides within the sound path of this delay line (see B). To increase spatial resolution, a special TIDT has been used [39].

Source: Courtesy T. Frommel.

For this purpose, we employ one of the temporarily unused delay lines on the chip to monitor the SAW transmission between them. Once a droplet is pushed into the sound path of this monitoring SAW, it is strongly attenuated. The corresponding SAW transmission signal can then be used to determine the position of the droplet on the chip.

The result of such a position measurement is shown in Figure 13.13. Here, we show a photograph of the chip and the droplet together with a transmission measurement of a perpendicularly oriented SAW delay line employing a network analyzer. In this case, so called tapered IDT (TIDT) have been used [39] to increase the spatial resolution of the experiment. A droplet in the sound path of the monitoring SAW leads to a significantly reduced transmitted intensity, as can be seen on the display of the network analyzer in Figure 13.13B. The attenuation of an SAW caused by a small droplet can exceed several dB, hence making it very simple to collect the data for a position analysis on the chip.

13.5 Applications

13.5.1 Microarray hybridization (biological application)

A first and very important application for the SAW-induced acoustic streaming as outlined above is its use for microarray hybridization. Small amounts of fluid containing an unknown constituent of DNA fragments is spread over a more or less densely packed array of “spots” containing different known constituents, acting as capture molecules for the unknown ones. The latter are being tagged with a fluorescent dye, in most cases. Upon successful hybridization between the target molecule in solution and a corresponding one on a spot, the local fluorescence intensity for this spot raises as compared to the areas without capture molecules or unspecific binding events somewhere else. Employing a sophisticated microarray layout and multicolor tagging schemes, a wealth of information about the unknown sample can be gained from such experiments. The probably best known example would be the “genetic fingerprint.”

Protein and DNA microarrays have thus become a standard tool in proteomics/genomics research. Up to several thousand spots of oligonucleotides or cDNA [40] probes with known identity are implemented on the chip in a checkerboard pattern. In gene expression profiling assays, the ratio of binding of complementary nucleic acids from test and control samples is determined. This allows a parallel, semiquantitative analysis of transcription levels in a single experiment. In order to guarantee fast and reproducible hybridization results, however, the diffusion limit must be overcome. Hybridization experiments are performed at either body or slightly elevated temperatures, and it turns out that diffusion—especially for large macromolecules like oligonucleotides, DNA fragments, or the like—is an extremely slow process. On the other hand, typical microarray areas are quite large, and the fluid film containing the precious sample is only a few tens of micrometers high, forming a capillary gap being spread over the microarray. Especially in case of low concentrated cDNA molecules corresponding to low expressed genes, the immediate vicinity of the corresponding probe spot will be quickly depleted. Without active agitation, diffusion is the only mechanism for the DNA strands to be transported to their complementary spots. It has been estimated that it would require weeks for the hybridization reaction to reach equilibrium [41,42].

To achieve reasonable hybridization time while saving precious sample and dye, stirring or mixing is an important issue. SAW microagitation chips efficiently agitate the smallest sample volumes (down to 10 µL and below) without introducing any dead volume. The advantages are reduced reaction time, increased signal-to-noise ratio, improved homogeneity across the microarray, and better slide-to-slide reproducibility. Such SAW micromixer chips are the heart of the Advalytix *ArrayBooster*, or the Advalytix *SlideBooster* [43], being compatible with all microarrays based on the microscope slide format.

Three different methods to apply the SAW agitation technique to microarray hybridization assays have been successfully demonstrated. First, in the so-called *ArrayBooster* geometry: an SAW mixer chip, embedded into a glass or epoxy

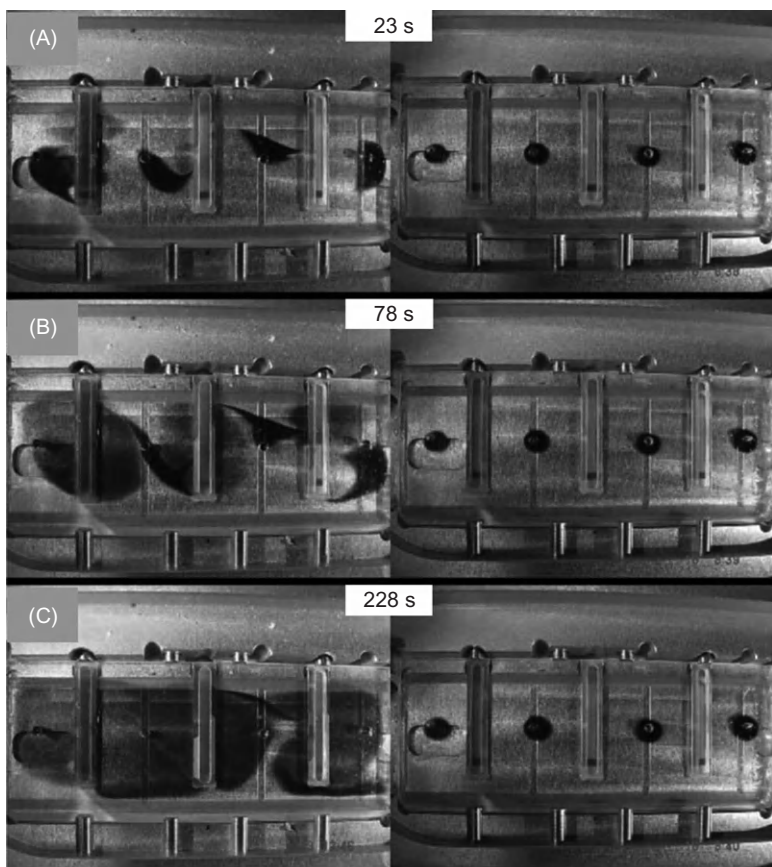
slide, is placed on top of the sample fluid from above. The SAW chip and the supporting glass or epoxy slide thus form a “mixer card,” and at the same time serve as the cover slip. Spacers between the mixer card and the slide containing the microarray define a well-controllable fluid layer, if the sandwich is filled with sample liquid. To visualize the mixing process, in the experiment shown in Figure 13.14, we drilled four holes into the mixer card, through which we pipetted small amounts of ink into the buffer solution confined between the slide and the mixer card. At the left of Figure 13.14A–C, the progress of the mixing can be observed, once the SAW mediated acoustic streaming takes place. In the right parts, the SAW had not been switched on. Hence, diffusion is the only source to act upon the ink, and nearly no spreading of the dye is observed.

A second method to apply SAW-induced acoustic streaming to a microarray assay is to couple the ultrasonic SAW energy through an index matching fluid and through the slide hosting the microarray into the sample fluid on top of it. Even without direct contact between the sample hybridization solution and the mixer chip, the SAW mediated agitation can be applied to the hybridization assay. This *SlideBooster* geometry [44] has proven to be particularly successful for protein and tissue microarrays for immunohistochemistry (IHC) applications. In both cases, the signal intensity as well as the homogeneity has been remarkably enhanced as compared to conventional methods. The third technique relies on the fact that mixing of a sample fluid in thin liquid layers is particularly effective if the sources of the ultrasonic energy are distributed randomly across the hybridization area on the microarray [43]. Although both the *ArrayBooster* and the *SlideBooster* geometries make use of a distributed source mixing by using multiple mixer chips containing multiple SAW transducers being operated at different frequencies (multiplexing), the distribution of SAW sources in these cases is spatially fixed and given by the layout of the mixer chips used. The frequency multiplexing distributes the sources of ultrasonic energy in time, following a predetermined protocol. In other words, a set of transducers is powered at a given SAW intensity over a certain period of time and hence induces a specific streaming pattern. After a certain dwell time, a second set of transducers with a second streaming pattern is powered, and so on.

Figure 13.15 is a typical example for such a fluorescently labeled microarray experiment. In (A), we show the fluorescence of a series of spots on the microarray, which has been hybridized employing a conventional cover slip technique [45], whereas panel (B) shows the same microarray after agitation during hybridization. Clearly, in (B), the fluorescence intensities and the homogeneity are much higher than in (A). Details for the hybridization parameters are found in Ref. [45]; many more examples for a successful application of agitation in the microarray field including protein microarrays and IHC applications can be found in Ref. [44].

13.5.2 Polymerase chain reaction

Many modern experiments and analytical techniques in genetics rely on the amplification of genetic material prior to microarray hybridization assays. The

**FIGURE 13.14**

Visualization of the SAW mediated agitation of a microarray sandwich. This top view into the hybridization chamber shows a mixer card with three SAW chips, which is used to confine a fluid layer of $d = 60 \mu\text{m}$ on top of a glass slide containing an oligonucleotide microarray. Ink is pipetted through four holes to visualize the agitation process. In the left part of the figure, the mixer chips are SAW activated. To the right, the SAW had been switched off, thus showing the effect of diffusion alone. After several minutes, the SAW-induced acoustic streaming led to a complete homogenization of the ink, indicating a very efficient mixing effect, whereas the ink in the “diffusion only” case has not spread at all.

Source: From Ref. [43] © 2005, JAI; reprinted with permission.

reason is that in some cases (e.g., for genetic fingerprinting), not enough material is available for further investigation. In other cases, the amplification of genetic material can also lead to a purification of the existing sample. The technique of choice for genetic amplification is the PCR, the invention of which was rewarded with the Nobel Price for chemistry in 1993 [46]. PCR is a biochemistry and

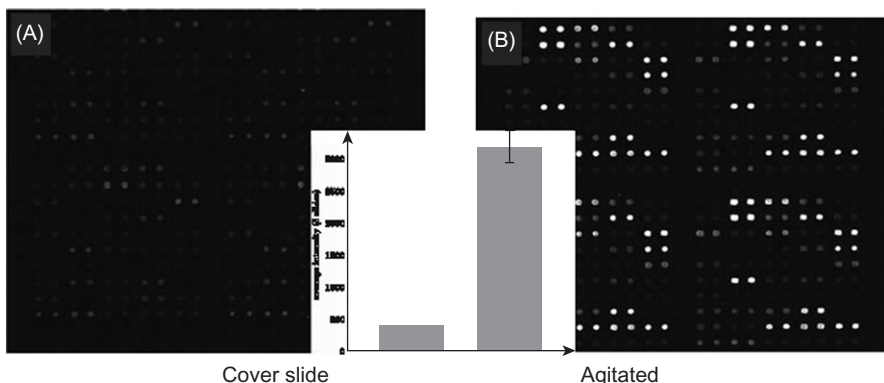


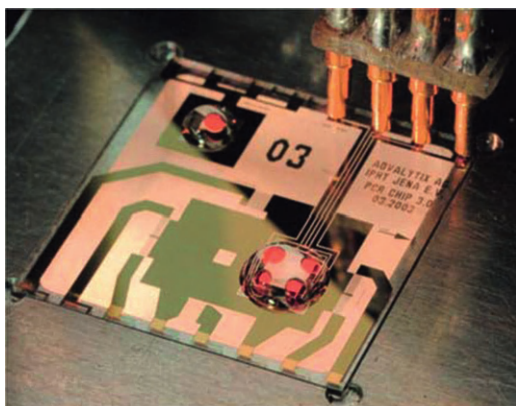
FIGURE 13.15

Fluorescence image of a typical microarray without (A) and with (B) microagitation. Clearly, a higher intensity and homogeneity due to agitation is observed. The inset shows the averaged intensities for five different slides.

Source: From Ref. [45] © 2003, JBT; reprinted with permission.

molecular biology technique for enzymatically replicating DNA without using a living organism. Like amplification using living organisms, the technique allows a small amount of DNA to be amplified exponentially. As PCR is an *in vitro* technique, it can be performed without restrictions on the form of DNA, and it can be extensively modified to perform a wide array of genetic manipulations. It is commonly used in medical and biological research laboratories for a variety of tasks, such as the detection of hereditary diseases, the identification of genetic fingerprints, the diagnosis of infectious diseases, the cloning of genes, paternity testing, and DNA computing [47].

In this section, we present a complete PCR laboratory on an SAW-driven chip, comprising many of the building blocks as described and outlined above. The whole chip has a size of about $2 \times 2 \text{ cm}^2$, and SAWs are generated by IDT structures being patterned by photolithography on a planar LiNbO_3 substrate. Employing the same process, other metal structures can be processed as well. This allows for building up a chip with different functional units. The transport of liquid between the units can then be achieved by SAW. Chemical surface functionalization is employed to dispense and guide droplets. The first functional structure on the chips is a metal thin film resistance heater with an integrated temperature sensor. The heater is $2 \times 2 \text{ mm}^2$ in size with a window in its center. This window allows for an optical monitoring through the transparent piezoelectric substrate. The temperature is computer controlled with 0.1 K accuracy. The chip heater is used for two processes in DNA analysis. The first is the amplification of a small amount of template DNA in a PCR where repeated cycles of three different temperatures lead to amplification of the DNA strand [48]. To finally analyze the amplified DNA, hybridization assays are commonly used, as has been

**FIGURE 13.16**

Programmable microfluidic biochip for multispot PCR. The sample solution in red is covered by a mineral oil layer to prevent evaporation at elevated temperatures. Apart from SAW-driven nanopumps for the fluid actuation, the chip also hosts a heater and a thermometer. The chip is connected to the outside via pogo contacts. Underneath the transparent piezoelectric substrate, a microscope objective is mounted for fluorescence monitoring of the PCR progress employing an intercalating dye. Microsystem realized by Avalytix and the Institute for Physical High Technology in Jena, Germany. (For interpretation of the references to color in this figure legend, the reader is referred to the web version of this book.)

Source: From A. Wixforth, *Flat fluidics: programmable on-chip networks for biological and chemical applications* © 2005, NSTI; reprinted with permission. [57]

described in the previous section. Employing this method, the binding of DNA in solution to surface-coupled complementary strands is observed, while the temperature is kept on a value characteristic for the reactants. This provides information on the corresponding nucleotide sequence.

With the two processes performed in series on one chip, a tool for complete DNA analysis is built suitable for various applications like the study of gene function, gene expression, and SNP [49]. A picture of such an SAW-driven PCR chip is shown in Figure 13.16. The chip shown in this figure allows for the so-called multispot PCR, where several samples are amplified simultaneously [44,48].

A severe drawback to the otherwise “open” geometry of SAW-driven programmable microfluidic chips is the sensitivity to elevated temperature and the related evaporation of the open droplets. To prevent this evaporation, the aqueous solution containing the PCR mix is covered with mineral oil, forming a semispherical cap due to the chemical modification of the surface. We recall here that the PCR mix consists of two oligonucleotide primers which hybridize to either side of the DNA region to be amplified, deoxynucleotide triphosphates, or dNTPs, the substrates for DNA synthesis, and the heat resistant Taq polymerase (an enzyme that comes from the bacterium *Thermophilus aquaticus* native to hot springs).

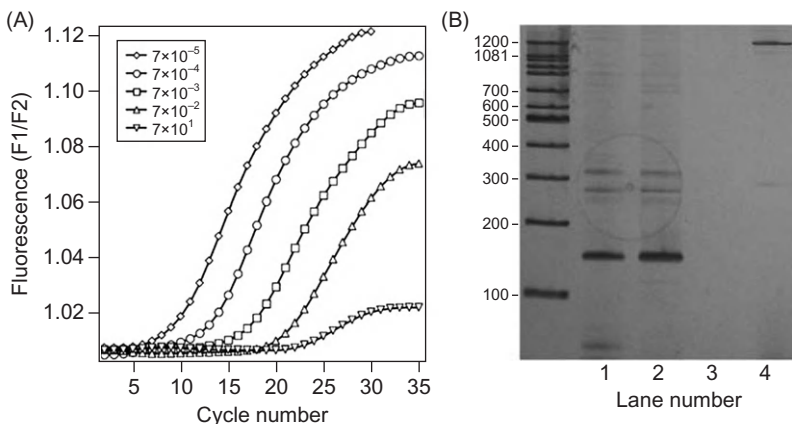


FIGURE 13.17

(A) Online PCR traces for five different template concentrations of plasmid: the threshold where the signal rises depends on the concentration. (B) Chip PCR (35 cycles) detected with electrophoresis gel. Lanes 1 and 2: 150 bp fragment of human genomic DNA cycled from 6000 genome equivalents (one genomic equivalent equals to 2×23 chromosomes); lane 3: no template; lane 4: 1382 bp fragment was amplified from six genome equivalents [48].

Source: Courtesy Advalytix.

This mix can either be applied as a liquid or be preloaded to the chip in dry form. In this case, sample buffer needs to be added, and SAW agitation is used to dissolve the PCR mix into solution. The application of the oil cap can also be achieved with the SAW by pushing the oil onto the water droplet, while the different surface tensions of the two liquids account for the spatial arrangement. Therefore, encapsulation of the PCR solution against evaporation can be reached much easier than with valves in a microfluidic channel system. The contact area of the oil/water droplet to the chip plane has about the size of the heater structure. This whole fluidic microchamber can be moved across the chip with the SAW.

PCR cycling has been described in detail in Chapter 6. Let us mention that to gain a better control over progress and efficiency of the PCR, an optical online monitoring system can be integrated. This is done with different fluorescent dye systems that exhibit varying emission intensities correlated with the amount of double stranded DNA or the concentration of a special DNA product with their emission intensity. To investigate the possibilities for a direct PCR process control on a planar chip, a small optical unit that can collect the light emitted from a dye inside the oil covered PCR droplet has been incorporated. The unit is placed below the transparent chip, and the optical path is focused through the window in the heater into the aqueous solution. Figure 13.17A shows the optically monitored increase of fluorescence intensity for an intercalating dye versus the number of PCR cycles and for different concentrations of the initial copies [44]. The

intensity is proportional to the actual number of copies after amplification. As can be seen from the figure, we observe a rapid increase in fluorescence for a few cycles, eventually saturating as the building blocks exhaust. Figure 13.17B shows a gel electrophorogram of the amplified DNA fragments. Lanes 1 and 2 represent a deliberate amplification from a given start copy concentration, lane 3 is a control experiment with no start copies at all, and lane 4 represents the result for a much lower start copy concentration as in lane 1. Within the experimental resolution, no cross contamination has been observed in this multispot PCR.

The leftmost lane in Figure 13.17B is a marker lane for calibration of the molecular weight of the amplicants. The on-chip PCR presented here is able to operate with submicroliter volumes at a significantly increased amplification speed. Moreover, for fortunate but still unknown reasons, the on-chip PCR seems to be much more resistant against (airborne) contamination than conventional approaches. For a detailed description of the PCR processes employed here, see Refs. [44,48] and references therein.

13.5.3 Cell adhesion

13.5.3.1 Blood flow on a chip

Another powerful application for SAW-driven microfluidic chips is the study of cell adhesion to either artificially fabricated surfaces or biological surfaces. This study is very useful for the investigation of cell adhesion to medical implants. These can be coarsely divided into two different types: one type is meant to adhere firmly to the biological environment, like tooth implants. The other group needs to avoid cell adhesion—like artificial hip joints. Both types of implants possess surfaces that can be deliberately functionalized to be optimized into one or the other direction.

The combination of planar (semiconductor) technology for SAW-driven fluidic chips is completely compatible with all kinds of thin film technologies. Hence, many different materials, textures, or functionalizations are easily investigated in terms of cell adhesion. For this purpose, closed loops of virtual fluidic tracks are used, where SAW induces acoustic streaming. As the SAW itself is attenuated over a propagation length of a few wavelengths, no real high-frequency effects remain in an even microscopic closed loop. Instead, the pressure difference between the SAW entrance and the fluid volume drives a homogeneous, easily controllable laminar flow whose profile covers the complete range of physiological flow and shear conditions from 0 to several $10,000\text{ s}^{-1}$ along the channel, which can be adjusted by means of the SAW amplitude. A simple version of such a “planar microflow chamber” is sketched in Figure 13.18. Employing a hydrophilic/hydrophobic surface functionalization, a closed loop virtual track is formed. In the case of Figure 13.18, the total volume is about $8\text{ }\mu\text{L}$.

Such acoustically driven planar microflow chambers provide many advantages for cell adhesion investigations. Apart from the advantages of using SAW as a localized nanopump, the free (functionalized) surface of the chip is easily

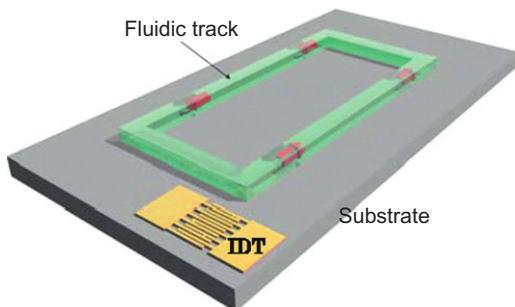


FIGURE 13.18

An SAW-driven microfluidic chip for cell adhesion measurements. An SAW, excited electrically, interacts with the confined liquid at the solid–liquid interface and induces liquid circulation. The surface wave basically acts as a localized pump, as its mechanical energy is absorbed by the liquid over only a few micrometers. Due to the small scales of this microfluidic system, it creates a homogeneous laminar flow along the channel. The total length of the track in this case is about $l = 40$ mm [50].

accessible to exchange buffers or reagents, or to monitor the flow optically. Moreover, the flow chamber and hence the flow within is electrically addressable, which makes it a versatile tool for investigations. As an example, we present here some recent investigations regarding blood flow and platelet adhesion. Studying cell or platelet adhesion (hemo-dynamics) in small capillaries and arteries is a particularly challenging topic, since it is difficult to be mimicked in an *in vitro* system and hard to access by optical or mechanical means. As the diameters of capillaries and arteries become as small as $1\text{ }\mu\text{m}$, the Reynolds number becomes very low, making the pumping mechanism extraordinarily difficult. Using the chip design shown in Figure 13.18, a blood vessel can be mimicked, allowing for the study of the blood flow and platelet adhesion. The flow chamber has no dead volume so that investigations of expensive or rare substrates—with a volume 100–1000 times less than usually required—are possible. The particularly small sample volume of only $8\text{ }\mu\text{L}$ is probably the most prominent advantage of the nanopump-driven planar flow chamber chip (FCC). Moreover, the chip components are inert and entirely compatible with biological systems and the system is free of all movable parts, making the handling extremely simple. The complete optical transparency of the LiNbO_3 substrate allows for individual cells to be tracked over long periods of time, when the μ -FCC is mounted directly onto a fluorescence microscope.

Lanes ranging from a few micrometers up to 10 mm both in width and length can be realized. The open structure on a free surface allows for direct access to the channel at all times (e.g., for the addition of antibodies or drugs). The technique also provides maximum freedom for mimicking all possible vessel architectures and conditions as they may exist in nature with curved, branched, or

restricted vessels. Finally, no restrictions are put on the surface functionalization. Artificial lipid membranes, protein coats, and even confluent cell layers have been prepared successfully.

13.5.3.2 Proteins in a microflow

Using the same microsystem, the effect of shear flow on a protein called von Willebrand factor (vWF) has been investigated [50]. This protein is a glycoprotein being synthesized and stored in endothelial cells, and has been found to play an important role for blood coagulation by adhesion of the platelets, particularly in regions where the shear rates are high. At first glance, this adhesion and subsequent coagulation behavior seems to be counterintuitive, but it is the very special nature of this mechanically activated macromolecule that helps us to resolve this contradiction: under normal conditions, it assembles into multimers (biopolymers) which, when stretched, can reach sizes as long as 100 μm . The monomeric length is unusually large ($\sim 100 \text{ nm}$) and contains 2050 amino acid residues. Intuitively, one would expect that blood platelet adhesion is always decreasing with increasing shear force applied to the platelet. Surprisingly, vWF mediated adhesion is strongly enhanced under high shear flow conditions [51]. vWF was spread over the hydrophilic track of the FCC and exposed to various shear flows. Images of vWF at concentrations typical for human blood ($c \approx 2 \mu\text{g/mL}$) are presented in the lower panel of Figure 13.19 for two different SAW-induced shear rates. At shear rates between $\dot{\gamma} \approx 10$ and 1000 s^{-1} , the biopolymer exhibits a compact conformation (Figure 13.19A). This compact conformation remains unchanged as long as the shear rate is maintained below a certain (critical) value $\dot{\gamma}_{\text{crit}} \sim 5000 \text{ s}^{-1}$. Increasing the shear rate, a shape transformation of the vWF fibers from a collapsed to a stretched conformation of length $l \approx 15 \mu\text{m}$ (Figure 13.19B) is observed. This transition is reversible, as we observe an immediate relaxation of the protein to its compact conformation when the flow is turned off.

This finding explains the apparent counterintuitive observation mentioned at the beginning of this section. Under high shear flow, vWF mediated blood platelet adhesion is more effective. In its collapsed state, all binding sites are buried inside the coil. Once the critical shear is exceeded, vWF stretches into a long thin fiber exposing all its binding sites. If vWF touches the surface in this conformation, it will immediately be immobilized and serve as a “sticky” grid for free floating blood platelets.

13.5.3.3 Cell–cell interactions on a chip

Although the simple planar flow chamber sketched in Figure 13.18 represents an elegant technique for examining many relevant topics, it does not perform satisfactorily for the direct culture of living cells on its surface: Initial attempts are hindered by the fact that the protein-rich media influenced the channel architecture due to the protein adsorption on the hydrophobic surface. As a result, this led to an unwanted inhomogeneous flow profile. To avoid this, a more sophisticated 3D version of the system has been developed which easily allows for successful

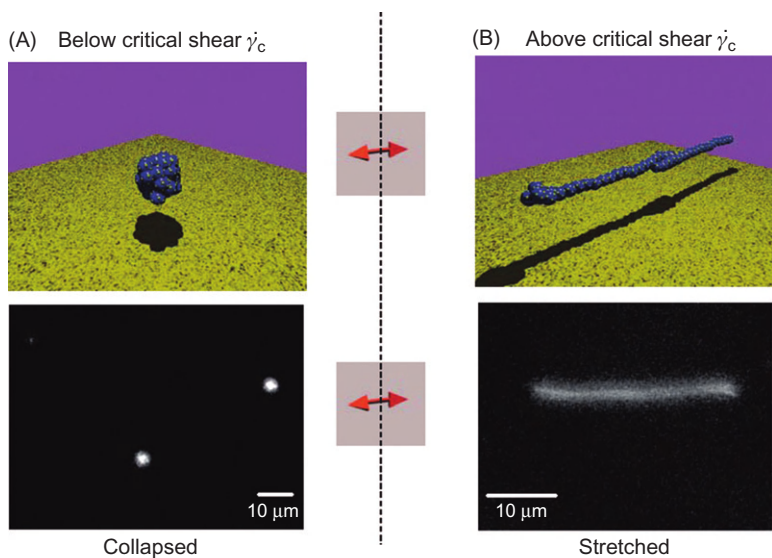


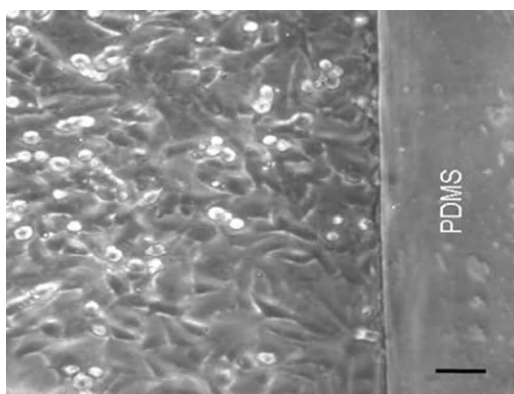
FIGURE 13.19

vWF proteins in a flow: the blood clotting protein vWF is exposed to various shear flow conditions. Only when a critical value is exceeded, the protein elongates in a reversible fashion. The unusually high shear rate levels could not be explained by conventional hydrodynamic models; and a new theory was developed [52].

cell culture while retaining all of the advantages of the planar system previously described. This was achieved by a flexible yet stable 3D architecture by adding “walls” to the channel employing the fully transparent, biocompatible synthetic elastomer PDMS. This system was devised by examining the adhesion of human melanoma cells at various shear rates. The results are shown in Figure 13.20, which shows the cell culture chip and the surrounding PDMS channel. Note that the cells form a confluent layer filling out the entire channel without growing outside of the boundaries. In addition, the cells appear healthy, divide readily, and are securely attached to the chip surface. This cultured layer remains completely unaffected by the SAW, which still induces a continuous flow along the channel. In such a biofunctionalized microfluidic chip, a true artificial blood vessel, for example, can be realized. We are presently investigating the possibilities of growing and culturing many different cell lines in such a channel, including endothelial cells.

13.5.3.4 Advanced applications

Using SAW-driven microfluidic chips, many other applications can be envisioned, some of which are presently under investigation. A representative example is SAW mediated alignment of carbon nanotubes (CNTs). CNTs are a self-assembled

**FIGURE 13.20**

Cell–cell interactions on a chip: cells are grown directly in the microfluidic channel delimited by PDMS walls. The cells form a confluent layer over the entire channel and do not grow on the boundaries (PDMS walls). The scale bar represents $50\text{ }\mu\text{m}$.

version of an ideal 1D electronic system and hence have recently attracted considerable interest in terms of future applications as electronic devices. The preparation of CNT is quite advanced, and CNT suspensions are commercially available. However, to actually integrate CNT into an electronic environment like a micro-electronic chip, a deliberate positioning with respect to the chip layout of the CNT is an important prerequisite.

Employing a flip-chip technique [53], an aqueous solution containing CNT in suspension is placed in a capillary gap in which a flow is induced by SAW technique. As CNTs are polarizable and possess a streaming resistance, the combination of SAW-induced piezoelectric fields and SAW-induced acoustic streaming results in an alignment of CNTs with respect to the substrate. This alignment exhibits a clear preferential direction, as can be seen in Figure 13.21.

Functionalization of the CNT, employing thiolization, makes the nanotubes stick to the gold electrodes. Using this technique, the SAW-induced alignment can be further improved and CNTs can be deliberately deposited between Au electrodes to investigate their electronic properties [54]. Recently, CNTs have been aligned between two Au electrodes even on a nonpiezoelectric substrate like silicon. Here, the same flip-chip technique as described in Ref. [53] has been employed. However, the cover slip was replaced by a silicon substrate on which an array of microfabricated Au electrodes had been previously deposited.

Depending on the CNT concentration, even single CNT can be “spanned” between the Au electrodes on the silicon substrate [55]. Moreover, it could be shown that they can even be processed to be freestanding between the Au “posts.” These devices represent a truly 1D electronic system with tunnel barrier contacts to manipulate them electrically. Using the very same SAW technique,

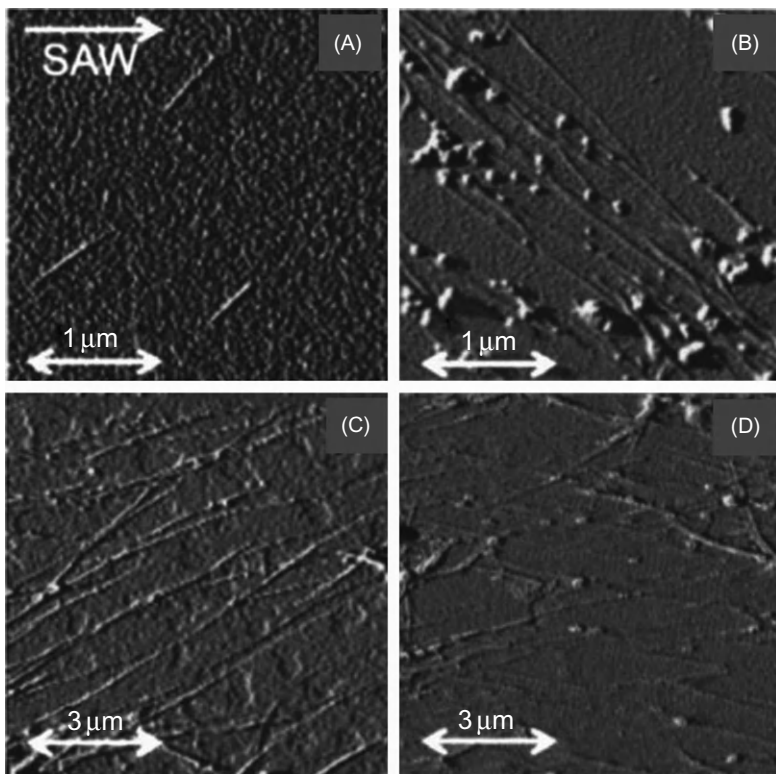


FIGURE 13.21

AFM images of aligned multiwall CNTs (MWNTs) with different concentrations of the suspension. After experiencing the SAW-induced shear flow in a capillary gap between the LiNbO₃ substrate and a cover slide, the MWNTs are aligned with an angle between $\pm 25^\circ$ and $\pm 45^\circ$ with respect to the SAW propagation direction.

Source: Reused with permission from Ref. [53] © 2004, American Institute of Physics.

acousto-electric currents can be induced in such 1D electronic systems. The difference with a quasi-2D system [16,18], however, is that the SAW represents a dynamical potential modulation acting like an escalator for single electrons. Hence, the SAW-induced acousto-electric current measured between the Au contacts consists of single electrons, one by one driven through the CNT by the SAW, and resulting in a quantized current [56].

13.6 Summary

SAWs induce an acoustically driven flow in fluids on the substrate surface on which they are propagating. SAWs are modes of elastic energy, propagating along

the surface of a solid. They are easily excited and detected once a piezoelectric substrate is used. The SAWs used in our experiments are mostly of the Rayleigh type, having large surface displacements normal to the surface plane. Fluids on this surface interact with the SAW by means of viscous damping and react to the interaction by developing an internal streaming. This streaming is very similar to the well-known acoustic streaming, originating from a sound-induced pressure gradient along the direction of propagation. For small SAW amplitudes or in confined geometries, this acoustic streaming effect leads to complex flow line patterns in the liquid. In a microfluidic system, viscous forces by far dominate inertial forces, which in turn restrict the flow in such systems to laminar regime. Especially for biological and chemical applications, this represents a drawback when compared to macroscopic fluidic systems, as diffusion is the only source for mixing. At higher SAW amplitudes, fluids confined in the form of droplets on the surface on which the SAW is propagating can be actuated as a whole. This observation led to the idea of chemically patterning the surface of an SAW chip in order to generate areas of preferred wettability (hydrophilic areas), surrounded by hydrophobic regions of the chip. Very similar to the metal strip lines and circuit paths on a microelectronic chip, this way “virtual fluidic tracks” can be created on a chip, on which acoustically actuated droplets can be maneuvered at will. The SAW generators are electrically excited and addressable, opening the doors for the creation of programmable microfluidic processors. However, the liquids are virtually confined by the surface functionalization and all liquid processing takes place on the planar chip surface.

Typical applications of SAW digital systems are microarray hybridization assays and other microfluidic applications, where efficient mixing and stirring of submicroliter volumes is required. These include mixing in open droplets, capillary gaps, microtiter-plate wells, and the like. The droplet-based fluidic systems have been shown to be able to perform very complex tasks, such as a complete on-chip PCR including microarray analysis for DNA amplification purposes. SAW-induced acoustic streaming in a planar microfluidic flow chamber has been used to investigate blood flow related phenomena. In a planar artificial blood vessel, specific macroproteins turn out to represent mechanically activated molecules with a specific switching behavior being related to their adhesion properties. Finally, cell culture and proliferation on such chips is possible; besides, SAW-induced acoustic streaming has found its way into nano-electronics. Here, we used the technique to deliberately align CNTs with respect to contacts on a silicon chip. These structures exhibit a quantized acousto-electronic current, a true indication for a quasi-1D behavior.

Acknowledgments

This work represents the summary of many years of effort by an even larger number of colleagues and students in the research group at Augsburg University and Advalytix. It is

nearly impossible to acknowledge all of their contributions in an appropriate manner, which, however, by no means should be forgotten at this point. At least, many of these invaluable contributions are summarized in the references to this chapter, which we refer the reader to. Special thanks, however, to our team of skilled technicians and administrative support in Augsburg: Funda Cevik, Sidonie Lieber, Andreas Spörhase, and Alexander Hupfer.

It is much easier to account for the financial support which enabled our research and led to the development of SAW-actuated chips. In a series of different research programs, we have been supported in part by the Bayerische Forschungsstiftung BFS, the Deutsche Forschungsgemeinschaft DFG, the Fonds der Chemischen Industrie, the Bundesministerium für Bildung und Forschung BMBF, and the European Community. This support is gratefully acknowledged.

References

- [1] E.M. Purcell, Life at low Reynolds number. *Am. J. Phys.* 45 (1977) 3.
- [2] J.G. Smits, Sensor Actuator A 21–23 (1990) 203.
- [3] A. Manz, C.S. Effenhauser, N. Burggraf, D.J. Harrison, K. Seiler, K. Fluri, *J. Micromech. Microeng.* 4 (1994) 257.
- [4] G.P. Lopez, H.A. Biebuyck, C.D. Frisbie, G.M. Whitesides, *Science* 260 (1993) 647.
- [5] G. Möller, M. Harke, H. Motschmann, *Langmuir* 14 (1998) 4955.
- [6] H. Gau, S. Herminghaus, P. Lenz, R. Lipowski, *Science* 283 (1999) 46.
- [7] S. Daniel, M.K. Chaudhury, J.C. Chen, *Science* 291 (2001) 633.
- [8] K. Ichimura, S.K. Oh, M. Nakagawa, *Science* 288 (2000) 1624.
- [9] R.M. Moroney, R.M. White, R.T. Howe, *Appl. Phys. Lett.* 59 (1991) 774.
- [10] M.A. Unger, H.P. Chou, T. Thorsen, A. Scherer, S.R. Quake, *Science* 288 (2000) 113.
- [11] W.L. Nyborg, in: W.P. Mason (Ed.), *Acoustic Streaming, in Physical Acoustics 2B*, Academic Press, Waltham, MA, 1965, p. 265.
- [12] A. Wixforth, *Superlattice Microstruc.* 33 (2003) 389–396.
- [13] C. Kittel, *Introduction to Solid State Physics*, sixth ed., John Wiley & Sons, Hoboken, NJ, 1986.
- [14] L. Rayleigh, *Proc. London Math. Soc.* 17 (1885) 4.
- [15] B.A. Auld, *Acoustic Fields and Waves in Solids*, John Wiley & Sons, New York, NY, 1973.
- [16] A. Wixforth, J.P. Kotthaus, G. Weimann, *Phys. Rev. Lett.* 56 (1986) 2104.
- [17] C. Rocke, S. Zimmermann, A. Wixforth, J.P. Kotthaus, G. Böhm, G. Weimann, *Phys. Rev. Lett.* 78 (1997) 4099.
- [18] M. Rotter, A.V. Kalameisev, A.O. Govorov, W. Ruile, A. Wixforth, *Phys. Rev. Lett.* 82 (1999) 2171. See also: M. Rotter, A. Wixforth, A.O. Govorov, W. Ruile, D. Bernklau, H. Riechert, *Appl. Phys. Lett.* 75 (1999) 965.
- [19] G.W. Farnell, *Elastic surface waves*, in: H. Matthews (Ed.), *Surface Wave Filters*, Wiley, New York, NY, 1977.
- [20] T. Frommelt, Dissertation, University of Augsburg, 2007.
- [21] C. Eckart, *Phys. Rev. Lett.* 73 (1948) 68.
- [22] M. Schindler, P. Talkner, P. Hänggi, *Phys. Fluid* 18 (2006) 103303.
- [23] R. Hui Liu, R. Lenigk, R.L. Druyor-Sanchez, J. Yang, P. Grodzinsky, *Anal. Chem.* 75 (8) (2003).

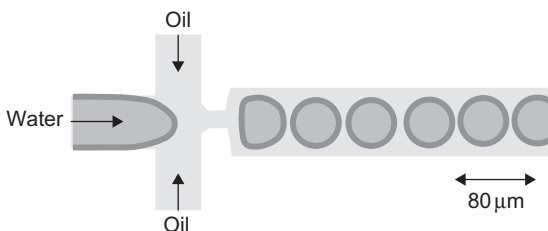
- [24] D. Gershon, *Nature* 416 (2002) 885–891.
- [25] Z. Wu, N.T. Nguyen, *J. Micromech. Microeng.* 15 (2005) R1–R16.
- [26] J. Knight, A. Vishwanath, J. Brody, R. Austin, *Phys. Rev. Lett.* 80 (1998) 3863.
- [27] Z. Wu, N.T. Nguyen, *Biomed. Microdevices* 7 (1) (2005) 13.
- [28] V. Hessel, S. Hardt, H. Löwe, F. Schönfeld, *AIChE J.* 49 (3) (2003) 556.
- [29] S. Hardt, F. Schönfeld, *AIChE J.* 49 (3) (2003) 578.
- [30] H. Chou, M.A. Unger, S.R. Quake, *Biomed. Microdevices* 3 (4) (2001) 323.
- [31] A. Scherer, S.R. Quake, *Science* 290 (2000) 1536.
- [32] A.D. Stroock, S.K.W. Dertinger, A. Adjari, I. Mezic, H.A. Stone, G.M. Whitesides, Chaotic mixer for microchannels, *Science* 295 (2002) 647–651.
- [33] S. Hardt, F. Schönfeld, *AIChE J.* 50 (4) (2004) 771.
- [34] A. Grossman, V. Steinberg, *Nature* 410 (2001) 905.
- [35] A. Vikhansky, *Phys. Fluid* 15 (2003) 108.
- [36] P. Tabeling, M. Chabert, A. Dodge, C. Julien, F. Okkles, *Philos. Trans. R. Soc. London Ser. A* 362 (2004) 987.
- [37] Z. Guttenberg, A. Rathgeber, S. Keller, J.O. Rädler, A. Wixforth, M. Kostur, et al., *Phys. Rev. E* 70 (2004) 056311.
- [38] K. Sritharan, C.J. Strobl, M.F. Schneider, A. Wixforth, Z. Guttenberg, *Appl. Phys. Lett.* 88 (2006) 054102.
- [39] M. Streibl, A. Wixforth, J.P. Kotthaus, A.O. Govorov, C. Kadov, A.C. Gossard, *Appl. Phys. Lett.* 75 (1999) 4139.
- [40] P. Hegde, R. Qi, K. Abernathy, *Biotechniques* 29 (2000) 548–550, 552–554, 556.
- [41] V. Chan, D.J. Graves, S.E. McKenzie, *Biophys. J.* 69 (1995) 2243–2255.
- [42] S.A. Allison, S.H. Northrup, J.A. McCammon, *Biophys. J.* 49 (1986) 167–175.
- [43] A. Rathgeber, M. Wassermeier, A. Wixforth, *J. ASTM Int.* 2 (2005) 1.
- [44] <http://www.Advalytix.de>.
- [45] A. Toegl, R. Kirchner, C. Gauer, A. Wixforth, *J. Biomol. Tech.* 14 (2003) 197–204.
- [46] K.B. Mullis, F.A. Faloona, *Meth. Enzymol.* 155 (1987) 335–350.
- [47] http://en.wikipedia.org/wiki/Polymerase_chain_reaction.
- [48] Z. Guttenberg, H. Müller, H. Habermüller, A. Geisbauer, J. Pipper, J. Felbel, et al., *Lab Chip* 5 (2005) 308–331.
- [49] S. Dong, E. Wang, L. Hsie, Y. Cao, X. Chen, T.R. Gingera, *Genome Res.* 11 (2001) 1418–1424.
- [50] S.W. Schneider, S. Nuschele, A. Wixforth, C. Gorzelannzy, A. Alexander-Katz, R.R. Netz, M.F. Schneider, *Proc. Natl. Assoc. Soc.* 104 (19) (2007) 7899–7903.
- [51] Z.M. Ruggeri, J. Thromb. Haemost. 1 (2003) 1335–1342.
- [52] A.A. Katz, M.F. Schneider, S.W. Schneider, A. Wixforth, R.R. Netz, *Phys. Rev. Lett.* 97 (2006) 138101.
- [53] C.J. Strobl, C. Schäflein, U. Beierlein, J. Ebbecke, A. Wixforth, *Appl. Phys. Lett.* 85 (2004) 1427.
- [54] T. Smorodin, U. Beierlein, J. Ebbecke, A. Wixforth, *Small* 1 (2005) 1188.
- [55] K.M. Seemann, J. Ebbecke, A. Wixforth, *Nanotechnology* 17 (2006) 4529.
- [56] J. Ebbecke, C.J. Strobl, A. Wixforth, *Phys. Rev. B.* 70 (2004) 233401.
- [57] A. Wixforth, Flat fluidics: programmable on-chip networks for biological and chemical applications, Technical Proceedings of the 2005 NSTI Nanotechnology Conference and Trade Show, Vol. 1, (2005) 571–574.

Introduction to Droplet Microfluidics and Multiphase Microflows

14

CHAPTER OUTLINE

14.1 Introduction	494
14.2 Two-phase flows: plugs in microchannels.....	494
14.2.1 Interface and meniscus.....	495
14.2.2 Dynamic contact angle.....	495
14.2.3 Plugs moving inside a capillary.....	498
14.2.3.1 <i>Cylindrical tube</i>	498
14.2.3.2 <i>Rectangular channel</i>	502
14.2.4 Hysteresis of static contact angle.....	502
14.2.5 Example of three-phase flow in a microchannel	503
14.3 Two-phase flows: flowing fluids separated by an interface	505
14.3.1 Introduction	505
14.3.2 Model.....	506
14.3.2.1 <i>Lozenge pillars</i>	507
14.3.2.2 <i>Circular pillars</i>	509
14.3.2.3 <i>Maximum stability length</i>	510
14.3.2.4 <i>Experimental results</i>	511
14.3.2.5 <i>Lozenge pillars</i>	511
14.3.2.6 <i>Circular pillars</i>	512
14.3.3 Discussion and conclusions.....	512
14.4 Droplets in two-phase flows.....	514
14.4.1 FFDs and T-junctions	514
14.4.1.1 <i>Droplet detachment in T-junctions</i>	515
14.4.1.2 <i>Flow focusing devices</i>	524
14.4.1.3 <i>Droplets or separated two-phase flow?</i>	526
14.4.2 Encapsulation	527
14.5 Summary	527
References	530

**FIGURE 14.1**

A continuous flow can be broken into discrete droplets [1].

14.1 Introduction

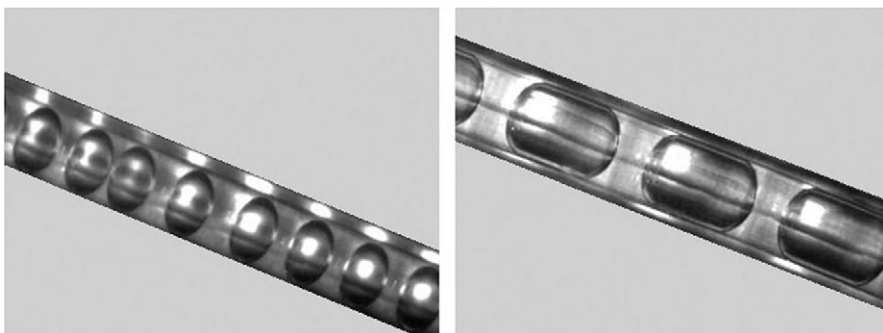
In the preceding chapters, we have studied the behavior of droplets placed on a planar surface. However, this is not the only way to manipulate droplets. Another approach, pioneered in the late 1990s, is usually called droplet microfluidics. In such an approach, immiscible discrete droplets are formed and transported by a continuous microflow (Figure 14.1).

It has been shown that these types of microflows, where droplets are continuously created and transported, can be of great interest for biological and chemical applications [2,3]. We emphasize here that digital microfluidics (planar microfluidics) and droplet microfluidics are not in opposition and, in fact, are complementary. They just do not address the same problems. For example, digital microfluidics is well adapted to biorecognition and biodiagnostics because only an extremely small volume of liquid is required and droplets can be carefully monitored until the detection step. On the other hand, droplet microfluidics is well adapted to continuous processes, as for example the production of a large number of encapsulated biological objects. From a general standpoint, digital (planar) microfluidics can treat very small volumes of liquid (stored in reservoirs) in parallel, whereas droplet microfluidics treats small liquid volumes in series (continuous online process).

More generally, droplet microfluidics can be considered as a subset of the more general two-phase or multiphase microflows. The physics of droplet microfluidics and multiphase flow is a vast domain and this chapter presents some introductory notions. First, we focus on the flow of liquid plugs in capillary tubes, then we analyze two-phase flows in parallel channels, and finally we present some aspects and applications of droplet microfluidics.

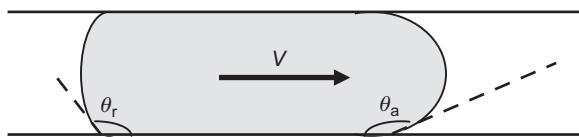
14.2 Two-phase flows: plugs in microchannels

Microflows are not always constituted by a single liquid. Frequently, one deals with small quantities of liquid (buffer liquid containing the molecules of interest)

**FIGURE 14.2**

Microdrops and plugs in a capillary tube

Source: Courtesy Y. Fouillet, CEA-LETI.

**FIGURE 14.3**

Schematic view of a liquid plug in a capillary tube with the advancing and receding contact angles.

under the form of liquid plugs moving inside capillary tubes and separated by inert, biocompatible, nonmiscible plugs of another liquid ([Figure 14.2](#)).

Conceptually, liquid plugs may be seen as a transitional state between micro-flows and digital microfluidics.

14.2.1 Interface and meniscus

The shape of a liquid plug in a capillary tube depends on the capillary forces. A liquid plug moving inside a capillary tube (or between two parallel plates) is limited by two menisci, one corresponding to the advancing front (index *a*), the other one corresponding to the receding front (index *r*) as shown in [Figure 14.3](#). In microcapillaries, menisci have spherical shapes. Note that receding, advancing, and static contact angles are not identical.

14.2.2 Dynamic contact angle

The contact angle formed between a flowing liquid front (advancing or receding) and a solid surface is not constant but reflects the balance between capillary

forces and viscous forces. The relative importance of these forces is often expressed by the nondimensional capillary number Ca defined by

$$Ca = \frac{\mu U}{\gamma}, \quad (14.1)$$

where μ is the dynamic viscosity of the moving fluid (unit kg/m/s), U its velocity (m/s), and γ its surface tension (N/m). The capillary number is a scale of the ratio between the drag force of the flow on a plug and the capillary forces. In a cylindrical tube of radius R , the friction pressure drop for a plug of length L is given by Washburn's law

$$\Delta P = \frac{8\mu UL}{R^2}. \quad (14.2)$$

We deduce an order of magnitude of the drag force (force necessary to push the plug in the tube):

$$F_{\text{drag}} \approx \Delta P \pi R^2 \approx \mu UL. \quad (14.3)$$

On the other hand, the capillary/wetting force is given by

$$F_{\text{cap}} \approx \gamma R. \quad (14.4)$$

From Eqs. (14.3) and (14.4), we deduce

$$\frac{F_{\text{drag}}}{F_{\text{cap}}} \approx \frac{\mu U L}{\gamma R} \approx Ca \frac{L}{R}. \quad (14.5)$$

Hoffman first proposed an expression for the dynamic contact angle based on experimental observations [4]; however, this correlation is rather complicated and Voinov and Tanner [5] have established the more workable correlation

$$\theta_d^3 - \theta_s^3 = A Ca, \quad (14.6)$$

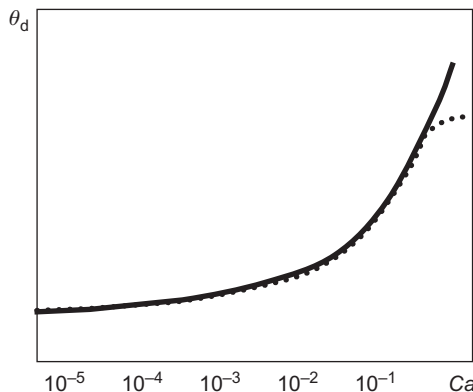
where θ_d and θ_s are the dynamic and static contact angles. The value of the coefficient A is $A \sim 94$ when θ is expressed in radians. Tanner's law is plotted in Figure 14.4.

For microflows, using the approximate values $\mu \sim 10^{-3}$ kg/m/s, $U \sim 10$ $\mu\text{m/s}$ to 1 cm/s, and $\gamma \sim 50 \times 10^{-3}$ N/m, we find that typical values of the capillary number are in the range 2×10^{-7} to 2×10^{-4} . The capillary number is then small and corresponds to the linear part of the Tanner's law. Linearization of Eq. (14.6) yields [6,7]

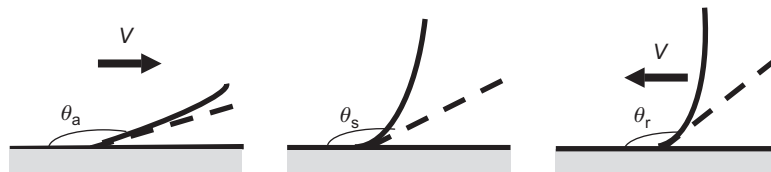
$$\theta_d = (\theta_s^3 + A Ca)^{\frac{1}{3}} \approx \theta_s \left(1 + \frac{1}{3} \frac{A Ca}{\theta_s^3} \right) \quad (14.7)$$

or

$$\theta_d - \theta_s \approx \frac{1}{3} \frac{A Ca}{\theta_s^2}. \quad (14.8)$$

**FIGURE 14.4**

Experimental results for the dynamic contact angle versus the capillary number (dots) and Tanner's relation (continuous line).

**FIGURE 14.5**

Sketch of an advancing, static, and receding contact angle. The advancing contact angle is larger than the static contact angle, which is in turn larger than the receding contact angle.

Note that the capillary number is signed. The relation (14.8) shows that $\theta_d - \theta_s$ is of the sign of Ca ; the values of the advancing and receding contact angles are then given by

$$\begin{aligned}\theta_a &\approx \theta_s + \frac{1}{3} \frac{A|Ca|}{\theta_s^2} \\ \theta_r &\approx \theta_s - \frac{1}{3} \frac{A|Ca|}{\theta_s^2},\end{aligned}\tag{14.9}$$

where θ_a and θ_r are, respectively, the advancing and receding contact angles. Relations (14.9) confirm the experimental observation that an advancing contact angle is larger than the static contact angle and a receding contact angle is smaller than the static contact angle (Figure 14.5).

14.2.3 Plugs moving inside a capillary

14.2.3.1 Cylindrical tube

In this section, we analyze the motion of one or more liquid plugs inside a cylindrical capillary tube. We use a lumped model and we show that Bernoulli's equation combined with Tanner's law explains the main features of the behavior of liquid plugs moving inside capillary tubes [6,7]. Flow regions may be decomposed in two (Figure 14.6): first, the regions where a fluid moves inside the capillary, inducing a friction pressure drop, and second, the interfaces that induce a capillary pressure drop.

The total pressure drop in the capillary is then

$$\Delta P_{\text{channel}} = \Delta P_{\text{cap}} + \Delta P_{\text{drag}}. \quad (14.10)$$

The pressure drop due to friction on the solid walls is given by Washburn's law [7,17]:

$$\Delta P_{\text{drag}} = \frac{8U}{R^2} (\mu_1 L_1 + \mu_2 L_2) \quad (14.11)$$

where indices 1 and 2 address liquid 1 (liquid plug) and liquid 2 (surrounding carrier fluid). R is the radius of the capillary, U the average liquid velocity, and L_1 , L_2 the total length of contact of liquid 1, 2 with the solid wall ($L_1 + L_2 = L$, total length of the tube). Each interface—advancing and receding—contributes (positively or negatively in function of the contact angles) to the capillary pressure drop. We have seen in Chapter 2 that the capillary pressure drop derives directly from Laplace's law which relates the pressure difference at a spherical interface of curvature radius a (Figure 14.7) by

$$\Delta P = \frac{2\gamma}{a}. \quad (14.12)$$

The meniscus has a spherical shape (if the capillary is small enough), and Figure 14.8 shows that the contact angle is related to the tube radius R and the curvature radius a by

$$\cos \theta = -\frac{R}{a}$$

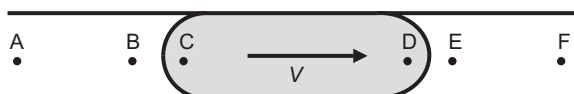
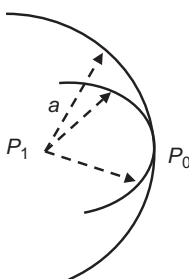
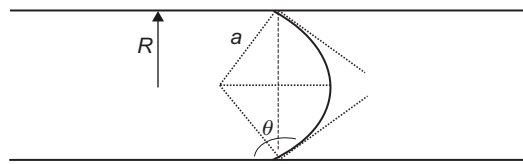


FIGURE 14.6

Decomposition of a two-phase flow in lumped elements. Between points A and B, C and D, E and F, the pressure drop is due to friction; between B and C, D and E the pressure drop results from capillary forces.

**FIGURE 14.7**

Sketch of a spherical interface separating two fluids. The pressure difference between the convex region and the outside region is $P_1 - P_0$ and is given by Laplace's law (see Chapter 1).

**FIGURE 14.8**

Schematic view of the meniscus in a cylindrical capillary tube.

Substitution of this relation into Eq. (14.12) yields

$$\Delta P_a = -\frac{2\gamma}{R} \cos \theta_a. \quad (14.13)$$

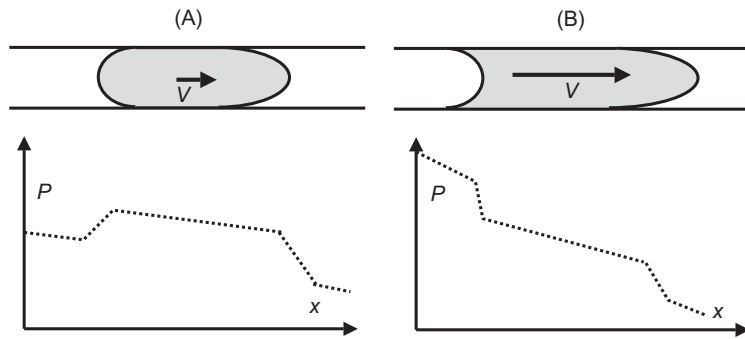
Similarly, the receding front contribution is given by the relation

$$\Delta P_r = -\frac{2\gamma}{R} \cos \theta_r. \quad (14.14)$$

In our convention, the pressure drop is always taken following the fluid flow. Consider the two configurations of Figure 14.9. If θ_a is larger than $\pi/2$, there is a positive pressure drop associated with the advancing interface. If θ_r is smaller than $\pi/2$, the receding front contributes positively to the pressure drop (Figure 14.9B) and negatively in the opposite case (Figure 14.9A).

The capillary pressure drop is due to the difference of the capillary forces between advancing and receding fronts because of the two different contact angles (advancing and receding) θ_a and θ_r :

$$\Delta P_{cap} = \frac{2\gamma}{R} (-\cos \theta_a + \cos \theta_r). \quad (14.15)$$

**FIGURE 14.9**

Two possible configurations for a plug moving inside a capillary tube: (A) at low velocity, the receding angle is larger than $\pi/2$ and the contribution to the pressure drop is negative and (B) at high velocity, θ_r is smaller than $\pi/2$ and the contribution to the pressure drop is positive. The slope of the pressure drop inside the different liquid is due to the friction pressure drop.

Equation (14.15) shows that too many plugs in the capillary may rapidly block the flow. For N plugs flow, we will have for some N :

$$\Delta P_{\text{cap}} = \frac{2\gamma}{R} N(-\cos \theta_a + \cos \theta_r) > P_i - P_o \quad (14.16)$$

and the flow will come to a stop (P_i and P_o are the inlet and outlet pressures). Let us introduce now the linearized Hoffman–Voinov–Tanner’s law—Eq. (14.7)—to find a more workable expression of the capillary pressure drop:

$$\theta_a = \theta_{s,a} \left(1 + \frac{1}{3} \frac{A Ca}{\theta_{s,a}^3} \right) \quad (14.17)$$

and

$$\theta_r = \theta_{s,r} \left(1 - \frac{1}{3} \frac{A Ca}{\theta_{s,r}^3} \right) \quad (14.18)$$

with

$$Ca = \frac{U \mu_1}{\gamma} \quad (14.19)$$

where the index s stands for the static contact angle, and $\theta_{s,r}$ and $\theta_{s,a}$ are the two static contact angles. They are equal if there is no static hysteresis, i.e., if the surface is perfectly smooth. The minus sign in Eq. (14.18) derives from the fact that we consider a positive Ca . After substitution of Eqs. (14.18) and (14.19) into

[Eq. \(14.16\)](#), and using some algebra, and keeping the higher order terms only, the capillary pressure drop can be cast under the form

$$\Delta P_{\text{cap}} \approx \frac{2\gamma}{R} N(-\cos \theta_{s,a} + \cos \theta_{s,r}) + \frac{2ANU\mu_1}{3R} \left(\frac{\sin \theta_{s,a}}{\theta_{a,s}^2} + \frac{\sin \theta_{s,r}}{\theta_{r,s}^2} \right). \quad (14.20)$$

14.2.3.1.1 No static hysteresis

If there is no static hysteresis of contact angle, the first term to the right-hand side of [Eq. \(14.20\)](#) vanishes and the capillary pressure drop is proportional to the average velocity U of the flow. As the friction pressure drop is also proportional to U , so is the total pressure drop:

$$\Delta P = U \left[\frac{8}{R^2} (\mu_1 L_1 + \mu_2 L_2) + \frac{2AN\mu_1}{3R} \left(\frac{\sin \theta_{s,a}}{\theta_{a,s}^2} + \frac{\sin \theta_{s,r}}{\theta_{r,s}^2} \right) \right]. \quad (14.21)$$

Let us write the ratio between the friction and capillary pressure drop

$$\frac{\Delta P_{\text{drag}}}{\Delta P_{\text{cap}}} = \frac{12(L_1 + (\mu_2/\mu_1)L_2)}{ANR((\sin \theta_{s,a}/\theta_{a,s}^2) + (\sin \theta_{s,r}/\theta_{r,s}^2))} \approx \frac{L}{12RN} \frac{\theta_s^2}{\sin \theta_s}, \quad (14.22)$$

where θ_s is the median value of the static contact angle. In [Eq. \(14.22\)](#), we have supposed that the viscosities of the two fluids were similar, and $L = L_1 + L_2$. Suppose that θ_s is of the order of $\pi/2$, then the ratio of the two types of pressure drop becomes $\Delta P_{\text{friction}}/\Delta P_{\text{capillary}} \approx (L/R)(1/5N)$. Depending on the aspect ratio L/R and on the number of plugs N , the friction pressure drop or the interface pressure drop governs the flow. In the example of [Figure 14.2](#), the capillary radius is $R = 100 \mu\text{m}$ and the length $L = 2 \text{ mm}$; the number of plugs N is larger than 40, hence the capillary pressure drop is 10 times larger than the friction pressure drop.

14.2.3.1.2 Static hysteresis

In case of hysteresis of static contact angle, at very low velocities, the pressure drop has an asymptotic value which is the first term of the right-hand side of [Eq. \(14.20\)](#):

$$\Delta P_{\text{cap}} \approx \frac{2\gamma}{R} N(-\cos \theta_{s,a} + \cos \theta_{s,r}). \quad (14.23)$$

In this case, the ratio of the friction to the capillary pressure drop is approximately

$$\frac{\Delta P_{\text{drag}}}{\Delta P_{\text{cap}}} \approx \frac{L}{RN} \frac{1}{(-\cos \theta_{s,a} + \cos \theta_{s,r})} Ca. \quad (14.24)$$

Relation (14.24) for the ratio of the two pressure drops is comparable to relation (14.5) for the ratio of the two forces inducing the pressure drops. Both ratios are proportional to the capillary number.

14.2.3.2 Rectangular channel

The same reasoning can be done for rectangular channels, with the precaution of substituting a capillary and a friction pressure drop adapted for rectangular micro-channels. The expression of the capillary pressure loss (14.13) becomes

$$\Delta P_a = -2\gamma \cos \theta_a \left(\frac{1}{h} + \frac{1}{w} \right)$$

where h and w are the height and width of the channel. On the other hand, the friction factor f is given by the Shah and London approximated expression [8]

$$f \text{Re} = 96(1 - 1.3553\alpha + 1.9467\alpha^2 - 1.7012\alpha^3 + 0.9564\alpha^4 - 0.2537\alpha^5) = 96g(\alpha),$$

where Re is the Reynolds number, α the ratio between the two dimensions of the rectangular channel $\alpha = \min(h/w, w/h)$. Note that α is smaller than 1. After substituting this relation in the Darcy–Weisbach's equation, we obtain

$$\Delta P_{\text{drag}} = f \frac{\rho}{2} U^2 \frac{L}{D_h} = \frac{8\eta UL}{w^2} \frac{3}{2} (1+\alpha)^2 g(\alpha).$$

A more compact form has been recently obtained by Bahrami et al. [9] (including many other geometries of cross-section):

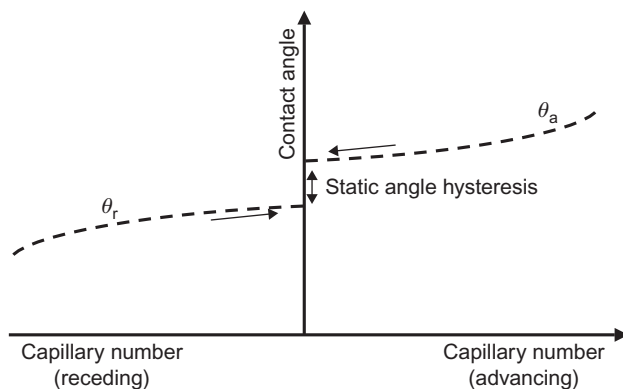
$$\Delta P_{\text{drag}} = \frac{8\eta UL}{w^2} = \frac{1}{2((1/3) - (64\alpha/\pi^5)\tanh(\pi/2\alpha))} = \frac{8\eta UL}{w^2} h(\alpha).$$

From hereon, the reasoning is the same as that detailed in the previous section.

14.2.4 Hysteresis of static contact angle

In Chapter 2, Young's law for contact angle was derived. Young's law predicts the value of the static contact angle as a function of the surface energy of the different materials (liquid plug, surrounding liquid, and solid substrate). Apparently, it should result in a unique value of the static contact angle. However, it happens frequently that the static contact angle is not uniquely defined. It can be comprised between two values, a first value obtained by slowing down to a stop an advancing front $\theta_{s,a}$, and another value (smaller) obtained by slowing down to a stop a receding front $\theta_{s,r}$ as shown in Figure 14.10.

In fact, Young's law applies only for a perfectly homogeneous solid substrate. If the substrate is disordered, the static contact angle is not uniquely defined. Hysteresis of contact angle is linked to the smoothness and homogeneity of the substrate [10–13].

**FIGURE 14.10**

Hysteresis of static contact angle and Hoffman–Tanner’s law for advancing and receding contact angles versus capillary number: the advancing contact angle is larger than the receding contact angle and there is a static hysteresis at zero velocity.

14.2.5 Example of three-phase flow in a microchannel

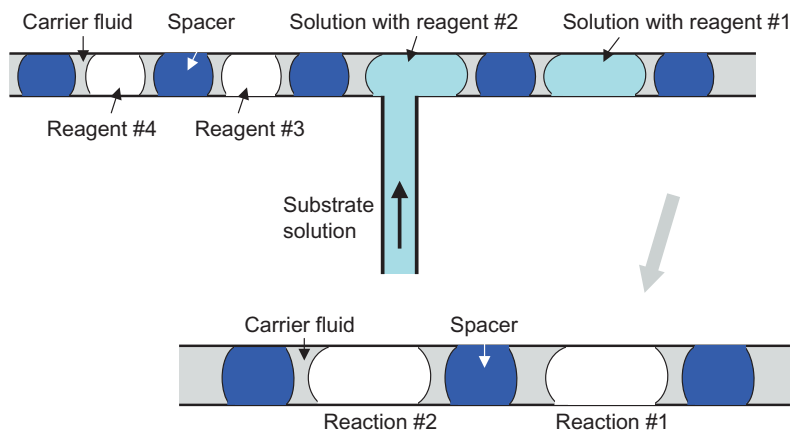
A promising way to perform biological and chemical reactions in microvolumes is to use plugs transported by an immiscible carrier fluid. Figure 14.11 shows the principle of such reactions. Different reagents transported by independent plugs are successively mixed with a solution containing a chemical or biochemical species. A condition for a proper functioning of such plug flow reactions is that the plugs do not coalesce. Coalescence would bring contamination between the liquids. Coalescence may occur when the plugs are not moving at the same velocity, due to differences of viscosity and surface tensions, according to Eqs. (14.22) and (14.24). In order to keep the plugs separated, Chen et al. [13] use spacer plugs constituted by a third immiscible liquid.

We place ourselves in the case of slow moving liquids (small capillary and Weber numbers) so that surface tension forces dominate inertia and viscous forces. We assume also that the carrier fluid is the only fluid wetting the solid walls.

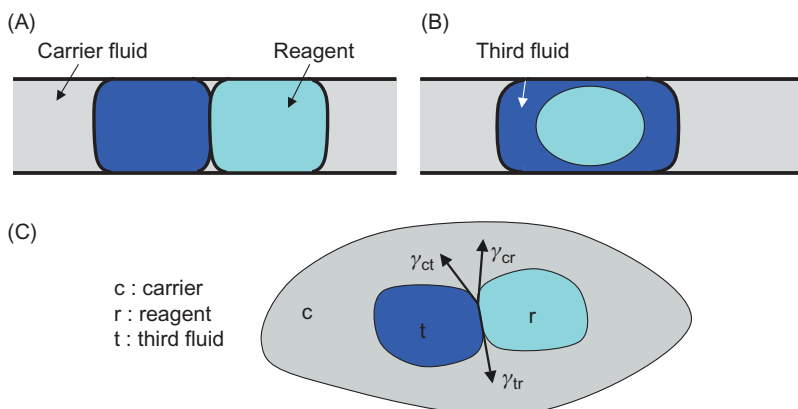
Obviously, a first condition for the efficiency of spacer plugs is that the liquid plugs do not engulf each other. Figure 14.12 shows the satisfactory arrangement of the plugs (A) and engulfment (B). The condition for stability of plugs in contact is given by the balance of the surface tension forces at the triple line (Neumann’s construction):

$$\vec{\gamma}_{ct} + \vec{\gamma}_{tr} + \vec{\gamma}_{rc} = 0. \quad (14.25)$$

Relation (14.25) can be satisfied only if the magnitude of every force is smaller than the sum of the magnitudes of the other two forces. This statement can be easily verified by remarking that if the magnitude of a force is larger than the sum of the magnitudes of the two others, equilibrium cannot be reached (Figure 14.13).

**FIGURE 14.11**

Principle of three-phase flow reactions: spacer plugs of immiscible liquid prevent coalescence of droplets.

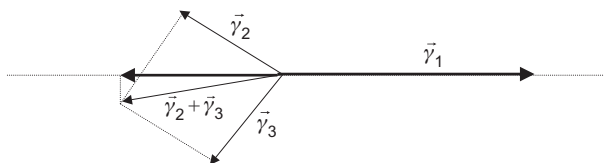
**FIGURE 14.12**

Sketch of two plugs in contact. (A) Plugs stay distinct; (B) spacer liquid plug engulfing reagent liquid; and (C) Neumann's construction for the equilibrium of the interfaces.

Hence, it can be shown that the condition for no engulfment is

$$\begin{aligned} \gamma_{rc} &< \gamma_{ct} + \gamma_{tr} \\ \text{and} \\ \gamma_{ct} &< \gamma_{tr} + \gamma_{rc} \end{aligned} \quad (14.26)$$

Gas bubbles usually satisfy relation (14.26). However, gas bubbles can induce pressure fluctuation in the system. Chen et al. [13] have found organic spacer liquids (SID, DTFS) adapted to fluorinated carrier fluids and aqueous reagent plugs.

**FIGURE 14.13**

Assuming that $\vec{\gamma}_1$ is larger than $\vec{\gamma}_2 + \vec{\gamma}_3$, the resultant of the forces $\vec{\gamma}_2 + \vec{\gamma}_3$ projected on the direction of $\vec{\gamma}_1$ cannot equilibrate $\vec{\gamma}_1$.

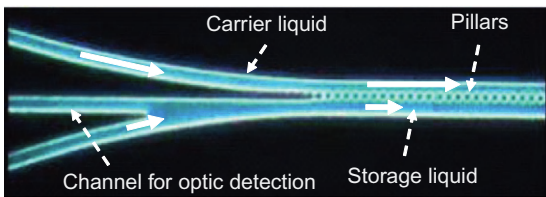
14.3 Two-phase flows: flowing fluids separated by an interface

In biotechnology and microchemistry, one frequently proceeds the transfer of a species contained in a liquid A (primary fluid) to another immiscible liquid B (secondary fluid). Mass transfer is facilitated when the interfacial area between the two immiscible flowing fluids is important, i.e., the case of microfluidic systems aimed at the detection of viruses or of traces of heavy metals in large volumes of liquids.

In this section, we focus on the extraction of target molecules from a primary liquid and concentration of these molecules in a secondary liquid. We present a system constituted of two adjacent microchannels geometrically separated by vertical micropillars [14]. The primary and secondary liquids are chosen immiscible, and vertical interfaces attached to the pillars separate the two fluids. The system must be designed to withstand the largest possible interfacial area to favor molecule transfer from primary to secondary fluids. Stability of the interface is then the key for the design of the system.

14.3.1 Introduction

The transfer and concentration of macromolecules from a flowing primary carrier fluid to a secondary storage liquid is the first step of any recognition process. In the literature, such types of concentration microdevices have already been proposed [15,16]. We analyze the case sketched in Figure 14.14 where the carrier fluid and the storage liquid are flowing side by side, separated by interfaces sustained by micropillars. The two immiscible fluids should not mix to form an emulsion, for two reasons: the system should use the economy of a demixing system and online detection is facilitated. The best efficiency of such devices is obtained for a largest possible interfacial area. However, it is observed that, for a given geometry of the pillars, there are only a limited number of interfaces that can be stable. We investigate here the stability of the interfaces in function of the geometry (channel length and width, morphology of the pillars) and flow parameters (flow rates in the channels).

**FIGURE 14.14**

Schematic of the microsystem.

Source: Reprinted with permission from Ref. [14] © 2007, NSTI.

14.3.2 Model

The two fluids flow in parallel with different velocities and their pressure evolves nearly independently—as long as the interfaces remain stable. Because of the differences of flow rate and geometry, a pressure difference between the two channels builds up. Hence the interfaces are submitted to two constraints: a normal stress due to the pressure difference between the two channels and a tangential stress exerted by the friction of the flowing fluids.

A calculation of the flow with the Comsol numerical software shows that the tangential stress on the interface is much less than the normal stress (Figure 14.15). Hence, we consider only the normal stress in the model.

Taking into account the outlet channels and using the Washburn's [17] equation for the pressure drop, modified by the Purday, Shah and London expressions for rectangular channels [7,8,18], the pressure is a function of the distance to the channel entrance, noted x , according to

$$P(x) - P_0 = cf(\mu, Q, a, b)x + cg(\mu, Q, D) \quad (14.27)$$

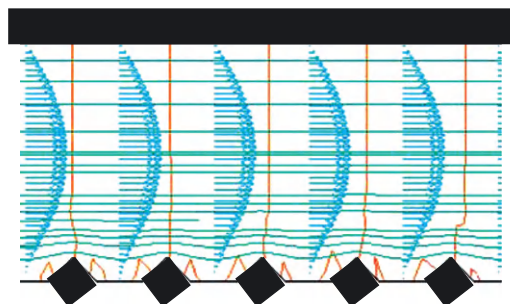
with the notations of Figure 14.16, where μ is the liquid dynamic viscosity. The functions f and g are respectively the pressure drop functions for the “transfer” channel and the outlet channel. The pressure difference across the interface in a cross-section of the transfer region is then

$$P_1(x) - P_2(x) = c_1[f(\eta_1, Q_1, a_1, b_1) - f(\eta_2, Q_2, a_2, b_2)]x + c_2[g(\eta_1, Q_1, D_1) - g(\eta_2, Q_2, D_2)] \quad (14.28)$$

If we specify the functions f and g , Eq. (14.28) yields

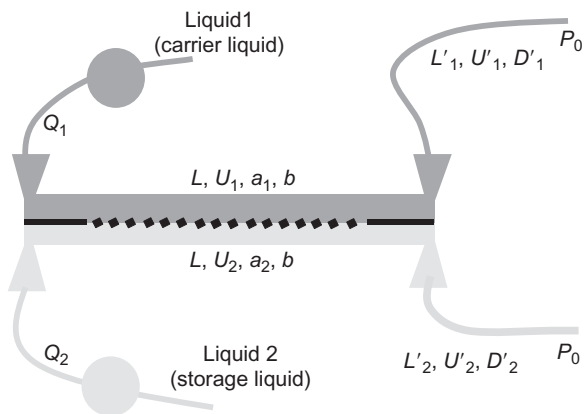
$$\begin{aligned} P_1(x) - P_2(x) &\cong 8(L-x) \left[\frac{\eta_1 Q_1}{((a_1^3 b^3)/(a_1+b)^2)} - \frac{\eta_2 Q_2}{((a_2^3 b^3)/(a_2+b)^2)} \right] \\ &+ 32 \left(\frac{\eta_1 Q_1 L_1}{\pi D_1^4} - \frac{\eta_2 Q_2 L_2}{\pi D_2^4} \right) \end{aligned} \quad (14.29)$$

The maximum pressure difference $P_1 - P_2$ for which an interface remains stable is related to the maximum theoretical stability length, sketched in

**FIGURE 14.15**

Velocity profile, pressure contour lines, and streamlines in a channel limited by lozenge pillars and a stable interface.

Source: Reprinted with permission from Ref. [14] © 2007, NSTI.

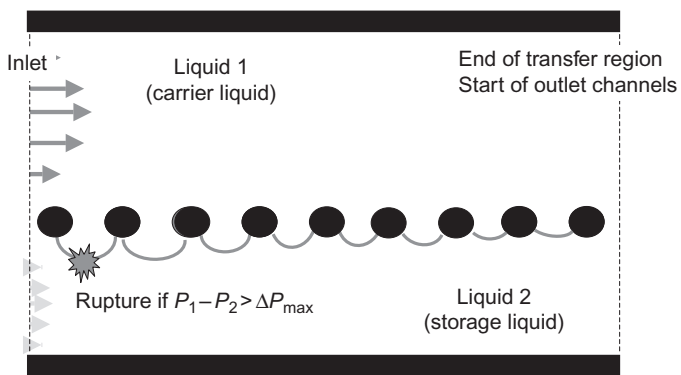
**FIGURE 14.16**

Schematic of the flow parameters: a is the channel width, b the channel depth, L stands for length, U for velocity, Q for flow rate, and D for hydraulic diameter.

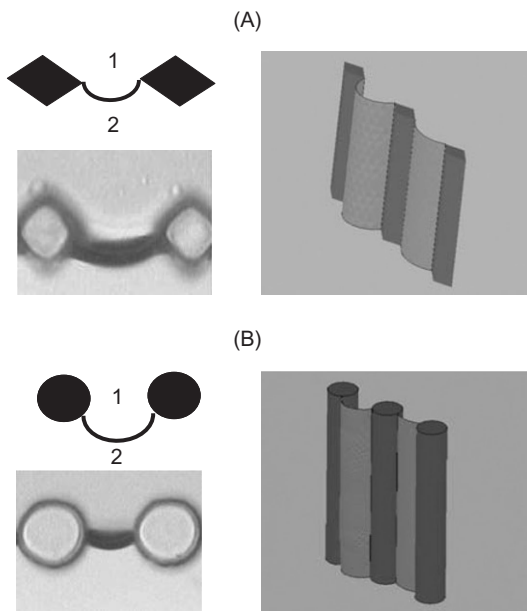
Figure 14.17. We analyze here the maximum pressure that an interface can withstand for lozenge and cylindrical pillars (Figure 14.18).

14.3.2.1 Lozenge pillars

The stability approach for lozenge pillars is identical to Tsori's approach for wedged pipettes [19] and we will not reproduce the equations here. It suffices to say that the interface is always anchored to the pillar edges (because the surfaces of the two adjacent pillars make sufficiently large angles). Hence, the

**FIGURE 14.17**

Sketch of the stability of the interfaces. The rupture occurs always at the beginning of the channel (under the condition of perfectly microfabricated pillars).

**FIGURE 14.18**

Interface position: (A) the interface is anchored to the pillar edge and (B) the interface adjusts to respect the Young's constraint. Experimental photographs (left) and Evolver calculation (right) [20].

Source: Reprinted with permission from Ref. [14] © 2007, NSTI.

maximum pressure difference that the interface can sustain (if the pillar edges are perfectly straight) is given by the Laplace's equation for a minimum curvature radius

$$\Delta P_{\max} = \frac{\gamma}{R} = \frac{2\gamma}{\delta} \quad (14.30)$$

where R is the curvature radius and $\delta = 2R$ is the distance between two pillar edges.

14.3.2.2 Circular pillars

In this case there is no pinning of the interface; the location of the triple contact line is determined by Young's constraints. Using the notations of [Figure 14.19](#), we locate the position of the contact point M by its angle ϕ and we have the following relation

$$\frac{h}{2} = r \sin \varphi + R \sin \beta. \quad (14.31)$$

The angle β can be expressed in function of the two angles ϕ and θ by

$$\left(\frac{\pi}{2} - \varphi\right) + (\pi - \beta) + \left(\theta - \frac{\pi}{2}\right) = \pi. \quad (14.32)$$

And we find

$$\beta = \theta - \varphi \quad (14.33)$$

Substitution of [Eq. \(14.33\)](#) in [Eq. \(14.31\)](#) produces the curvature radius

$$R = \frac{(h/2) - r \sin \varphi}{\sin(\theta - \varphi)}. \quad (14.34)$$

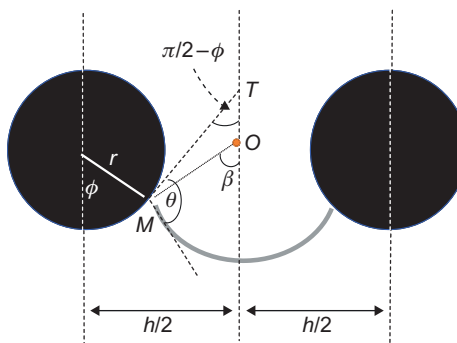


FIGURE 14.19

Schematic of the location of the interface. O is the curvature center, T the intersection of the tangent with the median axis, and M the contact point.

The pressure difference across the interface is then

$$\Delta P = \frac{\gamma}{R} = \frac{\gamma \sin(\theta - \varphi)}{(h/2) - r \sin \varphi}. \quad (14.35)$$

The important point now is that the function $\Delta P(\varphi)$ has a maximum; in other words, there is a position of the interface corresponding to a minimum curvature radius, i.e., to a maximum pressure difference. This position is determined by

$$\frac{\partial(\Delta P)}{\partial \varphi} = 0.$$

After some algebra, we find that the solution is given by

$$\varphi_{\max} = \theta - \arccos \left(\frac{2r \sin \theta}{h} \right). \quad (14.36)$$

And the maximum sustainable pressure is then

$$\Delta P_{\max} = \frac{\gamma \sin(\theta - \varphi_{\max})}{(h/2) - r \sin \varphi_{\max}}. \quad (14.37)$$

After examination of Eqs. (14.36) and (14.37), we deduce that the maximum pressure difference is a function of the Young's contact angle θ , the distance between two pillar centers h , and the radius of the pillar r .

14.3.2.3 Maximum stability length

On a general standpoint, the horizontal pressure profiles P_1 and P_2 along the channels are shown in Figure 14.20. According to Eq. (14.29), the profile is

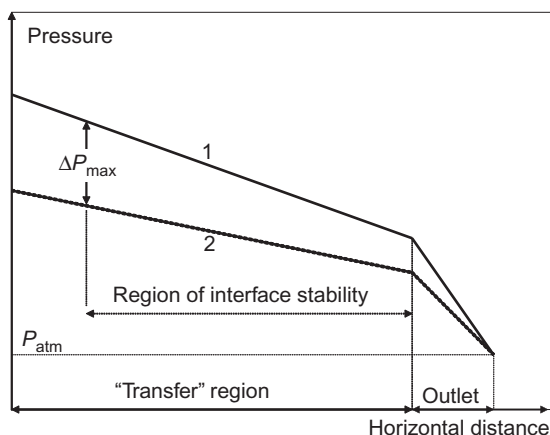


FIGURE 14.20

Pressure profiles and determination of the length of interface stability.

piecewise linear, with a jump of the slope between the “transfer” region and the outlet channels.

Examining the figure, we deduce that there is a maximum stability length corresponding to a pressure difference of ΔP_{\max} . Depending on the lozenge or circular geometry, we use Eq. (14.30) or (14.37). Substitution in Eq. (14.29) leads to the maximum value of the length of the transfer channel

$$\Lambda = \frac{\Delta P_{\max} - 32((\eta_1 Q_1 L_1 / \pi D_1^4) - (\eta_2 Q_2 L_2 / \pi D_2^4))}{8((\eta_1 Q_1) / ((a_1^3 b^3) / (a_1 + b)^2)) - ((\eta_2 Q_2) / ((a_2^3 b^3) / (a_2 + b)^2)))} \quad (14.38)$$

14.3.2.4 Experimental results

Experiments have been conducted using microfabricated channels of silanized Ordyl. Lozenge and circular pillars (150 μm high) have been tested. Stability has been investigated for water–cyclohexane interfaces.

14.3.2.5 Lozenge pillars

Interfaces attach to the edges of the pillars, as predicted by the theory. When the pressure increases above the rupture threshold or if the edge is not perfectly sharp, the interface slides along the sides of the pillars and carrier liquid invades the storage channel (Figure 14.21).

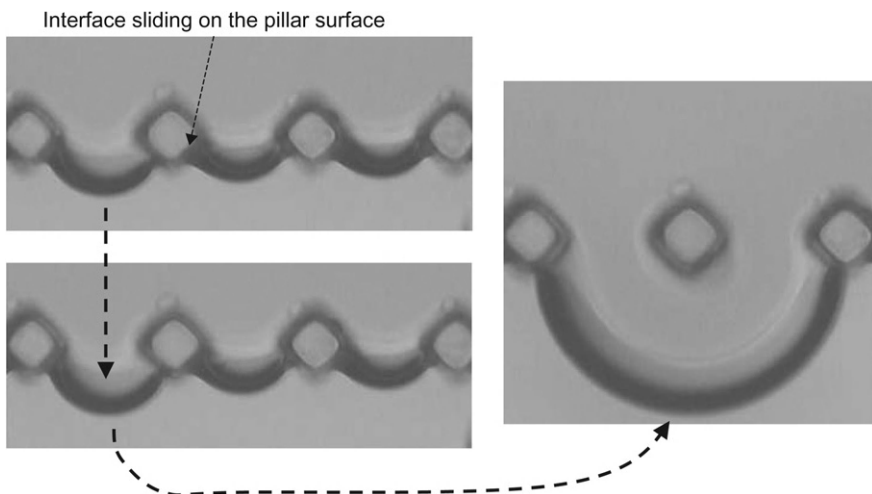


FIGURE 14.21

Once the triple contact line has detached from the edge—under the effect of the pressure difference or of a defect in the edge of the pillar—the interface inevitably invades the neighboring channel.

Source: Reprinted with permission from Ref. [14] © 2007, NSTI.

14.3.2.6 Circular pillars

We observe that interfaces take the position predicted by the theory, as shown in Figure 14.22. Beyond the limit angle ϕ_{\max} , the interface invades the other channel.

14.3.3 Discussion and conclusions

Relation (14.38) shows that, in order to maximize the stability length L_{\max} , it is necessary (i) to reduce as much as possible the difference of pressure drop in the outlet channels, (ii) to minimize the pressure drop difference in the transfer region, and (iii) to have the larger possible rupture threshold ΔP_{\max} . The rupture threshold ΔP_{\max} depends essentially on the free distance between two neighboring pillars, on the interface tension between the two liquids, and on the shape of the pillars. Figure 14.23 shows a comparison of the rupture pressure threshold between lozenge and circular pillars. Comparison has been performed by considering same exchange surfaces and same free distances between two pillars. The pinning of the interface on the lozenge arêtes stabilizes the interface. However, the model assumes perfectly microfabricated pillars. In reality, defects on edges deteriorate the pinning of the interface and may lead to a more unstable situation.

In conclusion, we have shown here that the outlet capillary tubes must be carefully designed (length and diameter adapted to the velocities) in order that their specific pressure drop is similar. It is advantageous to have the interfaces

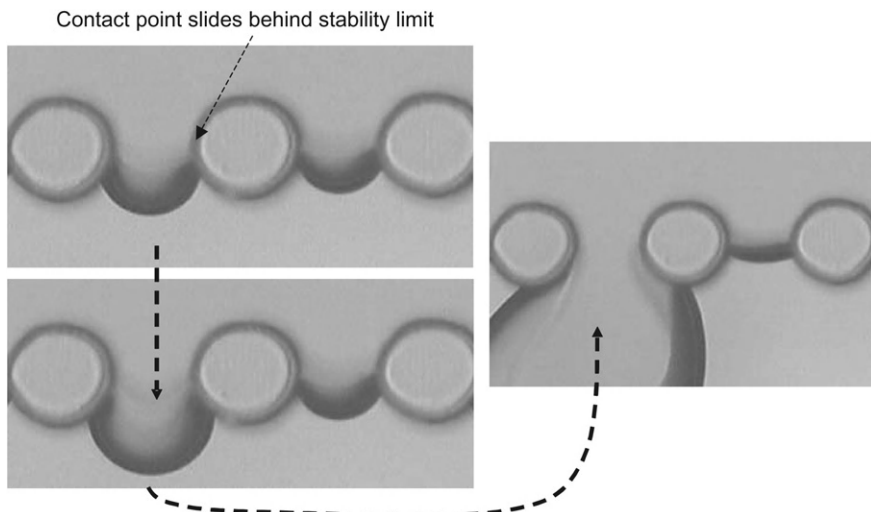


FIGURE 14.22

When the pressure difference becomes larger than ΔP_{\max} , the contact slides beyond the limit position, the interface invades the neighboring channel.

Source: Reprinted with permission from [14] © 2007, NSTI.

attached (pinned) to edges of the vertical pillars. However, if the quality of the edges is not satisfactory, the attachment is poor and sudden breakup of the interfaces can take place. Finally, Eqs. (14.30) and (14.37) show that the smaller the size of the interfaces, the larger the pressure difference sustained by the interface. Assuming that h denotes the distance between pillar center and r the radius or the 1/2 axial dimension of the pillars, let us analyze what happens when the dimensions are homothetically decreased, keeping the number r/h constant. Equation (14.30) can be rewritten as

$$\Delta P_{\text{lozenge,max}} = \frac{2\gamma}{h(1 - 2(r/h))} \propto \frac{1}{h}$$

and Eq. (14.37) can be cast under the form

$$\Delta P_{\text{cylinder,max}} = \frac{\gamma \sin(\theta - \varphi_{\max})}{h((1/2) - (r/h)\sin \varphi_{\max})} \propto \frac{1}{h}$$

Thus the maximum pressure that the interface can withstand is inversely proportional to h . At the same time, the interfacial area remains unchanged by the homothetic transform, because

$$\frac{S_i}{S} = \frac{n(h - 2r)}{nh} = 1 - 2\frac{r}{h}$$

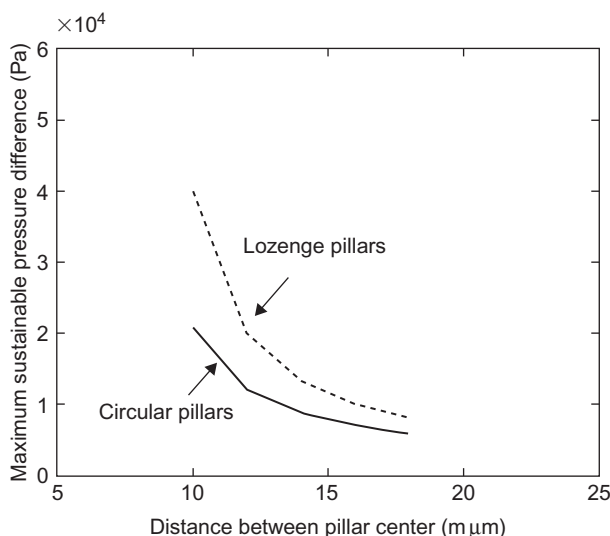


FIGURE 14.23

Comparison of stability between lozenge and circular pillars: maximum pressure difference ΔP_{\max} versus the distance between pillar centers.

where n is the number of intervals between pillars. Hence, it is advantageous to reduce the size of the interfaces together with the size of the pillars, the limit being the constraints of the microfabrication process.

14.4 Droplets in two-phase flows

In this section, we focus on the formation and behavior of droplets in a microflow and especially on the emission of monodispersed droplets. It is an extremely important challenge in biotechnology to be able to produce monodispersed droplets in a continuous flow. Such droplets can be produced in either T-junctions or flow focusing devices (FFDs) [21]. In this section, we investigate the mechanisms of droplet breakup; we show that the mechanisms are not the same for T-junctions and FFDs. Finally, we present applications of such devices in biology and biotechnology.

14.4.1 FFDs and T-junctions

Two different systems corresponding to two types of instabilities are used to create microdrops in a microflow. The first type of instability occurs in T-junctions at low velocity—small capillary and Weber numbers—where the detachment of a droplet is governed by the pressure drop created by the merging droplet (Figure 14.24A). The second type is obtained in FFDs and T-junctions with

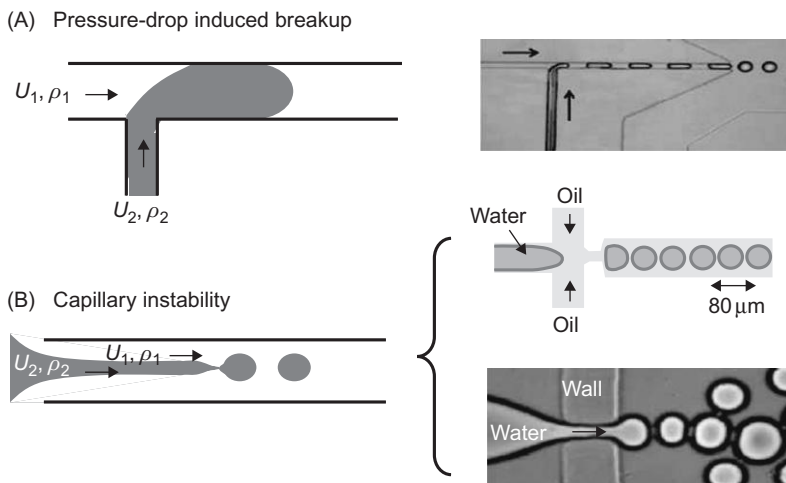
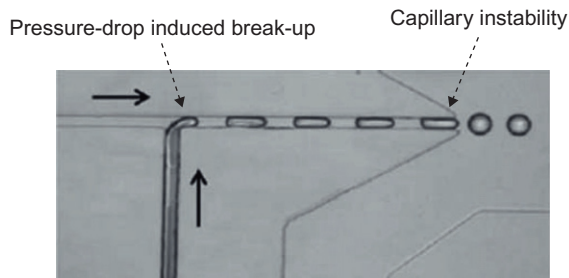


FIGURE 14.24

Two different types of instabilities leading to droplet breakup: (A) in a T-junction; (B) in an FFD.

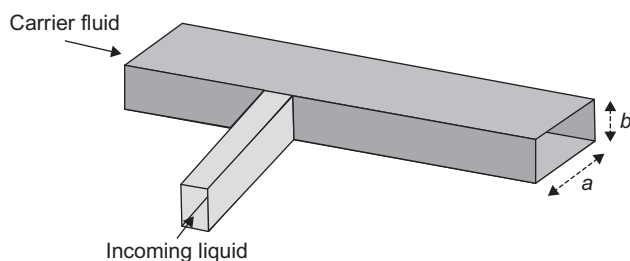
Source: (A) Reprinted with permission from Ref. [22] and (B) reused with permission from Ref. [21]

© 2003, American Institute of Physics.

**FIGURE 14.25**

The two types of instabilities can be used successively.

Source: From Ref. [22], reproduced by permission of the Royal Society of Chemistry.

**FIGURE 14.26**

Sketch of a T-junction composed of rectangular microfabricated channels.

higher flow velocity, where a flowing liquid is reduced to a filament under the action of another surrounding fluid (Figure 14.24B); because of the surface tension forces, the filament cannot be indefinitely stable; it breaks down in droplets at some distance to the channel entrance.

In the following sections, we present these two types of microdevices and show their applications for the encapsulation of liquids and particles. An important observation at this point is that multistep devices using T-junctions and FFDs can be realized, as shown in Figure 14.25. This principle is the key to multilayering encapsulation.

14.4.1.1 Droplet detachment in T-junctions

T-junctions that we consider are typical of microfluidics: due to microfabrication constraints, they are formed by two rectangular channels of the same depth b , usually merging at an angle of 90° (Figure 14.26). It has been observed that droplet detachment in T-junctions depends on the flow velocity: the instability leading to droplet detachment is different whether $Ca < 10^{-2}$ or $Ca > 10^{-2}$. Microsystems for biotechnology usually function with small flow rates, so that

we assume here that the carrier fluid (continuous phase) flows at low speed ($Ca < 10^{-2}$). The case of large velocities has been treated by Nisisako et al. [23] and Thorsen et al. [24]. We assume also that the carrier fluid wets the walls.

14.4.1.1.1 Principle of fluid segments (plugs) formation

T-junctions are one of the most frequently used microfluidic geometries to produce immiscible fluid segments (plugs) and droplets. The droplet formation proceeds in several steps: the liquid penetrates the main channel, forms a blob, and develops a neck. The neck elongates and becomes thinner as the blob advances downstream. It eventually breaks up and the droplet detaches.

At low capillary and Weber numbers, interfacial forces dominate shear stress, and breakup is triggered by the pressure drop across the droplet (or the bubble). In such a flow regime, the size of the droplets is determined solely by the ratio of the volumetric rates of flow of the two immiscible fluids. For rectangular cross-sections, if L is the length of the fluid segment, a the width of the channel, Q_{dis} and Q_{cont} the flow rates of the discontinuous and continuous phases, respectively, it has been observed that the relation

$$\frac{L}{a} = 1 + \alpha \frac{Q_{\text{dis}}}{Q_{\text{cont}}} \quad (14.39)$$

links the length L to the flow rates [25]. In relation (14.39), the constant α is positive and of the order of 1. Hence the length of the droplet L is always larger than a , and the droplet is in reality a fluid segment. Note that relation (14.39) is not valid for the entire domain of variation of the ratio $Q_{\text{dis}}/Q_{\text{cont}}$. For small values of this ratio, L is constant, as indicated in Figure 14.27. Relation (14.39) should be corrected by

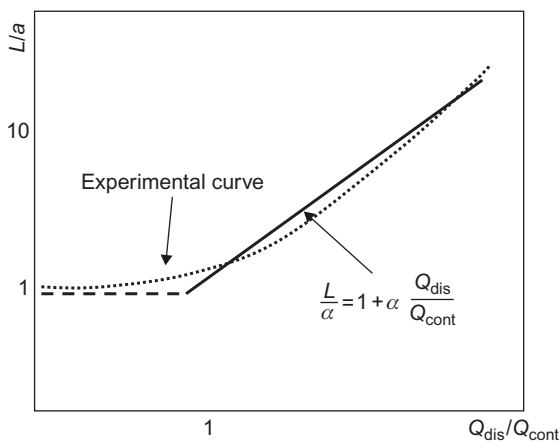
$$\frac{L}{a} = 1 + \alpha \frac{Q_{\text{dis}}}{Q_{\text{cont}}} H(Q_{\text{dis}} - Q_{\text{cont}}) \quad (14.40)$$

where H is the Heaviside's function: $H(x) = 1$ if $x > 0$, else $H(x) = 0$ [26].

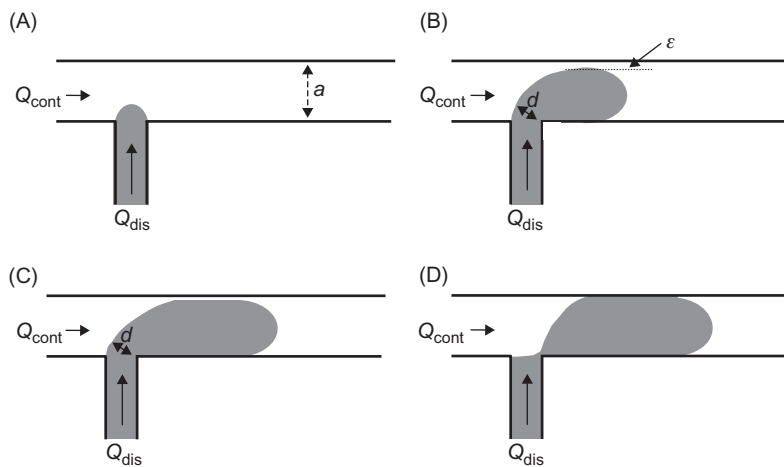
The physics behind Eq. (14.39) or (14.40) is complex. The process can be decomposed into four steps (Figure 14.28). In a first phase, the stream of discontinuous fluid enters the main channel. In a second phase, it forms a blob with approximately the size of main channel width ($L \sim a$). If the flow rate of “discontinuous” liquid Q_{dis} is sufficiently large compared to the flow rate of the “continuous” liquid Q_{cont} ($Q_{\text{dis}} > Q_{\text{cont}}$), the droplet elongates in the main channel. This third phase does not take place in the opposite case. Finally, the droplet detaches.

During the two first phases, the droplet reaches a length $L \sim a$. If $Q_{\text{dis}} < Q_{\text{cont}}$, the droplet does not have the time to elongate and separation occurs immediately. Hence, $L \sim a$ when $Q_{\text{dis}} < Q_{\text{cont}}$. Conversely, if $Q_{\text{dis}} > Q_{\text{cont}}$, the droplet elongates. Let us calculate the elongation length. During the elongation phase, the droplet growth rate is approximately given by

$$u_{\text{growth}} \approx \frac{Q_{\text{dis}}}{ab}. \quad (14.41)$$

**FIGURE 14.27**

Graph of L/a versus $Q_{\text{dis}}/Q_{\text{cont}}$: the relation is independent of the dynamic viscosity μ showing that the shear stress has no influence if the Capillary number is smaller than a critical value $Ca_{\text{crit}} \sim 10^{-2}$.

**FIGURE 14.28**

The four phases of droplet formation in a T-junction: (A) the stream of discontinuous fluid enters the main channel; (B) the stream blocks the main channel (nearly totally, except for a very small gap ε); (C) the droplet elongates downstream; and (D) the droplet separates from the inlet.

Remember that b is the height of the channel. On the other hand, the neck shrinks at a rate

$$u_{\text{squeeze}} \approx \frac{Q_{\text{cont}}}{ab} \quad (14.42)$$

If d denotes the width of the neck, the time needed to achieve the squeezing is approximately

$$\tau_{\text{squeeze}} \approx \frac{d}{u_{\text{squeeze}}} \approx \frac{dab}{Q_{\text{cont}}}.$$

The total length of the droplet when it detaches is then

$$L \approx a + u_{\text{growth}}\tau_{\text{squeeze}} \approx a + b \frac{Q_{\text{dis}}}{Q_{\text{cont}}}.$$

If we note $\alpha = d/a$ and scale by a , we nearly recover Eq. (14.39):

$$\frac{L}{a} \approx 1 + \frac{d}{a} \frac{Q_{\text{dis}}}{Q_{\text{cont}}} = 1 + \alpha \frac{Q_{\text{dis}}}{Q_{\text{cont}}}. \quad (14.43)$$

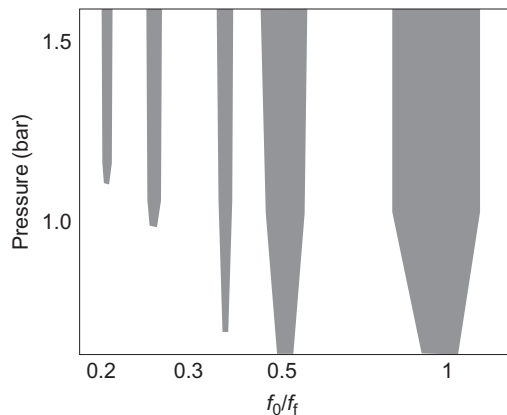
However, at this point, α is not a constant ($\alpha = d/a$), whereas in Eq. (14.40) α is a constant, with a value close to either 0 or 1. In the case where $Q_{\text{dis}} < Q_{\text{cont}}$, we have seen that $L \sim a$, which is equivalent to $d = 0$ in Eq. (14.43). In the case where $Q_{\text{dis}} > Q_{\text{cont}}$, $u_{\text{growth}} > u_{\text{squeeze}}$, which means that the growth velocity is larger than the squeeze velocity. It is observed that the width of the neck d does not vary quickly during the elongation phase; it suddenly goes to zero at breakup. This is due to a little gap between the blob and the wall (ε in Figure 14.28) that vanishes suddenly at breakup. Hence, the squeezing velocity is somewhat smaller than its value from Eq. (14.42). These observations explain why the ratio d/a can be approximated by a constant α , of the order of 1. Finally, we can approximate

$$\frac{d}{a} \approx \alpha H(Q_{\text{dis}} - Q_{\text{cont}})$$

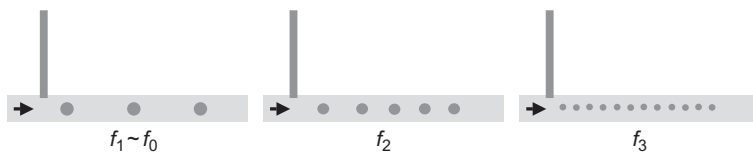
and relation (14.43) collapses to relation (14.40).

14.4.1.1.2 Droplet formation: frequency control of the droplet size

As we have seen above, according to Eq. (14.39) or (14.40), the size of the droplet is of the order of the channel width (always larger than the channel width). It has been found [27,28] that smaller droplet sizes can be produced if the incoming rate of liquid was modulated in frequency. Without frequency modulation, there is a natural frequency f_0 of droplet detachment. By superposing a tunable forcing frequency, resonances can be found leading to the formation of monodisperse droplets whose sizes differ notably from that of Eq. (14.39). Such regimes are called synchronized regimes. In such regimes, the system delivers regular drops at regular time intervals. One must be careful to avoid quasiperiodic regimes where droplets are emitted irregularly and have irregular sizes. The physics behind the

**FIGURE 14.29**

Arnold tongues: the gray areas correspond to the synchronized regimes. f_f is the forcing frequency.

**FIGURE 14.30**

Droplet size is inversely proportional to the frequency.

frequency actuated droplet emission is not yet completely understood. It involves complex nonlinear fluid dynamics. However, it has been observed [27,28] that, depending on the forcing frequency, there were domains of synchronized regimes. Such domains are shown in Figure 14.29 and are called “Arnold tongues.”

A very important experimental observation is that droplet volumes vary as the inverse of the emission frequency (Figure 14.30). Hence droplet volumes can be considerably reduced, approximately by an order of 10 and the range of droplet size is extended to the interval $[a/3, a]$; moreover, the size of the droplet can be adjusted in line by varying the frequency.

14.4.1.1.3 Mixing in T-junctions

As we have mentioned above, T-junctions are particularly well suited for biochemical and chemical reactions. However, the crux for obtaining a high efficiency of such reactions is that the constituents that react are well mixed in a very short time. For example, in the case of rapid polymerization, the components should be rapidly mixed in order to obtain a homogeneous polymerization.

**FIGURE 14.31**

(A) Stretching and folding a highly viscous fluid (or a very laminar flow). (B) Striation thickness.

Source: *Photograph by J. Tice; reprinted with permission from Ref. [33] © 2006, Wiley.*

Mixing in liquid plugs has been thoroughly studied by Handique and Burns [29], Song et al. [30], Tice et al. [31], and Bringer et al. [32].

The principle is the same that we developed in Chapter 5. In the process of folding and stretching, the striation thickness is the distance between the filets of the diffusing species (Figure 14.31); the diffusion time is then given by Fourier's law

$$t \approx \frac{s_t^2}{2D} \quad (14.44)$$

Ottino [33] has shown that the striation thickness is reduced after each folding of the filet according to

$$s_t(n) = s_t(0)\sigma^{-n} \quad (14.45)$$

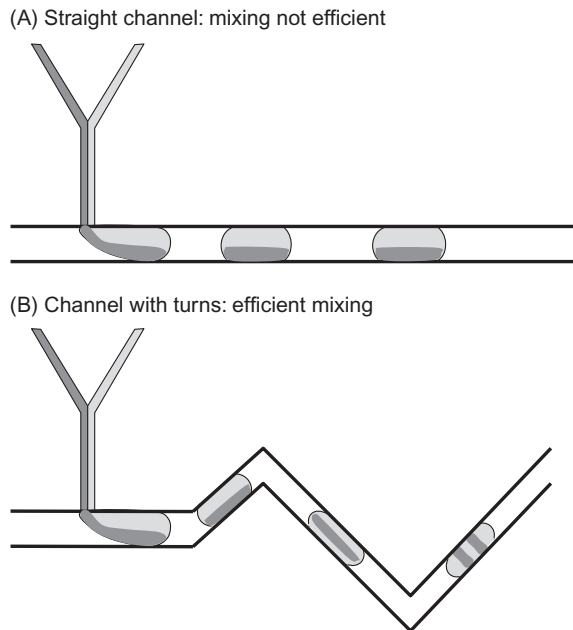
where σ is called the Lyapunov's coefficient. We analyze here two types of channels: straight channels and channels with turns (Figure 14.32). We show that the mixing process is much more efficient in channels with turns.

Suppose first that the microchannel is straight. Because the walls are fixed and the plug is moving, two recirculation patterns form inside the plug (Figure 14.33A). Striation thickness in the plug is given by the relation [29,33]

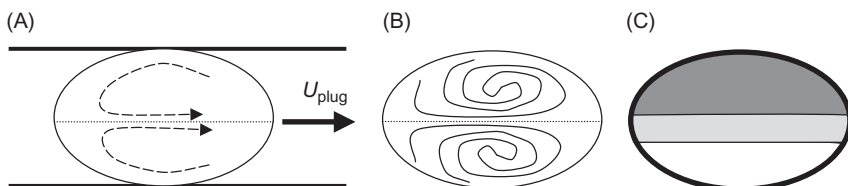
$$s_t = s_t(0) \frac{L}{d}, \quad (14.46)$$

where L is the length of the plug and d the distance traveled by the droplet. Each time the plug has traveled a distance $d = 2L$, the striation thickness is divided by two. Striation patterns are schematically shown in Figure 14.33B. The two halves homogenize first due to the reduction of the striation. Taking into account that $s_t(0) \approx a$ and using Eq. (14.44), the time for homogenization of each 1/2 plug is approximately

$$t \approx \frac{a^2 L^2}{2D d^2}. \quad (14.47)$$

**FIGURE 14.32**

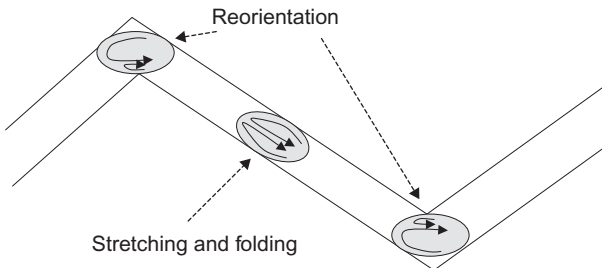
Two different types of microchannels: the channel with turns is much more efficient for mixing the components inside the droplets.

**FIGURE 14.33**

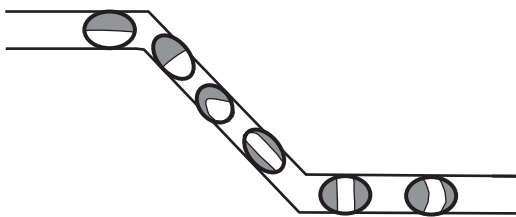
(A) Internal motion in a moving plug; (B) striation pattern in a moving plug; and (C) once diffusion has homogenized the two halves of the plug, the mixing is not complete.

However at this time, the concentration in the plug is not uniform and the situation is schematized in Figure 14.33C.

It has been observed that winding microchannels reduce homogenization time [34]. We analyze here the role of the turns of the capillary tube. Suppose we have a capillary tube constituted of n linear segments of length $d \sim 2L$, the segments being individualized by sufficiently pronounced turns. First, the recirculation flow inside the plug is modified by the turns, as shown in Figure 14.34.

**FIGURE 14.34**

Dissymmetry of internal recirculation flow is induced by turns of the capillary tube.

**FIGURE 14.35**

Sketch of the effect of stretching and folding in the straight parts and reorientation in the turns.

Second, the dissymmetry of the recirculation flow in the turns induces a reorientation of the fluid domains as shown in Figure 14.35. This reorientation is essential for the mixing of liquids in the plug. This phenomenon is called Baker's transformation and is schematized in Figure 14.36. Reorientation is necessary to increase the number of striations. Using Ottino's formula (14.45), the striation thickness is

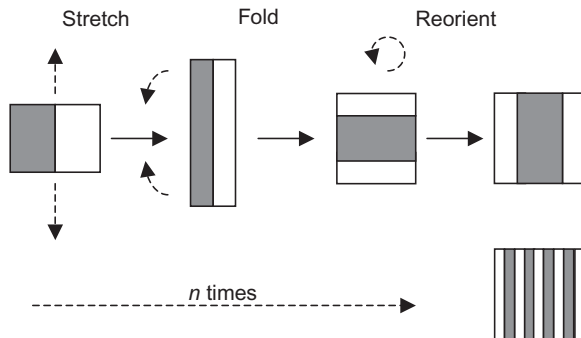
$$s_t(n) = a\sigma^{-n}$$

Using Eq. (14.46) with $d \sim 2L$, we find $\sigma = 2$. The diffusion time at step n is then derived from Eq. (14.44):

$$t_{\text{diffusion}}(n) = \frac{a^2 \sigma^{-2n}}{2D}. \quad (14.48)$$

On the other hand, because $d(1)$ is of the order of L , the convection time is given by

$$t_{\text{convection}}(n) \approx \frac{d(n)}{U} = n \frac{L}{U}. \quad (14.49)$$

**FIGURE 14.36**

Baker's transformation and reduction of the striation length.

Following Bringer et al. [32] and Stroock et al. [34], the mixing time is obtained by equating the diffusion and convection time, so that

$$t_{\text{convection}}(n) \approx n \frac{L}{U} \approx \frac{a^2 \sigma^{-2n}}{2D} = t_{\text{diffusion}}(n). \quad (14.50)$$

After rearrangement, we find

$$2n\sigma^{2n} \approx \frac{aU}{D} \frac{a}{L} \approx Pe \frac{a}{L}, \quad (14.51)$$

where $Pe = aU/D$ is the Peclet number. Equation (14.51) produces the value of n (number of segments) necessary to obtain mixing. Note that the solution of the equation $xe^x = q$ is given by the Lambert-W function [26]

$$x e^x = q \Rightarrow x = W(q)$$

The Lambert-W function is programmed in most numerical software. Then n is given by the relation

$$n \approx \frac{W(\ln \sigma Pe(a/L))}{2 \ln \sigma}. \quad (14.52)$$

Now we introduce the value $\sigma = 2$ of the Lyapunov's coefficient. Suppose that the flow rate $Q_{\text{dis}} < Q_{\text{cont}}$, Eq. (14.40) gives $L \sim a$ and Eq. (14.52) becomes

$$n \approx \frac{W(0.7 Pe)}{1.4}.$$

Using typical values of $D \sim 10^{-9} \text{ m}^2/\text{s}$, $U \sim 1 \text{ mm/s}$ and $a = 100 \mu\text{m}$, the value of the Peclet number is 100 and $n \sim 3$. In the case where $D \sim 10^{10} \text{ m}^2/\text{s}$, the number of segments required to obtain mixing is five. Hence, a small number of sharp turns of the capillary tube are very effective to completely mix the liquid.

14.4.1.2 Flow focusing devices

The principle of an FFD is shown in [Figure 14.37](#). A filament of core fluid forms at the nozzle and finally breaks up into a droplet. So far, the functioning of such devices has been mostly approached experimentally [21–23,35–39].

Contrary to T-junctions, little is known about the detailed physics of the droplet formation. The first theoretical investigations on the stability of micro-flows in FFD have been recently done by Guillot et al. [38]. It seems that there are two regimes depending on the velocities of the core flow: a dripping regime at low velocity and a jetting regime at high velocity. Here we focus on the low velocity case (dripping regime). Apparently, many parameters influence the droplet size: the ratio of the flow rates of the two fluids $Q_{\text{in}}/Q_{\text{ext}}$, the nozzle diameter D , the Reynolds numbers Re , the ratio of the densities of the two fluids $\rho_{\text{in}}/\rho_{\text{ext}}$, and the surface tension γ . For the geometry of [Figure 14.38](#), and a gaseous core, Ganan-Calvo and coworkers [21] have proposed the following correlation for the bubble diameter d :

$$d = \left(\frac{Q_{\text{in}}}{Q_{\text{ext}}} \right)^{\frac{1}{3}} D^{\frac{2}{3}} d_j^{\frac{1}{3}} f(Re_{\text{in}}) \quad (14.53)$$

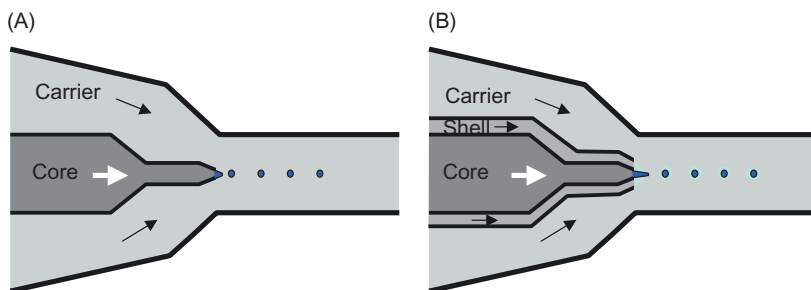


FIGURE 14.37

Principle of an FFD. (A) Monodispersed core liquid droplets and (B) encapsulated droplets.

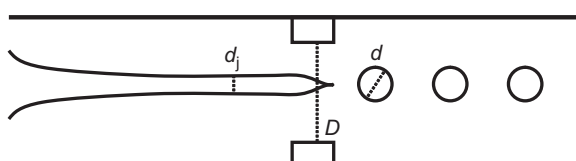


FIGURE 14.38

Sketch of an FFD.

where the filament diameter d_j is given by

$$d_j \approx \left(\frac{Q_{in}}{Q_{ext}} \right)^{\frac{1}{2}} D G(\rho_{ext}, \rho_{in}, D, \gamma). \quad (14.54)$$

A comparison with experimental results shows that the flow rates are the dominant terms in the correlation, and the correlation can be simplified by

$$\frac{d}{D} \approx \left(\frac{Q_{in}}{Q_{ext}} \right)^{0.37}. \quad (14.55)$$

The interesting thing here is that relation (14.55) shows that the ratio of the flow rates is controlling the droplet diameter. This observation confirms the results of Anna et al. [22]. The situation is then similar to that of the T-junction, with the exception that the diameter of the droplet is smaller than that of the orifice or nozzle.

Let us mention an interesting numerical approach has been performed by Davidson et al. [39] for an axisymmetric nozzle, using a volume of fluid (VOF) numerical method. Their numerical results show that the flow rate ratio is not the only parameter controlling the size of the produced droplets, and that the Reynolds and Weber numbers are also important parameters. Figure 14.39 shows the results for a ratio $Q_{in}/Q_{ext} = 0.025$, a Reynolds Rein number equal to 0.045 and a Weber number $We_{in} = 0.23 \times 10^{-5}$.

In conclusion, the detailed physics of FFD is not yet completely understood; however, the experimental approach has shown that FFD seems to be a very promising technique to realize online, monodispersed droplets, and especially to encapsulate liquids for biotechnological and pharmaceutical applications.

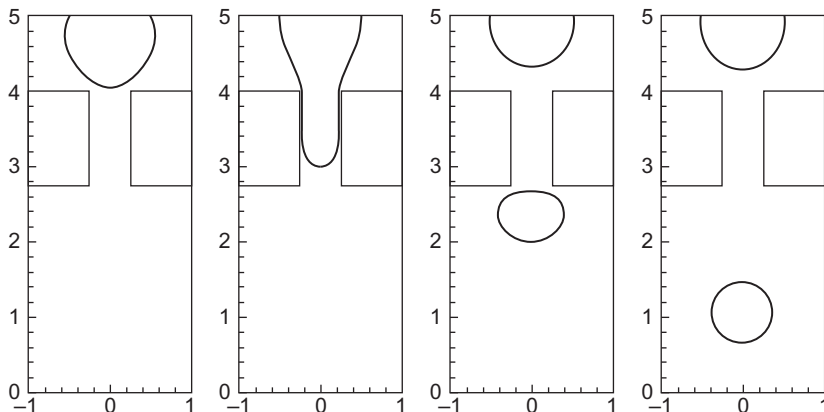
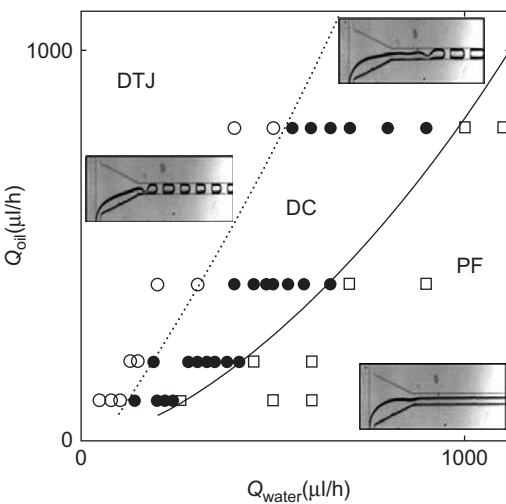


FIGURE 14.39

Numerical modeling of droplet breakup in an FFD [39].

**FIGURE 14.40**

Merging of water and oil microflows: three regimes are observed: parallel flows (PF) for small values of oil flow rate and large values of water flow rate, droplets in the channel (DC) at the inlet in the opposite case, and an intermediate regime with a short parallel flow that breaks up into droplets.

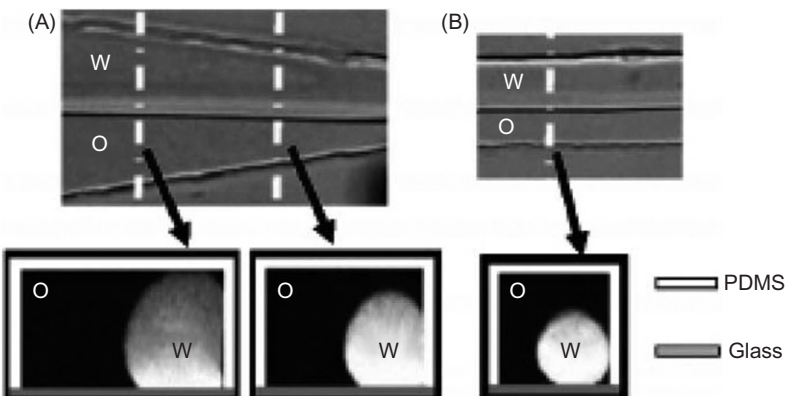
Source: Reprinted with permission from Ref. [38] © 2006, APS.

14.4.1.3 *Droplets or separated two-phase flow?*

We have seen in the preceding sections the formation of droplets in a microflow using T-junctions or FFDs. Let us remark here that the formation of droplets at the merging of two immiscible flows is not automatic. Guillot and Colin [38] have investigated the stability of parallel flows in a microchannel after a T-junction (Figure 14.40). They have observed different regimes depending on the flow rate of the two liquids (and more generally on the capillary numbers of the two regimes). Note that in their case, the bottom plate is hydrophilic (glass) and the other walls are hydrophobic (PDMS).

Based on similar considerations as those of Garstecki et al. [36], the authors have derived a semiempirical expression for the limit of the parallel flow domain.

However, not much is known on the stability of co-flowing immiscible fluids far from the inlet. In Section 14.3, we have investigated the case of co-flowing microflows when micropillars are present to increase the stability of the interface. The picture is largely different than that of macroscopic channels. In particular, the flows are not stratified because gravity is negligible at this scale (the Bond number $Bo = \rho g D_h^2 / \gamma$ is much smaller than 1), and the nonwetting liquid forms a cylindrical filament inside the channel, as shown in Figure 14.41. It appears that, if the filament touches the wall by capillary contact, the stability may be ensured

**FIGURE 14.41**

(A) Microchannel inlet: the oil–water interface forms a spherical segment. Progressively the water flow forms a filament attached to the hydrophilic glass plate. (B) At the outlet the two phases are still flowing in parallel and the water filament is nearly cylindrical.

Source: Reprinted with permission from Ref. [38] © 2006, APS.

on a long distance, but if it detaches from the wall, Rayleigh–Plateau type instabilities contribute to break the filament into droplets.

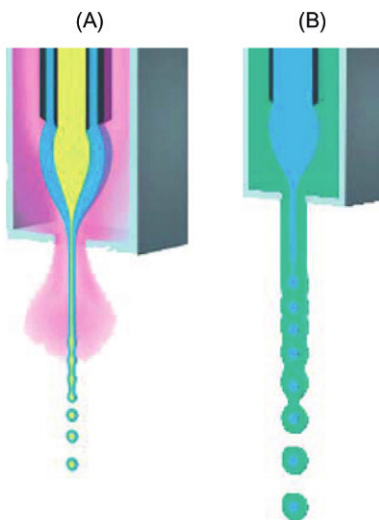
14.4.2 Encapsulation

Flow focusing techniques, and to a lesser extent T-junctions, are used in laboratories and in the industry to encapsulate liquids, bubbles, particles, and biological objects like proteins and cells. T-junctions can be used in series with FFD as shown in Figure 14.25. Figure 14.42 shows two types of FFDs aimed at producing encapsulated microdroplets [43].

Encapsulation is an essential process in many applications like drug delivery, protein crystallization [2,41], complex particles, and cell preservation [43]. According to the application, the coating may be programmed to become solid by polymerization, or the interior to crystallize when in contact with adequate chemical species. Figure 14.43 schematically shows some applications of encapsulation: (B) microdrops of two liquids (of different nature) encapsulated in a droplet of a third liquid obtained in a T-junction [44,45]; (C) a droplet of liquid ink encapsulated by a polymerized coating of resin [41]; (D) encapsulated live liver cells after 2 days storage in nonaseptic water [3].

14.5 Summary

In this chapter, we have introduced the physics of two-phase flows in microchannels, under the form of droplets and plugs, and the stability of an interface

**FIGURE 14.42**

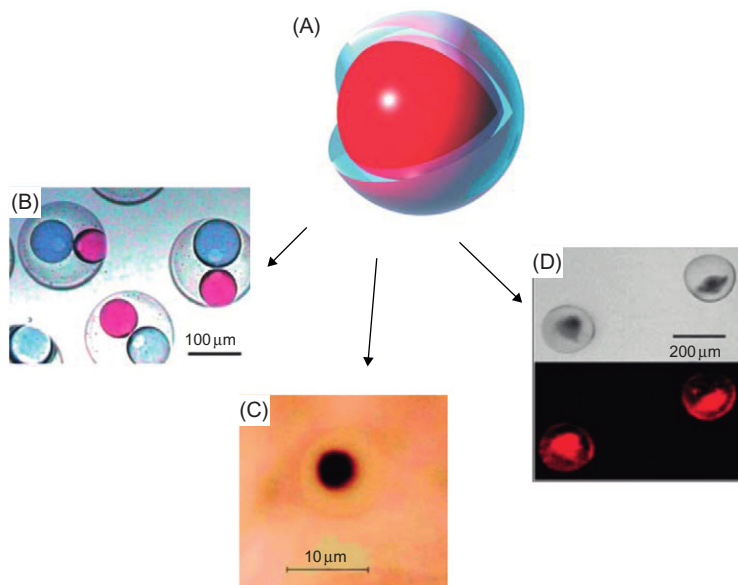
Two different FFDs for the encapsulation of droplets: (A) concentric nozzles can be used to create complex particles from two liquids or from a liquid and a gas resulting in the production of hollow spheres and (B) a funnel shaped lens of liquid can be used to create microencapsulated spheres.

Source: From Ref. [40], courtesy Flow Pharma Inc. of California, USA.

between two immiscible fluids flowing in parallel. The perspectives of droplet microfluidics are especially promising. Two-phase—and multiphase—flows are already used in T-junctions and FFDs to generate monodispersed droplets and to encapsulate them in a liquid or a gel and even a solid (polymerizable) coating, to generate applications in biology, biotechnology, and microchemistry.

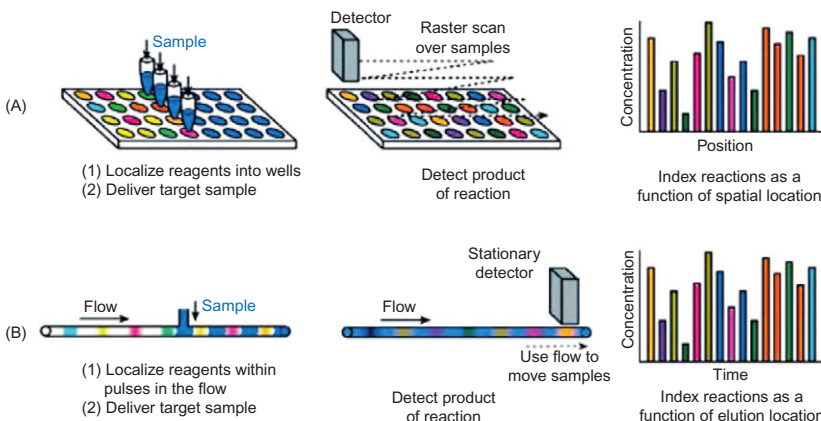
To this point, it may be useful to compare digital microfluidics, which we have presented in Chapters 4–8, and droplet microfluidics. In reality, the two techniques have different scopes of application; they address different problems. Digital microfluidics can handle extremely small volumes of liquids and realize operations and manipulation in parallel, and with great accuracy, whereas droplet microfluidics is well adapted to perform operations in series. These properties are illustrated in Figure 14.44.

Volumes and forces are generally smaller in digital microfluidics, and very small objects can be handled easily. Besides, the precision of the manipulations is very high. As a very coarse rule, digital microfluidics is particularly dedicated to precise biorecognition and bioanalysis, T-junctions are very efficient for online reactions, FFDs are essential for encapsulation processes, and separated two-phase microflows are particularly adapted as mass exchanger microdevices.

**FIGURE 14.43**

Encapsulation has many applications: (B) two immiscible liquids encapsulated by a third liquid; (C) liquid ink microdrop encapsulated by a polymer resin; and (D) live liver cells encapsulated in a protective gel, the fluorescent image below shows that the cells are still alive.

Source: (B) Reprinted with permission from Ref. [43] © 2004, American Chemical Society; (C) Reprinted with permission from Ref. [40], courtesy Flow Pharma Inc. of California, USA; and (D) Reprinted with permission from Ref. [3] © 2006, IOP.

**FIGURE 14.44**

Comparison between digital and droplet microfluidics.

Source: Reprinted with permission from Ref. [45] © 2006, Wiley.

References

- [1] M. Joanicot, A. Ajdari, Droplet control for microfluidics, *Science* 5 (2005) 887–888.
- [2] L.S. Bo Zheng, Roach, R.F. Ismagilov, Screening of protein crystallization conditions on a microfluidic chip using nanoliter-size droplets, *JACS* 125 (2003) 11170–11171.
- [3] Hyun-Jik Oh, So-Hyun Kim, Ju-Yeoul Baek, Gi-hun Seong, Sang-Hoon Lee, Hydrodynamic micro-encapsulation of aqueous fluids and cells via “on the fly” photo polymerization, *J. Micromech. Microeng.* 16 (2006) 285–291.
- [4] R.L. Hoffman, A study of advancing interface, *J. Colloid Interface Sci.* 50 (1975) 228–241.
- [5] M. Fermigier, P. Jenffer, An experimental investigation of the dynamic contact angle in liquid–liquid systems, *J. Colloid Interface Sci.* 146 (1990) 226–241.
- [6] J. Berthier, F. Ricoul, Numerical modeling of ferrofluid flow instabilities in a capillary tube at the vicinity of a magnet, in: Proceedings of the 2002 MSM Conference, 22–25 April 2002, San Juan, PR, 2002.
- [7] J. Berthier, P. Silberzan, *Microfluidics for Biotechnology*, Artech House Publishers, Norwood, MA, 2006.
- [8] R.K. Shah, A.L. London, Laminar flow forced convection in ducts, Supplement 1 to *Advances in Heat transfer*, eds. T.F. Irvine, J.P. Hartnett, Academic Press, New York, 1978.
- [9] M. Bahrami, M.M. Yovanovich, J.R. Culham, Pressure drop of laminar, fully developed flow in microchannels of arbitrary cross-section, *ASME J. Fluid Eng.* 126 (2006) 1036–1044.
- [10] E. Chibowski, A. Ontiveros-Ortega, R. Perea-Carpio, On the interpretation of contact angle hysteresis, *J. Adherence Sci. Technol.* 16 (10) (2002) 1367–1404.
- [11] S.M.M. Ramos, E. Charlaix, A. Benyagoub, Contact angle hysteresis on nanostructured surfaces, *Surf. Sci.* 540 (2003) 355–362.
- [12] J.L. Bo He, N.A. Patankar, Contact angle hysteresis on rough hydrophobic surfaces, *Colloids Surf. Physicochem. Eng. Aspects* 48 (2004) 101–104.
- [13] D.L. Chen, Liang Li, S. Reyes, D.N. Adamson, R.F. Ismagilov, Using three-phase flow of immiscible liquids to prevent coalescence of droplets in microfluidic channels: criteria to identify the third liquid and validation with protein crystallization, *Langmuir* 23 (2007) 2255–2260.
- [14] J. Berthier, Van Man Tran, H. Jeanson, N. Sarrut, On the stability length of fluid/liquid interfaces sustained by microfabricated pillars, in: Proceedings of the 2007 Nanotech Conference, 21–24 May, Santa Clara, CA, 2007.
- [15] A. Aota, M. Nonaka, A. Hibara, T. Kitamori, Micro counter-current flow system for high efficiency extraction, in: 7th International Conference on Miniaturized Chemical and Biochemical Analysis Systems, RSC (Royal Society of Chemistry), Squaw Valley, CA, 5–9 October, 2003.
- [16] W. van der Wijngaart, T. Frisk, G. Stemme, A micromachined interface for transfer of liquid or vapor sample to a liquid solution, in: Proceedings of the 13th International Conference on Solid-State Sensors, Actuators and Microsystems, SPIE International Society for Optics and Photonics, Seoul, 5–9 June, 2005.
- [17] E.W. Washburn, The dynamics of capillary flow, *Phys. Rev.* (1921) 273–283.

- [18] I. Papautsky, B.K. Gale, S. Mohanti, T.A. Ameel, A.B. Frazier, Effects of rectangular microchannel aspect ratio on laminar friction constant, Proc. SPIE 3877 (1999) 147–158, Microfluidic Devices and Systems II.
- [19] Y. Tsori, Discontinuous liquid rise in capillaries with varying cross-sections, Langmuir 22 (2006) 8860–8863.
- [20] K. Brakke, The surface evolver, Exp. Math. 1 (1992) 141.
- [21] A.M. Gañán-Calvo, J.M. Gordillo, Perfectly monodisperse microbubbling by capillary flow focusing, Phys. Rev. Lett. 87 n°27 (2001) 274501-1-4.
- [22] S.L. Anna, N. Bontoux, and H.A. Stone, Formation dispersions using “flow focusing” in microchannels, Appl. Phys. Lett. 82 n°3 (2003) 364–366.
- [23] T. Nisisako, T. Torii, T. Higuchi, Novel microreactors for functional polymer beads, Chemical Engineering Journal 101 (2004) 23–29.
- [24] T. Thorsen, R.W. Roberts, F.H. Arnold, S.R. Quake, Dynamic pattern formation in a vesicle-generating microfluidic device, Phys. Rev. Lett. 86 (2001) 4163–4166.
- [25] P. Garstecki, M.J. Fuerstman, H.A. Ston, G.M. Whitesides, Formation of droplets and bubbles in a microfluidic T-junction: scaling and mechanism of break-up, Lab. Chip. 6 (2006) 437–446.
- [26] Wolfram Mathworld, <http://mathworld.wolfram.com/HeavisideStepFunction.html>.
- [27] P. Tabeling, V. Barbier, J. Goulpeau, B. Lonetti, H. Willaime, Playing with actuators in microfluidic systems, Proceedings of the NSTI-Nanotech Conference 2006, Vol. 2, 2006.
- [28] H. Willaime, H., V. Barbier, L. Kloul, S. Maine, P. Tabeling, Arnold Tongues in a Microfluidic Drop Emitter, Phys. Rev. Lett. 96 (2006) 054501-1-4.
- [29] H. Handique, M.A. Burns, Mathematical modeling of drop mixing in a slit-type microchannel, J. Micromech. Microeng. 11 (2001) 548–554.
- [30] H. Song, J.D. Tice, R.F. Ismagilov, A microfluidic system for controlling reaction networks in time, Angew. Chem. 42 (2003) 767–771.
- [31] A. Günther, K.F. Jensen, Multiphase microfluidics: from flow characteristics to chemical and material synthesis, Lab. Chip. 6 (2006) 1487–1503.
- [32] S. Okushima, T. Nisisako, T. Torii, T. Higuchi, Controlled production of monodisperse double emulsions by two-step droplet breakup in microfluidic devices, Langmuir 20 (2004) 9905–9908.
- [33] T. Nisisako, T. Torii, T. Higuchi, Novel microreactors for functional polymer beads, Chem. Eng. J. 101 (2004) 23–29.
- [34] J.M. Ottino, The Kinematics of Mixing: Stretching, Chaos, and Transport, Cambridge University Press, 1988.
- [35] P. Garstecki, M.J. Fuerstman, H.A. Ston, G.M. Whitesides, Formation of droplets and bubbles in a microfluidic T-junction: scaling and mechanism of break-up, Lab. Chip. 6 (2006) 437–446.
- [36] P. Tabeling, V. Barbier, J. Goulpeau, B. Lonetti, H. Willaime, Playing with actuators in microfluidic systems, in: Proceedings of the NSTI-Nanotech Conference, vol. 2, 2006.
- [37] P. Garstecki, H.A. Stone, G.M. Whitesides, Mechanism for flow-rate controlled breakup in confined geometries: a route to monodisperse emulsions, Phys. Rev. Lett. 94 (2005) 164501-1-4.
- [38] A.M. Ganán-Calvo, L. Martin-Banderas, R. Gonzalez-Prieto, A. Rodriguez-Gil, T. Berdun-Alvarez, A. Cebolla, et al., Straightforward production of encoded

- microbeads by flow focusing: potential applications for biomolecule detection, *Int. J. Pharm.* 324 (2006) 19–26.
- [39] P. Guillot, A. Colin, Stability of parallel flows in a microchannel after a T-junction, *Phys. Rev. E* 72 (2005) 066301.
 - [40] M.R. Davidson, D.J.E. Harvie, J.J. Cooper-White, Flow focusing in microchannels, *ANZIAM J.* 46 (2005) C47–C58.
 - [41] J.T. Cabral, S.D. Hudson, Microfluidic approach for rapid multicomponent interfacial tensiometry, *Lab. Chip* 6 (2006) 427–436.
 - [42] S.L. Anna, N. Bontoux, H.A. Stone, Formation dispersions using flow focusing in microchannels, *Appl. Phys. Lett.* 82 (3) (2003) 364–366.
 - [43] A.M. Ganan-Calvo, J.M. Gordillo, Perfectly monodisperse microbubbling by capillary flow focusing, *Phys. Rev. Lett.* 87 (27) (2001) 274501-1-4.
 - [44] <<http://www.flowfocusing.com/Home>> Page Frameset Source/ff Home Content.htm.
 - [45] B. Zheng, J.D. Tice, R.F. Ismagilov, Formation and arrayed droplets by soft lithography and two-phase fluid flow and application in protein crystallization, *Adv. Mater.* 16 (15) (2004) 1365–1368.
 - [46] K. Liu, Hui-Jiang Ding, J. Liu, Y. Chen, Xing-Zhong Zhao, Shape-controlled production of biodegradable calcium alginate gel microparticles using a novel microfluidic device, *Langmuir* 22 (2006) 9453–9457.

Epilog

15

CHAPTER OUTLINE

15.1 Increasing the domain of EWOD applicability	533
15.2 Interconnecting the different microfluidic toolboxes	534
15.3 Miniaturization: nano-EWOD	536
15.4 Other applications specific to DMF	537
15.5 Summary	537
References	538

The place and importance of DMF in the development of microsystems have been pointed out throughout this book. It has been seen that the advantages of such systems are related to the reduction of the liquid volumes to be handled; besides, their high potential for reconfigurability has been shown by Chakrabarty and Su [1]. With the background acquired through the different chapters, a reflection on DMF and on its most needed and promising developments can be started. Questions such as “can miniaturization be pushed further?” and “what are the next developments that will extend the field of applications of DMF?” can reasonably be raised.

Of course, the answer to these questions is not straightforward and necessitates a long development. This epilog chapter only presents a few perspectives.

15.1 Increasing the domain of EWOD applicability

In Chapter 4, three limitations to the EWOD technology were pointed out: first, a minimum potential is required to move a droplet, due to contact angle hysteresis; second, the electrowetting force is limited by a maximum actuation potential linked to the saturation phenomenon; and third, the electrowetting force is also limited by a maximum potential linked to dielectric breakdown. Decreasing hysteresis and increasing the dielectric breakdown level require improving the electric characteristic and the surface quality of the materials separating the electrodes from the liquid: high-capacity layers supporting large critical electric

fields with highly hydrophobic surface are needed. This line of work is presently the subject of active research [2–5], and experimentation on new nano-textured surfaces is in progress.

15.2 Interconnecting the different microfluidic toolboxes

A second remark stems from the observation of Figure 1.1, redrawn slightly differently in [Figure 15.1](#): Is it possible to switch from one type of microfluidics to another one? Is it useful?

In [Figure 15.1](#), the interconnections between the different toolboxes have been materialized by arrows. A few connections have been developed (continuous arrows); for example, two microflows merging in a T-junction or in an FFD generate droplets or a two-phase microflow. It is also the case of ink-jet printing, or spotting robots, transforming a microflow into droplets. Conversely, Günther et al. [7] have shown it was possible to separate a plug flow into two single fluid microflows. However, many links are still missing.

The establishment of links between the different toolboxes is currently the object of active study: this is the case of the transformation of a two-phase microflow to droplet microflow [8,9]; it has been shown by Guillot et al. [10] that this

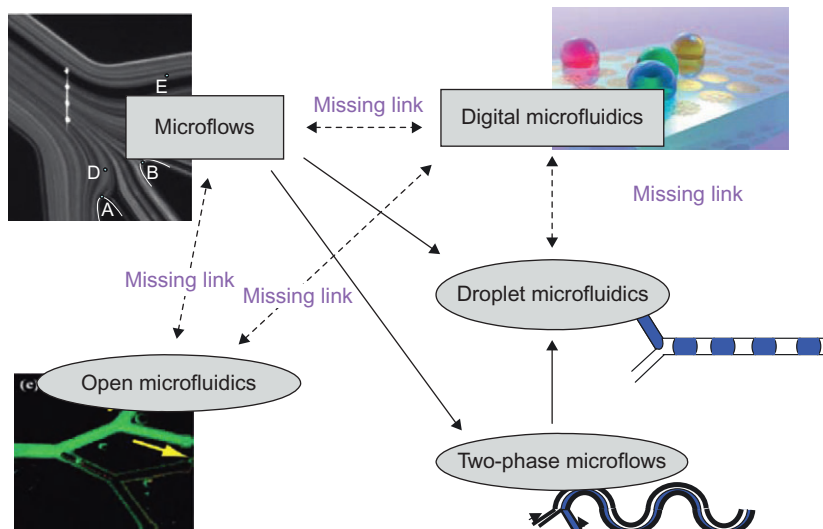


FIGURE 15.1

Sketch showing that links between the different types of microfluidics are still largely undeveloped.

Source: Photograph bottom left reprinted with permission from Ref. [6] © 2005, American Chemical Society.

Photograph top right courtesy Advalytix.

transformation depends heavily on the stability or the instability of the flow (Figure 15.2). This observation implies that the reverse path—from a droplet microflow (or an emulsion) to a separated two-phase flow—will be difficult.

Another missing link is presently under scrutiny: DMF would benefit from being connected to microflows. Indeed, DMF systems are currently manually loaded in sample liquids by using micropipettes, or in some cases by robots. Automatic loading of digital microsystems using a microflow would be a considerable improvement. The same reasoning applies for “open microfluidic” systems. It would also be useful to extract microdrops from a continuous flow and direct them onto a digital system. That would, for instance, improve substantially the detection of pathogens in flowing liquids. Conversely, it could be convenient to be able to convert a droplet or a digital microflow into a continuous flow. In particular, this would be an advantage for the manipulation and the study of cells. A first system of this kind has recently been studied by Berthier and Beebe [11] where droplets deposited on an inlet port give birth to a continuous, almost constant microflow, under the condition that a calibrated refill is implemented (Figure 15.3).

These few examples show that interconnections between the different types of microfluidics are essential. However, at the present time, they are still largely underdeveloped.

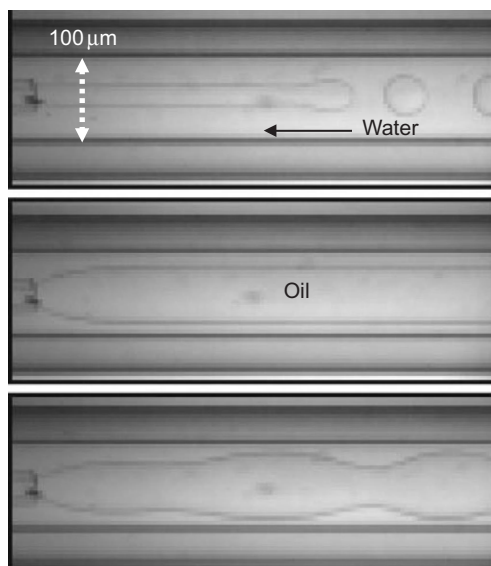
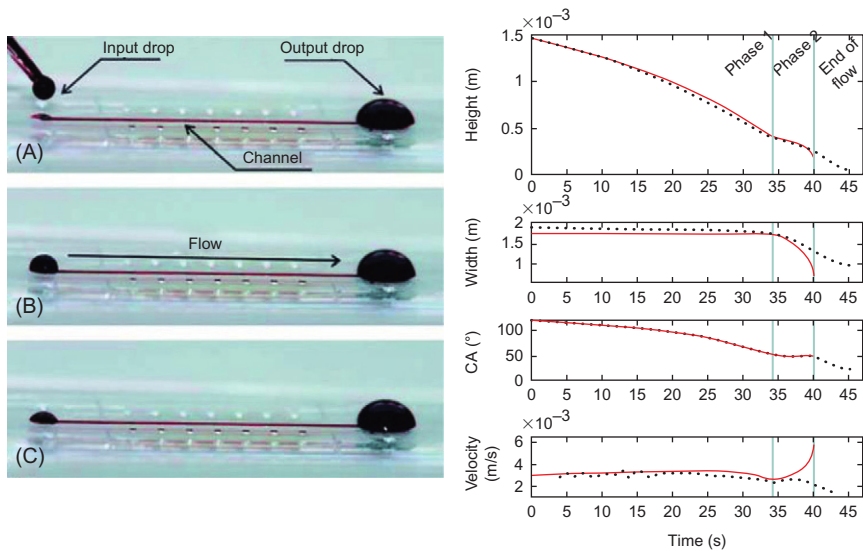


FIGURE 15.2

Two-phase flow degenerating into a droplet flow.

Source: From Ref. [10] © 2007 APS, reprinted with permission.

**FIGURE 15.3**

Droplet deposited on an inlet port gives birth to a continuous microflow (left). In the first phase, the contact area remains constant while the contact angle decreases; during this first phase, the velocity remains constant.

Source: Reprinted with permission from Ref. [11] © of the Royal Society of Chemistry (2007).

15.3 Miniaturization: nano-EWOD

It is obvious that the trend toward miniaturization has been the engine behind microsystems development. A second question that arises at this stage concerns miniaturization of DMF: can it be pursued further and what will it bring? The word nano-EWOD is even evoked to denote the scale down of EWOD-based microsystems. The idea behind this is the manipulation of droplets of less than 5–10 nL. One of the potential applications would be the manipulation of single cells, or at least small collections of cells, or bacteria, etc.

The first idea of a rule for downscaling is to homothetically reduce the dimensions of the usual EWOD-based systems described in Chapter 5. However, such a scale down raises some complicated questions, like: would the electrowetting force on the droplet be sufficient to perform all the operations required for the process? Remember that this force is proportional to the width of the electrode. And how can the hysteresis level be lowered sufficiently to palliate this loss of electrowetting force? Can the thickness of the dielectric layer be sufficiently reduced to compensate for the loss of electrowetting force? These two last questions refer to the remarks of Section 15.1. Another difficulty is the reduction of the size of the horizontal gap between the electrodes [12]: Can it be sufficiently

reduced to avoid pinning? And finally, what are the effects of the increase in microdrop pressure associated with the reduction of the vertical gap?

All these questions make nano-EWOD a difficult but interesting challenge.

15.4 Other applications specific to DMF

The focus of this book is mostly on biotechnological, biological, and chemical applications of DMF. However, DMF is not limited to biotechnology. New promising applications have recently appeared in optics, with the development of a “liquid” screen based on electrowetting display technology that becomes brighter in direct sunlight [13] and with the development of adjustable “liquid” lenses [14] (Figure 15.4). The principle derives directly from the electrowetting effect: in the case of the Liquavista™, each “pixel-electrode” of the screen is occupied by an oil droplet, and when the actuation is switched off, the droplet shrinks and is pushed toward a small corner of the pixel-electrode. In the case of the Varioptic™ lens, the convexity of the liquid lens is controlled by the intensity of the electric actuation.

15.5 Summary

This book has presented the background for the study of the behavior of micro-drops and its applications to digital and droplet microfluidics. Considering the whole domain of today’s microfluidics, schematized in Figure 15.1, the amount of progress done since the beginning of that science is considerable; however, a considerable amount of work remains to be done to cover all the applications that microtechnologies require. Coincidentally, the same conclusion can be made,

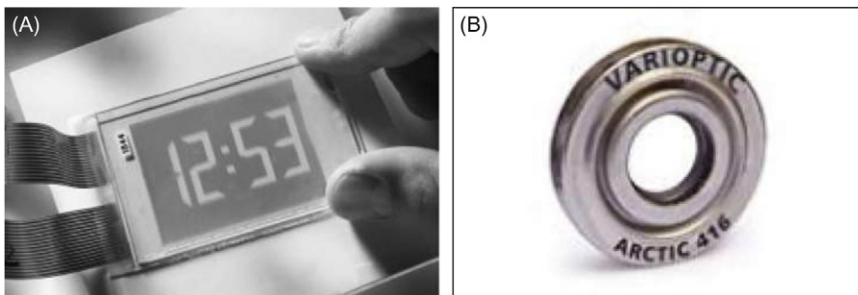


FIGURE 15.4

(A) Display screen based on electrowetting by Liquavista™: ColorMatch prototype display manufactured by Liquavista. The display diagonal is 2.5" [13]. (B) Adjustable optical lens by Varioptic™: Varioptic liquid lens Artic 416 [14].

based on totally different grounds, by comparison with the developments of microelectronics. The parallel is done principally because the first microfluidic systems were realized with devices obtained by microfabrication techniques used in microelectronics. The comparison is based on the following observation: it has taken approximately 50 years for microelectronics to become mature—approximately between the years 1950 and 2000. If the same is to be expected in the field of biotechnology, we are just midway in the development of microfluidic systems. And this leaves a considerable field for new developments in the years to come.

References

- [1] K. Chakrabarty, F. Su, *Digital Microfluidic Biochips: Synthesis, Testing, and Reconfiguration Techniques*, Taylor and Francis, Boca Raton, FL, 2007.
- [2] N. Verplanck, E. Galopin, J.-C. Camart, V. Thomy, Y. Coffinier, R. Boukherroub, Reversible electrowetting on superhydrophobic silicon nanowires, *Nano Lett.* 7 (3) (2007) 813–817.
- [3] T.N. Krupenkin, J.A. Taylor, T.M. Schneider, S. Yang, From rolling ball to complete wetting: the dynamic tuning of liquids on nanostructured surfaces, *Langmuir* 20 (2004) 3824–3827.
- [4] M.S. Dhindsa, N.R. Smith, J. Heikenfeld, P.D. Rack, J.D. Fowlkes, M.J. Doktycz, Reversible electrowetting of vertically aligned superhydrophobic carbon nanofibers, *Langmuir* 22 (2006) 9030–9034.
- [5] G. McHale, D.L. Hebertson, S.J. Elliott, N.J. Shirtcliffe, M.I. Newton, Electrowetting of nonwetting liquids and liquid marbles, *Langmuir* 23 (2007) 918–924.
- [6] W. Satoh, H. Hosono, H. Suzuki, On-chip microfluidic transport and mixing using electrowetting and incorporation of sensing functions, *Anal. Chem.* 77 (2005), 6857–6863.
- [7] A. Günther, M. Jhunjhunwala, M. Thalmann, M.A. Schmidt, K.F. Jensen, Micromixing of miscible liquids in segmented gas–liquid flow, *Langmuir* 21 (2005) 1547–1555.
- [8] T. Thorsen, R.W. Roberts, F.H. Arnold, S.R. Quake, Dynamic pattern formation in a vesicle-generating microfluidic device, *Phys. Rev. Lett.* 86 (18) (2001) 4163–4166.
- [9] J.D. Tice, H. Song, A.D. Lyon, R.F. Ismagilov, Formation of droplets and mixing in multiphase microfluidics at low values of the Reynolds and the capillary numbers, *Langmuir* 19 (19) (2003) 9127–9133.
- [10] P. Guillot, A. Colin, A.S. Utada, A. Ajdari, Stability of a jet in confined pressure-driven biphasic flows at low Reynolds numbers, *Phys. Rev. Lett.* 99 (2007) 104502.
- [11] E. Berthier, D.J. Beebe, Flow rate profile of a surface tension driven passive micro-pump, *Lab Chip* 11 (2007) 1475–1478.
- [12] J. Berthier, C. Peponnet, A model for the determination of the dimensions of dents for jagged electrodes in electrowetting on dielectric microsystems, *BioMicrofluidics* 1 (1) (2007) 014104.
- [13] Liquavista™. <<http://www.liquavista.com/files/LQV060828XYR-15.pdf>>.
- [14] Varioptic™. <<http://www.varioptic.com/en.tech/technology01.php>>.

Index

Note: Page numbers followed by “*f*” refer to figures respectively.

A

- Allele, 353
- Amplification, (DNA), 354–355, 479–482, 490
- Annealing, 346
- Area-tunable micromirrors (ATMM), 433–435
- Arnold tongues, 518–519, 519*f*

B

- Baker’s transformation, 522, 523*f*
- Bending stiffness, 445–446
- Biocatalytic reaction, 407
- Biocompatibility, 342
- Biofouling, 342, 355–356
- Biosensors, 321, 340
- Blood vessel network, 32–34
- Bond number, 58, 77–78, 85, 92, 169, 230, 332, 450, 526–527
- Bovine serum albumin (BSA), 342–343, 343*f*, 352–353

C

- Canthotaxis, 135–136, 245
- Cantilever, 443–445, 444*f*
- Capacitance, 162–166, 202, 206–208, 211, 313, 315, 317
- Capillary origami, 440, 445–447, 446*f*
- Capillary length, 30, 49–51, 77–79
- Capillary number, 132, 140–141, 235, 495–497, 497*f*, 503*f*, 517*f*, 526
- Capillary rise, 45–52, 45*f*, 46*f*, 49*f*, 55–56, 162–163, 313
- Carbon nano-tube (CNT), 26*f*, 487–488
- Casein, 342
- Cassie-Baxter law, 110–124, 218
- Catena, 107–108, 109*f*, 195*f*, 228–231, 259, 401*f*
- Cellomics, 367–368
- Cells, 100–101, 209, 211, 342–343, 362–363, 368–370, 376–378, 380*f*, 383–384, 486–487
- Coating (hydrophobic), 94, 96, 207, 393
- Concus-Finn relation, 94–96
- Concus-Finn-Brakke relation, 96–97
- Contamination, 355–356, 467, 484, 503
- Crenellated electrodes, 242–253
- Critical surface tension, 62, 64

- Curved EWOD substrates, 325–326, 326*f*, 330
- Cytomics, 367–368

D

- Darcy-Weisbach equation, 502
- DBS (Dried Blood Spot), 378, 378*f*
- Deformation tensor, 463–464
- Denaturation (DNA), 346
- Dengue virus, 352
- Dielectric constant, 169–170, 208, 211, 306, 308, 394–395, 447–448
- Dielectric film, 166, 179*f*
- Dielectrophoresis (DEP), 303
- Diffusion, 388, 396, 478, 480*f*, 522–523
- Disjoining pressure, 24–25, 66–67
- DMF (Digital Microfluidic), 2–3, 4*f*, 5–6, 8–10, 9*f*, 85, 90, 134, 151–152, 228, 237, 325, 342–343, 346–356, 360–361, 370–371, 379–383, 390, 422, 537
- DNA strands, 154, 321, 346, 347*f*, 357, 478, 481–482
- Double layer, 164–166, 168–169, 306, 388
- Droplet break-up, 514, 514*f*, 525*f*
- Droplet microfluidics, 2–6, 288–289, 494, 527–528, 529*f*

E

- Elasticity of the interface, 136, 260, 262
- Elasto-capillarity, 445–447, 448*f*
- Electro-convection, 405–406
- Electrode (jagged), 136, 242–243, 247–251, 249*f*
- Electro-elasto-capillarity, 447–448
- Electrokinetic effect, 459
- Electro-osmotic flow (EOF), 388, 389*f*
- Electrowetting display, 422–423, 422*f*, 537
- Electrowetting force, 193, 195–196, 216–217, 232, 233*f*, 234, 239, 244, 294, 318, 372–373, 394–395, 400, 402, 536–537
- Electrowetting number, 167, 176, 188*f*, 234, 268, 330, 375–376, 383
- Enzymatic repair activity, 357
- Evaporation, 144–156, 145*f*, 146*f*, 155*f*, 253, 288–289, 397–398, 482–483
- EWD (Electrowetting Device), 220*f*, 325, 378

EWOD (Electrowetting on Dielectric), 27, 107f, 162–163, 166, 171, 178–179, 185, 193–194, 196, 199f, 201–206, 211, 225, 303, 314, 317–318, 327–329, 339, 368–370, 375–378, 393–414, 436, 533–534, 536–537
Excision (DNA), 357

F

FAM (fluorophore), 143–144, 353, 357
Flow chamber chip (FCC), 484–485
Fluorescent energy transfer (FRET), 357, 358f
Fowkes method, 63–64
Frequency (droplet emission, natural), 518–519
Frequency-dependent permittivity, 395–396

G

Gauss' law, 173–174, 183
Genotyping, 346
Giant unilamellar vesicles (GUV), 321
Gibbs equation, 164–166, 288–289
Glucose microassay, 407
Good and Girifalco method, 62–63
Gravity, 57–60, 453–455
Green fluorescent protein (GFP), 358

H

Heat pump, 348
Helmholtz assumption, 164–166
Hooke's law, 464
Housing of single cells, 101f
Hydraulic diameter, 507f
Hydrogel disk, 379–383, 381f, 382f
Hysteresis, 131f

I

Incubation, 357–358, 397–398, 410
Interdigital transducer (IDT), 459, 466–467, 477f, 481–482
Interface, 11–14, 24f, 32f, 55, 85–86, 90–92, 93f, 95f, 137, 145f, 162, 172, 174, 176, 231, 244–245, 432f, 448–455, 452f, 495, 505–514, 508f, 509f, 510f
Interfacial surface, 14
In-tube PCR, 352–353
Ionic liquids, 138–139, 195, 247–248, 269–270, 289, 398–407, 410–414

J

Jackson-Meisenheimer complex, 409–410, 410f
Jagged electrodes, 250–251
Jurin's law, 46–47

K

Katayama-Guggenheim equation, 15
Korteweg-Helmholtz equation, 173–174

L

Lab-on-a-chip (LOC), 2–3, 100–101, 344–346, 388, 407, 468
Lambert W function, 523
Laplace law, 20–36, 39, 45, 67, 85–86, 106, 253, 362
Limit of detection (LOD), 345
Line tension, 39–41, 178
Lippmann law, 162–164, 166, 176–177, 239–240
Lippmann-Young law, 163, 166–172, 167f, 176–179, 181–184, 189–195, 207, 244, 253, 399
Liquid crystal (LC), 436
Liquid dielectrophoresis (LDEP), 303
Liquid lens, 422, 427–428, 429f, 430, 433f, 537
Lyapunov coefficient, 520, 523
Lyophilic surfaces, 103–104
Lyophobic surfaces, 103–104, 106, 136, 232

M

Marangoni convection, 15–17, 19f, 138–144, 140f, 152–153, 288–289
Marangoni number, 140, 142
Matrix Assisted Laser Desorption Ionization Mass Spectrometry (MALDI-Ms), 360–361
Maxwell's tensor, 173–174, 179, 244, 312
Mechanical elongation, 464
MEMS (Micro Electro-Mechanical Systems), 2–3, 322
Micro-mirrors, 433–435
Morphology (of microdrops), 2–5
Most unstable wavelength (Rayleigh instability), 318–320
Multiphase microflows, 3–4, 494
Murray's law, 32–33

N

Nano-EWOD, 536–537
Navier-Stokes equation, 468–469
Neumann's construction, 90–92, 440–441, 441f, 503, 504f
Neumann's triangle, 441f
Neuroblastoma, 363, 364f
Nucleotide, 352, 481–482

O

Ohnesorge number, 234–237, 253, 284, 318–319
 On-chip PCR, 353–354, 490
 Onium salt, 410–412, 415
 Optofluidics, 421

P

PCR-mix, 347, 353*f*, 357*f*, 482–483
 Peclet number, 523
 Pellat’s experiment, 309–312, 312*f*, 318
 Peltier device, 347*f*, 348–351
 Peltier effect, 348
 Permittivity (vacuum), 164–166, 208, 305, 311, 395–396
 Permittivity, 202*t*, 305, 313, 314*t*, 395–396
 Phonons, 461–462
 Phosphate buffered saline (PBS), 363
 Photoluminescence (PL), 462–463
 Piezoelectric stiffening, 465
 Piezoelectric substrates, 459, 462–463, 467*f*, 481–482, 482*f*, 489–490
 Placenta, 352–353
 Plasma, 113, 114*f*, 341
 Plateau-Rayleigh instability, 318–319, 320*f*
 PLL (Poly-L-Lysine), 376, 377*f*
 Plug, 30–32, 170, 389–390, 494–504, 516–518, 534
 Polymer dispersed liquid crystal (PDLC), 436
 Polymerase chain reaction (PCR), 140, 346–356, 479–484
 Ponderomotive force, 304, 311, 311*f*, 312*f*, 313
 PQRS model (Peykov-Quinn-Ralston-Sedev), 184–185, 203, 403
 Precursor film, 24–26, 26*f*, 27*f*, 65–66
 Primers, 346, 352–353, 482–483
 Proteins, 10*f*, 100–101, 211, 342, 360–362, 486

Q

Quencher, 357, 358*f*

R

Radio frequency (RF), 462, 466–467
 Rayleigh wave, 465–466
 Reorientation (plugs), 522
 Replication (DNA), 346
 Reynolds number, 235, 458, 473
 Room temperature ionic liquids (RTIL), 398, 398*f*, 415

S

Saturation, 179–193
 SAW-fluid interaction, 460–463, 468–469

Schwarz-Christoffel conformal mapping, 174–175, 210–211

Screen display, 422–427

Seebeck effect, 348

Semiconductor, 348, 462–463, 484

Sequence (DNA), 102, 346, 352

Shah and London friction factor, 502

Silanization, 145*f*, 460

Silicone oil, 37*f*, 93*f*, 342

Single nucleotide polymorphisms (SNP), 352

Stokes equation, 141, 468

Strain tensor, 463

Striation, 230–231, 284, 520–521, 520*f*

Surface acoustic waves (SAW), 459, 467*f*

Surface tension, 14–19, 38, 53–67

Surfactant, 17–19, 137–138

Switching frequency, 340–341, 341*f*

T

Taq-polymerase, 352–353

Task specific ionic liquids (TSIL), 399

Thermoelectric effect, 348

TNT, 409–410

Torkkeli’s equation, 217

Trapping of charges, 180–184

Trinitrotoluene (TNT), 409–410

Two-phase microflows, 5–6, 528

V

VIC (fluorophore), 353

Virtual fluidic tracks, 461*f*, 484

Virus, 346, 505

VM (Virtual Microwell), 371–378

Volatile organic solvent (VOS), 393–398

Volume of a droplet, 83–85, 87–89

Von Willebrand factor (protein), 486

W

Water microscope, 427–428

Weber number, 234–235, 525

Wenzel’s law, 109–110, 113–124

Wetting criteria, 246–248

Work of adhesion, 41–42

Work of cohesion, 42

Y

Young’s law, 38–41, 134, 170

Young–Dupré equation, 41–43

Z

Zisman plot, 64–66

Zisman’s criterion, 185